A FINITE PRESSURE ELEMENT APPROACH TO THE PLANING PROBLEM OF HIGH SPEED CRAFT

by

Tsz Kin Jimmy Tong, B.Sc

UNIVERSITY OF SOUTHAMPTON

FACULTY OF ENGINEERING AND APPLIED SCIENCE

Department of Ship Science

Ph.D. Thesis

(April, 1990)

Contents

UNIVERSITY OF SOUTHAMPTON

ABSTRACT

FACULTY OF ENGINEERING AND APPLIED SCIENCE
DEPARTMENT OF SHIP SCIENCE

Doctor of Philosophy

A FINITE PRESSURE ELEMENT APPROACH TO THE PLANING PROBLEM OF HIGH SPEED CRAFT

by Tsz Kin Jimmy Tong

A finite element method is presented for the steady motion of a craft planing over the surface of calm water. The fluid is assumed to be infinitely deep, inviscid, incompressible and without surface tension and the free surface is assumed to be of infinite extent. In addition, the angle of attack is assumed to be small and linearized potential flow theory is used. The method applies to the case of arbitrary Froude number and aspect ratio.

The presence of the craft is modelled by an unknown pressure distribution on its wetted bottom projected on the plane of the undisturbed free surface. This is represented by a finite element mesh consisting of a number of pressure elements, each of constant but different strength. The shape of the element can be arbitrary and therefore the theory can be applied to wetted planforms of any shape or configuration. The shape and extent of the wetted bottom is assumed to be known and the immersions along the transom are determined together with the pressures by satisfying the kinematic hull boundary condition at the centre of each element and the Kutta condition at a discrete number of points along the transom.

The finite element method has been applied to planing flat plate and prismatic hulls of constant deadrise angle. The derived lifts, centre of pressure locations and pressures have compared reasonably well with other experimental and theoretical results. An interpolating scheme for determining the operating trim angle and wetted length for a craft of specified loading condition and speed has also been developed.

The work also comprises a study of the hydrodynamics of planing craft under two conditions: firstly, when it is heeled at a small angle, and secondly, when it is yawed at a small angle. For the heel case, the theory predicts a decrease in roll stability when the craft is planing at high speed. The computed hydrodynamic force and moment derivatives have shown reasonably good agreement with the experiment data obtained by other authors. The behaviours of these hydrodynamic derivatives at high speed have also been investigated. For the yaw case, the theory predicts an interesting feature of the development of suctions under the outboard side of the hull at high planing speed. The theory also predicts a change in the direction of the induced roll moment which could well be directly related to the phenomena that some high speed crafts bank inwards during turning while others bank outwards.

Acknowledgements

The author would like to express his thanks to his Supervisor, Doctor J.F. Wellicome, for his encouragement and guidance throughout this work. The author would also like to acknowledge the encouragement of Professor G.J. Goodrich and the valuable advice of Mister P.A. Wilson on computational matters. Thanks are also due to the staff of the Ship Science Department for their help throughout this work.

I am grateful to my parents and especially to my wife, Vivien, for their endless support throughout the course of preparing this thesis.

Please note that the subscripts of the variables in the thesis may sometimes go from lower case to upper case due to typing inconsistencies - for example; Lw and Lw. However, both forms have the same meaning according to the Nomenclature.

Nomenclature

Alphabetic

A_R : Aspect ratio (B/L_W)

A_W : Wetted bottom area of planing surface

A_{Wu} : Wetted area under heeled up side of a planing hull

A_{Wd} : Wetted area under heeled down side of a planing hull

B : Transom wetted beam

B_u : Transom half beam (heeled up side)

B_d : Transom half beam (heeled down side)

C : Forward planing speed

C_{fy} : Sway force coefficient = $\dfrac{F_y}{{}^1/_2\rho g B^3 C_V^2}$

C_{fz} : Lift coefficient = $\dfrac{F_z}{{}^1/_2\rho g B^3 C_V^2}$

C_p : Bottom loading coefficient = $\dfrac{B\,L_k}{\nabla^{2/3}}$

C_{rm} : Roll moment coefficient = $\dfrac{M_r}{{}^1/_2\rho g B^4}$

C_V : Beam Froude number = $C/\sqrt{gB}$

C_{ym} : Yaw moment coefficient = $\dfrac{M_y}{{}^1/_2\rho g B^4}$

$f(x,y)$: Local hull displacement above transom level

$F_{a(x,y)}$: Free wave corner function at corner a

F_2 : Coefficient of sway force derivative = $\dfrac{1}{\Delta}\dfrac{\partial F_y}{\partial \phi}$

F_n : Froude number in general

F_y : Sway force

F_z : Lift force

$(F_z)_d$: Lift developed on heeled down side of the wetted bottom

$(F_z)_u$: Lift developed on heeled up side of the wetted bottom

g : Acceleration due to gravity

H : Predicted vertical locations across transom

$h(y)$: Unknown transom rise heights above undisturbed free surface

H^* : Mean transom vertical location

H_k : Immersion of transom at keel (deadrise surface)

H_{c2} : Immersion of transom at chine (heeled down side)

k : Wave number

k_o : Fundamental wave number = g/C^2

L^* : Non-dimensional distance of the longitudinal centre of gravity forward of the transom = $\frac{Lcg}{B}$

L_c : Wetted chine length for non-heeled constant deadrise surface

L_{c1} : Wetted chine length for heeled flat plate or heeled constant deadrise surface (up side)

L_{c2} : Wetted chine length for heeled flat plate or heeled constant deadrise surface (down side)

L_{cg} : Longitudinal centre of gravity forward of transom

L_{cL} : Longitudinal centre of lift forward of transom

L_{cLd} : Longitudinal centre of lift forward of transom (heeled down side of the wetted bottom)

L_{cLR} : Longitudinal centre of lateral resistance forward of transom

L_{cLu} : Longitudinal centre of lift forward of transom (heeled up side of the wetted bottom)

L_{cp} : Longitudinal centre of pressure forward of transom

$L_a(X,y)$: Local wave corner function at corner a

L_i : Immersed length for planing flat plate

L_{c2i} : Immersed chine length (heeled down side)

L_k : Wetted keel length for constant deadrise surface

L_{ki} : Immersed keel length (deadrise surface)

L_w : Mean wetted length for flat plate

: Mean wetted length for non-heeled constant deadrise surface $= \frac{(L_k+L_c)}{2}$

: Mean wetted length for heeled flat plate $= \frac{(L_{c1}+L_{c2})}{2}$

: Mean wetted length for heeled constant deadrise surface $= \frac{(2L_k+L_{c1}+L_{c2})}{4}$

M_1 : Coefficient of roll moment derivative with respect to drift angle $= \frac{1}{B\,\Delta}\,\frac{\partial M_r}{\partial \psi}$

M_2 : Coefficient of roll moment derivative with respect to heel angle $= \frac{1}{B\,\Delta}\,\frac{\partial M_r}{\partial \phi}$

M_r : Rolling moment about keel line

M_y : Yawing moment about transom

N_2 : Coefficient of yaw moment derivative with respect to heel angle $= \frac{1}{B\,\Delta}\,\frac{\partial M_y}{\partial \phi}$

N_F : Froude number based on wetted keel length $= C/\sqrt{gL_k}$

P : Pressure above atmospheric

P_o : Constant Pressure inside an element

$q(u,v,w)$: Fluid velocity vector

R : Rolling moment arm from keel line for heeled or drifted planing surface

τ_{m1} : Minimum trim angle required for the transom running beam to remain completely wetted at both sides of the hull

τ_{m2} : Minimun trim angle required for the transom running beam to remain completely wetted at the heeled down side of the hull

v : Sway velocity

W : Craft weight in Newtons

W^* : Non-dimensional craft weight $= \frac{W}{1/2 \rho g B^3}$

x, y, z : Cartesian Coordinates

$Z(x,y)$: Total hull displacement above undisturbed free surface

Greek

β : Deadrise angle

ϕ : Heel angle

θ : Wave angle

τ : Trim angle

ψ : Drift or yaw angle

ρ : Density of fluid

$\zeta_i(x,y)$, $\zeta(x,y)$: Free surface wave elevation

$\overline{\Phi}(x,y,z)$: Total velocity potential

$\phi_i(x,y,z)$, $\phi(x,y,z)$: Perturbation velocity potential

λ_{rp} : Average wetted length to beam ratio for deadrise surface in heel (used by Y.M.Jahangeer Ref.(66))

$$= \frac{2L_{c1} + L_k + L_{c2}}{4B}$$

∇ : Craft displacement volume (m^3)

Δ : Craft displacement in Newtons

CHAPTER (1) Introduction

1.1 General Background

When a surface craft moves at low speed through water, the weight of the craft is supported mainly by the hydrostatic forces. As the speed of the craft is increased so that the water surface separates smoothly from the trailing edge of the craft, the craft is said to be planing on the water surface. During planing motion, the lift is dominated by the hydrodynamic pressure generated on the wetted bottom of the craft.

Another important role played by the hydrodynamic pressure load developed during planing motion is its influence on the dynamic stability of the craft. There are two common types of instability problems associated with hard chine planing surface operating at high speed in calm water - the so called 'Chine Walking', which is a transverse instability resulting from a combination of rolling and yawing oscillations, and the combined longitudinal pitch and heave oscillation which is better known as 'Porpoising'. Although these two modes of instabilities frequently occur simultaneously, only the transverse instability will be considered in some details in this thesis. Thus, the roll, sway and yaw degree of freedoms are decoupled from the rest of the motions and the problem can be treated separately.

It is known from practical experience that a high speed craft can lose transverse and course keeping stabilities at high speed even though the static stability is adequate. The transverse dynamic stability of a craft can depend on a number of factors such as speed, displacement, hull geometry and the position of centre of gravity. The forces and torques generated by the propeller and rudder can also be significant especially during turning. When a planing craft is turning, it will roll, yaw and sway. Roll, yaw and sway are strongly coupled modes of motion. An introduction of heel angle results in net transverse loads which cause the craft to sway and yaw. Similarly, the asymmetric bottom pressures associated with sway and yaw motions will cause the craft to roll. Therefore, in order to carry out a thorough investigation into this dynamic problem, it would be necessary to take the roll, sway and yaw coupling into account.

1.2 Literature Review

Two of the earliest workers to study the hydrodynamics of two dimensional planing problem were Sretenskii (Ref.(1,2)) and Sedov (Ref.(3)). They used linearized potential flow theory and represented the pressure distributions under the surface of a planing plate by an infinite series. The first term of the series gave rise to a square root type of singularity at the leading edge which is well known in airfoil theory. The same problem was also tackled by Maruo (Ref.(4,5,6,7)). The experimental pressure results for planing flat plates presented in his 1959 paper were in good agreement with his theory, particularly at small trim angles and away from the pressure singularity at the leading edge. A similar approach to Sretenskii and Maruo was adopted by Squire (Ref.(8)) and the importance of satisfying the Kutta Condition at the trailing edge was outlined. In his solution, the transom rise height or the wetted length was treated as unknown and obtained as part of the solution together with the pressures, which satisfied the Kutta Condition at the trailing edge. Cumberbatch (Ref.(9)) solved the two dimensional problem using a high Froude number approximation. In his method, the kernel function of the integral equation was expanded into a series in inverse powers of Froude number and the solution was obtained by an iterative method. He also showed that an optimal shaped parabolic plate could greatly reduce the drag by eliminating the pressure singularity at the leading edge. More details of the above works were reviewed later by Wehausen and Laitone (Ref.(10)). Doctors (Ref.(11)) used a finite element method to solve the linear two dimensional planing problem at finite speed. In his method, the pressure distribution under the planing surface was represented by a number of equivalent pressure elements. In this way, the shape of the plate could be arbitrary. Several types of optimum forms based on maximizing the lift squared to drag ratio and on the elimination of the forward thrown splash jet were derived. These optimum forms were found to be similar to those obtained by Cumberbatch with the splash removed from the leading edge.

The non-linear planing problem in two dimensions has also been studied by a few authors with the restriction of zero gravitational

effect. Green (Ref.(12,13,14)) solved the two dimensional non-linear planing problem of a flat plate at infinite Froude number in both finite and infinite water depth using the method of conformal mapping. He showed explicitly that the solution obtained by neglecting the gravitational effect was not unique and the free surface slope approaches zero so slowly far away that there was no finite level asymptote. The anomalous behaviour of the flow at infinity in Green's solution was first treated satisfactory by Rispin (Ref.(15)) and Wu (Ref.(16)) using the method of matching asymptotic expansions. The flow problem was broken down into a 'near field' problem, which represents the flow close to the planing surface, and a 'far field' problem, which represents the free surface flow with waves, which could be solved individually and then matched. Other works related to this subject can be referred to those by Wu and Whitney (Ref.(17)) and Ting and Keller (Ref.(18)). They had also derived optimum shapes that resulted in a splash free condition.

The linearized three dimensional planing problem has been studied using potential flow theory but usually with some restrictions on aspect ratio and/or Froude number. Wagner (Ref.(19)) and Casling (Ref.(20)) solved the problem using a low aspect ratio assumption at infinite Froude number. Tulin (Ref.(21)) and Shuford (Ref.(22)) also tackled the problem of low aspect ratio planing. Maruo (Ref.(23)) solved the problem for both high and low aspect ratio delta planing surfaces. However, a high Froude number was required in his solution for the low aspect ratio planing surface and the method was not applicable to a rectangular planing planform. Shen (Ref.(24)) and Shen and Ogilive (Ref.(25)) tackled the problem with a high aspect ratio assumption. In the latter paper, non-linearity effect was also included for the case of infinite Froude number by extending the method of matching asymptotic expansions of Rispin (Ref.(15)) and Wu (Ref.(16)) into three dimensions. Wang and Rispin (Ref.(26)) extended Cumberbath's method (Ref.(9)) to three dimensions to solve the planing problem of rectangular plate with moderate aspect ratio at high Froude number. In their solution, the kernel function in the integral equation was expanded asymptotically for high Froude numbers, $Fr=C^2/gl$, up to Fr^{-2}. However, in the expansion, singularities were introduced at the tips of the plate due to

the chosen pressure form. Tuck (Ref.(27)) extended the works of Maruo (Ref.(23)) on low aspect ratio flat delta wing to finite Froude number. In his work, a cusped parabolic water plane shape with arbitrary section was considered and strong gravitational effects near the centre plane were demonstrated. Oertel (Ref.(28)) discussed the aspect of unknown wetted bottom area and its relation to the Kutta condition in some details. He considered the problem at an infinite Froude number and showed that the hull shape had to be determined as part of the solution once the wetted area was prescribed and the Kutta condition was satisfied. Doctors (Ref.(29)) extended his finite element method to solve three dimensional planing problem without any restriction on either aspect ratio or speed. In his solution, the weight and the longitudinal centre of gravity position of the craft were first prescribed, the wetted area, the transom rise height and the pressures were then determined by an iterative procedure based on the change in the trailing edge immersions with respect to the change in wetted lengths across the transom. The amount of wetted area predicted for the flat plates and the constant deadrise prismatic hulls were in good agreement with that derived from the Savitsky's empirical equations. Standing (Ref.(30)) and Huang and Wong (Ref.(31)) applied linearized potential flow theory to predict the free surface elevations induced by a constant pressure disturbance moving over a free surface. Their works was later extended by Wellicome and Jahangeer (Ref.(32)) to determine the pressures under planing surfaces using constant pressure rectangular elements. Various hull forms including flat plate, constant deadrise prismatic hulls and delta wing were considered. Two dimensional optimum forms similar to those obtained by Doctors (Ref.(11)) were also derived. His theory had also been applied to predict the amount of rolling moment induced by planing prismatic hulls and flat plate under heel condition, though the sway force and the yawing moment had not been considered.

There were a number of experimental results published. Some of the earliest experimental studies on planing surfaces were made by Baker (Ref.(33)), Sottorf (Ref.(34)), Shoemaker (Ref.((35)), Sambraus (Ref.(36)), Sedov (Ref.(37)) and Locke (Ref.(38)). Much experimental measurement and empirical analysis of planing phenomenon had been

conducted by the Davidson Laboratory of Stevens Institute of Technology (1947) under the sponsorship of the office of Naval Research U.S. Navy. The aim of these studies was to utilize existing planing data (including those obtained in Davidson Laboratory) and to establish empirical equations for the prediction of hydrodynamic performance of planing surfaces. In 1949, a summary report on these studies was published by Korvin-Kroukovsky and Savitsky (Ref.(39)). Later in 1954, a more extensive set of empirical equations was developed by Savitsky and Neidinger (Ref.(40)) which increased the range of applicability well beyond those in (Ref.(39)). These so called Savitsky's empirical equations, which apply mainly to planing flat plate and constant deadrise hulls, are frequently used for practical calculations owing to their simplicity. Other published experimental results include the works by Hadler (Ref.(41)), Kapryan and Boyd (Ref.(42)), Clement and Blount (Ref.(43)) and Savitsky (Ref.(44,45,46)).

It is known from practical experience that planing boats suffer from transverse instability when turning at high speed, even though the static stability is adequate. This behaviour can be explained in connection with the asymmetric hydrodynamic loads developed on the hull bottom as a result of roll, sway and yaw motions. This phenomenon had been studied by authors such as Du Cane (Ref.(47)), Lord (Ref.(48)) and Savitsky and Koelbel (Ref.(49)). Recently, particular attention has been paid to round bilge semi displacement hull forms which frequently encounter roll instability when operating at high speed. Marwood and Bailey (Ref.(50)) conducted model tests on a NPL round bilge series form fixed in sway and yaw. The model was allowed to roll freely and the relationship between roll angles and vertical centre of gravity positions were studied at various speeds. Suhrbier (Ref.(51)) also conducted similar experiments but paid particular attention to the effect of sway force on transverse stability.

Some researchers like Baba, Asai and Toki (Ref.(52)) and Mueller-Graf and Schmiechen (Ref.(53)) conducted captive model experiments to determine the hydrodynmaic coefficients of a round bilge hull form. The effects of rudder and spray strips on these coefficients had also been

investigated. Transverse stability criteria based on their experimental results and the manoeuvring equations of roll, sway and yaw degrees of freedom were derived. Other researchers like Millward (Ref.(54)) and Wakeling, Sproston and Millward (Ref.(55)) paid particular attention to the effect of hull form on the pressure distributions developed on the hull bottom. The pressure measurements on a round bilge form revealed that the instability problem was due to the negative pressure developed along the afterbody of the hull and was attributed to the unsatisfactory hull shape of the round bilge form for high speed.

The studies on the transverse dynamic stability of hard chine planing hull, particularly the constant deadrise prismatic hulls, have received little attention. Gill (Ref.(56)) determined the rolling moment on a prismatic hull when it is yawed relative to the flow. His theory, the so called 'Deadrise Effect', describes that the introduction of yaw angle is effectively to increase the trim angle on one side of the hull and to reduce it on the other. The rolling moment was calculated from the difference between the moments produced by the asymmetric lift loads developed on the two sides of the hull; the moment arms were taken to be a quarter of the beam from the keel. The empirical equations presented by Savitsky were employed for deriving this lift. Wellicome and Campbell (Ref.(57)) conducted model experiments similar to those of Mueller-Graf and Schmiechen to determine the hydrodynamic coefficients for a series of constant deadrise prismatic hulls. In their theory, however, all lateral forces were assumed to act at the longitudinal centre of gravity position of the craft so that no net yawing moment arises when the craft is under either heel or yaw condition. Simple transverse stability criteria were derived based on their experimental data and the coupled sway and roll manoeuvring equations.

1.3 Linearization of Planing Problem

The classical ship wave problem is a boundary value problem. The free surface boundary conditions for this problem are non-linear and lead to a complicated integral equation which is always difficult to solve. In order to simplify the problem, it is customary to linearize

the boundary conditions on the free surface. In order to achieve this, the disturbances to the fluid due to the motion of the ship are required to be small and the ship should be slender in the direction of its motion. The two most commonly known types of ship wave problems that can be linearized are the 'Thin Ship Problem' treated by Michell (Ref.(58)) and the 'Slender Ship Problem' treated by Vossers (Ref.(59)). The other type of ship wave problem that can be linearized is the 'Flat Ship Problem' in which the draught of the ship is much smaller than its length and width.

An important feature of planing motion is the development of a spray sheet thrown ahead and sideways of the planing surface. This gives rise to a region of highly non-linear flow near the spray root. Although the high speed planing hull form is a typical example of 'Flat Ship', the non-linear flow near the spray root region would make the small disturbances assumption of a linear theory invalid. Green's (Ref.(12, 13 and 14)) studies on the two dimensional non-linear flat plate planing at infinite Froude number in the absence of gravity has shown that at sufficiently small angle of attack (or trim angle), the thickness of the splash is proportional to the square of the angle of attack. Wagner (Ref.(19)) studied both the two and three dimensional planing at infinite Froude number with linearized free surface boundary conditions. In his solution, the governing equations were shown to be identical to those of the flows passing the lower surface of a thin airfoil with a square root type of pressure singularity at the leading edge. Wagner showed that linear planing theory can be adopted if the angle of attack is sufficiently small and that the same type of pressure singularity can be used to represent the splash at the leading edge and the configuration of the forward thrown splash jet can be ignored.

Throughout the work in this thesis, the angle of attack (or trim angle) is therefore assumed to be small so that the splash configuration can be ignored in the linearization of the free surface boundary conditions. In addition, the induced free surface elevations are also assumed to be small so that the linearized free surface boundary conditions can be applied on the mean free surface. The resulting

pressure distributions will therefore contain a square root type of singularity at the leading edge.

1.4 Present Work

The work in this thesis concerns a theoretical study of the steady motion of a craft planing over the surface of calm water. The water is assumed to be infinitely deep, inviscid, incompressible and free of surface tension. The free surface is assumed to extend to infinity and the flow is irrotational. The trim angle or the angle of attack is assumed to be small so that the splash configuration near the spray root can be ignored, and inviscid linearized potential flow theory is adopted.

The presence of the planing surface is modelled by an unknown pressure distribution on its wetted bottom projected on the plane of the undisturbed free surface. The projected wetted bottom is represented by an equivalent two dimensional finite element mesh which consists of a number of constant pressure elements, each of different strength. The elements derived in this thesis can be arbitrary in shape. In this way, both the shape of the wetted planform and the planing speed can be arbitrary, hence the restrictions of previous theories are avoided.

The solution to the problem consists of two parts. The first part of the solution is to evaluate the free surface wave patterns induced by these constant pressure elements. The theoretical derivation and numerical method involved will be discussed in detail in chapter two. The predicted wave patterns for various element shapes are to be compared with the results of other authors. The second part of the solution is to assemble these elements to form the projected wetted bottom of the craft. The unknown pressures and the unknown transom immersions are determined by satisfying the kinematic hull boundary condition at each element's centre and the Kutta condition at a discrete number of points along the transom. In the present method, the shape of the wetted planform and the planing speed are assumed to be known; the pressures and the immersions along the transom, hence the output hull shape, are determined as the solutions. More details of this method will

be discussed in chapter three.

The present finite element method will be applied particularly to study the hydrodynamics of a planing flat plate and constant deadrise prismatic surfaces, although the method can also be applied equally well to other forms such as twin-hull and warp surface. The predicted pressure distributions, lifts and longitudinal centre of pressure positions will be compared with the results obtained by other authors in chapter four and five. An interpolating procedure for determining the running wetted length and running trim angle for a craft of specified weight, longitudinal centre of gravity position and speed has also been developed.

Another main area of study in this thesis is the performance of planing craft under heel and drift (or yaw) conditions. The present theory has been applied to predict the pressure distributions, rolling moments, yawing moments and sway forces for planing craft under two conditions: firstly, when it is heeled at a small angle, and secondly, when it is yawed at a small angle. Again, flat plate and constant deadrise surfaces were considered, though only a planing flat plate has been studied in the later case. Based on these forces and moments results, an interpolating procedure to determine the hydrodynamic forces and moments derivatives for a particular craft's loading condition and speed has been developed. The predicted hydrodynamic forces and moments derivatives have been compared with the experimental measurements of Wellicome and Campbell (Ref.(57)) with reasonable agreement. These forces and moments derivatives are essential for the analysis of transverse stability of planing craft in turn. More details of these studies will be discussed in chapter six to chapter eight. Although it is a known fact that high speed planing craft can lose stability during turning, little work has been done to understand this particular phenomenon. It is hoped that the present studies can provide a better insight into the transverse stability of planing craft turning at high speed.

CHAPTER (2) Velocity Potential and Free Surface Elevation induced by a Constant Pressure Element in an Uniform Free Stream

2.1 The Constant Pressure Polygon

In this chapter, we will derive an expression for the velocity potential, $\underline{\Phi}(x,y,z)$, and the free surface elevation, $\xi(x,y)$, induced by a constant pressure element in an uniform stream of speed, C. The fluid is assumed to be inviscid, incompressible, infinitely deep and without surface tension. The free surface is assumed to be of infinite extent, the flow is assumed to be irrotational and linearized potential flow theory is adopted. The constant pressure element is assumed to cover an arbitrary area on the undisturbed free surface with pressure equal to P_o inside that area and zero elsewhere. The x-y-z Cartesian coordination system employed is shown in fig.(2.1), with the x-y plane lying on the undisturbed free surface, the x-axis pointing in a direction opposite to the flow and the z-axis pointing vertical upward in a direction opposite to the gravitational acceleration.

The arbitrary area of constant pressure on the free surface is then approximated by an equivalent constant pressure polygon, as shown in fig.(2.2a). The total velocity potential, $\underline{\Phi}(x,y,z)$, at a point, (x,y,z), inside the fluid due to this pressure disturbance can be considered as the sum of a perturbation potential, $\phi(x,y,z)$, and the disturbance due to the uniform free stream, thus,

$$\underline{\Phi}(x,y,z) = \phi(x,y,z) - Cx \qquad (2.1.1).$$

In order to further simplify the problem, it is more convenient to breakdown this constant pressure polygon into a number of constant pressure trapezia, each of pressure $\pm P_o$ extending downstream from the side of the polygon to $x=-\infty$, as shown in fig.(2.2b). Such a constant pressure trapezium is shown in fig.(2.2c). For an anticlockwise nodal numbering configuration, such as the one shown in fig.(2.2a), the pressure of the i^{th} trapezium is $+P_o$ if $(y_{i+1}-y_i)\geq 0$ and is $-P_o$ if $(y_{i+1}-$

$y_i)<0$. The perturbation velocity potential, $\phi(x,y,z)$, and the free surface elevation, $\mathcal{E}(x,y)$, due to the constant pressure polygon are then mathematically equivalent to the sums of the disturbances induced by these individual constant pressure trapezia. Thus,

$$\phi(x,y,z) = \sum_{i=1}^{n} \phi_i(x,y,z) \qquad (2.1.2)$$

and

$$\mathcal{E}(x,y) = \sum_{i=1}^{n} \mathcal{E}_i(x,y) \qquad (2.1.3),$$

where n is the number of sides of the constant pressure polygon, $\phi_i(x,y,z)$ and $\mathcal{E}_i(x,y)$ are the perturbation velocity potential and the free surface elevation induced by the i^{th} constant pressure trapezium of pressure $\pm P_o$. An expression for $\phi_i(x,y,z)$ and $\mathcal{E}_i(x,y)$ will be derived in the following section.

2.2 Theoretical Derivation of the Velocity Potential and the Free Surface Elevation induced by a Constant Pressure Trapezium

In this section, an expression is derived for the free surface elevation, $\mathcal{E}_i(x,y)$, and the velocity potential, $\phi_i(x,y,z)$, induced by a constant pressure trapezium of pressure $+P_o$ in an uniform stream of velocity, C. The geometry of the trapezium is shown in fig.(2.2c) with its four corners defined by the points (x_a,y_a), (x_b,y_b), $(-\infty,y_b)$ and $(-\infty,y_a)$. The ordinate, y_b, is assumed to be greater than y_a so that the area enclosed is positively defined. Making the usual assumptions, the total velocity potential, $\underline{\Phi}_i(x,y,z)$, induced by the constant pressure trapezium can be written as:

$$\underline{\Phi}_i(x,y,z) = \phi_i(x,y,z) - Cx \qquad (2.2.1),$$

where $\phi_i(x,y,z)$ is the perturbation potential and C is the uniform stream speed. The fluid velocity, q(u,v,w), at a point, (x,y,z), inside the fluid is then given by

$$u = \frac{\partial \phi_i(x,y,z)}{\partial x} - C \ , \quad v = \frac{\partial \phi_i(x,y,z)}{\partial y} \quad \text{and} \quad w = \frac{\partial \phi_i(x,y,z)}{\partial z} \qquad (2.2.2).$$

Inside the fluid, the velocity potential, $\underline{\Phi}_i(x,y,z)$, has to satisfy the Laplace equation:

$$\frac{\partial^2 \phi_i}{\partial x^2} + \frac{\partial^2 \phi_i}{\partial y^2} + \frac{\partial^2 \phi_i}{\partial z^2} = 0 \qquad (2.2.3).$$

On the free surface, $z=\varepsilon_i(x,y)$, one must also satisfy the non-linear free surface kinematic condition:

$$\frac{\partial \phi_i}{\partial z} = \frac{\partial \varepsilon_i}{\partial x}\left[\frac{\partial \phi_i}{\partial x} - C\right] + \frac{\partial \varepsilon_i}{\partial y}\frac{\partial \phi_i}{\partial y} \qquad (2.2.4)$$

on $z=\varepsilon_i(x,y)$

and the non linear free surface pressure condition derived from the Bernoulli equation:

$$\frac{P(x,y)}{\rho} + \frac{1}{2}\left[\left\{\frac{\partial \phi_i}{\partial x} - C\right\}^2 + \frac{\partial \phi_i}{\partial y}^2 + \frac{\partial \phi_i}{\partial z}^2\right] + g\,\varepsilon_i = \frac{1}{2}C^2 \qquad (2.2.5),$$

on $z=\varepsilon_i(x,y)$

where P(x,y) is the pressure on the free surface (above atmospheric pressure), g is the acceleration due to gravity and ρ is the density of the fluid.

Assuming that the induced disturbances ϕ_i and ε_i are both small so that the products of their derivatives, i.e. $(\partial\phi_i/\partial x)(\partial\varepsilon_i/\partial x)$ etc, are also small and can be neglected in the formulation of the free surface

boundary conditions, conditions (2.2.4) and (2.2.5) can be linearized by considering only the first order terms in ϕ_i and ε_i and can be applied on the undisturbed free surface, z=0, rather than on the actual free surface, $z= \varepsilon_i(x,y)$. It follows that the linearized free surface kinematic condition is

$$\frac{\partial \phi_i(x,y)}{\partial z} + C \frac{\partial \varepsilon_i(x,y)}{\partial x} = 0 \qquad \text{on } z=0 \qquad (2.2.6)$$

and the linearized free surface pressure condition is

$$\frac{P(x,y)}{\rho} - C \frac{\partial \phi_i(x,y)}{\partial x} + g\, \varepsilon_i(x,y) = 0 \qquad \text{on } z=0 \qquad (2.2.7).$$

A combined free surface boundary condition can then be obtained by eliminating $\varepsilon_i(x,y)$ from conditions (2.2.6) and (2.2.7), thus,

$$\frac{\partial^2 \phi_i(x,y)}{\partial x^2} + k_o \frac{\partial \phi_i(x,y)}{\partial z} = \frac{1}{\rho C} \frac{\partial P(x,y)}{\partial x} \qquad \text{on } z=0 \qquad (2.2.8),$$

where k_o is the fundamental wave number, g/C^2. For the case of infinitely deep water, the velocity potential is also required to satisfy an infinite depth condition,

$$\frac{\partial \phi_i}{\partial z} = 0 \qquad \text{as } z \to -\infty \qquad (2.2.9),$$

which ensures that the disturbance die away as $z \to -\infty$. In addition, it must also satisfy the radiation condition,

$$\vec{\nabla} \phi_i = 0 \qquad \text{as } x \to +\infty \qquad (2.2.10),$$

which ensures that gravity waves only exist downstream of the pressure.

The solution in $\phi_i(x,y,z)$ which satisfies the above conditions can be obtained by a double Fourier transform in the x-y domain. The details in deriving this velocity potential is given in appendix A and may also be found in references such as Wehausen and Laitone (Ref.(10), pg. 598). The solution is

$$\phi_i(x,y,z) =$$

$$\int_{-\frac{\pi}{2}}^{\frac{\pi}{2}} \frac{2\,\mathrm{Sec}(\theta)}{\rho C}\,d\theta \int_0^{\infty} \frac{k\,e^{kz}}{(k-k_1)} \{\mathrm{Re}[P(k,\theta)]\,\mathrm{Sin}(kw) - \mathrm{Img}[P(k,\theta)]\,\mathrm{Cos}(kw)\}\,dk$$

$$- \int_{-\frac{\pi}{2}}^{\frac{\pi}{2}} \frac{2\pi\,\mathrm{Sec}(\theta)k_1\,e^{k_1 z}}{\rho C} \{\mathrm{Re}[P(k_1,\theta)]\,\mathrm{Cos}(k_1 w) + \mathrm{Img}[P(k_1,\theta)\,\mathrm{Sin}(k_1 w)]\}\,d\theta \qquad (2.2.11),$$

where θ denotes the wave angle, k denotes the wave number,

$$k_1 = k_o\,\mathrm{Sec}^2(\theta) \qquad (2.2.12)$$

and

$$w = x\,\mathrm{Cos}(\theta) + y\,\mathrm{Sin}(\theta) \qquad (2.2.13).$$

The complex function, $P(k,\theta)$, is the Fourier transform of the free surface pressure function, $P(x,y)$, given by the following Fourier inversion formula:

$$P(k,\theta) = \mathrm{Re}[P(k,\theta)] + \mathrm{Img}[P(k,\theta)]\,i$$

$$= \frac{1}{4\pi^2} \int_S P(x,y)\, e^{ikw}\, dxdy \qquad (2.2.14),$$

where s denotes the free surface. The wave elevation, $\varepsilon_i(x,y)$, at a field point, (x,y), on the undisturbed free surface, z=0, can be obtained by substituting the above solution in $\phi_i(x,y,z)$ into the free surface pressure condition (2.2.7). This gives

$$\varepsilon_i(x,y) = \int_{-\pi/2}^{\pi/2} \int_0^{\infty} \frac{2k^2}{\rho g(k-k_1)} \{Re[P(k,\theta)]\, Cos(kw) + Img[P(k,\theta)]\, Sin(kw)\}\, dkd\theta$$

$$+ \int_{-\pi/2}^{\pi/2} \frac{2\pi}{\rho g} k_1^2 \{Re[P(k_1,\theta)]\, Sin(k_1 w) - Img[P(k_1,\theta)]\, Cos(k_1 w)\}\, d\theta$$

$$- \delta_i \qquad (2.2.15),$$

where $$\delta_i = \frac{P(x,y)}{\rho g} \qquad (2.2.16)$$

is the hydrostatic free surface wave elevation.

The velocity potential, $\phi_i(x,y,z)$, due to the present constant pressure trapezium of pressure + P_o can be obtained by substituting the following Fourier transform (see appendix A) into expression (2.2.11).

$$Re[P(k,\theta)] = \frac{-P_o}{4\pi^2} \frac{(Y_b - Y_a)}{(W_b - W_a)} \left[\frac{Cos(kW_b) - Cos(kW_a)}{k^2\, Cos(\theta)} \right] \qquad (2.2.17)$$

and $$\mathrm{Img}[P(k,\theta)] = \frac{-P_o}{4\pi^2}\ \frac{(Y_b-Y_a)}{(W_b-W_a)}\left[\frac{\mathrm{Sin}(kW_b)\ -\ \mathrm{Sin}(kW_a)}{k^2\ \mathrm{Cos}(\theta)}\right] \qquad (2.2.18),$$

where $$W_a = (x_a\mathrm{Cos}(\theta) + y_a\mathrm{Sin}(\theta)) \qquad (2.2.19)$$

and $$W_b = (x_b\mathrm{Cos}(\theta) + y_b\mathrm{Sin}(\theta)) \qquad (2.2.20).$$

Leading to

$$\phi_i(x,y,z) =$$

$$P_o \int_{-\frac{\pi}{2}}^{\frac{\pi}{2}} \frac{(y_b-y_a)\ \mathrm{Sec}^2(\theta)}{(W_b-W_a)\ 2\pi^2\rho C}\, d\theta \int_0^{\infty} e^{kz}\left[\frac{\mathrm{Sin}(k(w-Wa))-\ \mathrm{Sin}(k(w-W_b))}{k\ (k-k_1)}\right] dk$$

$$- P_o \int_{-\frac{\pi}{2}}^{\frac{\pi}{2}} \frac{(y_b-y_a)\ \mathrm{Sec}^2(\theta)\ e^{k_1 z}}{2\pi\rho C\ k_1\ (W_b-W_a)}\ \{\mathrm{Cos}(k_1(w-W_a)) - \mathrm{Cos}(k_1(w-W_b))\}\, d\theta$$

(2.2.21).

Similarly, substituting expressions (2.2.17) and (2.2.18) into expression (2.2.15) yields the free surface elevation,

$$\varepsilon_i(x,y) =$$

$$P_o \int_{-\frac{\pi}{2}}^{\frac{\pi}{2}} \frac{(y_b-y_a)\ \mathrm{Sec}(\theta)}{(W_b-W_a)\ 2\pi^2\rho\ g}\, d\theta \int_0^{\infty} \frac{\mathrm{Cos}(k(w-W_a)) - \mathrm{Cos}(k(w-W_b))}{(k-k_1)}\ dk$$

$$+ \quad P_o \int_{-\frac{\pi}{2}}^{\frac{\pi}{2}} \frac{(y_b - y_a)\,\mathrm{Sec}(\theta)}{2\pi\rho g\,(W_b - W_a)} \{\mathrm{Sin}(k_1(w - W_a) - \mathrm{Sin}(k_1(w - W_b)\}\, d\theta \quad - \quad \delta_i \qquad (2.2.22),$$

where $\delta_i = \frac{P_o}{\rho g}$ for a field point (x,y) inside the trapezium

$\delta_i = 0$ for a field point (x,y) outside the trapezium

$\delta_i = \frac{P_o}{2\rho g}$ for a field point (x,y) on the boundary of the trapezium.

As shown in appendix B, the inner k integrals in the above expression can be transformed by means of a suitable substitution into:

$$\int_0^\infty \frac{\mathrm{Cos}(k(w - W_a)}{(k - k_1)}\, dk \quad = \quad g(|\lambda_a|) - \mathrm{Sin}(|\lambda_a|)\,\pi \qquad (2.2.23),$$

where $\lambda_a = k_1\,(w - W_a)$ (2.2.24)

and g(Z) is the auxiliary cosine integral function:

$$g(Z) \quad = \quad \int_0^\infty \frac{\mathrm{Cos}(u)}{(u+Z)}\, du \qquad (2.2.25),$$

which is given in the 'Handbook of Mathematical Functions' by Abramowitz and stegun (Ref.(60) pg.232). Replacing the inner k integral in expression (2.2.22) by the form derived above gives

$$\varepsilon_i(x,y) = \frac{P_o}{\rho g} \left[\{La(x,y) + Fa(x,y)\} - \{Lb(x,y) + Fb(x,y)\} - \delta_i \right] \qquad (2.2.26),$$

where δ_i is now the non-dimensional hydrostatic free surface elevation:

$\delta_i = 1$ for a field point (x,y) inside the trapezium,

$\delta_i = 0$ for a field point (x,y) outside the trapezium

and $\delta_i = \frac{1}{2}$ for a field point (x,y) on the boundary of the trapezium,

$La(x,y)$ and $Lb(x,y)$ are the non-dimensional local wave corner functions given by:

$$La(x,y) = \int_{-H_M}^{H_M} \frac{(y_b - y_a)\,\mathrm{Sec}(\theta)\, g(|\lambda_a|)}{2\pi^2\,(W_b - W_a)}\, d\theta$$

and

$$Lb(x,y) = \int_{-H_N}^{H_N} \frac{(y_b - y_a)\,\mathrm{Sec}(\theta)\, g(|\lambda_b|)}{2\pi^2\,(W_b - W_a)}\, d\theta \qquad (2.2.27),$$

$Fa(x,y)$ and $Fb(x,y)$ are the non-dimensional free wave corner functions given by:

$$Fa(x,y) = [\mathrm{Sgn}(\lambda_a)-1] \int_{-H_N}^{H_N} \frac{(y_b - y_a)\,\mathrm{Sec}(\theta)\,\mathrm{Sin}(|\lambda_a|)}{2\pi\,(W_b - W_a)}\, d\theta$$

$$\text{and} \quad F_b(x,y) = [\mathrm{Sgn}(\lambda_b)-1] \int_{-\frac{\pi}{2}}^{\frac{\pi}{2}} \frac{(y_b - y_a)\,\mathrm{Sec}(\theta)\,\mathrm{Sin}(|\lambda_b|)}{2\pi\,(W_b - W_a)}\, d\theta \qquad (2.2.28)$$

$$\text{with} \qquad \mathrm{Sgn}(u) = +1 \qquad \text{if} \quad u > 0$$

$$\text{and} \qquad \mathrm{Sgn}(u) = -1 \qquad \text{if} \quad u < 0 \qquad (2.2.29)$$

2.3 The Corner Wave Functions

The terms $L_a(x,y)$ and $L_b(x,y)$ in equation (2.2.26) can be identified as the non-dimensional local wave corner functions, which are the near field disturbance generated by the pressure trapezium. The terms $F_a(x,y)$ and $F_b(x,y)$ are the non-dimensional free wave corner functions which contribute to the wave system progressing downstream. Since the free wave sine term in $F_a(x,y)$ and $F_b(x,y)$ oscillates rapidly without attenuation as $\theta \to \pm \pi/2$, it is more convenient to make the transformation, $t=\mathrm{Tan}(\theta)$, in the evaluation of these integrals. The functions, $g(|\lambda_a|)$ and $g(|\lambda_b|)$, are not oscillatory and decay through zero as $\theta \to \pm\frac{\pi}{2}$, therefore, this transformation is not essential for the evaluation of the local wave corner functions. However, there are some advantages in replacing the arguments in the sine and cosine functions by algebraic ones. Thus, following Huang and Wong (Ref.(31)) and Standing (Ref.(30)), the local and free wave corner functions are transformed by using $t=\mathrm{Tan}(\theta)$. Also, following the discussion in appendix G about the integrating limits of the free wave integral (2.2.28), the local and free wave corner functions can be expressed as:

$$L_a(x,y) = \frac{1}{2\pi^2} \int_{-\infty}^{+\infty} \frac{g(|\lambda_a|)}{(t - T_o)}\, dt \qquad (2.3.1)$$

and $$F_a(x,y) = -\frac{1}{\pi} \int_{-\infty}^{T_a} \frac{\mathrm{Sin}(|\lambda_a|)}{(t - T_o)}\, dt \qquad \text{for } (y-y_a)>0 \qquad (2.3.2)$$

or $$F_a(x,y) = -\frac{1}{\pi} \int_{T_a}^{+\infty} \frac{\mathrm{Sin}(|\lambda_a|)}{(t - T_o)}\, dt \qquad \text{for } (y-y_a)<0 \qquad (2.3.3)$$

or $$F_a(x,y) = -\frac{1}{\pi} \int_{-\infty}^{+\infty} \frac{\mathrm{Sin}(|\lambda_a|)}{(t - T_o)}\, dt \qquad \text{for } (y-y_a)=0 \text{ and } (x-x_a)<0 \qquad (2.3.4),$$

where $$\lambda_a = \{(x-x_a)+(y-y_a)t\} \sqrt{(1 + t^2)}\, k_o \qquad (2.3.5),$$

$$T_a = \frac{-(x - x_a)}{(y - y_a)} \qquad (2.3.6)$$

and $$T_o = \frac{-(x_b - x_a)}{(y_b - y_a)} \qquad (2.3.7).$$

For $(y-y_a)=0$ and $(x-x_a)>0$, the free wave corner function, $F_a(x,y)$, is equal to zero.

The difference in integrating the limits between the above free wave integrals, (2.3.2), (2.3.3) and (2.3.4), are inconvenient for programing. It was decided to make the transformation t=-t in the integrals (2.3.1) and (2.3.3) when $(y-y_a)<0$, though this transformation

is not essential for the evaluation of $L_a(x,y)$. Following this transformation, which is only applied when $(y-y_a)<0$, the final forms of the local and free wave corner functions are

$$L_a(x,y) = \frac{M_a}{2\pi^2} \int_{-\infty}^{+\infty} \frac{g(|\lambda_a|)}{(t - T_o)} \, dt \qquad (2.3.8)$$

and

$$F_a(x,y) = -\frac{M_a}{\pi} \int_{-\infty}^{T_a} \frac{\mathrm{Sin}(|\lambda_a|)}{(t - T_o)} \, dt \qquad (2.3.9),$$

where now

$$T_o = -M_a \frac{(x_b - x_a)}{(y_b - y_a)} \qquad (2.3.10),$$

$$T_a = \frac{-(x - x_a)}{|(y - y_a)|} \qquad \text{for } |y-y_a|>0 \qquad (2.3.11),$$

$$T_a = +\infty \qquad \text{for } (y-y_a)=0 \text{ and } (x-x_a)<0 \qquad (2.3.12),$$

$$\lambda_a = \{(x-x_a)+|(y-y_a)|t\} \sqrt{(1 + t^2)}\, k_o \qquad (2.3.13)$$

and

$$M_a = 1 \qquad \text{for} \qquad (y-y_a)\geq 0 \qquad (2.3.14)$$

$$M_a = -1 \qquad \text{for} \qquad (y-y_a)<0 \qquad (2.3.15).$$

Note that, mathematically, the transformation t=-t maps the original pressure trapezium, T, and the field point, p(x,y), to a mirror image

trapezium, T', and a mirror image field point, $p'(x,-y)$, about the reference x-axis, as shown in fig.(2.3). If the field point, $p(x,y)$, is located between the two sides of the trapezium, i.e. $(y-y_a)>0$ and $(y-y_b)<0$, the transformation $t=-t$ is only applied for evaluating the corner wave functions $L_b(x,y)$ and $F_b(x,y)$. For the case of (y_b-y_a) is zero, the trapezoid area shrinks to a line without any wavemaking. In this case, the wave elevation is taken to be zero. If the field point $p(x,y)$ is located at the corner (x_a,y_a) of the trapezium, the local wave integral in (2.3.8) is undefined. One should also note that both the local wave corner function, $L_a(x,y)$, in (2.3.8) and the free wave corner function, $F_a(x,y)$, in (2.3.9) are independent of the length of the forward facing segment of the pressure trapezium, i.e. the distance between the points (x_a,y_a) and (x_b,y_b), but dependent only on the angle, $\mathrm{Tan}^{-1}(T_o)$, it makes with the reference y-axis.

2.4 Numerical Evaluation of the Local Wave Corner Function

In this section, we deal with the numerical method for evaluating the local wave corner function, $L_a(x,y)$, in expression (2.3.8). The auxiliary cosine integral function, $g(|\lambda_a|)$, in the expression can be calculated quickly by using a rational polynomial approximation for $+\infty > |\lambda_a| > 1.0$, or a series expansion for $1.0 > |\lambda_a| > 0$. Both approximations can be found in the 'Handbook of Mathematical Functions' by Abramowitz and Stegun (Ref.(60) pg.232) and have also been enclosed in appendix C. The denominator inside the integral varies slowly, and although $g(|\lambda_a|) \to 0$ as $|\lambda_a| \to \pm\infty$, the decay may be slow and the infinite range often cannot be truncated. The infinite integral is then split up into two infinite ranges, $-\infty < t < T_1$ and $T_2 < t < +\infty$, and a finite range, $T_1 < t < T_2$, which contains the points of singularity. The number of singularities present in the finite integrating range varies with the position of the field point, (x,y), with respect to the trapezium. They can be categorized into the following three cases and will be considered separately.

Case (i) $|T_a-T_o|>0$ and $|y-y_a|>0$

The infinite integral is split up into three segments, $-\infty<t<T_1$, $T_1<t<T_2$, and $T_2<t<+\infty$, where

$$T_1 = (T_a+T_o)/2 - |T_a-T_o|/2 - 1.0$$

and

$$T_2 = (T_a+T_o)/2 + |T_a-T_o|/2 + 1.0$$

for $|T_a-T_o|>3.0$ and $|T_a-T_o|<2.0$, or

$$T_1 = (T_a+T_o)/2 - |T_a-T_o|$$

and

$$T_2 = (T_a+T_o)/2 + |T_a-T_o|$$

for $2.0<|T_a-T_o|<3.0$. There are two points of singularity in the finite integrating range. There is a logarithmic singularity at $t=T_a$, as $|\lambda_a|$ tends to zero and

$$g(|\lambda_a|) \rightarrow -\gamma - \mathrm{Log}(|\lambda_a|) \qquad (2.4.1)$$

(see equations (C.2) and (C.7) of appendix C), where γ is the Euler constant. The other singularity occurs at the pole, $t=T_o$, when the denominator of the integrand, $(t-T_o)$, tends to zero (for the definitions of T_o, T_a and $|\lambda_a|$, see expressions (2.3.8), (2.3.9) and (2.3.10)). These two singularities can be removed by rewriting the integral into the following form:

$$\int_{T_1}^{T_2} \frac{g(|\lambda_a|)}{(t-T_o)}\,dt = \int_{T_1}^{T_2} \frac{g(|\lambda_a|) + \mathrm{Log}(|t-T_a|) - H(T_o)}{(t-T_o)}\,dt$$

$$- \int_{T_1}^{T_2} \frac{\mathrm{Log}(|t-T_a|)}{(t-T_o)}\,dt + H(T_o)\,\mathrm{Log}\frac{|T_2-T_o|}{|T_1-T_o|} \qquad (2.4.2),$$

where

$$H(t) = g(|\lambda_a|) + \mathrm{Log}(|t-T_a|) \qquad (2.4.3).$$

As shown in appendix D, the compensating logarithmic integral in equation (2.4.2) can be expressed as:

$$\int_{T_1}^{T_2} \frac{\mathrm{Log}(|t-T_a|)}{(t-T_o)}\,dt = \int_{T_1-T_a}^{T_2-T_a} \frac{\mathrm{Log}(|u|)}{u-(T_o-T_a)}\,dt$$

$$= \mathrm{Ilg}[-(T_2-T_a)/(T_o-T_a)] - \mathrm{Ilg}[-(T_1-T_a)/(T_o-T_a)]$$

$$+ \mathrm{Log}(|T_o-T_a|)\,\mathrm{Log}\left|\frac{(T_2-T_a)-(T_o-T_a)}{(T_1-T_a)-(T_o-T_a)}\right| \qquad (2.4.4),$$

where the function Ilg(x) is defined as:

$$\mathrm{Ilg}(x) = \int_0^x \frac{\mathrm{Log}(|u|)}{(1+u)}\,du \qquad (2.4.5),$$

which can be evaluated using the series approximations given in appendix E. It should be noticed that although the function, $g(|\lambda_a|) + \mathrm{Log}(|t-T_a|) - H(T_o)$, is continuous at $t=T_a$, its slope is discontinuous. Therefore, the integrating process stops and restarts at the point, $t=T_a$, to minimize errors. At $t=T_a$, the value of the integrand inside the

first integral on the right hand side of equation (2.4.2) can be obtained by considering its limiting value as $t \to T_a$, thus,

$$\lim_{t \to T_a} \frac{g(|\lambda_a|) + \mathrm{Log}(|t-T_a|) - H(T_o)}{(t - T_o)}$$

$$= \frac{-\gamma - \mathrm{Log}[k_o\sqrt{(1+T_a^2)}\,|y-y_a|] - H(T_o)}{(T_a - T_o)} \qquad (2.4.6).$$

Similarly, the limiting value of the integrand at $t=T_o$ is

$$\lim_{t \to T_o} \frac{g(|\lambda_a|) + \mathrm{Log}(|t-T_a|) - H(T_o)}{(t - T_o)}$$

$$= [\, g(|\lambda_a|)'\, |\lambda_a|']_{t=T_o} + \frac{M_o}{(T_o-T_a)} \qquad (2.4.7),$$

where $g(u)'$ is the derivative of the function, $g(u)$, with respect to u and $|\lambda_a|'$ is the derivative of the function, $|\lambda_a|$, with respect to t. The derivative, $g(u)'$, for positive real values of u can be evaluated by a series approximation for $1>u>0$ or by a rational polynomial approximation for $+\infty>u>1$. Both approximations are given in appendix F. The derivative of $|\lambda_a|$ with respect to t at $t=T_o$ is

$$|\lambda_a|'_{t=T_o} = k_o \frac{T_o\,[\,|(x-x_a)+|(y-y_a)|T_o|\,]}{(1 + T_o^2)^{1/2}} + M_o\sqrt{(1+T_o^2)}\,|y-y_a| \qquad (2.4.8),$$

where $M_o = 1$ if $T_o > T_a$

and $M_o = -1$ if $T_o < T_a$.

Over the infinity ranges, $-\infty < t < T_1$ and $T_2 < t < +\infty$, the integrals are transformed using $1/v = (t-T_a)$. It follows that

$$\int_{-\infty}^{T_1} + \int_{T_2}^{+\infty} \frac{g(|\lambda_a|)}{(t-T_o)}\,dt = \int_{(T_1-T_a)^{-1}}^{0} \frac{g(|\lambda_a|)}{(1-(T_o-T_a)v)v}\,dv + \int_{0}^{(T_1-T_a)^{-1}} \frac{g(|\lambda_a|)}{(1-(T_o-T_a)v)v}\,dv \qquad (2.4.9),$$

where $$\lambda_a = \frac{k_o|y-y_a|\sqrt{v^2+(1+T_a v)^2}}{v^2} \qquad (2.4.10).$$

There is no problem in evaluating the above integrals since there is no singularity inside the integrating ranges. The integrating process stops and restarts at v=0, though this is not essential since the integrand is well behaved. At $v = 0$, as $|\lambda_a| \to +\infty$ and $g(|\lambda_a|) \to 1/|\lambda_a|^2$, the value of the integrand is given by:

$$\lim_{v\to 0} \frac{g(|\lambda_a|)}{(1-(T_o-T_a)v)v} = \lim_{v\to 0} \frac{1}{|\lambda_a|^2(1-(T_o-T_a)v)v} = 0 \qquad (2.4.11).$$

Significant contributions to the local wave corner function, $L_a(x,y)$, are expected to come from the regions around the logarithmic singularity, $t=T_a$, and the pole, $t=T_o$. For the case of $|T_a-T_o|>3.0$, the finite integrating range may be large, therefore the integral over the range, $[(T_a+T_o)/2-|T_a-T_o|/2+1.0] > t > [(T_a+T_o)/2+|T_a-T_o|/2-1.0]$, is also evaluated using the transformation, $1/v=(t-T_a)$. Note that the integral over this range does not contain any singularity.

Case (ii) $(T_a-T_o)=0$ and $|y-y_a|>0$

For a field point, (x,y), lying on the line passing through the two corners, (x_a,y_a) and (x_b,y_b), of trapezium, the logarithmic singularity and the pole singularity occur simultaneously at $t=T_a$. In this case, we have $T_o=T_a$ and there is only one singularity in the range of integration. The infinite integral is split up into three segments, $-\infty < t < T_1$, $T_1 < t < T_2$ and $T_2 < t < +\infty$, where

$$T_1 = T_a - 1.0$$

and

$$T_2 = T_a + 1.0$$

The singularity occurs in the finite integrating range, $T_1 < t < T_2$, when both $|\lambda_a|$ and $(t-T_o)$ tend to zero simultaneously at $t=T_a$ can also be removed by rewriting the integral in the form of (2.4.2) with the value of $H(T_o)$ replaced by $H(T_a)$, where

$$H(T_a) = \lim_{t \to T_a} [g(|\lambda_a|) + \mathrm{Log}(|t-T_a|)]$$

$$= -\gamma - \mathrm{Log}\left[k_o|y-y_a|\sqrt{1+T_a^2} \right] \qquad (2.4.12).$$

The limiting value of the integrand inside the first integral on the right hand side of equation (2.4.2) at $t=T_a$ is now given by:

$$\lim_{t \to T_a} \frac{g(|\lambda_a|) + \mathrm{Log}(|t-T_a|) - H(T_a)}{(t - T_a)} = \frac{-T_a}{1 + T_a^2} \qquad (2.4.13).$$

Note that the integrands inside the second and third compensating integrals of equation (2.4.2) are now odd function of t about the point $t=T_a$. It follows that by taking the integrating ranges symmetrically about the point, $t=T_a$, the contributions of these two integrals are both

zero. As before, the integration process stops and restarts at $t=T_a$ to minimize errors. Over the infinity ranges, $-\infty<t<T_1$ and $T_2<t<+\infty$, the integrals are evaluated by using the transformation, $1/v=(t-T_a)$. Note that the value of (T_a-T_o) in (2.4.9) is now zero. Again, there is no problem in evaluating these integrals since there is no singularity in the integrating ranges and the integrating process stops and restarts at $v=0$. At $v=0$, the limiting value of the integrand is zero.

Case (iii) $y-y_a=0$ and $|x-x_a|>0$

For a field point, (x,y), lying on the side of the trapezium, $(y-y_a)=0$, the logarithmic singularity does not exist since the function, $|\lambda_a|$, is greater than zero for all values of t. However, the singularity at the pole, $t=T_o$, still exists. As before, the infinite integral is split up into three segments, $-\infty<t<T_1$, $T_1<t<T_2$ and $T_2<t<+\infty$, with

$$T_1 = T_o - 1.0$$

and

$$T_2 = T_o + 1.0$$

The singularity in the finite range, $T_1<t<T_2$, is removed by Monacella's method (Ref.(61)). Thus, the integral is made regular by writing

$$\int_{T_1}^{T_2} \frac{g(|\lambda_a|)}{(t-T_o)}\,dt = \int_{T_1}^{T_2} \frac{g(|\lambda_a|)-H(T_o)}{(t-T_o)}\,dt + H(T_o)\,\mathrm{Log}\frac{|T_2-T_o|}{|T_1-T_o|} \qquad (2.4.14),$$

where now

$$H(t) = g(|\lambda_a|) \qquad (2.4.15)$$

and

$$\lambda_a = (x-x_a)\sqrt{(1+t^2)}\,k_o \qquad (2.4.16).$$

At $t=T_o$, the limiting value of the integrand inside the first integral on the right hand side of equation (2.4.14) is given by:

$$\lim_{t \to T_o} \frac{g(|\lambda_a|) - H(T_o)}{(t-T_o)} = [g(|\lambda_a|)' \; |\lambda_a|']_{t=T_o} \qquad (2.4.17),$$

where $g(u)'$ is the derivative of $g(u)$ with respect to u, which can be computed by the methods given in appendix F, and $|\lambda_a|'$ is the derivative of $|\lambda_a|$ with respect to t. Note that the value of $(y-y_a)$ in the expression (2.4.8) for $|\lambda_a|'$ is now zero. Also note that if the integrating range is taken to be symmetrical about the point, $t=T_o$, the contribution of the second term on the right hand side of equation (2.4.14) is zero. There is no singularity in the infinity ranges, $-\infty < t < T_1$ and $T_2 < t < +\infty$, the integrals are transformed using $1/v=(t-T_o)$ into

$$\int_{-\infty}^{T_1} + \int_{T_2}^{\infty} \frac{g(|\lambda_a|)}{(t-T_o)}\, dt = \int_{(T_1-T_o)^{-1}}^{0} \frac{g(|\lambda_a|)}{v}\, dv + \int_{0}^{(T_2-T_o)^{-1}} \frac{g(|\lambda_a|)}{v}\, dv \qquad (2.4.18),$$

where $$\lambda_a = \frac{k_o |x-x_a| \sqrt{(v^2+(1+T_o\, v)^2)}}{v} \qquad (2.4.19).$$

The integration process stops and restarts at $v=0$. At $v=0$, the value of the integrand is zero. Note that if both $(x-x_a)$ and $(y-y_a)$ are equal to zero, the local wave corner function, $L_a(x,y)$, is undefined.

2.5 Numerical Evaluation of the Free Wave Corner Function

Recapping from section (2.3), equations (2.3.9) to (2.3.15), the free wave corner function, $F_a(x,y)$, is

$$F_a(x,y) = -\frac{M_a}{\pi}\int_{-\infty}^{T_a}\frac{\sin(|\lambda_a|)}{(t-T_o)}\,dt \qquad (2.5.1),$$

where
$$T_a = \frac{-(x-x_a)}{|(y-y_a)|} \qquad \text{for } |y-y_a|>0 \qquad (2.5.2)$$

$$T_o = -M_a\,\frac{(x_b-x_a)}{(y_b-y_a)} \qquad (2.5.3),$$

$$\lambda_a = \{(x-x_a)+|(y-y_a)|t\}\sqrt{(1+t^2)}\,k_o \qquad (2.5.4),$$

and
$$M_a = 1 \qquad \text{for} \qquad (y-y_a)\geq 0$$
$$M_a = -1 \qquad \text{for} \qquad (y-y_a)<0 \qquad (2.5.5).$$

As explained in appendix G, the upper limit of the free wave integral in (2.5.1) is equal to $+\infty$ when $(y-y_a)=0$ and $(x-x_a)<0$, while for $(y-y_a)=0$ and $(x-x_a)>0$ the free wave integral is equal to zero. Thus, the free wave corner integral, $F_a(x,y)$, at a point upstream from the corner (x_a,y_a) along the line $(y-y_a)=0$ is zero. However, one should notice that the free wave corner integral, $F_b(x,y)$, along the line $(y-y_a)=0$ forward of the corner (x_a,y_a) is not equal to zero. Also note that, for the case of $(y-y_a)=0$ and $(x-x_a)<0$, M_a is taken as +1 in the present program though the same numerical result can also be obtained by taking M_a equal to -1.

The difficulties in evaluating the free wave corner function are caused by a slow decay of the integrand combined with the highly oscillatory behaviour resulting from the rapid rate of change of the phase function $|\lambda_a|$ as $t\to\pm\infty$. Significant contributions to the integral are expected to come from the regions around $t=T_a$, the pole $t=T_o$, and

the points of stationary phase where the slope of the phase function, $|\lambda_a|$, changes sign. Thus, the points of stationary phase are given by the real roots of the following quadratic equation:

$$\frac{d\lambda_a}{dt} = k_o \left[\frac{2|y-y_a|t^2 + (x-x_a)t + |y-y_a|}{(1+t^2)} \right] = 0 \qquad (2.5.6).$$

The roots of the above equation for $|y-y_a|>0$ are

$$t = 1/4 \{ T_a \pm \sqrt{(T_a^2 - 8)} \} \qquad (2.5.7).$$

There are two points of stationary phase inside the integrating range, $-\infty < t < T_a$, if $T_a > 2(2)^{1/2}$, one if $T_a = 2(2)^{1/2}$ and none otherwise. For $T_a = 2(2)^{1/2}$, the point of stationary phase is located at $t = 1/(2)^{1/2}$ which is at a distance $3/(2)^{1/2}$ from the upper limit of the integral, T_a, in descending values of t. Standing (Ref.(30)) pointed out that when T_a is just smaller than $2(2)^{1/2}$, the influence of the complex stationary phase points can still be felt around $t=T_a/4$, and this region may contribute significantly to the integral. Therefore, the integrating range starting at $t=T_a$ should include the region around $t=T_a/4$ when T_a is just smaller than $2(2)^{1/2}$. Note that for the case of $(y-y_a)=0$ and $(x-x_a)<0$, the point of stationary phase is located at t=0 and the integrating range is from $t=-\infty$ to $t=+\infty$.

Case (i) $|T_a-T_o|>0$ and $|y-y_a|>0$

For the case where $|T_a-T_o|>0$ and $|y-y_a|>0$, there is a pole at $t=T_o$, if $T_a>T_o$ and none if $T_a<T_o$. The integrating range is divided into two segments, $-\infty < t < T_1$ and $T_1 < t < T_a$. The latter is arranged to include the pole at $t=T_o$ if $T_a>T_o$. The point $t=T_1$ is chosen to be at least two complete wave cycles from the point $t=T_a-2.5$ if $T_a<T_o$, or from the point $t=T_o-2.5$ if $T_a>T_o$, in descending values of t and located at a maximum or minimum of the function, $\mathrm{Sin}(|\lambda_a|)$, where $\mathrm{Cos}(|\lambda_a|)=0$. The point, $t=T_a-$

2.5 or $t=T_o-2.5$, is chosen on the ground that the influence of the complex stationary phase points around the region $t=T_a/4$ will be included in the integrating range when T_a is just smaller than $2(2)^{1/2}$. The singularity at the pole, $t=T_o$, if present in the range, $T_1<t<T_a$, is removed by Monacella's method (Ref.(61)). The integral is made regular by writing

$$\int_{T_1}^{T_a} \frac{\mathrm{Sin}(|\lambda_a|)}{(t-T_o)}\,dt = \int_{T_1}^{T_a} \frac{\mathrm{Sin}(|\lambda_a|)-H(T_o)}{(t-T_o)}\,dt + H(T_o)\,\mathrm{Log}\left|\frac{T_a-T_o}{T_1-T_o}\right| \qquad (2.5.8),$$

where
$$H(t) = \mathrm{Sin}(|\lambda_a|) \qquad (2.5.9).$$

As before, the value of the integrand in the first integral on the right hand side of equation (2.5.8) at $t=T_o$ can be obtained by considering its limiting value as $t\to T_o$. Thus,

$$\lim_{t\to T_o} \frac{\mathrm{Sin}(|\lambda_a|)-H(T_o)}{(t-T_o)} = [\,\mathrm{Cos}(|\lambda_a|)\,|\lambda_a|'\,]_{t=T_o} \qquad (2.5.10),$$

where $|\lambda_a|'$ is the derivative of the function $|\lambda_a|$ with respect to t given in expression (2.4.8).

The integral over the infinite range, $-\infty<t<T_1$, is truncated using the method proposed by Huang and Wong (Ref.(31)). The infinite range is truncated after a few cycles at a maximum or minimum of the function $\mathrm{Sin}(|\lambda_a|)$. The resulting integral is roughly a 'mean' value and further extension of the range results in oscillations about this mean level. Suppose that $|\lambda_a|$ varies monotonically with t and $(t-T_o)$ has the same sign for $t<T_1$. The infinite range can be rewritten as:

$$\int_{-\infty}^{T_1} \frac{\mathrm{Sin}(|\lambda_a|)}{(t - T_o)}\,dt = \sum_{k=1}^{+\infty} \int_{T_{k+1}}^{T_k} \frac{\mathrm{Sin}(|\lambda_a|)}{(t - T_o)}\,dt \qquad (2.5.11),$$

where the points T_k and T_{k+1} $(T_k > T_{k+1})$ are chosen to be at successive half cycle apart of the function $\mathrm{Sin}(|\lambda_a|)$ in descending values of t, and located at a maximum or a minimum of $\mathrm{Sin}(|\lambda_a|)$, where $\mathrm{Cos}(|\lambda_a|)=0$. The contributions to the integral from successive half cycles can be regarded as terms in an alternating series which are normally of decreasing magnitude and the series has the property that the difference between its exact sum and its partial sum is not greater than the first neglected term. Thus, the error in truncating the integral at $t=T_n$ can be estimated by the value of the integral over the next successive half cycle. The integrating process therefore starts at $t=T_a$, integrating through descending values of t to the point $t=T_1$, then it starts to estimate the error in truncating the infinite range at $t=T_1$ by integrating over the next successive half cycle. The integration process stops when the estimated error is less than 1.0E-5. The program then checks whether the points of stationary phase are included in the integrating range. If not, the integrating process starts again at the points of stationary phase, integrates through descending and ascending values of t in both directions for at least two complete wave cycles in each direction to a maximum or minimum of $\mathrm{Sin}(|\lambda_a|)$. The truncating process is then repeated in both directions. The integrating range is checked in each stage throughout the above process to ensure that no part of the range is covered twice.

Case (ii) $(T_a-T_o)=0$ and $|y-y_a|>0$

For the case where $T_a=T_o$ and $|y-y_a|>0$, the pole is located at the upper limit of the integral, $t=T_a$. However, the integrand itself is not singular at $t=T_a$ since both $|\lambda_a|$ and $(t-T_a)$ tend to zero as t tends to T_a. The limiting value of the integrand as t approaches T_a from t less than T_a is

$$\lim_{t\to T_a} \frac{\sin(|\lambda_a|)}{(t-T_a)} = -k_o\sqrt{(1+T_a^2)}\,|y-y_a| \qquad (2.5.12).$$

Note that the integrand has a jump at the point $t=T_a$, where its value is negative when t is just less than T_a and is positive when t is just greater than T_a. As in case (i), the integral is divided into two segments, $-\infty<t<T_1$ and $T_1<t<T_a$, where the point $t=T_1$ is chosen to be at least two complete wave cycles to the negative t direction from the point $t=T_a-2.5$ and is located at a maximum or minimum of $\sin(|\lambda_a|)$. There is no problem in evaluating these integrals as there is no singularity present in both integrating ranges. The methods of truncating the infinite range, $-\infty<t<T_1$, and the integrations around the stationary phase points are the same as those in case (i).

Case (iii) $(y-y_a)=0$ and $|x-x_a|>0$

For the case where $y-y_a=0$ and $|x-x_a|>0$, the upper limit of the integration is $+\infty$. The integral is then divided into three segments, $-\infty<t<T_1$, $T_1<t<T_2$ and $T_2<t<+\infty$. The points, T_2 and T_1, are chosen to be at least two complete wave cycles of the function, $\sin|\lambda_a|$, from the points, $t=T_o\pm2.5$, and are located at a maximum or minimum of $\sin(|\lambda_a|)$. The singularity at $t=T_o$ presents in the range, $T_1<t<T_2$, is removed by Monacella's method (Ref.(61)) (see expression (2.5.8)) and the point itself is stepped over symmetrically to minimize errors. The truncations of the infinite ranges, $-\infty<t<T_1$ and $T_2<t<+\infty$, are proceed in both directions from the points, T_1 and T_2. The truncating process about stationary phase point at t=0 is then followed, if this region has not yet been covered by the above integrations.

2.6 Some Computational Results for the Free Surface Elevation

In order to validate the present computing program with respect to the evaluation of the free surface wave pattern generated by a constant pressure element in an uniform stream, longitudinal and transverse wave profiles induced by elements of various shapes were computed and

compared with the numerical results published by Standing (Ref.(30)), Huang and Wong (Ref.(31)) and Everest and Hogben (Ref.(63)). The computed wave profiles are presented in a non-dimensional form, $\rho gz/P_o$, where z is the free surface elevation, ρ is the density of the fluid, g is the acceleration due to gravity and P_o is the pressure inside the element.

Fig.(2.5a), fig.(2.5b) and fig.(2.5c) show the longitudinal wave profiles along the centre line, y=0, of a non-drifted rectangular element (geometry shown in fig.(2.4a)) of aspect ratio, B/L, of 10.0, 1.0 and 4.0, at a Froude number, $Fn=C/(gL)^{1/2}$, of 0.57, where B is the element's width, L is the element's length and C is the uniform stream speed. It can be seen that the profiles obtained by the present computational method are in excellent agreement with the results obtained by Standing (Ref.(30)). For the high aspect ratio rectangle of B/L=10.0, the present profile also reproduces Lamb's (Ref.(62)) two dimensional result closely with the wave length of the downstream wave equal to $2\pi Fn^2$ L. The accuracy of the present computations is indicated by the degree of smoothness of the curves and in particular, the way the waves die away upstream of the elements. Note that for the case of B/L=0.4 in fig.(2.5c), there is a region of ripples developed downstream from the element. These ripples are a genuine feature of the free wave system, which has also appeared in the computational results obtained by Standing (Ref.(30)), and are not due to numerical inaccuracies of the present computations. Fig.(2.5d) shows a three dimensional plot of the wave pattern produced by the same rectangular element of B/L=0.4 at Fn=0.57. Since the wave pattern is symmetric about the element's centre line, y=0, only the results for positive values of y are shown in the figure. It can be seen clearly from this plot that the ripples displayed in fig.(2.5c) are part of the diverging wave systems which originate from the corners of the rectangle. The formation of these ripples, however, may be due to the absence of viscous and surface tension effects in the present linearized theory. More details about these corner wave systems will be discussed in section 3.6.

Fig.(2.6) shows the non-dimensional transverse wave profiles along the lateral centre line, x=0, along the forward face, x=0.5L, and along

the rearward face, x=-0.5L, of a non-drifted rectangular element of aspect ratio of 0.4, at a higher Froude number of 2.12. Again, the present profiles are in exact agreement with those obtained by Standing (Ref.(30)). Good agreement also exists between the present computational results and those from Huang and Wong (Ref.(31)). However, in Huang and Wong's solution, there are some oscillations in the bow profile, along x=0.5L, near the corner of the element. These oscillations may indicate that there are some numerical instability problems in their solution around the element's corner. No such oscillations were found either in the present computations or in Standing's results. The transverse wave profile at a distance x=-L downstream from the centre of the same element is shown in fig.(2.7a). The present results confirm the ripples developed around the element's side, y=0.2L, in Standing's solutions. Similar sort of ripples were also observed in the transverse wave profile further downstream at a distance x=-2L from the element's centre, as shown in fig.(2.7b). Again, these ripples appear around the element's side are a genuine feature of the present solutions and are not due to numerical inaccuracies. It can be seen from fig.(2.5d) that they are also part of the diverging wave systems produced by the pressure element although the two Froude numbers are not the same. The reason for the formation of these ripples will be discussed further in section (8.2). Note that these ripples are roughly antisymmetric about the element's side, y=0.2L.

Fig(2.8a) and fig.(2.8b) show the wave profiles around the periphery of a rectangular element of aspect ratio of 2/3, at a drift angle of 30° (geometry shown in fig.(2.4b)) and at a Froude number of 0.6. Again, the present results are in exact agreement with those obtained by Standing (Ref.(30)). Generally good agreement also exists between the present profiles and the free wave profiles obtained by Everest and Hogben (Ref.(63)) for the same rectangle in a channel of finite width. Note that the present wave profiles along the forward facing edges, AD and AB, have different mean levels from those obtained by Everest and Hogben. These differences may due to the contribution of the local wave terms, which have been neglected in Everest and Hogben's solutions. However, a further computation of the profiles along AD and AB excluding

the local wave terms has only produced a slightly better agreement between the two results.

The final set of comparisons are for the longitudinal wave profiles along y=0, y=0.24D and y=0.42D of a circular element of diameter D. As shown in fig.(2.4c), the circle was represented by a 12-sided polygon and two Froude numbers, $Fn=C/(gD)^{1/2}$, of 0.4 and 0.5 were considered. The profiles obtained by the present computational method together with those obtained by Standing (Ref.(30)) are shown in fig.(2.9a,b,c) and fig.(2.10a,b,c). Again, excellent agreement has been obtained between the two results.

The generally good agreements between the present computational results and those obtained by other authors confirm the validity of the present computing program used in the evaluation of the free surface elevations induced by constant pressure elements in an uniform stream. The application of these elements to the determination of the pressure distribution under a planing surface will be discussed in the following chapter.

CHAPTER (3) The Application of Constant Pressure Elements to Planing Problem

3.1 Formulation of the Problem

In this chapter, the constant pressure elements derived in the preceding chapter will be applied to determine the pressures under the wetted bottom of a planing craft. We will consider the steady state motion of a craft gliding at a constant speed, C, over the surface of calm water. The trim angle or the angle between the wetted surface and the undisturbed free surface is assumed to be small so that the splash configuration at the leading edge can be ignored and linearized potential flow theory can be adopted.

When a craft is planing over a water surface, the wetted bottom of the craft is divided into two regions. A sketch of the typical wetted bottom of a planing prismatic surface is shown in fig.(5.1). The area forward of the spray root line (stagnation line) is known as the spray area and the area behind the spray root line is the pressure area. The pressure in the spray area is nearly atmospheric, therefore it only contributes to the total drag and does not carry any portion of pressure load. The pressure area is the load carrying area of the planing bottom. The 'wetted bottom area' used in the present computations refer to this load carrying area of the wetted bottom and does not include the forward thrown spray sheet.

The x-y-z Cartesian coordinate system adopted is the same as that in chapter two. The motion is made steady by fixing the frame of reference in space and imposing an uniform stream of velocity, C, to the negative x-direction. The presence of the planing surface is modelled by an unknown pressure distribution on its wetted bottom projected on the plane of the undisturbed free surface. Making the usual assumptions of irrotational linearized potential flow, the flow field generated by these unknown pressures can be represented by a total velocity potential, $\Phi(x,y,z)$, given by a perturbation velocity potential, $\phi(x,y,z)$, and the imposed uniform free stream of velocity, C. Thus,

$$\underline{\Phi}(x,y,z) = \phi(x,y,z) - Cx \qquad (3.1.1)$$

and the corresponding fluid velocity vector, q(u,v,w), at the point (x,y,z) inside the fluid domain is given by:

$$q(u,v,w) = \tilde{\nabla} \left(\phi(x,y,z) - Cx \right) \qquad (3.1.2).$$

By means of discretization, the unknown continuous pressure distribution on the projected wetted bottom of the planing surface can be replaced by an equivalent finite element mesh consisting of a number of constant pressure elements, each of different strength. Typical finite element meshes representing the projected wetted bottom of a planing flat plate and a planing prismatic surface are shown in fig.(4.2) and fig.(5.2). It has been shown in chapter two that the perturbation velocity potential, $\phi_i(x,y,z)$, induced by the i^{th} element of constant pressure, P_i, which satisfied the Laplace equation (2.2.3), the linearized free surface kinematic and pressure conditions (2.2.6) and (2.2.7), the infinite depth condition (2.2.9) and the radiation condition (2.2.10), can be expressed in the form of

$$\phi_i(x,y,z) = P_i \, \overline{\phi_i}(x,y,z) \qquad (3.1.3),$$

where $\overline{\phi_i}(x,y,z)$ denotes the perturbation velocity potential induced by the i^{th} element of unit pressure. From the linearized free surface pressure condition (2.2.6), the free surface elevation induced by the i^{th} element, $\mathcal{E}_i(x,y)$, is

$$\mathcal{E}_i(x,y) = P_i \, \overline{\mathcal{E}_i}(x,y) \qquad (3.1.4),$$

where $$\overline{\hat{\varepsilon}_i}(x,y) = \left[\frac{c}{g} \frac{\partial \overline{\phi_i}}{\partial x} - \delta_i \right]_{z=0} \qquad (3.1.5)$$

and $\delta_i = 1/\rho g$ for a field point (x,y) inside the element

$\delta_i = 0$ for a field point (x,y) outside the element

$\delta_i = 1/2\rho g$ for a field point (x,y) on the boundary of the element.

If the projected wetted bottom of the planing surface is represented by a number of n constant pressure elements, the total velocity potential, $\underline{\Phi}(x,y,z)$, induced by the discretized pressure distribution at a point (x,y,z) inside the fluid domain is

$$\underline{\Phi}(x,y,z) = \sum_{i=1}^{n} P_i \, \overline{\phi_i}(x,y,z) - Cx \qquad (3.1.6).$$

Similarly, the free surface elevation, $\mathcal{E}(x,y)$, at a point (x,y) on the free surface due to the discretized pressure distribution is

$$\mathcal{E}(x,y) = \sum_{i=1}^{n} P_i \, \overline{\mathcal{E}_i}(x,y) \qquad (3.1.7).$$

Inside the fluid domain, the total velocity potential, $\underline{\Phi}(x,y,z)$, is required to satisfy the Laplace equation, thus

$$\sum_{i=1}^{n} \left[\frac{\partial^2 \overline{\phi_i}}{\partial x^2} + \frac{\partial^2 \overline{\phi_i}}{\partial y^2} + \frac{\partial^2 \overline{\phi_i}}{\partial z^2} \right] P_i = 0 \qquad (3.1.8).$$

Assuming that the fluid disturbance generated by the planing motion and the deformation of the free surface are both small, the linearized free surface pressure condition applied on the undisturbed free surface, z=0, is

$$\left[\sum_{i=1}^{n} \frac{C}{g} \frac{\partial \overline{\phi_i(x,y)}}{\partial x} P_i \right] - \frac{P(x,y)}{g\rho} = \sum_{i=1}^{n} P_i \overline{\mathcal{E}_i}(x,y) = \mathcal{E}(x,y) \qquad (3.1.9)$$

on z=0

and the linearized free surface kinematic condition applied on z=0 is

$$\sum_{i=1}^{n} \frac{\partial \overline{\phi_i(x,y)}}{\partial z} P_i = - C \sum_{i=1}^{n} \frac{\partial \overline{\mathcal{E}_i(x,y)}}{\partial x} P_i = -C \frac{\partial \mathcal{E}(x,y)}{\partial x} \qquad (3.1.10),$$

on z=0

where P(x,y) is the pressure on the free surface. It is clear that P(x,y) is equal to zero, i.e. atmospheric pressure, on the part of the free surface outside the projected planing wetted bottom. Inside the projected wetted bottom, P(x,y) is the unknown pressure distribution represented by the n unknown pressure strengths (P_1 to P_n). $\mathcal{E}(x,y)$ and $\partial\mathcal{E}(x,y)/\partial x$ denote the free surface elevations and free surface slopes, which are equal to the hull displacements and hull slopes on the part of the free surface covered by projected planing wetted bottom. In addition, the velocity potential, $\underline{\Phi}(x,y,z)$, is also required to satisfy the infinite depth condition:

$$\sum_{i=1}^{n} \frac{\partial \overline{\phi_i}}{\partial z} P_i = 0 \qquad \text{as } z \to -\infty \qquad (3.1.11)$$

and the radiation condition:

$$\vec{\nabla} \sum_{i=1}^{n} \overline{\phi_i} P_i = 0 \qquad \text{as } x \to +\infty \qquad (3.1.12),$$

which assures that no gravity wave will propagate upstream.

Since the form of the velocity potentials, $P_i\overline{\phi_i}$ (i=1 to n), of the n elements is chosen in such a way that each potential satisfies the Laplace equation, the infinite depth condition and the radiation condition, conditions (3.1.8), (3.1.11) and (3.1.12) will be satisfied by any arbitrary pressure distribution (P_1 to P_n). Either the linearized free surface pressure condition (3.1.9) or the free surface kinematic condition (3.1.10) can be used to set up the rigid hull boundary condition under the planing bottom for solving the unknown pressures. In addition, it is also required to satisfy a Kutta condition at the trailing edge of the planing surface in order to ensure that the flow separates smoothly from the transom. It should be noticed that the pressure solution obtained from either rigid hull boundary condition will satisfy both free surface conditions (3.1.9) and (3.1.10), since both the linearized free surface pressure and kinematic conditions have been satisfied in deriving the basic velocity potential, $P_i\ \overline{\phi_i}$, and the corresponding free surface elevation, $P_i\ \overline{\zeta_i}$. Both methods of solution will be considered in the following section.

3.2 The Hull Boundary Condition

The total displacement, Z(x,y), of a planing hull above the undisturbed free surface can be expressed as the sum of the local hull displacement above the transom level, f(x,y), and the rise height along the transom above the level of the undisturbed free surface, h(y). Thus,

$$Z(x,y) = f(x,y) + h(y) \qquad (3.2.1),$$

where the distance, x, is measured forward from the transom and the distance, y, is measured from the centre line of the projected wetted bottom. Since the shape of the projected wetted bottom is assumed to be known in the present computational method, the transom rise heights, h(y), have to be treated as unknowns and determined as part of the solution. If the projected wetted bottom is divided into **m** buttock strips (as shown in fig.(4.2) for m=5 and in fig.(5.2) for m=4), this will introduce an extra **m** number of unknown rise heights, one at the trailing edge of each buttock. Thus, the known quantities are the local hull displacement function, f(x,y), the speed, C, and the shape and extent of the projected wetted bottom and the solutions required to be determined are the **n** unknown pressures (P_1 to P_n) and the **m** unknown trailing edge rise heights (h_1 to h_m).

As mentioned in section (3.1), there are two ways to set up the rigid hull boundary condition under the wetted bottom for determining these unknowns. The rigid hull boundary condition can be derived either by equating the free surface slopes to the hull slopes using the linearized free surface kinematic condition (3.1.10), or by equating the free surface elevations to the hull displacements using the linearized free surface pressure condition (3.1.9).

First, we will consider the hull boundary condition derived from the free surface kinematic condition. This hull boundary condition requires that

$$\frac{1}{C}\,\frac{\partial\phi(x,y)}{\partial z} = \frac{-\partial Z(x,y)}{\partial x} = -\frac{\partial f(x,y)}{\partial x} \qquad \text{on } z=0 \qquad (3.2.2a)$$

to be satisfied at the field points, (x,y), on the part of the free surface covered by the projected wetted bottom. By applying the discretized form of condition (3.2.2a) to the control points of the **n** elements, we have at the control point of the j^{th} element,

$$\frac{1}{C}\sum_{i=1}^{n}\frac{\partial\overline{\phi_i}(x_j,y_j)}{\partial z}P_i = -\frac{\partial f(x_j,y_j)}{\partial x} \qquad \text{on } z=0 \qquad (3.2.2b),$$

$$\text{for } j = 1 \text{ to } n$$

where (x_j,y_j) denotes the coordinates of the control point inside the j^{th} element. These provided a number of n linear simultaneous equations for solving the n unknown pressures. However, it can be seen that equations (3.2.2b) do not involve the determination of the unknown trailing edge rise heights (h_1 to h_m). The extra m equations required to determine these unknown trailing edge rise heights can be derived from the Kutta condition, which states that the flow should be separated smoothly from the transom edge of the planing bottom. In order to maintain the continuity of the flow from the planing bottom to the part of the free surface of atmospheric pressure, the rise heights along the trailing edge must equal to the free surface elevations induced by the pressure distribution there. Thus, by applying the linearized free surface pressure condition (3.1.9) to the points lying just outside the trailing edge of the m buttock strips where the pressures are atmospheric, we have at each such points,

$$h_k = \sum_{i=1}^{n}\frac{C}{g}\frac{\partial\overline{\phi_i}(x_k,y_k)}{\partial x}P_i \qquad \text{on } z=0 \qquad (3.2.3),$$

$$\text{for } k= 1 \text{ to } m$$

where m is the total number of buttock strips, (x_k,y_k) is the coordinates of the chosen point lying just outside the trailing edge of the k^{th} buttock strip and (P_1 to P_n) are the pressure solution determined from the system of linear simultaneous equations (3.2.2b). The locations of the points, (x_k,y_k), with respect to the projected wetted bottom are shown in fig.(4.2) and fig.(5.2), where the k^{th} buttock is denoted by B_k in the figures. The total hull displacement along the k^{th} buttock strip at a distance, x, from the transom is then given by the sum of h_k and $f(x,y_k)$. It should be noted that the above method of solution involves the evaluation of two sets of integrals,

$\partial\overline{\phi_i}/\partial z$ for solving the n unknown pressures and $\partial\overline{\phi_i}/\partial x$ for determining the m unknown trailing rise heights.

An alternative method of solution is to set up the rigid hull boundary condition under the planing bottom using the linearized free surface pressure condition (3.1.9). This approach is preferred to the one discussed above since it only involves the evaluation of one set of integrals, $\partial\overline{\phi_i}/\partial x$ or $\overline{\varepsilon_i}$, and the unknown trailing edge rise heights are determined as part of the solution together with the unknown pressures. To satisfy this rigid hull boundary condition, the total hull displacement at a field point, (x,y), on the part of the free surface covered by the projected wetted bottom must equal to the free surface elevation induced by the unknown pressures there. Thus, on this part of the free surface, we have

$$\frac{c}{g}\frac{\partial\phi(x,y)}{\partial x} - \frac{P(x,y)}{\rho g} = f(x,y) + h(y) \qquad \text{on } z=0 \qquad (3.2.4a).$$

By applying the discretized form of (3.2.4a) to the control points of the n elements, we then have at the control point of the j^{th} element,

$$\left[\sum_{i=1}^{n} \frac{c}{g}\frac{\partial\overline{\phi_i}(x_j,y_j)}{\partial x} P_i\right] - \frac{P_j}{\rho g} = \sum_{i=1}^{n} P_i\,\overline{\varepsilon_i}(x_j,y_j) = f(x_j,y_j) + h_k$$

$$\text{on } z=0 \quad \text{for } j=1 \text{ to } n \qquad (3.2.4b),$$

where (x_j,y_j) is the coordinates of the control point inside the j^{th} element and h_k is the trailing edge rise height of the k^{th} buttock strip containing the j^{th} element (see fig.(4.2) and fig.(5.2)). Condition (3.2.4b) only provides n linear simultaneous equations. The extra m equations required are obtained by satisfying the Kutta condition at the trailing edge of each individual buttock strips, which eventually leads to the m simultaneous linear equations given in (3.2.3). It should be

noted that, now, the pressures (P_1 to P_n) in (3.2.3) are unknowns and have to be determined together with the unknown transom rise heights (h_1 to h_m) by solving the **m+n** linear simultaneous equations given in (3.2.3) and (3.2.4b). Once again, the author would like to point out that although only the linearized free surface pressure boundary condition has been satisfied explicitly in setting up the above **m+n** linear simultaneous equations, the linearized free surface kinematic boundary condition will be satisfied implicitly since the chosen form of the basic velocity potentials, $P_i\ \overline{\phi_i}$, and the basic free surface elevations, $P_i\ \overline{\zeta_i}$, individually satisfy both linearized free surface boundary conditions.

3.3 The Kutta Condition

It has already been mentioned in the previous section that the present method of solution requires the shape of the projected wetted bottom to be prescribed, as well as the local hull displacement above the transom level, f(x,y), and the planing speed, C. Therefore, an unique pressure solution can only be obtained if the trailing edge rise heights, h(y), are also treated as unknowns and determined as part of the solution of the problem. This aspect of non-uniqueness can clearly be seen by considering the set of **n** linear simultaneous equations derived in (3.2.4b). One can solve this set of equations for the **n** unknown pressures by prescribing arbitrary values of h(y), however, the resulting pressure solution will not be necessarily correct and unrealistic pressure distribution could result. This is due to the incompatibility between the prescribed wetted bottom shape and the prescribed transom rise heights. This aspect of non-uniqueness in the solution has also been discussed by other authors such as Tuck (Ref.(27)) and Oertel (Ref.(28)).

In the present method of solution, the extra equations required for solving these unknown trailing edge rise heights are provided by the Kutta condition at the trailing edge of the planing bottom. When a surface is under planing condition, the Kutta condition requires that the fluid under the planing bottom to separate smoothly from the transom edge. The method adopted in section (3.2) to satisfy this condition is

to ensure that the free surface wave profile induced by the unknown pressures (P_1 to P_n) is continuous at the trailing edge of the planing bottom so that the smooth flow separation condition is maintained.

Alternatively, the Kutta condition can also be satisfied by ensuring that the fluid pressures go to zero, i.e. atmospheric pressure, at the trailing edge of the planing bottom so that there is no discontinuity of pressure as the fluid leaves the transom edge. This 'Kutta zero pressure condition' at the transom edge can be achieved by adding one extra element of zero pressure to the trailing edge of each buttock strip. Since the pressure of these extra elements are prescribed to be zero, the number of unknown pressures and unknown trailing edge rise heights required to be determined are unaltered. By applying the rigid hull boundary condition (3.2.4b) to the control points of the additional m elements will then give the **m** extra equations required to solve for the **n** unknown pressures and the **m** unknown trailing edge rise heights. If the lengths of these extra elements are small so that their control points lie just outside the trailing edge of the buttock strips, it can be shown that the extra **m** equations obtained from this 'Kutta zero pressure condition' are identical to those obtained by the method adopted in section (3.2).

In the present computational method, the Kutta condition is only satisfied at the trailing edge of the planing bottom. From a physical point of view, this seems to be sufficient. Doctors (Ref.(29)) suggested that in the non-linear viscous situation with surface tension, there is effectively a Kutta condition to be applied along the entire perimeter of the planing surface.

In order to verify that the Kutta condition has been satisfied satisfactory at the transom edge so that there is no discontinuity in the flow as the fluid leaves the planing bottom, the wake depression behind a planing flat plate of wetted length to beam ratio, Lw/B, of 2.0, at a beam Froude number, Cv, of 3.17 was computed. These wake profiles were computed by substituting the pressure solution obtained by the method discussed in section (3.2) into the linearized free surface pressure condition (3.1.9) and evaluated on the undisturbed free

surface, z=0. The rectangular wetted bottom of the planing flat plate were divided into five equal sized buttock strips and the resulting pressure distribution is shown in fig.(4.6d). It can be seen that the resulting pressure distribution has a singularity at the leading edge and the pressures go to zero at the trailing edge. This leading edge pressure singularity, which represents the splash configuration at the spray root region and is ignored in a linear theory, is a common characteristic of all the pressure distribution obtained by the present theory.

The computed wake profiles along the centre line, y=0, along y=0.4B and along y=0.7B outside the planing bottom are shown in fig.(3.1a), fig(3.1b) and fig.(3.1c) in a non-dimensional form, $z/(B \tan(\tau))$, where τ is the trim angle, z is the wave elevation and B is the wetted beam. In these figures, the trailing edge of the projected wetted bottom is located at x=0 and the leading edge is located at x=2.0B. Note that although the predicted pressure distribution is a step function, the free surface wave profiles induced by these discretized pressures are continuous along the free surface. It can be clearly seen that the wake separates smoothly from the transom which confirms that the Kutta condition has been satisfied at the trailing edge of the plate. The formation of the splash is also observed in fig.(3.1c). One can also seen that these wave profiles have died away smoothly upstream from the leading edge, indicating that the radiation condition has also been satisfied. The present centre line wake profile has also been compared with the wake depression formula developed by Epshtein (Ref.(64)):

$$z = h \cos(kx) + \frac{\tau_c \sin(kx)}{k} \qquad (3.3.1),$$

where

$$k = \frac{(8/\pi)^{1/2}}{B\ Cv^2} \quad ,$$

z is the free surface depression (downward positive) at a distance x downstream from the transom, h is the immersion of the transom below the

undisturbed free surface and τ_c is the trim angle in radians. The centre line transom immersion predicted by the present theory, which is $h/(B\ \tau_c) = 1.666$, was used in the above formula to obtain the wake profile. As shown in fig.(3.1a), reasonably good agreement exists between the two results. In particular that the present wake profile seems to confirm the zero crossing point given by the formula. The accuracy of the present computations is also indicated by the degrees of smoothness of these curves.

3.4 Output Hull Shapes

In the present computational method, the vertical locations at the trailing edge of the buttock strips, h(y), cannot be prescribed because the shape of the projected wetted bottom has already been assumed. As a consequence, the transverse section shape of the planing surface will also be part of the solution though the longitudinal hull profile can be specified by the input local hull displacement function, f(x,y), above the transom level. The output vertical locations above the undisturbed free surface, Z(x,y), across a transverse section at a distance, x, forward of the transom are given by:

$$Z(x,y) = f(x,y) + h(y) \qquad (3.4.1),$$

which are dependent on the output rise heights, h(y), along the transom as well as the input function, f(x,y). Note that h(y) is constant along a given buttock strip.

The transverse transom shape is presumably dependent on the shape of the prescribed projected wetted bottom and in particular, the geometry of the spray root profile. For example, as shown in fig.(3.2a) and fig.(3.2b), for an input local hull displacement above the transom level defined by the function $f(x,y)= x\mathrm{Tan}(\tau)$, a nearly flat transverse transom will be obtained if the projected wetted bottom is rectangular in shape, while a swept back spray root profile will result in a vee-shape transverse transom. The predicted shape of the transoms shown in these figures are slightly curved instead of being perfectly straight.

This is due to the slight imperfection in the assumed spray root profiles, which should have a slight curvature in practical situations. The present computations also show that these output section shapes are dependent on the spray root geometry but are independent of the planing speed.

Obviously, a direct approach to the problem is to prescribe the hull shape and to determine the required wetted bottom shape and transom rise height, which is constant along the transom, as part of the solution together with the pressure distribution. This can be achieved by an iteration process based on the change in transverse transom shape against the change in spray root geometry - i.e. the change in wetted length of each buttock strip (also see section 3.7). However, such an approach could be time consuming since it will require the recalculation of the pressure distribution at each stage of the iteration. Furthermore, the rate of convergence is dependent primarily on the initial estimation of the wetted bottom shape and consequently convergence might be difficult to achieve.

3.5 Convergence Behaviour

In this section, we investigate the convergence behaviour of the present finite element method on the determination of the pressure distribution under a planing surface. As in any finite element scheme, the fineness of the mesh has to be varied until the computed quantity converges. It is of particular importance to have a good understanding of the convergence behaviour of this method in order to optimize the number of elements used in the finite element mesh, hence the computing time, and to avoid any divergence in the computed quantity. Both the transverse and the longitudinal convergences of the pressure distribution will be investigated aiming to optimize the number of buttock strips and the number of longitudinal elements in each buttock. The longitudinal convergence of the pressure distribution for a given wetted bottom is obtained by fixing the number of buttock strips and increasing the number of elements in each strip until the pressure distribution converges. Similarly, the transverse convergence of the pressure distribution is achieved by fixing the number of elements in

each buttock strip and the number of buttocks is increased until the pressure distribution converges.

It was found that for a fixed number of buttock strips, the computed pressure distribution converged fairly rapidly with the increase in the number of elements in each buttock. Fig.(3.3a,b) and fig.(3.4a,b) show the predicted pressure distributions along the centre line and along the chine of a planing flat plate with wetted length to beam ratios, Lw/B, of 2.7 and 1.2, at beam Froude numbers, $C/(gB)^{1/2}$, of 3.5 and 2.42 respectively. The rectangular wetted bottom of the plate was divided into five buttock strips, each of equal width, and each strip was sub-divided into 5 to 50 equal sized elements. It can be seen from the figures that the pressure distributions converge rapidly both along the centre line and the chine of the plate. Even with only 10 elements in each buttock, the pressures predicted are in good agreement with those obtained when 50 elements are used. Equally fast convergence rates were also evident in the predicted lifts, longitudinal centre of pressure positions and transom rise heights. Fig.(3.5a,b,c) and fig.(3.6a,b,c) show these computed quantities as a percentage of their respective values computed using 50 elements in each buttock. It was found that even with only five equal sized elements in each buttock strip, the results obtained were over 94% of those predicted by using 50 elements.

However, unfortunately, the convergence of the pressure distribution in the transverse sense is not as well-behaved. It was found that the pressure solutions obtained by the present method have a divergent tendency when the number of buttock strips is increased. For a planing flat plate with a rectangular wetted bottom, this pressure divergence was found to occur initially at the chine, near the trailing edge of the plate. Further increases in the number of buttock strips resulted in the spreading of this divergence toward the leading edge and the centre line of the plate. It was also found that the number of buttock strips that could be used before there is any sign of divergence in the pressure distribution varies directly with the speed and the aspect ratio, B/Lw, of the plate. Fig.(3.7a) and fig.(3.7b) show the lateral pressure distributions at various distances along the length of a rectangular wetted bottom of Lw/B ratio of 0.5, at beam Froude numbers of 1.5 and

2.5, when different number of buttock strips are used. Again, equal size rectangular elements were used in the computations with each buttock divided into 15 elements. It can be seen that in the high beam Froude number case, i.e. Cv=2.5, the present computational method is comparatively more stable and there is no sign of pressure divergence up to eleven buttock strips being used. However, at a lower beam Froude number of 1.5, divergence in the predicted pressure distribution is spotted at the chine at station (A), at a distance of Lw/30 forward of the trailing edge, when only seven buttock strips are used. The spreading tendency of this pressure divergence with the increase in the number of buttocks is also demonstrated in fig.(3.7b).

Unrealistic oscillatory pressure results were also obtained for rectangular wetted bottom of large Lw/B ratio at low beam Froude number when large number of buttocks were used. These oscillatory pressures are shown in fig.(3.8a) and fig.(3.8b) for rectangular wetted bottom of Lw/B ratio of 1.8, at a beam Froude number of 1.5 when nine buttock strips are used. Note that the pressure oscillation along the chine is more violent than that along the centre line with a region of negative pressure developed near the trailing edge. Also note that the oscillation has completely died away both along the chine and the centre line when the number of buttock strips is reduced to five. Similar oscillatory and divergent behaviours were also observed in the pressure solutions obtained from wetted bottoms with a swept-back spray root. But in this case, as shown in fig.(5.9) of chapter five for Cv=1.512, the divergence and the oscillation are originated from the region near the centre line, where the wetted length is maximum.

3.6 The Causes of Pressure Divergence and Pressure Oscillation

Doctors' finite element method (Ref.(29)) also showed a similar type of deteriorated pressure distribution to those displayed in fig.(3.8), especially for planing surfaces - his theory had only been applied to flat plate and constant deadrise prismatic surfaces - of large wetted length to beam ratio at low beam Froude number. Doctors suggested that these deteriorated pressures were probably due to the imprecision of the influence coefficients in the matrix, and this inaccuracy coupled with

the round-off error inherent in a large matrix system may be responsible for the occurrence of this pressure divergence. However, when the accuracy of the present integration was increased by assigning smaller step sizes in the integrating process, there was no change in the resulting pressure distribution nor in the free surface response produced by a single element. Moreover, if there was any serious round-off error problem, it should have manifested itself by preventing the pressure distribution converging in the longitudinal sense.

Since the hull displacement vector - defined by the input local hull displacement function $f(x,y)$ - is not oscillatory, these pressure oscillations can only be caused by some oscillatory patterns built into the system matrix. For a rectangular projected wetted bottom divided into equal sized rectangular pressure elements, the influence coefficients in the system matrix are basically equal to the free surface response produced by an element of unit pressure. A close examination on the free surface wave profiles produced by such an element reveals that a more likely cause for this divergence and oscillation is the type of element used. Fig.(3.9) shows the non-dimensional free surface wave profiles along the centre line of a constant pressure rectangular element of width 1/5 B and length 1/10 B at various beam Froude numbers, where B is the beam of the rectangular projected wetted bottom. It can be seen that there is an increase in the number of wave cycles in the downstream wave profile as the beam Froude number decreases from 5.0 to 1.5. One can also see from the non-dimensional wave profiles presented in fig.(3.10a,b,c) that, for a fixed beam Froude number and element's length, the wave length of these downstream waves decrease with the width of the element. It is now clear that the oscillatory patterns in the system matrix are caused by these short period downstream waves, and as a result, the pressure solution is forced to oscillate in order to satisfy the hull boundary condition set up on the planing wetted bottom. Wave profiles such as those shown in fig.(3.9) and fig.(3.10) can therefore be used as a guide-line for estimating the approximate number of buttocks that can be used for a particular wetted length to beam ratio and beam Froude number before any oscillation in the pressure distribution occurs. It was found that the maximum buttock length has to be less than about three quarters of the

first downstream wave length produced by the leading edge element in order to avoid the pressure oscillation problem.

Perhaps a better way to understand the reason for the formation of these short period downstream waves is to consider the wave pattern produced by the corner wave function. The presence of a constant pressure rectangular element can be represented by four corner wave sources, each at a corner of the rectangle and each mathematically equivalent to the sum of the local wave and the free wave corner functions at that corner, as shown in fig.(3.11a). Thus, we can write the free surface elevation at a field point (x,y) given by a rectangular element of constant pressure, P_o, as:

$$\zeta(x,y) = \frac{P_o}{\rho g} [\, C(x-x_A, y-y_A) - C(x-x_B, y-y_B) + C(x-x_C, y-y_C) - C(x-x_D, y-y_D) + \delta \,] \qquad (3.6.1),$$

where (x_A, y_A), (x_B, y_B) etc are the coordinates of the corners of the rectangle as shown in fig.(3.11a), δ has its usual meaning of either 1, $^1/_2$ or 0 according to the location of field point (x,y) with respect to the rectangle and C(X,Y) is the non-dimensional corner wave function given by:

$$C(X,Y) = L(X,Y) + F(X,Y) \qquad (3.6.2).$$

For a rectangular element with T_o equal to zero in expressions (2.3.8) and (2.3.9), the non-dimensional local and free wave corner functions can be written as:

$$L(X,Y) = \frac{M}{2\pi^2} \int_{-\infty}^{+\infty} \frac{g(|\lambda|)}{t} \, dt \qquad (3.6.3)$$

and

$$F(X,Y) = -\frac{M}{\pi} \int_{-\infty}^{T} \frac{\mathrm{Sin}(|\lambda|)}{t} \, dt \qquad (3.6.4),$$

in which

$$\lambda = k_o \, (X + |Y|t \,) \, (1 + t^2)^{1/2} \qquad (3.6.5)$$

and, with $(x-x_a)$ and $(y-y_a)$ replaced by X and Y, M and T have the same meanings as M_a and T_a in the expressions. For a rectangular element, it can be shown that $C(X,Y) = -C(X,-Y)$. Further, as mentioned earlier in section (2.3), the wave pattern produced by each corner wave function, $C(X,Y)$, is speed dependent but does not depend on the length and the width of the element.

Fig.(3.11b) shows two three dimensional plots of the non-dimensional corner wave function, $C(X,Y)$, of a constant pressure rectangular element at different view angles. The horizontal distances X and Y are non-dimensionized using the fundamental wave number, $k_o=g/C^2$, as k_oX and k_oY so that the function is independent of speed. It can be seen from these 3-D plots that there is a diverging wave system originating from the corner (X=0 and Y=0). One can also see that, for large values of k_oY, the transverse wave length is equal to $2\pi/k_o$ which is the downstream wave length along the centre line of a rectangular element of infinitely large width to length ratio. This corresponds to a wave length of $2\pi C_v^2 B$ if B is the projected wetted beam of the planing plate and C_v is the beam Froude number. It is clear that the wave length of these transverse waves is much longer than those shown in fig.(3.9) and fig.(3.10) and should not be responsible for producing the short period downstream

waves shown in the figures. It was found that the diverging waves produced by the four corner wave functions are responsible for the formation of these short period downstream waves.

The interaction between the four corner diverging wave systems is a complex phenomenon. However, for simplicity, we can combine the two corner wave functions at corners A and D, and also the two at corners B and C, to form two wave patterns originated from the corners A and B, as shown in fig.(3.11c). Note that each of these combined wave patterns is now a function of element length, but is still independent of the width of the element. Now, it can be seen clearly from fig.(3.11c) that the formation of the short period downstream waves along the element's centre line is caused by the interference between the two diverging wave systems produced by the two combined corner wave functions at corners A and B. Furthermore, for a fixed element length, the width of the element can then be adjusted by varying the lateral distance between the two combined corner wave functions. It can be seen from fig.(3.11d) that the effect of reducing the element's width is to produce more oscillations in the downstream wave profile along the centre line of the element.

Fig.(3.12a,b) demonstrates the effect of element's length on the resulting free surface wave profiles. At each of the two speeds considered, the width of the element is fixed at B/5 and the length of the element is allowed to vary from B/40 to B/5. The distance, x, in the figures is measured from the centre of the elements. It can be seen that there is no phase shift in the downstream wave profiles for the range of element's lengths considered, while the wave amplitudes vary fairly linearly with the area of the element. This would explain the good behaviour of the pressure solutions obtained when the number of elements is increased in the longitudinal sense.

Returning to the pressure divergence and oscillation problems, since the formation of these short period downstream waves is a genuine characteristic of the present constant pressure element and is not due to numerical inaccuracy, a cure to the problem can only be sought by deriving elements of different form or by considering alternative approaches to the problem. For a Kelvin wavemaking source, it is known

that in practice situation with viscous effects and surface tension included, the diverging wave crests will not extend to the source itself. It is therefore very likely that the neglect of these viscous effect and surface tension in the present theory are responsible for the formation of these short period waves at low speed. It would be tempting to suggest that the re-formulation of the present theory by including the effects of viscous and surface tension or some sort of artificial damping in the governing equations could well be a direct way to overcome the present convergence difficulty and oscillatory pressure problem. In order to avoid the oscillation in the pressure solution, a maximum number of six buttock strips will be used in the later computations so that reasonably good results can be expected. On the other hand, a few elements in each buttock strip will be adequate to achieve reasonably good results.

3.7 The Determination of Wetted Lengths and Trim Angles for a given Craft's Loading Condition

For a particular craft, the hull geometry, displacement and centre of gravity position are specified. At a given speed, the equilibrium of the craft can only be maintained if the lift generated by the planing motion is equal to the weight of the craft and the pitching moment produced by the bottom pressures is zero about the craft's centre of gravity. Therefore, the direct approach to the problem is clearly to determine the unknown running trim, wetted bottom area, transom immersion and bottom pressures which will provide for these equilibrium conditions. As mentioned earlier in section (3.4), this direct problem would be difficult to solve since it involves the integration over an unknown wetted area and the convergence of the iteration process in obtaining the right wetted bottom shape might also be difficult to achieve.

However, such a direct approach to the problem has been achieved by Doctor (Ref.(29)) who also used a finite element method. The pressure elements used were rectangular in shape with a pyramidal pressure distribution and the method has been applied to both planing flat plate and prismatic hulls. In his solution, the weight and the longitudinal

centre of gravity position of the craft were derived from its hydrostatic condition. An initial estimation of the wetted length was obtained from Savitsky's empirical formula for the longitudinal location of centre of pressure (4.4.1). The solutions were then determined by an iterative procedure. For an estimated wetted bottom shape, the pressure distribution, trim angle and trailing edge immersions were obtained by satisfying the rigid hull boundary condition, the Kutta condition and the equilibrium conditions of the craft. At each stage of iteration, correction to each buttock length was made by considering the change in the errors in not satisfying the Kutta condition at the trailing edge of the buttocks due to an increment in the length of each buttock in turn. The method predicted the amount of wetted area of flat plates and prismatic hulls to within a few percent of those derived from the Savitsky's formula.

In the present approach, the shape of the wetted bottom, the trim angle, the wetted beam and the speed are required to be prescribed and the lift, the longitudinal centre of pressure location and the immersions at the trailing edge of each buttock are determined as the solution. In order to obtain the running trims and running wetted lengths for a craft of specified loading condition for a given speed range, it would be necessary to carry out computations for the lift and longitudinal centre of pressure position for an assumed range of wetted length to beam ratios and trim angles at each speed. The required running trim and running wetted length can then be determined by an interpolating method based on matching the weight and the longitudinal centre of gravity position of the craft to the pre-calculated lifts and longitudinal centre of pressure positions. For a heeled or yawed craft, one can also pre-calculate the rolling moments, yawing moments and sway forces arising from the asymmetric bottom pressures for the assumed ranges of trim angles and wetted length to beam ratios. The required rolling moment, yawing moment and sway force for the heeled or yawed craft at a particular loading condition can then be determined by a similar interpolating process once the running trim and running wetted length have been obtained. The following flow diagram outlines the general procedures of the solution scheme. More details concerning this interpolating method will be discussed in the later chapters.

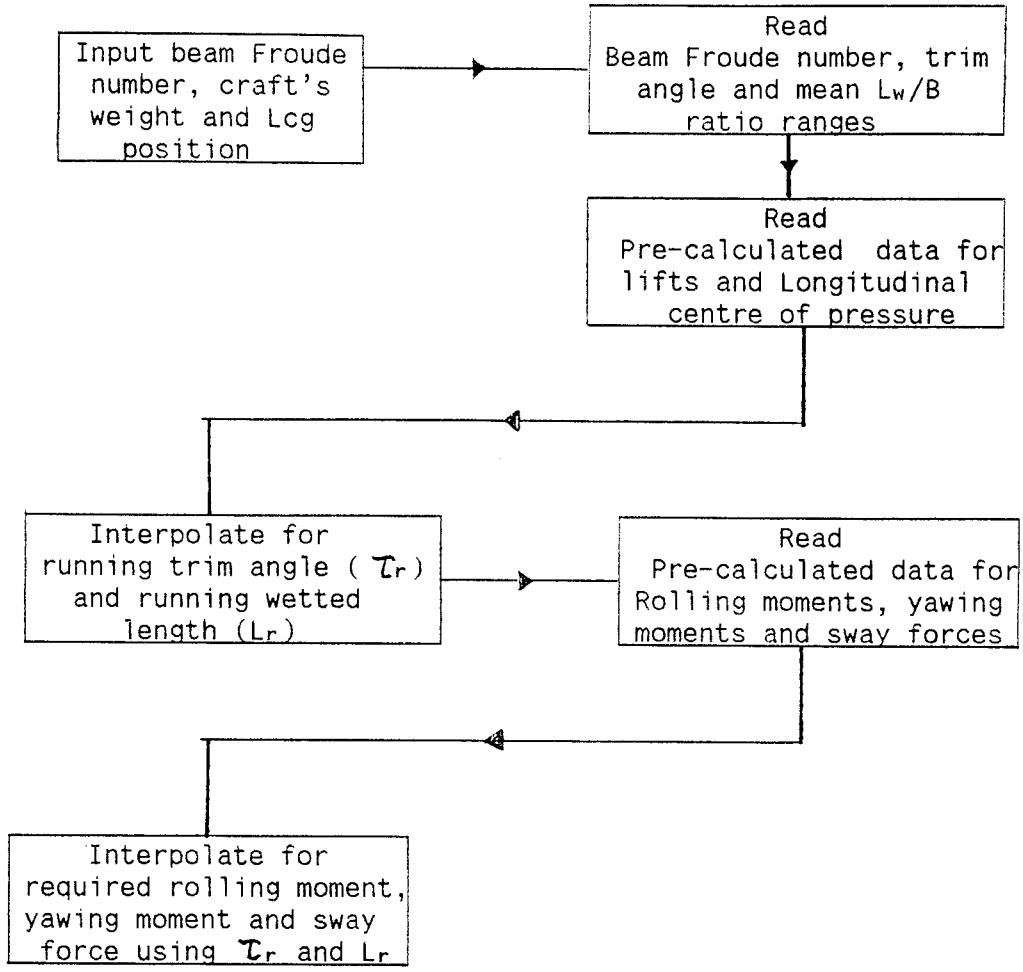

Fig.(3.13) General Procedures for the present Interpolating Method of Solution

CHAPTER (4) Some Results for the Planing of a Flat Plate

4.1 Introduction

This chapter presents results derived from the present theory for planing flat plates. As shown in fig.(4.1), the projected wetted bottom of the planing plate was taken to be rectangular in shape and the slight curvature at the spray root was ignored. A typical finite element representation of this rectangular projected wetted bottom is shown in fig.(4.2). The number of buttock strips used in the computations varied from three at low Froude numbers to five at high Froude numbers. The input local hull surface displacement above the transom level was defined by the function, $f(x,y)=x$, instead of $f(x,y)=\mathrm{Tan}(\tau)x$. Therefore, the resulting solutions were $P/\mathrm{Tan}(\tau)$ and $H/\mathrm{Tan}(\tau)$, where P is the pressure under the wetted bottom and H is the transom immersion of the individual buttocks, both being independent of the trim angle, τ.

The transom immersions, lift coefficients and longitudinal centre of pressure positions predicted by the present theory will be compared with the results obtained from the Savitsky's empirical equations (Ref.(44)) and the theoretical predictions of Wang and Rispin (Ref.(26)) and Doctors (Ref.(29)) in sections (4.2), (4.3) and (4.4). The Savitsky's empirical equations, which are applicable to both flat plate and constant deadrise prismatic hulls, were derived by fitting simple formulae to a large collection of experimental data. The accuracy of these equations is not exactly known; however they do give an overall representation of the experimental values for a wide range of speeds, trim angles and wetted lengths. Comparisons of the present pressure distribution have been made with the experimental results of Sottorf (Ref.(34)) and Jahangeer (Ref.(66)) and the theoretical curves of Wang and Rispin (Ref.(26)), and these results will be presented in section (4.5). Finally, the method to determine the running trim angle and running wetted length for a planing plate of specified weight and longitudinal centre of gravity location will be discussed in section (4.6).

4.2 Output Transom Shape and Immersed Length

The results for the immersed length, i.e. the length of the plate below the undisturbed free surface, and the predicted transom shape are presented in this section. Five different beam Froude numbers, Cv, of 1.512, 2.309, 3.5, 5.0 and 8.0 and a wetted length to beam ratio, Lw/B, up to 3.0 were considered. Five buttock strips of equal width were used for the cases of Cv greater than 2.309 and three buttocks were used otherwise. In order to save computing time, equal sized rectangular elements were used. At each speed, the influence coefficients were evaluated for a rectangular wetted bottom of Lw/B ratio of 3.0 with 60 elements along each buttock strip. Reduction in Lw/B ratio was then achieved by discarding a single row of leading edge elements along the length at a time. In this way, the results for the entire range of Lw/B ratios can be obtained by evaluating only the influence coefficients for the case of Lw/B=3.0. As mentioned earlier in section (3.5), the computed quantities converge very rapidly with the number of elements in each buttock strip, hence reasonably good accuracy can also be expected from the results obtained for wetted bottoms of small Lw/B ratio.

Fig.(4.3) shows the predicted transom shapes and vertical locations for various wetted length to beam ratios and beam Froude numbers. The ordinate of the graph is the non-dimensional transom rise height, H/(Tan(τ) B), where H is the transom rise height above the undisturbed free surface, B is the wetted beam and τ is the trim angle. Note that at small trim angles, Tan(τ) is equivalent to the trim angle in radians. As mentioned in section (3.4), the output transoms are slightly cambered as a result of ignoring the curvature at the spray root. It can be seen that the amount of camber remains fairly constant over the entire range of Cv and Lw/B ratios. This suggests that the output transom shape is only a function of the spray root geometry.

For planing flat plates, Savitsky (Ref.(44)) gave the following pair of equations for the relationship between immersed length to beam ratio, L_i/B, and the wetted length to beam ratio, Lw/B:

$$L_w/B = L_i/B + 0.3 \qquad \text{for} \quad 1.0 \leq L_i/B \leq 4.0$$

and $$L_w/B = 1.6\, L_i/B - 0.3\, (L_i/B)^2 \qquad \text{for} \quad 0.0 \leq L_i/B \leq 1.0 \qquad (4.2.1),$$

which are applicable to trim angles ranging from 2° to 24°; $L_w/B \leq 4.0$; and $0.6 \leq Cv \leq 25.0$. Since in the present theory, the predicted trailing edge immersion of the individual buttocks are of slightly different values, a mean immersed length to beam ratio has to be defined:

$$\frac{L_i}{B} = \frac{H^*}{B\,\tau_c} = \frac{H^*}{B\,\mathrm{Tan}(\tau)} \qquad (\text{for Small } \tau) \qquad (4.2.2),$$

where H^* is the mean transom immersion obtained by fitting a least-squares straight line through the predicted immersions along the transom and τ_c denotes the trim angle in radians. The present predictions for L_i/B are shown in fig.(4.4) together with the Savitsky's curve and the theoretical predictions of Doctors (Ref.(29)). For L_w/B ratios greater than 0.9, the present predictions are in excellent agreement with the Savitsky's curve but there is some discrepancies between the two results at lower L_w/B ratios. On the other hand, the present results seem to verify that the immersed lengths are independent of the planing speeds, as was apparent in Savitsky's curve.

4.3 Coefficient of Lift

Savitsky (Ref.(44)) derived the following empirical equation for the lift coefficient, C_{fz}, of planing flat plate:

$$C_{fz} = \tau^{1.1} \left[0.012\, (L_w/B)^{1/2} + \frac{0.0055\, (L_w/B)^{5/2}}{Cv^2} \right] \qquad (4.3.1),$$

which is valid for $0.6 \leq Cv \leq 13.0$; $2^o \leq \tau \leq 15^o$ and $Lw/B \leq 4.0$,

where $$Cfz = \frac{Fz}{1/2\,\rho\, Cv^2 g B^3} \qquad (4.3.2),$$

Fz is the lift, g is the acceleration due to gravity and τ is the trim angle in degrees. In order to make comparison with the results obtained by the present linear theory, for small trim angles the term $\tau^{1.1}$ in equation (4.3.1) is taken to be equal to τ and is expressed in radians (or $\mathrm{Tan}(\tau)$) to give

$$\frac{Cfz}{\mathrm{Tan}(\tau)} = 57.296 \left[0.012(Lw/B)^{1/2} + \frac{0.0055(Lw/B)^{5/2}}{Cv^2} \right] \qquad (4.3.3).$$

Fig.(4.5a,b,c and d) compare the predicted lift slopes, $Cfz/\mathrm{Tan}(\tau)$, with the empirical lift equation (4.3.3) for beam Froude numbers, Cv, of 1.512, 2.309, 3.5, 5.0 and 8.0. For Cv of 1.512 and Lw/B ratios greater than about 2.2, the predicted pressure distributions have generally deteriorated. As these deteriorated pressures might lead to unreliable results, they have not been shown in fig.(4.5a). For Cv less than 3.5, the lift slopes predicted by the present theory are generally larger than those obtained from the Savitsky's lift equation (4.3.3), but a better agreement is observed at small Lw/B ratios. On the other hand, at Cv=2.309, the theoretical predictions of Doctors (Ref.(29)) are around 30% less than the values obtained from equation (4.3.3), while the present result is about 30% larger than the respective value given by the empirical lift equation at Lw/B=3.0. For high beam Froude numbers, the present theory gives results that are generally below the Savitsky's curve for Lw/B ratios greater than about 1.6, and an error of up to 30% is observed at Lw/B=3.0 for Cv=8.0.

An interesting feature of equation (4.3.3) is that the gravitational effect, which corresponds to the second term of the equation, gives an

increase to the lift coefficient, C_{Fz}, regardless of the wetted length to beam ratio. In the present predictions, however, it was found that the lift coefficient increases with the decrease of Cv for large L_w/B ratios, while the tendency is reversed at small L_w/B ratios (i.e. lift coefficient decreases with Cv). The same tendencies have also been observed in the case of planing prismatic hulls and are clearly shown in fig.(5.7) of chapter five. These would imply that the gravitational effect gives an increase to the lift coefficient for a large L_w/B ratio planing surface but reduces it for a small L_w/B ratio. These tendencies agree with the theoretical predictions of Maruo (Ref.(23)) for the cases of high and low aspect ratio approximations as well as the experimental results of Sambraus (Ref.(36)). The theoretical results of Jahangeer (Ref.(66)) and Wang and Rispin (Ref.(26)) also showed similar effects. At high speed, the hydrodynamic effect becomes dominant and the lift coefficient becomes independent of beam Froude number. This aspect of planing is demonstrated by the results presented in fig.(4.5d) for the cases of Cv=5.0 and 8.0 and is particularly true for small L_w/B ratio planing surfaces. This hydrodynamic effect is also indicated by the Savitsky's empirical lift equation (4.3.3).

Finally, the present results are compared with the theoretical predictions of Wang and Rispin (Ref.(26)). In their theory, the unknown pressure distribution, P(x,y), under the plate was expressed in the form of:

$$P(x,y) = \sum_{m=0}^{\infty} \sum_{n=0}^{\infty} A_{mn}\, y^m\, (1 - y^2)^{1/2}\, I_n(x) \qquad (4.3.4),$$

where $I_n(x)$ is the Birnbaum expansion (Ref.(65)) derived from thin airfoil theory which contains a square root type of singularity at the leading edge, A_{mn} are unknown coefficients to be determined and all distances are non-dimensionalized against the semi-span width of the plate. The kernel function in the integral equation was expanded asymptotically for large Froude number, $Fr = C^2/(gl)$, up to Fr^{-2},

where l is the half beam of the plate. In the expansion, singular behaviour was introduced at the tips of the plate, as $y \to \pm 1$, by the chosen pressure form, P(x,y). For large aspect ratio, B/L_w, the expansions used in their theory are not valid, while for small aspect ratio their theory becomes inaccurate as the tip effect predominates.

The comparison between the present lift slopes and the theoretical predictions of Wang and Rispin is shown in fig.(4.6a) for a Froude number, $Fn=C/(gL_w)^{1/2}$, of 2.24. It can be seen that there is a good agreement exists between the two theories for the range of aspect ratios considered. Fig.(4.6b) compares the present centre of pressure to wetted length ratios, L_{cp}/L_w, with their theoretical predictions. Reasonably good agreement has been obtained between the two results for large aspect ratios while the centre of pressure positions predicted by the present theory are more forward from the transom for aspect ratios less than about 1.0. The discrepancy between the two results at small aspect ratios is probably due to the predominance of the tip effect in their theory.

Fig.(4.6c) and fig.(4.6d) compare the present centre line and chine pressure distributions with the theoretical curves of Wang and Rispin for two L_w/B ratios of 1.0 and 2.0, both at a Froude number of 2.24. In both cases, good agreement is found along the centre line of the plate but the chine pressure distributions of Wang and Rispin show higher pressures at the region near the trailing edge. This could also due to the singular behaviour introduced at the tips of the plate by their theory. Of the two cases, the chine pressures of the smaller L_w/B ratio (larger aspect ratio) plate shows better agreement.

4.4 Longitudinal Centre of Pressure Location

The Savitsky's empirical equation (Ref.(44)) for the location of the longitudinal centre of pressure forward of the transom, L_{cp}, of planing flat plate and planing constant deadrise prismatic hulls is

$$\frac{L_{cp}}{B} = \left[0.75 - \frac{1}{(5.21\ Cv^2/(L_w/B)^2 + 2.39)} \right] \frac{L_w}{B} \qquad (4.4.1),$$

which is independent of the trim and deadrise angles. This equation was derived by considering the moments produced by the hydrodynamic lift, i.e. the first term of equation (4.3.1), and the buoyant lift, i.e. second term of (4.3.1), separately. The centre of pressure of the hydrodynamic lift was taken to be at 75% of the mean wetted length forward of the transom and the centre of pressure of the buoyant force was taken to be at 33% of the mean wetted length forward of the transom. Therefore, this empirical equation should be valid for the same working ranges as those given in equation (4.3.1).

Fig.(4.7a) to fig.(4.7d) show the comparison between the present predictions for L_{cp}/B and the results obtained from equation (4.4.1) for beam Froude numbers ranging from 1.512 to 8.0, together with the theoretical predictions of Doctors (Ref.(29)). It can be seen that the present centre of pressure positions are generally more forward from the transom than those given by the Savitsky's equation. However, a reverse tendency is observed at large L_w/B ratio for $Cv \leq 3.5$. The maximum error between the two results in the range of Cv and L_w/B ratios considered was found to be about 19%. On the other hand, Doctors' results for Cv of 1.512 and 2.309 show very good agreements with the Savitsky's curves especially for L_w/B less than 2.0, despite the fact that his pressure distribution curves have generally deteriorated.

At a high beam Froude number of 8.0 and L_w/B ratio of 3.0, the present theory gives a centre of pressure location at about 89% of the wetted length forward of the transom. This corresponds to an increase of about 14% of the wetted length when compared with the 75% given by the Savitsky's empirical equation (4.4.1), but a much better agreement of about 76% was obtained for L_w/B ratios less than 0.5. This is not a surprising outcome since the location of the hydrodynamic centre of pressure in the Savitsky's equation was based on the result derived from two dimensional planing flat plate, which is at 75% of the wetted length forward of the transom. At high speed, the present theory has actually shown a very good agreement with this two dimensional limit when the

wetted length to beam ratio is small and the flow can be regarded as two dimensional. Furthermore, it is a known fact that the hydrodynamic centre of pressure of a flat plate airfoil will move toward the leading edge from the 75% chord point when its chord length to width ratio is increased from the two dimensional limit.

4.5 Some Results for Pressure Distribution

Fig.(4.8) to fig.(4.10) show the predicted pressure results for rectangular wetted bottoms with wetted length to beam ratios of 3.0, 2.0 and 1.0, at beam Froude numbers, Cv, of 2.309, 3.5 and 8.0. At relatively low beam Froude numbers of 3.5 and 2.309, strong gravitational effect can be seen in the predicted pressure distributions, particularly for the case of $L_w/B=3.0$. This gravitational effect is to increase the pressures toward the trailing edge and to reduce the pressures along the forward half of the plate. At high speed, the hydrodynamic pressures become dominant and, as shown in fig.(4.10) for Cv=8.0, the 'pressure hump' produced by the gravitational effect near the trailing edge has disappeared even at a large wetted length to beam ratio of 3.0. Comparing the pressure distributions in fig.(4.8a) for Cv=2.309 with those in fig.(4.10a) for Cv=8.0, one can clearly see that the gravitational effect is to shift the centre of pressure toward the transom as the speed decreases. The theoretical pressure results of Wang and Rispin (Ref.(26)) have also demonstrated similar gravitational effect.

Fig.(4.11a) and fig.(4.11b) compare the present centre line pressure distributions with the experimental measurements of Sottorf (Ref.(34)) for two L_w/B ratios of 1.49 and 0.82, at a beam Froude number of 3.5. For the higher wetted length to beam ratio case, the present theory predicts pressure result that is over 50% higher than the experimental measurements at the afterbody of the plate, but a better agreement is obtained near the leading edge. For wetted length to beam ratio of 0.82, the agreement between the two pressure results is generally better, though a larger discrepancy is observed near the leading edge. However, surprisingly, the integrated lift coefficient slopes, $C_{fz}/\mathrm{Tan}(\tau)$, are in

much better agreement with Sottorf's experimental values with an under prediction of only 10% for the higher L_w/B ratio case and an over prediction of only 2.5% for the lower L_w/B ratio case. These relatively small discrepancies are probably due to the fact that, in the present theory, most of the lift is generated by the pressures near the leading edge which are higher than the experimental pressures in both cases. Also because of these relatively high leading edge pressures predicted by the present theory, a more forward centre of pressure position could be expected. The numerical values of both the present and Sottorf's lift coefficient slopes are displayed in the figures.

Fig.(4.12) shows the predicted pressure distribution along the centre line of a flat plate of L_w/B ratio of 2.4, at a beam Froude number of 2.42 and at a trim angle of 6° together with the experimental measurements of Jahangeer (Ref.(66)). Reasonably good agreement can be seen between the two pressure results, in particular that the discrepancy near the leading edge is not as pronounced as that in the comparisons with Sottorf's results.

4.6 Determination of Running Wetted Length and Trim Angle

In this section, we consider the problem of predicting the running wetted length, running trim angle and transom immersion of a planing flat plate of specified weight, longitudinal centre of gravity position and speed. It has been mentioned earlier in section (4.1) that, in the present computational method, the predicted pressures, i.e. $P/\mathrm{Tan}(\tau)$, and the predicted transom immersions, i.e. $H/\mathrm{Tan}(\tau)$, are independent of the trim angles for a particular L_w/B ratio and beam Froude number. It follows that both the lift coefficient, C_{fz}, and the mean transom immersion, H^*, are directly proportional to the angle of trim and, if the pressure drag is neglected at small trim angles, the longitudinal centre of pressure ratio, L_{cp}/B, is independent of trim angle.

Now, consider the equilibrium condition of the craft, at any given speed the weight of the craft must be equal to the lift generated by the bottom pressure and its longitudinal centre of gravity position must

also match with the position of the longitudinal centre of pressure. Based on the above equilibrium condition and the present computing program, the following procedures were developed to predict the unknown running wetted length, running trim angle and transom immersion for a planing flat plate of specified weight, W, and specified longitudinal centre of gravity position, Lcg, forward of the transom.

(1) Determination of running wetted length

If the minor effect of the drag force is ignored, the L_{cp}/B ratio of a planing flat plate is only dependent on its wetted length to beam ratio and the planing speed and is independent of the trim angle. Therefore, the running wetted length to beam ratio at a particular beam Froude number, say $[L_w/B]_o$, can be obtained by matching the L_{cp}/B ratio to the Lcg/B ratio of the plate using the L_{cp}/B curve computed at that speed, such as those presented in fig.(4.7a) to fig.(4.7d). This can be easily achieved by some interpolating methods.

(2) Determination of running trim angle

With the running wetted length to beam ratio predicted from (1), the respective lift coefficient slope, say $[C_{fz}/\mathrm{Tan}(\tau)]_o$, at that speed can be obtained from the computed lift slope curve, such as those presented in fig.(4.5a) to fig.(4.5d). The running trim angle, τ_o, can then be obtained from the relation:

$$\mathrm{Tan}(\tau_o) = \frac{2W}{[C_{fz}/\mathrm{Tan}(\tau)]_o} \quad \frac{1}{{}^1/_2\rho g C_v^2 B^3} \qquad (4.6.1),$$

where B is the wetted beam of the plate and Cv is the corresponding beam Froude number.

(3) Determination of unknown transom immersion

Similarly, with the running wetted length to beam ratio predicted from (1), the respective non-dimensional mean transom immersion, say $[H^*/(B\mathrm{Tan}(\tau))]_o$, can be determined from the computed results presented in fig.(4.4). The required transom immersion, say H_o^*, is then given by:

$$H_o^* = \left[\frac{H^*}{B\ \mathrm{Tan}(\tau)}\right]_o B\ \ \mathrm{Tan}(\tau_o) \qquad (4.6.2).$$

It should be noticed that the present linear theory is only valid for small angles of trim as non-linear effects can be significant at large angle of attack. The procedure discussed above is not applicable to prismatic surfaces or other planing forms with a spray root geometry that varies with the trim angle. This is because both the L_{cp}/B ratio and the lift slope, $C_{fz}/\mathrm{Tan}(\tau)$, are now dependent on the angle of trim as well as the mean wetted length to beam ratio. A different approach for the prismatic hulls will be discussed in the next chapter. Owing to the limited number of speeds computed, the method has not been demonstrated in this section. However, the method has been applied to predict the running trim angles and wetted lengths of a heeled planing flat plate and the results are presented in fig.(6.11a) and fig.(6.11b) of chapter six.

CHAPTER (5) Some Results for the Planing of Constant Deadrise Prismatic Hulls

5.1 Introduction

The results for planing prismatic hulls of constant deadrise angle are presented in this chapter. Since the present linearized theory is only applicable for small free surface disturbances, both the trim and deadrise angles are required to be small and only deadrise angles up to 15° will be considered. Fig.(5.1) shows a typical wetted bottom of a planing prismatic surface. As mentioned earlier in section (3.1), the forward thrown spray area, which only contributes drag forces, and the slightly convex curvature at the swept-back spray root are both ignored in the present theory. The mean wetted length to beam ratio, L_w/B, or the wetted area to beam squared ratio of the wetted bottom pressure area can therefore be defined as:

$$\frac{L_w}{B} = \frac{(L_k + L_c)}{2\,B} \qquad (5.1.1),$$

where L_k is the wetted keel length, L_c is the wetted chine length and B is the transom wetted beam. The present finite element representation of this wetted bottom area is shown in fig.(5.2). A different finite element mesh consisting of triangular elements at the spray root and rectangular elements along each buttock as the one shown in fig.(5.3) has also been tried, but the pressure solution obtained has a region of small negative pressures developed along the aft body, near the keel of the wetted bottom. These unrealistic negative pressures were found to be caused by the incompatibility between the phase angles of the downstream waves generated by the rectangular and the leading edge triangular elements. The finite element mesh shown in fig.(5.2) does not suffer from this incompatibility problem simply because the triangular elements are now located at the trailing edge so that the downstream waves of these elements are no longer required in the formation of the system of simultaneous linear equations for determining the unknown pressures. One

should also note that the upstream waves do not cause any problem since they die away quickly ahead of the elements and do not contain any phase change.

Beam Froude numbers ranging from 1.512 to 8.0 and mean wetted length to beam ratios up to 3.0 have been considered. Four buttock strips of equal width were used in the computations. The solution procedure is the same as that for planing flat plates and the input local hull surface displacement above the transom level is defined by the function, $f(x,y) = x$. In order to save computing time, the method of discarding leading edge elements discussed in section (4.2) has also been employed. Section (5.2) discusses the relation between the spray root geometry and the output hull shape. In sections (5.3) and (5.4), the present lift coefficients and longitudinal centre of pressure locations will be compared with the Savitsky's empirical equations (Ref.(44)) as well as the theoretical and experimental results of Jahangeer (Ref.(66)). The present pressure distributions will be compared with the experimental measurements obtained by Sottorf (Ref.(34)) and Jahangeer (Ref.(66)) in section (5.5). Finally, a method for determining the running trim angle and the running mean wetted length of a planing prismatic hull under specified loading condition will be discussed in sections (5.6) and (5.7), together with some work examples for the cases of beam Froude number equal 3.0 and 5.0.

5.2 Output Transom Shape and Immersed Keel Length

Based on the $\pi/2$ wave-rise factor computed by Wagner (Ref.(19)) for a two dimensional wedge penetrating vertically into a fluid surface, Savitsky (Ref.(44)) derived the following relation for the spray root geometry of a planing prismatic surface:

$$\frac{L_K - L_C}{B} = \frac{\tan(\beta)}{\pi \tan(\tau)} \qquad (5.2.1),$$

where B is the transom wetted beam, τ is the trim angle, β is the deadrise angle, L_k is the wetted keel line and L_c is the wetted chine length.

Fig.(5.4) shows the predicted transom shapes and vertical locations for various mean wetted length to beam ratios, L_w/B, and beam Froude numbers, Cv. As before, the ordinate of the graph is $H/(\mathrm{Tan}(\tau)\ B)$, where H is the transom rise height above the undisturbed free surface. The geometry of the spray root used for the computations was defined by the ratio, $(L_k-L_c)/B=0.8115$, which corresponds to a trim angle of 6° and a deadrise angle of 15° according to the Savitsky's expression (5.2.1). This does not strictly agree with the present results. The finite element method generally gives a trim angle slightly larger than that suggested by expression (5.2.1) for a given spray root geometry and deadrise angle and, in this particular case, the output trim angle is about 6.6° for a deadrise angle of 15°. However, the present results seem to agree with expression (5.2.1) that both the planing speed and the mean L_w/B ratio have little effect on the output transom slope, $\mathrm{Tan}(\beta)/\mathrm{Tan}(\tau)$. Over the range of beam Froude numbers and mean L_w/B ratios considered, the variation in the output transom slopes is not more than 2.5%. Note that the output transoms should be slightly curved instead of perfectly straight (see fig.(3.2a)) as the curvature at the spray root has been ignored. The results in fig.(5.4) do not display this feature simply because only four buttock strips were used to represent the wetted bottom.

Fig.(5.5) shows the non-dimensionalized immersed keel length, L_{ki}/B, as a function of mean L_w/B ratio for $(L_k-L_c)/B$ = 0.8115 and 0.5340 at various beam Froude numbers. For small angles of trim, the present immersed keel length, L_{ki}, is given by $H_k/\mathrm{Tan}(\tau)$ where H_k is the predicted transom immersion at the keel. For prismatic surfaces, Savitsky (Ref.(44)) noted that up to a trim angle of approximately 15° there appears to be no noticeable pile-up of water at the keel line. Thus, the immersed keel length in this case is equal to the wetted keel length, L_k. However, the present theory has predicted that the immersed keel lengths are less than the respective wetted keel lengths for both

$(L_k-L_c)/B$ ratios. This would imply that there is water piling up ahead of the keel. The same tendency has also been predicted by Doctors (Ref.(29)) and Jahangeer (Ref.(66)). For both $(L_k-L_c)/B$, a difference of around 0.3 was observed between the predicted L_{ki}/B ratio and the L_k/B ratio, regardless of the beam Froude numbers and the mean L_w/B ratios. This result seems to agree better with Savitsky's expression (4.2.1) - for the relationship between the immersed wetted length, L_i, and the overall wetted length, L_w, of planing flat plates - when L_w and L_i in the expression are replaced by L_k and L_{ki}. The agreement is particularly good for $L_k > 1.0$. On the other hand, Savitsky's observation about no water piling up at the keel line might not be strictly accurate.

5.3 Coefficient of Lift

For a given trim angle and mean L_w/B ratio, the effect of increasing deadrise angle is to reduce the planing lift. This is primarily due to the reduction in the stagnation pressure at the leading edge of the wetted bottom. Taking this lift reduction into account, Savitsky (Ref.(44)) derived the following empirical lift equation for constant deadrise prismatic planing surfaces:

$$C_{fz} = [C_{fz}]_{\beta=o} - 0.0065 \ (\ [C_{fz}]_{\beta=o} \ )^{0.6} \qquad (5.3.1),$$

in which C_{fz} is the lift coefficient of the constant deadrise surface, $[C_{fz}]_{\beta=o}$ is the lift coefficient of a flat plate operating at the same trim angle, wetted area to beam squared ratio (L_w/B) and beam Froude number as the deadrise surface and β is the deadrise angle in degrees. The expression for the lift coefficient of a planing flat plate is given in equation (4.3.1). To compare with the results derived from the present linear theory, the second term of equation (5.3.1) is neglected in the limit of small deadrise angle. As in the case of planing flat plate, for small trim angles, the term, $[C_{fz}]_{\beta=o}$, in equation (5.3.1) is expressed as:

$$\frac{C_{fz}}{Tan(\tau)} = 57.296 \left[0.012(L_w/B)^{1/2} + \frac{0.0055(L_w/B)^{5/2}}{Cv^2} \right] \qquad (5.3.2),$$

where L_w/B in the above expression is the mean wetted length to beam ratio of the prismatic surface given by expression (5.1.1).

Fig.(5.6a) to fig.(5.6h) compare the present lift coefficient slopes, $C_{fz}/Tan(\tau)$, with expression (5.3.2) for beam Froude numbers ranging from 1.512 to 8.0. Two deadrise angles of 10° and 15° are considered. Also shown in fig.(5.6a) and fig.(5.6f) are the theoretical predictions of Jahangeer's finite element method (Ref.(66)) at Cv=1.512 and 5.0, together with his experimental measurements at Cv=1.512. The comparison between the present predictions and expression (5.3.2) show similar trends as those for the planing flat plates. On the other hand, the present results show reasonably good agreement with the theoretical predictions and the experimental measurements of Jahangeer. As shown in fig.(5.9), at a beam Froude number of 1.512 and mean L_w/B ratios greater than 2.0, the predicted pressure distributions have generally deteriorated and violent oscillations have been observed as L_w/B approaches 3.0. However, these deteriorated pressures do not seem to affect the results for the lift coefficient slope and longitudinal centre of pressure location. In the later case, the results are in unexpectedly good agreement with the Savitsky's empirical equation for the location of centre of pressure (5.3.1) as shown in fig.(5.7a). The reason for these results not displaying the oscillatory behaviour of the pressure solution is probably that they represent an integrated effect of the pressures.

The results presented in fig.(5.6a,b,d,f and h) also demonstrate the effect of deadrise angle on the lift coefficient slope. For the two deadrise angles considered, the results show little effect of deadrise on the lift coefficient slope for a given mean L_w/B ratio and beam Froude number. Fig.(5.6g) shows that the lift coefficient becomes independent of the beam Froude number for Cv greater than 6.0. This suggests that the hydrodynamic lift becomes predominant at high planing

speed and the static pressure effect on lift coefficient can be ignored. This aspect of planing is also apparent in the Savitsky's lift equation and the semi-empirical equation developed by Shuford (Ref.(22)).

It has been mentioned in section (4.3) that the Savitsky's empirical lift equation (5.3.2) does not shows the gravitational effect of reducing lift coefficient on a small L_w/B ratio planing surface. This gravitational effect can be seen more clearly by plotting the lift coefficient slopes, $C_{fz}/\mathrm{Tan}(\tau)$, against the beam Froude numbers. Such a plot is shown in fig.(5.7) for a 15° constant deadrise prismatic surface with a $(L_k-L_c)/B$ ratio of 0.8115. It can be seen clearly from the figure that for a small mean L_w/B ratio surface the lift coefficient decreases with decreasing beam Froude number due to the negative gravitational effect, while the tendency reverses at large mean L_w/B ratios. The dividing mean L_w/B ratio in this case is about 0.7.

5.4 Longitudinal Centre of Pressure Location

As mentioned in section (4.4), the Savitsky's empirical equation for the location of the longitudinal centre of pressure forward of the transom, L_{cp}, of constant deadrise prismatic planing surfaces is

$$\frac{L_{cp}}{B} = \left[0.75 - \frac{1}{(5.21\ C_v^2/(L_w/B)^2 + 2.39)} \right] \frac{L_w}{B} \qquad (5.4.1),$$

which is independent of trim angle and deadrise angle for a given mean L_w/B ratio and C_v.

The comparisons between the present predictions for L_{cp}/B ratio and the Savitsky's empirical equation (5.4.1) are shown in fig.(5.8a) to fig.(5.8h), for two deadrise angles of 10° and 15° and for beam Froude numbers ranging from 1.512 to 8.0. As in the case of planing flat plate, the present predictions are usually above the Savitsky's curve, though, for $C_v \leq 3.0$ and large mean L_w/B ratios, results below the Savitsky's curve have also been obtained. On the other hand, as shown in fig.(5.8a) and fig.(5.8f) for C_v=1.512 and 5.0, a very good agreement generally

exists between the present predictions and the theoretical and experimental results of Jahangeer (Ref.(66)). At Cv=1.512, excellent agreement has been obtained between the present results and the Savitsky's empirical equation, even though the predicted pressure distributions for mean wetted length to beam ratios greater than 2.0 have generally deteriorated. These deteriorated pressure solutions are shown in fig.(5.9). The results presented in fig.(5.8a,b,d,f and h) also seem to verify that the deadrise angle has little effect on the centre of pressure ratio, L_{cp}/B, for a given mean wetted length to beam ratio and beam Froude number. The reduction in static pressure effect on the centre of pressure location at high planing speeds can be seen in fig.(5.8g), where the L_{cp}/B ratio has almost become independent of the beam Froude number for Cv greater than 6.0.

5.5 Some Results for Pressure Distribution

Fig.(5.9) shows the pressure distribution curves obtained for a 15° constant deadrise surface with $(L_k-L_c)/B=0.8115$ at various mean wetted length to beam ratios and beam Froude numbers. At Cv=1.512, it is observed that the pressure oscillation starts to build up for mean L_w/B >2.0 and has become quite violent as L_w/B reached 3.0. At higher speeds, the pressure solutions are well behaved and no such pressure oscillation is evident up to a mean L_w/B ratio of 3.0. The cause of these pressure oscillations has already been discussed in section (3.6), but it should be pointed out that, unlike the pressure oscillations in the flat plate cases, these oscillations originate at the region near to the centre line rather than at the region near to the chine. As in the planing of flat plate, the present pressure results have also demonstrated that there is a strong gravitational effect on large mean L_w/B ratio planing surfaces operating at low speed. Note that for beam Froude numbers greater than 6.0, the shape of these non-dimensionalized pressure distribution curves, $P/(^1/_2\rho\ C^2\mathrm{Tan}(\tau))$, have almost become independent of the beam Froude number for a given mean L_w/B ratio. This would imply that the hydrodynamic bottom pressures are directly proportional to the square of the planing speed.

As shown in fig.(5.2), the present wetted bottom grid does not allow us to prescribe a set of control points along the keel line, hence the pressure distribution along the keel cannot be obtained. For comparison purpose, however, the pressure distribution along the first buttock strip from the keel line will be used to compare with the keel pressure distribution obtained by other authors.

Fig.(5.10) compares the present pressure distributions with the experimental measurements of Sottorf (Ref.(34)) for a 15° constant deadrise surface of mean L_w/B ratio of 1.754, $(L_k-L_c)/B$ ratio of 0.7012, at a beam Froude number of 3.5. As in the flat plate pressure distributions shown in fig.(4.11a,b), the present theory has predicted pressure results that are more than 50% lower than Sottorf's experimental measurements both along the chine and along the keel (the present keel pressure distribution refers to that along the line at a distance of B/12 from the keel line), but the agreement is much better near the leading edge of the chine. Comparison of the present keel pressure distribution (B/8 from keel line) with the experimental measurements of Jahangeer (Ref.(66)) is shown in fig.(5.11) for a deadrise angle of 15°, mean L_w/B ratio of 2.87, trim angle of 6° and beam Froude number of 2.54. The agreement between the two results is reasonably good, considering that the pressures at the keel should be slightly higher than those at a distance B/8 from the keel, especially around the region near to the leading edge.

5.6 Variation of Lift Coefficient and Centre of Pressure Ratio with Trim Angle

For a given constant deadrise surface, the effect of decreasing trim angle is to increase the swept-back angle at the spray root. This alters the shapes and sizes of the triangular fore-piece and the rectangular tail of the wetted bottom even though the wetted bottom area is kept constant. It follows that the L_{cp}/B ratio and the lift coefficient slope, $C_{fz}/\mathrm{Tan}(\tau)$, of a constant deadrise hull are not necessarily constant over the entire range of trim angles for a given mean wetted length to beam ratio and speed.

Fig.(5.12a and b) and fig.(5.13a and b) show the predicted lift coefficients, C_{fz}, and centre of pressure ratios, L_{cp}/B, as a function of trim angle and mean L_w/B ratio for a 10° constant deadrise surface at beam Froude numbers of 3.0 and 5.0. For each of the trim angles, τ, considered, an initial estimate of the swept-back angle, i.e. $(L_k-L_c)/B$, was obtained from the Savitsky's expression (5.2.1). The trim angle was then determined from the output transom slope, $\mathrm{Tan}(\beta)/\mathrm{Tan}(\tau)$, for the given value of β. It can be seen that the slope of the lift coefficient curve for each mean L_w/B ratio is fairly constant throughout the range of trim angles considered. This aspect seems to agree with the Savitsky's empirical lift equation (5.3.2), although the exact values of the two lift slopes are not the same. The predicted longitudinal centre of pressure locations, L_{cp}, have a tendency of shifting toward the transom as the trim angle decreases. This tendency is particularly pronounced at small trim angles. The overall decrease in L_{cp}/B, however, is not more than 0.1 over the ranges of trim angles and L_w/B ratios considered. It would appear that this decrease in L_{cp}/B ratio is due to the increase in the swept-back angle at the spray root (or $(L_k-L_c)/B$ ratio), which could result in a reduction in the pitching moment produced by the pressures near the chines. On the other hand, the Savitsky's empirical equation (5.4.1) suggests that the centre of pressure ratio, L_{cp}/B, is independent of the trim angle for a given mean L_w/B ratio and Cv. The slight unsmoothness of the curves can be ascribed to the difference in the sizes of elements used in the computations.

An interesting feature about the planing wetted bottom of constant deadrise hulls is that the trim angle and the deadrise angle can have an infinite number of values that can produce a particular spray root geometry (or $(L_k-L_c)/B$). This special feature is displayed explicitly in expression (5.2.1) and would allow us to obtain the lifts and the centres of pressure for a range of deadrise angles from the results computed for a particular deadrise angle. For instance, if the predicted trim angle, lift coefficient and longitudinal centre of pressure ratio for a 10° constant deadrise surface of particular wetted bottom geometry at a particular beam Froude number are $\tau_{10°}$, $[C_{fz}]_{10}$ and $[L_{cp}/B]_{10}$, then the corresponding trim angle, say τ_{β} °, for a surface of constant

deadrise angle of β° can simply be obtained from the relation:

$$\text{Tan}(\tau_\beta^\circ) = \frac{\text{Tan}(\tau_{10}^\circ)}{\text{Tan}\ (10^\circ)}\ \text{Tan}(\beta^\circ) \qquad (5.6.1).$$

The lift coefficient, say $[C_{fz}]_\beta$, for the β° constant deadrise surface at the trim angle of τ_β° is

$$[C_{fz}]_\beta = \frac{[C_{fz}]_{10}}{\text{Tan}(10^\circ)}\ \text{Tan}(\beta^\circ) \qquad (5.6.2)$$

and the corresponding longitudinal centre of pressure ratio at τ_β° is equal to $[L_{cp}/B]_{10}$ if the pitching moment produced by the pressure drag is ignored.

5.7 Determination of Running Mean Wetted Length and Running Trim Angle

The method for determining the running trim angle and running wetted length for planing flat plate has already been discussed in section (4.6). In this section, we will extend this method to constant deadrise planing hulls (or any hull form in general). Again, the method developed here is based on matching the craft's weight and craft's centre of gravity position to the planing lift and centre of pressure position. A simple interpolating program has been developed for this purpose and a third order Lagrange interpolating polynomial has been employed in the interpolating procedures.

For a particular constant deadrise hull, the weight, W, and the distance of the longitudinal centre of gravity forward of the transom, L_{cg}, can be expressed in the following non-dimensional forms:

$$W^* = \frac{W}{1/2\,\rho\, gB^3} \qquad \text{and} \qquad L^* = \frac{Lcg}{B} \qquad (5.7.1).$$

For a given beam Froude number, the program determines the possible combinations of trim angle and mean Lw/B ratio that can provide the required weight coefficient, W*, from the pre-calculated lift data shown in fig.(5.12a) and fig.(5.13a). Similarly, the possible combinations of trim angle and mean Lw/B ratio that can provide the required L* are determined from the pre-calculated centre of pressure data shown in fig.(5.12b) and fig.(5.13b). For example, these trim angles and mean Lw/B ratios predicted for W*=1.3, L*=1.6 and β=10° are shown in fig.(5.14a) and fig.(5.14b) for beam Froude numbers of 3.0 and 5.0. Curves (A) in these figures represent the possible combinations of trim angle and mean Lw/B ratio for producing a weight coefficient, W*, of 1.3 and Curves (B) represent those for producing a centre of gravity ratio of 1.6. The trim angle and mean Lw/B ratio which satisfy both the required weight and centre of gravity conditions are given by the intersection of the two curves.

Fig.(5.15a) and fig.(5.15b) compare the predicted running trim angles and running wetted length to beam ratios with the results obtained from the Savitsky's empirical equations (5.3.2) and (5.4.1) for a 10° deadrise surface. For demonstration purposes, only two beam Froude numbers of 3.0 and 5.0 have been considered. The weight coefficient, W*, is fixed at 1.3 and the trim angle and mean Lw/B ratio results are plotted as a function of centre of gravity ratio, L*. Both the present and Savitsky's results show the tendencies of decrease in trim angle and increase in mean Lw/B ratio as the centre of gravity moves toward the bow. The agreement between the two results is reasonable with a difference of not more than 1° for the trim angles and 0.3 for the mean Lw/B ratios. However, for the two speeds considered, the present theory usually gives a larger trim angle and a smaller mean Lw/B ratio than those obtained from the empirical equations for a value of W* and L*. This could be due to the fact that, as mentioned in section (4.4), the hydrodynamic centre of pressure in the Savitsky's empirical equation for the centre of pressure location is taken to be at 75% of the mean wetted length forward of the transom which is less than that one would expect from a moderate aspect ratio lifting surface.

CHAPTER (6) Some Results for the Planing of a Flat Plate in Heel Condition

6.1 Introduction

In this chapter, we consider the planing motion of a flat plate in heel condition. Again, only small heel and trim angles will be considered in the present linear theory. When a planing flat plate is heeled, the wetted bottom becomes asymmetrical about the centre line. This gives rise to an asymmetrical bottom pressure load about the plate centre line, which can result in a net rolling moment, a net yawing moment and a net sway force. A sketch of the wetted bottom of a planing flat plate in heel condition is shown in fig.(6.1). As before, the forward spray area is ignored in the present computations on the ground that this area only contributes to the total drag and does not carry any pressure load. In addition, the sightly convex curvature at the spray root is also ignored and the running beam at the transom is assumed to be completely wetted during the planing motion. Thus, the mean wetted length to beam ratio, L_w/B, or the wetted area to beam squared ratio for a planing flat plate in heel can be defined as:

$$\frac{L_w}{B} = \frac{(L_{c2} + L_{c1})}{2B} \qquad (6.1.1),$$

where B is transom wetted beam, L_{c1} and L_{c2} are the wetted chine lengths at the heeled up and the heeled down sides of the plate respectively. A typical finite element mesh representing the wetted bottom pressure area of a planing flat plate in heel is shown in fig.(6.2). As in the case of planing prismatic surfaces, the triangular elements have been located at the trailing edge in order to avoid incompatibility in the phase angles between the two types of element used. The input local hull displacement function above the transom level is the same as before, thus, $f(x,y)=x$.

In section (6.2), an analytical expression is derived for estimating the spray root geometry of a planing flat plate in heel condition.

Sections (6.3) and (6.4) discuss the effect of heel angle on the induced roll moment for a fixed trim condition and the effect of trim angle on the roll moment for a fixed heel condition. Section (6.5) compares the present computational results with the theoretical predictions and the experimental measurements of Jahangeer (Ref.(66)). Finally, a method for determining the derivatives of roll moment and sway force with respect to the heel angle for a planing flat plate of specified loading condition will be discussed in section (6.6).

6.2 Spray Root Geometry and Predicted Transom Shape

In this section, an analytical expression is derived for the relationship between the spray root geometry, which can be defined by the ratio of $(L_{c2}-L_{c1})/B$, the heel angle and the trim angle for a planing flat plate in heel condition. The analogy employed here is similar to the one used by Savitsky (Ref.(44)) for deriving the spray root geometry of planing constant deadrise prismatic hulls.

For an observer fixed in space and located at the vertical plane through centre line of the heeled plate, the passage of the heeled planing flat plate to the observer can be regarded as the motion of a two dimensional wedge immersing vertically into the water surface. This being the case, the $\pi/2$ wave rise factor computed by Wagner (Ref.(19)) for a two dimensional wedge penetrating vertically into a fluid surface is applicable. Now, consider the cross section A-A in fig.(6.3a) of a heeled planing flat plate, at a distance, X, from the calm water intersection of the chine (heeled down side). According to the $\pi/2$ wave rise factor computed by Wagner (Ref.(19)), the relationship between the actual wetted width, B_1, and the wetted width, B_2, defined by the calm water intersection with the plate surface is

$$B_1 = \frac{\pi}{2} B_2 \qquad (6.2.1).$$

Under the assumption of no pile-up of water at the chine line (heeled down side), it can be shown from the wetted bottom geometries in fig.(6.3b) and fig.(6.3c) that the wetted widths B_2 and B_1 are

$$B_2 = \frac{d}{\mathrm{Tan}(\phi)} = \frac{X\,\mathrm{Tan}(\tau)}{\mathrm{Tan}(\phi)} \qquad (6.2.2)$$

and

$$B_1 = \mathrm{Tan}(\alpha)\,X = \frac{B}{(L_{c2} - L_{c1})}\,X \qquad (6.2.3).$$

Thus, the difference between the wetted chine lengths, L_{c2} and L_{c1}, for a planing flat plate in heel is given by:

$$\frac{L_{c2} - L_{c1}}{B} = \frac{2\,\mathrm{Tan}(\phi)}{\pi\,\mathrm{Tan}(\tau)} \qquad (6.2.4),$$

where B is the transom wetted beam, τ is the trim angle and ϕ is the heel angle. A similar expression has also been derived by Jahangeer (Ref.(66)).

Fig.(6.4) shows the transom shapes and vertical locations predicted from wetted bottoms with a spray root profile defined by $(L_{c2}-L_{c1})/B$ =1.0518 at various beam Froude numbers. As a result of neglecting the curvature at the spray root, the output transoms are slightly cambered. In order to determine the transom slope, $\mathrm{Tan}(\phi)/\mathrm{Tan}(\tau)$, a least-squares straight line was fitted through the predicted vertical locations along the transom. As suggested by expression (6.2.4), for a given spray root geometry, the output transom slopes are almost independent of the planing speed and the mean L_w/B ratio. However, the present theory always gives a smaller value of $\mathrm{Tan}(\phi)/\mathrm{Tan}(\tau)$ than that suggested by the analytical expression. In the present case, with $(L_{c2}-L_{c1})/B$=1.0518, the least-squares straight line fitting gives a transom slope, $\mathrm{Tan}(\phi)/\mathrm{Tan}(\tau)$, of about 1.4. This corresponds to a reduction of 15% when

compared with the value of 1.65 given by expression (6.2.4). The output transom slope, however, is very much dependent on the way that a straight line is fitted through the predicted vertical locations along the transom and an error of few percents between different fitting methods is not unusual.

Fig.(6.5) shows the variation of immersed chine length to beam ratios, L_{c2i}/B, against mean L_w/B ratios for $(L_{c2}-L_{c1})/B$ of 1.0518 and 0.4235, at two beam Froude numbers of 3.0 and 5.5. The immersed chine length at the heeled down side of the plate, L_{c2i}, can be obtained from the relation

$$\text{Immersed Chine Length (heeled down side)} \quad L_{c2i} = \frac{H_{c2}}{\text{Tan}(\tau)} \qquad (6.2.5),$$

where H_{c2} is the predicted transom immersion at the chine (heeled down side). On the other hand, in deriving expression (6.2.4), it has been assumed that there is no pile-up of water at the chine (heeled down side). Based on this assumption, the immersed chine length, L_{c2i}, is simply equal to the wetted chine length, L_{c2}. It can be seen from fig.(6.5) that the present immersed chine length to beam ratios, L_{c2i}/B, are less than the assumed values of L_{c2}/B for both $(L_{c2}-L_{c1})/B$ ratios. This would suggest that there is water piling up at the chine of the heeled down side of the plate during the planing motion.

6.3 Variation of Hydrodynamic Forces and Moments with Heel Angle

Strictly speaking, for a planing surface supported mainly by hydrodynamic pressures on the wetted bottom, the introduction of a heel angle results in a net transverse load which gives rise to a net rolling moment, a net yawing moment and a net sway force. For a heeled planing flat plate, however, both the sway force and the lift force are acting at the centre of pressure (not in the case of prismatic surface), therefore causing no net yawing moment about this point. It follows that the introduction of heel angle will only cause the plate to sway but not to yaw.

Fig.(6.6a) shows the sign conventions for the sway force, F_y, the rolling moment, M_r, and the heel angle, ϕ. Rolling to the starboard and swaying to the port are treated as positive. The sway force, F_y, can be obtained from the simple relation

$$F_y = - \mathrm{Tan}(\phi)\, F_z \qquad (6.3.1),$$

where F_z is the bottom lift. The total roll moment about the centre line, M_r, can be considered to be made up of two components - one is the roll moment produced by the lift and the other is the roll moment produced by the sway force. If R denotes the distance from the transverse centre of pressure to the plate centre line as shown in fig.(6.6b), it can be shown from the geometry of the heeled plate that the roll moment produced by the lift is $-R\,\mathrm{Tan}(\phi)\,F_z$ and the roll moment produced by the sway force is $-R\,\mathrm{Tan}^3(\phi)\,F_z$. Thus, for small heel angles, the roll moment produced by the sway force is only a minor part of the total roll moment. A non-dimensional roll moment coefficient, C_{rm}, is defined as:

$$C_{rm} = \frac{M_r}{1/2\,\rho\, g B^4} \qquad (6.3.2)$$

and the rolling moment arm ratio, R/B, is

$$\frac{R}{B} = \frac{M_r}{(F_z^2+F_y^2)^{1/2}\, B} \qquad (6.3.3).$$

Fig.(6.7a) and fig.(6.7b) show the variations of $R/(B\mathrm{Tan}(\phi))$ and $C_{rm}/\mathrm{Tan}(\phi)$ against heel angle for various mean L_w/B ratios, at a trim angle of 6° and beam Froude numbers of 3.0 and 5.5. It can be seen that, up to a heel angle of 10.75°, the predicted roll moment coefficient

slopes, $C_{rm}/\mathrm{Tan}(\phi)$, are almost independent of the heel angles for a given mean L_w/B ratio, trim angle and beam Froude number. The predicted $R/(B\mathrm{Tan}(\phi))$ ratios also exhibit the same feature, although slightly larger discrepancies have been observed at Cv=3.0 for large mean L_w/B ratios. The corresponding lift coefficient slopes, $C_{fz}/\mathrm{Tan}(\tau)$, and longitudinal centre of pressure ratios, L_{cp}/B, are shown in fig.(6.7c) and fig.(6.7d). The results in fig.(6.7c) show little effect of heel angle on the lift coefficient for a given mean L_w/B ratio, trim angle and beam Froude number. On the other hand, the centre of pressure tends to shift toward the transom as the heel angle increases, but the difference in any case is not more than 6%.

In an equilibrium condition at any given speed, the weight of the plate must be equal to the planing lift and the longitudinal centre of gravity must be at the same location as the longitudinal centre of pressure. The above results would imply that the roll moment coefficient slope, $C_{rm}/\mathrm{Tan}(\phi)$, for a heeled planing flat plate of specified loading condition is independent of the angle of heel.

6.4 Variation of Hydrodynamic Forces and Moments with Trim Angle

Another interesting feature about the predicted roll moment coefficient slope, $C_{rm}/\mathrm{Tan}(\phi)$, is that, at a small trim and heel condition, the trim angle also has a very minor effect on the roll moment coefficient slope. Consider a set of input to the program consisting of:

(1) a given projected wetted bottom geometry, in this case, defined by the spray root profile, $(L_{c2}-L_{c1})/B$, the transom wetted beam, B, and the wetted bottom area, A_w,

(2) a given beam Froude number,

(3) a given local hull surface displacement above the transom level, in this case, defined by the function, $f(x,y) = x$.

The output solutions are the bottom pressures, $P/\mathrm{Tan}(\tau)$, and the transverse section shape defined by the ratio, $\mathrm{Tan}(\phi)/\mathrm{Tan}(\tau)$. For a small heel angle, ϕ, the roll moment produced by the sway force can be ignored on the ground that its magnitude is in the order of $\mathrm{Tan}^2(\phi)$ of that produced by the lift. Thus, the roll moment coefficient slope, $C_{rm}/\mathrm{Tan}(\phi)$, or to be precise, the roll moment coefficient slope due to the lift force, $[C_{rm}/\mathrm{Tan}(\phi)]_z$, is given by:

$$\left[\frac{C_{rm}}{\mathrm{Tan}(\phi)}\right]_z = \int_{A_w} \frac{P}{\mathrm{Tan}(\tau)}\, y\, dxdy\, \frac{\mathrm{Tan}(\tau)}{\mathrm{Tan}(\phi)}\, \frac{1}{1/2\,\rho g B^4} \qquad (6.4.1),$$

where the distance, y, is measured from the centre line. It is clear that both the pressure term, $P/\mathrm{Tan}(\tau)$, and the ratio, $\mathrm{Tan}(\tau)/\mathrm{Tan}(\phi)$, in expression (6.4.1) are independent of the trim angle. Therefore, for a given set of input to the program, $[C_{rm}/\mathrm{Tan}(\phi)]_z$ is constant for any combinations of heel angle and trim angle provided that both angles are small and their ratio is the same as the output $\mathrm{Tan}(\phi)/\mathrm{Tan}(\tau)$. Since we have already shown in the previous section that $C_{rm}/\mathrm{Tan}(\phi)$ is independent of the heel angle for a given trim angle, the above argument would imply that, for a given beam Froude number and mean L_w/B ratio, $C_{rm}/\mathrm{Tan}(\phi)$ is also independent of the trim angle.

Furthermore, for a given projected wetted bottom and beam Froude number, the integrated lift coefficient, C_{fz}, varies linearly with the trim angle and, if the drag is ignored, the L_{cp}/B ratio is independent of the trim angle. It follows that, ignoring the minor effect due to the sway force, the roll moment coefficient slope, $C_{rm}/\mathrm{Tan}(\phi)$, of a heeled planing flat plate only depends on the planing speed and its longitudinal centre of gravity position and is independent of its weight.

Returning to the results in fig.(6.7b,c and d) computed from four different spray root geometries. For each set of $(L_{c2}-L_{c1})/B$ ratio, beam

Froude number and mean L_w/B ratio considered, the heel angle can be fixed at a certain value and the trim angle can be altered according to the predicted transom slope, $Tan(\phi)/Tan(\tau)$. Thus, the results in these figures can also represent the roll moment coefficient slopes (ignoring sway force effect), lift coefficient slopes and centre of pressure ratios for different trim angles at a fixed heel condition. These results therefore verify that the weight (or trim angle) of the plate has little effect on $C_{rm}/Tan(\phi)$ for a given L_{cg} position (or mean L_w/B ratio) at a given beam Froude number. Note that although the lift coefficient slope remains unchanged during this scaling process, the lift itself has been varied according to the changes in trim angle.

6.5 Comparison of Results

In this section, the results derived from the present theory are compared with the theoretical predictions and the experimental measurements of Jahangeer (Ref.(66)). Jahangeer also used a finite element method to determine the bottom pressures of planing surfaces. However, the constant pressure elements used in his solution are rectangular in shape, therefore the spray root geometry cannot be prescribed as accurately as in the present theory. The wetted bottom used for the comparison has a $(L_{c2}-L_{c1})/B$ ratio of 1.0518 and a mean wetted length to beam ratio of 2.36. Beam Froude numbers ranging from 2.0 to 10.5 are considered. Four buttock strips were used in the computations, except in the comparison of pressure distributions where five buttock strips were used in order to obtain the pressure distribution along the centre line of the plate.

Fig.(6.8a) compares the present predictions for the roll moment coefficient slope, $C_{rm}/(Tan(\phi)Tan(\tau))$, with Jahangeer's theoretical and experimental results. The non-dimensional ordinate $C_{rm}/(Tan(\phi)Tan(\tau))$ in the figure was used in Jahangeer's original graph and does not mean that $C_{rm}/Tan(\phi)$ varies linearly with the trim angle. It has already been shown in the previous section that the trim angles have little effect on $C_{rm}/Tan(\phi)$ for a given mean L_w/B ratio and Cv. It can be seen that there is an excellent agreement between the two theoretical curves beyond beam

Froude number of 3.5, while the present theory predicts lower values at smaller beam Froude numbers. On the other hand, the present result agrees exactly with Jahangeer's experimental measurement at Cv=2.42. Fig.(6.8b) shows the variation of the non-dimensional rolling moment arm, $R/(B\tan(\phi))$, against beam Froude number. As before, the present non-dimensional rolling moment arms are smaller than the theoretical predictions of Jahangeer for beam Froude numbers less than 3.5. At a beam Froude number of 2.42, the present prediction is also smaller than his experimental measurement. The discrepancy between the present prediction and the experimental measurement, however, can be ascribed to the difference between the lift obtained by the present theory and the experiment. Both the $C_{rm}/(\tan(\phi)\tan(\tau))$ and the $R/(B\tan(\phi))$ curves have a peak at beam Froude number of about 2.6 and decrease rapidly as the speed is further increased. This would imply a decrease in roll stability at high speeds.

The results for the lift coefficient slopes, $C_{fz}/\tan(\tau)$, are shown in fig.(6.8c). Excellent agreement has been obtained between the present results and Jahangeer's theoretical predictions. At Cv=2.42, the present lift coefficient slope is slightly larger than Jahangeer's experimental measurement. Fig.(6.8d) shows the results for the longitudinal centre of pressure ratio, L_{cp}/B. The longitudinal centre of pressure positions predicted by the present theory are consistently less forward from the transom than Jahangeer's theoretical results for all the beam Froude numbers considered. The discrepancy between the two theoretical curves is rather large, but the present result agrees much better with his experimental measurement at a beam Froude number of 2.42.

Fig.(6.9) compares the present pressure distributions with the experimental measurements obtained by Jahangeer for a heeled planing flat plate of mean L_w/B ratio of 2.36, at a trim angle of 6°, heel angle of 10° and at a beam Froude number of 2.42. Good agreement has been obtained between the theoretical and the experimental pressure distributions along the centre line of the plate, while larger discrepancies have been found along the chines. It has been observed that the chine pressures obtained by using four buttock strips are in

better agreement with the experimental measurements, and this could be the reason for the very encouraging roll moment result obtained at Cv=2.42. One should be aware that the chine pressures are more important as far as the calculation of rolling moment is concerned.

6.6 Determination of Hydrodynamic Forces and Moments acting on a Heeled Planing Flat Plate of Specified Loading Condition

In this section, we consider the problem of determining the rolling moment and the sway force acting on a heeled planing flat plate under a specified loading condition. For a heeled planing flat plate, the sway force, F_y, is independent of the speed and the position of the centre of gravity and, according to the sign convention shown in fig.(6.6a), can be obtained from the relation

$$F_y = - W \, Tan(\phi) \qquad (6.6.1),$$

where W is the weight of the plate and ϕ is the angle of heel. Following the earlier discussion in section (6.3), at sufficiently small heel and trim angles, the roll moment coefficient, C_{rm}, can be expressed as:

$$C_{rm} = \frac{\partial C_{rm}}{\partial \phi} \, \phi \qquad (6.6.2),$$

where ϕ is the heel angle in radians and $\partial C_{rm} / \partial \phi$ is the partial derivative of the roll moment coefficient with respect to the heel angle which can be regarded as a function of the weight, the longitudinal centre of gravity position and the planing speed. At small heel angles , $\partial C_{rm} / \partial \phi$ is independent of ϕ and is equal to the roll moment coefficient slope, $C_{rm}/Tan(\phi)$.

To determine these roll moment derivatives, $\partial C_{rm}/\partial \phi$, one can fix the angle of heel and carry out computations for an assumed range of mean Lw/B ratios and trim angles at each beam Froude number, and then

interpolate between these results to obtain the right lift, longitudinal centre of pressure position and roll moment. However, this could be a time consuming process, since several trim angles will be required for each assumed mean L_w/B ratio and beam Froude number. In order to save computing time, a slightly different approach is adopted here. This approach, which will be discussed later in this section, is based on the results obtained from wetted bottoms of a fixed spray root geometry, i.e. a fixed ratio of heel to trim angles, and therefore only requires one computation for each assumed mean L_w/B ratio and beam Froude number.

Computations have therefore been carried out for a series of wetted bottoms with spray root geometry defined by $(L_{c2}-L_{c1})/B=1.0518$. The computed lift coefficient slopes, centre of pressure ratios and roll moment coefficient slopes are shown in fig.(6.10a), fig.(6.10b) and fig.(6.10c) as a function of mean L_w/B ratio and beam Froude number. The output transom slopes, $\mathrm{Tan}(\phi)/\mathrm{Tan}(\tau)$, of these wetted bottoms have a mean value of 1.4 with a discrepancy, in any case, of not more than $\pm$ 2% about this mean level. The roll moment coefficient slopes, $[C_{rm}/\mathrm{Tan}(\phi)]_z$, presented in fig.(6.10c) are the components due to the lift forces. These roll moment coefficient slopes, as discussed earlier in section (6.4), are independent of the trim and the heel angles. The total roll moment coefficient slope, $[C_{rm}/\mathrm{Tan}(\phi)]_{\phi=\phi_1}$, at a particular heel angle, ϕ_1, including the effect of the sway force can be obtained from the relation:

$$\left[\frac{C_{rm}}{\mathrm{Tan}(\phi)}\right]_{\phi=\phi_1} = \left[\frac{C_{rm}}{\mathrm{Tan}(\phi)}\right]_z \left(1.0 + \mathrm{Tan}^2(\phi_1)\right) \qquad (6.6.3).$$

Note that, according to the sign convention shown in fig.(6.6a), the negative values of $[C_{rm}/\mathrm{Tan}(\phi)]_z$ in the figure indicate positive righting moments. At beam Froude number of 2.0 and mean $L_w/B > 2.2$, the predicted centre of pressure ratios, L_{cp}/B, have suffered badly from the pressure divergence problem discussed in section (3.6), although oscillations were not observed in the pressure solutions. However, the effect of these deteriorated pressures on the lift coefficient slopes and the roll moment coefficient slopes is less pronounced.

The weight, W, and the position of the centre of gravity forward of the transom, L_{cg}, of a heeled planing flat plate can be defined by the weight coefficient, $W^*=W/(^1/_2\rho gB^3)$, and the ratio, L_{cg}/B. The procedure for determining the running mean L_w/B ratio (wetted bottom area to beam squared ratio), the running trim angle, and the roll moment coefficient slope under this loading condition can be described as follows:

(1) Determination of running mean L_w/B ratio

For a given beam Froude number, the longitudinal centre of pressure ratios, L_{cp}/B, predicted from wetted bottoms with a fixed spray root geometry are only dependent on the mean wetted length to beam ratios. The running mean wetted length to beam ratio at a given Cv, say $[L_w/B]_1$, can therefore be obtained by matching the longitudinal centre of gravity ratio, L_{cg}/B, of the plate to the computed centre of pressure ratios, L_{cp}/B, presented in fig.(6.10b). This procedure is the same as the one discussed in section (4.6) for a non-heeled planing flat plate.

(2) Determination of running trim and heel angles

The lift coefficient slope, say $[C_{fz}/\mathrm{Tan}(\tau)]_1$, at the mean wetted length to beam ratio, $[L_w/B]_1$, and the starting beam Froude number is then obtained from the computed lift coefficient slopes shown in fig.(6.10a). The running trim angle, say τ_1, can be obtained by matching the weight of the plate to the planing lift. Since the lift varies linearly with the angle of trim for a wetted bottom of fixed spray root geometry, τ_1 is simply given by:

$$\mathrm{Tan}(\tau_1) = \frac{W^*}{Cv^2\ [C_{fz}/\mathrm{Tan}(\tau)]_1} \qquad (6.6.4).$$

The heel angle, say ϕ_1, required to produce the spray root geometry, $(L_{c2}-L_{c1})/B=1.0518$, is given by:

$$\mathrm{Tan}(\phi_1) = \left[\frac{\mathrm{Tan}(\phi)}{\mathrm{Tan}(\tau)}\right] \mathrm{Tan}(\tau_1) \qquad (6.6.5),$$

where $[\mathrm{Tan}(\phi)/\mathrm{Tan}(\tau)]$ is the output transom slope and, in this case, is equal to 1.4.

(3) Determination of roll moment coefficient slope

We have shown in section (6.4) that, for a given mean L_w/B ratio, spray root geometry and beam Froude number, the roll moment coefficient slope, $[C_{rm}/\mathrm{Tan}(\phi)]_z$, produced by the lift is independent of both the trim and the heel angles. Having determined the required running mean wetted length to beam ratio, $[L_w/B]_1$, at the starting Cv from (1), the $[C_{rm}/\mathrm{Tan}(\phi)]_z$ at this running condition can be obtained by interpolating between the computed $[C_{rm}/\mathrm{Tan}(\phi)]_z$ results presented in fig.(6.10c). The total roll moment coefficient slope, say $[C_{rm}/\mathrm{Tan}(\phi)]_{\phi=\phi_1}$, at $\phi=\phi_1$ is then obtained from the relation given in expression (6.5.3).

Although the above procedure places no restriction on the weight of the plate, however, one must always be aware of the fact that both the trim and the heel angles have to be small in order to satisfy the basic assumptions of a linearized theory.

The method discussed above has been applied to heeled planing flat plates of weight coefficient, $W^*=1.3$, and L_{cg}/B ratios ranging from 1.05 to 1.45. Again, a third order Lagrange interpolating polynomial was employed for the interpolating processes. Since the heel angle has been shown to have little effect on the lift and the longitudinal centre of pressure position, the predicted running mean L_w/B ratios and running trim angles will be compared with those obtained from the Savitsky's empirical equations (4.3.3) and (4.4.1). The present predictions are shown in fig.(6.11a) and fig.(6.11b) as a function of beam Froude number, together with the results obtained from the empirical equations for the cases of $L_{cg}/B=1.05$ and 1.45. Each of the predicted trim angle

curves in fig.(6.11b) are extended backward to the point at Cv=0.0. The lift at rest is produced purely by buoyant effect, and the trim angle at rest, τ_o, is given by:

$$\mathrm{Tan}(\tau_o) = \frac{W^*}{(L_w/B)_o^2} \qquad (6.6.6),$$

where $(L_w/B)_o$ is the wetted length to beam ratio at rest given by:

$$(L_w/B)_o = 3\,(L_{cg}/B) \qquad (6.6.7).$$

It can be seen from fig.(6.11a) that, for a fixed load and fixed longitudinal centre of gravity position, both the present theory and the Savitsky's empirical equation (4.4.1) show the tendency of decreasing in mean wetted length to beam ratio with the increase of speed. Generally speaking, the present theory usually gives smaller mean L_w/B ratios than the empirical equation, though this tendency seems to have reversed at low speeds. At high beam Froude numbers, the present L_{cg}/L_w ratio approaches a constant value of about 0.8. This corresponds to an increase of about 7% when compared to the value of 0.75 given by the empirical equation.

An interesting feature displayed in fig.(6.11b) is that the running trim angle rises initially above its respective rest value as the plate moves from rest. This initial rise in trim angle can be caused by two factors; one is due to the rapid reduction in wetted length as the speed increases from rest and the other is due to the negative hydrodynamic effect on the lift at low speed. Savitsky (Ref.(44)) noted that at a very low speed, the hydrodynamic reaction of the water actually reduced the lift below the value which would be expected on a purely displacement basis. At high beam Froude numbers, the present trim angles agree very well with the values obtained from the Savitsky's empirical equations (4.3.3) and (4.4.1). At low beam Froude numbers, however, the

present theory has predicted trim angles that are much smaller than those obtained from the empirical equations. On the other hand, it is known that the Savitsky's empirical equations are less accurate at low speeds.

The results for the roll moment coefficient slopes, $C_{rm}/Tan(\phi)$, are shown in fig.(6.11c). It can be seen that, for a given load, the predicted roll moment coefficient slope in general increases with the centre of gravity ratio, L_{cg}/B, of the plate. This would imply that the roll stability can be improved by shifting the centre of gravity forward from the transom. The results indicate that the improvement could be quite significant at the lower speed range. However, one must also notice that this might reduce the craft's performance in other aspects - for example, the increase in bottom drag. One can also see from fig.(6.11c) that the roll moment slopes decrease continuously as the speed increases. In particular, the rapid drop in roll moment coefficient slope between beam Froude numbers of 2 and 4 suggests that a rapid decrease in roll stability at this speeds. It should be noted that the transom running beam of the heeled plate is assumed to be completely wetted in the present solution. In the case of very low L_{cg}/B ratio, the transom running beam at the heeled up side of the plate can become partially dry. This could give rise to an increase in righting moment as a result of the rapid loss in wetted area under the heeled up side of the plate.

CHAPTER (7) Some Results for the Planing of Constant Deadrise Prismatic Hulls in Heel Condition

7.1 Introduction

In this chapter, we will apply the present finite element method to predict the pressures under the bottom of a constant deadrise prismatic hull when it is planing in a heel condition. Again, only small heel, trim and deadrise angles will be considered. Fig.(7.1) shows a sketch of the asymmetrical wetted bottom of a planing constant deadrise prismatic hull in heel condition. As before, the forward thrown spray sheet and the slightly curvature at the spray root will be ignored in the present computations and the running beam at the transom is assumed to be completely wetted during the planing motion. The mean wetted length to beam ratio, L_w/B, or the wetted area to beam squared ratio for such a wetted bottom can be defined in terms of its transom wetted beam, B, its wetted keel length, L_k, and its wetted chine lengths, L_{c1} (heeled up side) and L_{c2} (heeled down side), as:

$$\frac{L_w}{B} = \frac{2L_k + L_{c1} + L_{c2}}{4B} \qquad (7.1.1).$$

An 'average wetted length to beam ratio', λ_{rp}, for planing prismatic hulls in heel was used by Jahangeer (Ref.(66)):

$$\lambda_{rp} = \frac{1}{2B}\left[\frac{L_k + L_{c2}}{2} + L_{c1}\right] \qquad (7.1.2).$$

This 'average wetted length to beam ratio' is not the wetted area to beam squared ratio of the wetted bottom and should not be confused with the present definition. A typical finite element representation of the projected wetted bottom of a planing prismatic hull in heel condition is shown in fig.(7.2). The input local hull displacement function above the transom level is the same as that for the zero heel angle case.

An interesting feature of heeled planing prismatic hulls is that the point associated with zero yawing moment (longitudinal centre of lateral resistance) can be well separated from the point associated with zero pitching moment (longitudinal centre of lift). Thus, in addition to a rolling moment and a sway force, there is also a net yawing moment acting about the centre of gravity of the craft. This is different from a heeled planing flat plate in which the net yawing moment about the centre of gravity is zero. This particular aspect of planing has been confirmed by the experimental measurements of Wellicome and Campbell (Ref.(57)) and has also been observed in the present computational results.

Section (7.2) discusses the relationship between the spray root geometry, the heel angle, the trim angle and the deadrise angle. Section (7.3) investigates the effect of the heel angle on the induced sway force, rolling moment and yawing moment for a fixed trim condition. The computational results suggest that, for a given loading condition and planing speed, these hydrodynamic force and moments vary linearly with the angle of heel. Section (7.4) compares the present results with the theoretical predictions and the experimental measurements of Jahangeer (Ref.(66)) for a 15° constant deadrise hull in heel condition. The application of the present finite element method to the determination of the hydrodynamic forces and moments derivatives, $\partial C_{fy}/\partial\phi$, $\partial C_{rm}/\partial\phi$ and $\partial C_{ym}/\partial\phi$, for a prismatic hull of fixed loading condition will be discussed in section (7.5). Finally, the hydrodynamic forces and moments derivatives predicted for a 10° constant deadrise hull will be compared with the experimental measurements of Wellicome and Campbell (Ref.(57)) in section (7.6).

7.2 Selection of Spray Root Profile

Based on the $\pi/2$ wave rise factor computed by Wagner (Ref.(19)) for a two dimensional wedge penetrating vertically into a fluid surface and the assumption of no water piling up at the keel line, it can be shown analytically, as for the heeled planing flat plate discussed in section

analytically, as for the heeled planing flat plate discussed in section (6.2), that the spray root geometry of a planing constant deadrise prismatic hull in heel condition is given by:

$$\frac{(L_k - L_{c1})}{B} = \frac{\mathrm{Sin}(\beta+\phi)}{\pi \mathrm{Cos}(\beta)\ \mathrm{Tan}(\tau)} \qquad (7.2.1a)$$

and

$$\frac{(L_k - L_{c2})}{B} = \frac{\mathrm{Sin}(\beta-\phi)}{\pi \mathrm{Cos}(\beta)\ \mathrm{Tan}(\tau)} \qquad (7.2.1b),$$

where β is the deadrise angle, τ is the trim angle, ϕ is the heel angle, B is the transom wetted beam, L_k is the wetted keel length and L_{c1} and L_{c2} are the wetted chine lengths at the heeled up and the heeled down sides respectively.

Fig.(7.3) shows the shape of the transoms obtained from a spray root profile of $(L_k-L_{c1})/B=0.958$ and $(L_k-L_{c2})/B=0.587$ for various mean L_w/B ratios and beam Froude numbers. The wetted bottoms were divided symmetrically into six buttock strips, each of equal width, and it can be seen that the predicted transoms are slightly curved as a result of ignoring the curvature at the spray root. However, unfortunately, oscillatory pressure solutions were observed at Cv=2.5 for moderate mean L_w/B ratios, though, surprisingly, they have not manifested themselves in the results for the vertical location along the transom. The number of buttock strips was then reduced to four in the latter computations in order to obtain more satisfactory pressure results at lower beam Froude numbers.

Table (7.1) compares the computed trim angles and heel angles with the estimations from expressions (7.2.1a) and (7.2.1b) for a 10° constant deadrise hull. For an assumed heel angle, trim angle and deadrise angle, an initial estimate of the spray root geometry was first obtained from the analytical expressions. The output trim and heel angles for a given mean L_w/B ratio and beam Froude number were then determined from the output transom slopes, $\mathrm{Tan}(\beta+\phi)/\mathrm{Tan}(\tau)$ (heeled up side) and $\mathrm{Tan}(\beta-\phi)/\mathrm{Tan}(\tau)$ (heeled down side). Four buttock strips of

equal width were used in these computations. In general, the heel angles predicted by the present theory are in very good agreement with those obtained from expressions (7.2.1a) and (7.2.1b), with a difference of not more that $\pm$1.4% between the two results. The computed trim angles, however, have consistently shown an increase of about 11% when compared with the corresponding values given by the analytical expressions. Again, a possible cause of these differences could be the assumption of no water piling up at the keel line in deriving the analytical expressions, which itself may not be strictly accurate. On the other hand, the results presented in table (7.1) and fig.(7.3) seem to agree with the the analytical expressions that the output transom shape is only dependent on the geometry of the spray root but not dependent on the mean L_w/B ratio and the planing speed.

7.3 Variation of Hydrodynamic Forces and Moments with Heel Angle

In this section, we investigate the effect of the heel angle on the the sway force, the rolling moment and the yawing moment induced by the planing motion of a heeled prismatic hull. The aim of this investigation is to confirm the linear relationships between the heel angle and these hydrodynamic forces and moments at small angle of heel.

The sign conventions for the lift force, the sway force, the rolling moment, the yawing moment and the heel angle are shown in fig.(7.4). The datum of these force and moments is taken to be at the intersection of the keel line and the transom. Rolling to the starboard, swaying and yawing to port are treated as positive. For a heeled constant deadrise prismatic hull, the sway forces and the yawing moments, as well as the rolling moments, contributed by the bottom pressures on the port and starboard sides of the hull are acting in an opposite direction. Thus, the relationship given in (6.3.1) is no longer applicable here. The resultant sway force, yawing moment and rolling moment are therefore obtained from the differences between their corresponding port and starboard components. The non-dimensional sway force coefficient, C_{fy}, yaw moment coefficient, C_{ym}, and roll moment coefficient, C_{rm}, are defined as follows:

$$C_{fy} = \frac{F_y}{{}^1/_2\,\rho g B^3\, Cv^2} \qquad (7.3.1),$$

$$C_{ym} = \frac{M_y}{{}^1/_2\,\rho\, g B^4} \qquad (7.3.2)$$

and

$$C_{rm} = \frac{M_r}{{}^1/_2\,\rho\, g B^4} \qquad (7.3.3),$$

where F_y is the sway force, M_y is the yawing moment about the transom and M_r is the rolling moment about the keel. As in the case of heeled planing flat plate, a non-dimensional rolling moment arm, R/B, can be defined as:

$$\frac{R}{B} = \frac{M_r}{(F_z^2+F_y^2)^{1/2}\, B} \qquad (7.3.4).$$

It can also be shown from the hull geometry of a heeled prismatic hull that the sway force is not necessary acting at the same point as the resultant of the drag and the lift forces. It follows that the net yawing moment about the centre of gravity of the craft is not necessary equal to zero. This suggests that the introduction of a heel angle will cause the craft to roll, to sway and to yaw. Thus, there is a coupling between the sway, yaw and roll motions. Neglecting the effect of pressure drag at small trim angles, the longitudinal centre of lateral resistance, L_{CLR}, - i.e. the point associated with zero net yawing moment - forward of the transom is given by:

$$L_{CLR} = \frac{\text{Yawing Moment about Transom } (M_y)}{\text{Sway Force } (F_y)} \qquad (7.3.5)$$

and the longitudinal centre of lift, L_{CL}, - i.e. the point associated with zero pitching moment - forward of the transom is given by:

$$L_{CL} = \frac{\text{Pitching Moment about Transom}}{\text{Lift Force}} \qquad (7.3.6).$$

Fig.(7.5a) to fig.(7.5g) show the computational results obtained for a 15° constant deadrise hull in heel condition. Two beam Froude numbers, Cv, of 3.0 and 5.5 and heel angles ranging from 3° to 10° were considered. The output transom shapes give a trim angle of about 7°. It can be seen from fig.(7.5a) and fig.(7.5b) that for a given mean L_W/B ratio, trim angle and beam Froude number, the predicted lift coefficient slopes, $C_{fz}/\mathrm{Tan}(\tau)$, and longitudinal centre of lift ratios, L_{CL}/B, are almost independent of the heel angles. Also shown in the same figures are the lift coefficient slopes and the longitudinal centre of lift ratios computed for the case of zero heel angle at the same angle of trim and beam Froude numbers. These also nearly fall on the theoretical curves for the heeled cases, justifying the present definition of mean L_W/B ratio, i.e. wetted bottom area to beam squared ratio, rather than λ_{rp}. For the mean L_W/B ratios and beam Froude numbers considered, the discrepancies in lift coefficient slopes and longitudinal centre of lift ratios between different heel angles are in the order of 3% and 4% respectively.

The results for the roll moment coefficient slopes, $C_{rm}/\mathrm{Tan}(\phi)$, and the rolling moment arm ratios, $R/(B\mathrm{Tan}(\phi))$, are shown in fig.(7.5c) and fig.(7.5d). The very close agreement between the values of $C_{rm}/\mathrm{Tan}(\phi)$ obtained at different heel angles suggests that, for a given mean L_W/B ratio, trim angle and beam Froude number, a linear relationship exists between the rolling moment and heel angle. In general, the computed rolling moment arm ratios, $R/(B\mathrm{Tan}(\phi))$, also display the same feature, although a slightly larger discrepancy of around 9% has been found at large L_W/B ratio for the case of beam Froude number equal to 3.0.

Fig.(7.5e) and fig.(7.5f) show the variations of the sway force

coefficient slopes, $C_{fy}/(\mathrm{Tan}(\tau)\mathrm{Tan}(\phi))$, and the yaw moment coefficient slopes, $C_{ym}/(\mathrm{Tan}(\tau)\mathrm{Tan}(\phi)Cv^3)$, against heel angles. The overall results also seem to suggest that, for a given mean L_W/B ratio, trim angle and beam Froude number, both the sway force and the yaw moment vary linearly with the angle of heel. Again, for the sway force coefficient slopes, a slightly larger discrepancy of about 6% has been found at large mean L_W/B ratio for the case of beam Froude number equal to 3.0. Since both the sway force and the yawing moment about the transom vary linearly with the heel angle, it can be expected that the corresponding longitudinal centre of lateral resistance, L_{CLR}/B, is independent of the heel angle. This aspect also seems to be verified by the present computations for L_{CLR}/B, as shown in fig.(7.5g). Finally, the results for the distance of the longitudinal centre of lateral resistance forward of the longitudinal centre of lift, $(L_{CLR}-L_{CL})/B$, are shown in fig.(7.5h). As the yawing moment about the centre of lift/centre of gravity is equal the product of the distance, $(L_{CLR}-L_{CL})$, and the sway force, F_y, $(L_{CLR}-L_{CL})/B$ can be regarded as the non-dimensional yawing moment arm for the net yawing moment about the centre of lift position. The overall results for $(L_{CLR}-L_{CL})/B$ seem to suggest that the yawing moment arm about the centre of lift position is independent of the heel angle for a given mean L_W/B ratio, trim angle and beam Froude number. Furthermore, as the sway force varies linearly with the heel angle, the results would imply that the yawing moment about the centre of lift position also varies linearly with the heel angle. Note that at a beam Froude number of 3.0, the present theory predicts positive values of $(L_{CLR}-L_{CL})/B$ for large mean L_W/B ratios. This suggests that a reverse in the direction of the yawing moment about the centre of lift position (for sign convention, see fig.(7.4)).

To summarize, the above investigation indicates two important aspects. They are

(1) for a given mean L_W/B ratio, trim angle and beam Froude number, the sway force, the rolling moment and the yawing moment all vary linearly with the heel angle, and

(2) for a given mean L_w/B ratio, trim angle and beam Froude number, both the lift and the longitudinal centre of lift position are independent of the heel angle.

These would imply that, for a given craft's loading condition and speed, these hydrodynamic forces and moments vary linearly with the heel angle. At sufficiently small heel angles, the sway force coefficient, C_{fy}, the roll moment coefficient, C_{rm}, and the yaw moment coefficient, C_{ym}, can therefore be expressed as:

$$C_{fy} = \frac{\partial C_{fy}}{\partial \phi} \phi$$

$$C_{rm} = \frac{\partial C_{rm}}{\partial \phi} \phi$$

and

$$C_{ym} = \frac{\partial C_{ym}}{\partial \phi} \phi \qquad (7.3.7),$$

where ϕ is the heel angle in radians, $\partial C_{fy}/\partial \phi$, $\partial C_{rm}/\partial \phi$ and $\partial C_{ym}/\partial \phi$ are the partial derivatives of the sway force coefficient, the roll moment coefficient and the yaw moment coefficient with respect to the heel angle which are equal to $C_{fy}/\mathrm{Tan}(\phi)$, $C_{rm}/\mathrm{Tan}(\phi)$ and $C_{ym}/\mathrm{Tan}(\phi)$. Each of these derivatives can be regarded as a function of planing speed, craft's weight and craft's longitudinal centre of gravity position (running trim and running mean wetted length to beam ratio). The method for determining these derivatives will be discussed further in section (7.5).

7.4 Comparison of Results

In this section, the present computational results are compared with the theoretical predictions and experimental measurements of Jahangeer

(Ref.(66)) for a 15° constant deadrise hull in heel condition. The spray root geometry of the projected wetted bottom is defined by $(L_k-L_{c1})/B=1.325$ and $(L_k-L_{c2})/B=0.273$, which corresponds to a trim angle of 6° and heel angle of 10° according to expressions (7.2.1a) and (7.2.1b). The trim angles and heel angles determined from the output transom slopes have a mean value of about 7° and 9.7° respectively. Two mean wetted length to beam ratios, L_w/B, of 2.67 and 2.08 and a range of beam Froude numbers, from 2.0 to 10.5, are considered. Note that the corresponding 'average wetted length to beam ratios (λ_{rp})' in Jahangeer's paper were 2.38 and 1.7 respectively.

Besides the differences in element types and sizes, there is another major difference between the present and Jahangeer's wetted bottom grids. As shown in fig.(7.2), the projected wetted bottom used in the present computations is divided into four buttock strips, each of equal width. In Jahangeer's calculations, however, the projected wetted bottom was divided in an asymmetrical fashion with three buttock strips on the heeled up half of the wetted bottom and two buttocks on the other, as shown in fig.(7.6). As mentioned in the previous section, the resultant sway force, rolling moment and yawing moment are calculated from the differences between the pressure forces and moments acting on the port and starboard sides of the hull about the keel line. By arranging the buttock strips symmetrically about the keel, the errors in calculating these pressure forces and moments on the two sides of the hull should be of the same order and therefore the errors in calculating the resultant sway force, rolling moment and yawing moment will be largely reduced by the subtracting process. Thus, as far as the calculations of these hydrodynamic forces and moment are concerned, a symmetrical buttocks configuration should give a better accuracy. This aspect could be important in particular that when a small number of buttock strips are used.

Fig.(7.7a) and fig.(7.7b) compare the present lift coefficient slopes, $C_{fz}/\mathrm{Tan}(\tau)$, and longitudinal centre of lift ratios, L_{cL}/B, with the theoretical predictions and experimental measurements of Jahangeer. In general, there is a reasonable agreement between the present

lift coefficient slopes and Jahangeer's results, although the present theory has predicted larger values than his theoretical predictions for beam Froude numbers less than 3.0 and his experimental measurement at Cv=2.52 and L_w/B=2.67. As in the planing of a heeled flat plate, for both mean L_w/B ratios, the longitudinal centre of lift positions predicted by Jahangeer are generally more forward from the transom than those predicted by the present theory. However, as before, the present result is in better agreement with his experimental measurement at L_w/B=2.67 and Cv=2.52.

Good agreement also exists between the present roll moment coefficient slopes, $C_{rm}/(\mathrm{Tan}(\phi)\mathrm{Tan}(\tau))$, non-dimensional rolling moment arms, $R/(B\mathrm{Tan}(\phi))$, and Jahangeer's experimental results as shown in fig.(7.7c) and fig.(7.7d). However, at high beam Froude numbers, the righting moments predicted by the present theory are considerably larger than Jahangeer's theoretical predictions. As mentioned earlier in this section, the heeled up half of the wetted bottom in Jahangeer's calculation was divided into three buttock strips and this could produce a larger negative righting moment, i.e. positive M_r, about the keel due to the increase in the moment arms of the pressures at outer most buttock. The large discrepancy between the two theoretical predictions at high speeds might be due to the difference in the element arrangements of the present and Jahangeer's wetted bottom grids. Note that the wetted bottom grid in fig.(6.2) used for the heeled planing flat plate calculations has the same buttocks layout, i.e. four buttocks arranged symmetrically about the centre line, as that used in Jahangeer's calculations. The results for the roll moment coefficient slope presented in fig.(6.8a) are, not surprisingly, in good agreement with Jahangeer's predictions.

The predicted sway force coefficient slopes, $C_{fy}/(\mathrm{Tan}(\phi)\mathrm{Tan}(\tau))$, yaw moment coefficient slopes, $C_{ym}/(\mathrm{Tan}(\phi)\mathrm{Tan}(\tau)Cv^3)$, and longitudinal centre of lateral resistance ratios, L_{CLR}/B, are shown in fig.(7.7e), fig.(7.7f) and fig.(7.7g) respectively. Like the longitudinal centre of lift, the longitudinal centre of lateral resistance for each mean L_w/B ratio has approached a constant distance forward of the transom at high

beam Froude numbers. However, the later computational results and the experimental measurements of Wellicome and Campbell (Ref.(57)) have shown that the centre of lateral resistance can be situated at a point behind the transom at high speed when the associated trim angle and mean wetted length to beam ratio are small. The later computational results also suggest that both $C_{Fy}/Tan(\phi)$ and $C_{ym}/Tan(\phi)$ do not vary linearly with the trim angle for a given mean L_w/B ratio and beam Froude number. That is to say the results presented in these figures are only valid for the present wetted bottom. These sway forces, yawing moments and longitudinal centre of lateral resistance ratios had not been computed or measured by Jahangeer.

Fig.(7.8) compares the present pressure distributions with the experimental measurements of Jahangeer for a mean L_w/B ratio of 2.67 and a beam Froude number of 2.54. Reasonable agreement has been obtained between the predicted and measured pressure distributions along the chines, especially at the heeled up side where the present computations confirmed the experimental measurements closely. As shown in fig.(7.2), the present wetted bottom grid does not allow a set of control points to be located along the keel line. However, judging from the means of the pressures predicted along the lines $\pm$ B/8 from the keel, the present theory seems to have under-estimated the experimental pressure measurements along the forward half of the keel.

7.5 Determination of Hydrodynamic Forces and Moments acting on a Heeled Planing Prismatic Hull of Specified Loading Condition

As mentioned in the preceding chapters, the shape and extent of the projected wetted bottom is required to be prescribed in the present computational method, therefore, the hydrodynamic forces and moments derivatives, $\partial C_{Fy}/\partial\phi$, $\partial C_{rm}/\partial\phi$ and $\partial C_{ym}/\partial\phi$, for a craft of specified loading condition cannot be directly predicted. Again, these forces and moments derivatives can be determined by means of interpolating methods. For a given deadrise hull, this would require computations for an assumed range of trim angles, mean wetted length to beam ratios and

speeds to be carried out at a fixed heel condition. For each beam Froude number considered, the following parameters are required to be computed as a function of mean L_W/B ratio and trim angle:

(a) lift coefficient (C_{fz}),

(b) longitudinal centre of lift ratio (L_{cL}/B),

(c) sway force coefficient slope ($C_{fy}/\mathrm{Tan}(\phi)$),

(d) yaw moment coefficient slope about the transom ($C_{ym}/\mathrm{Tan}(\phi)$),

(e) roll moment coefficient slope about the keel ($C_{rm}/\mathrm{Tan}(\phi)$).

The computed lift coefficients (a) and longitudinal centre of lift ratios (b) allow us to determine the running trim angle and the running mean wetted length to beam ratio for a particular craft's loading condition. The interpolating procedure for matching the computed lift and longitudinal centre lift position to the craft's weight and the craft's longitudinal centre of gravity position is the same as the one discussed in section (5.7) for the non-heeled case. Once the running trim angle and the running mean wetted length to beam ratio have been obtained, the corresponding hydrodynamic forces and moments derivatives can be easily determined from the computed sway force coefficient slopes (c), yaw moment coefficient slopes (d) and roll moment coefficient slopes (e) by interpolation. The longitudinal centre of lateral resistance ratio, L_{cLR}/B, can be obtained by dividing the predicted yawing moment by the predicted sway force. Note that the method to scale the trim angle and the heel angle using a fixed spray root geometry, as discussed in section (6.5) for a heeled planing flat plate, cannot be applied in the present case. This is because, now, for a fixed spray root geometry, i.e. fixed output transom slopes $\mathrm{Tan}(\beta+\phi)/\mathrm{Tan}(\tau)$ and $\mathrm{Tan}(\beta-\phi)/\mathrm{Tan}(\tau)$, there could only be one solution in the heel angle, ϕ, and the trim angle, τ, for a given deadrise angle, β.

Computations have been carried out to determine the above (a), (b), (c), (d) and (e) for a 10° constant deadrise prismatic hull. Beam Froude numbers ranging from 2.0 to 6.5 (increasing at 0.25 increment) have been

considered. The spray root geometries used for the computations together with the output trim angles (ranging from 2.5° to 7.2°) and the output heel angles (mean value of about 3.62°) are shown in table (7.1). For Cv>4.0, however, the trim range has been reduced to 2.5° to 6° simply because the running trim angle required to produce a given craft's weight reduces with the planing speed. A range of mean L_W/B ratios from 1.65 to 2.85 have been considered for all beam Froude numbers, with the exception of the cases of Cv = 2.25 and 2.0 in which the range has been reduced to 1.65 to 2.40 and 1.65 to 2.15 due to the oscillatory pressure solutions encountered at higher mean L_W/B ratios. Note that a further reduction in mean L_W/B ratio at small trim angle can result in partial dryness of the transom running beam at the heeled up side of the hull.

Some of these computational results are shown in fig.(7.9.1) and fig.(7.9.2). It can be seen from the results in these figures that, for a given mean L_W/B ratio and beam Froude number, the computed lift coefficient, C_{fz}, varies linearly with the trim angle and the location of the longitudinal centre of lift gradually moves toward the transom as the trim angle decreases. These tendencies have also been observed in the zero heel angle case and are shown in fig.(5.12) and fig.(5.13). Like the longitudinal centre of lift, the longitudinal centre of lateral resistance, L_{CLR}, also moves toward the transom as the trim angle decreases. However, the rate of decrease of the longitudinal centre of lateral resistance to beam ratio, L_{CLR}/B, is considerably higher than that of the longitudinal centre of lift to beam ratio, L_{CL}/B, and this is particular true for small mean L_W/B ratio and small trim angle when the swept back angle at the spray root becomes large. Strictly speaking, for a given mean L_W/B ratio and beam Froude number, both the sway force coefficient slope, $C_{fy}/\mathrm{Tan}(\phi)$, and the yaw moment coefficient slope, $C_{ym}/\mathrm{Tan}(\phi)$, do not vary linearly with the trim angle. Fig.(7.10a) and fig.(7.10b) show the variation of roll moment coefficient slope, $C_{rm}/\mathrm{Tan}(\phi)$, against trim angle for beam Froude numbers of 3.0 and 5.5. For a heeled planing flat plate, it has been shown in section (6.3) that the trim angle has little effect on the roll moment coefficient slope. The present results also display this feature to some extent, though a difference of up to $\pm$ 20% about the mean level (denoted by the solid

lines in the figures) has been observed between the values of $C_{rm}/Tan(\phi)$ at different trim angles. These differences, however, might be due to the variation in the shape and the size of the elements used in the computations. For interpolating purpose, the roll moment curves have been smoothed out by plotting $C_{rm}/(Tan(\phi)Tan(\tau))$, instead of $C_{rm}/Tan(\phi)$, against the trim angles as shown in fig.(7.9.1f) and fig.(7.9.2f).

Although computations have only been carried out for a 10° constant deadrise hull, the results for other planing surfaces can also be obtained in a similar manner. The 'data-base' for feeding the interpolating program can be expanded to cover a wide range of deadrise angles, mean L_w/B ratios, trim angles and speeds. This would allow users to estimate the hydrodynamic forces and moments derivatives together with the running trim and the running wetted length quickly for a wide range of craft's displacements and craft's longitudinal centre of gravity positions without going through the tedious integration process. This implies that the use of the present interpolation scheme in engineering design would be a practical proposition.

7.6 Comparison of Hydrodynamic Forces and Moments Derivatives for fixed Bottom Loading Coefficient and Wetted Keel Length to Beam Ratio

The hydrodynamic forces and moments derivatives derived from the present theory for a 10° constant deadrise hull have been compared with the experimental measurements obtained by Wellicome and Campbell (Ref.(57)). Wellicome and Campbell conducted model tests to measure the hydrodynamic forces and moments for a series of constant deadrise prismatic hulls under restrained roll and yaw conditions. Models with deadrise angles ranging from 10° to 30° were tested. The roll restrained models in their experiments were free to heave and trim but were restrained to a given heel angle. The displacement of the model was defined by a non-dimensional bottom loading coefficient,

$$C_p = \frac{L_K B}{\nabla^{2/3}} \qquad (7.6.1),$$

where ∇ is the static displacement volume. The value of C_p was chosen to be constant over the range of wetted keel length to beam ratios, L_k/B, with C_p=5.7 for L_k/B=2.0, 2.5, 3.0, 3.5 and 4.0, C_p=7.8 for L_k/B=2.0, 3.0 and 3.5 and C_p=8.1 for L_k/B=4.0. For each deadrise angle, bottom loading coefficient, speed and wetted keel length, the roll moments and the sway forces were measured using force and moment dynamometers at a number of different heel angles between $\pm$ 7.5°. The roll moment and sway force derivatives were then determined from the slopes of the roll moment against heel angle curve and the sway force against heel angle curve by fitting straight lines to the experimental data. The sway force and roll moment derivatives were presented in non-dimensional forms,

$$F_2 = \frac{\partial F_y}{\partial \phi}\,\frac{1}{\Delta} \qquad \text{and} \qquad M_2 = \frac{\partial M_r}{\partial \phi}\,\frac{1}{\Delta B} \qquad (7.6.2),$$

where Δ is the weight of the model in Newtons. These results were plotted against Froude numbers based on the wetted keel length, $N_F=C/(gL_k)^{1/2}$. Some results for the location of the longitudinal centre of lateral resistance for the 25° deadrise model were also recorded. Note that although the bottom loading coefficient, C_p, was kept constant for the entire range of wetted keel length to beam ratios, the actual model displacement, Δ, for each L_k/B ratio was not the same. Also note that, for a given L_k/B ratio and C_p, the longitudinal centre of gravity location of the craft is a function of planing speed.

In order to compare with these experimental results, it was necessary to convert the characteristic length ratio, L_w/B, of the 'pre-calculated' data to L_k/B. Since the relationship between L_w/B and L_k/B at each calculated trim angle was known from the geometry of the input wetted bottom, there was no problem in obtaining the corresponding results for a particular L_k/B ratio. Again, this was achieved by an interpolating process which employed a third order Lagrange interpolating polynomial. For the cases of L_k/B=3.0 and $C_V \leq 2.25$ ($N_F \leq$ 1.3), however, extrapolation was used as the 'pre-calculated' data did not extend up to this particular L_k/B ratio for these speeds (see section 7.5).

The lift coefficient, C_{fz}, required to produce a given C_p for a given L_k/B ratio and beam Froude number can be obtained from the relation

$$C_{fz} = \frac{(L_k/B)^{1.5}}{{}^1/_2 \, C_p{}^{1.5} \, C_V{}^2} \qquad (7.6.3)$$

and the trim angle required to produce this lift was determined by interpolating the lift coefficient against trim angle curve for the given L_k/B ratio and beam Froude number. The sway force, roll moment and yaw moment derivatives and the L_{CL}/B ratio at the predicted trim angle were then obtained from their respective relations with the trim angles. The predicted yaw moment derivatives (about the transom) are also presented in a non-dimensional form,

$$N_2 = \frac{\partial M_y}{\partial \phi} \frac{1}{\Delta B} \qquad (7.6.4).$$

Unfortunately, no yaw moment data is available in Wellicome and Campbell report (Ref.(57)). The centre of lateral resistance ratio, L_{CLR}/B, was then calculated from the predicted sway force and yaw moment derivatives. Extrapolation had also been used in some high beam Froude number cases if the running trim angle required to produce the given C_p exceeded the lower limit of the assumed trim range.

As shown in fig.(7.11), the roll moment results presented in Wellicome and Campbell report are referred to a datum point which is located at the intersection of the keel line and the vertical plane through the centre of gravity of the craft. This is different from the present case where the roll moment is computed about the keel line (see fig.(7.4). In order to transform the predicted roll moment derivatives to the datum point shown in fig.(7.11), it was necessary to know the longitudinal centre of gravity locations and trim angles measured during

the experiments. However, these values are not presented in the report so the values predicted by the present theory were used instead. The predicted roll moment derivatives were then corrected, by taking into account of the interaction between the sway force, yawing moment and rolling moment, using the predicted trim angles and longitudinal centre of lift locations.

Following the above procedures, the coefficients, F_2, M_2 and N_2, and the ratios, L_{CLR}/B and L_{CL}/B, for a 10° deadrise hull have been obtained for three bottom loading coefficients, C_p=7.8, 5.7, and 3.3, and for two wetted keel length to beam ratios, L_K/B=2.5 and 3.0. Due to the oscillatory pressure solutions associated with large L_K/B ratios at low speeds, the results for L_K/B >3.0 have not been computed, although the present theory is quite capable to obtain results for L_K/B=3.5 and 4.0 at higher speeds, say Cv>4.0. The experiment measurements presented in (Ref.(57)) for the 10° deadrise model lie between the speed range $0.85 \leq N_F \leq 1.35$ for L_K/B=3.0 and $1.0 \leq N_F \leq 1.48$ for L_K/B=2.5, therefore only a few data spots are available for comparing with the present results. The present predictions together with the experimental measurements are shown in fig.(7.12a to e) to fig.(7.16a to e). The dotted curves shown in fig.(7.12) to fig.(7.14) for C_p=5.7 and 7.8 denote results obtained by extrapolation because the trim angles required to produce these C_p have exceeded the lower limit of the assumed trim range at these high speeds (trim angle reduces with the increase of speed for a given C_p). The trim angles associated with these extrapolated results are, in all cases, within 0.85° beyond the lower limit of the assumed trim range, therefore reasonable accuracy could still be expected. No extrapolation was required for the higher displacement case of C_p=3.3.

Fig.((7.12a), fig.(7.13a) and fig.(7.14a) compare the computed sway force derivative coefficients, F_2, with the experimental measurements of Wellicome and Campbell (Ref.(57)). In general, there is a reasonable agreement between the computational and the experimental results, although a rather large discrepancy of 30% is observed in the case of C_p=5.7 and L_K/B=3.0. The computed results indicate an overall increase in F_2 with the increase in displacement for a given L_K/B ratio. All the

computed F_2 curves (fig.(7.12a) to fig.(7.16a)) have reached a peak value at high speed. For the case of $L_K/B=2.5$, as shown fig.(7.14a) and fig.(7.16a), a declining tendency in F_2 is spotted at high speed. This declining tendency is shown explicitly in the experimental results of Wellicome and Campbell for models with higher deadrise angles, in which the declination occurs at a lower speed.

This declining tendency, which only seems to occur at high speed, could be related to the geometry of the planing wetted bottom. The sway force to planing lift ratio, F_y/F_z, can be obtained from the relation

$$\frac{F_y}{F_z} = \frac{(F_z)_u}{(F_z)_u+(F_z)_d} \mathrm{Tan}(\beta+\phi) - \frac{(F_z)_d}{(F_z)_u+(F_z)_d} \mathrm{Tan}(\beta-\phi) \qquad (7.6.5),$$

where $(F_z)_u$ and $(F_z)_d$ denote the planing lifts under the heeled up and the heeled down halves of the hull respectively. If we assume that $(F_z)_u$ and $(F_z)_d$ are equal to one half of the planing lift of a constant deadrise surface of deadrise angles $(\beta+\phi)^o$ and $(\beta-\phi)^o$, then, at small trim angles, $(F_z)_u$ and $(F_z)_d$ can be estimated from the Savitsky's empirical lift equation (5.3.2). As we are only interested in the sway force to planing lift ratio at high speed, the buoyant force term in the equation will be ignored and the planing lifts, $(F_z)_u$ and $(F_z)_d$, produced by pure hydrodynamic effect are given by:

$$(F_z)_u = \mathrm{Tan}(\tau)\ 57.296\ (0.012\ [A_{Wu}/2B_u^2]^{1/2})\rho\, B_u^2 C^2$$

and $$(F_z)_d = \mathrm{Tan}(\tau)\ 57.296\ (0.012\ [A_{Wd}/2B_d^2]^{1/2})\rho\, B_d^2 C^2 \qquad (7.6.6),$$

where A_{Wu} and A_{Wd} denote the wetted bottom areas under the heeled up and heeled down halves of the planing hull and B_u and B_d denote their respective half beams. Fig.(7.17) shows the typical variation in wetted bottom shape with the decrease of trim angle (or increase in speed) for a constant deadrise hull planing in heel condition. As shown in the

figure, for $\tau \geq T_{m1}$, the transom running beam is completely wetted at both sides of the hull and in this case $B_u = B_d = B/2$. If $T_{m2} \leq \tau < T_{m1}$, however, the transom running beam at the heeded up side of the hull will be partially dried and therefore $B_u < B/2$. The minimum trim angle, T_{m1}, in degrees required to keep the transom running beam completely wetted at both sides of the hull can be estimated using expression (7.2.1a):

$$T_{m1} = \mathrm{Tan}^{-1}\left[\frac{B}{L_k}\,\frac{\mathrm{Sin}(\beta+\phi)}{\pi\,\mathrm{Cos}(\beta)}\right] \qquad (7.6.7).$$

Similarly, from expression (7.2.1b), the minimum trim angle, T_{m2}, in degrees required for just the transom running beam at the heeled down side to remain completely wetted is

$$T_{m2} = \mathrm{Tan}^{-1}\left[\frac{B}{L_k}\,\frac{\mathrm{Sin}(\beta-\phi)}{\pi\,\mathrm{Cos}(\beta)}\right] \qquad (7.6.8).$$

The wetted area to beam squared ratios, A_{Wu}/B^2 and A_{Wd}/B^2, for $\tau \geq T_{m1}$ can be obtained from expressions (7.2.1a) and (7.2.1b):

$$\frac{A_{Wu}}{B^2} = \frac{(L_k+L_{c1})}{2}\,\frac{B}{2}\,\frac{1}{B^2} = \left[\frac{L_k}{B} - \frac{\mathrm{Sin}(\beta+\phi)}{2\pi\,\mathrm{Cos}(\beta)\mathrm{Tan}(\tau)}\right]\frac{1}{2} \qquad (\text{for } \tau \geq T_{m1})$$

and

$$\frac{A_{Wd}}{B^2} = \frac{(L_k+L_{c2})}{2}\,\frac{B}{2}\,\frac{1}{B^2} = \left[\frac{L_k}{B} - \frac{\mathrm{Sin}(\beta-\phi)}{2\pi\,\mathrm{Cos}(\beta)\mathrm{Tan}(\tau)}\right]\frac{1}{2} \qquad (\text{for } \tau \geq T_{m1})$$

(7.6.9).

For $T_{m2} \leq \tau < T_{m1}$, the wetted keel length to half beam ratio, L_k/B_u, can be derived, as discussed in section (6.2), from the $\pi/2$ wave rise factor computed by Wagner (Ref.(19)) for a two dimensional wedge penetrating vertically into a fluid surface. This gives

$$\frac{L_k}{B_u} = \frac{2\,\mathrm{Sin}(\beta+\phi)}{\pi\,\mathrm{Cos}(\beta)\mathrm{Tan}(\tau)} \qquad (7.6.10),$$

(for $\tau_{m2} \le \tau < \tau_{m1}$)

and the corresponding wetted area to beam squared ratio, A_{Wu}/B^2, is

$$\frac{A_{Wu}}{B^2} = \frac{1}{2B^2} B_u L_k = \frac{\mathrm{Cos}(\beta)\mathrm{Tan}(\tau)\,\pi}{4\,\mathrm{Sin}(\beta+\phi)} (L_k/B)^2 \qquad (7.6.11).$$

(for $\tau_{m2} \le \tau < \tau_{m1}$)

Substituting expression (7.6.6) into (7.6.5), we then have

$$\frac{F_y}{F_z} = \frac{(A_{Wu}/B^2)^{1/2}\,(B_u/B)\,\mathrm{Tan}(\beta+\phi) - (A_{Wd}/B^2)^{1/2}\,(B_d/B)\,\mathrm{Tan}(\beta-\phi)}{(A_{Wu}/B^2)^{1/2}\,(B_u/B) + (A_{Wd}/B^2)^{1/2}\,(B_d/B)} \qquad (7.6.12),$$

where the parameters A_{Wu}/B^2, B_u/B, A_{Wd}/B^2 and B_d/B can be evaluated using the above expressions according to the trim condition. Expression (7.6.12) suggests that, at high speed, the sway force to lift ratio is governed by the wetted bottom geometry and is not directly dependent on the planing speed.

The tabulated results in table(7.2) (for β=10° and 20°, L_k/B=2.5 and ϕ=3.62°) show that the area difference, $(A_{Wd}-A_{Wu})/B^2$, increases with the decrease of trim angle and it is not surprise that the sway force to planing lift ratio, which is calculated from expression (7.6.11) for high speed consideration, decreases with the trim angle. Since the decrease in trim angle can be interpreted as the increase in planing speed, the results would imply that, at high speed, F_2 (or $[F_y/F_z]/\mathrm{Tan}(\phi)$) decreases with the increase of planing speed. The results in table(7.2) also indicate that the direction of the sway force could be reversed, i.e. positive F_2, at very small trim angles. It would appear that the reverse in the direction of F_2 displayed in fig.(25) and fig.(28) of Ref.(57) for the 30° deadrise model is due to the rapid loss

in the wetted area under the heeled up side of the hull at small running trim condition. Note that the minimum trim angle, τ_{m1}, for a 30° deadrise surface is considerably larger than that for a 10° deadrise surface and this could encourage the above mentioned reverse tendency to occur at a lower speed.

The comparison between the present roll moment derivative coefficients, M_2, and the experimental results of Wellicome and Campbell (Ref.(57)) are shown in fig.(7.12b) to fig.(7.14b). The agreement between the two results is reasonable, though not as good as that for F_2. Again, a rather large error of about 27% is spotted at C_p=5.7 and L_k/B=3.0. The present theory predicts a peak value in M_2 around 1.26 <N_F< 1.58 (depending on the values of C_p and L_k/B), with the exception of C_p=5.7 and L_k/B=2.5 where the peak does not occur inside the speed range considered. This is followed by a rapid decline in M_2 as the speed is further increased. There is an overall decrease in M_2 with the increase of displacement for a given L_k/B ratio. Note that a possible cause of the differences between the computational and experimental values of M_2 could be the differences in the computed and the measured longitudinal centre of gravity locations and running trim angles.

The results for the yaw moment derivative coefficients, N_2, and the longitudinal centre of lateral resistance ratios, L_{CLR}/B, are shown in fig.(7.12c) to fig.(7.16c) and fig.(7.12d) to fig.(7.16d) respectively. Both the computed N_2 and L_{CLR}/B curves increase initially with the planing speed. This is followed by a rapid decline at higher speeds. Negative values of L_{CLR}/B, i.e. centre of lateral resistance behind the transom, have been obtained in the lower displacement cases of C_p=5.7 and 7.8. The same tendency also appears in the experimental results of Wellicome and Campbell (Ref.(57)) for the 25° deadrise model with C_p=5.7 and L_k/B=3.0 as shown in fig.(7.13d). For a given L_k/B ratio, the rates of decline of N_2 and L_{CLR}/B have been found to reduce with the increase of displacement and the L_{CLR}/B ratios predicted for the higher displacement case of C_p=3.3 remain positive for the speed range considered.

These negative L_{CLR}/B, which seem to occur only at high speed, might also be related to the geometry of the planing wetted bottom. The yawing moment (about the transom) to lift-beam ratio, $M_y/(F_z B)$, can be calculated from the relation

$$\frac{M_y}{B\,F_z} = \frac{(F_z)_u}{(F_z)_u+(F_z)_d}\,\frac{L_{CLu}}{B}\,\mathrm{Tan}(\beta+\phi) - \frac{(F_z)_d}{(F_z)_u+(F_z)_d}\,\frac{L_{CLd}}{B}\,\mathrm{Tan}(\beta-\phi) \qquad (7.6.13),$$

where L_{CLu} and L_{CLd} denote the distances of the centres of pressure forward of the transom and the subscripts u and d have their usual meanings of representing parameters with respect to the heeled up and the heeled down sides of the hull. Ignoring the buoyant effect at high speed, the locations of these centres of pressure can be taken at 75% of the respective mean wetted lengths forward of the transom, thus,

$$\frac{L_{CLu}}{B} = 0.75\,\frac{(L_k + L_{c1})}{2B} \qquad (\text{for } \tau \geq \tau_{m1})$$

or

$$\frac{L_{CLu}}{B} = 0.75\,\frac{L_k}{2B} \qquad (\text{for } \tau_{m1} > \tau \geq \tau_{m2}) \qquad (7.6.14)$$

and

$$\frac{L_{CLd}}{B} = 0.75\,\frac{(L_k + L_{c2})}{2B} \qquad (\text{for } \tau \geq \tau_{m2}) \qquad (7.6.15).$$

Under these assumptions together with the hydrodynamic lifts given in expression (7.6.6), the yawing moment to lift-beam ratio, $M_y/(F_z B)$, can be written as:

$$\frac{M_y}{B\,F_z} = 0.75\left[\frac{(A_{Wu}/B^2)^{3/2}\,\mathrm{Tan}(\beta+\phi) - (A_{Wd}/B^2)^{3/2}\,\mathrm{Tan}(\beta-\phi)}{(A_{Wu}/B^2)^{1/2}\,(B_u/B) + (A_{Wd}/B^2)^{1/2}\,(B_d/B)}\right] \qquad (7.6.16),$$

which would indicate that $M_y/(F_zB)$ is also dependent primarily on the wetted bottom geometry at high speed. The tabulated results for $N_2=M_y/(\mathrm{Tan}(\phi)F_zB)$ in table(7.2) suggest that the yawing moment can also reverse in direction, i.e. N_2 becomes positive, at small running trim condition (or high planing speed). This would imply negative value of L_{CLR}/B which seems to agree with the trends of the present computational results and the experimental measurements of Wellicome and Campbell (ref.(57)). Note that the trim angle for N_2 to reverse in direction is larger than that for F_2 to reverse in direction. Therefore, if the trim angle decreases continuously (increase in speed), both the sway force and the yawing moment will eventually become negative and hence there will appear a sudden jump in the L_{CLR}/B ratio from a large negative value to a positive one. On the other hand, the results shown in table(7.2) suggest that, for a given displacement and L_K/B ratio, the increase in deadrise angle could encourage these positive N_2 and negative L_{CLR}/B ratio to appear at a smaller trim angle, hence at a lower planing speed. Although only the hydrodynamic effect is considered in the above analyses, the buoyant effect, if required, can also be easily included. In this case, the full expressions for the lift and the centre of pressure location in (5.3.2) and (5.4.1) should be used.

The results for the longitudinal centre of lift ratios, L_{CL}/B, are shown in fig.(7.12e) to fig.(7.16e). As mentioned earlier in this section, for a given L_K/B ratio and craft's displacement, the longitudinal centre of lift position is a function of speed. An unusual feature displayed in these figures is that the longitudinal location of the centre of lift moves toward the transom at high speeds. This is due to the loss in wetted bottom area, i.e. decrease in mean L_W/B ratio, resulted from the reduction in the trim angle as the speed increases. One should note that, although the L_K/B ratio is kept constant, the corresponding mean L_W/B ratio decreases with the angle of trim. The deduction in L_W/B can be of significant amount as indicated by the tabulated results in table(7.2). This effect of decreasing in mean L_W/B ratio, however, has not manifested itself at the lower speed range because the effect of the speed, which moves the centre of lift forward

from the transom, is predominant. If the characteristic length ratio, L_W/B, was used instead of L_K/B, the L_{CL}/B ratio would approach a constant value at high speed.

One of the assumptions of the present theory is that the transom running beam remains completely wetted on both sides of the hull during the planing motion. The forces and moments derivatives, however, can behave quite differently once the transom wetted beam at the heeled up side of the hull starts to run dry. The most obvious phenomena that would result is the reverse in the direction of the sway force which is due to the loss in wetted area under the heeled up side of the hull. Clearly, there is scope for further investigation in this area.

The computed coefficients F_2 and M_2 are terms related to the transverse dynamic stability criteria derived by Wellicome and Campbell (Ref.(57)) for planing craft. Other hydrodynamic terms involved in these criteria are the derivatives of sway force and rolling moment with respect to the yaw/drift angle obtained from their yaw restrained models. These transverse stability criteria, however, were derived based on the coupled sway and roll manoeuvring equations in which the yaw coupling has been ignored. The present computational results as well as their later experimental measurements for the 25° deadrise model have shown that the net yawing moment about the longitudinal centre of gravity position are, in fact, not zero. This implies that the yaw coupling will be present in the dynamic problem. Including this yaw coupling, the characteristic equation for deriving the transverse dynamic stability criteria will become more complicated and will involve additional terms such as the yawing moment derivative with respect to heel angle (N_2), the yawing moment derivative with respect to yaw angle and the sway force, rolling moment and yawing moment derivatives with respect to yaw rate. The computational method developed in this chapter, however, can be regarded as a useful tool to provide some of the information essential for determining the transverse dynamic stability of a high speed craft. Some considerations of a planing flat plate in drift/yaw condition will be discussed in the next chapter.

CHAPTER (8) Some Results for the Planing of a Flat Plate in Drift Condition

8.1 Introduction

In this chapter, we consider the motion of a drifted planing flat plate. When a planing craft is turning, it will sway and yaw as well as heel. The resultant of the sway motion and the forward motion of the craft will cause it to plane at a drift angle. The initial onset of the sway motion can be the introduction of dynamic sway forces produced by the reaction of the water on a heeled planing hull or/and the sway forces produced by the rudder during turning. As shown in fig.(8.1), with respect to a reference axes system fixed in space, the drifting motion is a translational motion in which no rotational motion about the centre of gravity of the craft is involved. The hydrodynamic forces and moments induced by this motion should not be confused with those induced by the introduction of yaw velocity at the centre of gravity of the craft.

When a craft is planing at a drift angle, the flow under the bottom of the craft will become asymmetric about the centre line. This gives rise to an asymmetric bottom pressure load, resulting in a net sway force, a net yawing moment and a net rolling moment. However, the problem can be less complicated for a drifted planing flat plate. Thus, if the plate remains perfectly upright during the planing motion, both the sway force and the yawing moment will be equal to zero. Furthermore, as the sway force induced by the motion of a drifted and heeled planing flat plate is always acting at the centre of pressure, thus causing no net yawing moment about the centre of gravity, the yaw motion can be decoupled from the sway and roll motions in treating the transverse stability problem.

Fig.(8.2) shows a sketch of the wetted bottom of a drifted planing flat plate together with the body axes and the global axes systems. These global axes are defined in such a way that the global x-axis is always pointing in the direction of the resultant motion. Drift angle measured from the plate centre line to the starboard side of the plate

is treated as positive. As in the heel cases in chapter six, rolling moments were computed about the centre line of the plate and rolling to the starboard side is treated as positive. If swaying to port is treated as positive, then at a small drift angle (or yaw angle), ψ, the sway velocity, v, can be related to the planing speed, C, by the equation:

$$v = -\psi C \qquad (8.1.1),$$

where ψ is in radians. The derivative of roll moment with respect to sway velocity, $\partial Mr/\partial v$, is therefore given by:

$$\frac{\partial Mr}{\partial v} = -\frac{1}{C}\frac{\partial Mr}{\partial \psi} \qquad (8.1.2),$$

where $\partial Mr/\partial \psi$ is the derivative of roll moment with respect to drift or yaw angle. At small drift angles, the projected wetted bottom of the drifted plate was taken to be rectangular in shape. Drifted constant pressure rectangular elements were used to assemble this rectangular wetted area as shown in fig.(8.3). Note that the coordinates of the wetted bottom grid must be defined with respect to the global axes system. In addition to the usual restriction in the number of buttock strips that can be used to represent the wetted bottom (see section 3.6), it was also necessary to restrict the drift angle to a very small value. The reason for this will be explained in the following section.

It is hoped that the present drift investigation together with the results obtained from the heel investigation in the preceding chapters can provide a better insight into the transverse stability of a planing craft turning at high speed.

8.2 Free Surface Ripples induced by a Drifted Constant Pressure Rectangular Element

In the attempt to compute the pressure solutions for a flat plate planing at small drift angle (3° to 7°), periods of highly oscillatory

pressures were always found in the predicted pressure distributions along the length of the plate, regardless of the beam Froude number. This pressure oscillation problem was particularly serious for wetted bottom of large wetted length to beam ratio at large drift angle. A close examination into the free surface wave profiles produced by a single drifted constant pressure rectangular element revealed that these oscillatory pressure solutions are caused by the short period ripples developed in the wave profiles downstream from the element.

Fig.(8.4) shows a sketch of the diverging wave systems produced by the four corner wave functions of a drifted constant pressure rectangular element of length l and width b. Like the non-drifted constant pressure rectangular element discussed in section (3.6), the wave system produced by a drifted constant pressure rectangular element can also be represented by four corner wave sources, each mathematically equivalent to the sum of the corner wave functions at a corner of the rectangle. The interaction between the four corner wave systems is a complex phenomenon, however, one can predict the approximate locations of the ripples in the downstream waves by simply considering the geometry of the diverging wave envelopes of these corner wave systems. For instance, let us consider the wave profiles along the lines $y=b$, $y=0$ and $y=-b$ with respect to the element's axes system as shown in fig.(8.4). It can be seen from the figure that the line $y=b$ has cut through the four corner diverging wave systems at the regions around the points

$$A_1(-[b/(2\mathrm{Tan}(\psi))-l/2],b), \qquad A_2(-[b/(2\mathrm{Tan}(\psi))+l/2],b),$$

$$B_1(-[3b/(2\mathrm{Tan}(\psi))-l/2],b) \quad \text{and} \quad B_2(-[3b/(2\mathrm{Tan}(\psi))+l/2],b)$$

from the element's centre, where ψ is the drift angle. This suggests that short period ripples will appear in the wave profile along the line y=b at these intersecting regions. For short element length and small drift angle, the ripples around A_1 and A_2, and similarly for those around B_1 and B_2, will merge into a single whole due to the interference between the corner waves at the overlapping region. Thus, two

distinct patterns of ripples will appear in the wave profile along the line y=b. Similarly, for the wave profile along the line y=0, a single period of ripples will spread around the points

$$C_1(-[b/(2\mathrm{Tan}(\psi))-l/2],0) \quad \text{and} \quad C_2(-[b/(2\mathrm{Tan}(\psi))+l/2],0)$$

from the element's centre. Clearly, the locations of these points, i.e. A_1, A_2 etc, are speed independent though the actual bandwidths of these ripples, i.e. distances D_A, D_B and D_C in fig.(8.4), can vary slightly with the speed. Unfortunately, these bandwidths cannot be easily predicted. Note that no such ripples will appear in the wave profiles along any lines with $y \leq -b$, therefore, these wave profiles are not responsible for producing the oscillatory pressures.

In order to verify the above phenomenon, longitudinal wave profiles induced by a drifted constant pressure rectangular element were computed at a number of drift angles and speeds. Drifted rectangular element of length l =B/10 and width b =B/4, which is the typical element size used in the pressure calculations, was used in the computations. Wave profiles were computed along the lines y=b, y=0 and y=$-b$ with respect to the element's axes. The computational results for the drift angles and the beam Froude numbers ($Cv=C/(gB)^{1/2}$) considered are shown in the figures listed in the table below.

Locations of Ripples predicted from fig.(8.4)

Fig.	Cv	ψ	Along y=b				Along y=0	
			A_1	A_2	B_1	B_2	C_1	C_2
8.5 (a,b,c)	4.0	7°	-0.97B	-1.07B	-3.00B	-3.10B	-0.97B	-1.07B
8.6 (a,b,c)	2.5	7°	-0.97B	-1.07B	-3.00B	-3.10B	-0.97B	-1.07B
8.7 (a,b,c)	4.0	4°	-1.74B	-1.84B	-5.31B	-5.41B	-1.74B	-1.84B

Table (8.1) Predicted Locations of Ripples in the Wave Profiles along y=b and y=0

As expected, in each of the cases considered, there are two distinct patterns of short period ripples in the wave profile computed along the line y=b, one in the wave profile along the line y=0 and none in the wave profile along the line y=-b. The computational results closely confirm the predicted locations of these ripples, i.e. A_1, A_2 etc, given in the above table. The wave profiles shown in fig.(8.5) and fig.(8.6) for Cv=2.5 and 4.0, at a drift angle of 7°, also seem to agree with the earlier prediction that the locations of these ripples are independent of the speed. Note that for the case of Cv=4.0 and ψ =4°, the second period of ripples in the wave profile along y=*b* has not been shown in fig.(8.7a). The computational results suggest that the bandwidth of these ripples decreases with the increases of speed and drift angle.

Recalling from fig.(2.7a) and fig.(2.7b), the same sort of ripples have also appeared in the transverse wave profiles downstream from a non-drifted constant pressure rectangular element. These ripples and those obtained from the present drifted rectangular elements are a genuine feature of the present solution and are not due to numerical inaccuracies. However, as mentioned in section (3.6), the formation of these ripples might be due to the absence of viscous damping and surface tension in the present linear theory. Once again, the author would like to point out that these ripples are formed by the four corner diverging wave systems but not the transverse wave systems. In the viscous situation with surface tension, these diverging waves will not extend to the corners of the rectangle.

In order to avoid the oscillations in the pressure solutions, the influence of these ripples in the system matrix for solving the unknown pressures must be removed. This would require the ripples produced by the pressure elements in the finite element mesh to be shifted to a distance far downstream from the trailing edge so that their effects cannot be felt around the part of the free surface covered by the projected wetted bottom of the plate. Mathematically, this implies that a condition of

$$\frac{b}{2\mathrm{Tan}(\psi)} - \frac{l}{2} \gg L_w \qquad (8.2.1)$$

has to be placed upon the selection of element size for a given drift angle and wetted length, where $b/(2\mathrm{Tan}(\psi))-l/2$ denotes the approximate location of the first ripples, i.e. A_1 and C_1, produced by the leading edge elements downstream from their centres. In addition, except for very small L_w/B ratio or very large beam Froude number, the number of buttock strips that can be used are restricted to three to five, therefore, condition (8.2.1) usually can only be achieved by reducing the drift angle, ψ.

Fig.(8.8a,b and c) show the longitudinal wave profiles along $y=b$, $y=0$ and $y=-b$ for the same rectangular element at a even smaller drift angle of $^1/_2°$ and at a beam Froude number of 4.0. The first period of ripples in the wave profiles along $y=0$ and $y=b$ are expected to develop at a distance around 14.25B downstream from the element's centre. As can be seen from fig.(8.8a) and fig.(8.8b), the wave profiles along $y=0$ and $y=b$ are, indeed, free of ripples within a distance of 3B downstream from the centre of the element. Note that the ripples in the wave profiles along any lines with $y>b$ will be developed at a distance further downstream from $x=-14.25B$, hence their effects on the pressure solution are comparatively less significant than those in the wave profiles along $y=b$ and $y=0$.

Due to the formation of these ripples, the drift angle has to be restricted to very small values, usually less than 1° for a L_w/B ratio of about 3.0 when four buttock strips are used, in order that more realistic pressure results can be obtained. Although the drift angle is small, it appears that significant difference still exists between the predicted pressures on the port and the starboard sides of the plate. The theory in its present form, i.e. without viscous damping and surface tension, may not be an ideal method for treating the problem of a drifted planing surface. However, the results obtained at this small drift angle could still provide some useful information for predicting the behaviour of a planing craft in turn.

8.3 Output Transom Shapes

As shown in fig.(8.3), the projected wetted bottom of the drifted planing flat plate was taken to be rectangular in shape. The vertical locations along the transom predicted from such a rectangular wetted bottom can be expected to be asymmetric about the centre line. Thus, as well as having drifted, the plate will also be slightly heeled instead of perfectly upright.

Fig.(8.9) shows the output transom shapes predicted from rectangular wetted bottoms of L_w/B ratios of 1.5, 2.0 and 2.5, at a drift angle of 0.5° and at beam Froude numbers of 2.5, 4.5 and 6.5. Again, it can be seen from the figure that the predicted transoms are slightly cambered as a result of neglecting the curvature at the spray root. For the present small drift angle the output transoms are almost perfectly upright. However, the least-squares straight lines fitted through the predicted vertical locations along the transoms suggest a transom slope, $\mathrm{Tan}(\phi)/\mathrm{Tan}(\tau)$, of about 0.013. This would imply that the plates have actually heeled very slightly to the starboard side. For a given L_w/B ratio, the output vertical locations along the transom are almost independent of speed as shown in fig.(8.9).

Strictly speaking, if a planing plate is heeled as well as drifted, the rolling moment will consist of two components - one due to the introduction of the drift angle (or sway velocity) and the other due to the introduction of the heel angle. In order to obtain the roll moment derivative with respect to the drift angle, $\partial M_r/\partial \psi$, the relation

$$\begin{array}{lcl} \text{Total Rolling Moment Computed} & = & \text{Rolling Moment due to Heel} + \text{Rolling Moment due to Drift} \\ & = & \dfrac{\partial M_r}{\partial \phi}\,\phi + \dfrac{\partial M_r}{\partial \psi}\,\psi \end{array} \qquad (8.3.1)$$

has been assumed, where ϕ and ψ are the heel and drift angles in

radians. The term $\partial M_r/\partial\phi$ in expression (8.3.1) denotes the roll moment derivative with respect to the heel angle for a heeled planing flat plate whose lift and longitudinal centre of pressure location are equal to those predicted from the drifted rectangular planform. This $\partial M_r/\partial\phi$ can be obtained by the interpolating method discussed in section 6.5 together with the results presented in fig.(6.10a) to fig.(6.10c). Although the predicted heel angle in the present case is so small that the rolling moment due to heel should not be a significant portion of the total moment, the effect of heel will nevertheless be taken into account in section (8.5).

8.4 Some Results for Pressure Distribution

Fig.(8.10a,b,c) to fig.(8.12a,b,c) show the pressure distributions along the length of the 0.5° drifted flat plates, for wetted length to beam ratios of 1.5, 2.0 and 2.5 and for beam Froude numbers of 2.5, 3.5 and 6.5. It can be seen from these figures that the pressures on the port side of the plate are significantly different from those on the starboard side. At relatively low beam Froude numbers of 2.5 and 3.5, as shown in fig.(8.10) and fig.(8.11), there is a region of high pressures developed near the trailing edge on the starboard side of the plate. These pressures are particularly pronounced at large wetted length to beam ratio and are considerably higher than those developed on a non-drifted planing plate. The most interesting result of all perhaps is the development of suctions, i.e. negative pressures, on the starboard side of the plate at high speeds. These suctions are shown in fig.(8.12) for a beam Froude number of 6.5. The development of these suctions is presumably due to the increase in cross flow velocity, $\frac{1}{2}\rho C$, on the wetted bottom. It has been found that these suctions increase with the increase of drift angle.

8.5 Some Results for Hydrodynamic Forces and Moments

The predicted lift coefficient slopes, $C_{fz}/\mathrm{Tan}(\tau)$, and longitudinal centre of pressure ratios, L_{cp}/B, for the 0.5° drifted flat plates are shown in fig.(8.13a) and fig.(8.13b), for L_w/B ratios of 1.5, 2.0 and

2.5 and for beam Froude numbers ranging from 2.5 to 7.0. Also shown in the figures are the results for non-drifted planing flat plates of the same L_w/B ratios. As far as small drift angle is concerned, the introduction of drift angle seems to have little effect on the lift coefficient slopes, though the reduction in lift due to the suctions developed at high speed is recognizable. On the other hand, the drift effect on the centre of pressure location is more pronounced, and the longitudinal centre of pressure of the drifted plates tend to be further forward from the transom than those of the non-drifted ones.

It has been mentioned earlier in section (8.2) that the plates predicted from the present 0.5° drifted rectangular wetted planforms are slightly heeled as well as drifted. In order to obtained the roll moment due to drift only, i.e. $(\partial M_r/\partial\psi)\psi$, the predicted moment has been corrected by subtracting the component due to heel, i.e. $(\partial M_r/\partial\phi)\phi$, using expression (8.3.1).

The roll moment components due to heel and due to drift are shown in fig.(8.13c) for a L_w/B ratio of 2.0. These roll moments are presented in the following non-dimensional forms:

$$\frac{\partial C_{rm}}{\partial \phi}\ \frac{\phi}{\tau} \qquad \text{for the heel component}$$

and

$$\frac{\partial C_{rm}}{\partial \psi}\ \frac{\psi}{\tau} \qquad \text{for the drift component} \qquad (8.5.1),$$

where C_{rm} is the coefficient of roll moment, ϕ, ψ and τ are the heel, drift and trim angles in radians. As expected, the roll moments due to heel are quite insignificant when compared with the components due to drift. Note that the output transom slope, ϕ/τ, is constant for a given L_w/B ratio and beam Froude number. Also note that, as explained in section (6.3), if the sway force is neglected at small heel angle the roll moment coefficient derivative, $\partial C_{rm}/\partial\phi$, is independent of the trim angle. Therefore the term, $(\partial C_{rm}/\partial\phi)\ \phi/\tau$, can be regarded as constant

for a given longitudinal centre of pressure ratio (or Lw/B) and beam Froude number.

Perhaps a better way to present the results for the roll moment derivative with respect to drift angle is to non-dimensionalize them using the lift, F_z, and the wetted beam, B. Thus,

$$\frac{\partial M_r}{\partial \psi}\ \frac{1}{F_z\ B} = \frac{\partial C_{rm}}{\partial \psi}\ \frac{\psi}{\tau}\ \frac{1}{\psi}\ \frac{1}{C_V^2\ (C_{fz}/\tau)} = M_1 \qquad (8.5.2),$$

where C_{fz}/τ is the lift coefficient slope and all the angles are in radians. Fig.(8.13d) shows the variation of M_1 (with the correction of the roll moment due to heel) against beam Froude number for Lw/B ratios of 2.5, 2.0 and 1.5. It can be seen that, for a given load, the roll moment for each Lw/B ratio has approached a constant value at high speeds. The results for Lw/B ratios of 2.5 and 2.0 also display an interesting feature of the change in the direction of the roll moment - initially rolling the plate to the port side at low speeds while rolling it to the starboard side at high speeds. This could well be one of the explanations for the phenomenon that some high speed crafts bank inwards during turning, while others bank outwards.

Although the present theory can also be applied equally well to drifted constant deadrise hulls (with the restriction of small drift angle), unfortunately, the problem has not been studied due to the limitation of time. It would be of great interest if the sway forces, rolling moments and yawing moments for the constant deadrise hulls could be obtained to compare with the experimental measurements of Wellicome and Campbell (Ref.(57)).

Chapter (9) Conclusion and Further Work

9.1 Conclusion of Present Work

A finite element procedure has been presented in this thesis for the prediction of the hydrodynamic performance of planing craft in calm water. An important feature in planing motion is the development of a spray sheet thrown ahead and sideways of the planing surface which gives rise to a region of highly non-linear flow near the spray root. In order to simplify the problem, however, it has been necessary to assume a small angle of attack (or trim angle) so that the splash configuration can be ignored in the linearization of the problem. In addition, the viscous effects and surface tension have also been neglected in the present linear theory.

The main advantage of the present theory over most of the previous planing theories is that the present theory has no restrictions on either the aspect ratio or/and the planing speed. Further, although it has not been demonstrated in this work, the present finite element method can be applied to crafts with multi-planform configuration which has also been restricted in most of the other theories.

In the present work, the finite element method has been applied particularly to study the hydrodynamics of planing flat plate and constant deadrise hulls. The results derived from the theory have compared favourably with other theoretical and experimental data. Reasonably good agreement has also been obtained with the empirical equations developed by Savitsky (Ref.(44)). However, in contrast with the empirical lift equation, the present results have indicated that the gravitational effect reduces the lift coefficient of large aspect ratio (B/L_w) planing surfaces but increases it for small aspect ratios. These tendencies confirm the experimental results of Sambraus (Ref.(36)) as well as the theoretical predictions of Maruo (Ref.(23)), Wang and Rispin (Ref.(26)) and Jahangeer (Ref.(66)).

For the longitudinal centre of pressure location, the Savitsky empirical equation does not seem to have correctly taken into account of

the location of the hydrodynamic centre of pressure. The present theory has shown that the effect of increasing the wetted length to beam ratio (Lw/B) of a planing surface is to move the hydrodynamic centre of pressure further forward from the transom - from 75% of the wetted length forward of the transom for very small Lw/B ratios to about 90% of the wetted length forward of the transom for a Lw/B ratio of 3.0. In comparison with the empirical equation, in which the hydrodynamic centre of pressure is taken to be at 75% of the wetted length forward of the transom regardless of the wetted length to beam ratio, the present results would seem to be more reasonable. This is certainly so, when one considers the fact that the hydrodynamic centre of pressure of a flat plate airfoil moves toward the leading edge from the 75% chord point with the increase in the chord length to width ratio. Further, one must always bear in mind that empirical equations themselves are fitted curves; although they are frequently used in practical calculations because of their simplicity.

In practical design calculations, it is often required to predict the running trim angle and the running wetted area (mean wetted length) for a craft of specified loading condition at certain speeds. The direct approach to the problem is obviously to determine these unknown parameters such that the lift generated by the bottom pressures and the centre of pressure location are correctly matched with the weight and the centre of gravity location of the craft. In the present method of solution, however, because the shape and extent of the projected wetted bottom, the trim angle as well as the planing speed are assumed to be known, the pressures and the immersions along the transom are determined as the solution, these running trim angle and running wetted area cannot be directly predicted. Instead, they have been determined by an interpolating method based on matching the craft's weight and craft's centre of gravity position to the computed lifts and computed centre of pressure positions. This would of course require computations to be carried out for an assumed range of trim angles, mean wetted lengths and speeds for the given craft. However, once these results have been obtained, it would allow users to estimate the operating trim angle and mean wetted length for a wide range of craft displacements and craft

centre of gravity locations without going through the tedious integration process. This implies that the use of the present interpolation scheme would be a practical proposition in engineering design. The results obtained in such a way have compared reasonably well with those obtained from the Savitsky's empirical equations for a 10° constant deadrise hull. A similar interpolation scheme has also been developed for determining the hydrodynamic derivatives of a heeled planing surface.

Another topic studied in this thesis has been the hydrodynamics of planing hulls under heel condition. Again, flat plate and constant deadrise hulls have been considered. The computational results have shown that, for a given craft's loading condition (or a given trim angle and mean wetted length to beam ratio) and speed, the induced sway force, rolling moment, and yawing moment vary linearly with the angle of heel up to an angle of about 10°, this being the largest heel angle considered in this work. For the case of a heeled planing flat plate, it has been further shown that the craft's weight (or trim angle) has very little effect on the rolling moment as far as small heel angle is concerned.

The pressure distributions, the roll moment coefficients, the lift coefficients and the centre of lift locations predicted for a flat plate and a 15° constant deadrise hull in heel condition have been compared with the theoretical and experimental results of Jahangeer (Ref.(66)) with reasonably close agreements. However, for the constant deadrise hull, the agreement between the two theories on the roll moment coefficients was not particular good though the present results agreed very well with his experimental measurements. As mentioned in section 7.4, this could due to the difference in the element arrangement between the present and Jahangeer's wetted bottom grids. The present theory has predicted a decrease in righting moment with the increase in planing speed and this would imply a decrease in roll stability at high speed. In addition, the sway force coefficients and the yaw moment coefficients for the heeled constant deadrise hull have also been derived. These force and moment coefficients had not been considered by Jahangeer (Ref.(66)).

Results for the hydrodynamic forces and moments have been derived as a function of planing speed, trim angle and mean wetted length to beam ratio for a 10° constant deadrise hull under heel condition. Based on these results and the interpolating procedure developed in section 7.5, non-dimensional sway force, roll moment and yaw moment derivatives have been obtained for craft with fixed bottom loading coefficients and wetted keel length to beam ratios at various speed coefficients. These force and moment derivatives have shown reasonable agreement with the experimental data of Wellicome and Campbell (Ref.(57)), though, unfortunately, there is no experimental result for the yaw moment derivative in Ref.(57) available for comparison.

The most interesting result of all has been the behaviour of these hydrodynamic force and moments at high speed. The present theory has predicted that both the sway force and the yaw moment have a tendency of reversing in direction at high speed. These were found to be in line with the experimental measurements obtained by Wellicome and Campbell (Ref.(57)) for models with higher deadrise angles, in which this reverse tendency occurred at lower speeds. It should be pointed out that although there are no yaw moment result presented in Ref.(57), the reverse tendency of the yaw moment is clearly indicated by their experimental measurements for the longitudinal centre of lateral resistance (the point associated with zero yawing moment) obtained from a 25° deadrise model. Negative centre of lateral resistance, i.e. behind the transom position, has also been obtained, a feature which has also been evident in their experimental measurements. The analogy using the Savitsky's empirical equations discussed in section 7.6 has indicated that the reverse tendency of the sway force and the yaw moment at high speed could be directly related to the rapid loss of wetted area under the heeled up side of the hull when the craft is operating at small trim angle and wetted bottom area.

The motion of a planing flat plate under drift/yaw condition has also been considered. The results displayed an interesting feature of the development of suctions (negative pressures) on the outboard side of

the wetted bottom at high speed. This is presumably due to the increase in cross flow velocity under the wetted bottom. The present theory has predicted a change in the direction of the induced rolling moment with the increase in planing speed, and this could well be one of the explanations for the phenomenon that some high speed crafts bank inwards during turning, while others bank outwards. It would be of great interest if the hydrodynamic forces and moments derivatives for a yawed constant deadrise hull could be obtained to compare with the experimental results of Wellicome and Campbell (Ref.(57)).

The hydrodynamic force and moment derivatives derived in this thesis are terms related to the transverse dynamic stability criteria for planing craft. The present results have shown that the net yawing moment about the centre of gravity of the craft is not zero (except for flat plate). This would imply that, in addition to the sway and roll coupling as treated by Wellicome and Campbell (Ref.(57)), the yaw coupling will also be present in this dynamic problem. In order to have a thorough investigation into this dynamic problem, however, additional terms such as the hydrodynamic forces and moments derivatives with respect to the yaw angle and the yaw rate would need to be determined. Although these hydrodynamic terms have not been derived in this thesis, the present computational method can nevertheless be regarded as a tool to provide some of the information essential for determining the transverse dynamic stability of high speed craft. Clearly, there is scope for further research in this area.

9.2 Further Work

Whilst the present finite element method has worked reasonably well with respect to the determination of the pressures and the hydrodynamic forces and moments developed under the wetted bottom of a planing hull, there is room for further improvement and development.

There have been two major difficulties associated with the present method of solution. First, as mentioned in section 3.5, the pressure solution obtained by the present method has a divergent tendency when a

large number of buttock strips are used in the representation of the projected wetted planform. For planing surfaces of large wetted length to beam ratio, oscillatory pressure results have also been obtained at low speed. In order to avoid the noted divergence and oscillation, a maximum number of six buttock strips could only be used. As a consequence, the transverse hull shape could not be prescribed as accurately as it should be and detailed lateral pressure distributions could not be obtained. A similar type of oscillatory pressure solution had also been obtained by Doctors' finite element method (Ref.(29)). Secondly, for the drifted/yawed planing surface discussed in chapter eight, in addition to this restriction, it has also been necessary to restrict the drift angle to an usually small value of less than 1° due to the highly oscillatory pressures obtained at larger drift angles.

The reasons for these difficulties have been fully traced and have already been discussed in detail in sections 3.6 and 8.2. The investigation of the free surface responses produced by the present constant pressure element has revealed that the viscous effects and surface tension neglected in the present theory are most likely to be responsible for the convergence and the pressure oscillation problems. It has been suggested that the reformulation of the theory by including these viscous and surface tension effects or some sort of artificial damping in the governing equations could be a direct way to overcome these problems. The non-linear effects, which have been strictly ignored in the present linear theory, might also have a part to play but this is very unlikely since the pressure divergence and oscillation did not always occur near the chine.

On the other hand, the projected wetted planform can be assembled using a different type of element. Recalling from section 3.6, the unrealistic pressure oscillations were caused by some unwanted oscillatory patterns inherent in the system matrix. These unwanted oscillatory patterns are formed by the interaction between the diverging wave systems produced by the corner wave functions of each individual element. It may perhaps be worthwhile to divide the projected planform into a number of transverse strips, each has a continuous but unknown pressure distribution across the width of the planform. It should be

pointed out that the discontinuity of the pressure between the elements in the longitudinal sense should not produce any convergence difficulty since the pressure solutions obtained by the present theory converged fairly rapidly and was well behaved when the number of elements was increased in the longitudinal sense.

Alternatively, based on the Green's second identity, a boundary element method of solution could be derived. In such a method, it will be necessary to layout elements on the boundaries of the fluid domain as well as on the wetted surface of the body. In a three dimensional situation, however, it may be difficult to allocate a suitable boundary limit away from the body and the representation of the far field disturbances could also be a problem. Furthermore, the size of the matrix involved could be large, but the method can nevertheless be amenable to solution.

Although the work in this thesis only concerns the motion of planing craft in calm water, the theory could well be extended to cover rough water. On the other hand, if the interest is in the added mass and damping coefficient, elements with oscillating pressure strength could be used. Rectangular element of constant but oscillating pressure distribution has been derived by Chen (Ref.(67)) and would be well suited for this particular purpose.

References

(1) Sretenskii, L.N. "On the Motion of a Glider on Deep Water", Izv. Akad. Nauk SSSR., Otdel. Mat. Estest. Nauk, pp.817-835, 1933.

(2) Sretenskii, L.N. "On the Theory of the Glider", Izv. Akad. Nauk SSSR., Otdel. Tekhn. Nauk, No.7, pp.3-16, 1940.

(3) Sedov, L.I. "The Plane Problem of Gliding on the Surface of a Heavy Fluid", Trudy Konferentsii po Teorii Volnovogo Soprotivleniya, Moscow, pp.7-30, 1936.

(4) Maruo, H. "Two Dimensional Theory of the Hydroplane", Proc. First Japan Nat. Cong. Appl. Mech., Science Council of Japan, Tokyo, pp.409-415, 1952.

(5) Maruo, H. "Hydrodynamic Researches of the Hydroplane, Part 1", J. Zosen Kiokai (J. Soc. Nav. Arch. Japan), Vol.91, pp.9-16, 1956.

(6) Maruo, H. Ibid, Part 2, Vol.92, pp.57-63, 1957.

(7) Maruo, H. Ibid, Part 3, Vol.105, pp.23-26, 1959.

(8) Squire, H.B. "The Motion of a Simple Wedge along the Water Surface", Proc. Roy. Soc. London, Series A, Vol.243, pp.48-64, 1957.

(9) Cumberbatch, E. "Two Dimensional Planing at high Froude number", J. Fluid Mechanics, Vol.4, Part 5, pp.466-478, 1958.

(10) Wehausen, J.V. and Laitone, E.V. "Surface Waves",

Encyclopedia of Physics, Vol. 9, Fluid Dynamics 3, ed. by S. Flugge, Springer-Verlag, Berlin, pp.446-815, 1960.

(11) Doctors, L.J. "Representation of Planing Surfaces by Finite Pressure Elements",

Proc. Fifth Australasian Conference on Hydraulics and Fluid Mechanics, Vol.2, pp.480-488, 1974.

(12) Green, A.E. "The Gliding of a Plate on a Stream of Finite Depth, Part 1",

Proc. Cambridge Phil. Soc., Vol.31, pp.589-603, 1935.

(13) Green, A.E. "The Gliding of a Plate on a Stream of Finite Depth, Part 2",

Proc. Cambridge Phil. Soc., Vol.32, pp.67-85, 1936.

(14) Green, A.E. "Note on the Gliding of a Plate on the Surface of a Stream",

Proc. Cambridge Phil. Soc., Vol.32, pp.248-252, 1936.

(15) Rispin, P. "A Singular Perturbation Method for Non-linear Water -waves past an Obstacle",

Ph.D. thesis, California Inst. of Tech., 1966.

(16) Wu, T.Y. "A Singular Preturbation Theory for Nonlinear Free-surface Flow Problems",

Int. Shipbuilding Progress, Vol.14, No.151, pp.88-97, 1967.

(17) Wu, T.Y. and Whitney, A.K. "Theory of Optimum Shapes in Free -surface Flows, part 1, Optimum Profile of Sprayless Planing Surface",

J. fluid Mechanics, Vol.55, part 3, pp.439-455, 1972.

(18) Ting, L. and Keller, J.B. "Optimal Shape of a Planing Surface at High Froude Number",

J. of Ship Research, Vol.21, No.1, pp.40-43, 1977.

(19) Wagner, H. "Uber Stross-und Gleitvorgange an der Oberflachen von Flussigkeiten",

Zeitschrift fur Angewandte Mathematik und Mechanik, Vol.12, No.4, pp.193-215, 1932.

(20) Casling, E.M. "The Planing of a Low-Aspect-Ratio Flat Ship at Infinite Froude Number",

J. Engineering Mathematics, 31 pp., 1977.

(21) Tulin, M.P. "The Theory of Slender Surfaces Planing at high Speeds",

Schiffstechnik, Vol.4, No.21, pp.125-133, 1957.

(22) Shuford, C.L. "A Theoretical and Experimental Study of Planing Surfaces Including Effects of Cross Section and Plan Form"

National Advisory Committee for Aeronautics, Report 1335, 45 pp., 1958.

(23) Maruo, H. "High and Low Aspect Ratio Approximation of Planing Surfaces",

Schiffstechnik, Vol.14, No.72, pp.57-64, 1967.

(24) Shen, Y.T. "Theory of High Aspect Ratio Planing Surfaces",

Department of Nav. Arch. and Marine Eng., Univ. Michigan, Ann Arbor, Michigan, Rep.102, 123 + vii pp., 1970.

(25) Shen, Y.T. and Ogilvie, T.F. "Non Linear Hydrodynamic Theory for Finite-Span Planing Surfaces",

J. Ship Research, Vol.16, No.1, pp.3-20, 1972.

(26) Wang, D.P. and Rispin, P. "Three-Dimensional Planing at High Froude Number",

J. Ship Research, Vol.15, No.3, pp.221-230, 1971.

(27) Tuck, E.O. "Low Aspect Ratio Flat Ship Theory",

J. Hydronautics, Vol.9, No.1, January, pp.3-12, 1975.

(28) Oertel, R.P. "The Steady Motion of a Flat Ship Including an Investigation of Local Flow near the Bow",

Ph.D. thesis, Dept. Applied Mathematics, Univ. Adelaide, Adelaide, Australia, 113 +vii pp., 1975.

(29) Doctors, L.J. "Representation of Three Dimensional Planing Surfaces by Finite Elements",

Proc. 1st. Int. Conf. on Numerical Ship Hydrodynamics, David Tayor Naval Ship Research and Development Center, October, pp.517-537, 1975.

(30) Standing, R.G. "Experience in Computing the Wavemaking of Hovercraft",

NPL. Report, Ship 191, Sept., 1975.

(31) Huang, T.T. and Wong, K.K. "Disturbance Induced by a Pressure Distribution Moving Over a Free Surface",

J. Ship Research, Vol.14, pp.195-203, 1970.

(32) Wellicome, J.F. and Jahangeer, J.M. "The Prediction of Pressure Loads on Planing Hulls in Calm Water",

R.I.N.A. Trans., April, pp.53-70, 1978.

(33) Baker, G.S. "Some Experiments in connection with the Design of Floats for Hydro-areoplanes",

ARC (British), R & M, No.70, 1912.

(34) Sottorf, W. "Experiments with Planing Surfaces",

NACA TM 661, 1932 and NACA TM 739, 1934.

(35) Shoemaker, J.M. "Tank Tests of Flat and Vee-Bottom Planing Surfaces",

NACA TN 509, November, 1934.

(36) Sambraus, A. "Planing Surface Tests at Large Froude Numbers - Airfoil Comparsion",

NACA TM 848, February, 1938.

(37) Sedov, L.I. "Scale Effect and Optimum Relation for Sea Surface Planing",

NACA TM 1097, February, 1947.

(38) Locke, F.W.S. "Tests of a Flat Bottom Planing Surface to Determine the Inception of Planing",

Navy Department, BuAer, Research Division Report, No.1096, December, 1948.

(39) Korvin-Kroukovsky, B.V., Savitsky, D. and Lehman, F. "Wetted Area and Center of Pressure of Planing Surfaces",

Stevens Institute of Technology, Davidson Laboratory Report No.360, August, 1949.

(40) Savitsky, D. and Neidinger, J.W. "Wetted Area and Center of Pressure of Planing Surfaces at Very Low Speed Coefficients",

Stevens Institute of Technology, Davidson Laboratory Report No.493, July, 1954.

(41) Hadler, J. "The Prediction of Power Performance on Planing Craft",

Tran. Soc. Naval Arch. and Marine Engineers,Vol.74, pp.563-610, 1966.

(42) Kapryan, J. and Boyd, G.M. "Hydrodynamic Pressure Distributions obtained during a Planing Investigation of five Related Prismatic Surfaces",

NACA TN 3477.

(43) Clement, E.P. and Blount, D.L. "Resistance Tests of a Systematic Series of Planing Hull Forms",

Trans. Soc. Naval Arch. and Marine Engineers, vol.71, pp.491-579, 1963.

(44) Savitsky, D. "Hydrodynamic Design of Planing Hulls",

Marine Technology, Vol.1, No.1, pp.71-95, 1964.

(45) Savitsky, D. "Planing Craft",

Panel Discussion, Proc. Seventh Symposium on Naval Hydrodynamics, Office of Naval Research, Aug. 25-30, Rome, pp.1163-1168, 1968.

(46) Savitsky, D. "Hydrodynamic Development of a High Speed Planing Hull for Rough Water",

Proc. Ninth Symposium on Naval Hydrodynamics, Office of Naval Research, August 20-25, Paris, pp.419-461, 1972.

(47) Du Cane, P. "High Speed Small Craft, 4th Edition",

David and Charles, Newton Abbort, U.K., 1974.

(48) Lord, L. "Naval Architecture of Planing Hulls, 3rd Edition",

Cornell Maritime Press, 1963.

(49) Savitsky, D. and Koelbel, J.G., Jr. "Seakeeping Consideration in Design and Operation of Hard Chine Planing Hulls",

Combatant Craft Engineering Department, Naval Ship Engineering Center, May, 1978.

(50) Marwood, W.J. and Bailey, D. "Transverse Stability of Round-Bottomed High Speed Craft Underway",

N.P.L. Ship Report 98, October, 1968.

(51) Suhrbier, K.R. "An Experimental Investigation of the Roll Stability of a Semi-Displacement Craft at Forward Speed",

R.I.N.A. Symposium Small Fast Warships, March, 1978.

(52) Baba, E., Asai, S. and Toki, N.
"A Simulation Study on Sway-Roll-Yaw Coupled Instability of Semi Displacement Type High Speed Craft",

Second International Conference on the Stability of Ships and Ocean Vehicles, Tokyo, October, 1982.

(53) Mueller-Graf, B. and Schmiechen, M.
"On the Stability of Semi Displacement Crafts",

Second International Conference on the Stability of Ships and Ocean Vehicles, Tokyo, October, 1982.

(54) Millward, A. "A Preliminary Measurements of Pressure Distribution to Determine the Transverse Stability of a Fast Round Bilge Hull",

International Shipbuilding Progress, Vol.26, No.297, May, 1979.

(55) Wakeling, B.P., Sproston, J.L. and Millward, A.
"Transverse Stability of a Fast Bilge Hull",

International Conference on Design Considerations for Small Crafts, 13-15, February, 1984.

(56) Gill, J.D. "A Note on Some Roll Phenomena Associated with High Performance Boats",

Proceedings, Symposium on the Design and Construction of Recreational Power Boats, University of Michigan, Ann Arbor, August, 20-25, 1979.

(57) Wellicome, J.F. and Campbell, I.M.C. " The Transverse Dynamic Stability of Planing Craft",

University of Southampton, Ship Science Dept., Report No.12, Jan. 1984.

(58) Michell, J.H. "The Wave Resistance of a Ship",

Philosophical Magazine, Ser.5, Vol.45, pp.106-123, 1898.

(59) Vossers, G. "Some Applications of the Slender Body Theory to Ship Hydrodynamics",

Ph.D. Thesis, Technische Hogeschool, Delft, 1962.

(60) Abramowitz, M. and Stegun, I.A. "Handbook of Mathematical Functions",

Dover, 1965.

(61) Monacella, V.J. "The Disturbance due to a Slender Ship Oscillating in Waves in a Fluid of Finite Depth"

J. of Ship Research, Vol.10, pp.242-252, 1966.

(62) Lamb, H. "Hydrodynamics",

Cambridge University Press, pp.437, 1932.

(63) Everest, J.T. and Hogben, N. "A Theoretical and Experimental Study of the Wavemaking of Hovercraft of Arbitrary Planform and Angle of Yaw",

R.I.N.A. Trans., 111, pp.343-365, 1969.

(64) Epshtein, L.A. "Determination of the Depression behind a Finite-Span Underwater Wing and Gliding Flat Plate",

N.E. Zhukovskii Central Aeohydrodynamics Institute, Moscow.

(65) Birnbaum, W. "Die Tragende Wirbelflache als Hilfsmittel zur Behandlung des Ebenen Problems der Tragflugeltheorie",

Z. Angew. Math. Mech., Vol.3, pp.290-297, 1923.

(66) Jahangeer, Y.M. "A Finite-Element Approach to the Hydrodynamic Performance of Planing Craft"

P.H.D. Thesis, University of Southampton, Dept. of Ship Science

(67) Chen, H.H. "On a Rectangular Pressure Distribution of Oscillating Strength Moving Over a Free Surface",

Journal of Ship Research, Vol.21, No.1, March, pp.11-23, 1977.

Appendix A Velocity Potential and Free Surface Elevation induced by a Pressure Disturbance in an Uniform Free Stream

The velocity potential, ϕ_r, which satisfies the Laplace equation (2.2.3) and the infinite depth condition (2.2.9) can be represented by a double Fourier integral:

$$\phi_r(x,y,z) = \mathrm{Re} \int_{-\pi}^{+\pi} \int_{0}^{+\infty} A(k,\theta)\, e^{kz}\, e^{-ikw}\, dk d\theta \qquad (A.1),$$

where k is the wave number, θ is wave angle and

$$w = x\,\mathrm{Cos}(\theta) + y\,\mathrm{Sin}(\theta) \qquad (A.2).$$

For a linear theory, this velocity potential must also satisfy the linearized kinematic condition (2.2.6) and the linearized pressure condition (2.2.7) on the undisturbed free surface. A combined free surface boundary condition derived from expressions (2.2.6) and (2.2.7) to be satisfied on the undisturbed free surface, z=0, is

$$\frac{\partial^2 \phi_r(x,y)}{\partial x^2} + k_o \frac{\partial \phi_r(x,y)}{\partial z} = \frac{1}{\rho C} \frac{\partial P(x,y)}{\partial x} \qquad \text{on } z=0 \qquad (A.3),$$

where P(x,y) is the pressure disturbance on the free surface, k_o is the fundamental wave number given by g/C^2, and C is the speed of the uniform free stream. The free surface pressure disturbance, P(x,y), can be represented by the double Fourier integral:

$$P(x,y) = \mathrm{Re} \int_{-\pi}^{+\pi} \int_{0}^{+\infty} k\, P(k,\theta)\, e^{-ikw}\, dk d\theta \qquad (A.4),$$

where the Fourier transform of the pressure, $P(k,\theta)$, is given by the following Fourier inversion formula:

$$\mathrm{Re}[P(k,\theta)] + \mathrm{Img}[P(k,\theta)]\, i = \frac{1}{4\pi^2} \int_{-\infty}^{+\infty} \int_{-\infty}^{+\infty} P(x,y)\, e^{ikw}\, dxdy \qquad (A.5).$$

The function, $A(k,\theta)$, can be obtained by substituting (A.1) and (A.4) into condition (A.3) and evaluated on the undisturbed free surface, $z=0$. This gives

$$\phi_r(x,y,z) = \mathrm{Re} \int_{-\pi}^{+\pi} \int_{0}^{\infty} \frac{ik\, \mathrm{Sec}(\theta)\, P(k,\theta)\, e^{kz}\, e^{-ikw}}{\rho C\, (k - k_1)}\, dkd\theta \qquad (A.6),$$

where $k_1 = k_o\ \mathrm{Sec}^2(\theta)$. One can reduce the integrating range of the θ integral in the above expression from $-\pi<\theta<+\pi$ to $-\pi/2<0<+\pi/2$. This can be achieved by dividing the θ integral into three ranges; I_1 $(-\pi < \theta < -\pi/2)$, I_2 $(-\pi/2 <\theta <+\pi/2)$ and I_3 $(+\pi/2< \theta <+\pi)$; the integrals I_1 and I_3 are then transformed by making the substitutions $\beta = \pi + \theta$ and $\beta = \theta - \pi$ respectively into:

$$I_3 + I_1 = \mathrm{Re} \int_{-\pi/2}^{0} + \int_{0}^{+\pi/2} \left[\frac{-ik\, \mathrm{Sec}(\beta)\, \overline{P(k,\beta)}\, e^{kz}\, \overline{e^{-ikw}}}{\rho C\, (k - k_1)} \right] dkd\beta \qquad (A.7),$$

where $\overline{P(k,\beta)}$ and $\overline{e^{-ikw}}$ are the complex conjugates of the functions $P(k,\beta)$ and e^{-ikw} obtained from the relations

$$P(k,\beta \pm \pi) = \overline{P(k,\beta)} \qquad (A.8),$$

which is a property of the inversion formula (A.5), and

$$\exp[-ik\{x\cos(\beta\pm\pi)+y\sin(\beta\pm\pi)\}] = \overline{\exp[-ik\{x\cos(\beta)+y\sin(\beta)\}]} \qquad (A.9).$$

After making use of the identity

$$\mathrm{Re}[\,P(k,\beta)\,e^{-ikw}\,i] = \mathrm{Re}[-\,\overline{P(k,\beta)}\;\overline{e^{-ikw}}\,i] \qquad (A.10)$$

and summing up the three integrals, I_1, I_2 and I_3, the velocity potential becomes

$$\phi_r(x,y,z) = \mathrm{Re}\int_{-\frac{\pi}{2}}^{+\frac{\pi}{2}}\int_{0}^{+\infty}\frac{2i\,k\,\mathrm{Sec}(\theta)\,P(k,\theta)\,e^{kz}\,e^{-ikw}}{\rho C\,(k-k_1)}\,dk\,d\theta \qquad (A.11).$$

The above solution for $\phi_r(x,y,z)$ is not unique and it generates both the downstream waves and the unwanted upstream waves. In order to satisfy the 'radiation condition', which ensures that gravity waves only exist downstream of the pressure disturbance, a cancelling potential, $\phi_p(x,y,z)$, has to be introduced. This cancelling potential can be obtained by considering the limit of $\phi_r(x,y,z)$ as x tends to positive infinity. As $x \to +\infty$, the inner k integral in (A.11) is dominated by the contribution at the pole, $k=k_1$, and its limiting value is

$$\lim_{x\to+\infty}\int_{0}^{+\infty}\frac{k\,P(k,\theta)\,e^{kz}\,e^{-ikw}}{(k-k_1)}\,dk = \pm\pi k_1\,P(k_1,\theta)\,e^{k_1 z}\,e^{-ik_1 w}\,i \qquad (A.12),$$

where the pole value should be taken as positive if $w<0$ and negative if $w>0$. Since in the present case where $-\pi/2 < \theta < +\pi/2$, the negative value

is then chosen. It follows that the limit of $\phi_r(x,y,z)$ as x tends to positive infinite is

$$\phi_p(x,y,z) = \lim_{x\to+\infty} \phi_r(x,y,z) = + \int_{-\frac{\pi}{2}}^{+\frac{\pi}{2}} \frac{2\pi \mathrm{Sec}(\theta)}{\rho C} k_1 P(k_1,\theta) e^{k_1 z} e^{-ik_1 w} d\theta \qquad (A.13).$$

Finally, the velocity potential with the upstream waves cancelling term is given by:

$$\phi_i(x,y,z) = \mathrm{Re}\,[\phi_r(x,y,z) - \phi_p(x,y,z)] \qquad (A.14)$$

and the resulting velocity potential is

$$\phi_i(x,y,z)$$

$$= \int_{-\frac{\pi}{2}}^{+\frac{\pi}{2}} \frac{2\,\mathrm{Sec}(\theta)}{\rho C} d\theta \int_{0}^{+\infty} \frac{k\, e^{kz}}{(k-k_1)} \left[\mathrm{Re}[P(k,\theta)]\,\mathrm{Sin}(kw) - \mathrm{Img}[P(k,\theta)]\,\mathrm{Cos}(kw) \right] dk$$

$$- \int_{-\frac{\pi}{2}}^{+\frac{\pi}{2}} \frac{2\pi}{\rho C} \mathrm{Sec}(\theta)\, k_1\, e^{k_1 z} \left[\mathrm{Re}[P(k_1,\theta)]\,\mathrm{Cos}(k_1 w) + \mathrm{Img}[P(k_1,\theta)]\,\mathrm{Sin}(k_1 w) \right] d\theta$$

(A.15).

The corresponding free wave elevation, $\zeta_i(x,y)$, can be obtained by substituting the above potential into the linearized free surface pressure condition (2.2.7) and evaluated on the undisturbed free surface, z=0. This gives

$$\zeta_i(x,y) = \frac{C}{g}\left[\frac{\partial\phi_i(x,y,z)}{\partial x}\right]_{z=0} - \frac{P(x,y)}{\rho g} \qquad (A.16)$$

$$\zeta_i(x,y) = \int_{-\frac{\pi}{2}}^{+\frac{\pi}{2}}\int_{0}^{+\infty} \frac{2k^2}{\rho g(k-k_1)}\left[\mathrm{Re}[P(k,\theta)]\,\mathrm{Cos}(kw) + \mathrm{Img}[P(k,\theta)]\,\sin(kw)\right] dk d\theta$$

$$+ \int_{-\frac{\pi}{2}}^{+\frac{\pi}{2}} \frac{2\pi}{\rho g} k_1^2\left[\mathrm{Re}[P(k_1,\theta)]\,\mathrm{Sin}(k_1 w) - \mathrm{Img}[P(k_1,\theta)]\,\mathrm{Cos}(k_1 w)\right] d\theta$$

$$- \frac{P(x,y)}{\rho g} \qquad (A.17).$$

For the constant pressure trapezium shown in fig.(2.2c), the pressure is defined as:

$$P(x,y) = +P_o \quad \text{if} \quad y_a < y < y_b \quad \text{and} \quad -\infty < x < my + c$$

and $$P(x,y) = 0 \quad \text{if} \quad y_a < y \quad \text{or} \quad y > y_b \quad \text{or} \quad x > my + c \qquad (A.18),$$

where $x=my+c$ is the equation of the straight line passing through the two corners, (x_a,y_a) and (x_b,y_b), of the trapezium and

$$m = \frac{(x_b - x_a)}{(y_b - y_a)} \qquad (A.19).$$

The Fourier transform, $P(k,\theta)$, of the this pressure function can be obtained by substituting (A.18) into the inversion formula (A.5):

$$\mathrm{Re}[P(k,\theta)] + \mathrm{Img}[P(k,\theta)]\, i = \frac{1}{4\pi^2} \int_{y_a}^{y_b} \int_{-\infty}^{x=my+c} P_o\, e^{ikw}\, dxdy \qquad (A.20),$$

this gives

$$\mathrm{Re}[P(k,\theta)] = \frac{-P_o}{4\pi^2} \frac{(y_b-y_a)}{(W_b-W_a)} \left[\frac{\mathrm{Cos}(kW_b) - \mathrm{Cos}(kW_a)}{k^2\, \mathrm{Cos}(\theta)} \right] \qquad (A.21)$$

and $$\mathrm{Img}[P(k,\theta)] = \frac{-P_o}{4\pi^2} \frac{(y_b-y_a)}{(W_b-W_a)} \left[\frac{\mathrm{Sin}(kW_b) - \mathrm{Sin}(kW_a)}{k^2\, \mathrm{Cos}(\theta)} \right] \qquad (A.22),$$

where $$W_b = x_b\, \mathrm{Cos}(\theta) + y_b\, \mathrm{Sin}(\theta) \qquad (A.23)$$

and $$W_a = x_a\, \mathrm{Cos}(\theta) + y_a\, \mathrm{Sin}(\theta) \qquad (A.24).$$

Having derived the function, $P(k,\theta)$, for the constant pressure trapezium, the velocity potential, $\phi_i(x,y,z)$, and the free surface elevation, $\varepsilon_i(x,y)$, can then be obtained by substituting (A.21) and (A.22) into (A.15) and (A.17). The results are

$$\phi_i(x,y,z) =$$

$$P_o \int_{-\frac{\pi}{2}}^{+\frac{\pi}{2}} \frac{(y_b-y_a)\, \mathrm{Sec}^2(\theta)}{(W_b-W_a)\, 2\pi^2 \rho C}\, d\theta \int_0^{+\infty} e^{kz} \left[\frac{\mathrm{Sin}(k(w-W_a) - \mathrm{Sin}(k(w-W_b)}{k\,(k-k_1)} \right] dk$$

$$- \quad P_o \int_{-\frac{\pi}{2}}^{+\frac{\pi}{2}} \frac{(y_b-y_a)\ \mathrm{Sec}^2(\theta)\ e^{k_1 z}}{2\pi\rho C\ k_1\ (W_b-W_a)} \quad \{\mathrm{Cos}(k_1(w-W_a) - \mathrm{Cos}(k_1(w-W_b)\}\ d\theta$$

(A.25)

and

$$\xi_i(x,y) =$$

$$P_o \int_{-\frac{\pi}{2}}^{+\frac{\pi}{2}} \frac{(y_b-y_a)\ \mathrm{Sec}(\theta)}{(W_b-W_a)\ 2\pi^2\rho g}\ d\theta \int_0^{+\infty} \left[\frac{\mathrm{Cos}(k(w-W_a) - \mathrm{Cos}(k(w-W_b)}{(k-k_1)}\right] dk$$

$$+ \quad P_o \int_{-\frac{\pi}{2}}^{+\frac{\pi}{2}} \frac{(y_b-y_a)\ \mathrm{Sec}(\theta)}{2\pi\rho g\ (W_b-W_a)} \quad \{\mathrm{Sin}(k_1(w-W_a) - \mathrm{Sin}(k_1(w-W_b)\}\ d\theta \quad - \quad \delta_i$$

(A.26),

where $\delta_i = \frac{P_o}{\rho g}$ for a field point (x,y) lying inside the trapezium

$\delta_i = 0$ for a field point (x,y) lying outside the trapezium

$\delta_i = \frac{P_o}{2\rho g}$ for a field point (x,y) lying on the periphery of the trapezium.

Note that the pressure is discontinuous around the periphery of the trapezium. From the double Fourier pressure integral (A.20), however, it can be shown that the pressure at the periphery is equal to $+P_o/2$, which is the average of the pressures $P(x,y)=+Po$ inside the trapezium and

$P(x,y)=0$ outside the trapezium. Therefore, when evaluating the free surface elevation at the element's periphery, the hydrostatic pressure term in expression (A.26) should be taken as $+Po/2\rho g$.

Appendix B The Inner k Integral

Recapping from expression (2.2.23) of section (2.2), the inner k integral of the free surface elevation integral (2.2.22) can generally be expressed as:

$$I = \int_0^{+\infty} \frac{\mathrm{Cos}(k(w - W_a))}{(k - k_1)}\, dk = \int_0^{+\infty} \frac{\mathrm{Cos}(k|w - W_a|)}{(k - k_1)}\, dk \qquad (B.1),$$

where

$$w = x\,\mathrm{Cos}(\theta) + y\,\mathrm{Sin}(\theta) \qquad (B.2),$$

$$W_a = x_a\,\mathrm{Cos}(\theta) + y_a\,\mathrm{Sin}(\theta) \qquad (B.3)$$

and

$$k_1 = k_o\,\mathrm{Sec}^2(\theta) \qquad (B.4).$$

The integral, I, is transformed by making the substitution, $u=k|w-W_a|-Z$, into:

$$I = \int_{-Z}^{+\infty} \frac{\mathrm{Cos}(u+Z)}{u}\, du \qquad (B.5),$$

where

$$Z = \left|k_1 (w - W_a)\right| \qquad (B.6)$$

and Z is not equal to zero. The function, Cos(u+Z), in (B.5) is then expanded to give

$$I = \mathrm{Cos}(Z) \int_{-Z}^{+\infty} \frac{\mathrm{Cos}(u)}{u}\,du - \mathrm{Sin}(Z) \int_{-Z}^{+\infty} \frac{\mathrm{Sin}(u)}{u}\,du \qquad \text{(B.7)}.$$

The cosine and sine integrals in expression (B.7) can be written as:

$$\int_{-Z}^{+\infty} \frac{\mathrm{Cos}(u)}{u}\,du = \int_{-\infty}^{+\infty} \frac{\mathrm{Cos}(u)}{u}\,du - \int_{-\infty}^{-Z} \frac{\mathrm{Cos}(u)}{u}\,du \qquad \text{(B.8)}$$

and

$$\int_{-Z}^{+\infty} \frac{\mathrm{Sin}(u)}{u}\,du = \int_{-\infty}^{+\infty} \frac{\mathrm{Sin}(u)}{u}\,du - \int_{-\infty}^{-Z} \frac{\mathrm{Sin}(u)}{u}\,du \qquad \text{(B.9)}.$$

Since Cos(u)/u is an odd function of u, it follows that

$$\int_{-\infty}^{+\infty} \frac{\mathrm{Cos}(u)}{u}\,du = 0 \qquad \text{(B.10)}.$$

By means of an integration around a suitable contour in the complex plane, it can be shown that

$$\int_{-\infty}^{+\infty} \frac{\mathrm{Sin}(u)}{u}\,du = +\pi \qquad \text{(B.11)}.$$

The results derived in (B.10) and (B.11) are then substituted back into (B.7) and after making use of the relationships,

$$\int_{-\infty}^{-Z} \frac{\mathrm{Cos}(u)}{u}\,du = \int_{+\infty}^{+Z} \frac{\mathrm{Cos}(u)}{u}\,du = -\int_{+Z}^{+\infty} \frac{\mathrm{Cos}(u)}{u}\,du \qquad \text{(B.12)}$$

and

$$\int_{-\infty}^{-Z} \frac{\mathrm{Sin}(u)}{u}\,du = -\int_{+\infty}^{+Z} \frac{\mathrm{Sin}(u)}{u}\,du = \int_{+Z}^{+\infty} \frac{\mathrm{Sin}(u)}{u}\,du \qquad \text{(B.13)},$$

the integral, I, becomes

$$I = \mathrm{Cos}(Z)\int_{+Z}^{+\infty} \frac{\mathrm{Cos}(u)}{u}\,du + \mathrm{Sin}(Z)\int_{+Z}^{+\infty} \frac{\mathrm{Sin}(u)}{u}\,du - \pi\,\mathrm{Sin}(Z) \qquad \text{(B.14)}.$$

The cosine and sine integrals in the above expression can be identified as the cosine and sine integral functions, $C_i(Z)$ and $s_i(Z)$, given in Abramowitz and Stegun (Ref.(60)) for positive non-zero values of Z. The integral is rewritten as:

$$I = -C_i(Z)\,\mathrm{Cos}(Z) - s_i(Z)\,\mathrm{Sin}(Z) - \pi\,\mathrm{Sin}(Z) \qquad \text{(B.15)}$$

or

$$I = g(Z) - \pi\,\mathrm{Sin}(Z) \qquad \text{(B.16)}.$$

The methods for evaluating the integral functions, $C_i(Z)$, $s_i(Z)$ and $g(Z)$ are given in appendix C and can also be found in the 'Handbook of Mathematical Functions' by Abramowitz and Stegun (Ref.(60)),p 232).

Appendix C Evaluation of the Integral Functions g(Z) and f(Z)

The auxiliary cosine and sine integrals, g(Z) and f(Z), given in Abramowitz and Stegun (Ref.(60)),p 232) for non-zero positive values of Z are defined as:

$$g(Z) = \int_0^{+\infty} \frac{\mathrm{Cos}(u)}{(u+Z)}\,du = \int_Z^{+\infty} \frac{\mathrm{Cos}(u-Z)}{u}\,du \qquad (C.1)$$

or $$g(Z) = -\,C_i(Z)\,\mathrm{Cos}(Z) - s_i(Z)\,\mathrm{Sin}(Z) \qquad (C.2)$$

and $$f(Z) = \int_0^{+\infty} \frac{\mathrm{Sin}(u)}{(u+Z)}\,du = \int_Z^{+\infty} \frac{\mathrm{Sin}(u-Z)}{u}\,du \qquad (C.3)$$

or $$f(Z) = C_i(Z)\,\mathrm{Sin}(Z) - s_i(Z)\,\mathrm{Cos}(Z) \qquad (C.4),$$

where $$C_i(Z) = -\int_z^{+\infty} \frac{\mathrm{Cos}(u)}{u}\,du \qquad (C.5)$$

and $$s_i(Z) = -\int_z^{+\infty} \frac{\mathrm{Sin}(u)}{u}\,du \qquad (C.6).$$

For $0 < Z \leq 1.0$, g(Z) and f(Z) can be evaluated by using the following infinite series approximations for $C_i(Z)$ and $s_i(Z)$ given in Ref.(60):

$$Ci(Z) = \gamma + \ln(Z) + \sum_{n=1}^{\infty} \frac{(-1)^n Z^{2n}}{(2n)!\ 2n} \qquad (C.7)$$

and $$Si(Z) = -\frac{\pi}{2} + \sum_{n=0}^{\infty} \frac{(-1)^n Z^{2n+1}}{(2n+1)!(2n+1)} \qquad (C.8),$$

where γ is the Euler Constant equal to 0.5772156649 and n is integer. Both of the above alternating series converge rapidly and are truncated when the value of their n^{th} terms is less than 1.0E-6.

For $1.0 \leq Z < +\infty$, g(Z) and f(Z) are evaluated by using the following rational approximation formulae given in Ref.(60):

$$g(Z) = \frac{(Z^8 + A_1 Z^6 + A_2 Z^4 + A_3 Z^2 + A_4)}{Z^2\ (Z^8 + B_1 Z^6 + B_2 Z^4 + B_3 Z^2 + B_4)} + E(Z) \qquad (C.9),$$

where

A_1=42.242855 A_2=302.757865 A_3=352.018498 A_4= 21.821899

B_1=48.196927 B_2=482.485984 B_3=1114.978885 B_4=449.690326

, with the error term $E(Z) < 3.0E-7$ and

$$f(Z) = \frac{(Z^8 + C_1 Z^6 + C_2 Z^4 + C_3 Z^2 + C_4)}{Z\ (Z^8 + D_1 Z^6 + D_2 Z^4 + D_3 Z^2 + D_4)} + E(Z) \qquad (C.10),$$

where

C_1=38.027264 C_2=265.187033 C_3=335.677320 C_4= 38.102495

D_1=40.021433 D_2=322.624911 D_3=570.236280 D_4=157.105423

, with the error term $E(Z) < 5.0E-7$.

Appendix D The Compensating Logarithmic Integral

Recapping from equation (2.4.4) of section (2.4), the compensating logarithmic integral can generally be expressed as:

$$I = \int_{a}^{b} \frac{\mathrm{Log}(|t-T_a|)}{(t - T_o)}\, dt \qquad (D.1),$$

where b is greater than a and T_a is not equal to T_o. The integral is first transformed by using the substitution, $v=(t-T_a)$, into:

$$I = \int_{a-T_a}^{b-T_a} \frac{\mathrm{Log}(|v|)}{(v - \beta)}\, dv \qquad (D.2)$$

where $$\beta = (T_o - T_a) \qquad (D.3).$$

A further transformation using the substitution, $v = \beta u$, gives

$$I = \int_{x1}^{x2} \frac{\mathrm{Log}(|\beta u|)}{(u - 1)}\, du$$

$$I = \int_{x1}^{x2} \frac{\mathrm{Log}(|\beta|)}{(u - 1)}\, du + \int_{x1}^{0} \frac{\mathrm{Log}(|u|)}{(u - 1)}\, du + \int_{0}^{x2} \frac{\mathrm{Log}(|u|)}{(u - 1)}\, du \qquad (D.4),$$

where $x_1 = \frac{a - T_a}{\beta}$ and $x_2 = \frac{b - T_a}{\beta}$ (D.5).

The first integral on the right hand side of equation (D.4) can be evaluated analytically, and the second and third integrals are transformed by using u=-u. It follows that

$$I = \left[\text{Log}(|\beta|)\ \text{Log}(|u-1|) \right]_{x1}^{x2} - \int_0^{-x1} \frac{\text{Log}(|u|)}{(u+1)}\, du + \int_0^{-x2} \frac{\text{Log}(|u|)}{(u+1)}\, du$$

$$I = \text{Log}(|\beta|)\ \text{Log}\left|\frac{(x_2 - 1)}{(x_1 - 1)}\right| - \text{Ilg}(-x_1) + \text{Ilg}(-x_2) \qquad (D.6),$$

where $\text{Ilg}(x) = \int_0^{x} \frac{\text{Log}(|u|)}{(u+1)}\, du$ (D.7).

The method for evaluating the logarithmic integral, Ilg(x), is given in appendix E.

Appendix E Evaluation of the Integral Function Ilg(x)

The logarithmic integral function, Ilg(x), in equation (2.4.5) of section (2.4) is defined as:

$$Ilg(x) = \int_0^x \frac{Log(|u|)}{(1+u)}\, du \qquad (E.1)$$

and integrating by parts gives

$$Ilg(x) = Log(|1+x|)\, Log(|x|) - \int_0^x \frac{Log(|1+u|)}{u}\, du \qquad (E.2).$$

For the case of $|x|<1.0$, the term $Log(|1+u|)$ in the above integral can be expanded into an infinite series in u, thus,

$$Ilg(x) = Log(|1+x|)\, Log(|x|) - \int_0^x \sum_{n=1}^{\infty} (-1)^{n-1} \frac{(u)^{n-1}}{n}\, du \qquad (E.3).$$

The series is then integrated term by term to give

$$Ilg(x) = Log(|1+x|)\, Log(|x|) + \sum_{n=1}^{\infty} \frac{(-x)^n}{n^2} \quad \text{for } |x|<1.0 \qquad (E.4).$$

Note that the above series is also convergent at x=1.0, where

$$\sum_{n=1}^{\infty} \frac{(-1)^n}{n^2} = -\frac{\pi^2}{12} \qquad \text{(E.5)},$$

and at x=-1, where

$$\sum_{n=1}^{\infty} \frac{1}{n^2} = \frac{\pi^2}{6} \qquad \text{(E.6)}$$

(also see Abramowitz and Stegun (Ref.(60)), equ. 4.1.55 and 4.1.56). For x >1.0, expression (E.2) is rewritten as:

$$Ilg(x) = Log(|1+x|)\,Log(|x|) - \int_1^x \frac{Log(|1+1/u|)}{u}\,du$$

$$- \int_1^x \frac{Log(|u|)}{u}\,du - \int_0^1 \frac{Log(|1+u|)}{u}\,du$$

$$Ilg(x) = Log(|1+x|)\,Log(|x|) - \int_0^x \frac{Log(|1+1/u|)}{u}\,du$$

$$- \frac{(Log(|x|))^2}{2} - \frac{\pi^2}{12} \qquad \text{(E.7)}.$$

The term Log(|1+1/u|) in the above expression is then expanded into an infinite series in inverse power of u:

$$Ilg(x) = Log(|x|)\ Log\left|\frac{(1+x)}{x^{1/2}}\right| - \int_1^x \sum_{n=1}^{\infty} \frac{(-1/u)^{n+1}}{n}\ du - \frac{\pi^2}{12} \qquad (E.8)$$

and the series is integrated term by term to give

$$Ilg(x) = Log(|x|)\ Log\left|\frac{(1+x)}{x^{1/2}}\right| - \sum_{n=1}^{\infty} \frac{(-1/x)^n}{n^2} - \sum_{n=1}^{\infty} \frac{(-1)^n}{n^2}$$

$$- \frac{\pi^2}{12} \qquad (E.9).$$

Using the result in (E.5), the above infinite series can be further simplified into:

$$Ilg(x) = Log(|x|)\ Log\left|\frac{(1+x)}{x^{1/2}}\right| - \sum_{n=1}^{\infty} \frac{(-1/x)^n}{n^2} - \frac{\pi^2}{6} \qquad (E.10).$$

for $x > 1.0$

For the case of $x < -1.0$, the indefinite integral is written as:

$$Ilg(x) = Log(|1+x|)\ Log(|x|) - \int_{-1}^{x} \frac{Log(|1+1/u|)}{u}\ du$$

$$- \int_{-1}^{x} \frac{Log(|u|)}{u}\ du - \int_{0}^{-1} \frac{Log(|1+u|)}{u}\ du \qquad (E.11).$$

Similarly, the term Log(|1+u|) can be expanded in inverse power of u to give

$$Ilg(x) = Log(|x|)\,Log\left|\frac{(1+x)}{x^{1/2}}\right| - \int_{-1}^{x} \sum_{n=1}^{\infty} \frac{(-1/u)^{n+1}}{n}\,du + \frac{\pi^2}{6} \qquad (E.12).$$

As before, the series is integrated term by term to give

$$Ilg(x) = Log(|x|)\,Log\left|\frac{(1+x)}{x^{1/2}}\right| - \sum_{n=1}^{\infty} \frac{(-1/x)^n}{n^2} + \sum_{n=1} \frac{1}{n^2} + \frac{\pi^2}{6} \qquad (E.13).$$

Using the result in (E.6), the above infinite series can be written as:

$$Ilg(x) = Log(|x|)\,Log\left|\frac{(1+x)}{x^{1/2}}\right| - \sum_{n=1}^{\infty} \frac{(-1/x)^n}{n^2} + \frac{\pi^2}{3} \qquad (E.14).$$

for $x < -1.0$

The series given in (E.4), (E.10) and (E.14) all converge as n tends to infinity, however, the rate of convergence varies with the value of x. Standing (Ref.(30)) has pointed out that the maximum error when the series is summed to N terms is occur at x=-1.0 and can be estimated by considering

$$\sum_{n=N+1}^{\infty} \frac{1}{n^2} = \sum_{n=N+1}^{2N} \frac{1}{n^2} + \sum_{n=2N+1}^{4N} \frac{1}{n^2} + \sum_{n=4N+1}^{8N} \frac{1}{n^2} + \cdots\cdots\cdots$$

$$< \frac{N}{N^2} + \frac{2N}{(2N)^2} + \frac{4N}{(4N)^2} + \cdots\cdots\cdots\cdots\cdots\cdots\cdots$$

$$< \quad 1/N \quad (1 + 1/2 + 1/4 + 1/8 + \cdots\cdots\cdots\cdots\cdots\cdots\cdots\cdots$$

$$< \quad 2/N \qquad\qquad (E.15).$$

Thus, the maximum error in summing the series to N terms is less than 2/N. In the present program, the series are truncated when the n^{th} term is less than 1.0E-6 and this is equivalent to a maximum error of less than 2.0E-3 for x=-1.0. However, the actual error at x=-1.0 was found to be approximately equal to one half of the maximum error deduced from (E.15). The details presented above are based on reference (30), and are included for completeness.

Appendix F Evaluation of the Derivatives of g(Z) and f(Z)

As mentioned in appendix C, the auxiliary cosine and sine integral functions, g(Z) and f(z), are defined as:

$$g(Z) = -C_i(Z)\,\mathrm{Cos}(Z) - s_i(Z)\,\mathrm{Sin}(Z) \qquad (F.1)$$

and

$$f(Z) = C_i(Z)\,\mathrm{Sin}(Z) - s_i(Z)\,\mathrm{Cos}(Z) \qquad (F.2),$$

in which the integrals $C_i(Z)$ and $s_i(Z)$ are given in expressions (C.5) and (C.6). The non-zero positive value Z in the above expressions is now treated as a function of t:

$$Z = \left| k_o \sqrt{1 + t^2}\ \{ (x-x_a) + |(y-y_a)|t \} \right| \qquad (F.3).$$

The derivatives of g(Z) and f(Z) with respect to t may be obtained by means of a numerical differentiation procedure, such as the finite difference method. In the present case, however, they are obtained by directly differentiating the functions themselves. Using the chain rule of differentiation, the derivatives of g(Z) and f(Z) with respect to t can be written as:

$$\frac{dg(Z)}{dt} = \frac{dZ}{dt}\,\frac{dg(Z)}{dZ} \qquad (F.4)$$

and

$$\frac{df(Z)}{dt} = \frac{dZ}{dt}\,\frac{df(Z)}{dZ} \qquad (F.5),$$

where

$$\frac{dZ}{dt} = k_o \left[\left[\frac{(x-x_a)+|(y-y_a)|t}{(1 + t^2)^{1/2}} \right] t + M_o(1 + t^2)^{1/2}\,|y-y_a| \right] \qquad (F.6)$$

and $M_o = 1$ for $t > \frac{-(x-x_a)}{|y-y_a|}$ (F.7)

or $M_o = -1$ for $t < \frac{-(x-x_a)}{|y-y_a|}$ (F.8).

From expressions (F.1) and (F.2), the derivatives of g(Z) and f(Z) with respect to Z can be written as:

$$\frac{dg(Z)}{dZ} = -\frac{dC_i(Z)}{dZ}\,\mathrm{Cos}(Z) + C_i(Z)\,\mathrm{Sin}(Z) - \frac{ds_i(Z)}{dZ}\,\mathrm{Sin}(Z) - s_i(z)\,\mathrm{Cos}(Z) \qquad (F.9)$$

and

$$\frac{df(Z)}{dZ} = \frac{dC_i(Z)}{dZ}\,\mathrm{Sin}(Z) + C_i(Z)\,\mathrm{Cos}(Z) - \frac{ds_i(Z)}{dZ}\,\mathrm{Cos}(Z) + s_i(Z)\,\mathrm{Sin}(Z) \qquad (F.10),$$

where the functions $C_i(Z)$ and $s_i(Z)$ are evaluated by the methods discussed in appendix C. For $0 < Z \leq 1.0$, $dC_i(Z)/dZ$ and $ds_i(Z)/dZ$ can be evaluated by directly differentiating the series expansions given in (C.7) and (C.8), thus,

$$\frac{dC_i(Z)}{dZ} = \frac{1}{Z} + \sum_{n=1}^{\infty} \frac{(-1)^n\, Z^{2n-1}}{(2n)!} \qquad (F.11)$$

and

$$\frac{ds_i(Z)}{dZ} = \sum_{n=0}^{\infty} \frac{(-1)^n\, Z^{2n}}{(2n+1)!} \qquad (F.12).$$

Both of the above alternating series are truncated when the value of their n^{th} terms is less than 1.0E-6. For $1.0 < Z < +\infty$, dg(Z)/dZ and

$df(Z)/dZ$ are evaluated by directly differentiating the rational approximation formulae for $g(Z)$ and $f(Z)$ given in expressions (C.9) and (C.10). Thus,

$$\frac{dg(Z)}{dZ} = \frac{(8Z^6 + 6A_1Z^4 + 4A_2Z^2 + 2A_3)}{Z\,(Z^8 + B_1Z^6 + B_2Z^4 + B_3Z^2 + B_4)}$$

$$- (Z^8 + A_1Z^6 + A_2Z^4 + A_3Z^2 + A_4)\ \frac{(10Z^8 + 8B_1Z^6 + 6B_2Z^4 + 4B_3Z^2 + 2B_4)}{Z^3\,(Z^8 + B_1Z^6 + B_2Z^4 + B_3Z^2 + B_4)^2} \qquad (F.13)$$

and

$$\frac{df(Z)}{dZ} = \frac{(8Z^6 + 6C_1Z^4 + 4C_2Z^2 + 2C_3)}{(Z^8 + D_1Z^6 + D_2Z^4 + D_3Z^2 + D_4)}$$

$$- (Z^8 + C_1Z^6 + C_2Z^4 + C_3Z^2 + C_4)\ \frac{(9Z^8 + 7D_1Z^6 + 5D_2Z^4 + 3D_3Z^2 + D_4)}{Z^2\,(Z^8 + D_1Z^6 + D_2Z^4 + D_3Z^2 + D_4)^2} \qquad (F.14),$$

where the coefficients A_1, B_1, C_1 and D_1 etc have the same meanings as those in expressions (C.9) and (C.10).

Appendix G Integrating Limits of the Free Wave Corner Function

Following the transformation, $t=\mathrm{Tan}(\theta)$, the free wave integral, $F_a(x,y)$, in expression (2.2.28) is transformed into:

$$F_a(x,y) = \frac{1}{2\pi} \int_{-\infty}^{+\infty} [\mathrm{Sgn}(\lambda_a)-1] \quad \frac{\mathrm{Sin}(|\lambda_a|)}{(t - T_o)} \, dt \qquad (G.1),$$

where $$\lambda_a = \{(x-x_a)+(y-y_a)t\} \sqrt{(1 + t^2)}\, k_o \qquad (G.2),$$

$$T_o = \frac{-(x_b - x_a)}{(y_b - y_a)} \qquad (G.3)$$

and $\mathrm{Sgn}(\lambda_a) = +1$ for $(\lambda_a) > 0$

or $\mathrm{Sgn}(\lambda_a) = -1$ for $(\lambda_a) < 0$ (G.4).

For $|(y-y_a)|>0$, (λ_a) is equal to zero at $t=T_a$, where

$$T_a = \frac{-(x - x_a)}{(y - y_a)} \qquad (G.5).$$

First, let us consider the variations of the functions $(x-x_a)+(y-y_a)t$ and $\mathrm{Sgn}(\lambda_a)$ in expression (G.1) with t for the case of $(y-y_a)>0$.

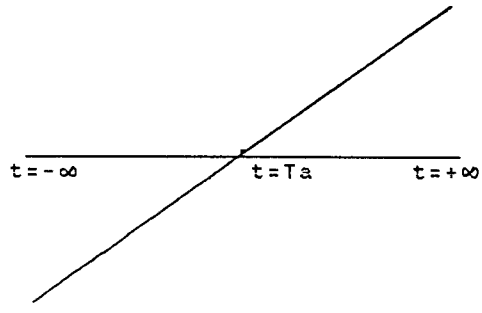

Function $(x-x_a)+(y-y_a)t$ for $(y-y_a)>0$

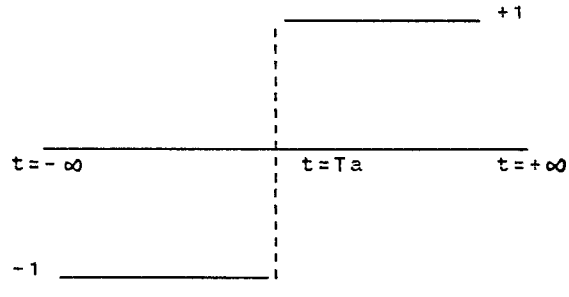

Function $\mathrm{Sgn}(\lambda_a)$ for $(y-ya)>0$

As shown in the diagrams above, the value of (λ_a) is less than zero for $t<T_a$ and greater than zero for $t>T_a$, it follows that $[Sgn(\lambda_a)-1]=-2$ for $t<T_a$ and $[Sgn(\lambda_a)-1]=0$ for $T>T_a$. In this case, the free wave corner function, $F_a(x,y)$, in expression (G.1) becomes

$$F_a(x,y) = \frac{-1}{\pi} \int_{-\infty}^{T_a} \frac{Sin(|\lambda_a|)}{(t - T_o)}\, dt \qquad \text{for } (y-y_a)>0 \qquad (G.6).$$

Now, consider the case of $(y-y_a)<0$ where the variations of the functions $(x-x_a)+(y-y_a)t$ and $Sgn(\lambda_a)$ against t are shown in the diagrams below.

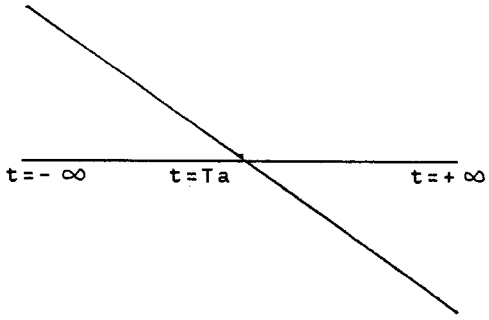

Function $(x-x_a)+(y-y_a)t$ for $(y-y_a)<0$

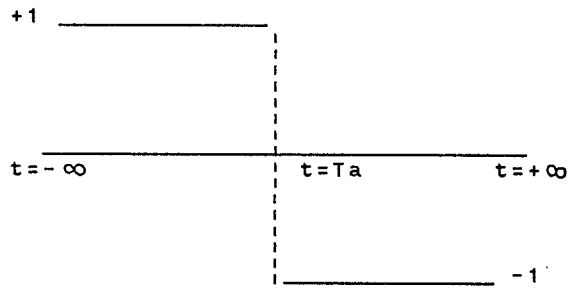

Function $Sgn(\lambda_a)$ for $(y-ya)<0$

In this case, $[Sgn(\lambda_a)-1]=0$ for $t<T_a$ and $[Sgn(\lambda_a)-1]=-2$ for $t>T_a$, therefore the free wave corner function, $F_a(x,y)$, in expression (G.1) becomes

$$F_a(x,y) = \frac{-1}{\pi} \int_{T_a}^{+\infty} \frac{Sin(|\lambda_a|)}{(t - T_o)}\, dt \qquad \text{for } (y-y_a)<0 \qquad (G.7).$$

For the case of $(y-y_a)=0$ and $(x-x_a)<0$, $Sgn(\lambda_a)=-1$ for all values of t, therefore the free wave corner function, $Fa(x,y)$, in expression (G.1) becomes

$$Fa(x,y) = \frac{-1}{\pi} \int_{-\infty}^{+\infty} \frac{Sin(|\lambda_a|)}{(t - T_o)}\, dt \qquad \begin{matrix} \text{for } (y-y_a)=0 \\ \text{and } (x-x_a)<0 \end{matrix} \qquad \text{(G.8).}$$

Finally for the case of $(y-y_a)=0$ and $(x-x_a)>0$, where $(\lambda_a)>0$ and $Sgn(\lambda_a)=+1$ for all values of t, the free wave corner function, $Fa(x,y)$, in expression (G.1) is equal to zero.

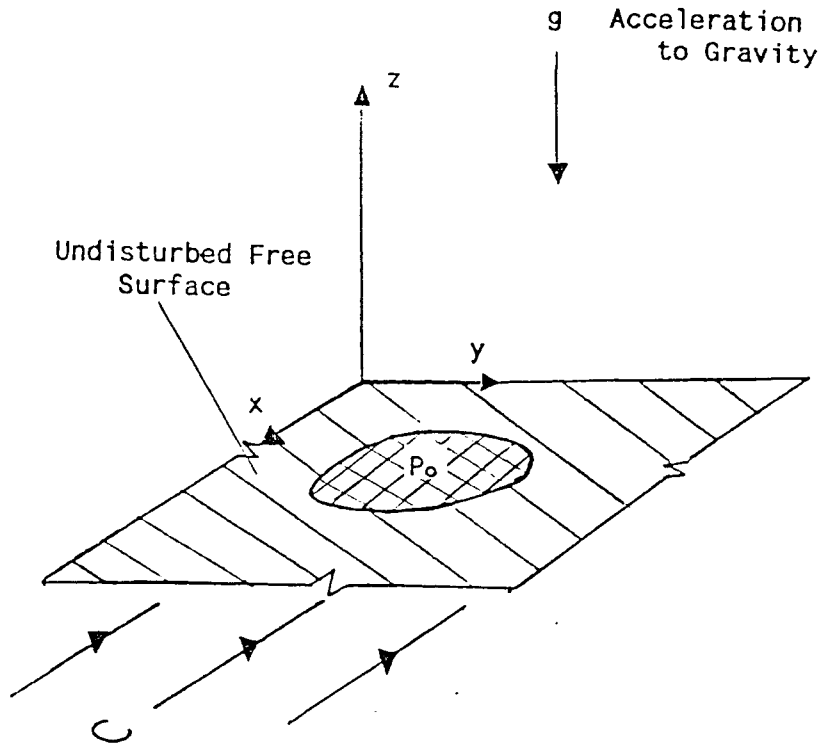

Fig.(2.1) x-y-z Cartesian Coordination System with the Undisturbed Free Surface Lies on the x-y Plane

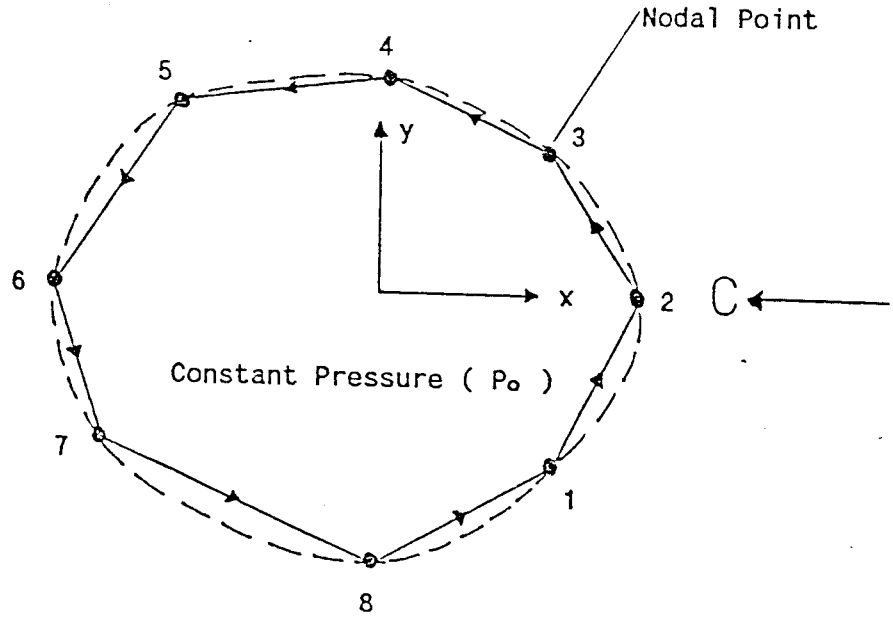

Fig.(2.2a) Representing an Irregular Area by an Equivalent Polygon and Nodal Numbering System

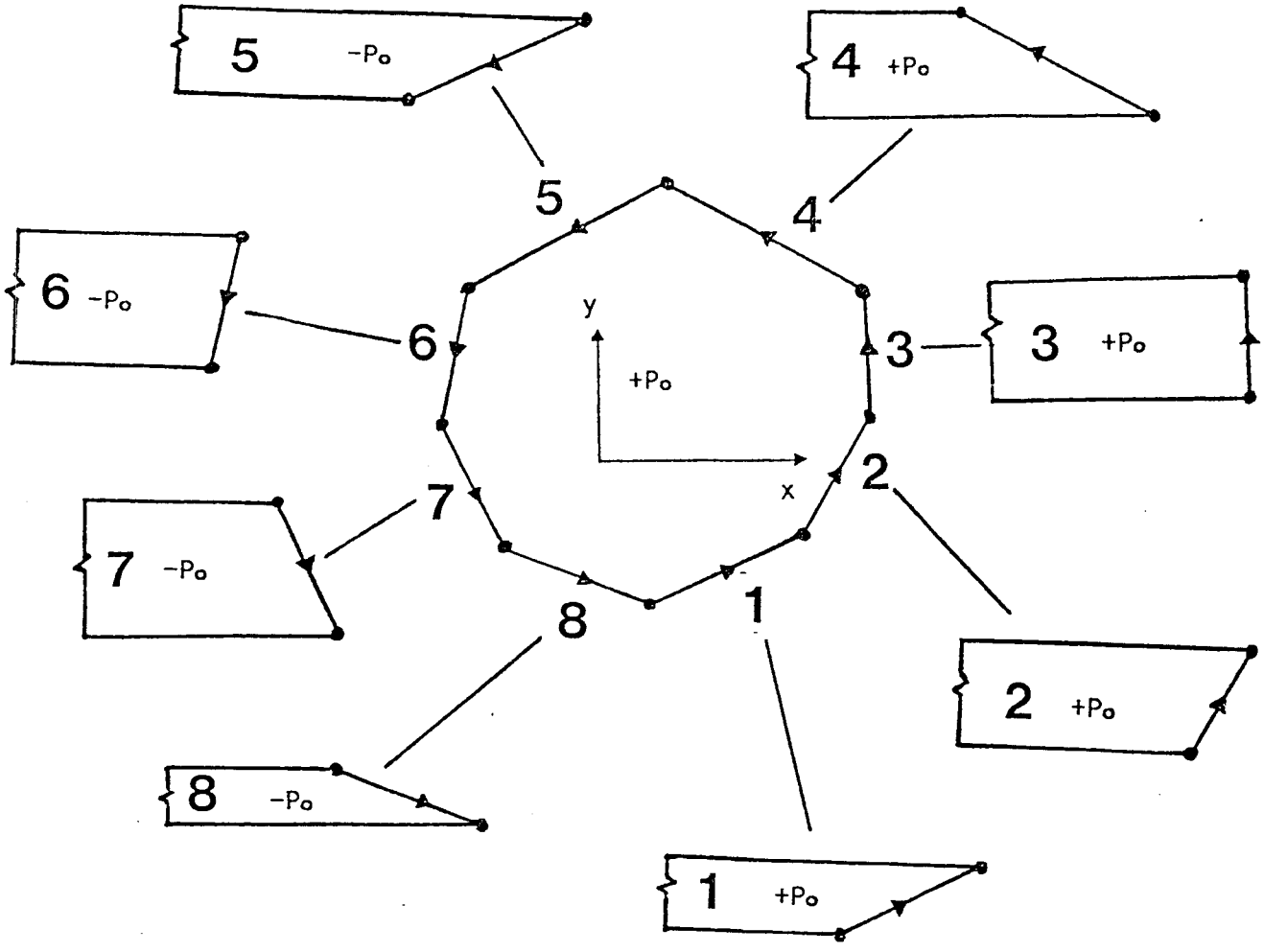

Fig.(2.2b) Breakdown of a Constant Pressure Polygon into Constant Pressure Trapeziums

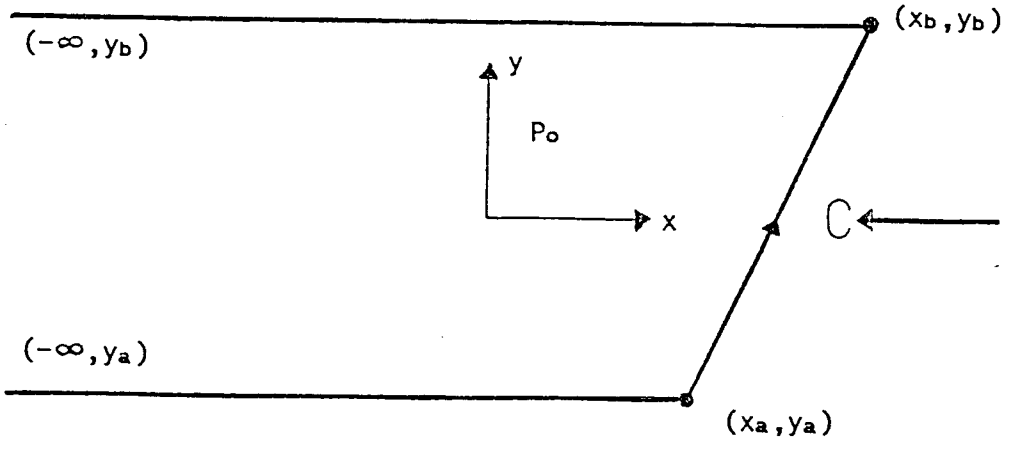

Fig.(2.2c) A Constant Pressure Trapezium

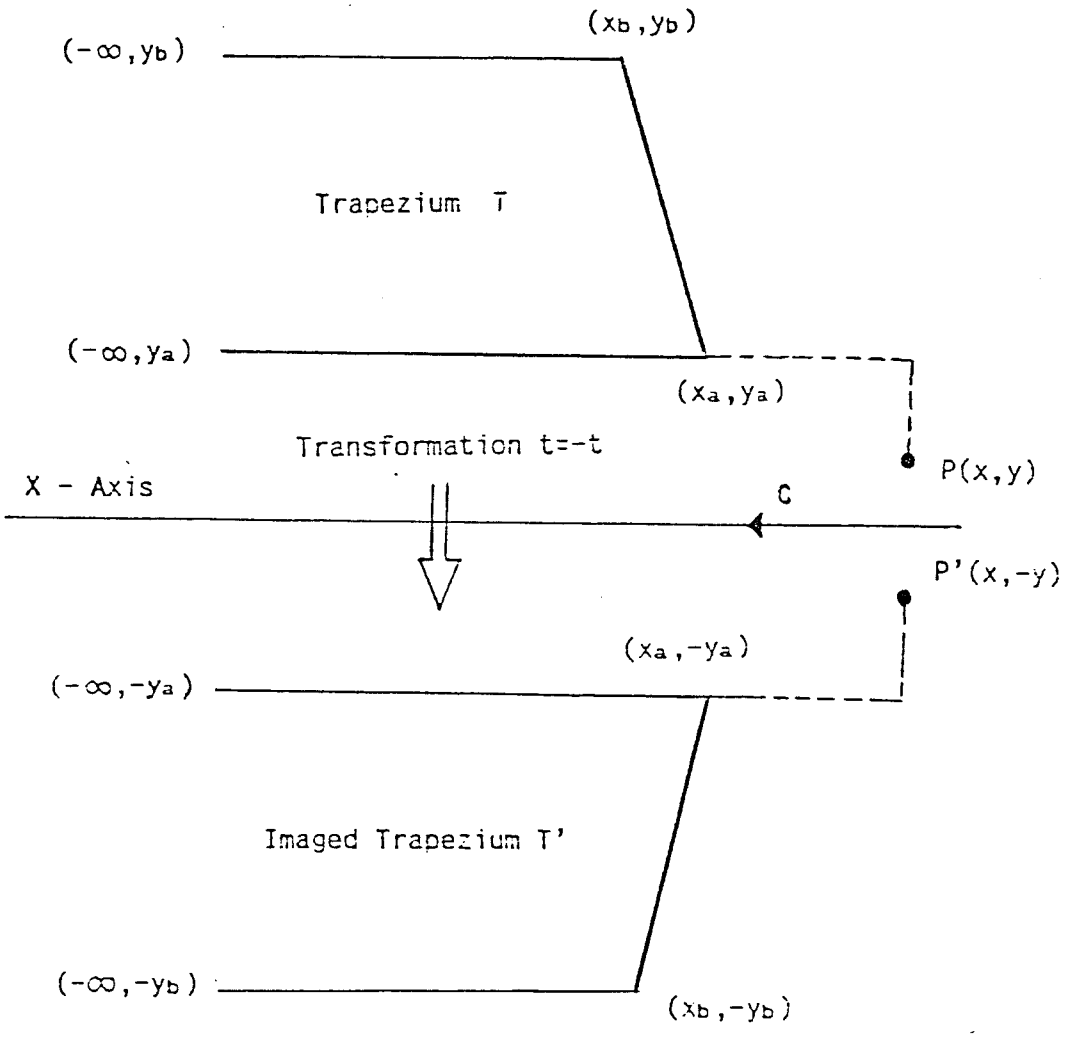

Fig.(2.3) Constant Pressure Trapezium, T, and Field point , P, and the Mirror Imaged Trapezium, T', and Mirror Imaged Field Point, P', about the x-Axis (Note that the surface elevation at P due to T is equal to that at P' due to T')

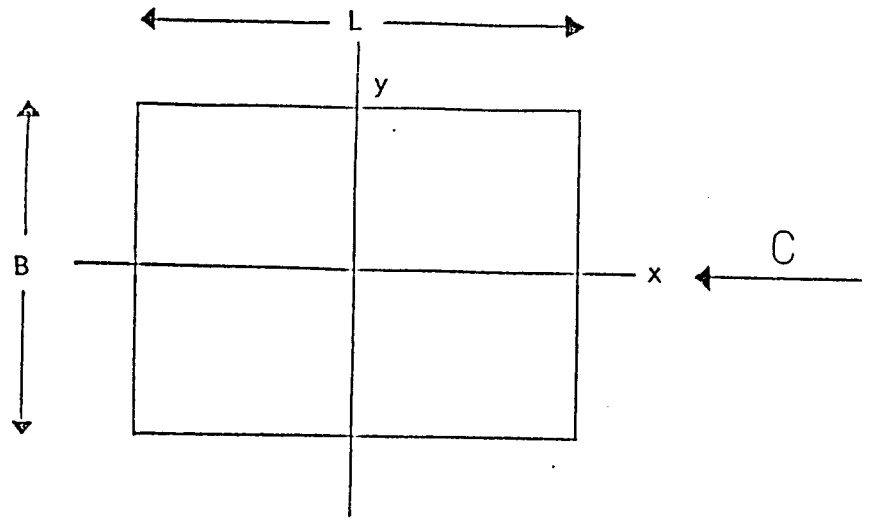

Fig.(2.4a) Non-drifted Rectangular Element

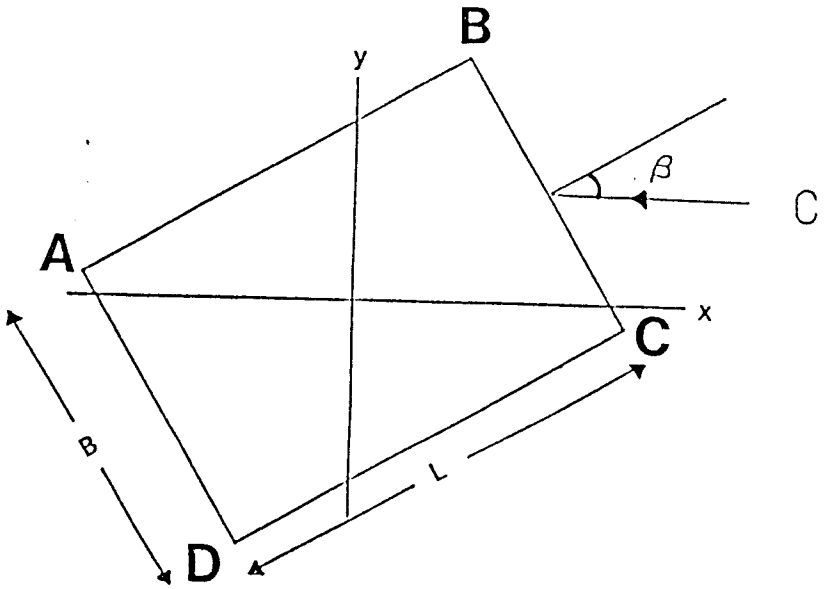

Fig.(2.4b) Drifted Rectangular Element

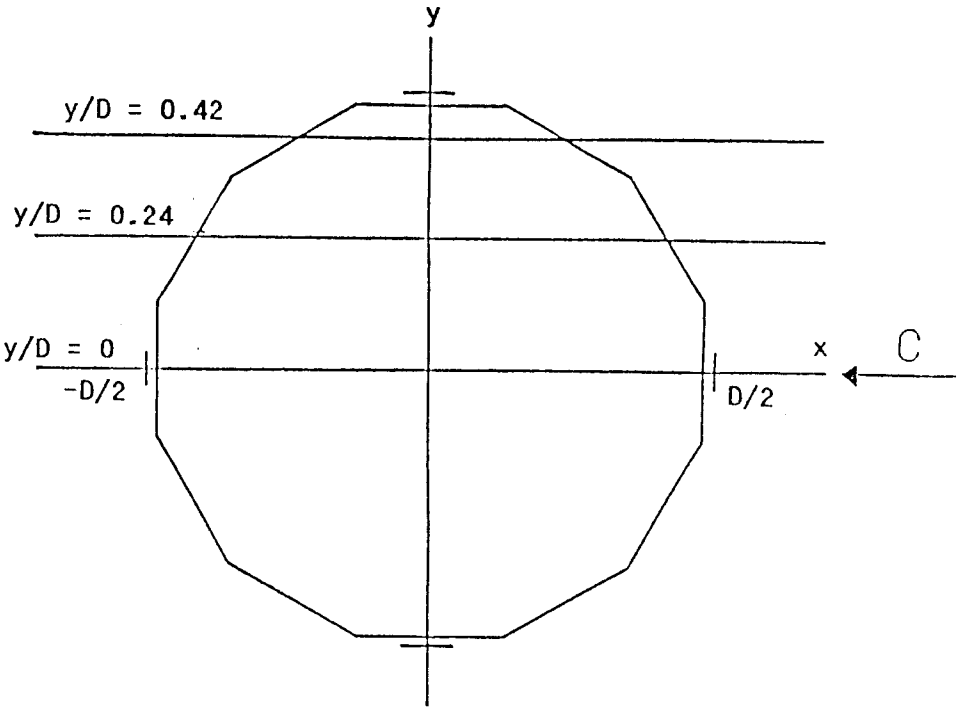

Fig.(2.4c) 12-sided Polygon Representation of a Circular Element

Fig.(2.5a) Longitudinal Wave Profile for Rectangular Element

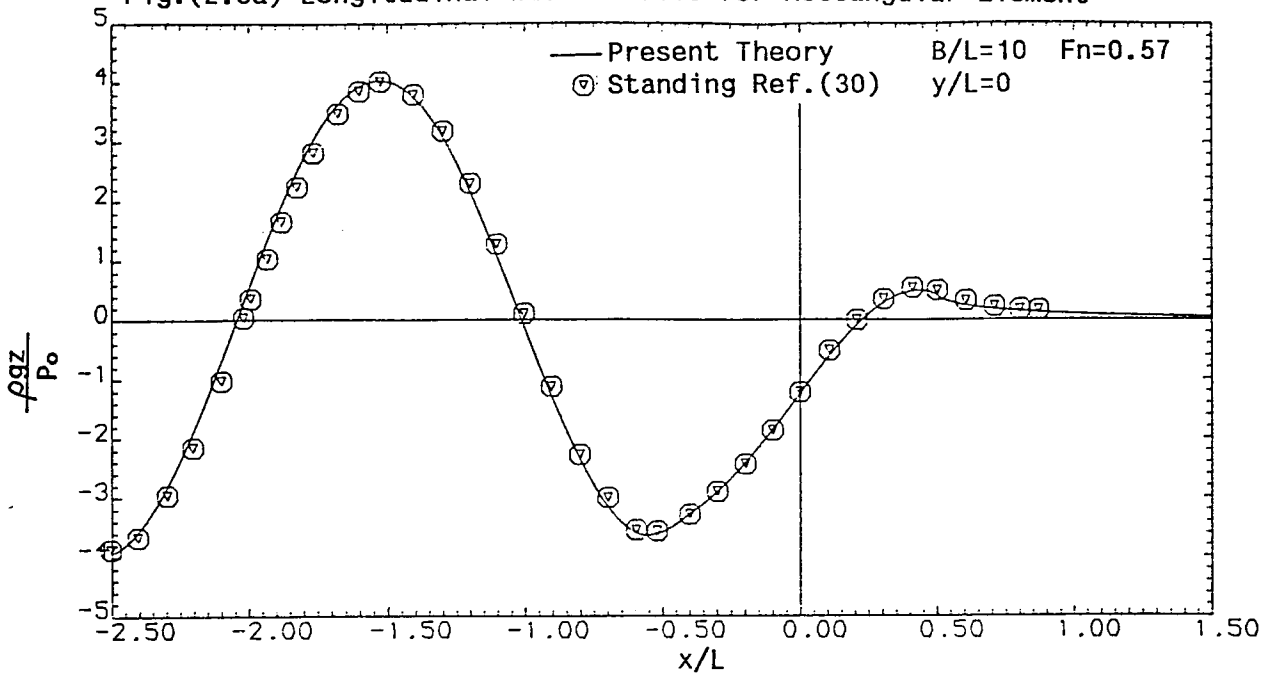

Fig.(2.5b) Longitudinal Wave Profile for Rectangular Element

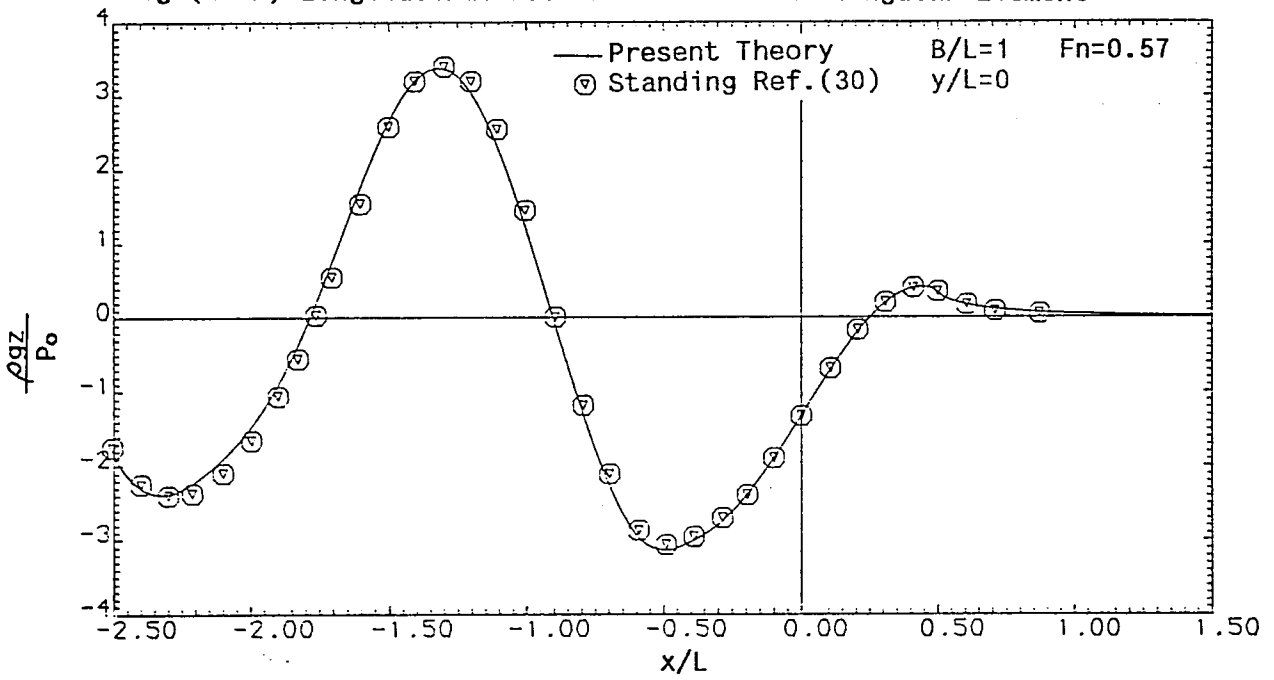

Fig.(2.5c) Longitudinal Wave Profile for Rectangular Element

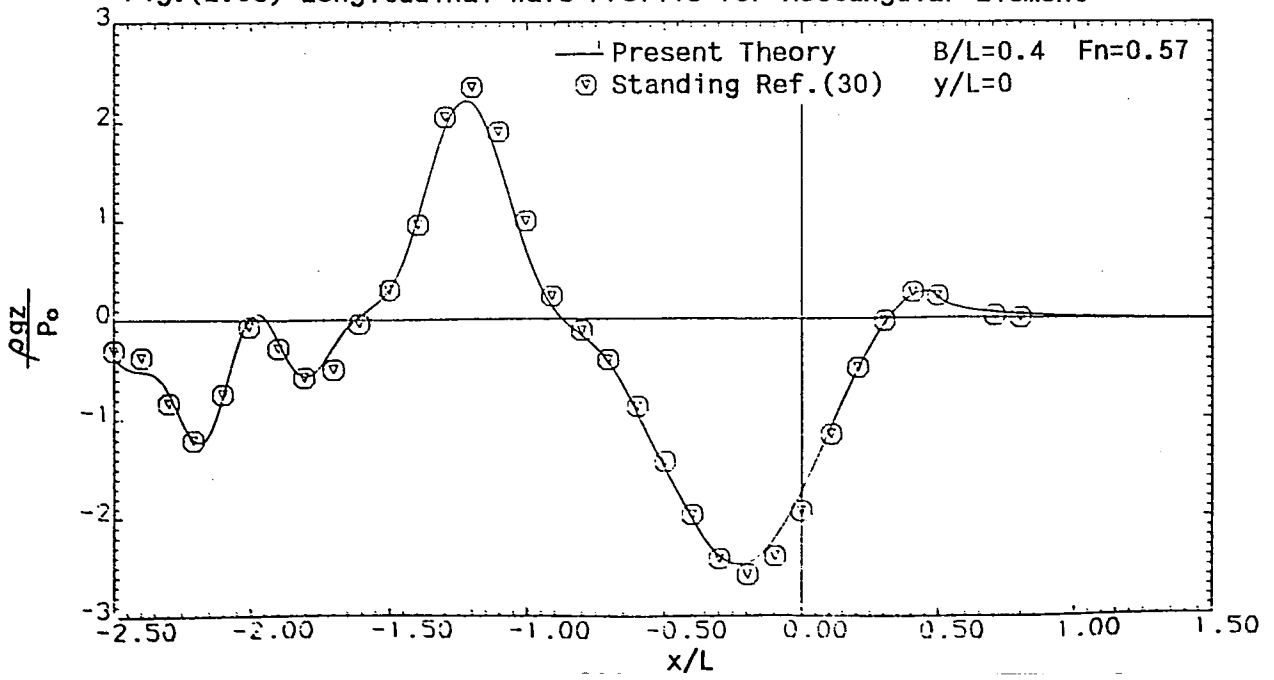

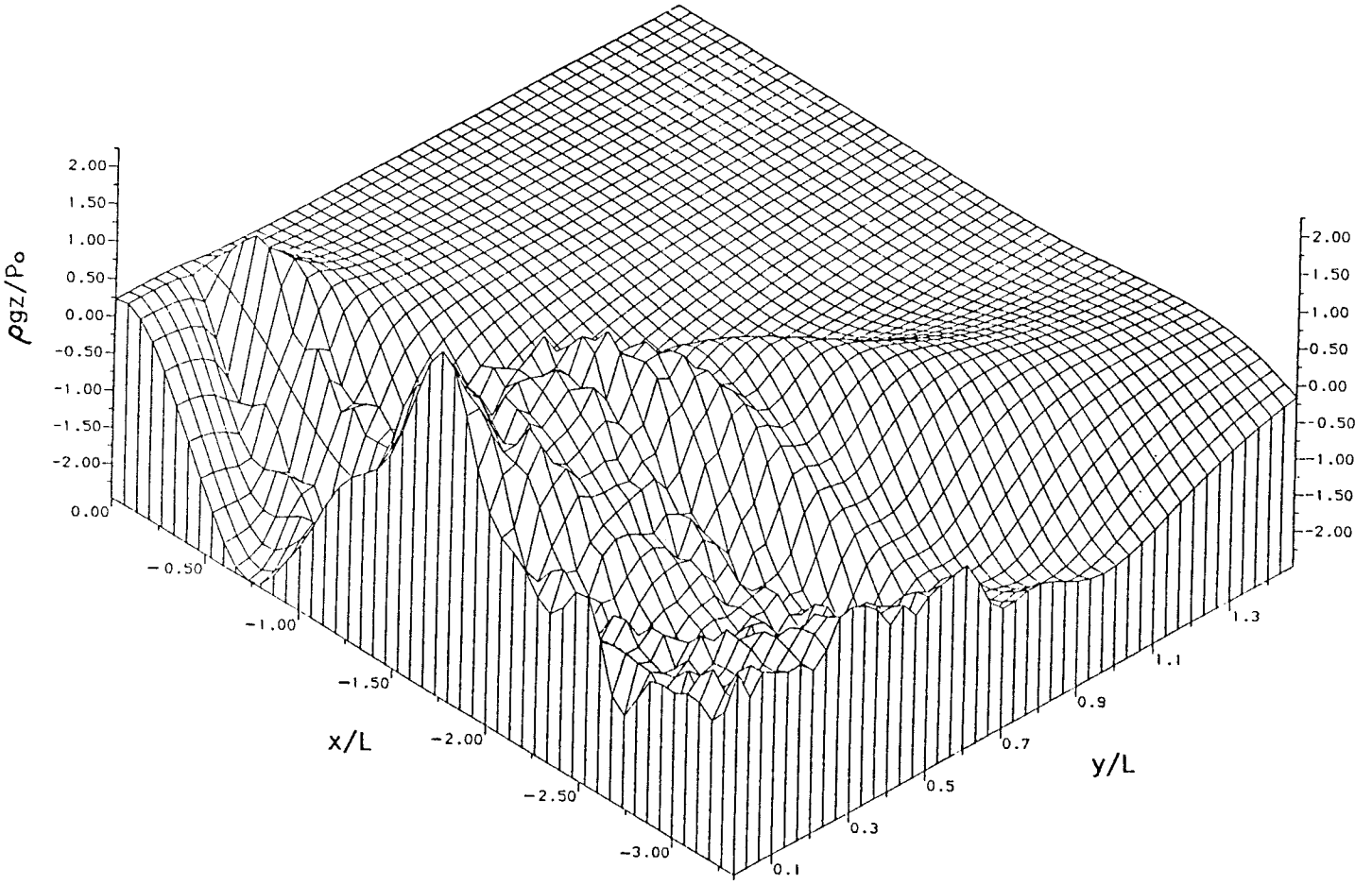

Corners' Coordinates of Rectangle	
x/L	y/L
0.00	-0.20
-1.00	-0.20
-1.00	0.20
0.00	0.20

Fig.(2.5d) Free Surface Elevation produced by a Constant Pressure Rectangular Element

(F_n = 0.57 B/L = 0.4)

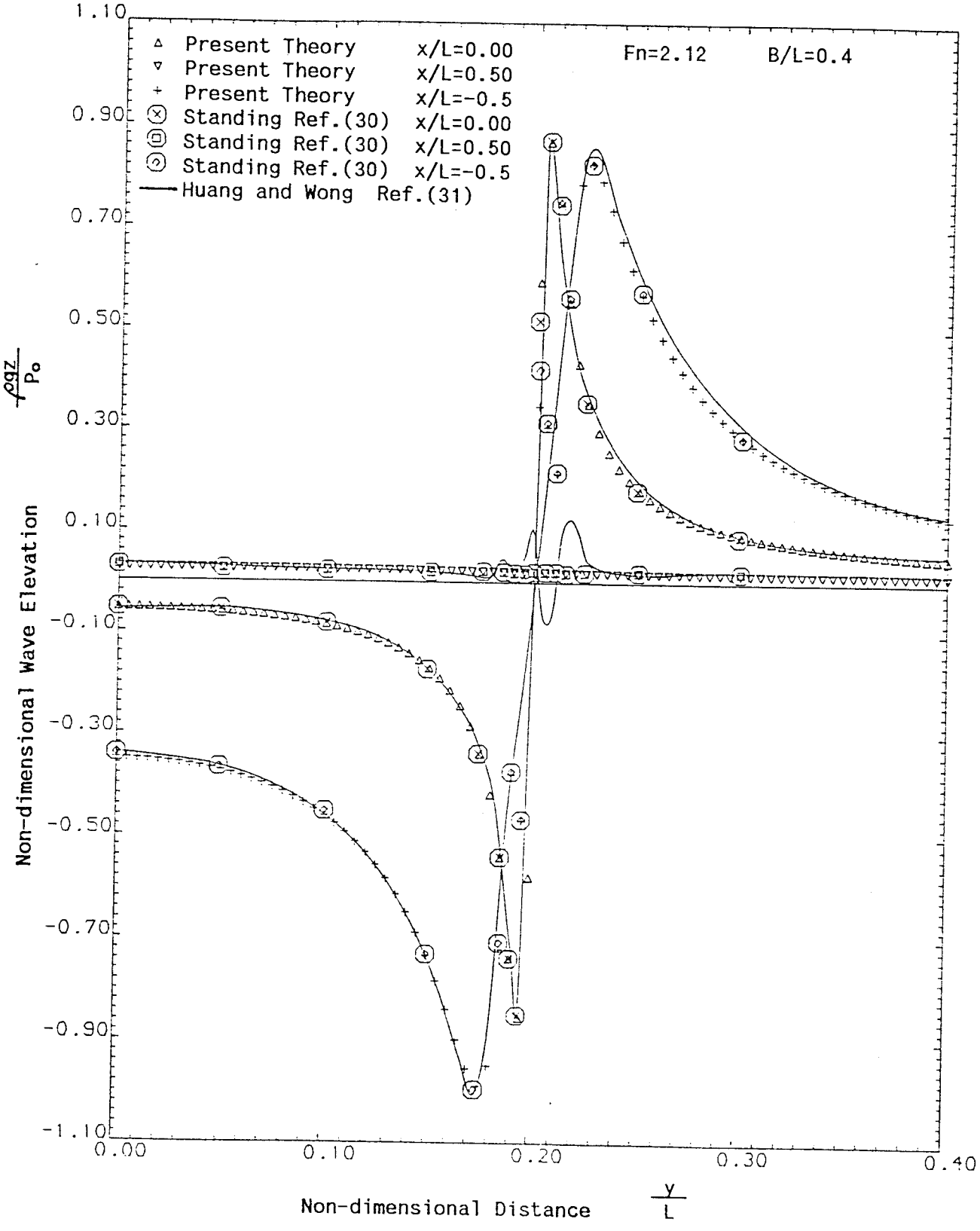

Fig.(2.6) Transverse Wave Profiles for non-drifted Rectangular Element

Fig.(2.7a) Transverse Wave Profile for Rectangular Element

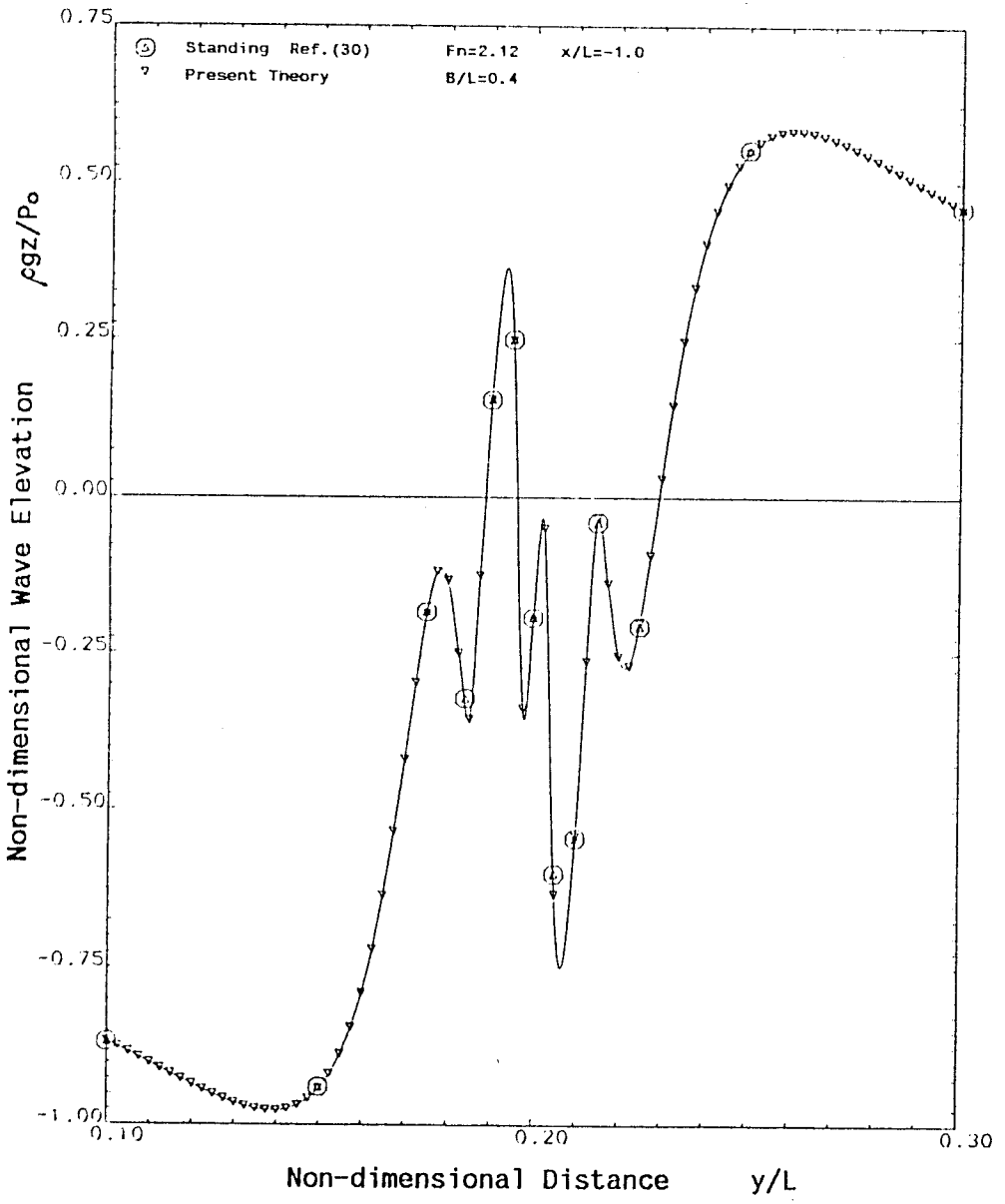

Fig.(2.7b) Transverse Wave Profile for Rectangular Element

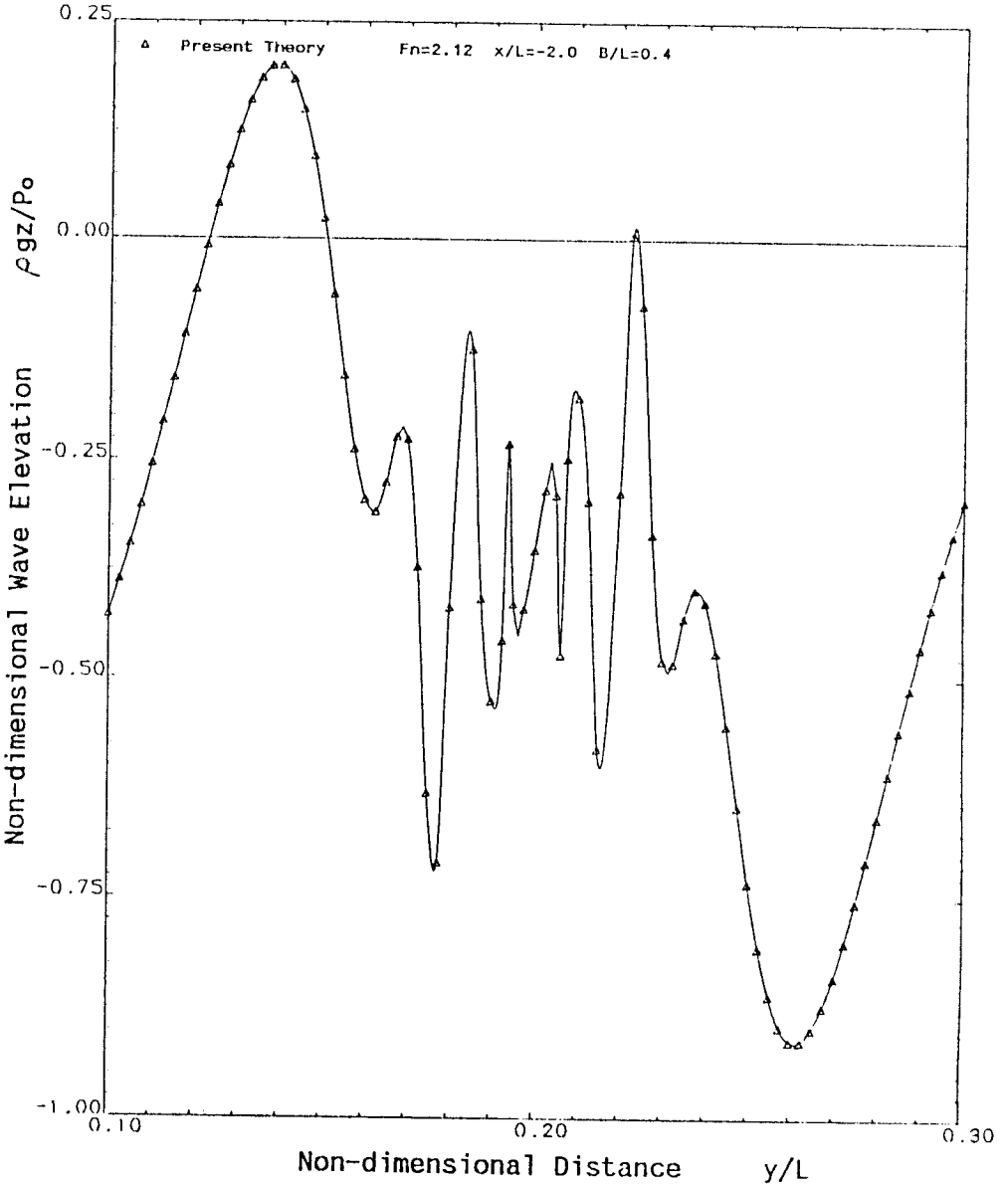

Fig.(2.8a) Longitudinal Wave Profiles for 30° Drifted Rectangular Element

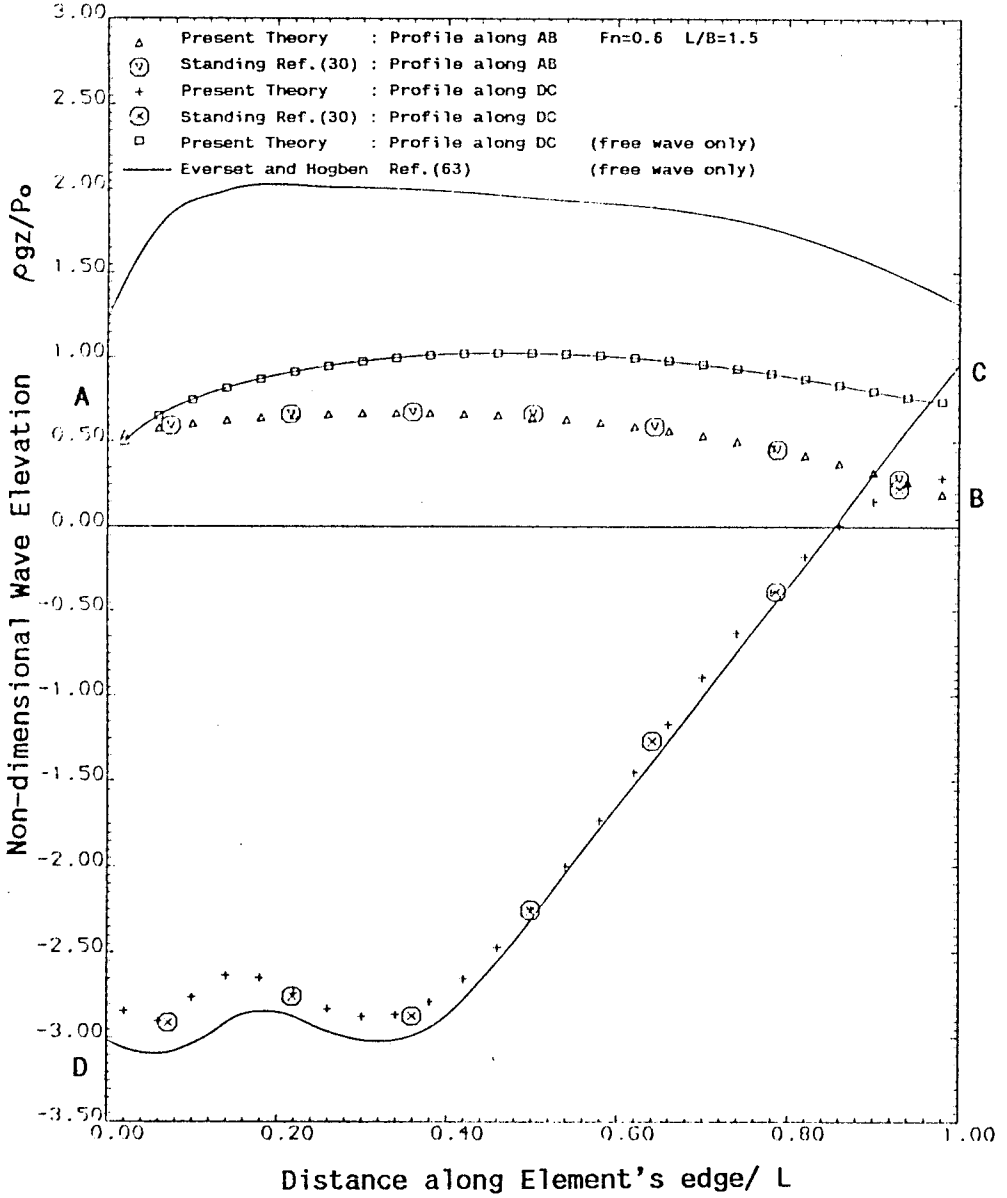

Fig.(2.8b) Transverse Wave Profiles for 30° Drifted Rectangular Element

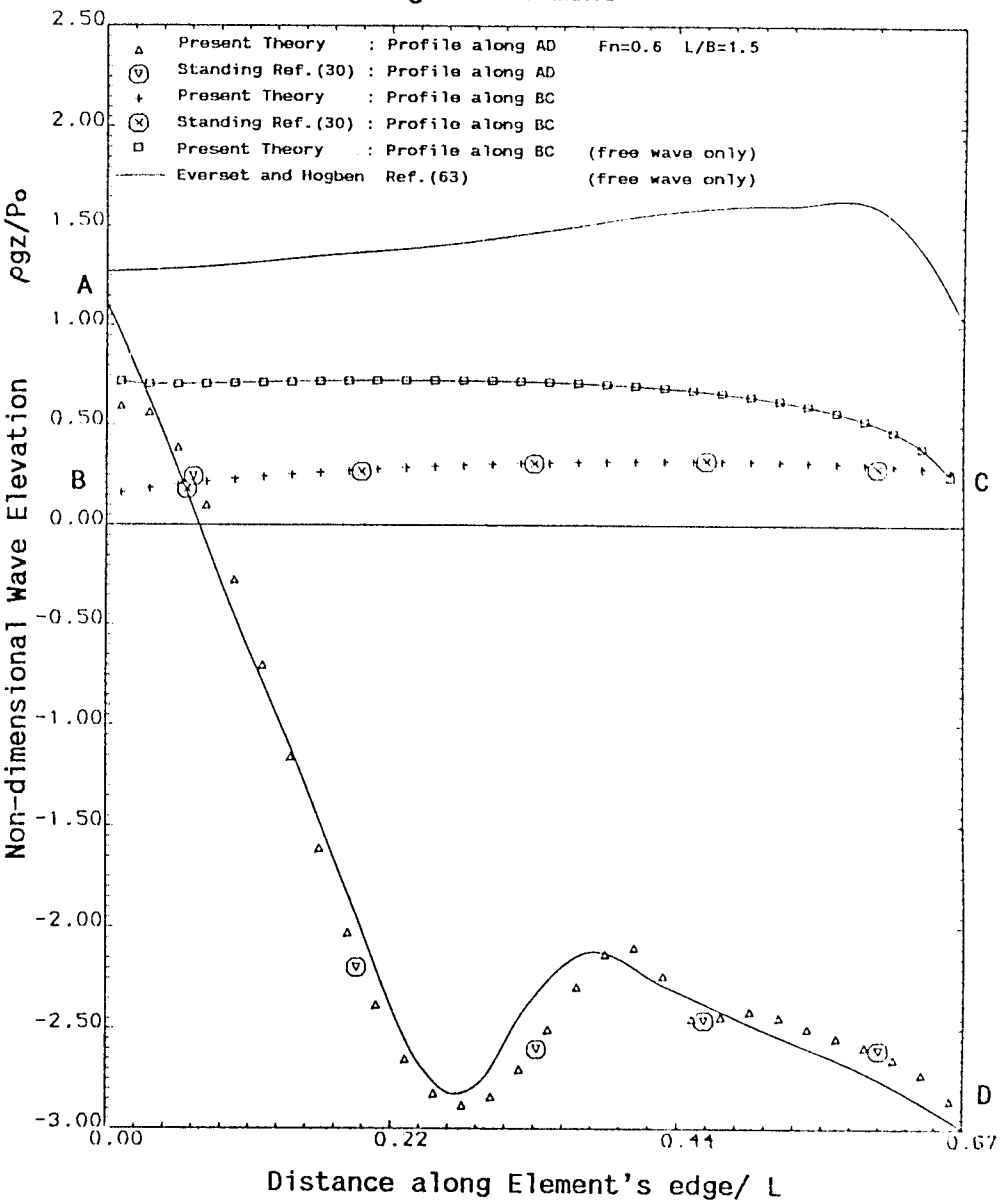

Fig.(2.9a) Longitudinal Wave Profile for Circular Element (Fn=0.4)

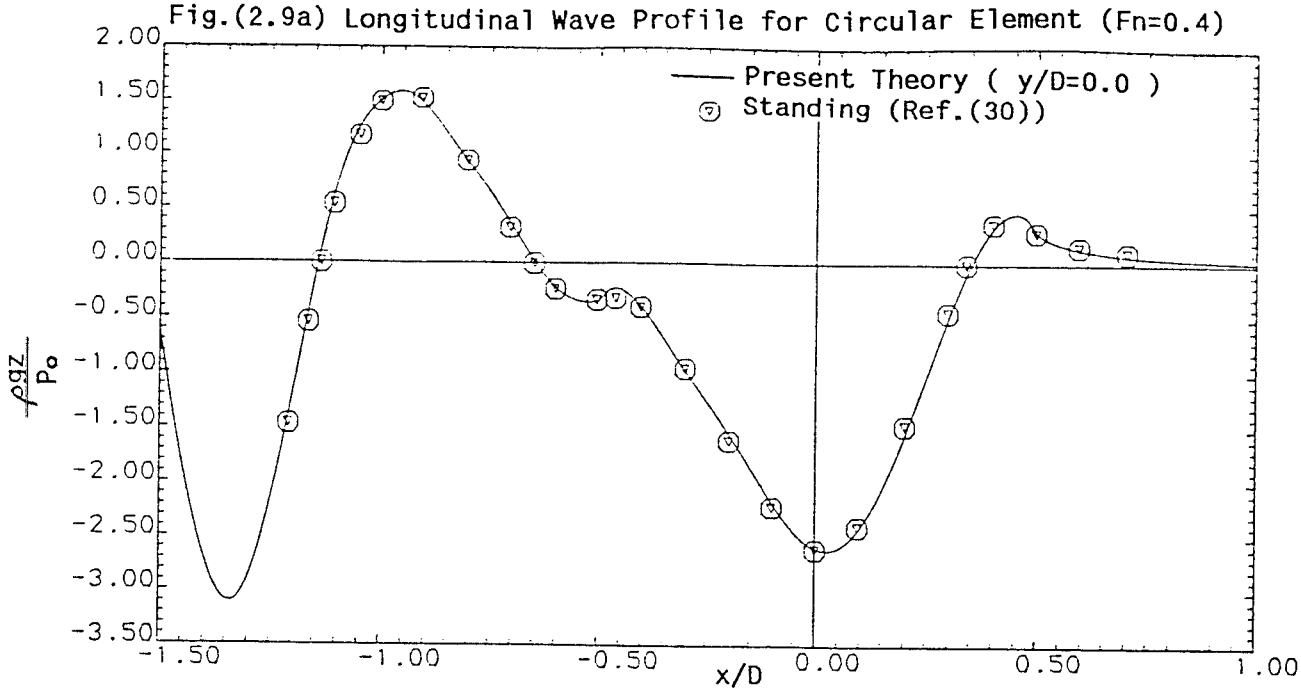

Fig.(2.9b) Longitudinal Wave Profile for Circular Element (Fn=0.4)

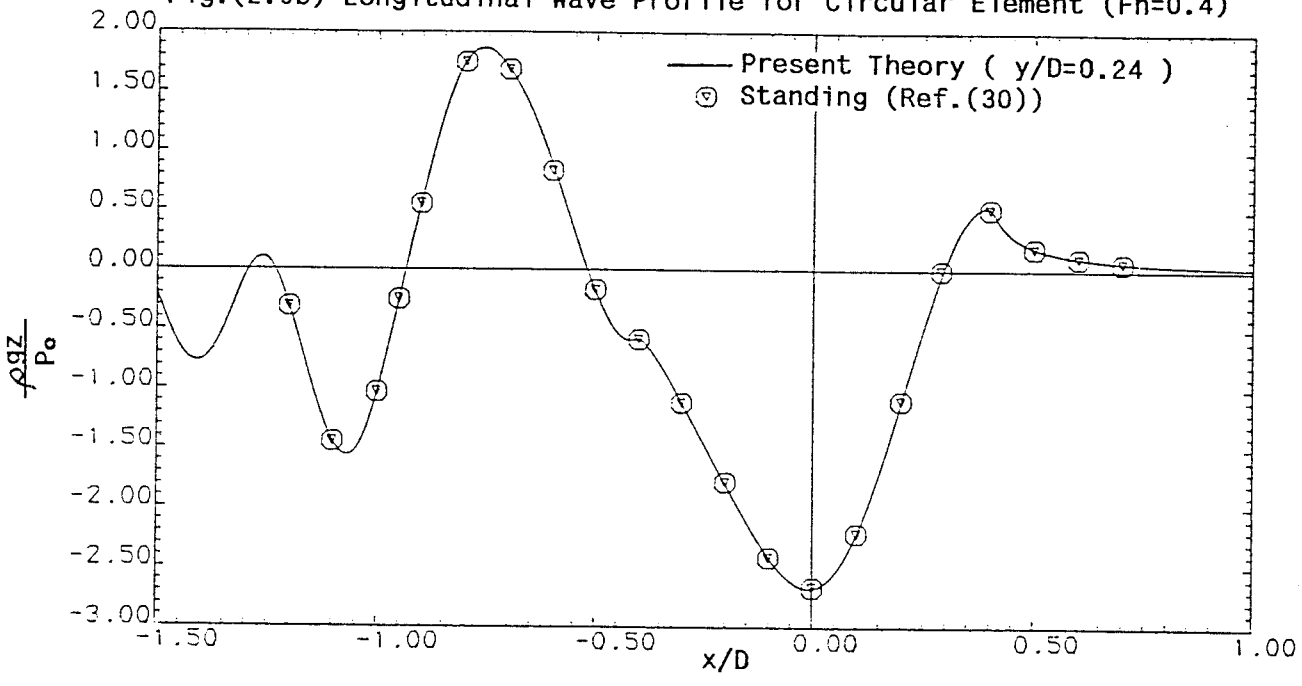

Fig.(2.9c) Longitudinal Wave Profile for Circular Element (Fn=0.4)

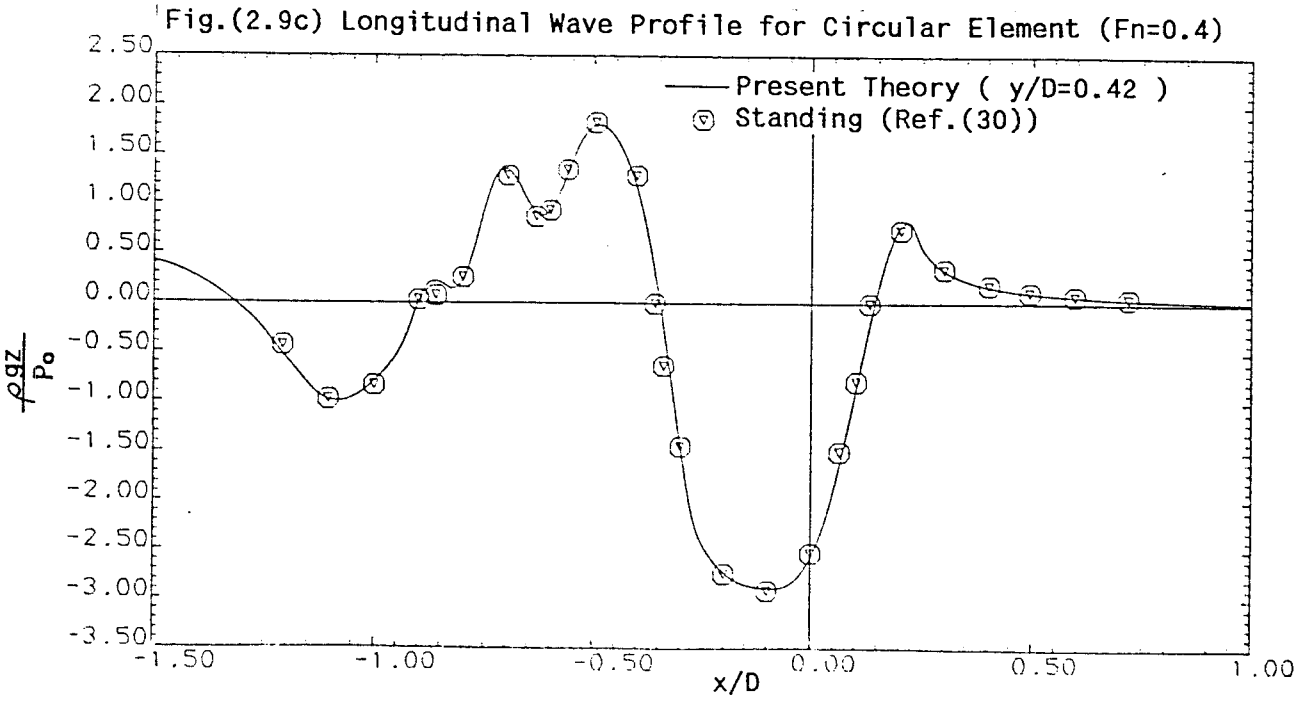

Fig.(2.10a) Longitudinal Wave Profile for Circular Element (Fn=0.5)

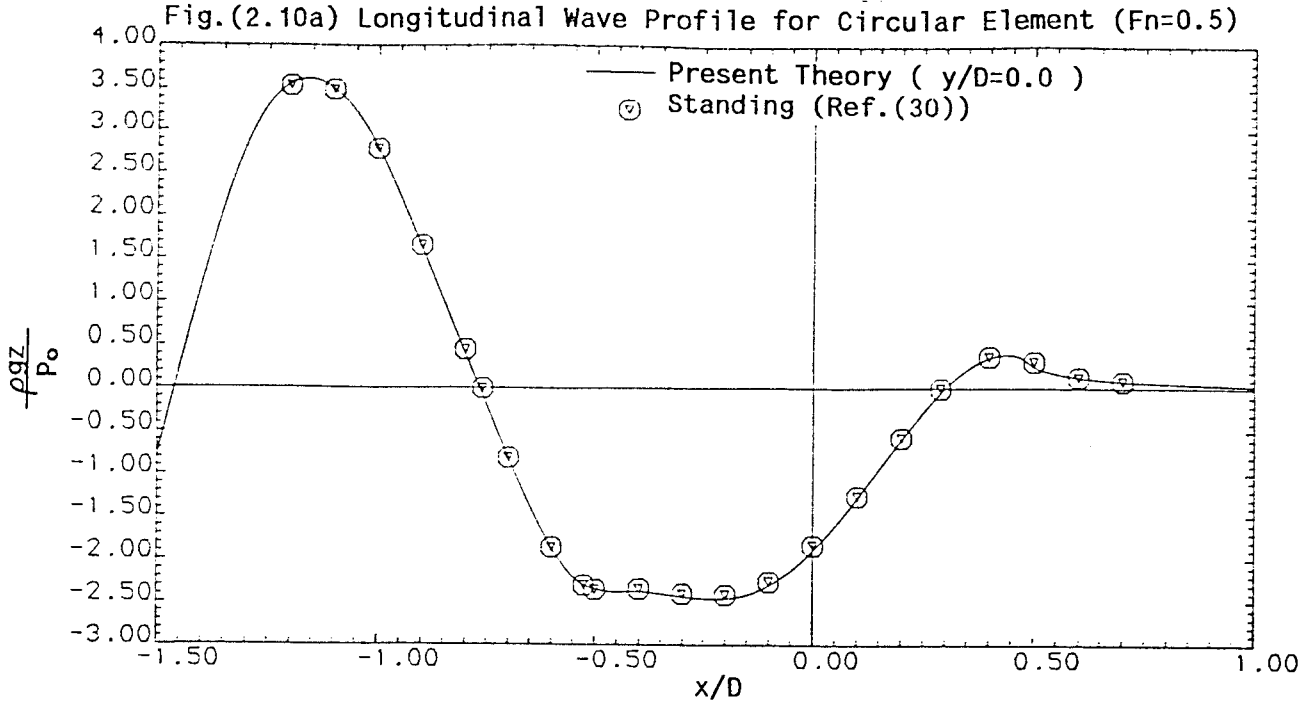

Fig.(2.10b) Longitudinal Wave Profile for Circular Element (Fn=0.5)

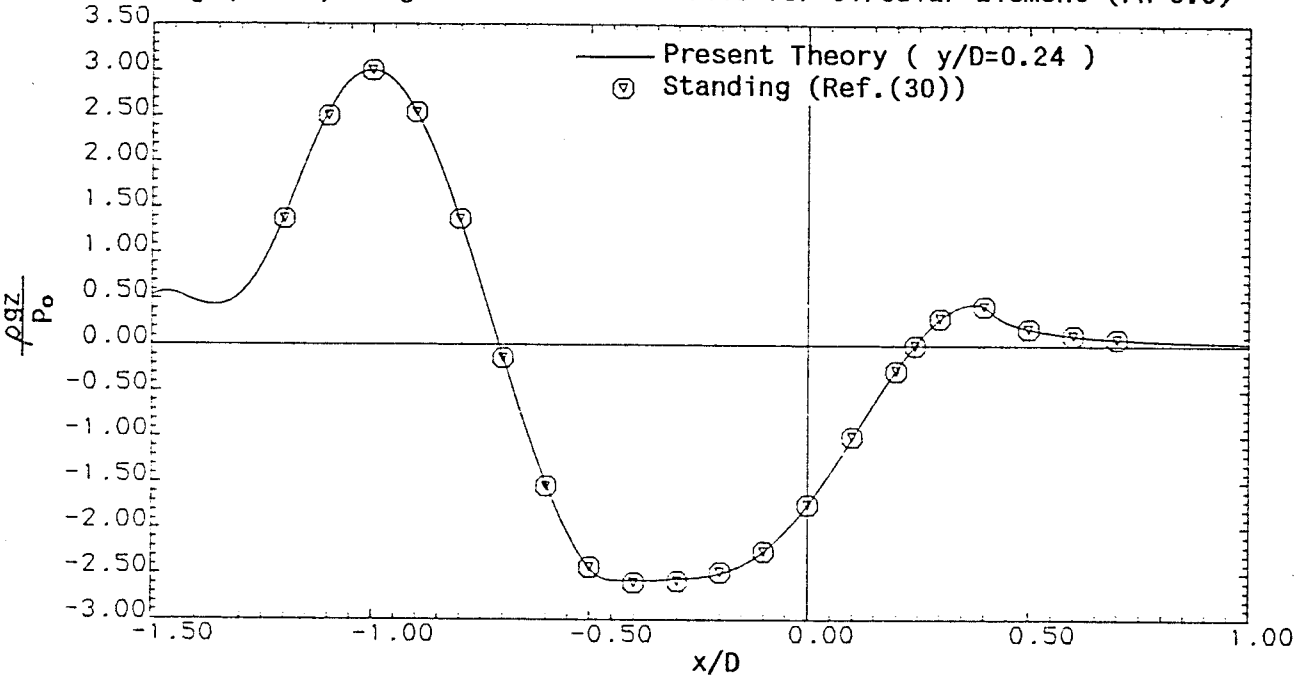

Fig.(2.10c) Longitudinal Wave Profile for Circular Element (Fn=0.5)

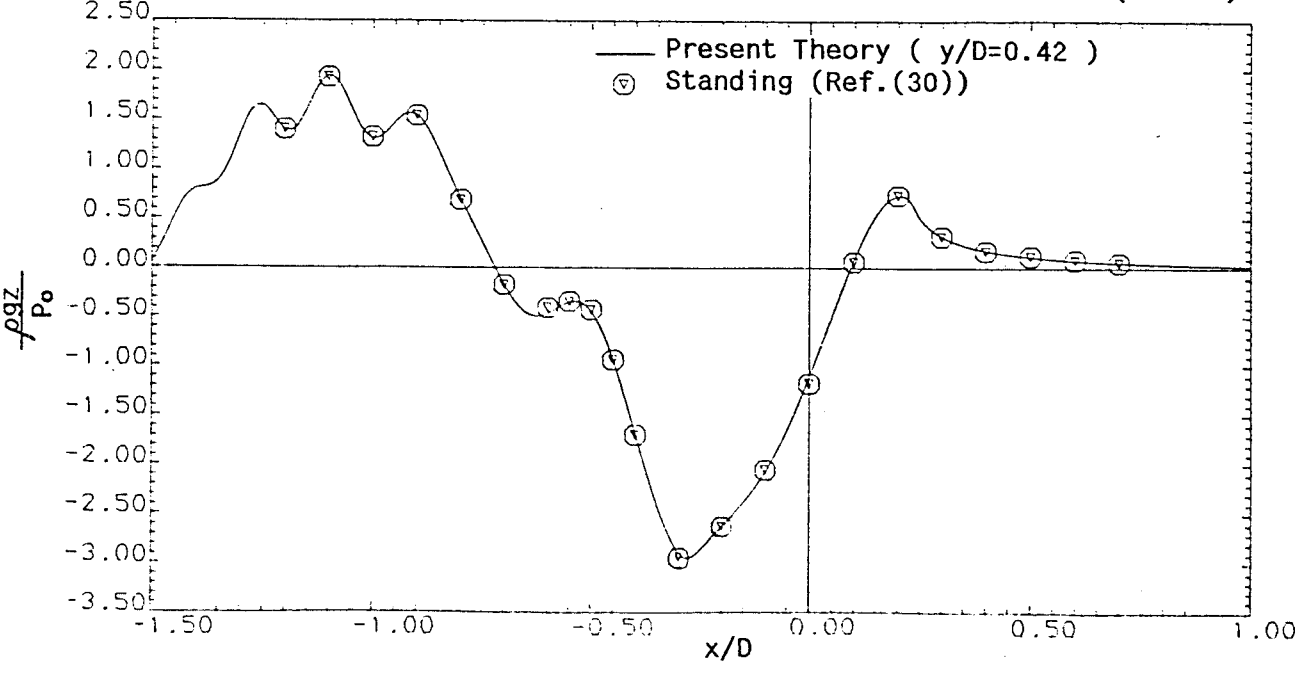

Fig.(3.1a) Computed Wake Profile for Planing Flat Plate (Centre Line)

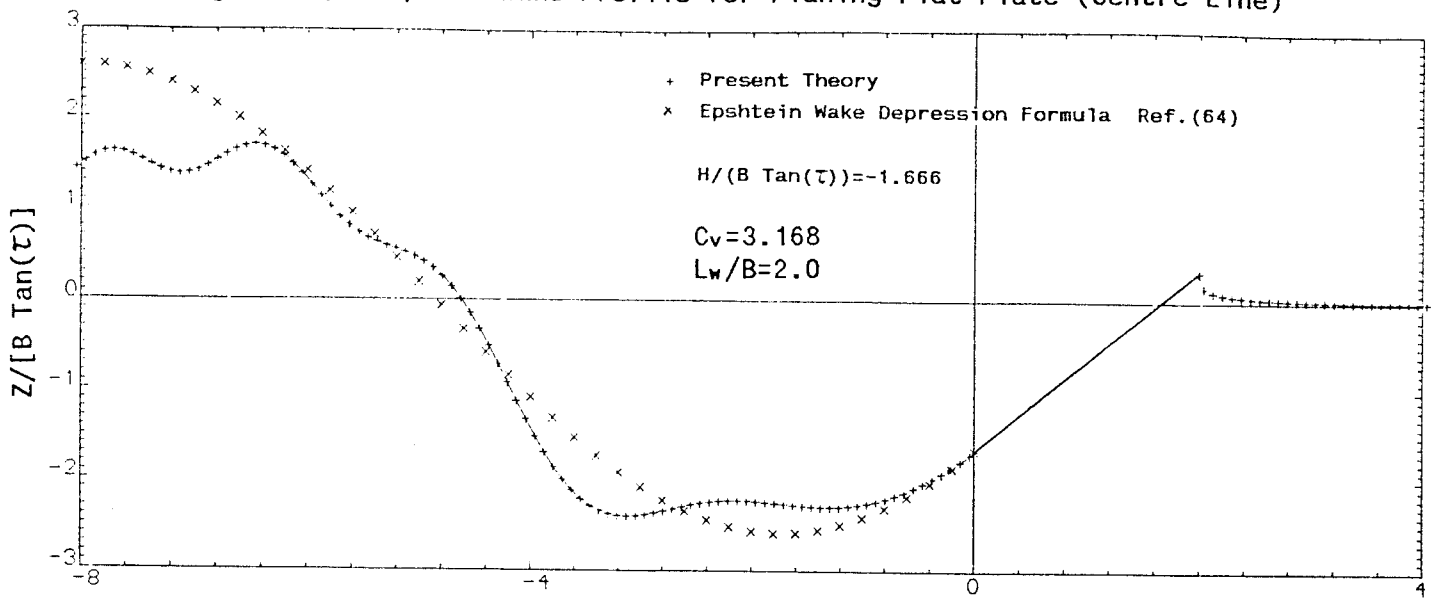

Fig.(3.1b) Computed Wake Profile for Planing Flat Plate (y=0.4B)

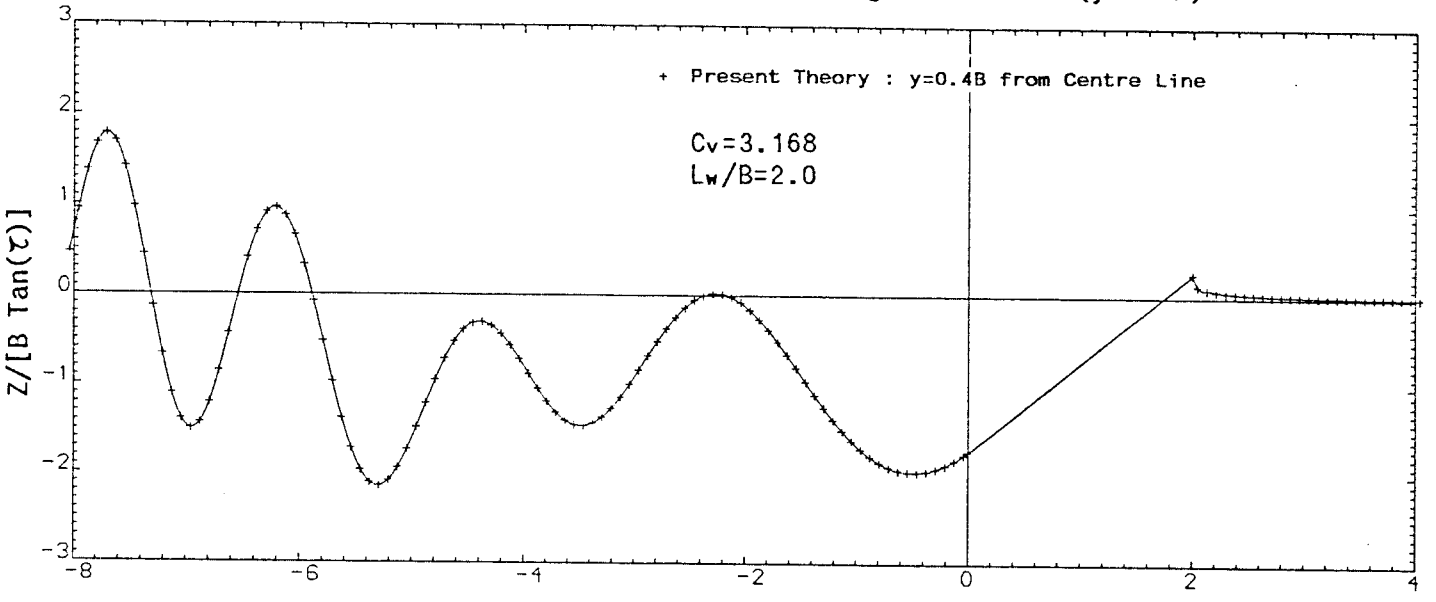

Fig.(3.1c) Computed Wake Profile for Planing Flat Plate (y=0.7B)

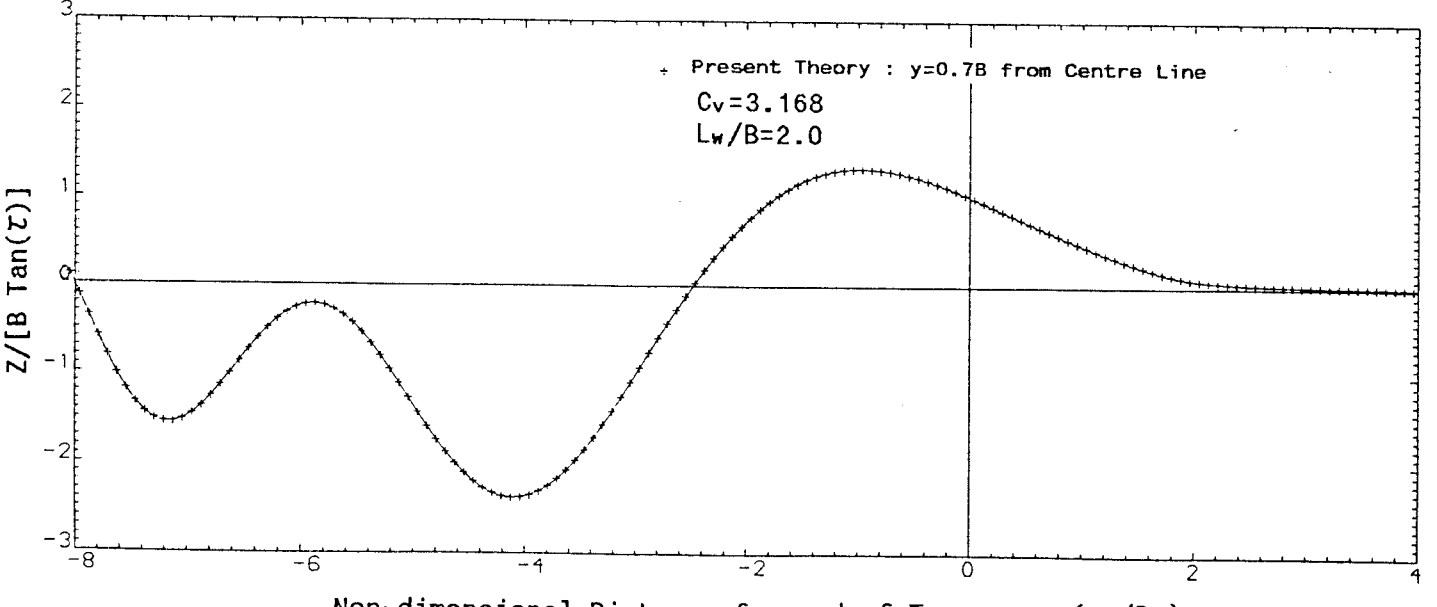

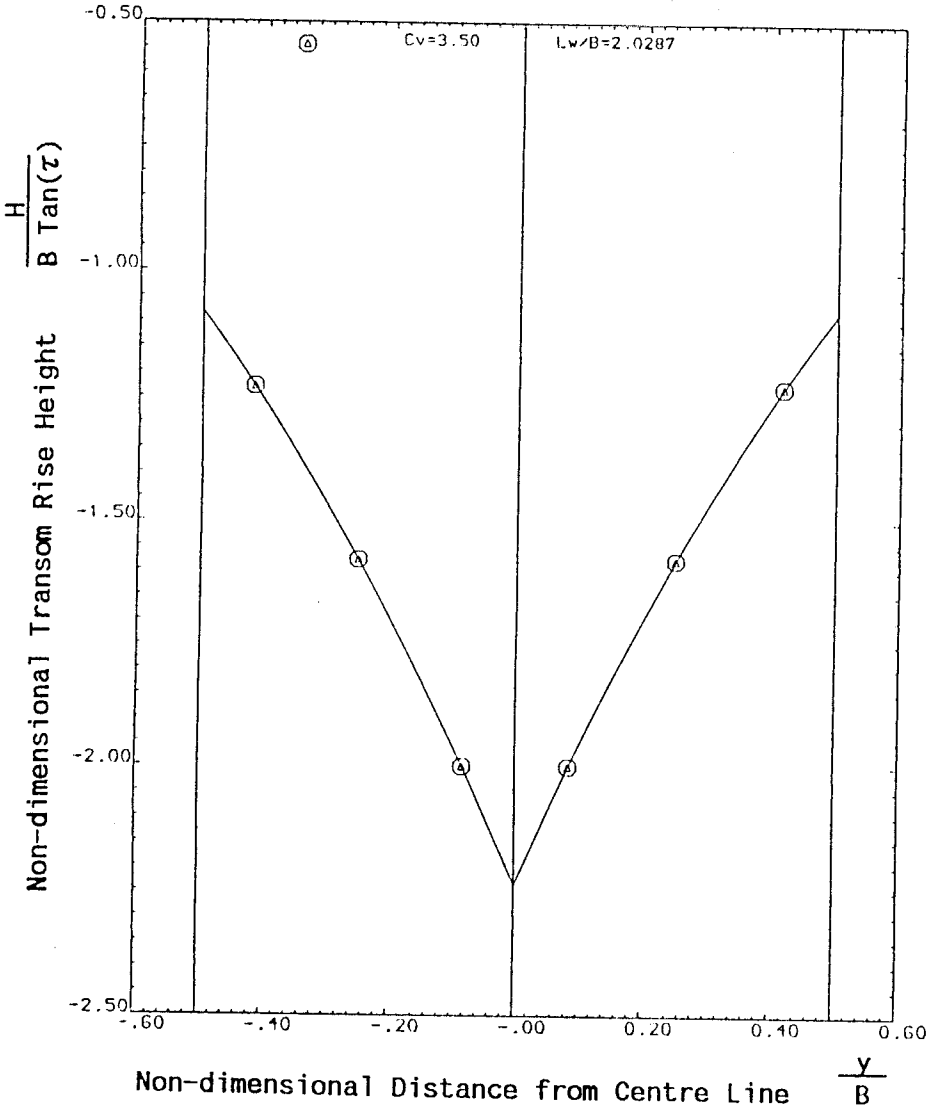

Fig.(3.2a) Transom Shape computed from Wetted Bottom with Swept-back Spray root: $\frac{(L_k - L_c)}{B} = 0.8115$

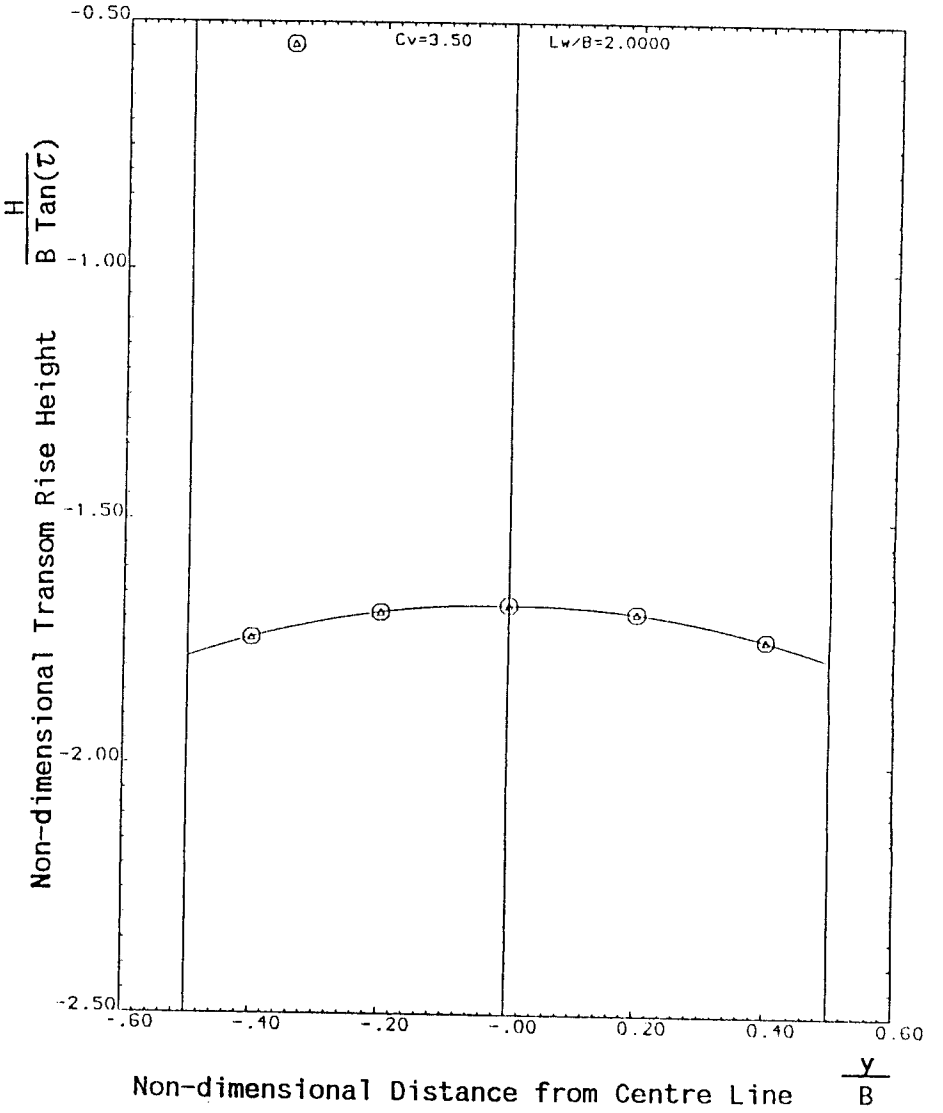

Fig.(3.2b) Transom Shape computed from Wetted Bottom with Straight Spray Root

Fig.(3.3a,b) and fig.(3.4a,b) Longitudinal Convergence of Pressure Distribution for Rectangular Wetted Bottoms

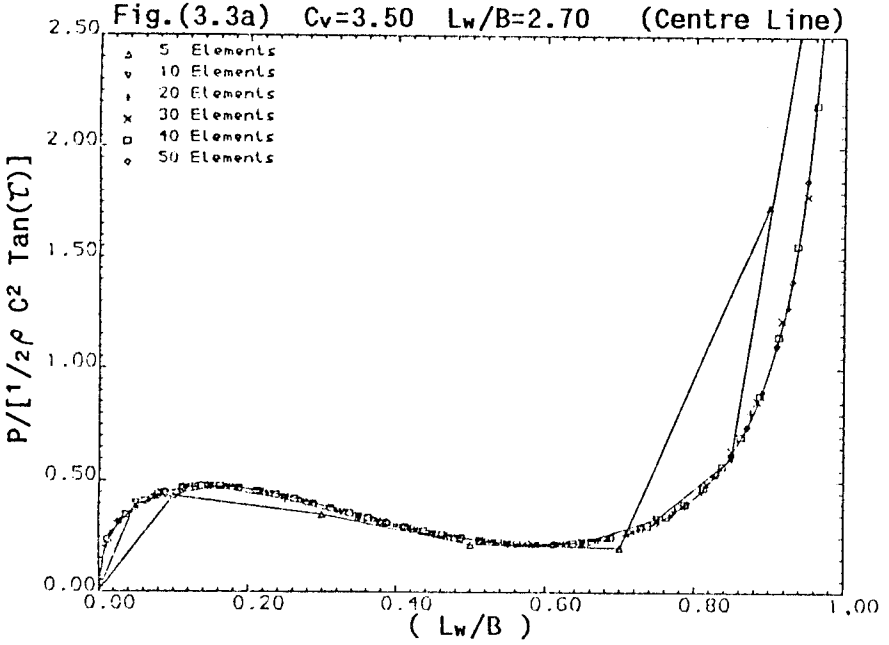

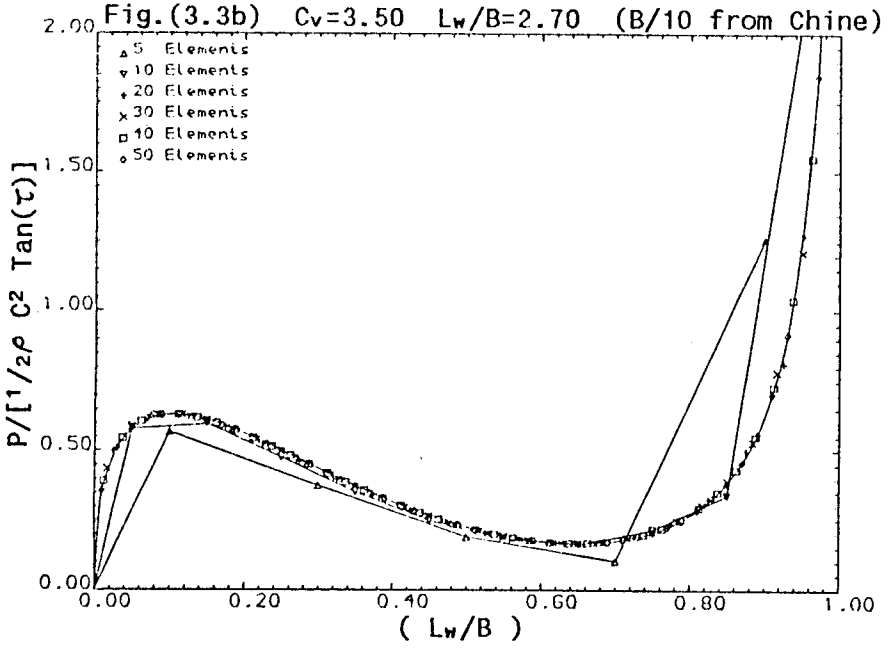

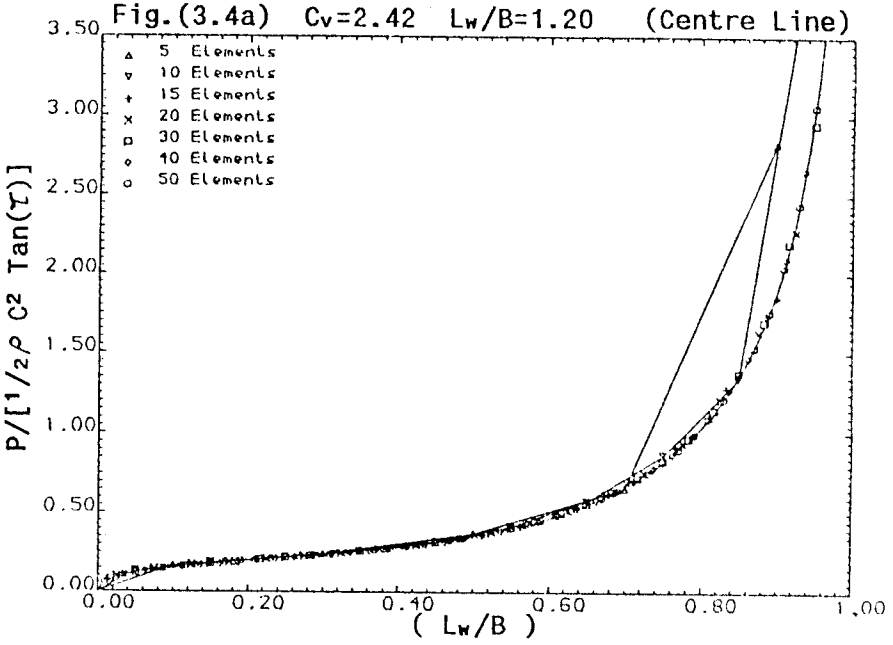

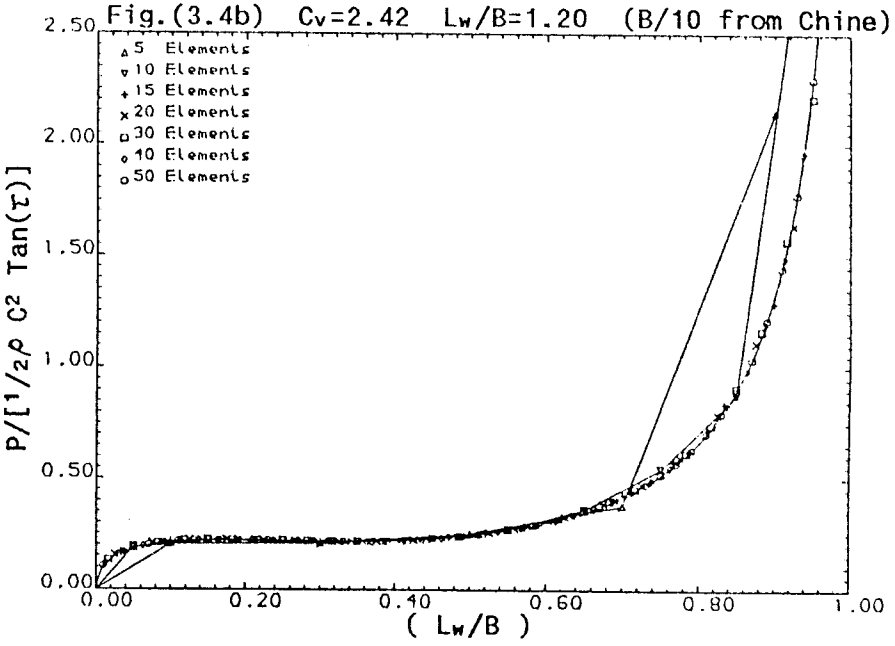

Fig.(3.5) and Fig.(3.6) Longitudinal Convergence of Lift Coefficient, Centre of Pressure Ratio and Transom Immersion for Rectangular Wetted Bottom

Fig.(3.5a,b,c) Cv=3.50, Lw/B=2.7

Fig.(3.6a,b,c) Cv=2.42, Lw/B=1.2

Fig.(3.5a)

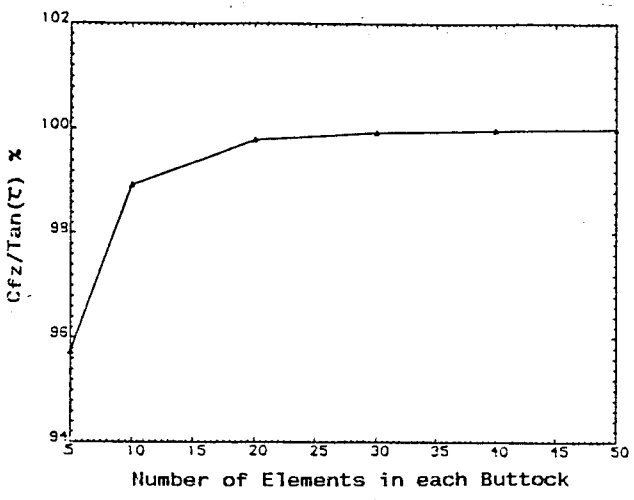

Fig.(3.6a)

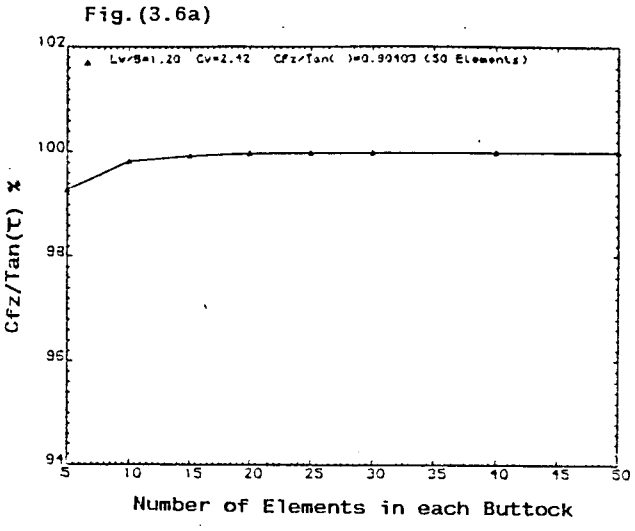

Fig.(3.5b)

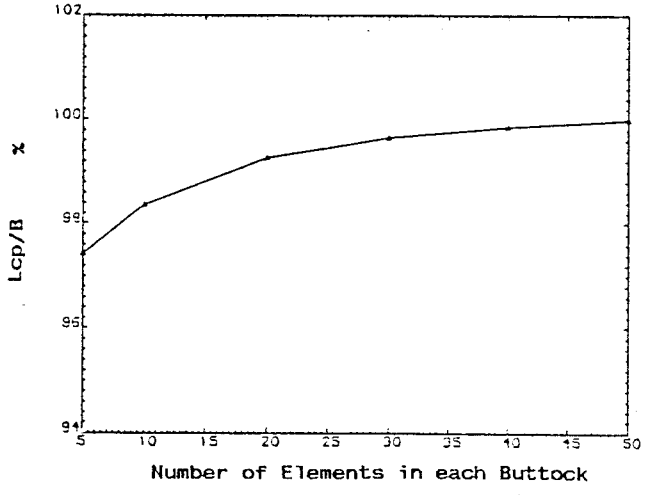

Fig.(3.6b)

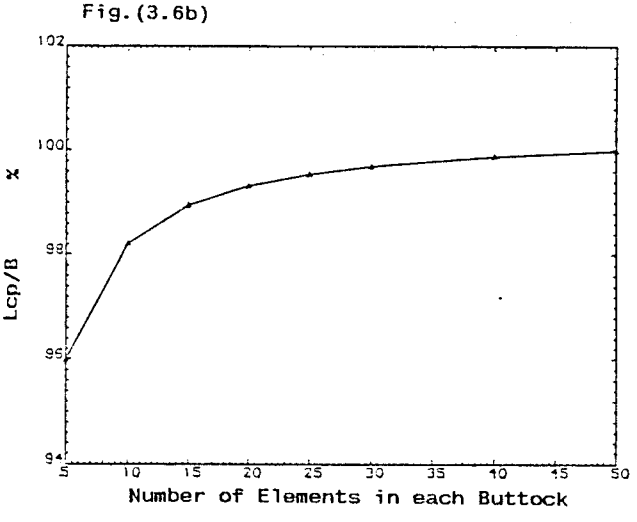

Fig.(3.5c)

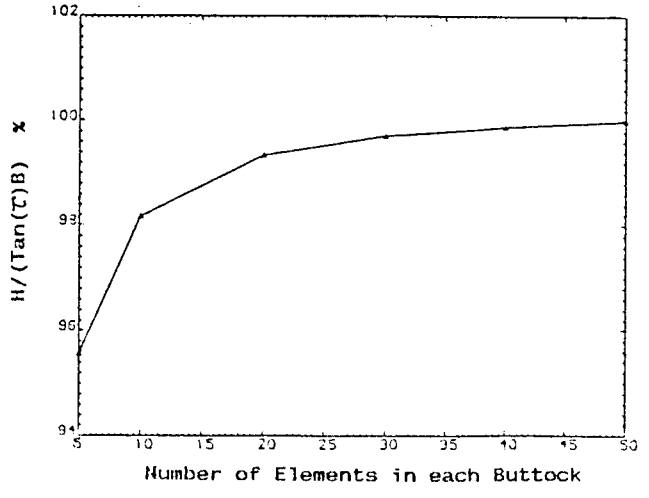

Fig.(3.6c)

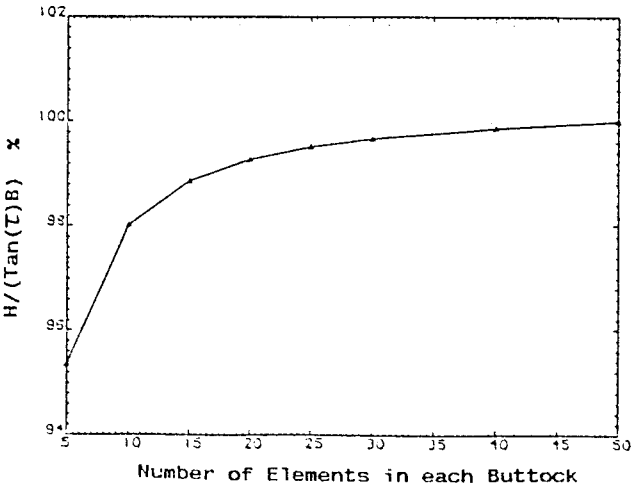

Computed quantities presented as a percentage of the respective values computed using 50 elements in each buttock

Fig.(3.7a) Transverse Convergence of Pressure Distribution for Rectangular Wetted Bottom (C_v=2.5 L_w/B=0.5)

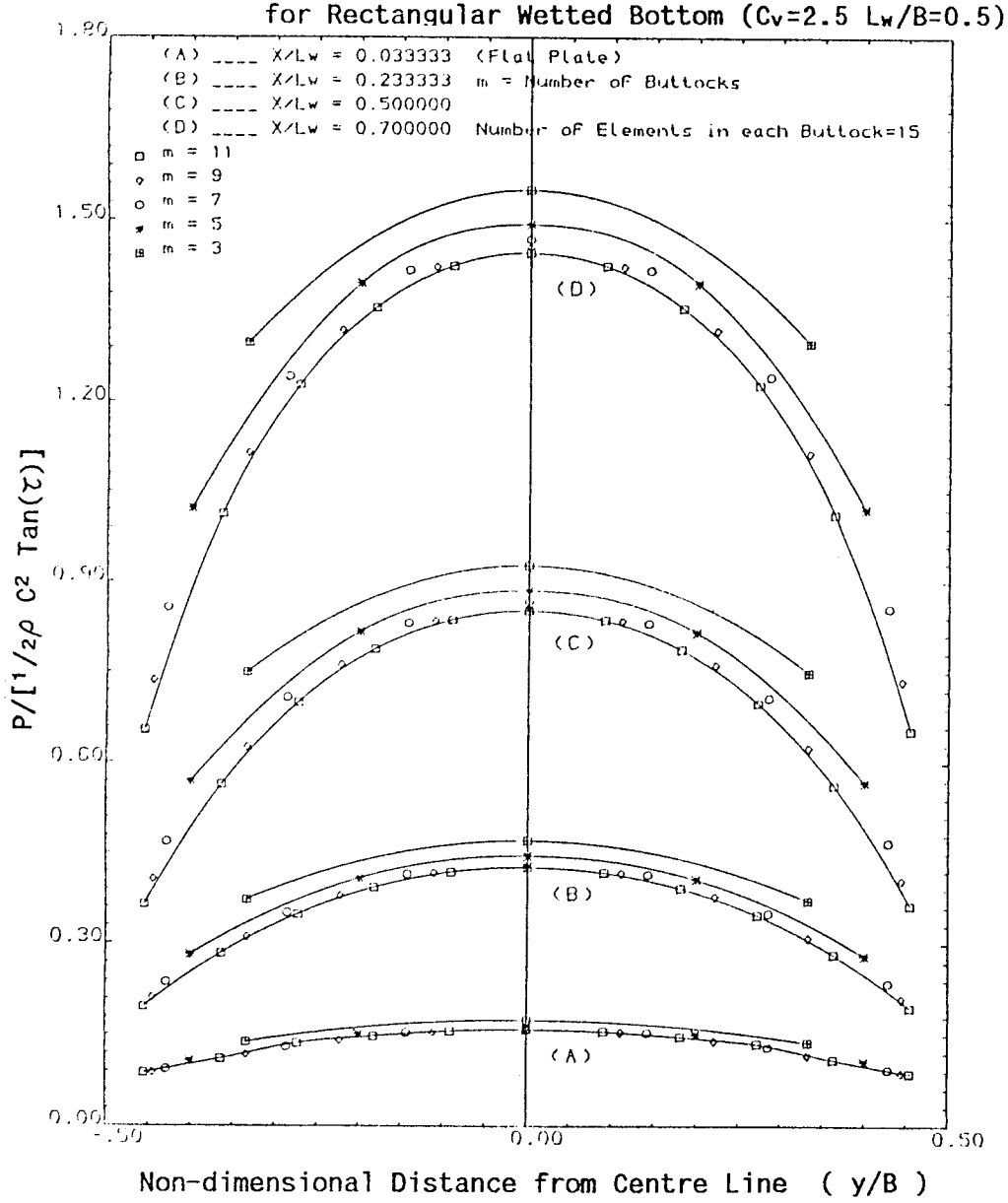

Fig.(3.7b) Transverse Convergence of Pressure Distribution for Rectangular Wetted Bottom (C_v=1.5 L_w/B=0.5)

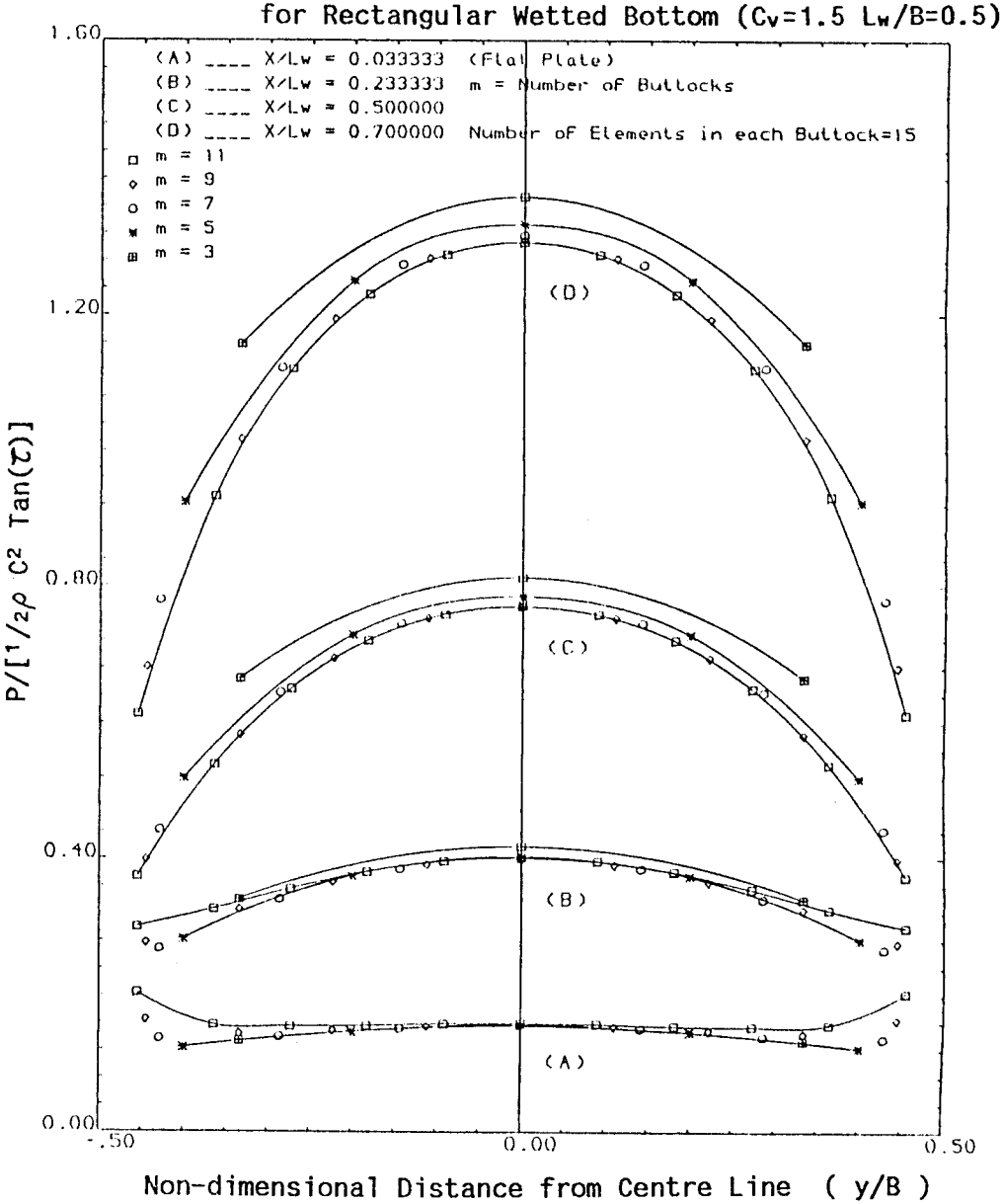

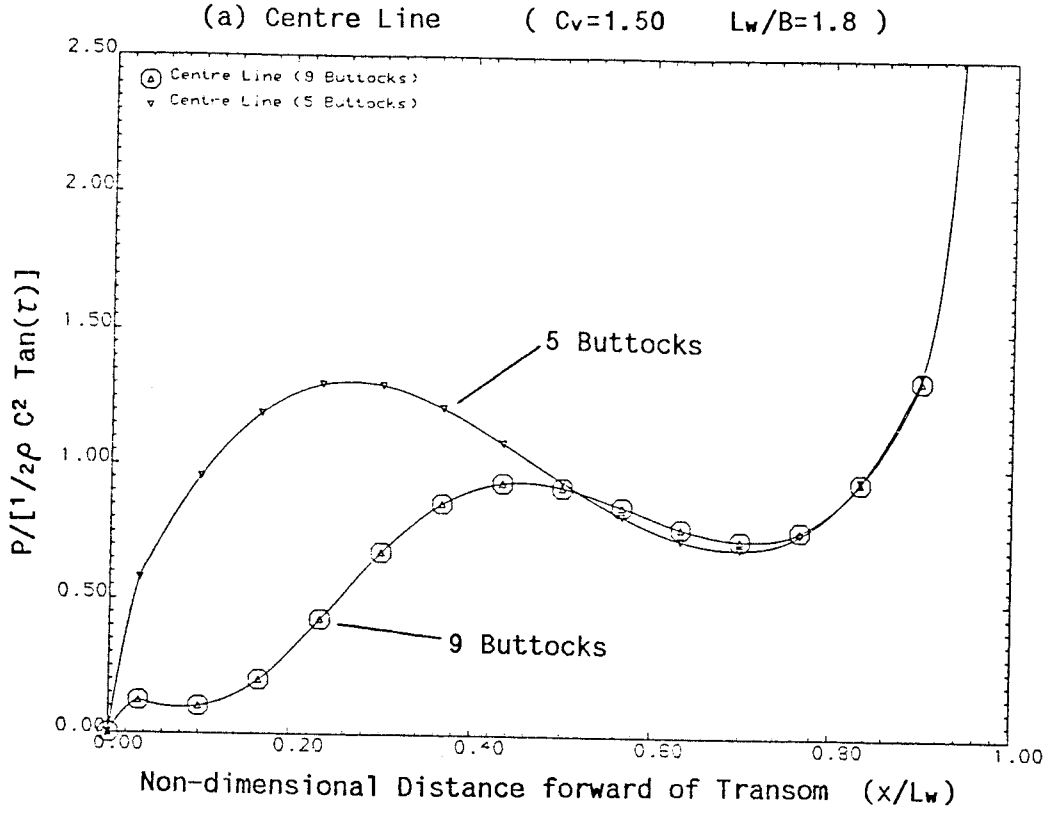

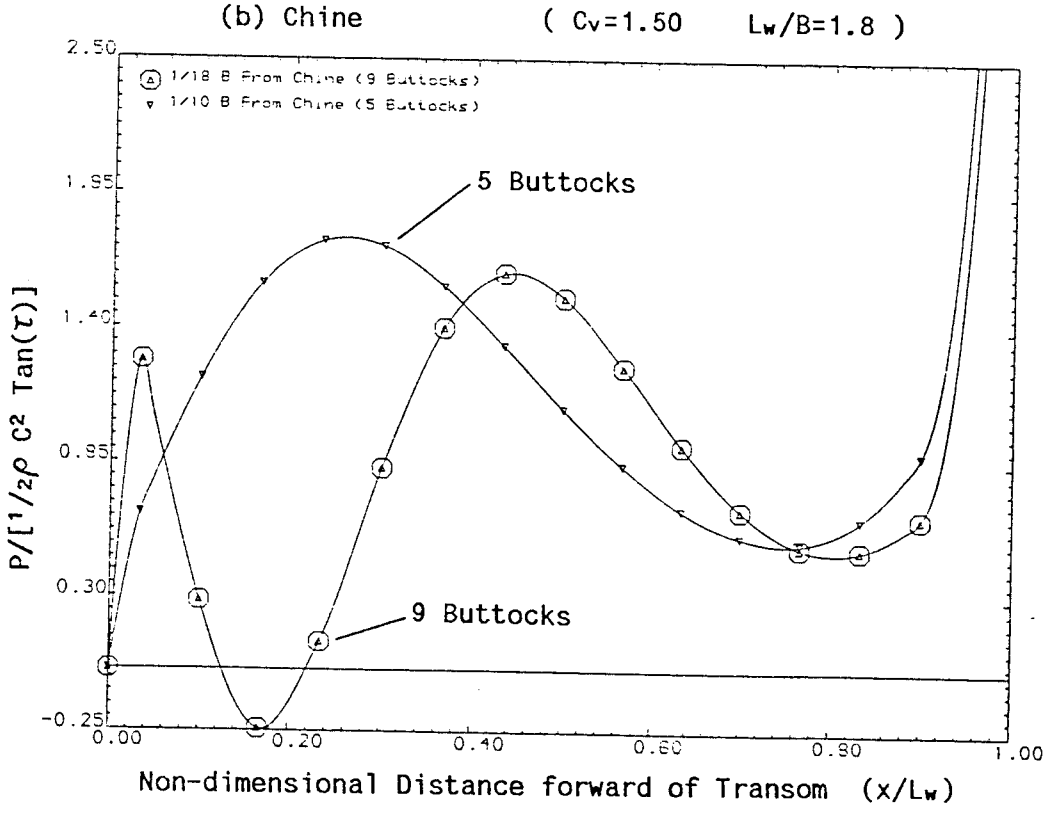

Number of Elements in each Buttock Strip = 15

Fig.(3.8a,b) Oscillatory Pressure Solution obtained from Rectangular Wetted Bottom using large number of Buttock Strips

Fig.(3.9) Centre Line Wave Profiles for Rectangular Element at Different Speeds (Element's Length = B/10 Element's Width = B/5)

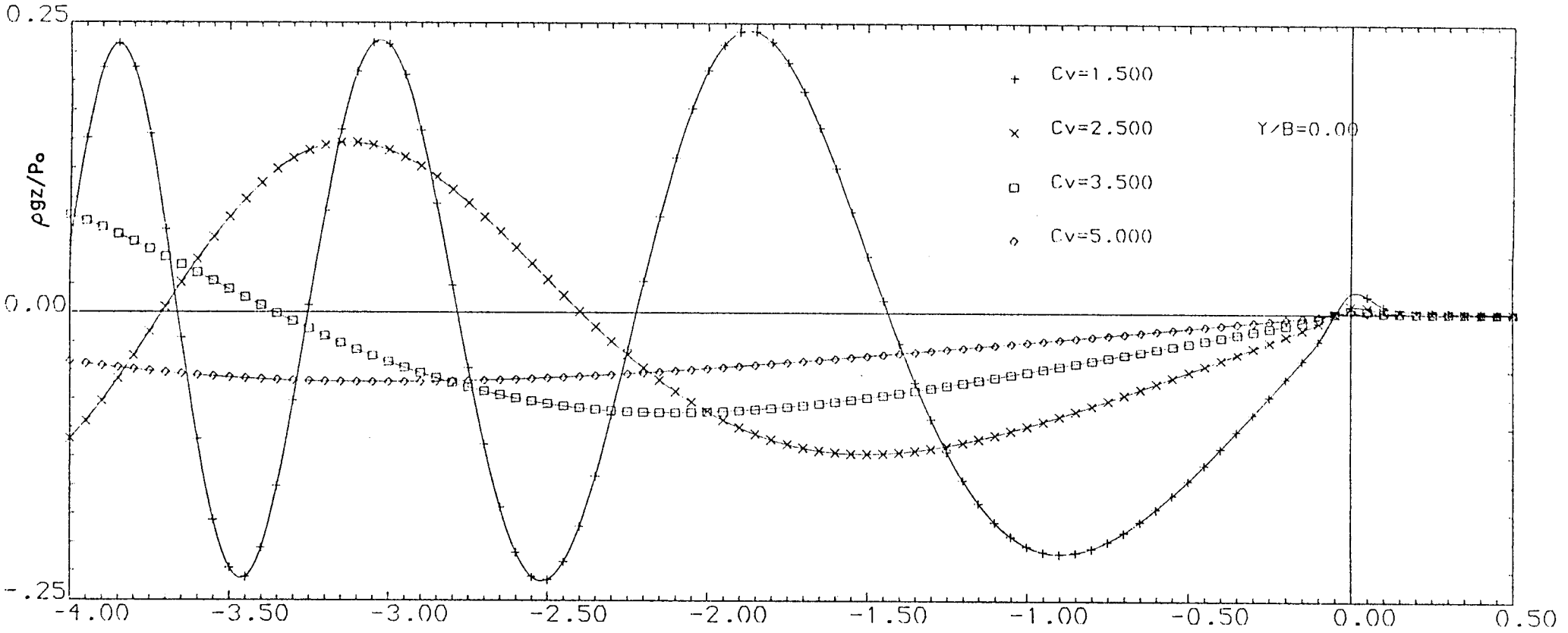

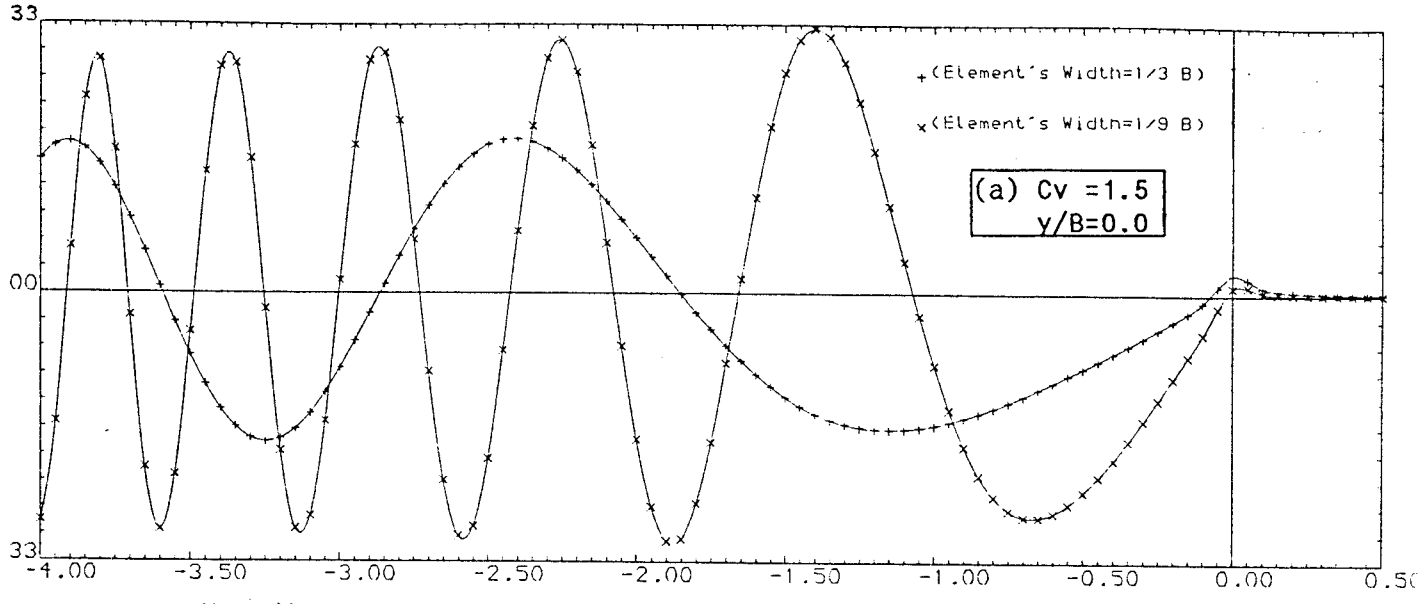

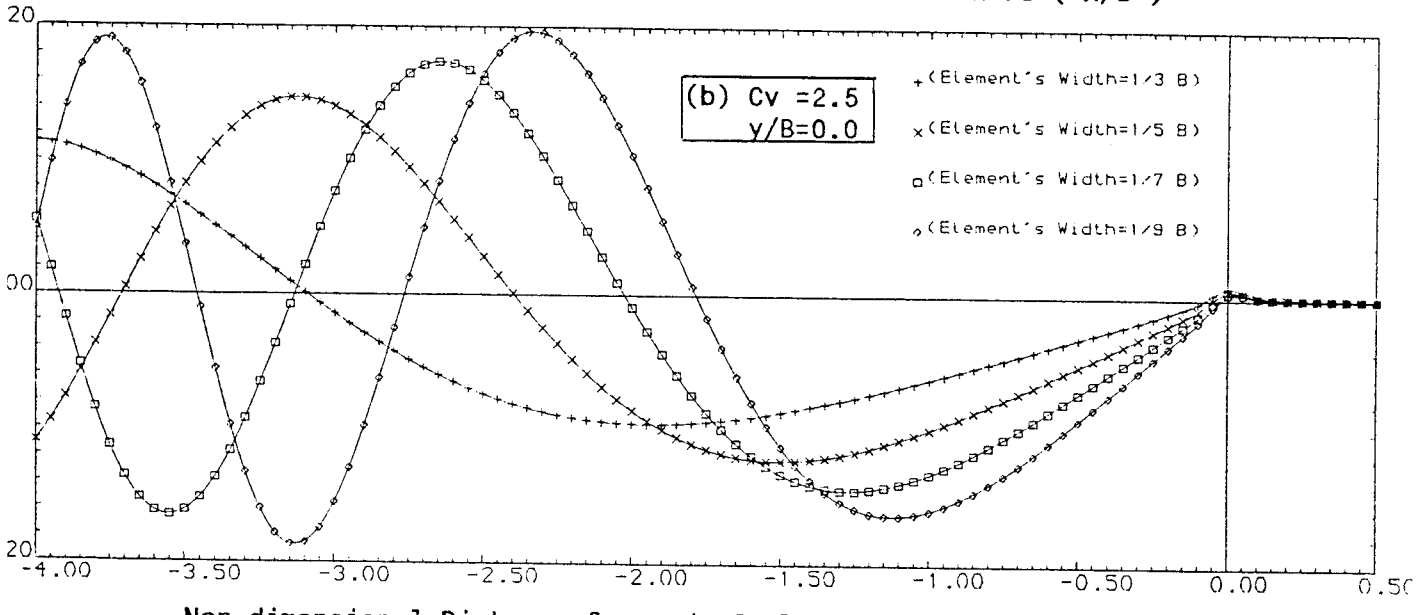

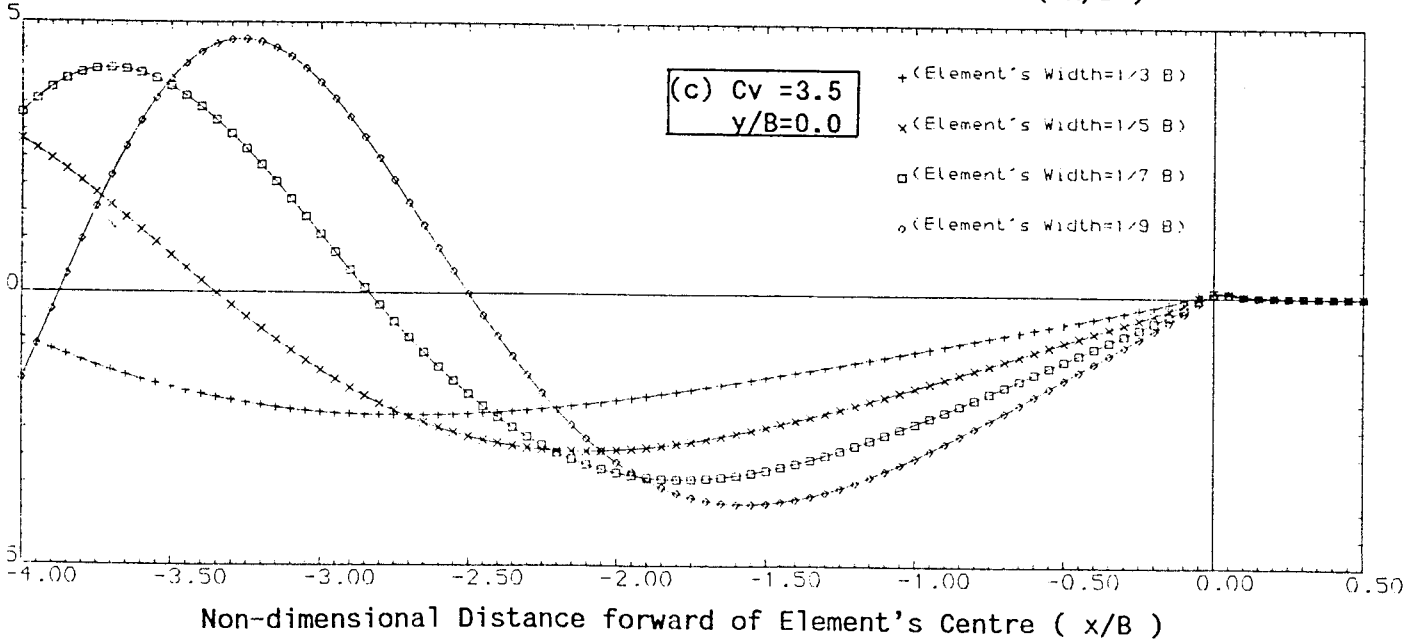

Fig.(3.10a,b,c) Centre Line Wave Profiles for Rectangular Elements of Different Widths (Elements' Length = B/10)

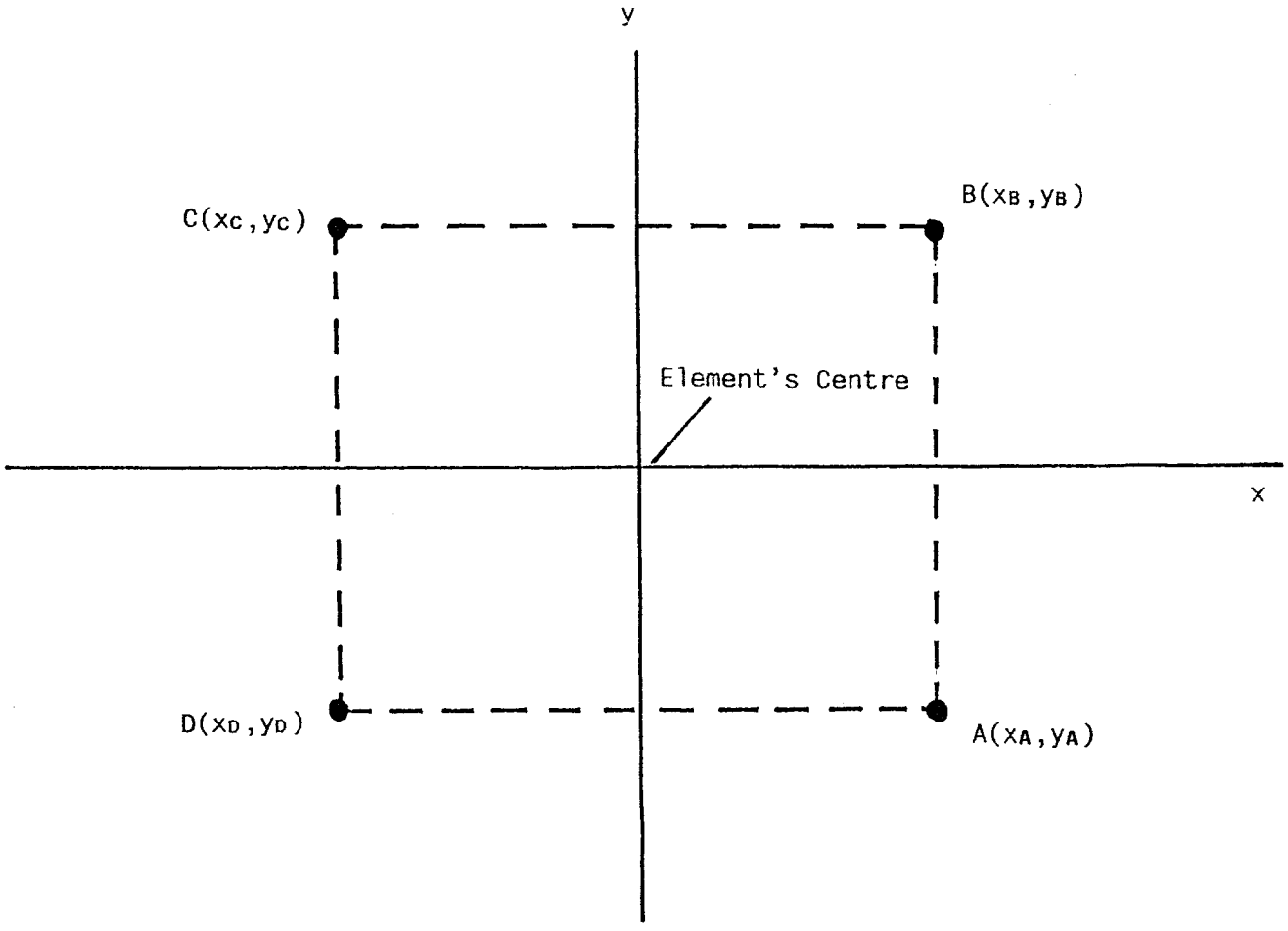

Fig.(3.11a) Representation of a Constant Pressure Rectangular Element by Corner Wave Functions

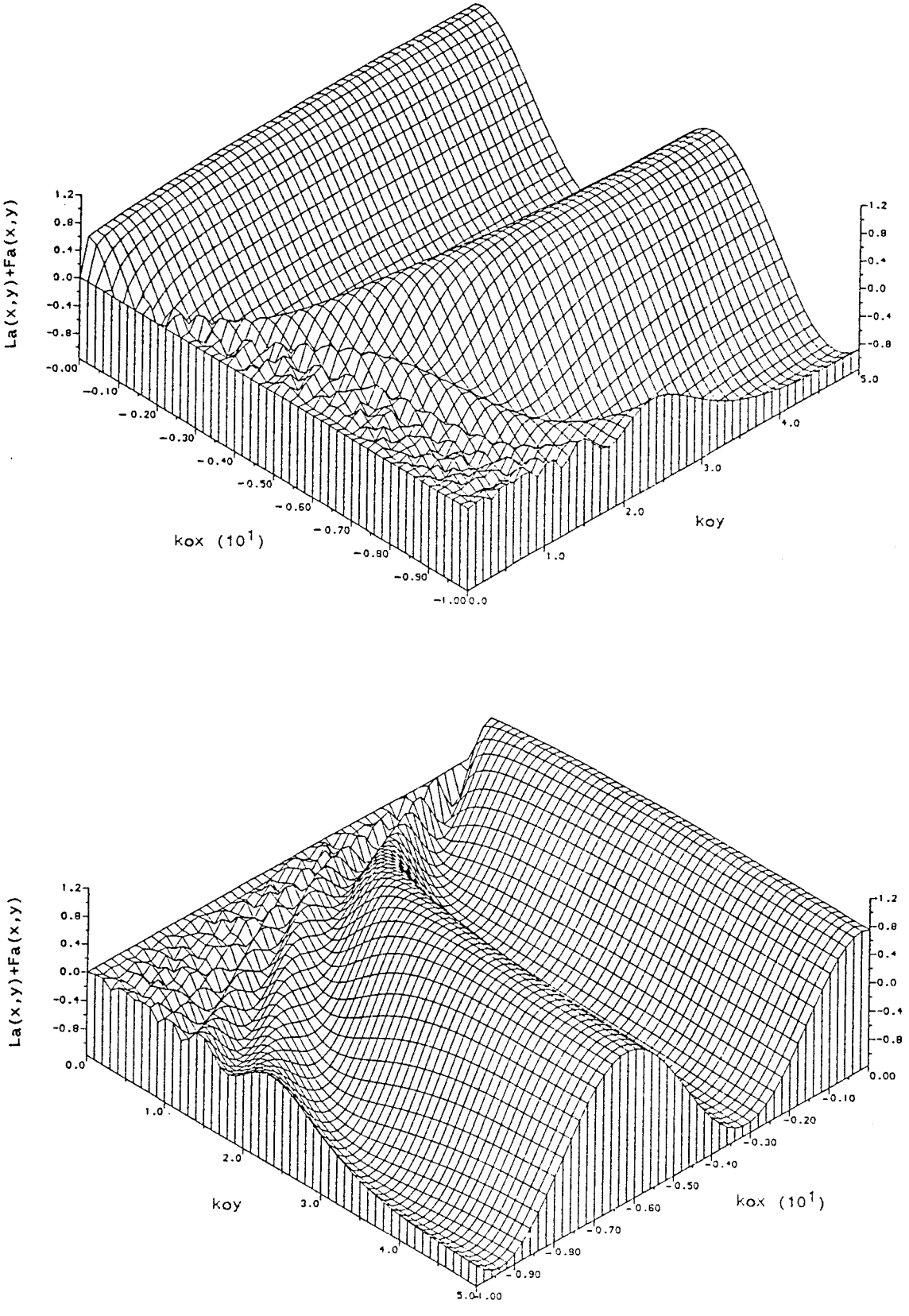

Fig.(3.11b) Non-dimensional Corner Wave Function ($L_a(x,y)+F_a(x,y)$) of a Constant Pressure Rectangular Element ($T_o=0$)

Note: ($L_a(x,y)+F_a(x,y)$) is an odd function of y for $T_o=0$

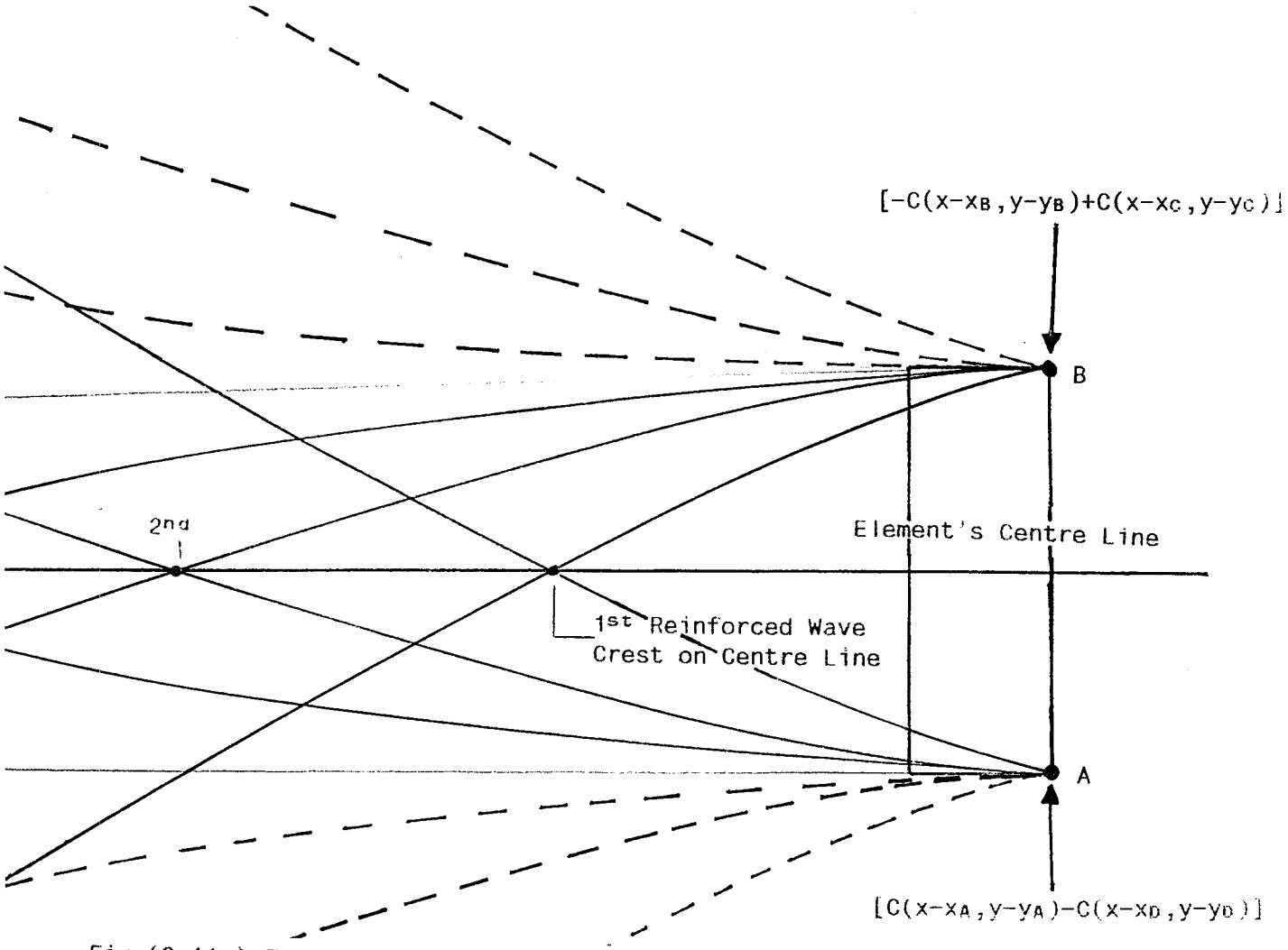

Fig.(3.11c) Two Identical Wave Patterns Produced by Combining the Corner Wave Functions at Corners A and D, and at Corners B and C

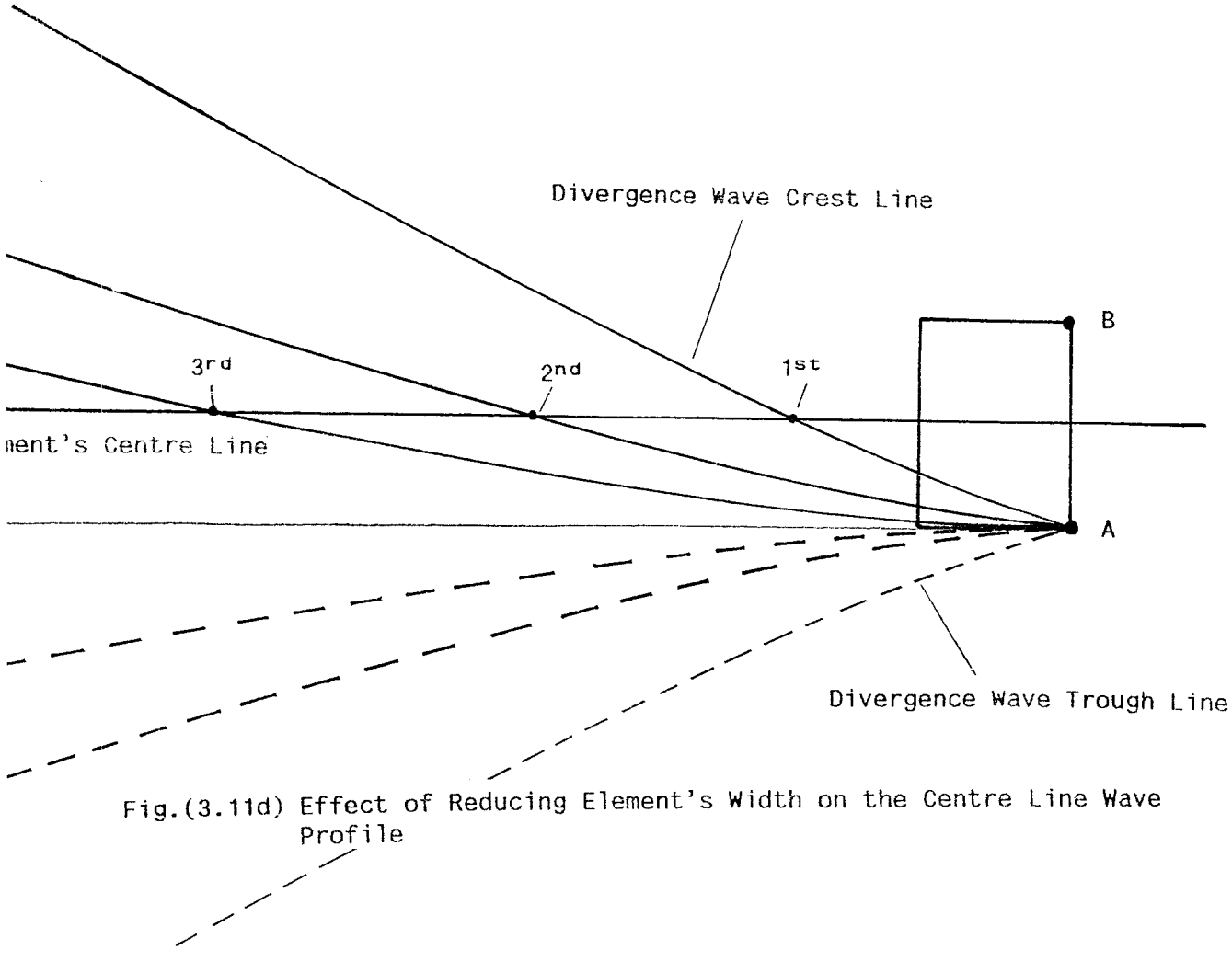

Fig.(3.11d) Effect of Reducing Element's Width on the Centre Line Wave Profile

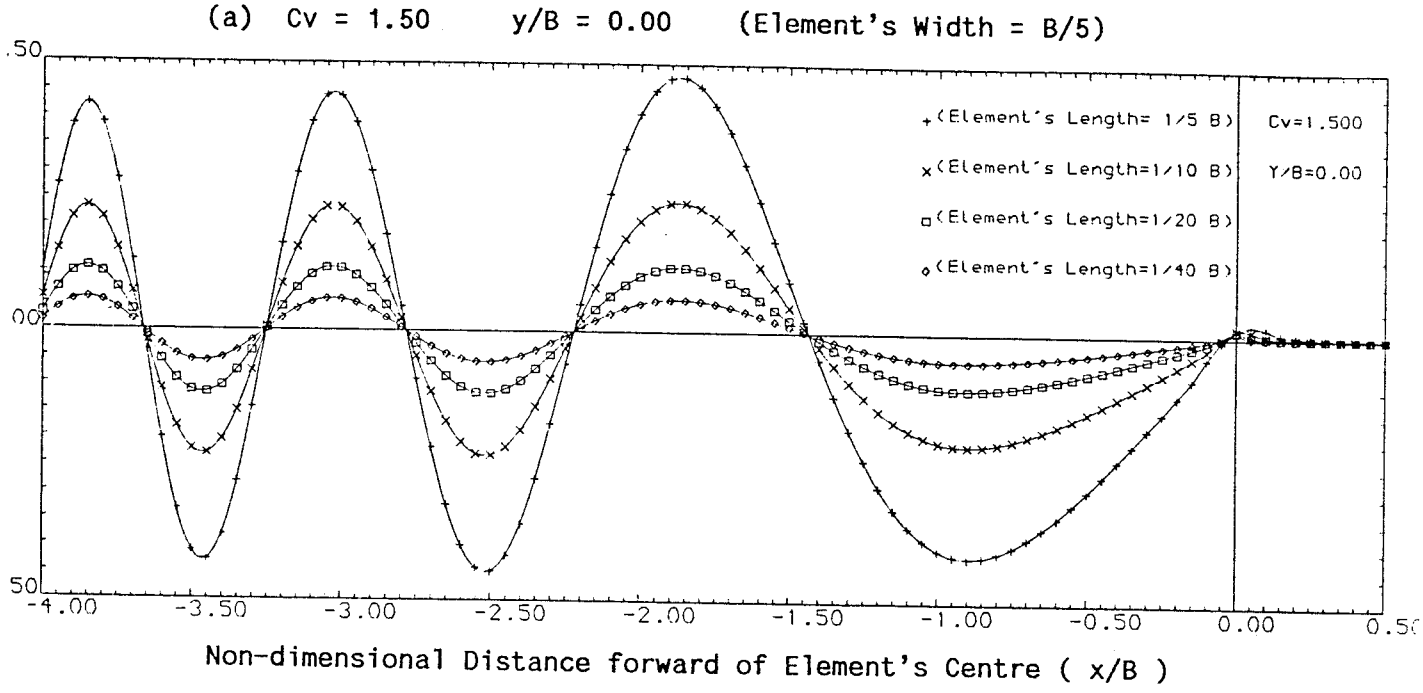

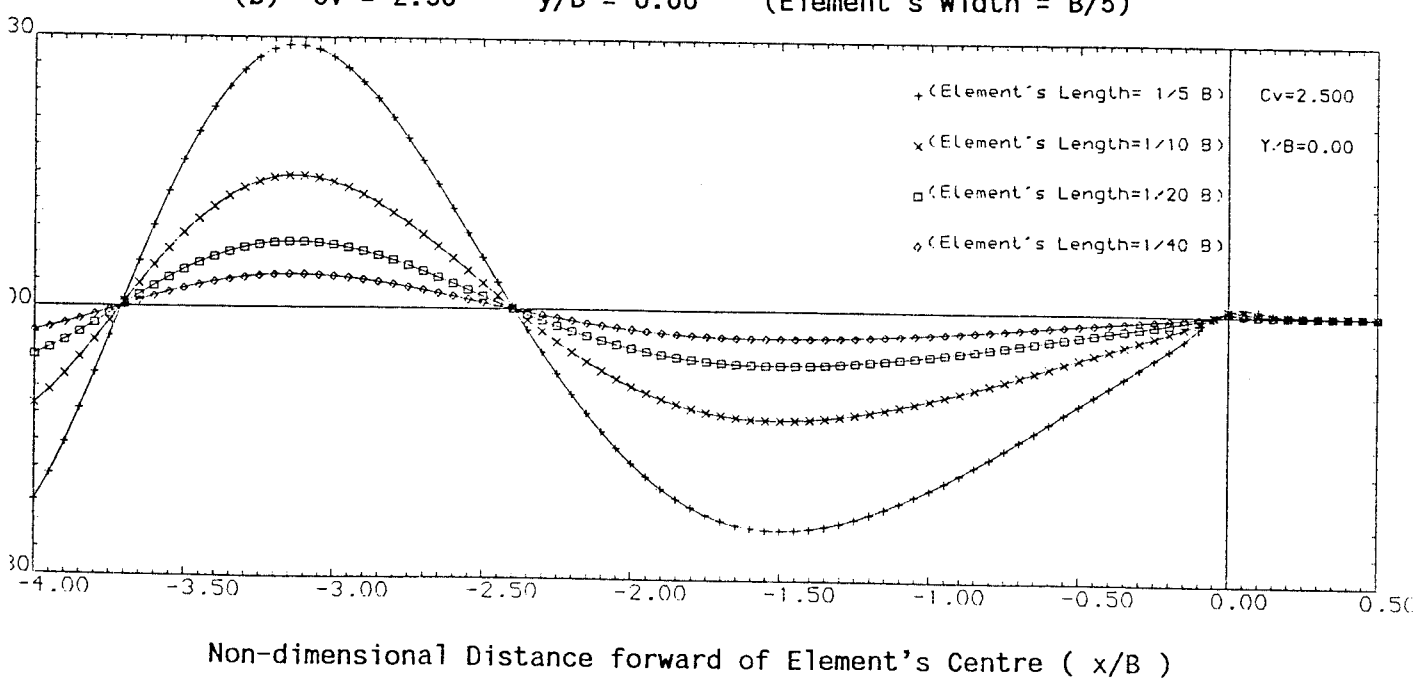

Fig.(3.12a,b) Centre Line Wave Profiles for Rectangular Elements of Different Lengths

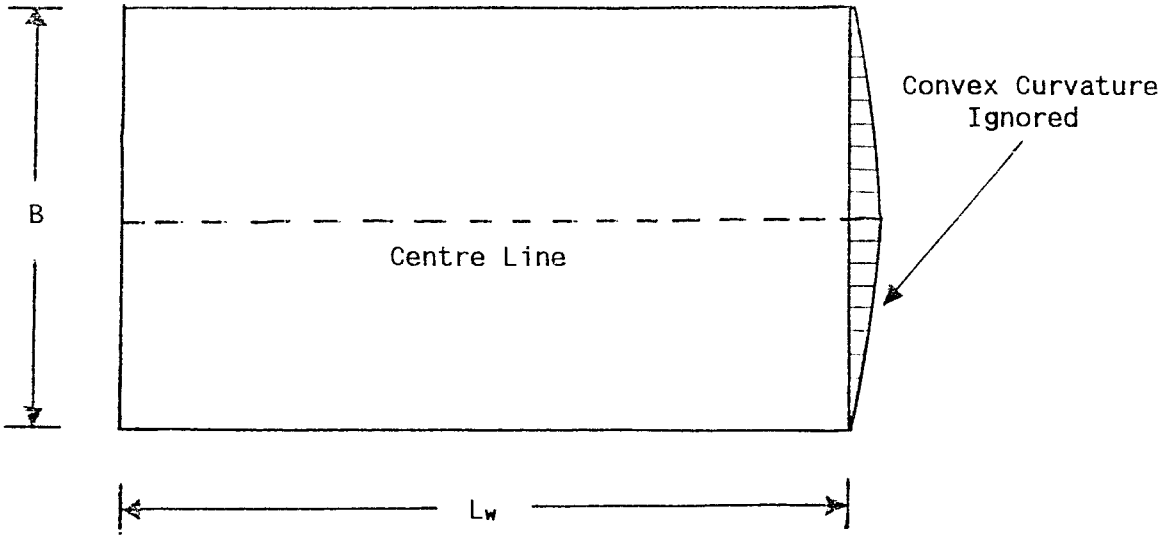

Fig.(4.1) Projected Wetted Bottom of a Planing Flat Plate

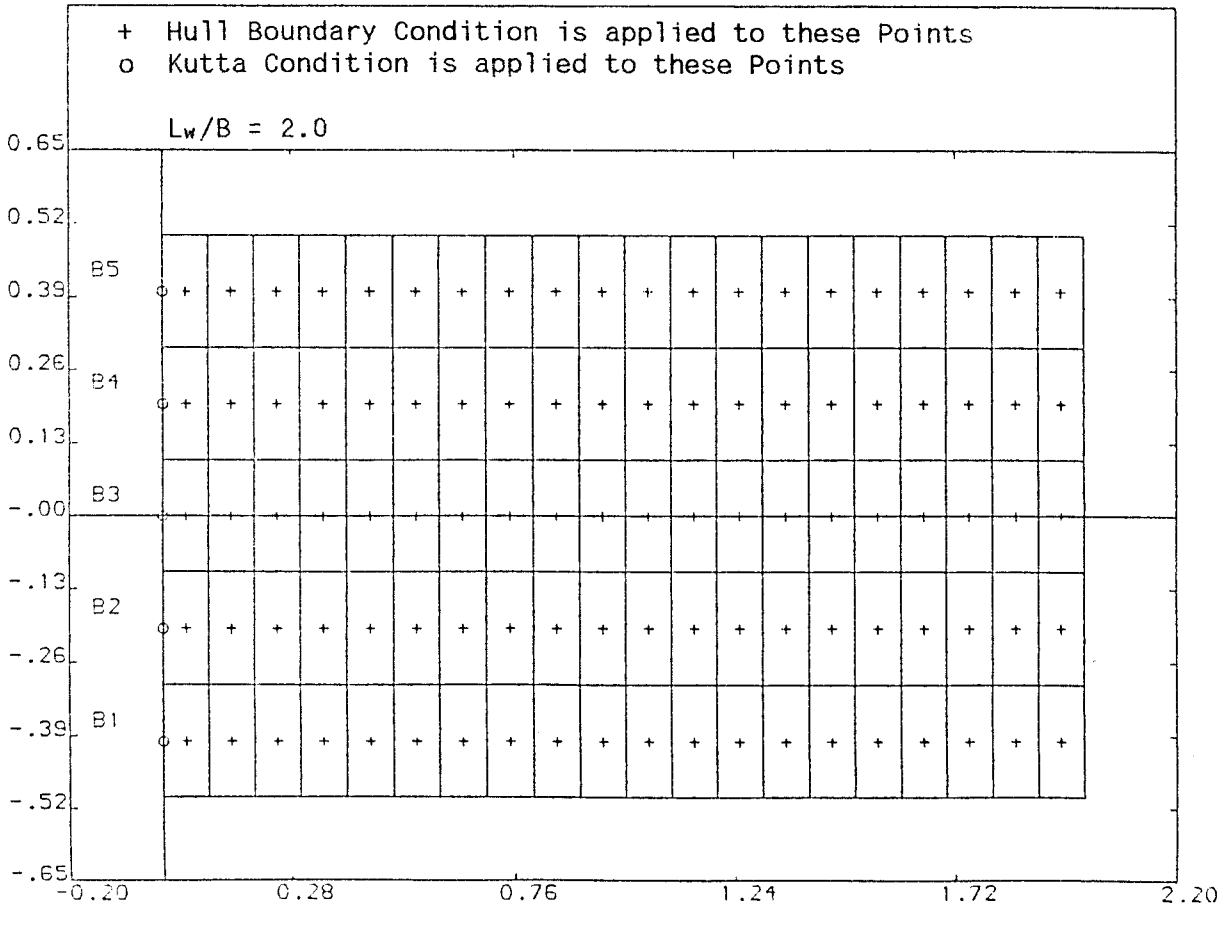

Fig.(4.2) Finite Element Representation of Projected Wetted Bottom

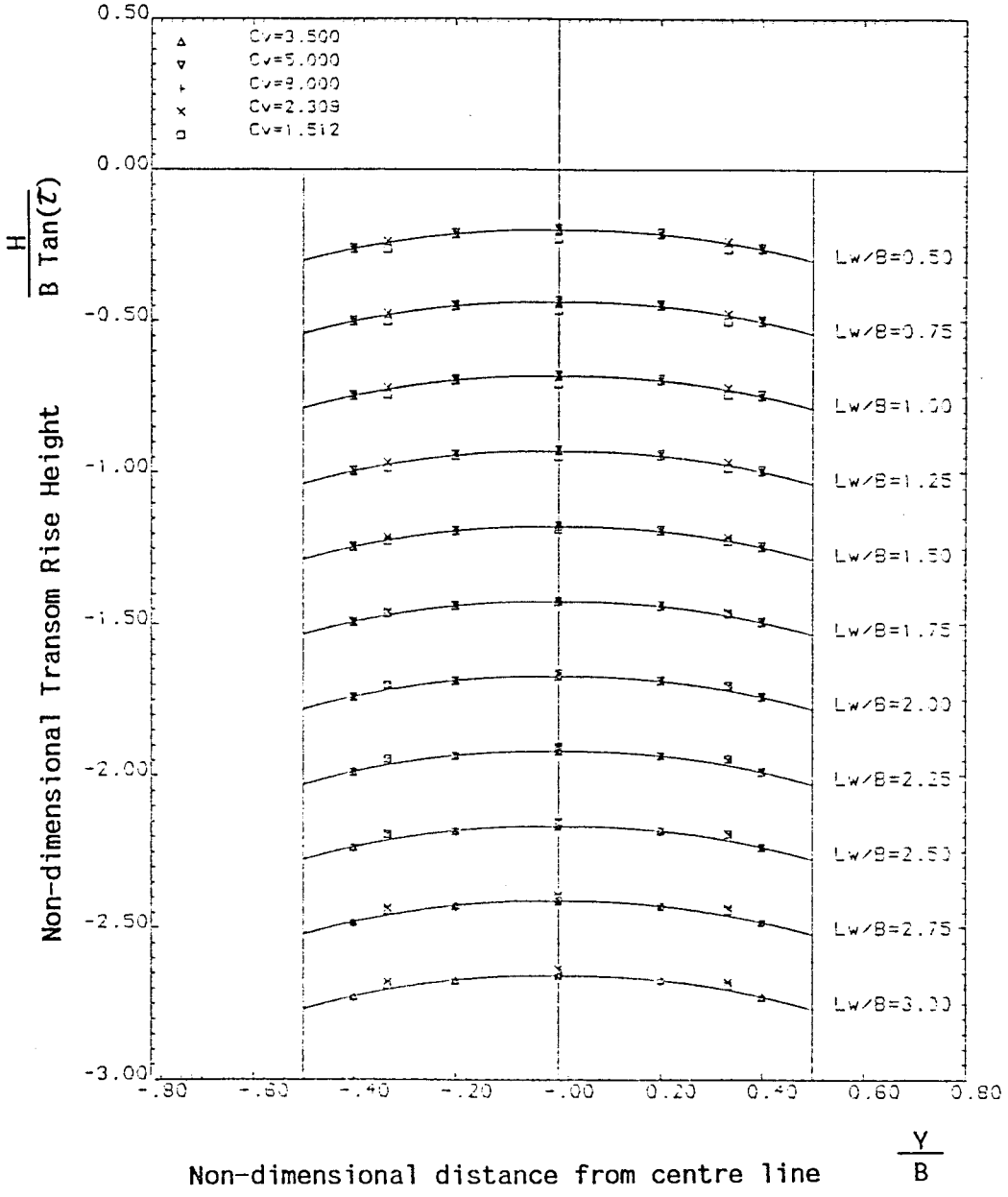

Fig.(4.3) Transom Shapes and Vertical Locations computed from Rectangular Wetted Bottoms

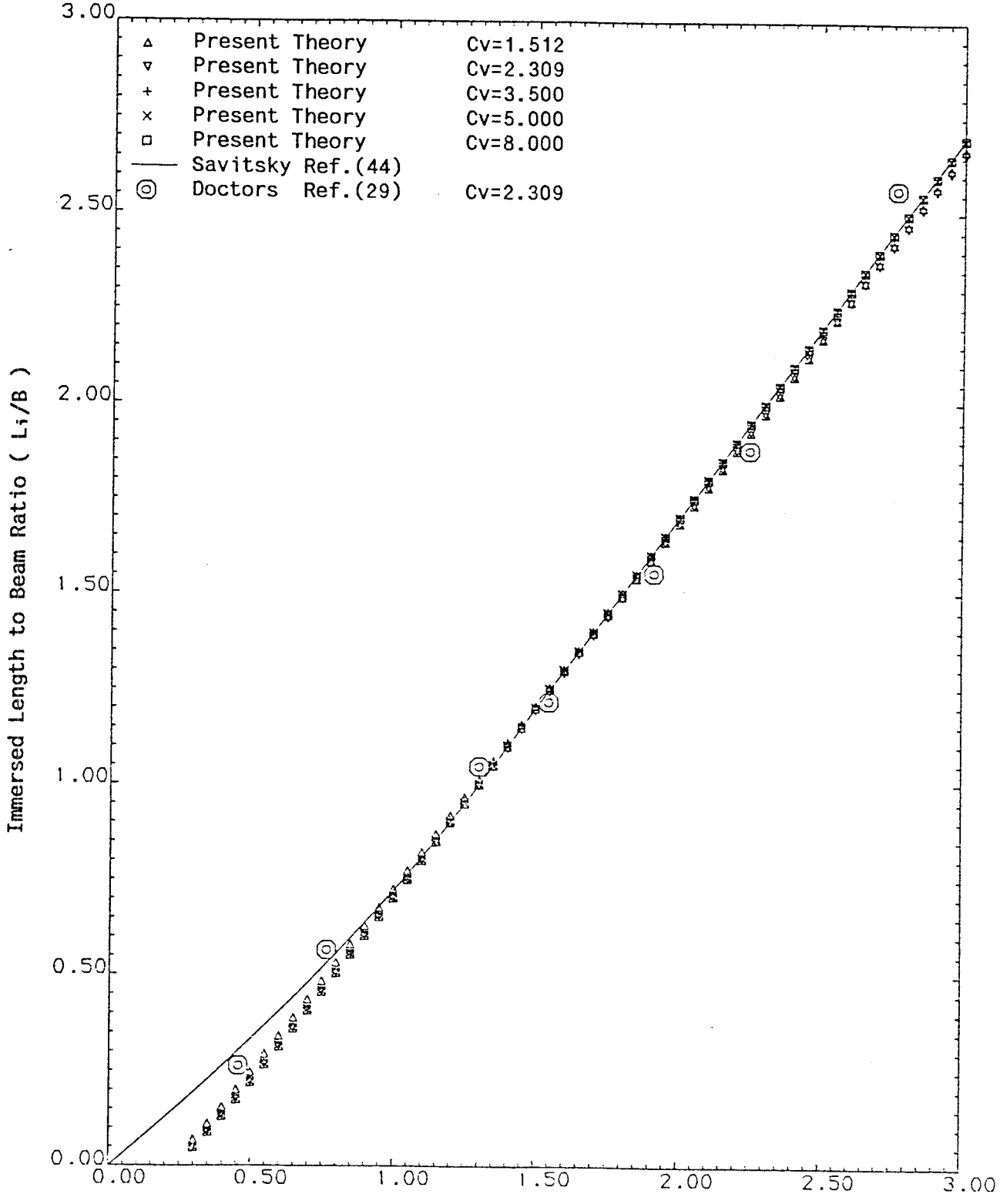

Fig.(4.4) Immersed Length below Undisturbed Free Surface to Beam Ratio for Planing Flat Plate

Fig.(4.5a) Lift Coefficient Slope for Planing Flat Plate

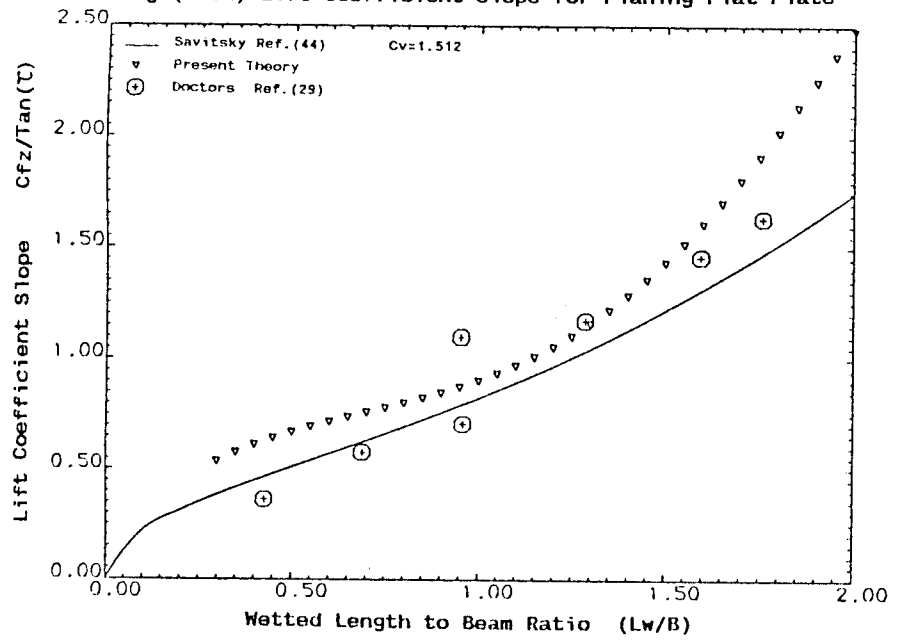

Fig.(4.5b) Lift Coefficient Slope for Planing Flat Plate

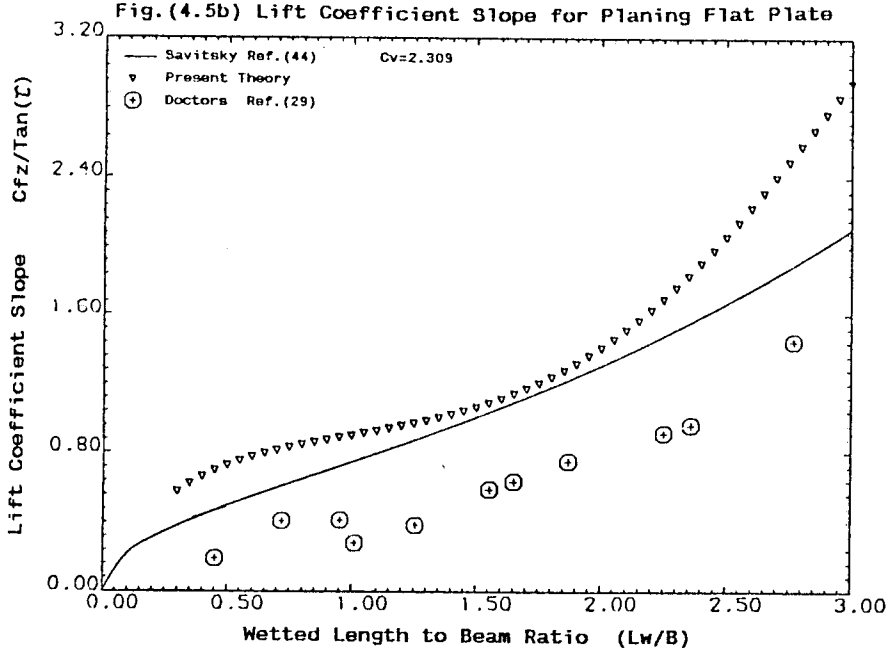

Fig.(4.5c) Lift Coefficient Slope for Planing Flat Plate

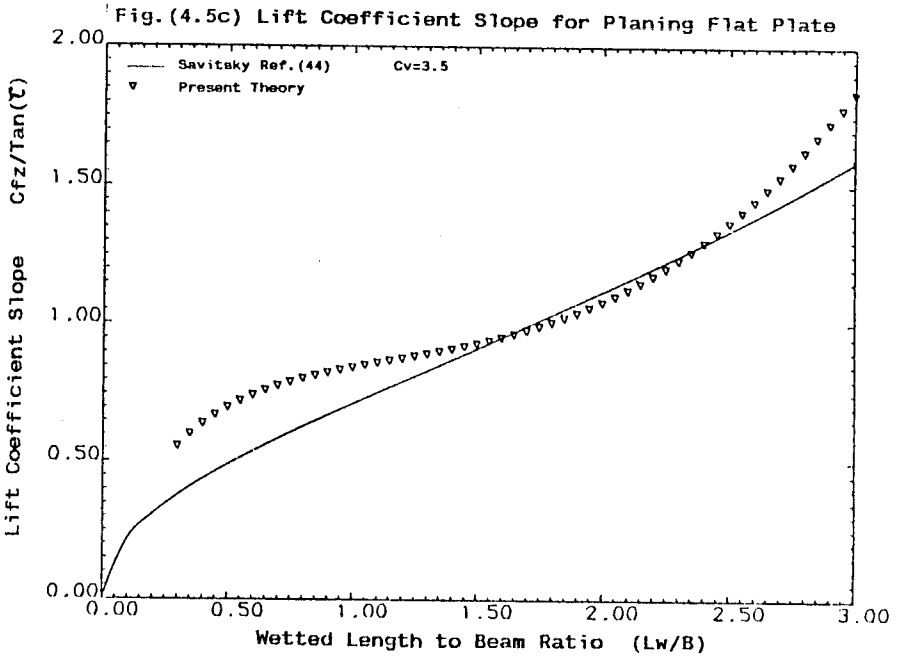

Fig.(4.5d) Lift Coefficient Slope for Planing Flat Plate

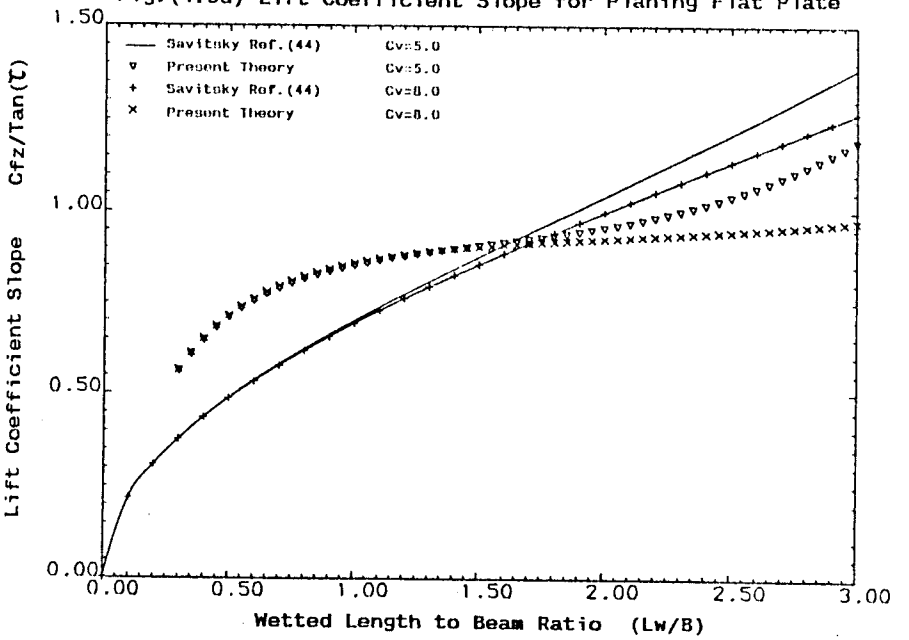

Fig.(4.6c) Pressure Distribution for Planing Flat Plate

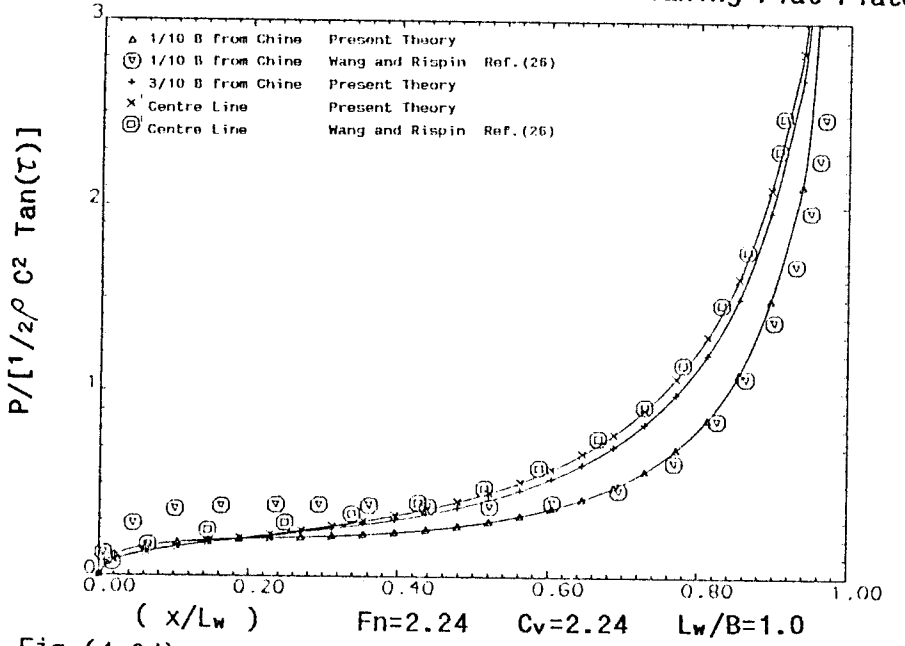

Fig.(4.6d) Pressure Distribution for Planing Flat Plate

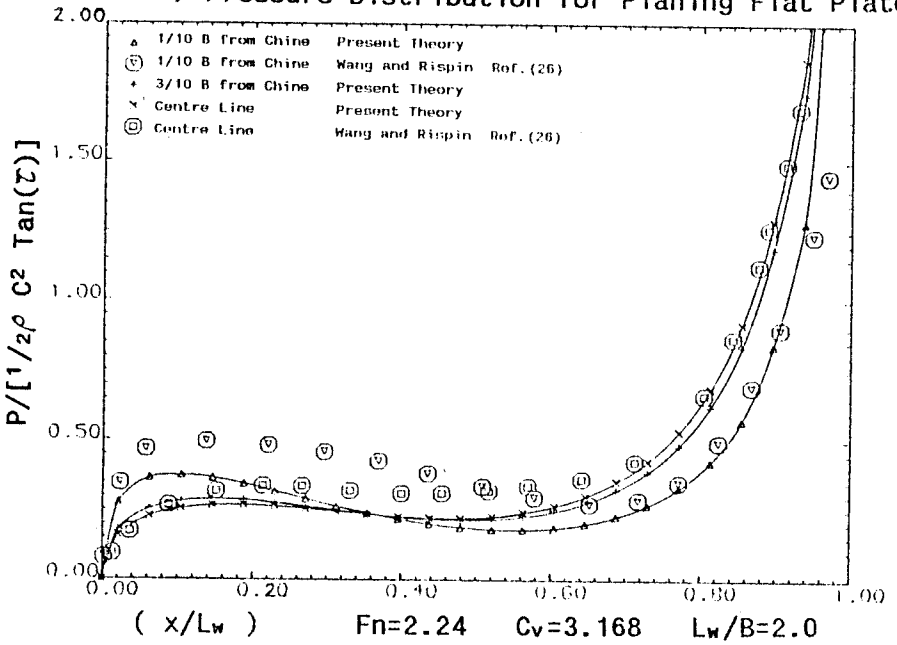

Fig.(4.6a) Lift Coefficient for Planing Flat Plate

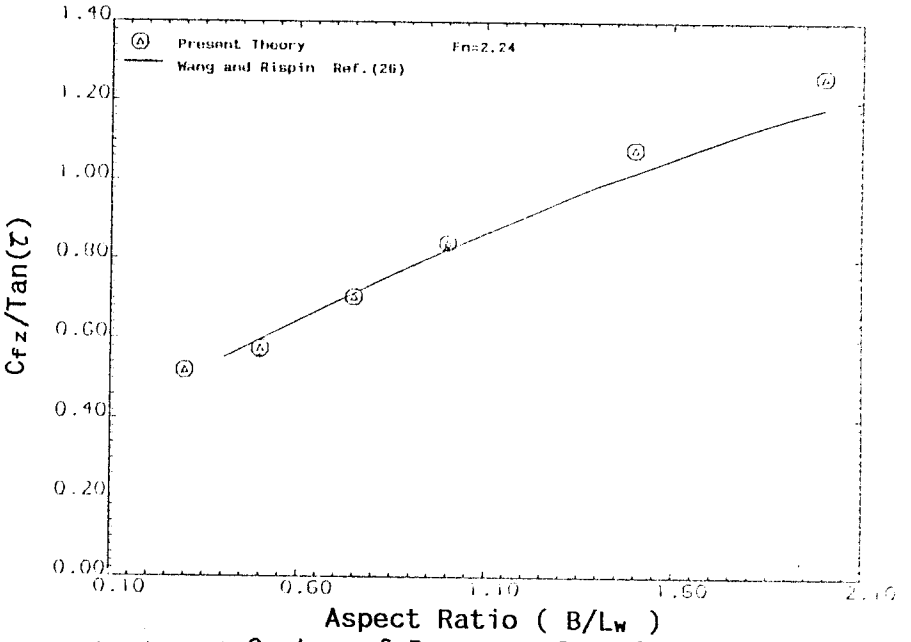

Fig.(4.6b) Centre of Pressure for planing Flat Plate

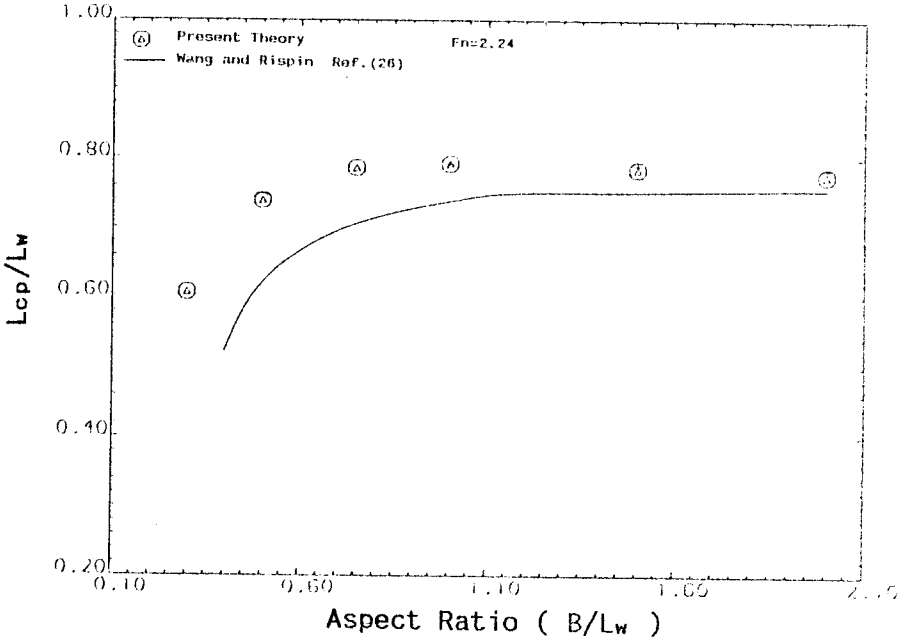

Fig.(4.7a) Centre of Pressure Ratio for Planing Flat Plate

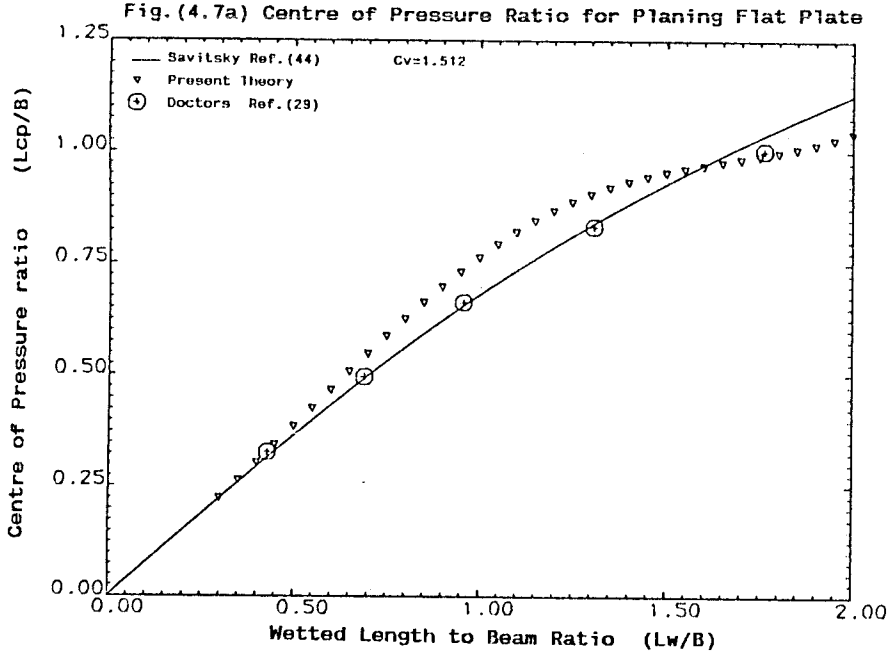

Fig.(4.7b) Centre of Pressure Ratio for Planing Flat Plate

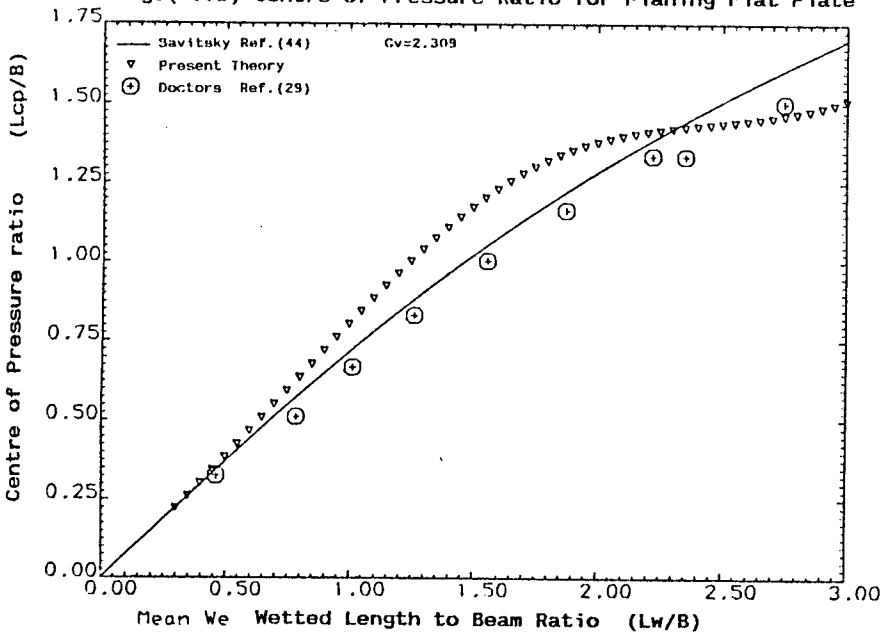

Fig.(4.7c) Centre of Pressure Ratio for Planing Flat Plate

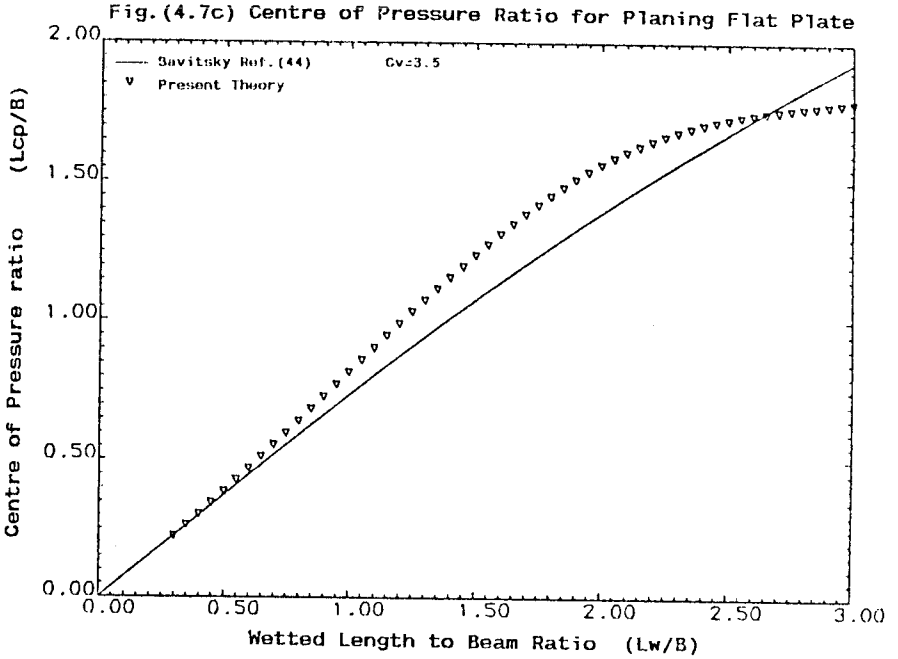

Fig.(4.7d) Centre of Pressure Ratio for Planing Flat Plate

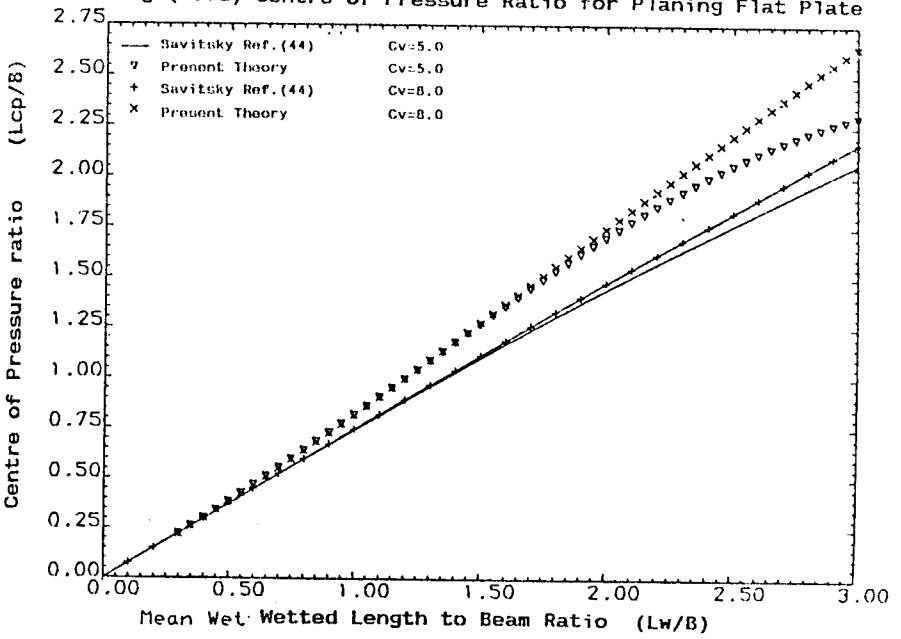

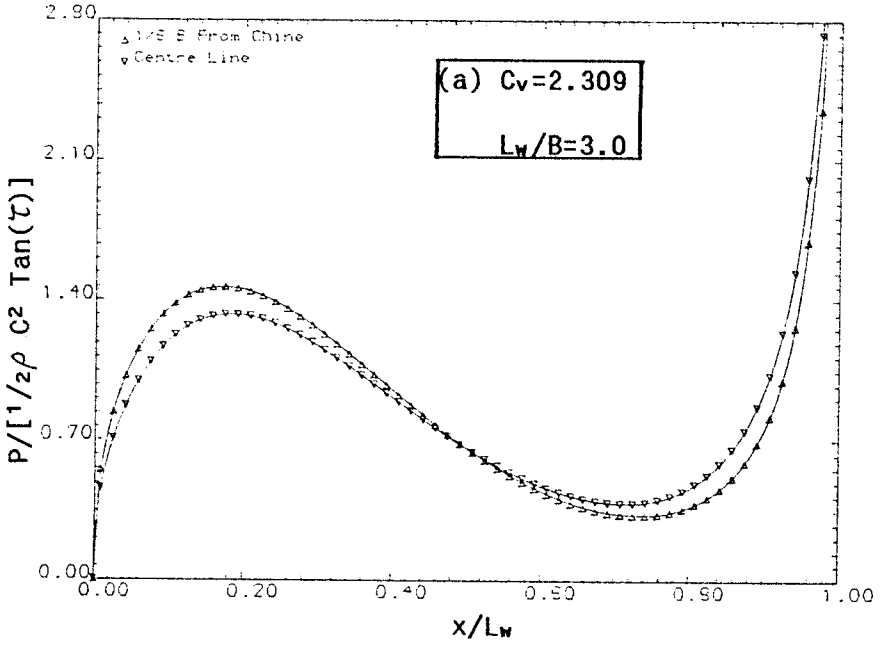

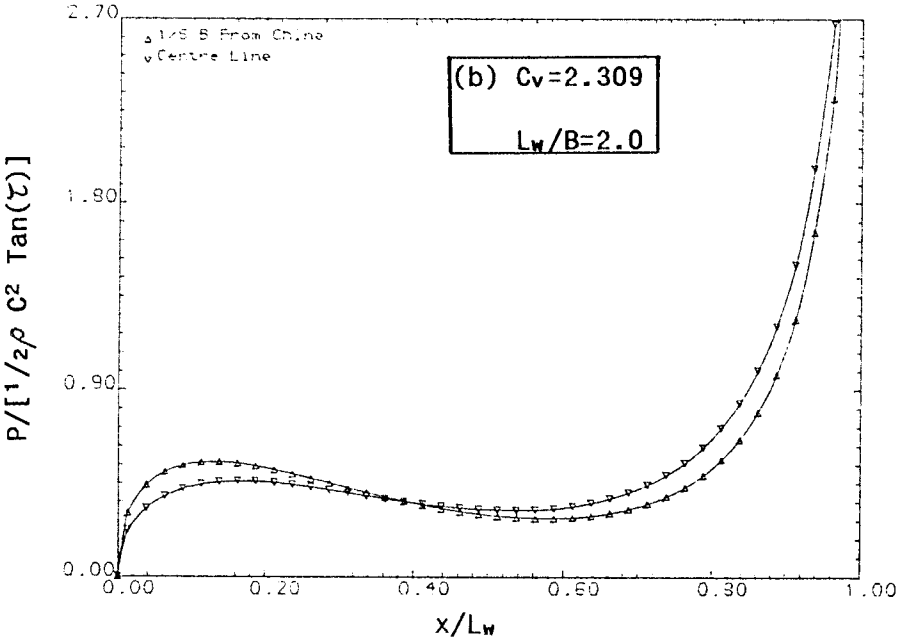

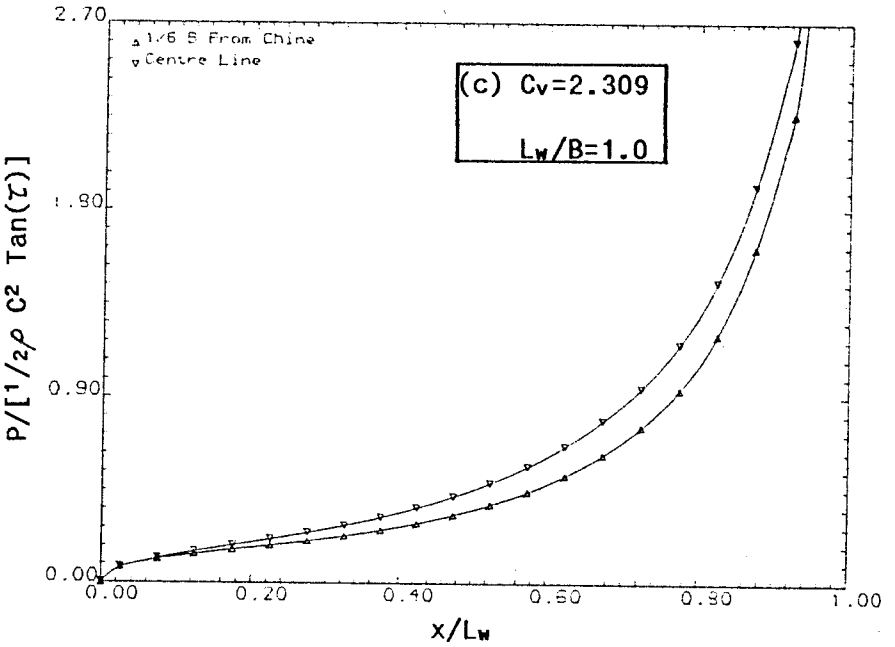

$\frac{x}{L_w}$ = non-dimensional distance forward of the transom

Fig.(4.8a,b,c) Pressure Distributions for planing Flat Plate

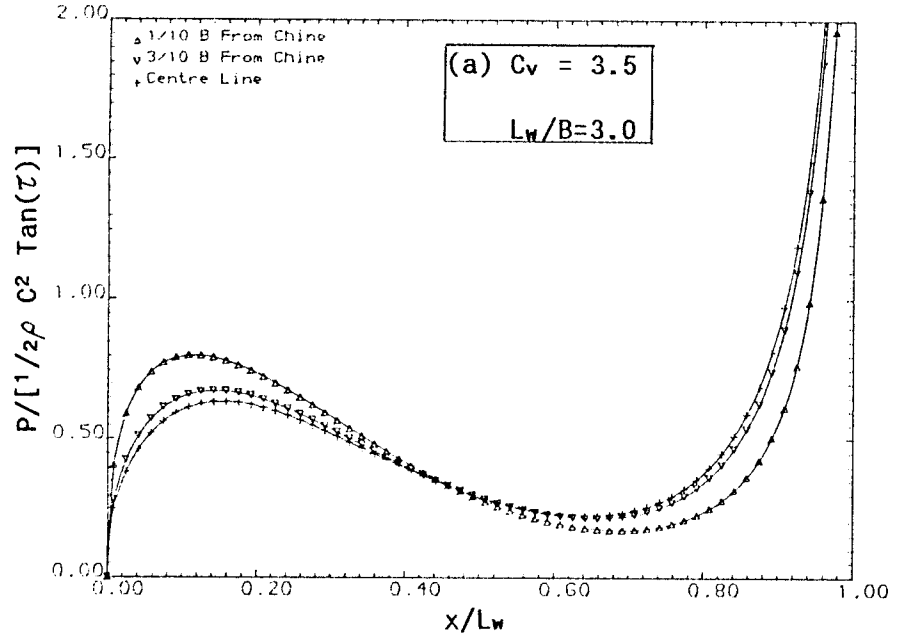

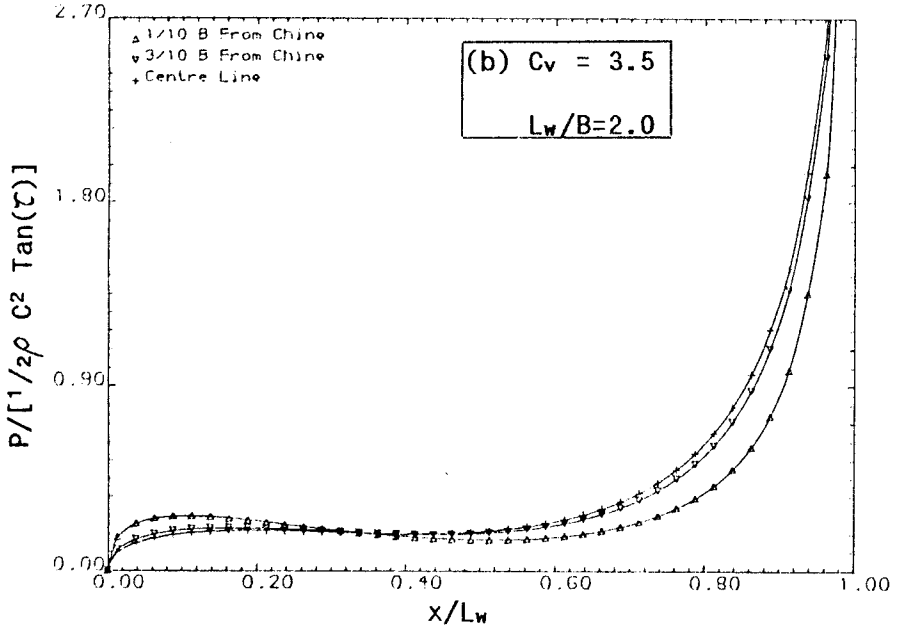

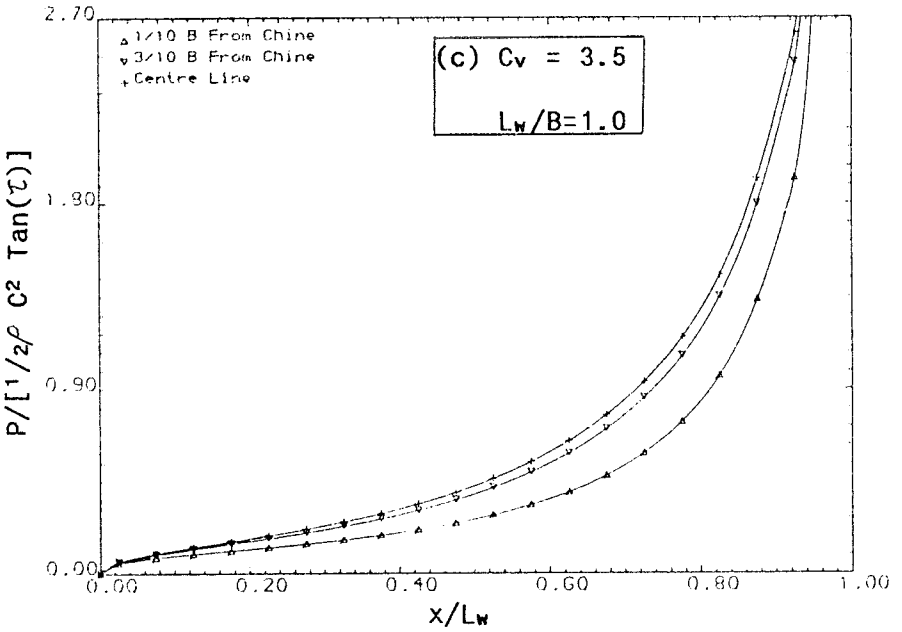

$\frac{x}{L_w}$ = non-dimensional distance forward of the transom

Fig.(4.9a,b,c) Pressure Distributions for planing Flat Plate

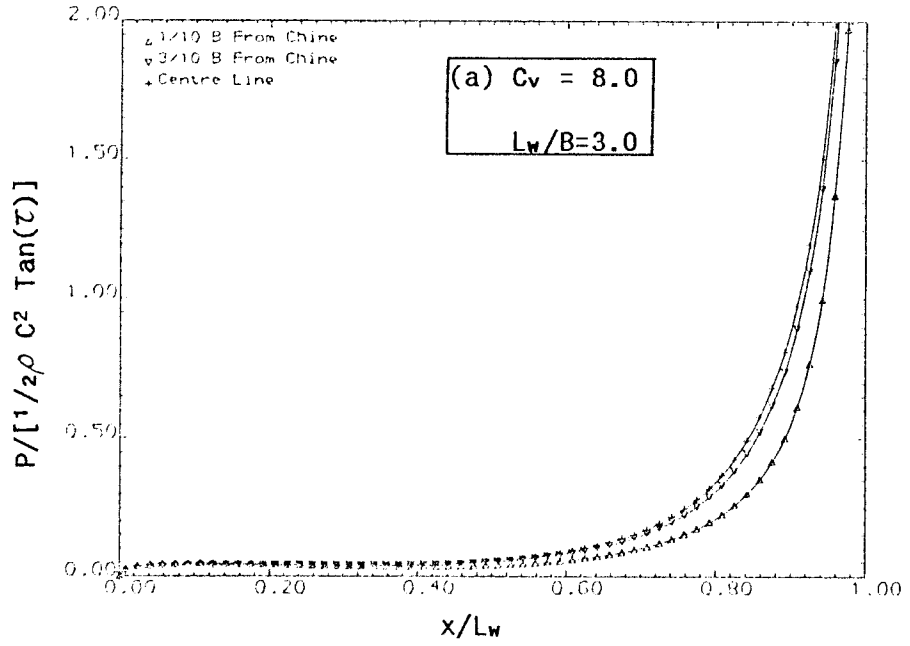

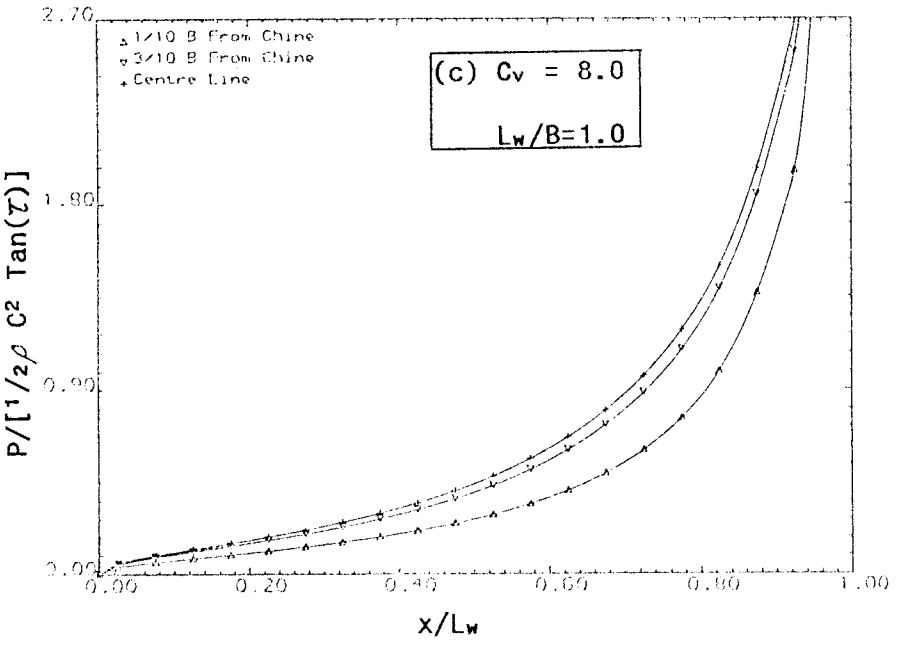

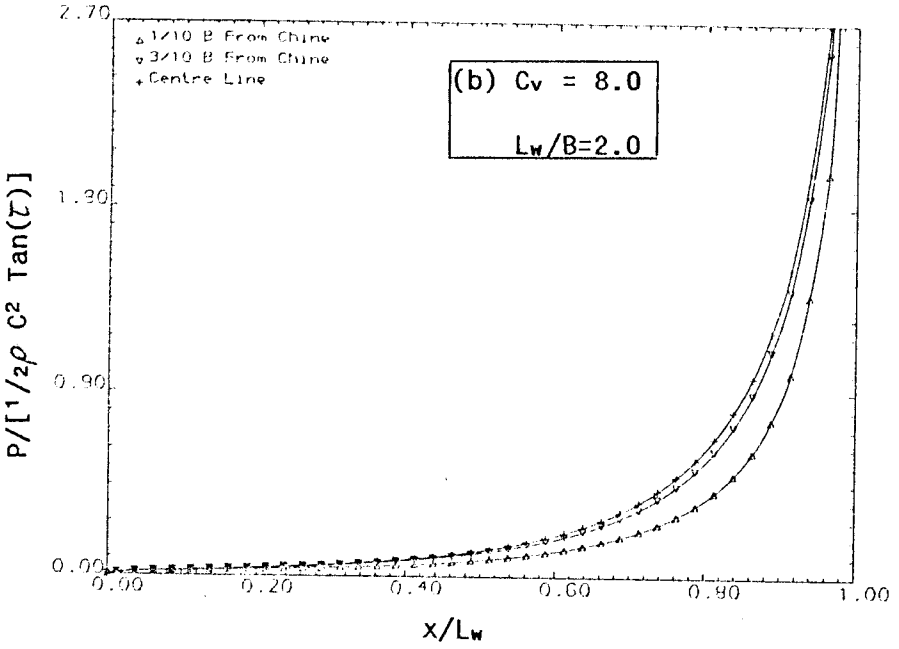

$\frac{x}{L_w}$ = non-dimensional distance forward of the transom

Fig.(4.10a,b,c) Pressure Distributions for planing Flat Plate

Fig.(4.11a) Pressure Distributions for planing Flat Plate

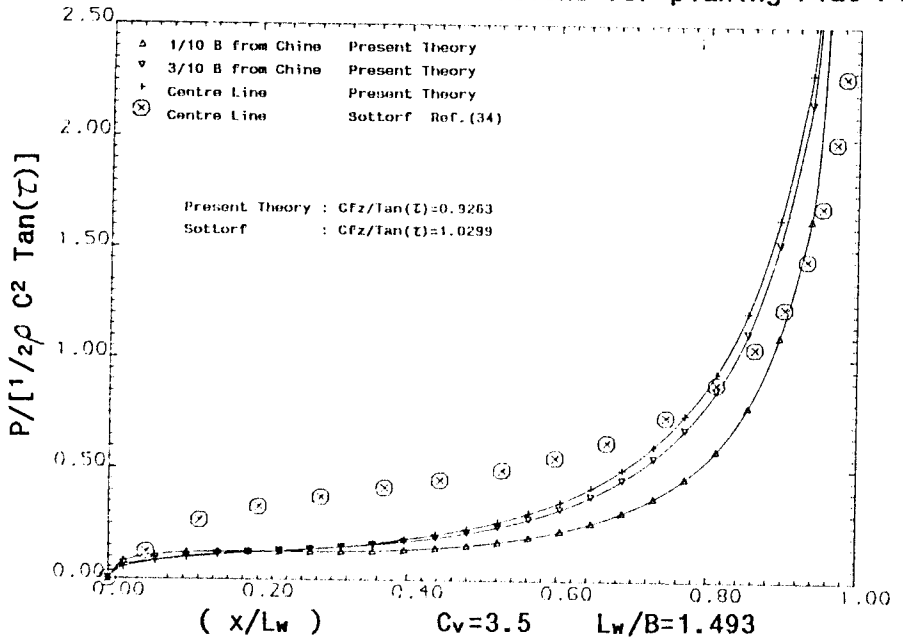

Fig.(4.11b) Pressure Distributions for planing Flat Plate

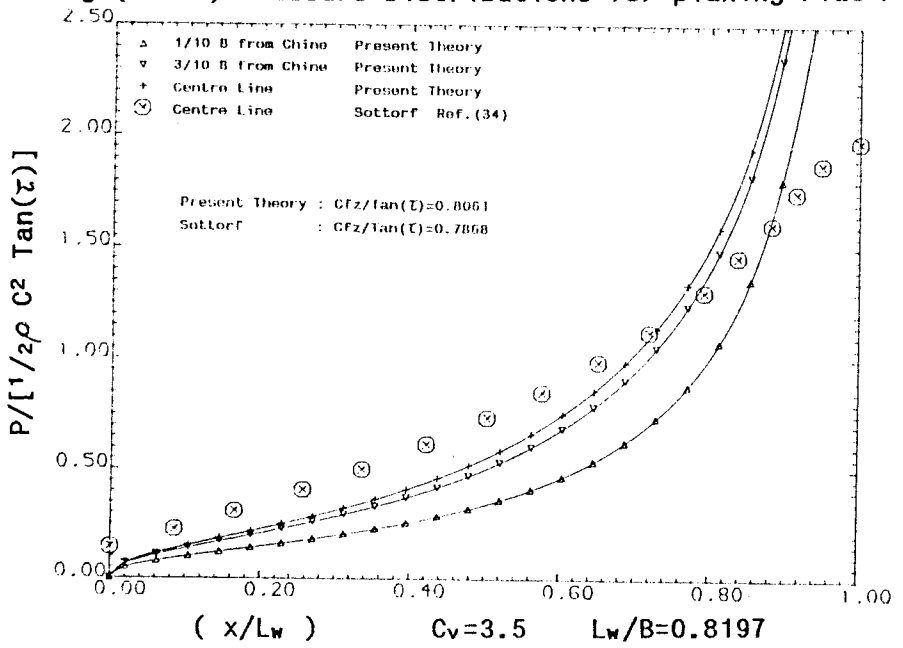

Fig.(4.12) Centre Line Pressure Distribution for Planing Flat Plate

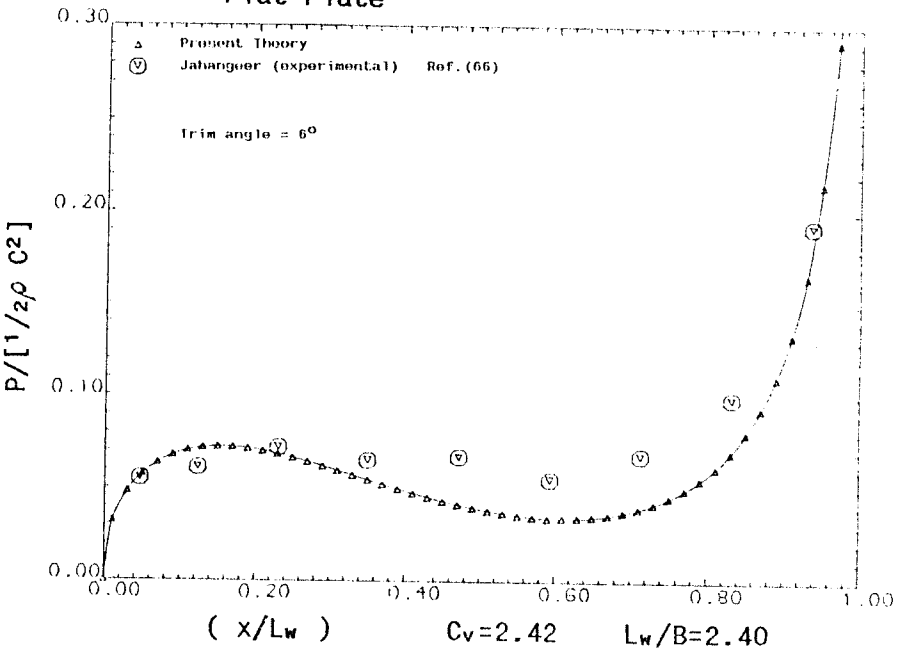

$\frac{x}{L_w}$ = non-dimensional distance forward of the transom

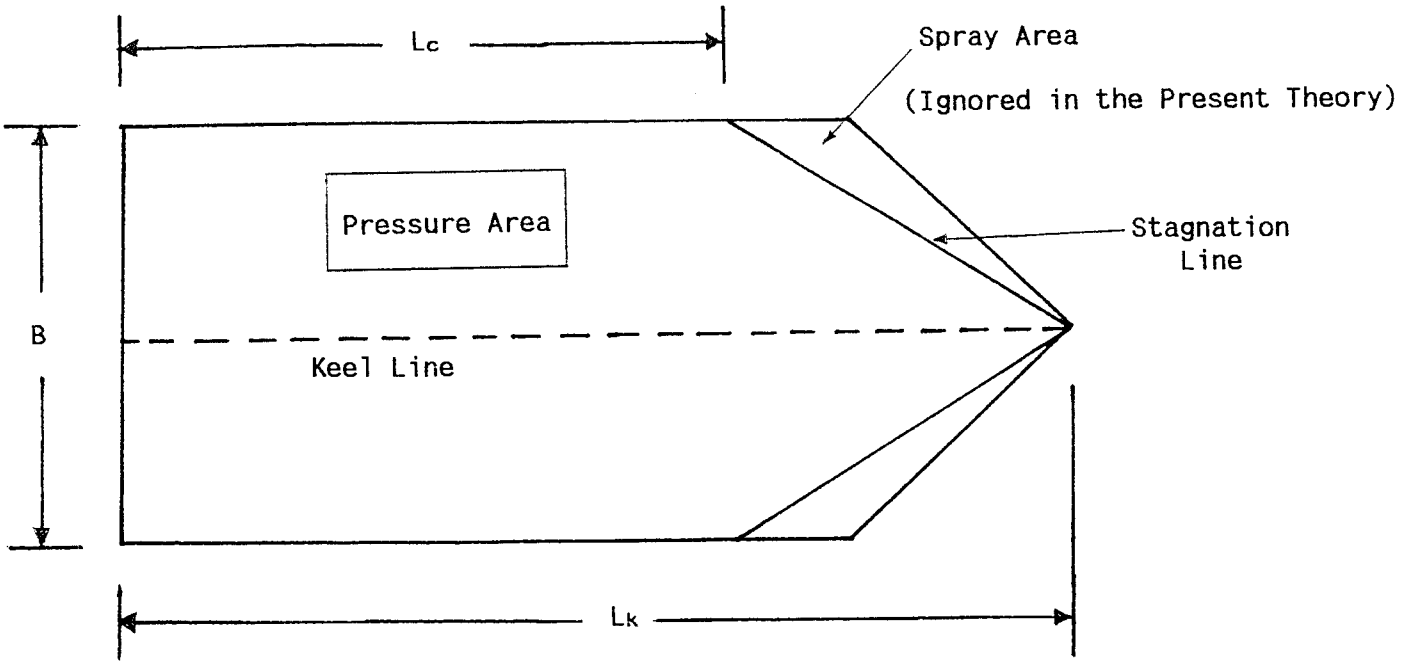

Mean Wetted Length (L_w) = $\frac{(L_k + L_c)}{2}$

Fig.(5.1) Projected Wetted Bottom of Planing Constant Deadrise Surface

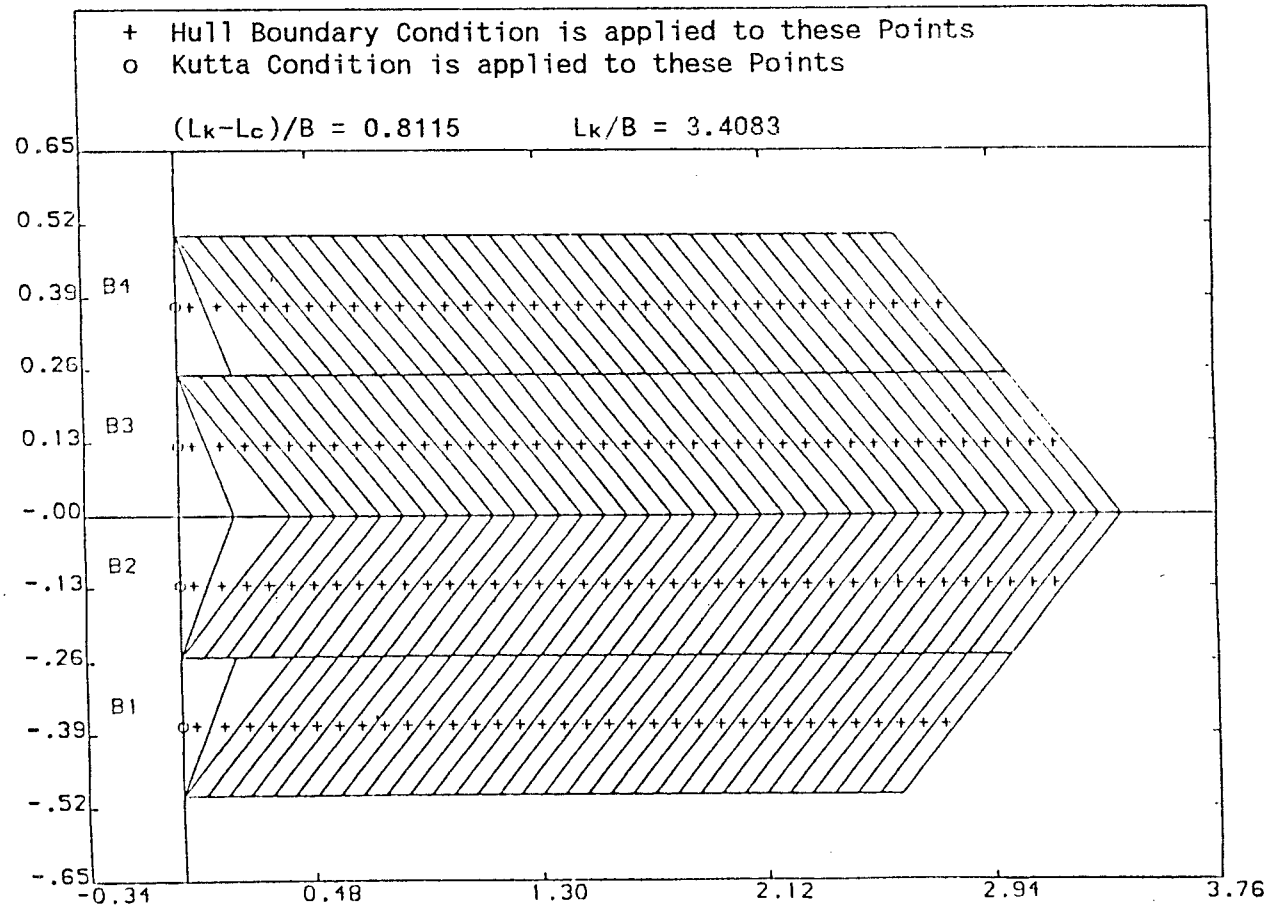

Fig.(5.2) Finite Element Representation of Projected Wetted Bottom

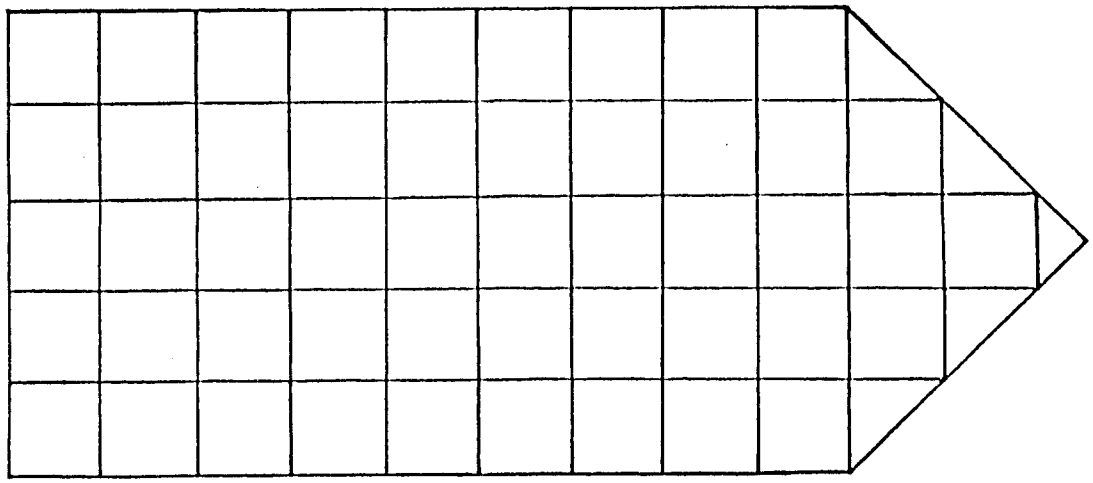

Fig.(5.3) An Alternative Wetted Bottom Grid that gives unsatisfactory Pressure Results

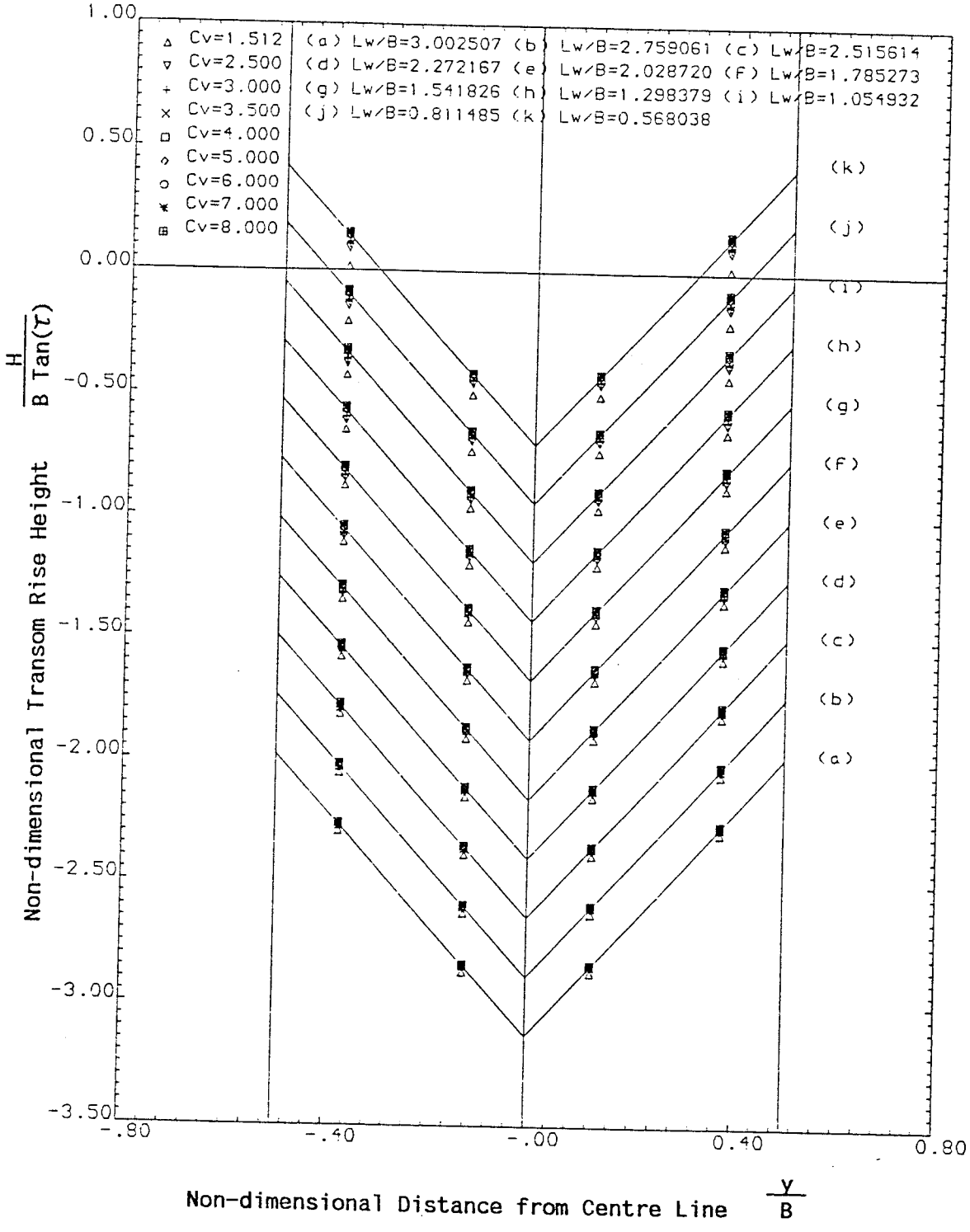

(Number of Buttock Strips = 4)

Fig.(5.4) Transom Shapes and Vertical Locations computed from Wetted Bottoms with $\frac{(L_k - L_c)}{B} = 0.8115$

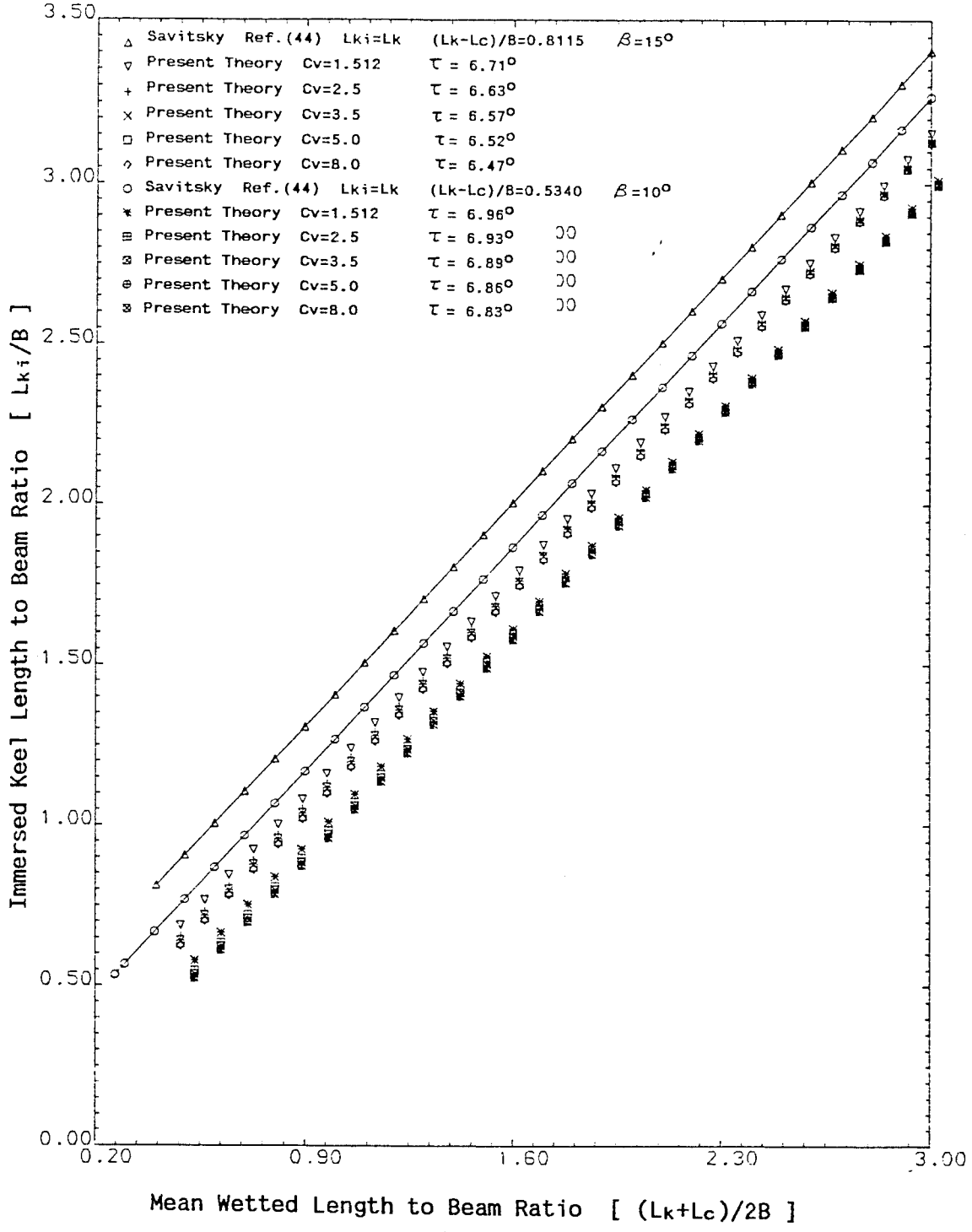

Fig.(5.5) Immersed Keel Length below Undisturbed Free Surface to Beam Ratio for Constant Deadrise Surfaces

Fig.(5.6a) Lift Coefficient Slopes for Constant Deadrise Hull (C_V=1.512)

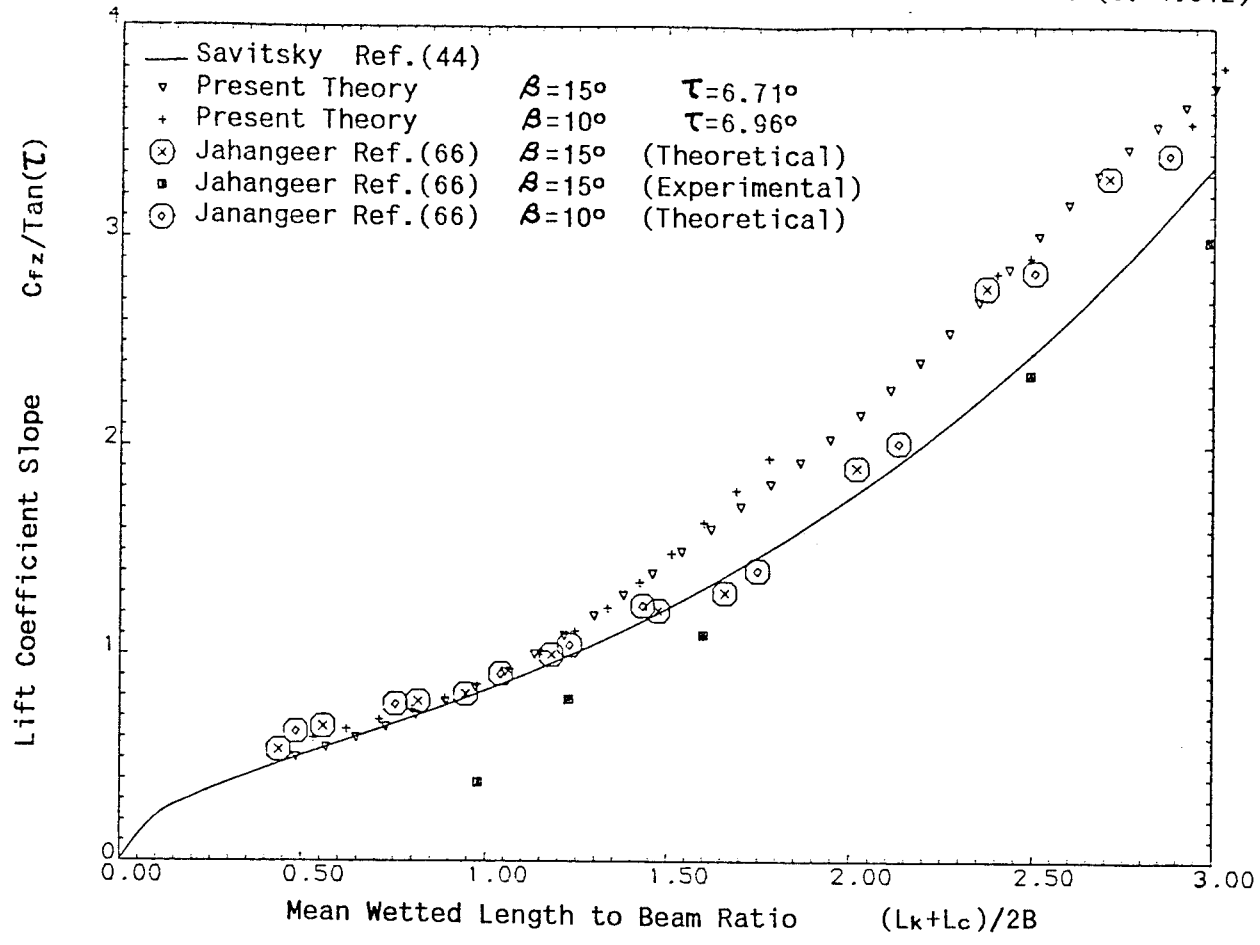

Fig.(5.6b) Lift Coefficient Slopes for Constant Deadrise Hull (C_V=2.5)

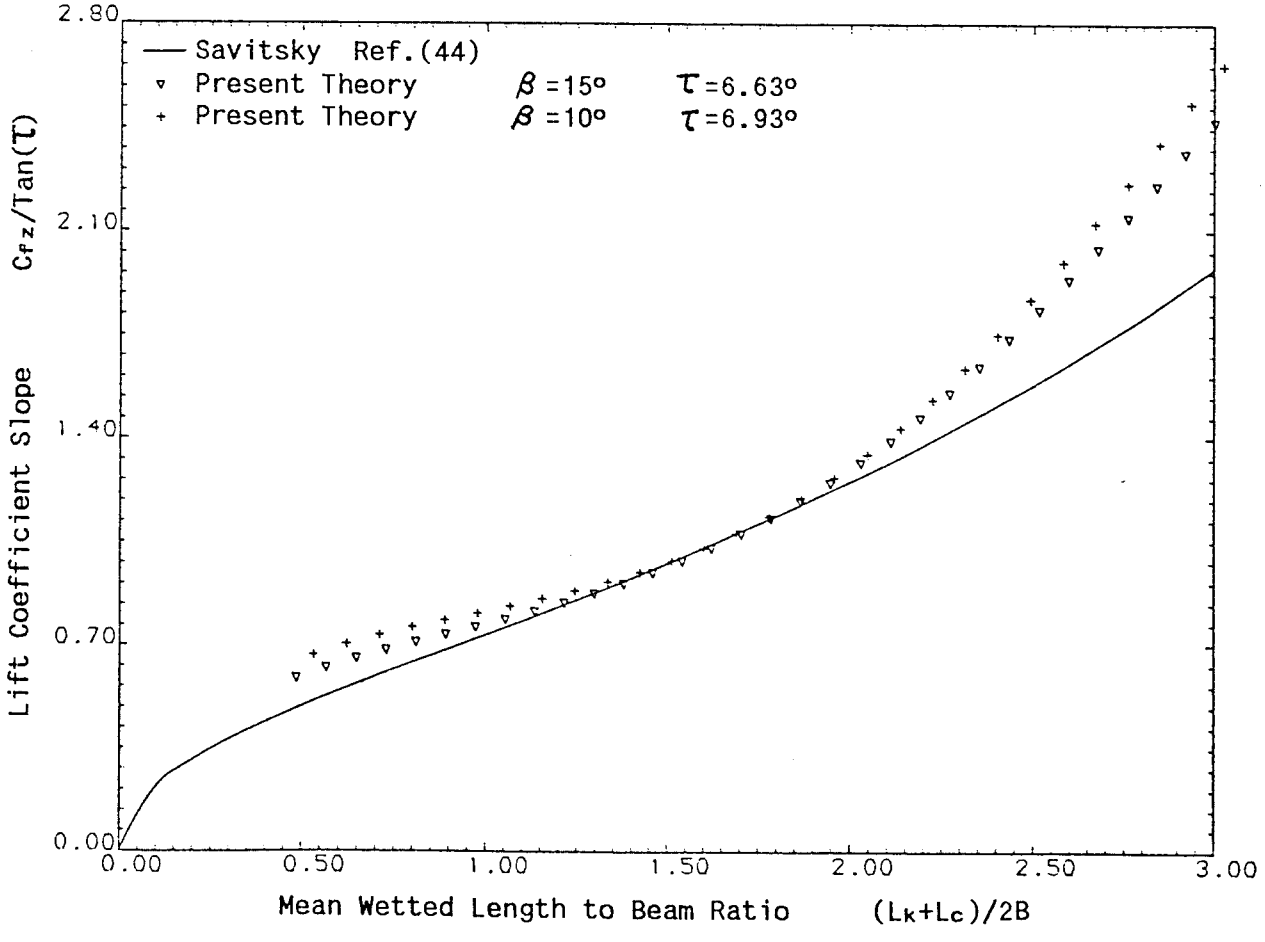

Fig.(5.6c) Lift Coefficient slopes for Constant Deadrise Hull (C_V=3.0)

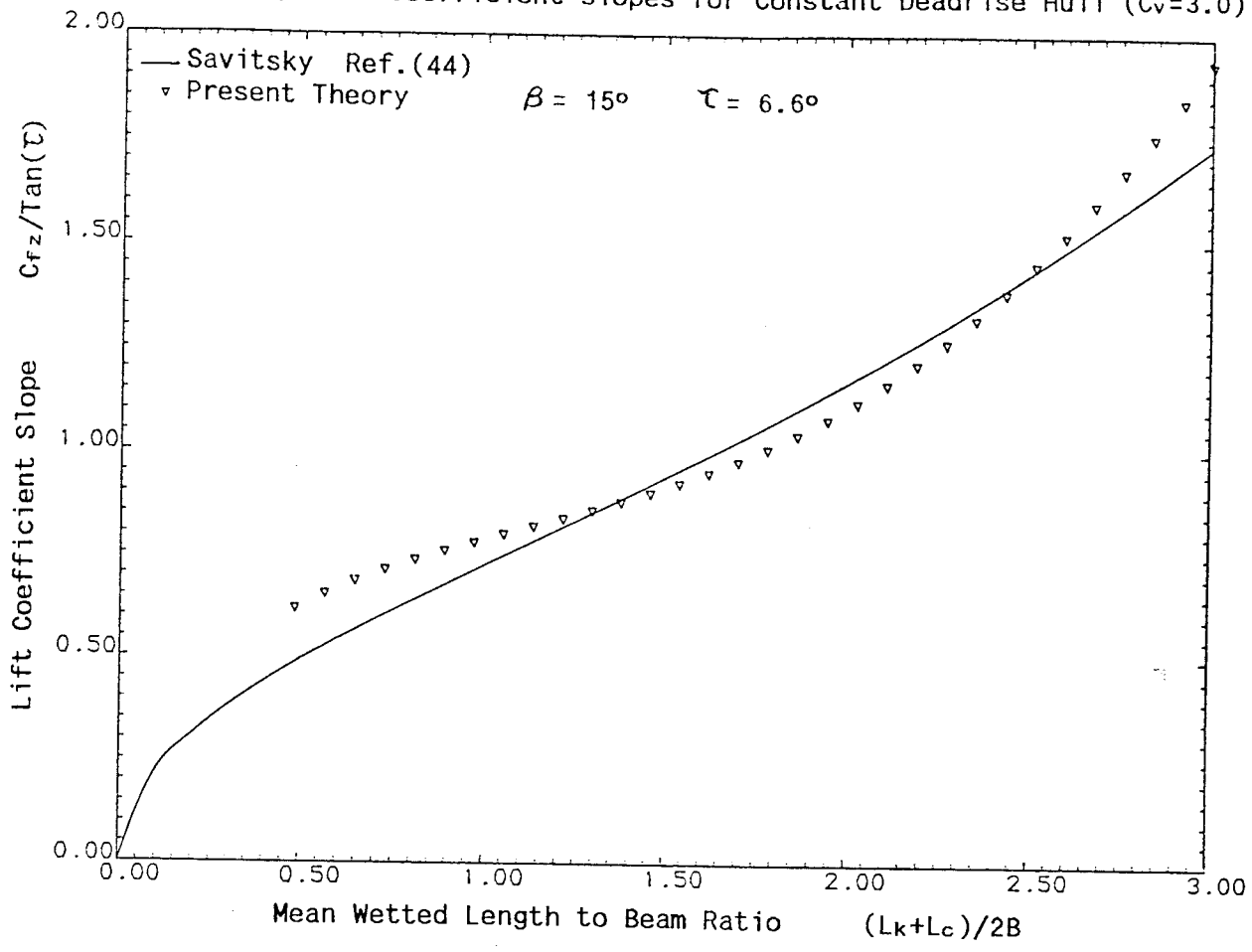

Fig.(5.6d) Lift Coefficient slopes for Constant Deadrise Hull (C_V=3.5)

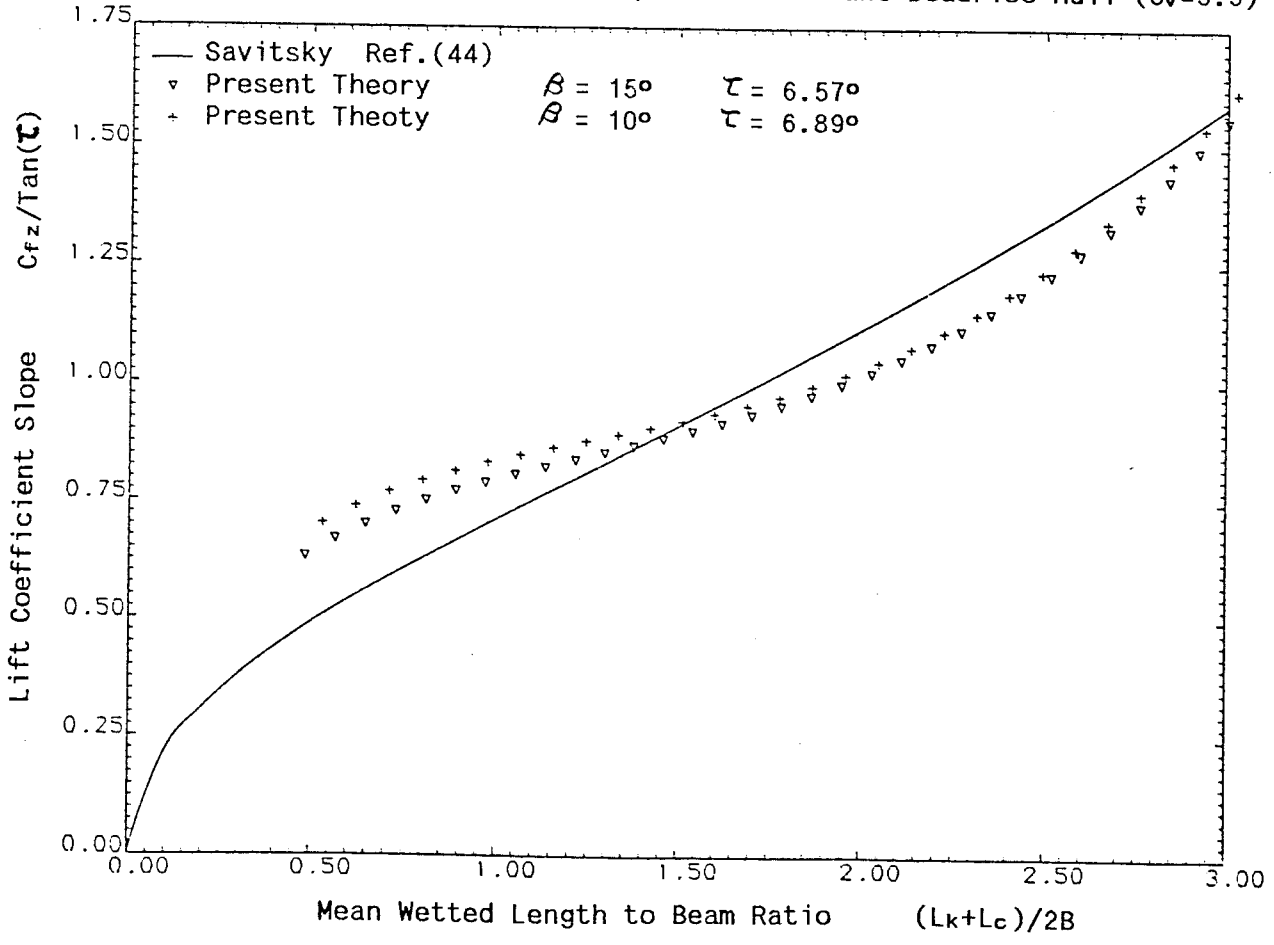

Fig.(5.6e) Lift Coefficient Slopes for Constant Deadrise Hull (C_V=4.0)

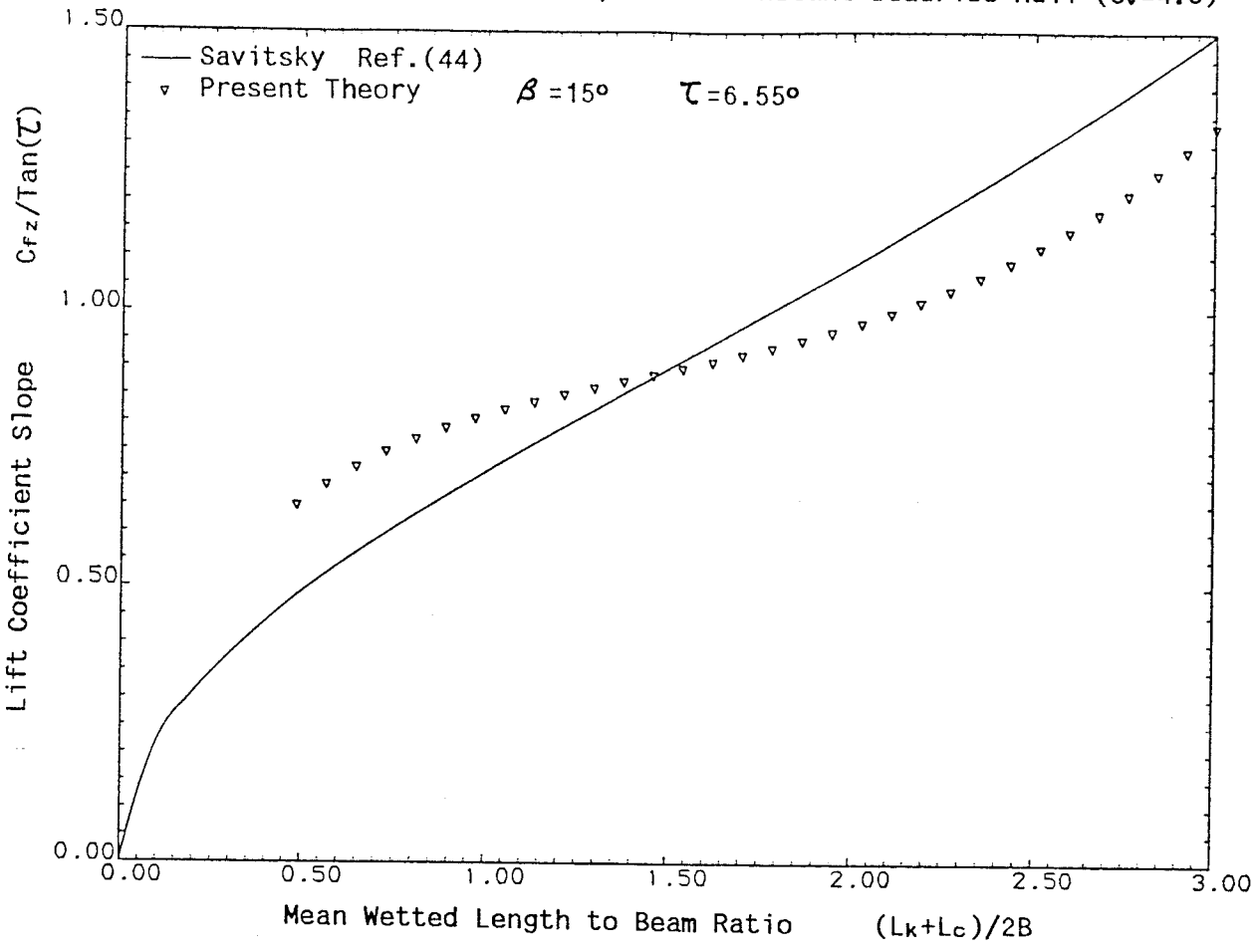

Fig.(5.6f) Lift Coefficient Slopes for Constant Deadrise Hull (C_V=5.0)

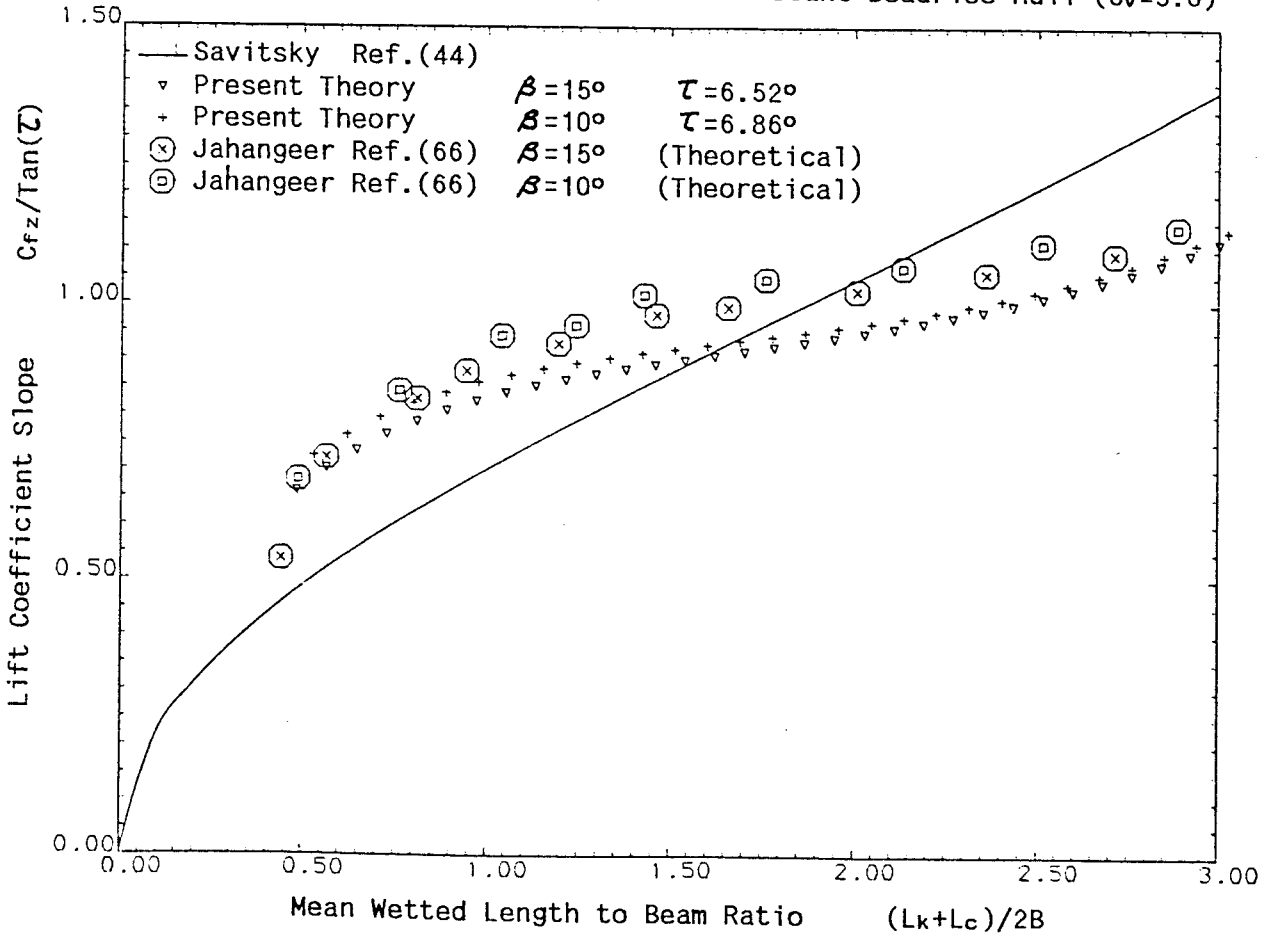

Fig.(5.6g) Lift Coefficient slopes for Constant Deadrise Hull

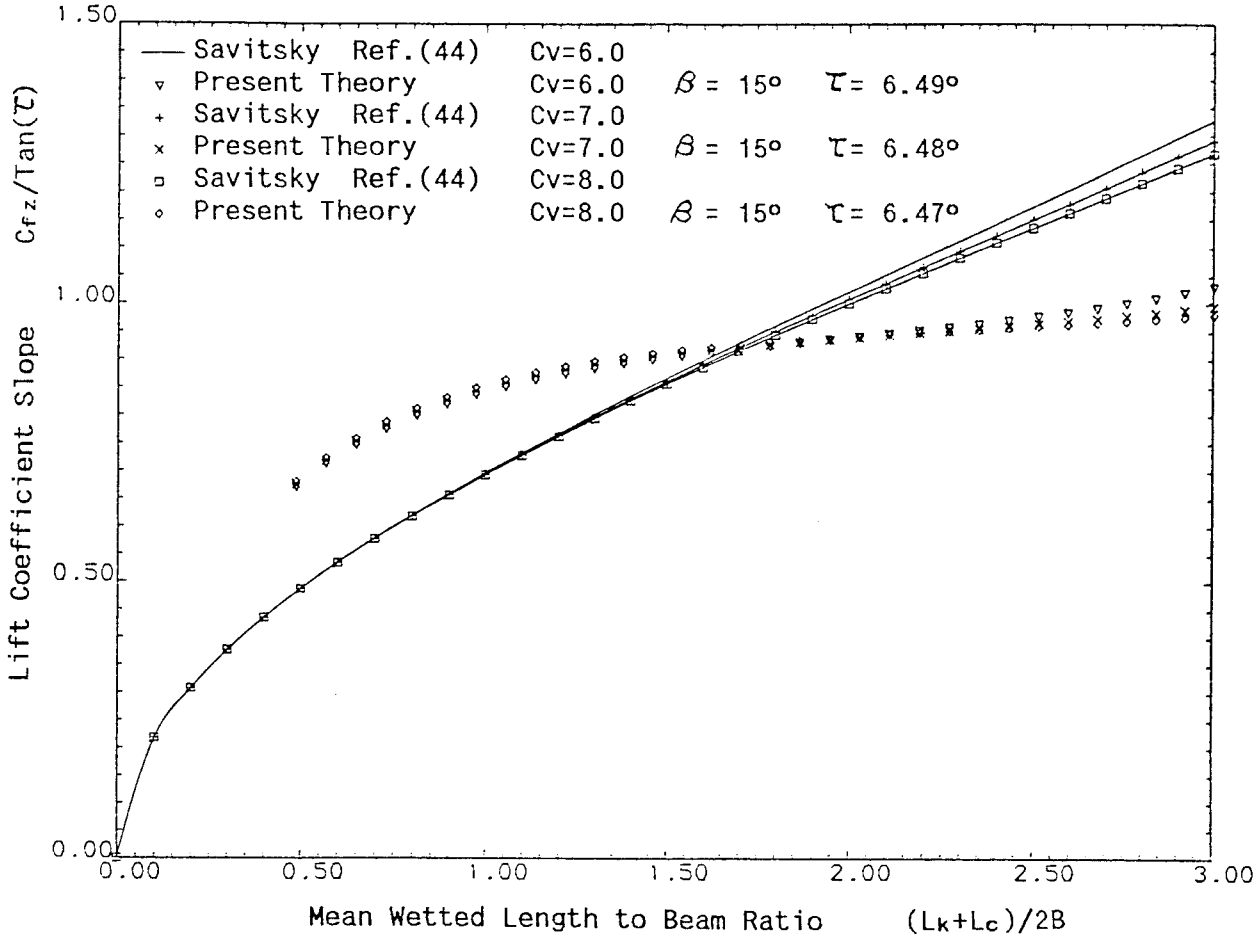

Fig.(5.6h) Lift Coefficient slopes for Constant Deadrise Hull

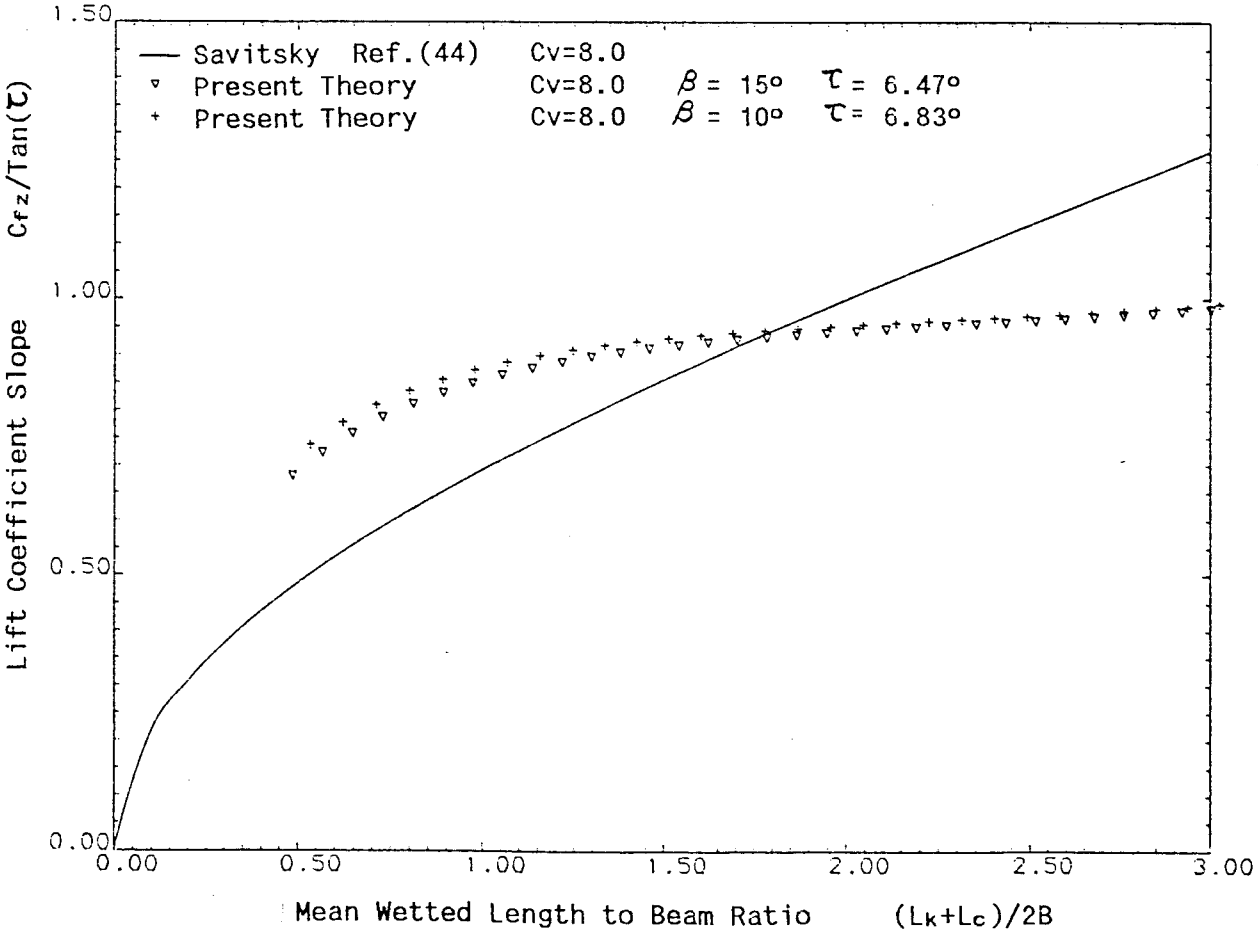

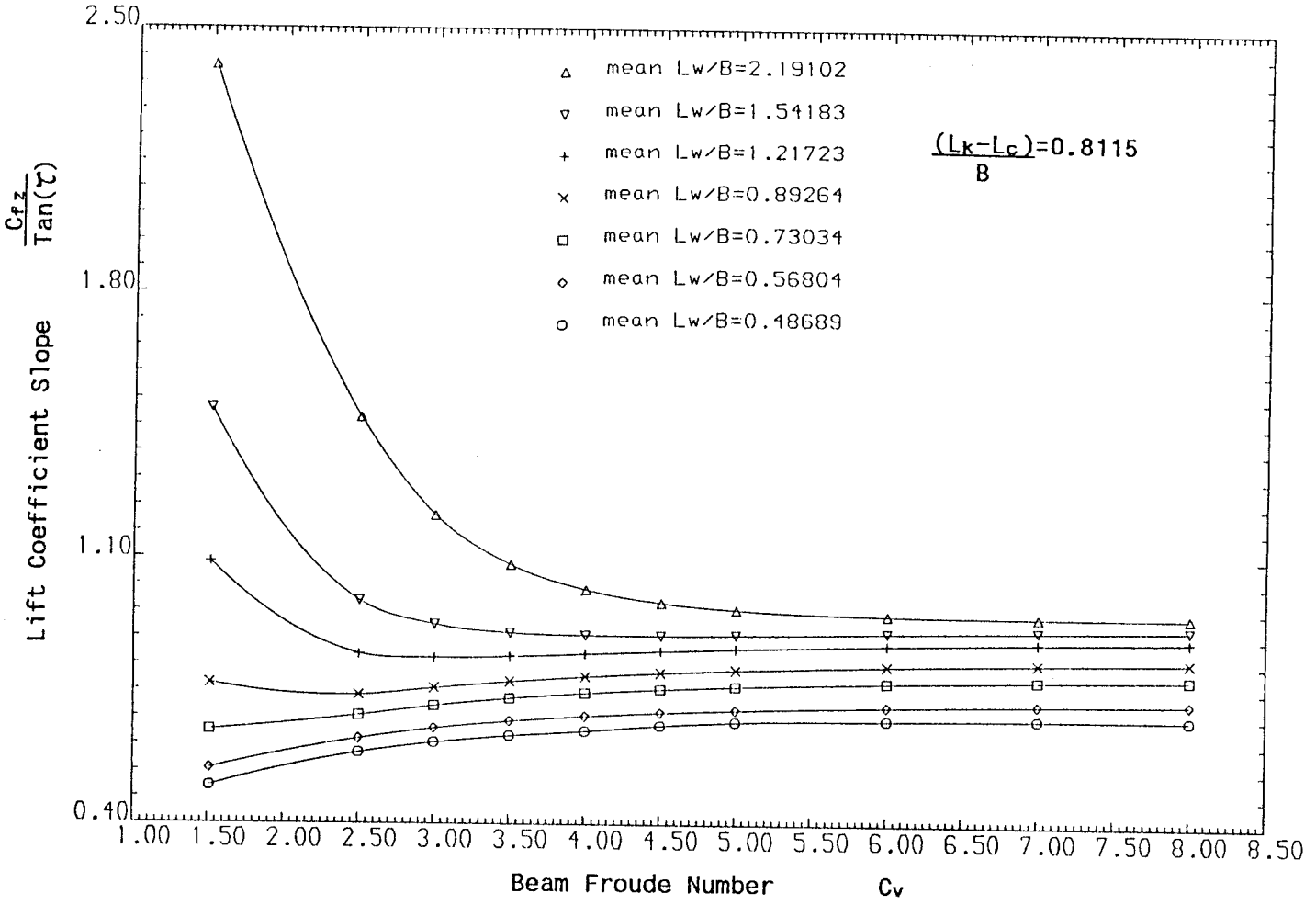

Fig.(5.7) Slopes of Lift Coefficient plotted against Beam Froude Number for a 15° Constant Deadrise Planing Surface

Fig.(5.8a) Centre of Pressure Ratios for Constant Deadrise Hull (C_v=1.512)

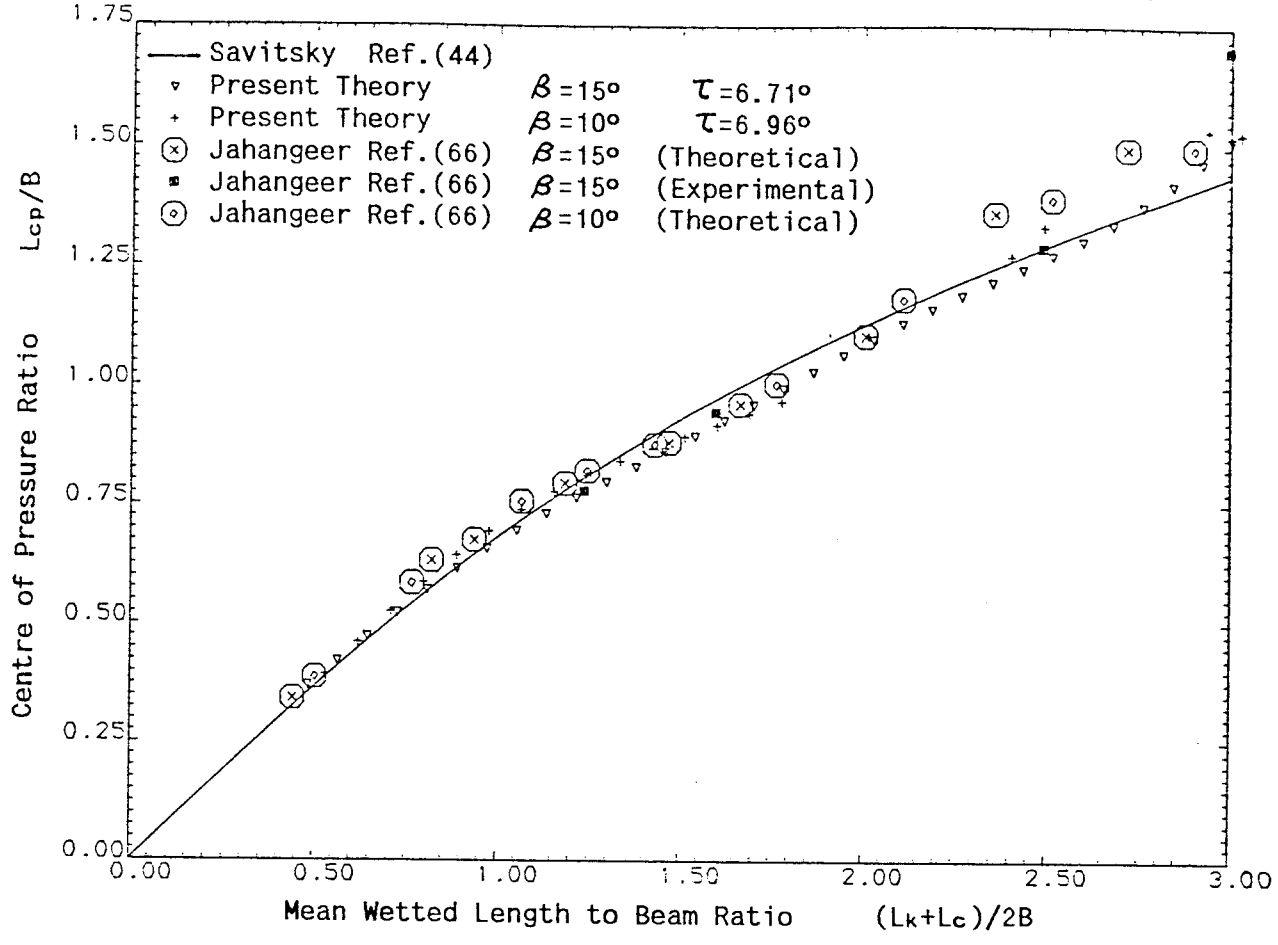

Fig.(5.8b) Centre of Pressure Ratios for Constant Deadrise Hull (C_v=2.50)

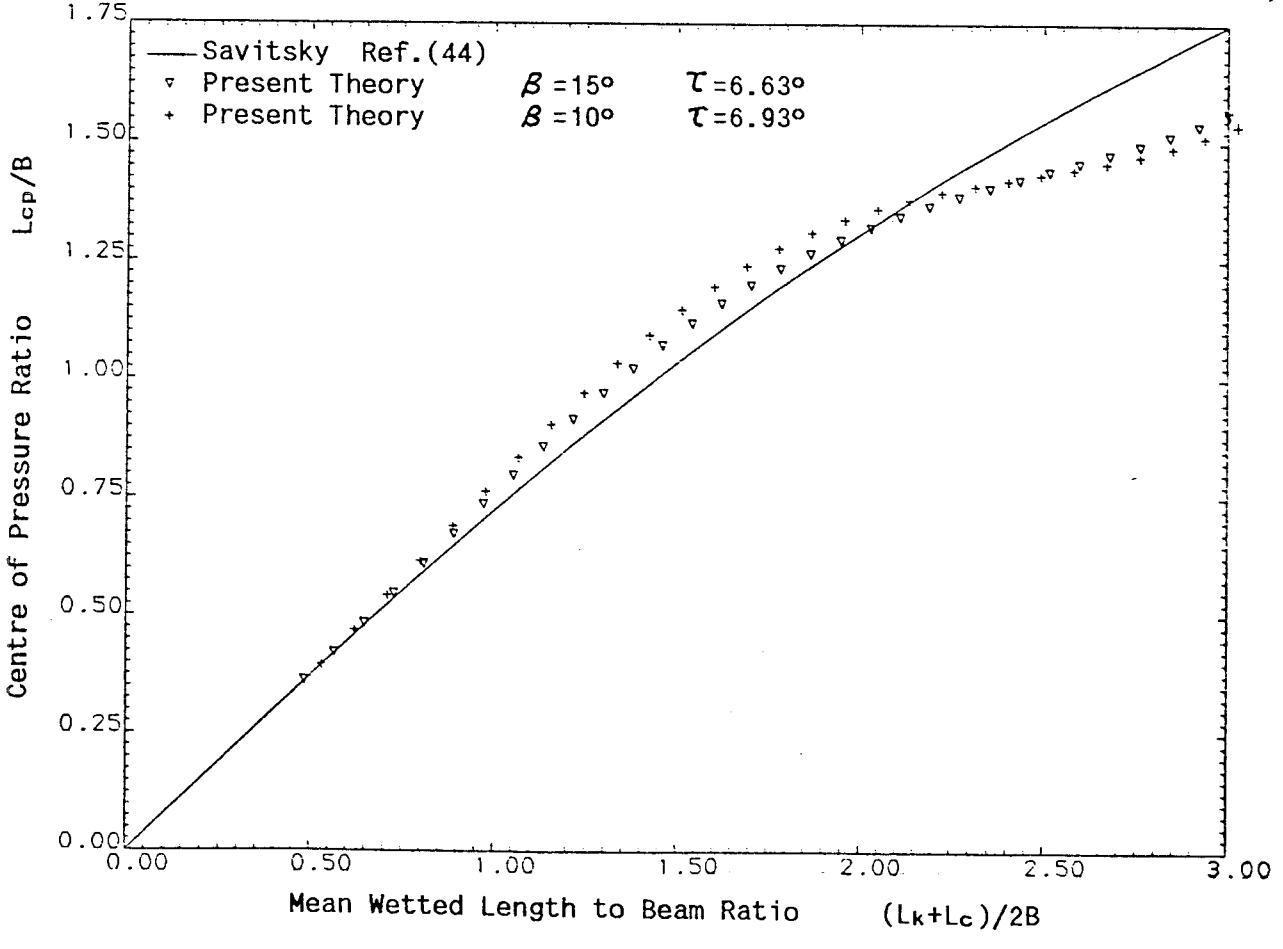

Fig.(5.8c) Centre of Pressure Ratios for Constant Deadrise Hull (C_v=3.0)

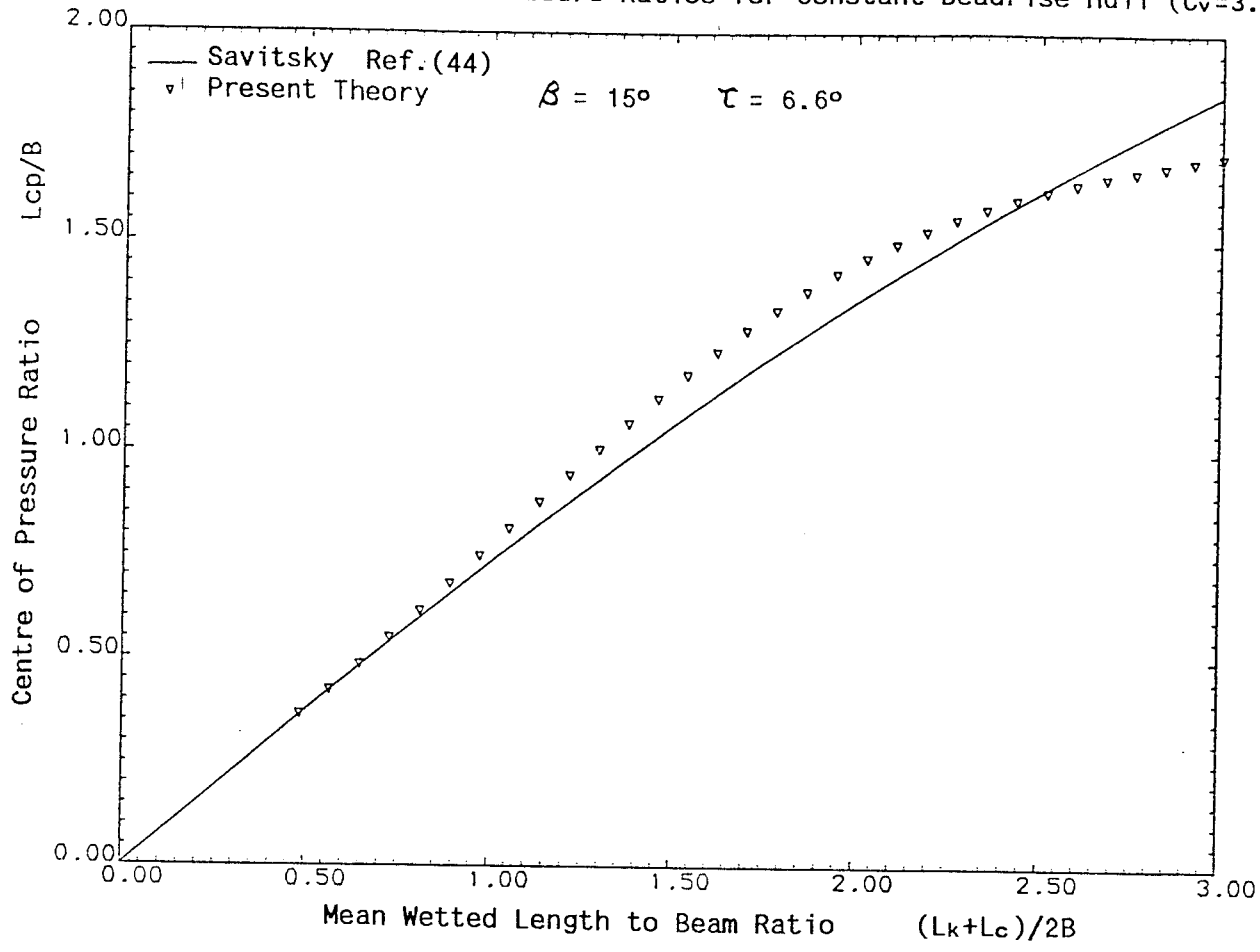

Fig.(5.8d) Centre of Pressure Ratios for Constant Deadrise Hull (C_v=3.5)

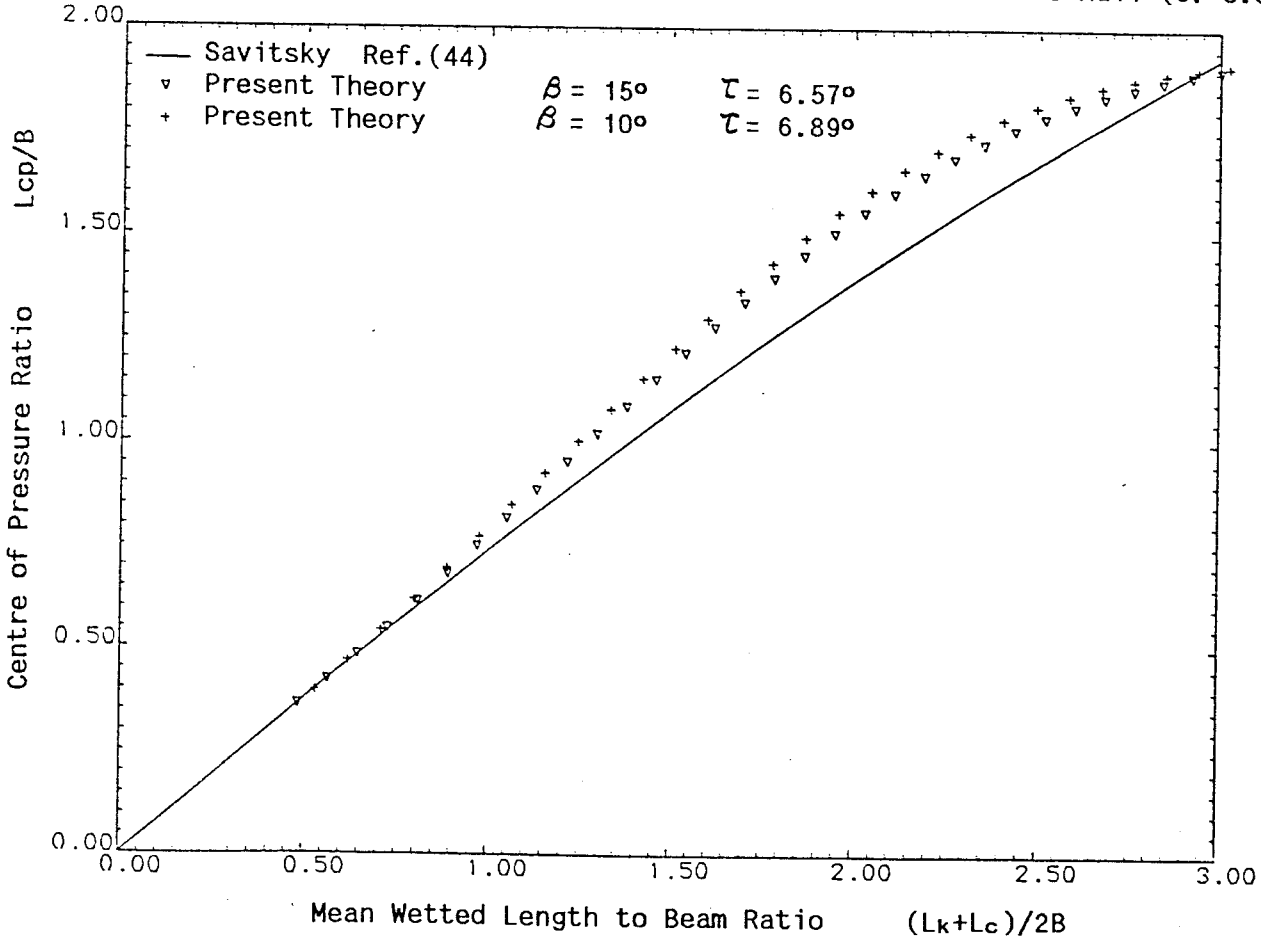

Fig.(5.8e) Centre of Pressure Ratios for Constant Deadrise Hull (C_V=4.0)

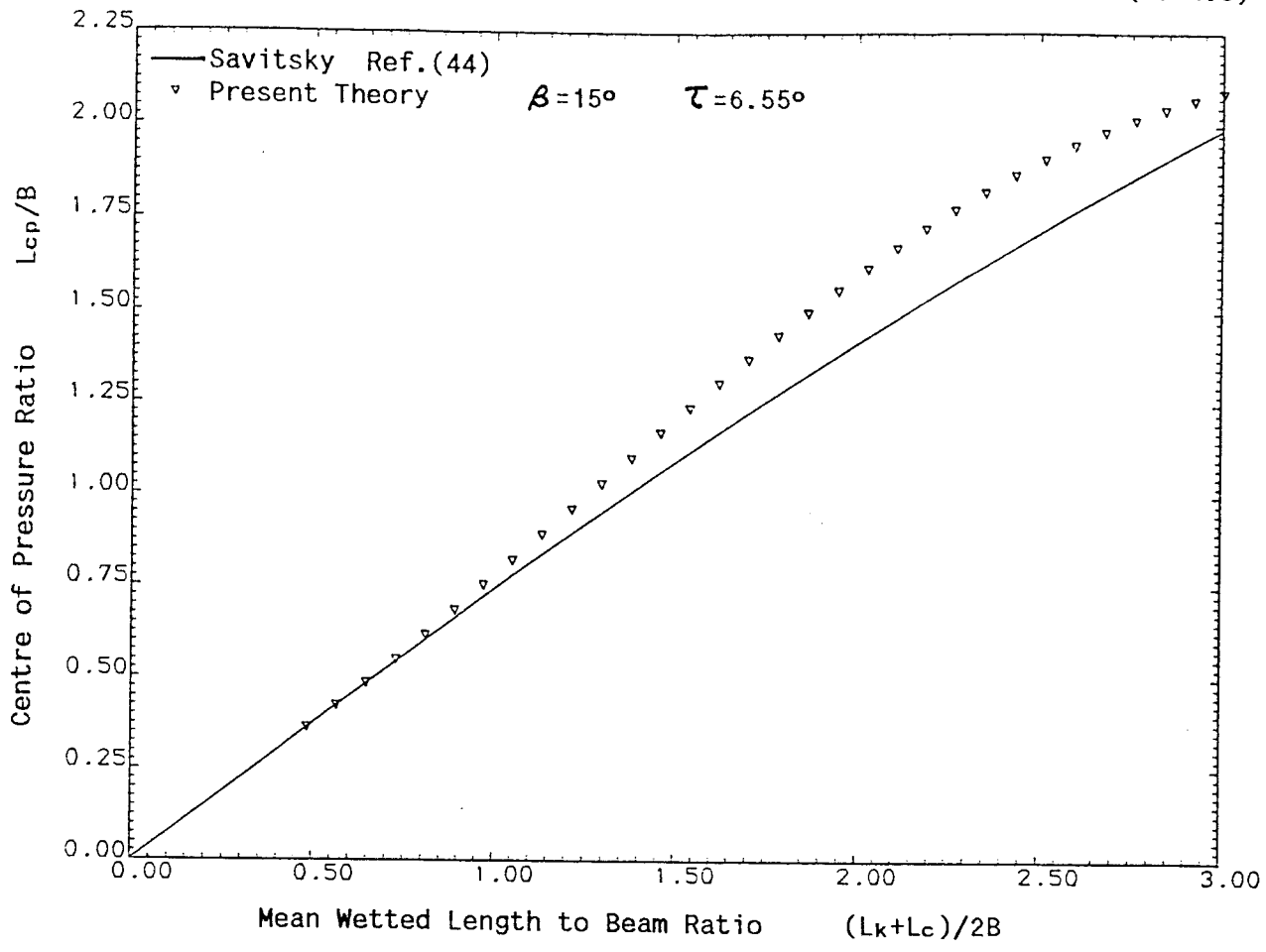

Fig.(5.8f) Centre of Pressure Ratios for Constant Deadrise Hull (C_V=5.0)

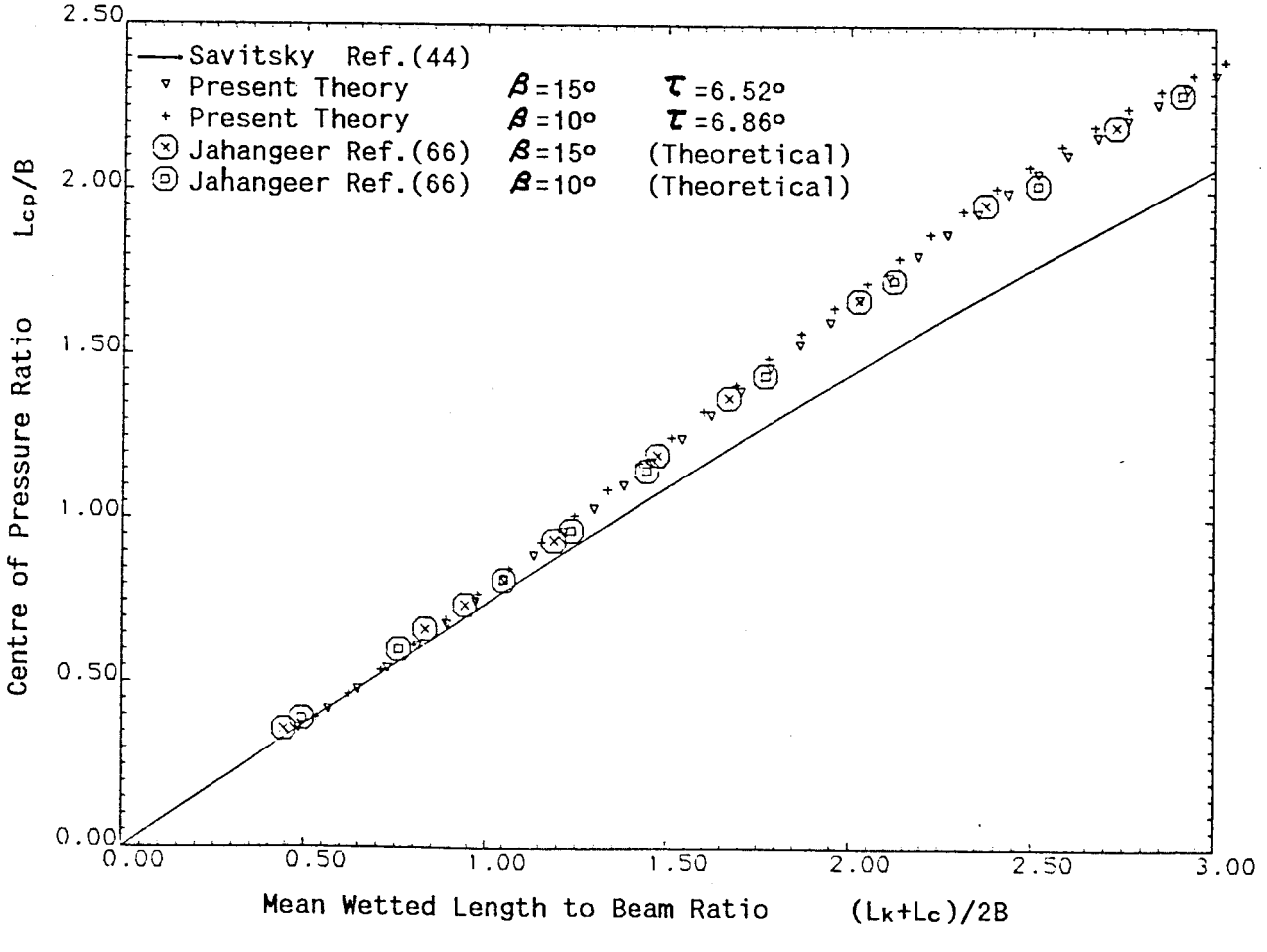

Fig.(5.8g) Centre of Pressure Ratios for Constant Deadrise Hull

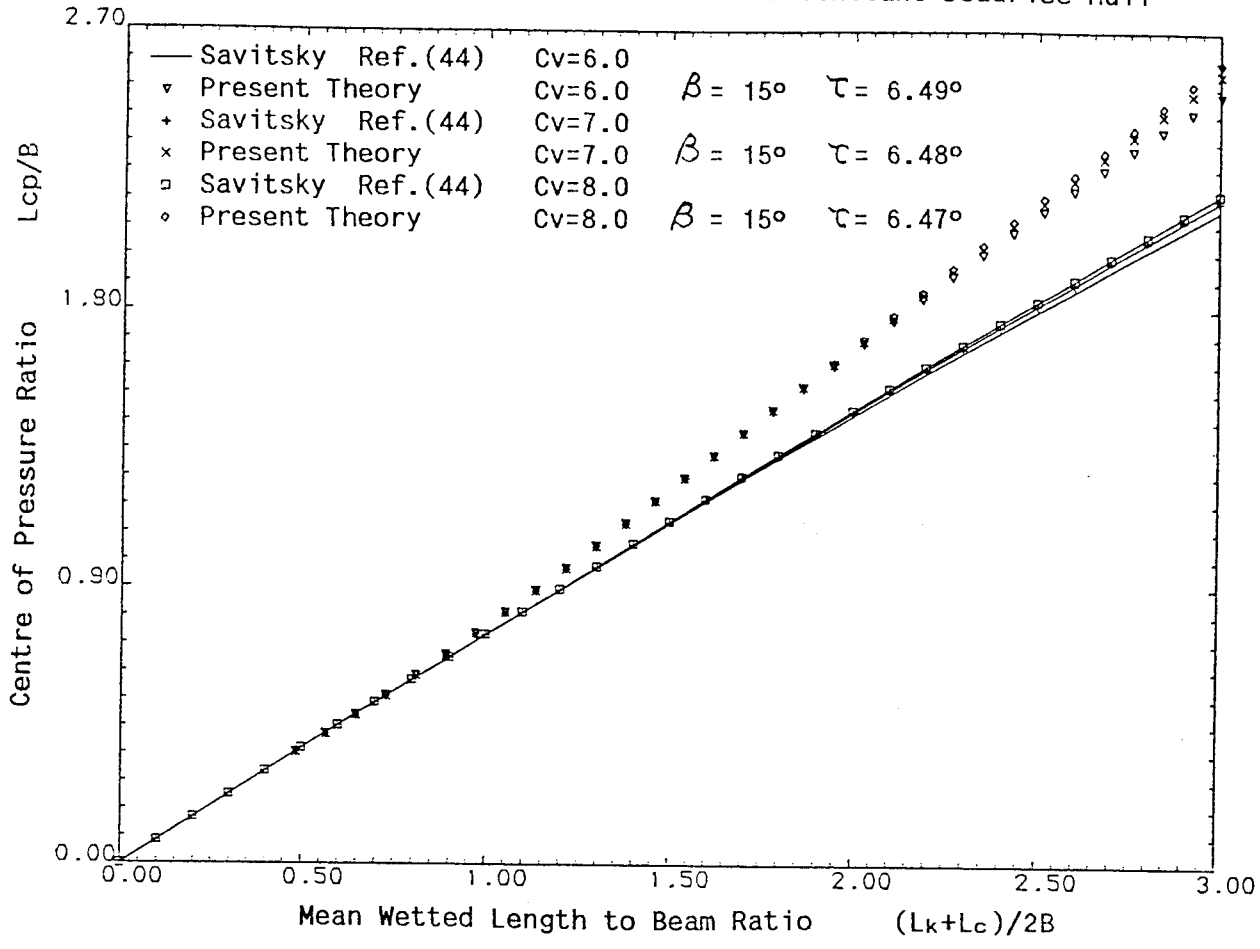

Fig.(5.8h) Centre of Pressure Ratios for Constant Deadrise Hull

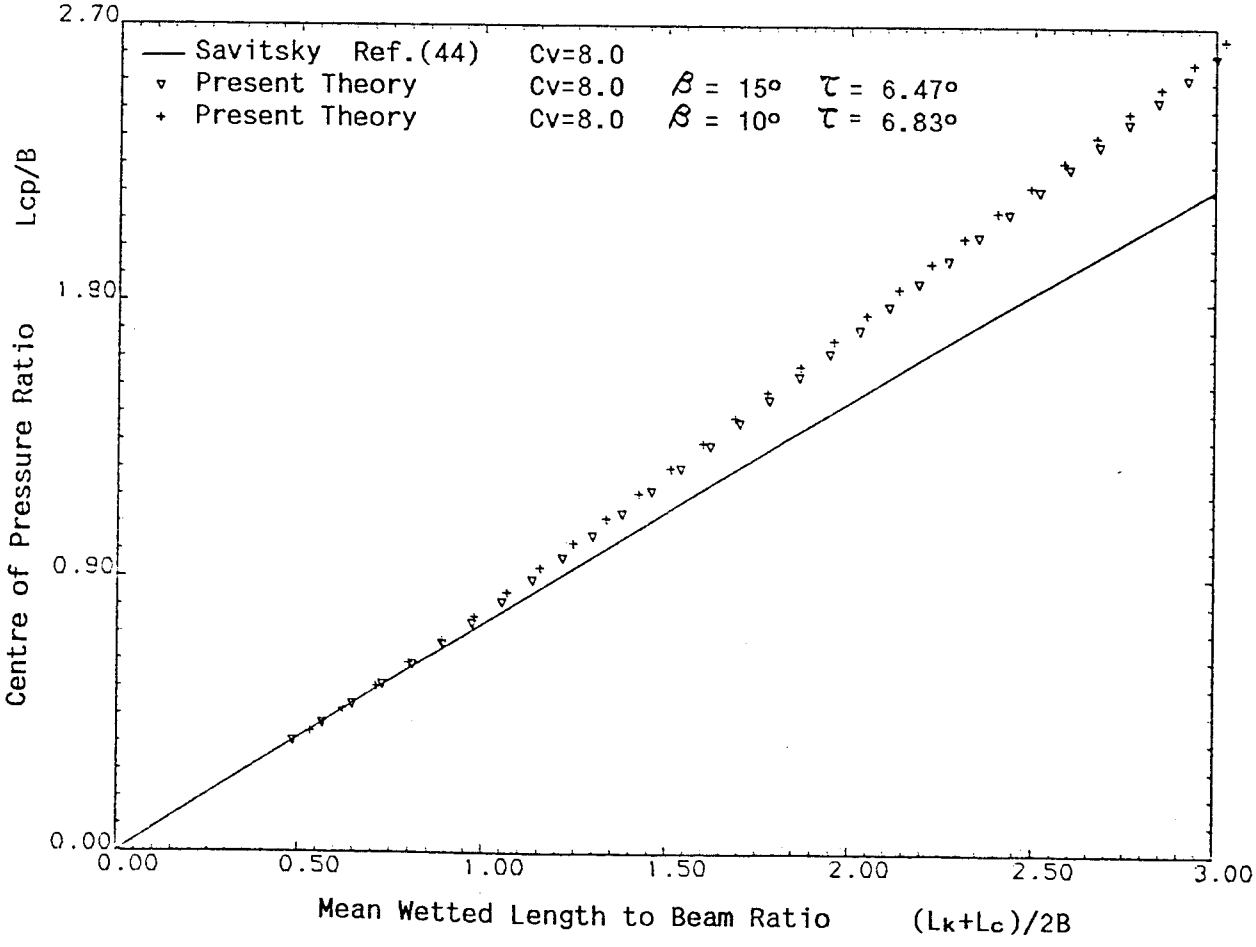

Fig.(5.9a) Pressure Distributions for 15° Constant Deadrise Hull (Cv=1.512)

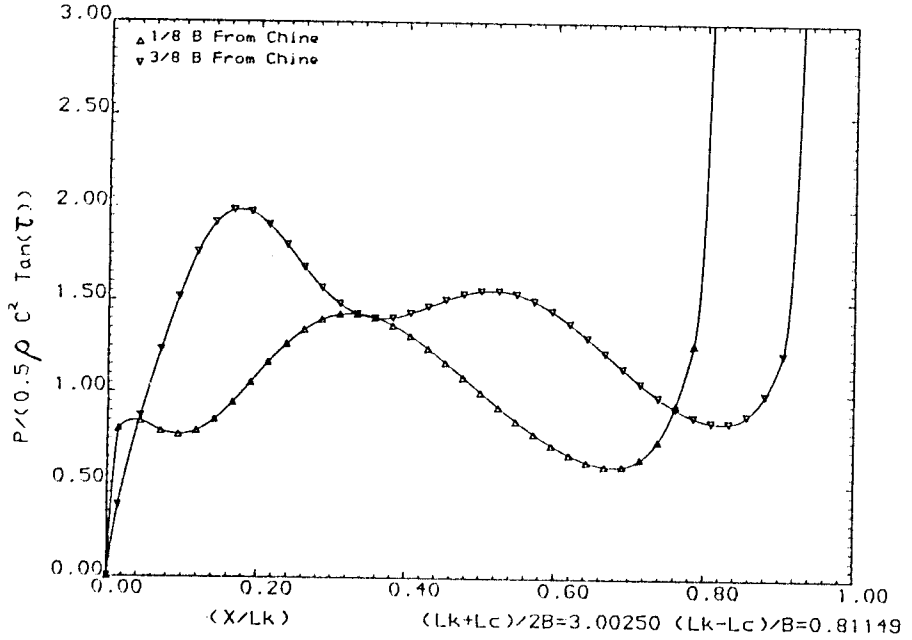

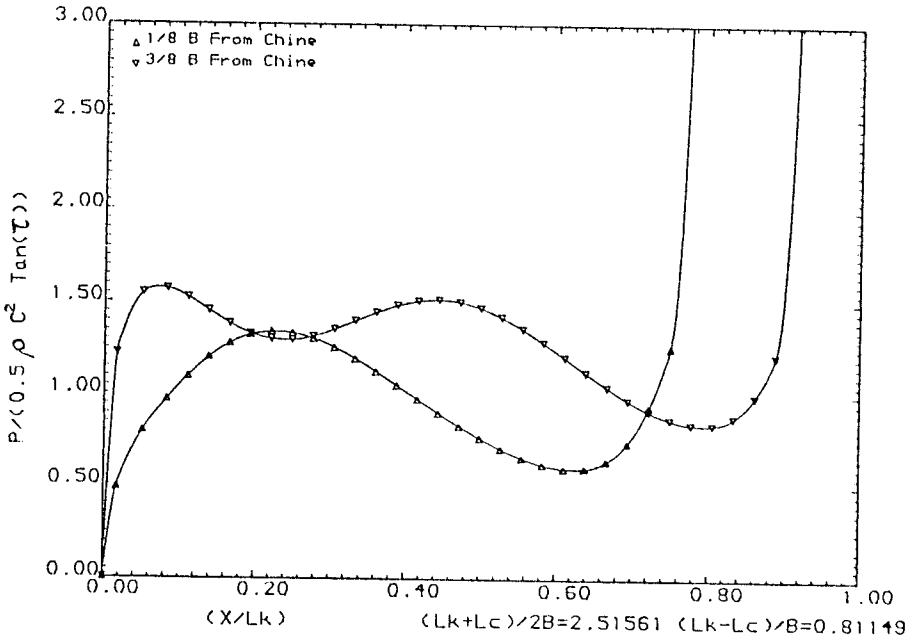

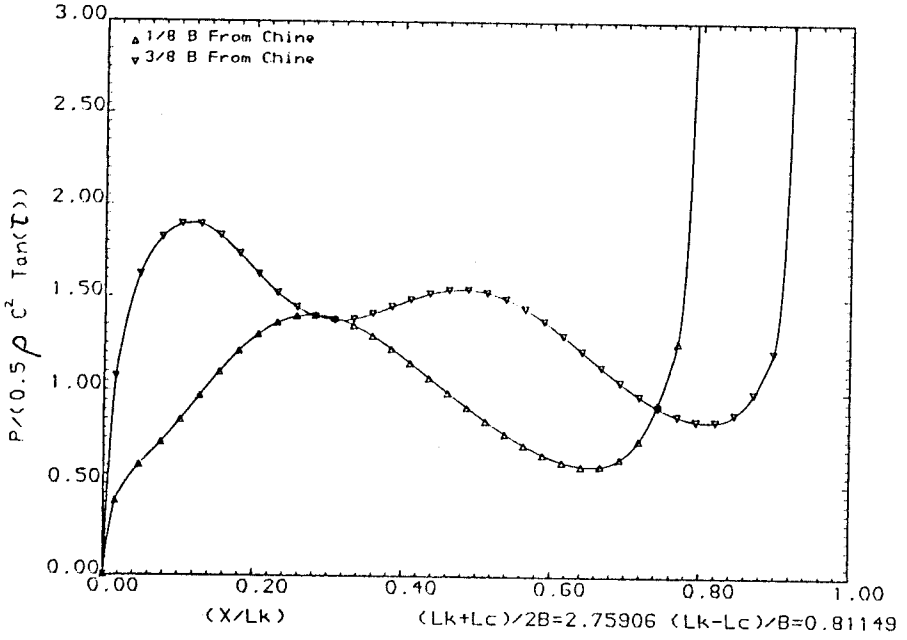

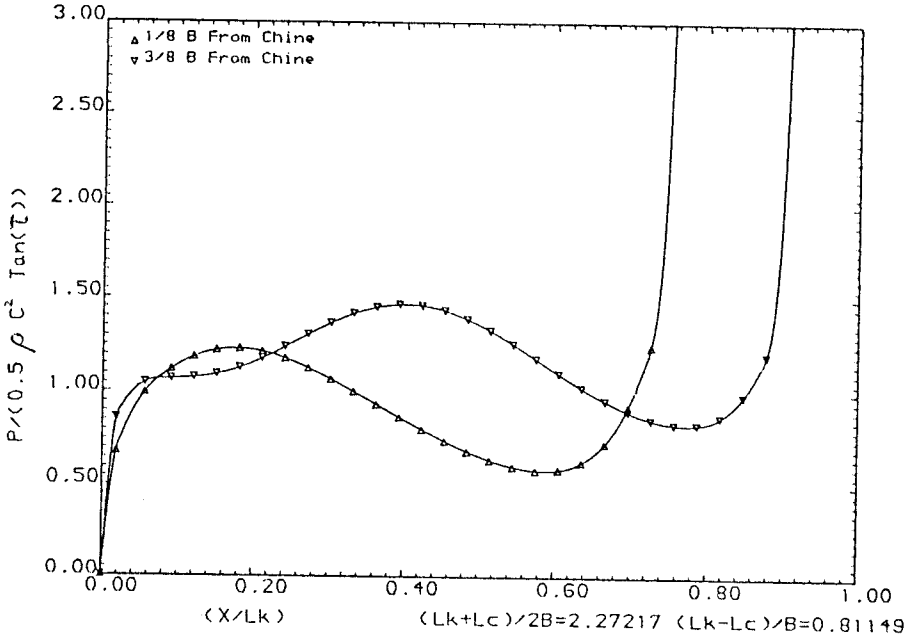

Fig.(5.9a) Pressure Distributions for 15° Constant Deadrise Hull (Cv=1.512)

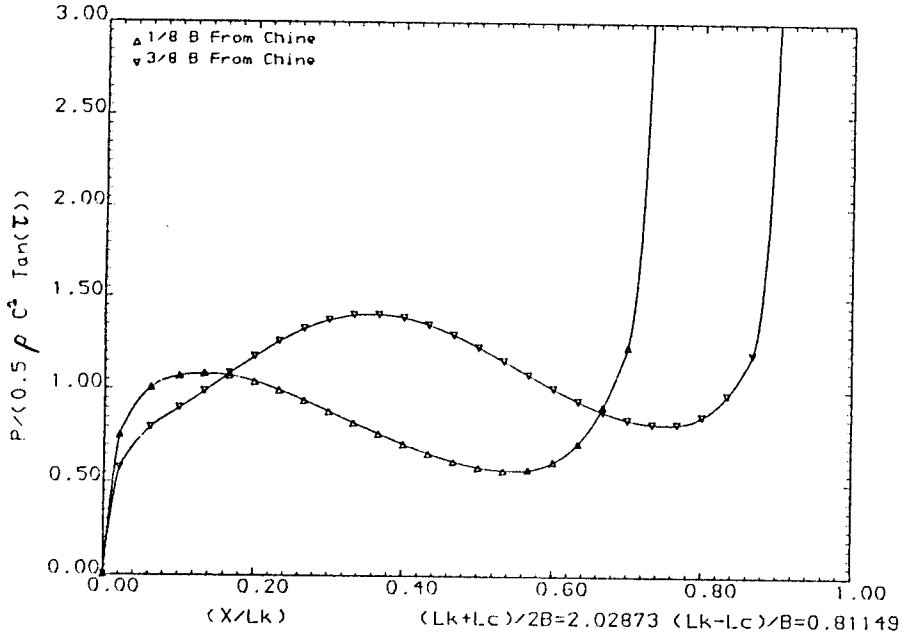

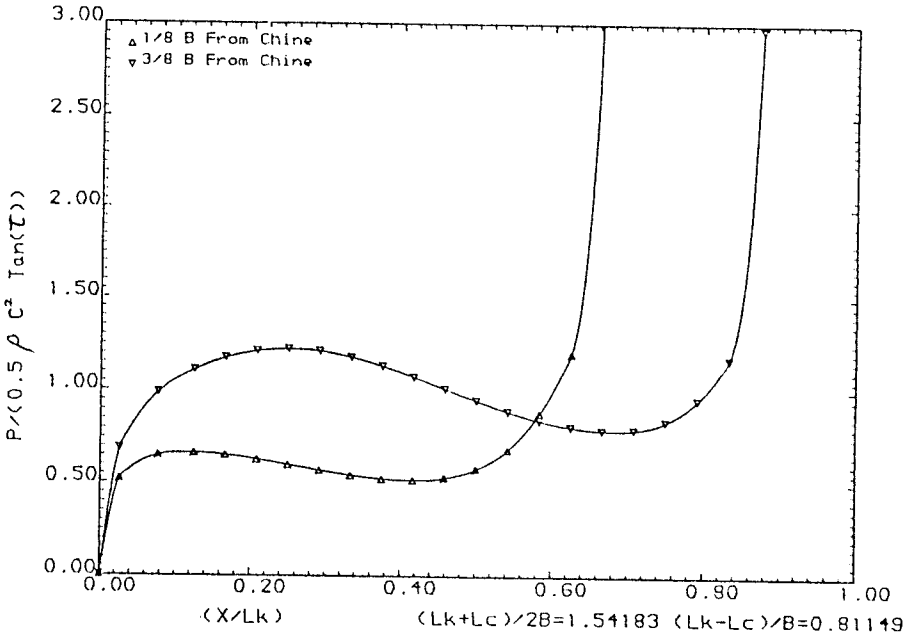

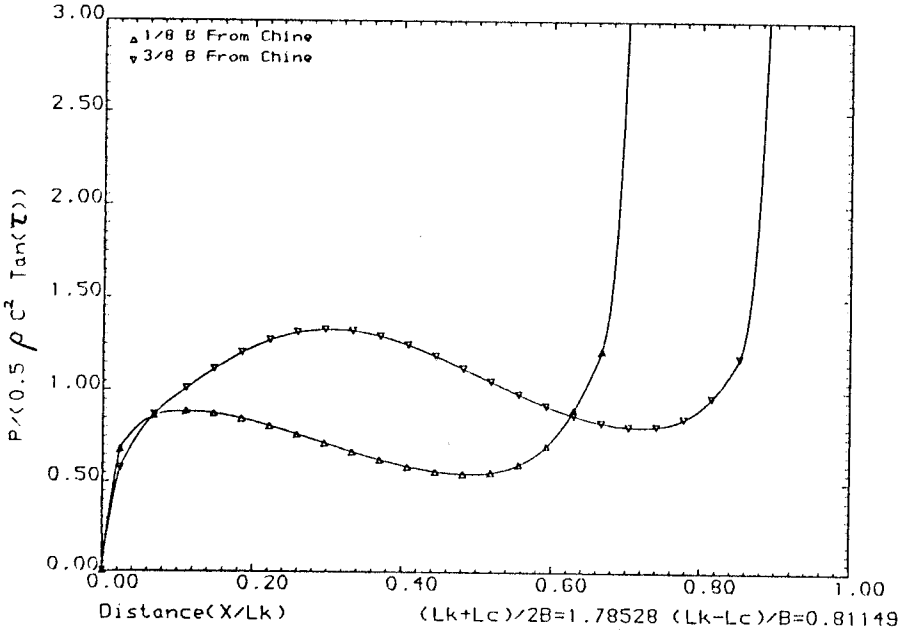

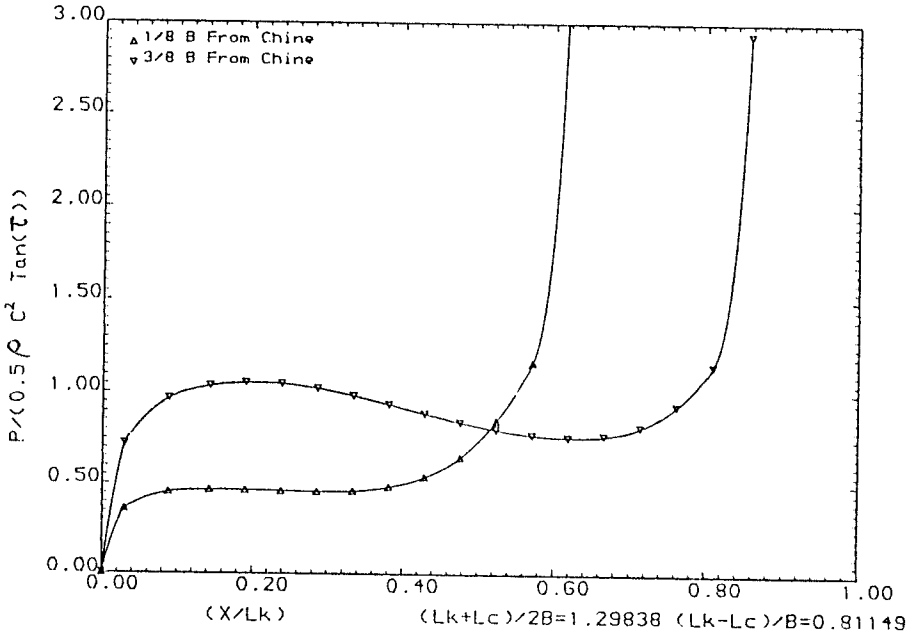

Fig.(5.9b) Pressure Distributions for 15° Constant Deadrise Hull (Cv=2.5)

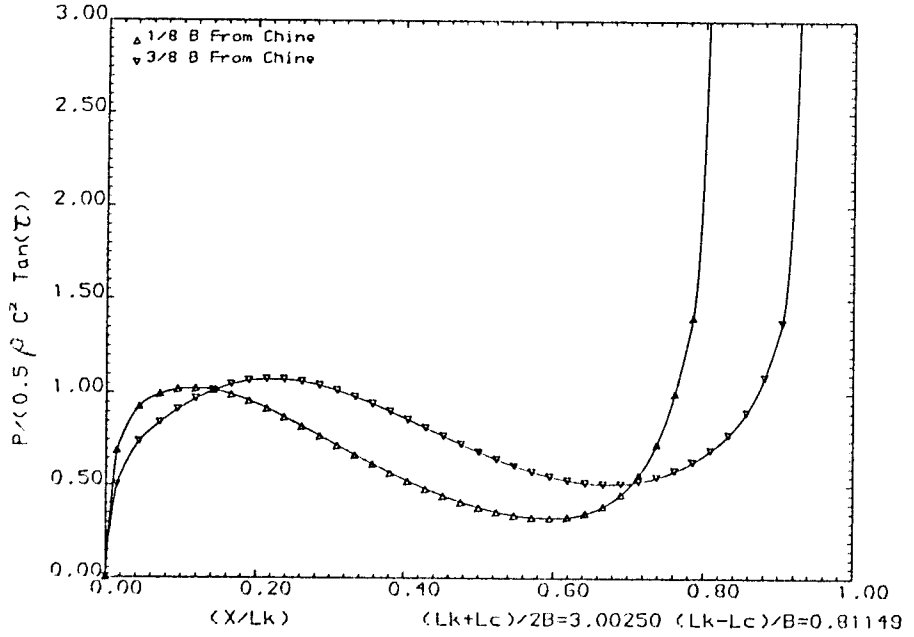

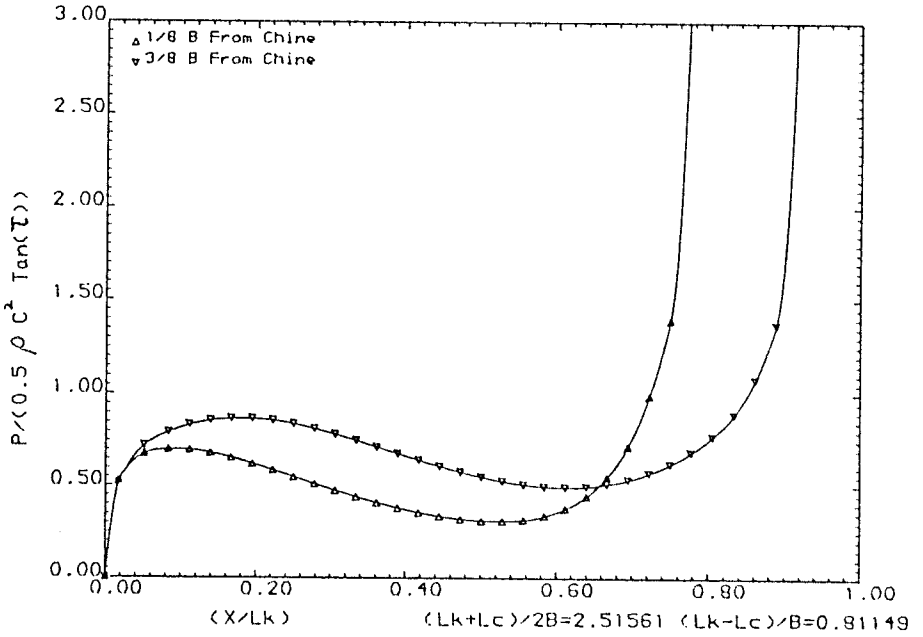

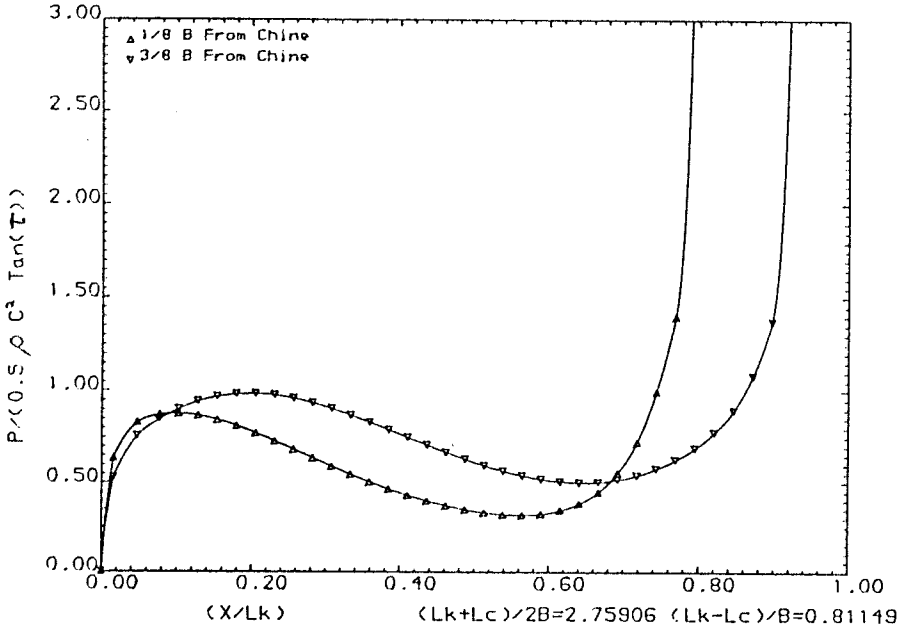

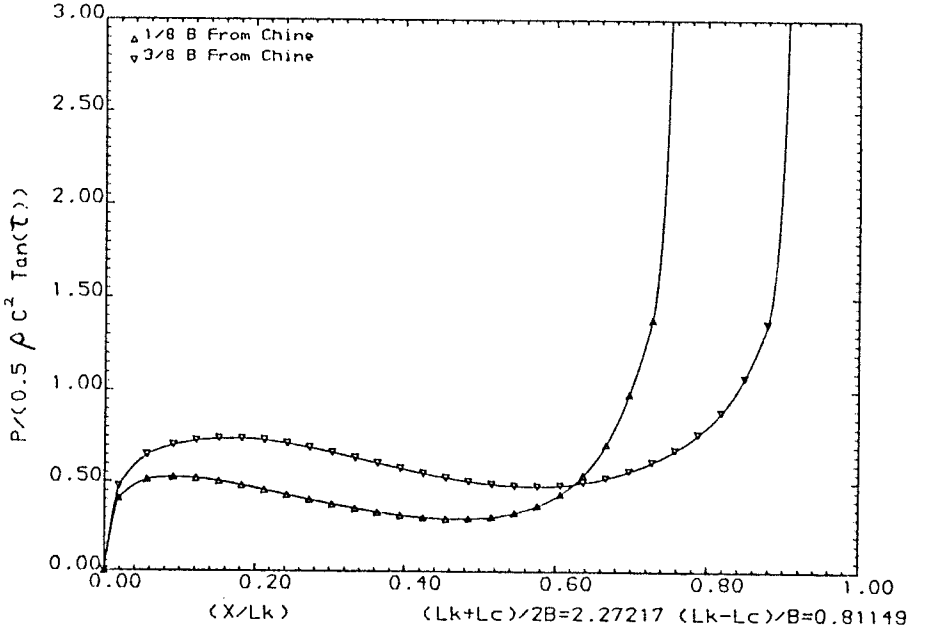

Fig.(5.9b) Pressure Distributions for 15° Constant Deadrise Hull (Cv=2.5)

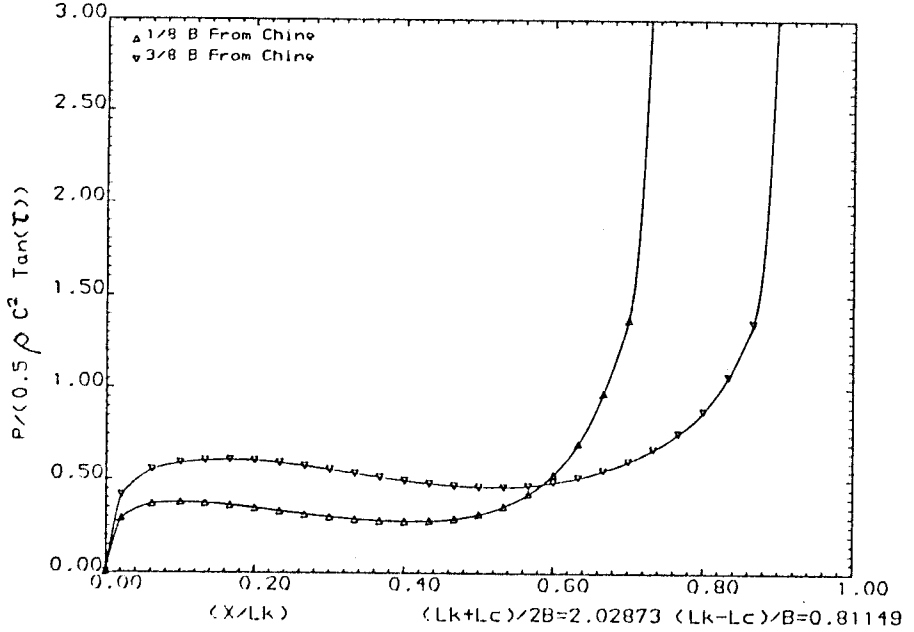

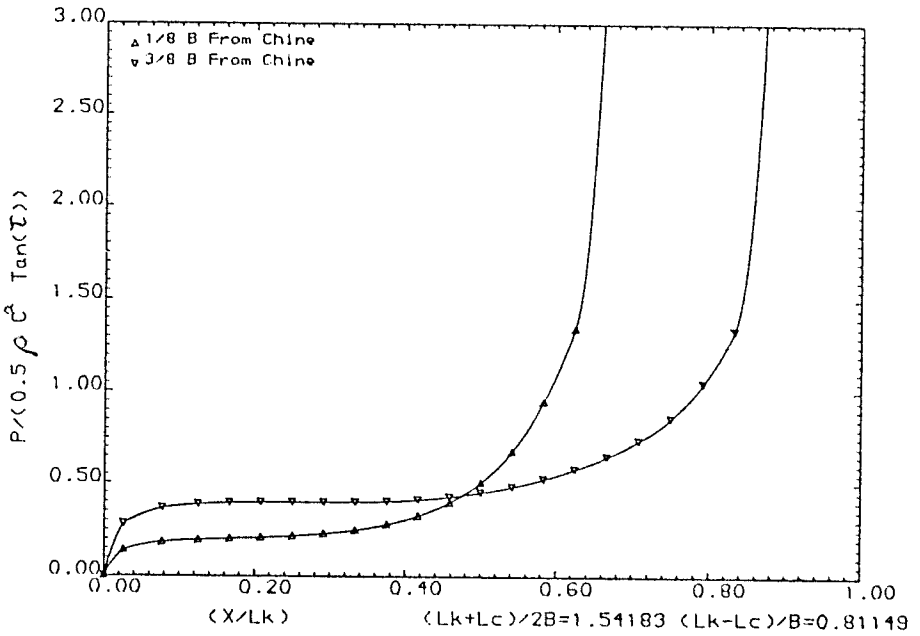

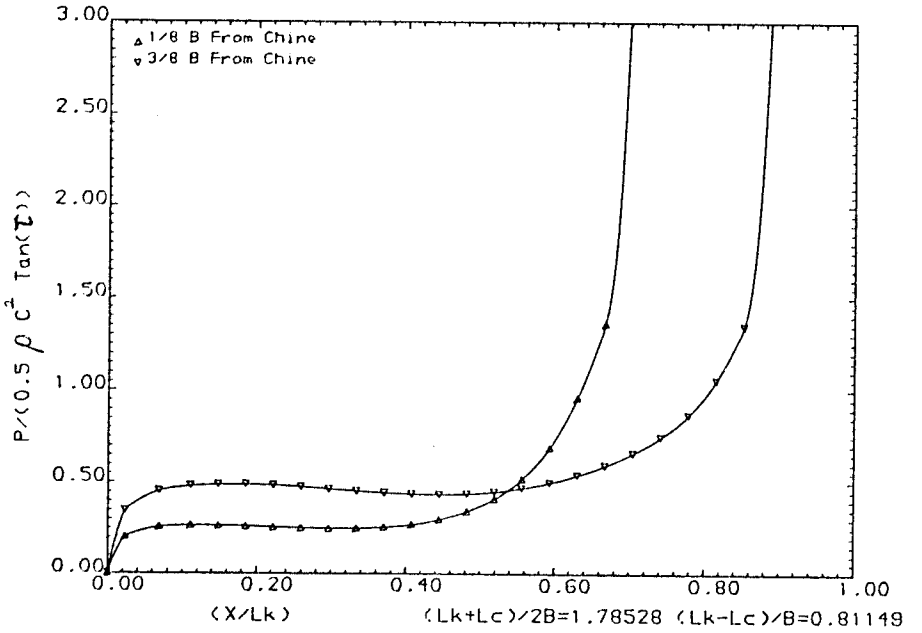

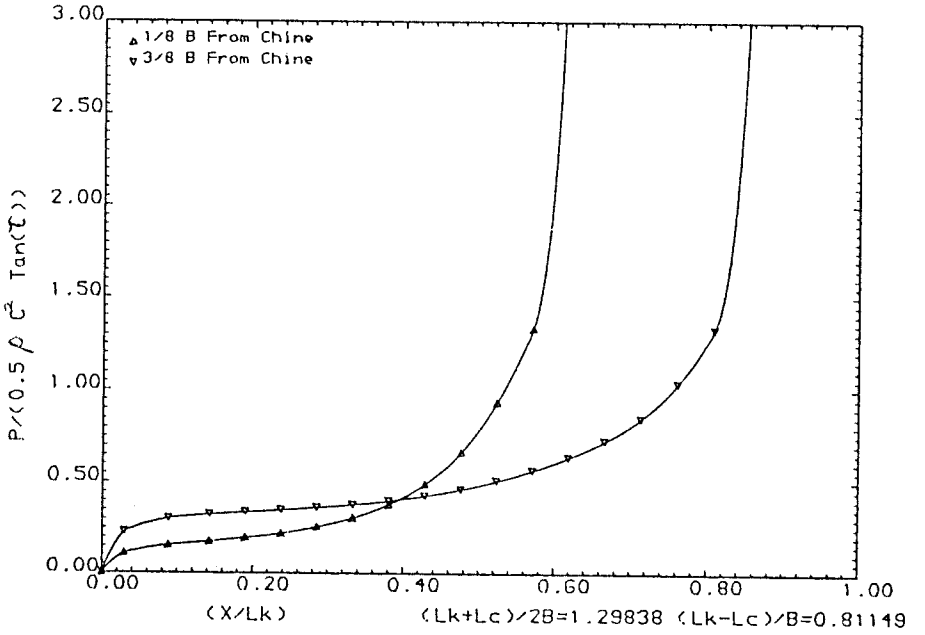

Fig.(5.9c) Pressure Distributions for 15° Constant Deadrise Hull (Cv=6.0)

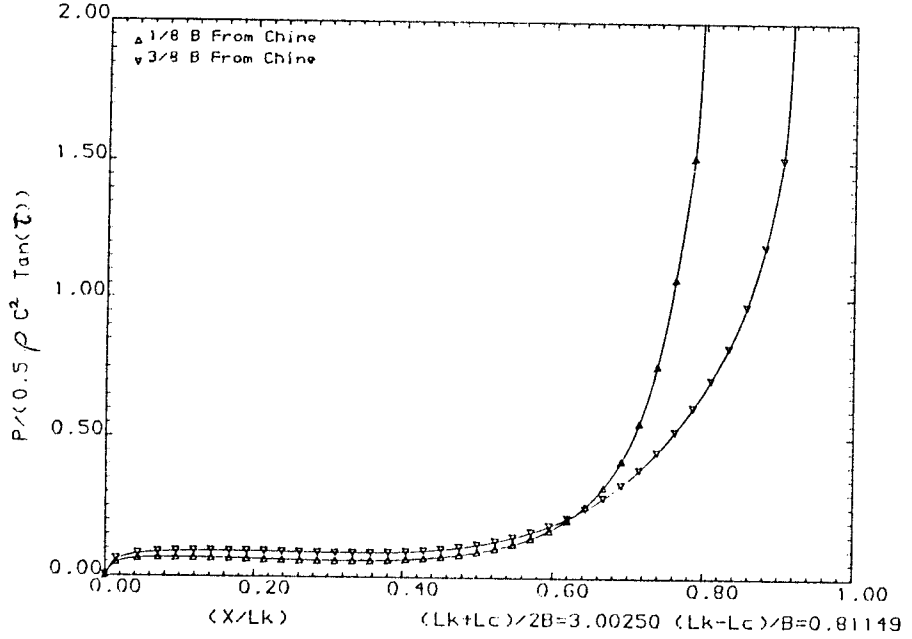

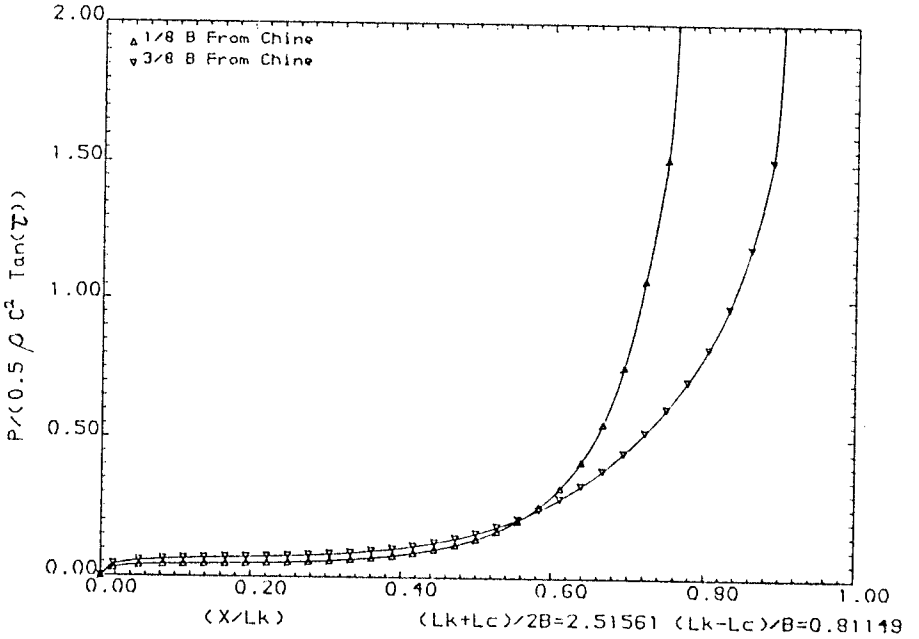

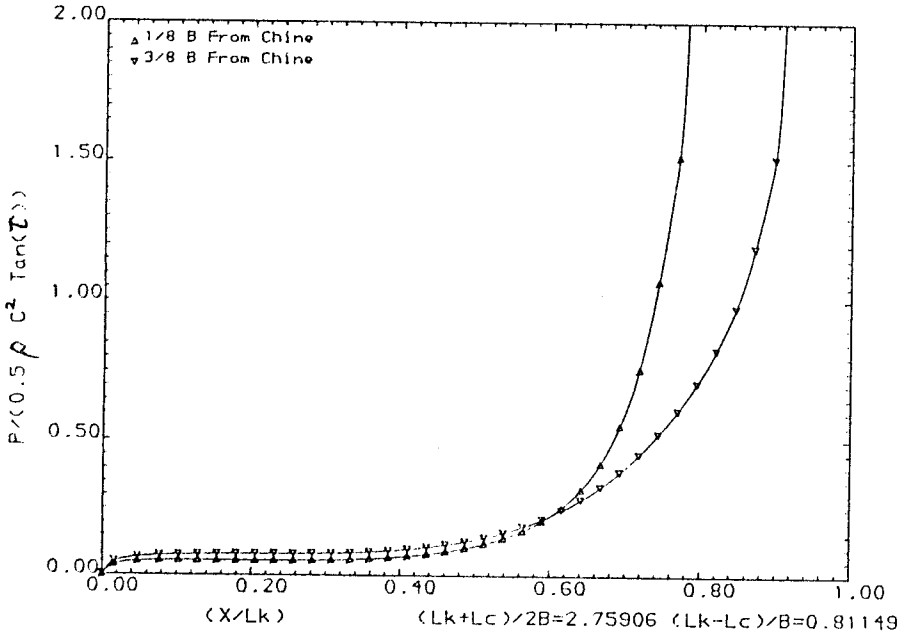

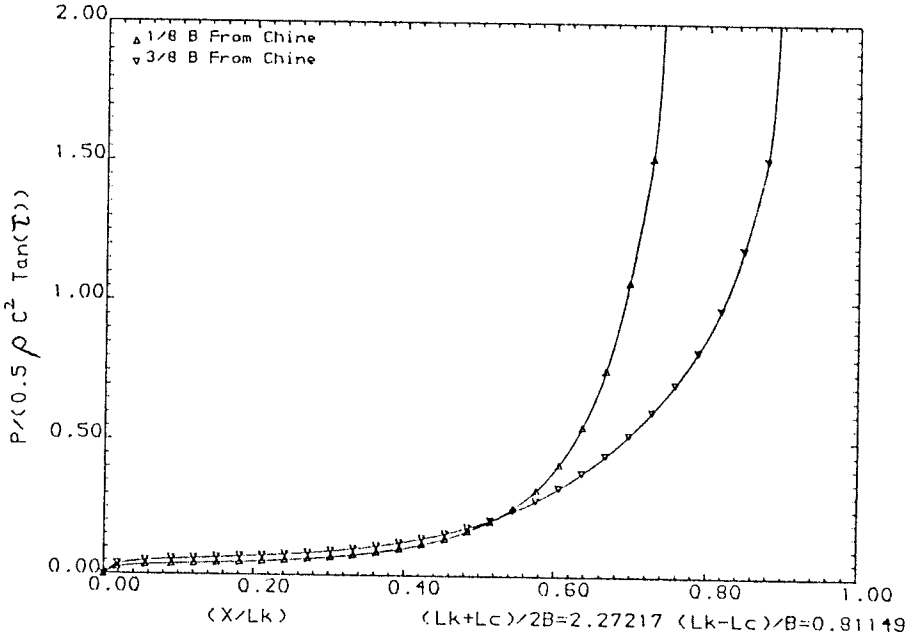

Fig.(5.9c) Pressure Distributions for 15° Constant Deadrise Hull (Cv=6.0)

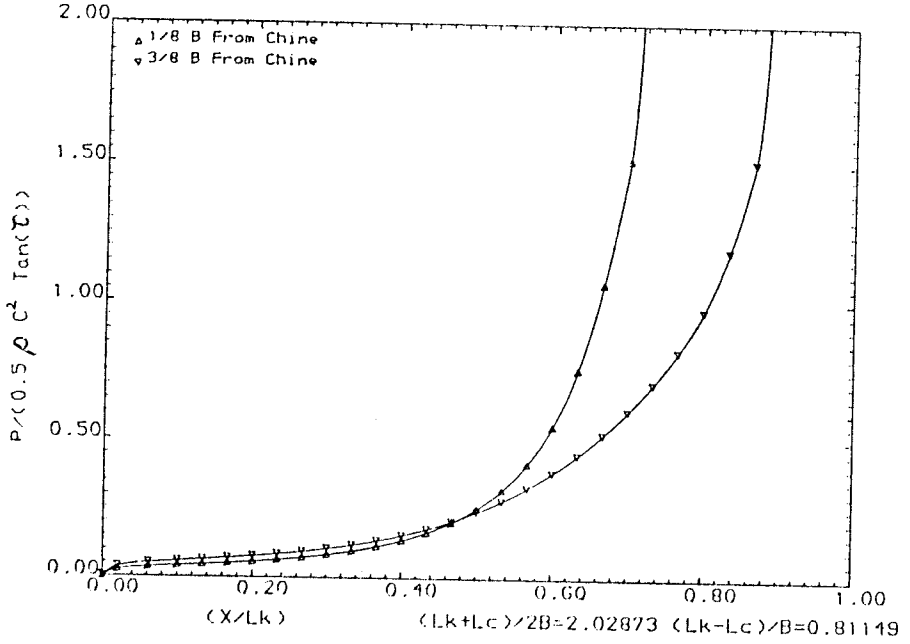

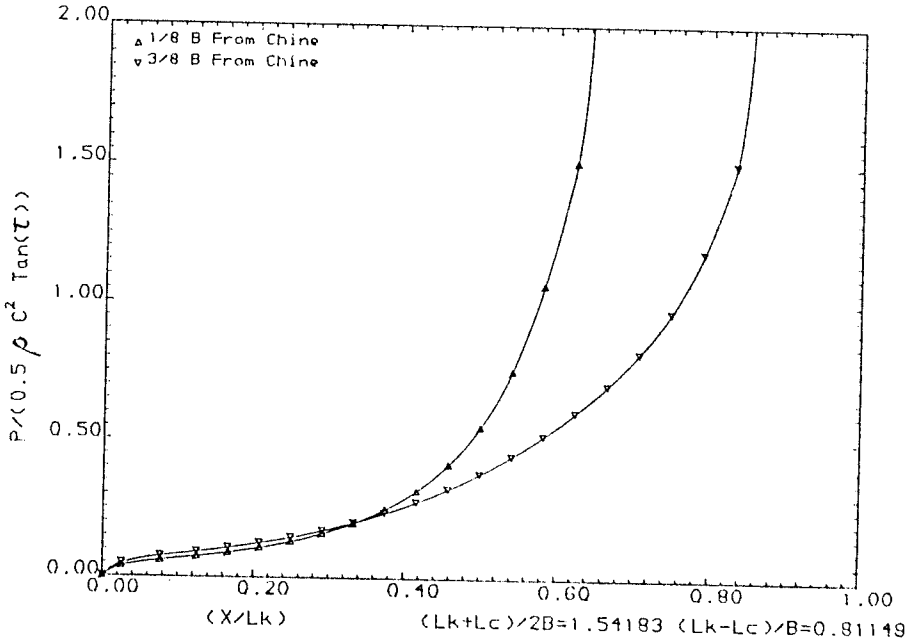

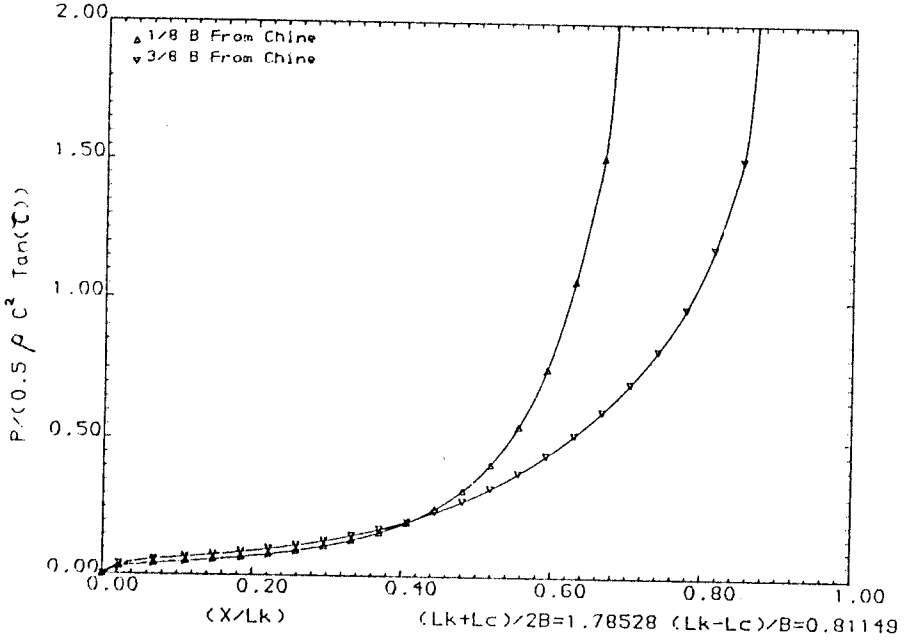

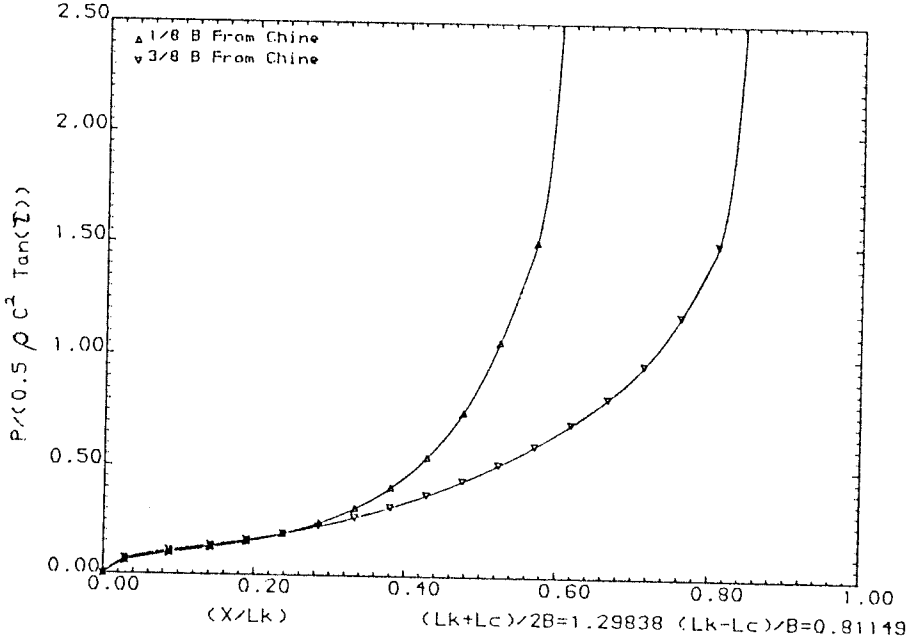

Fig.(5.9d) Pressure Distributions for 15° Constant Deadrise Hull (Cv=8.0)

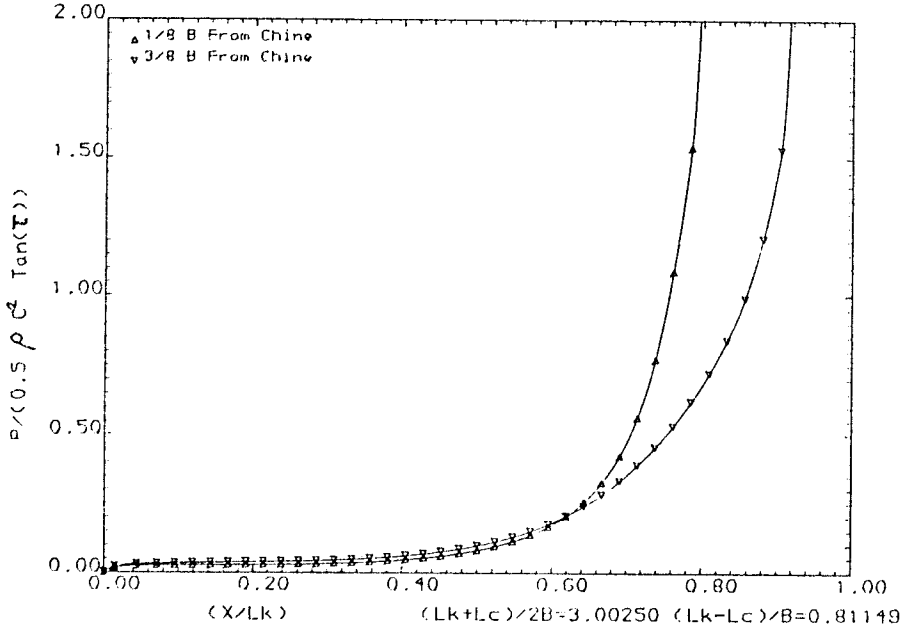

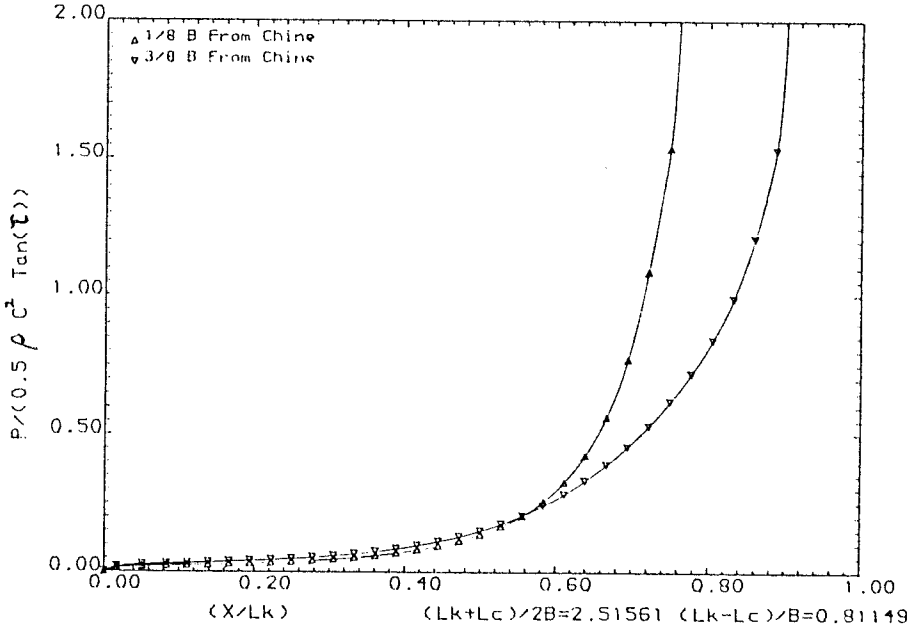

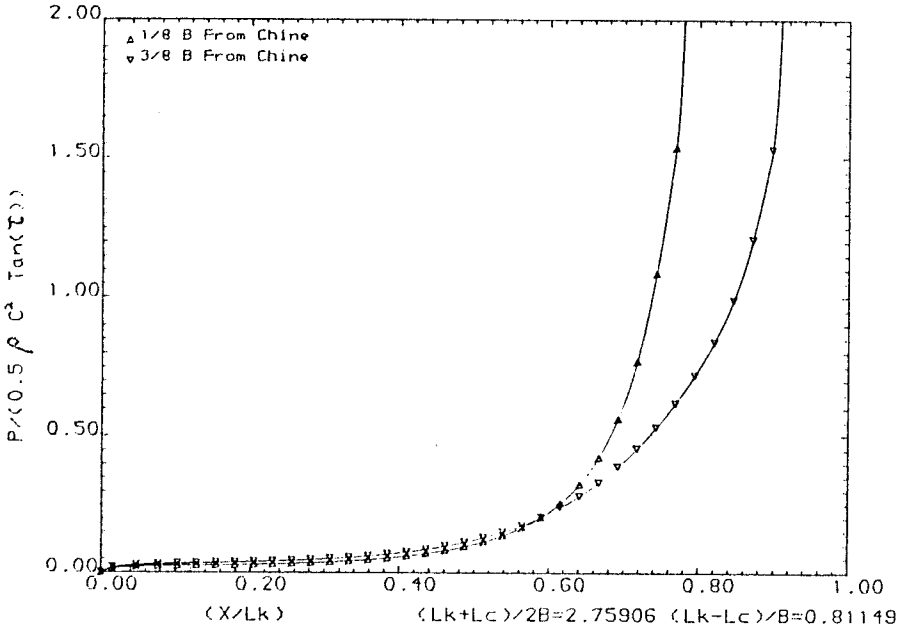

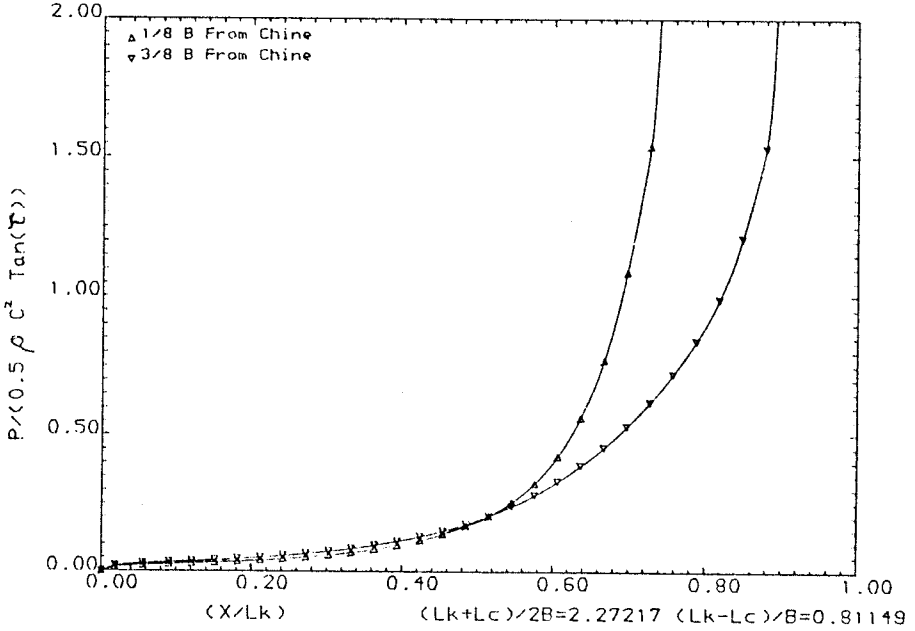

Fig.(5.9d) Pressure Distributions for 15° Constant Deadrise Hull (Cv=8.0)

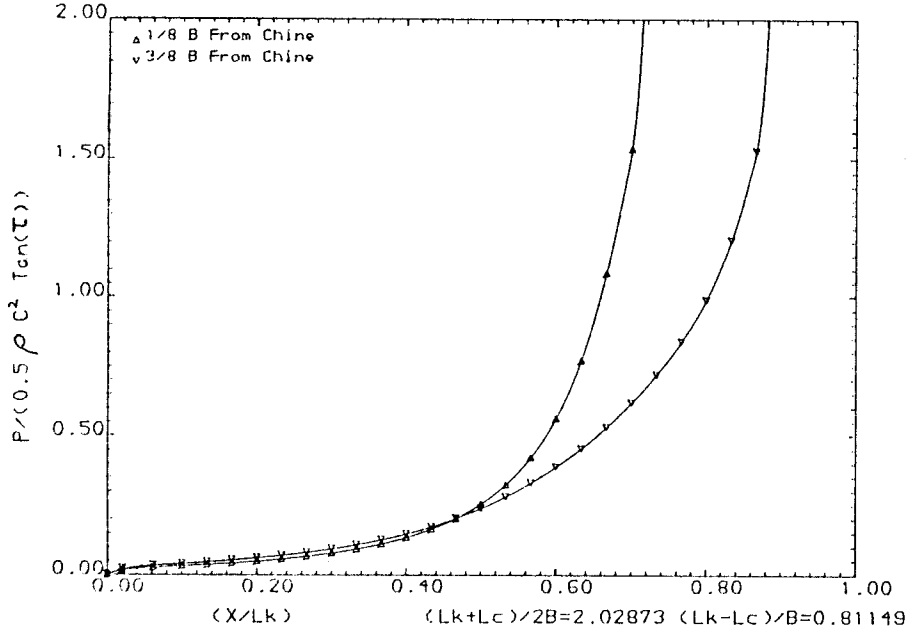

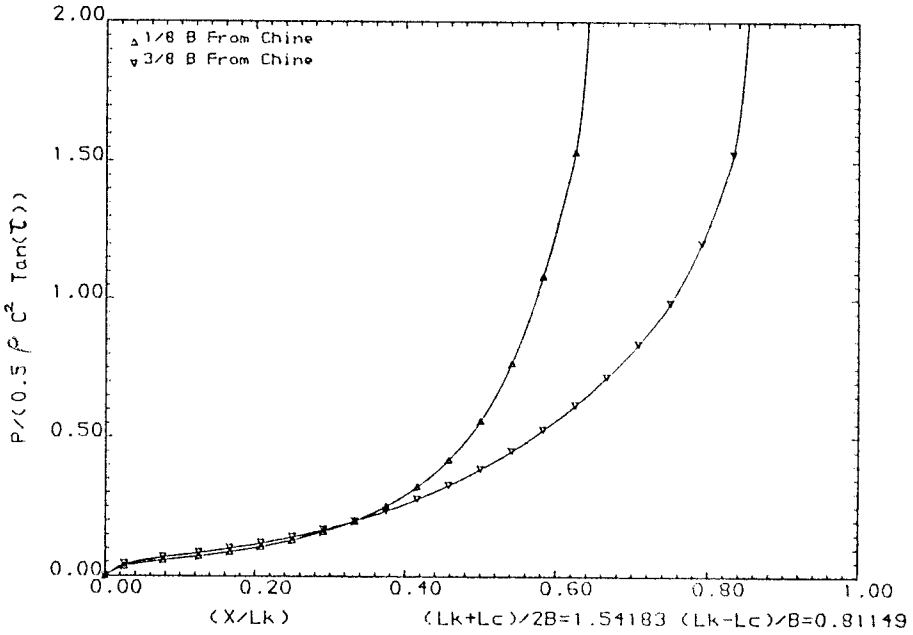

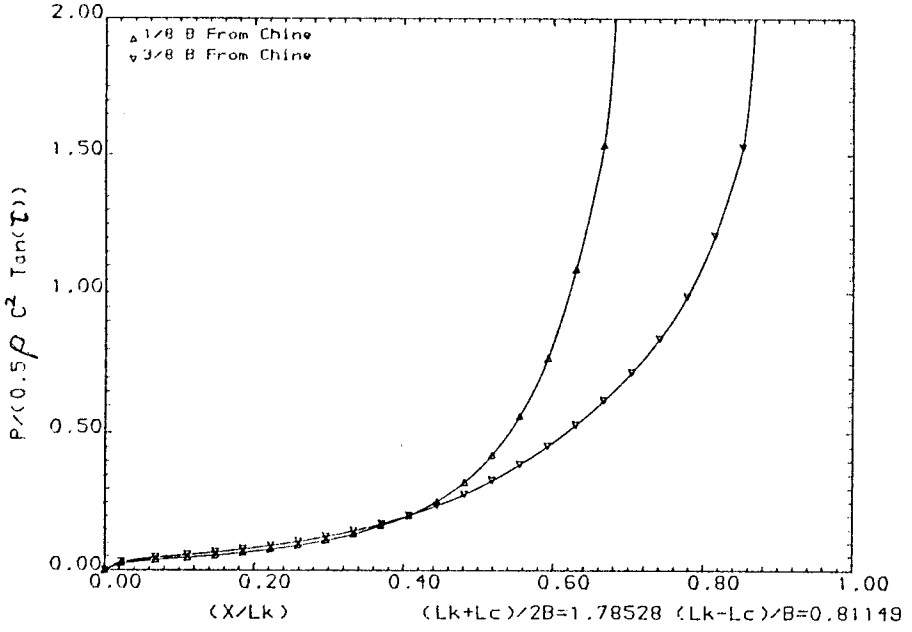

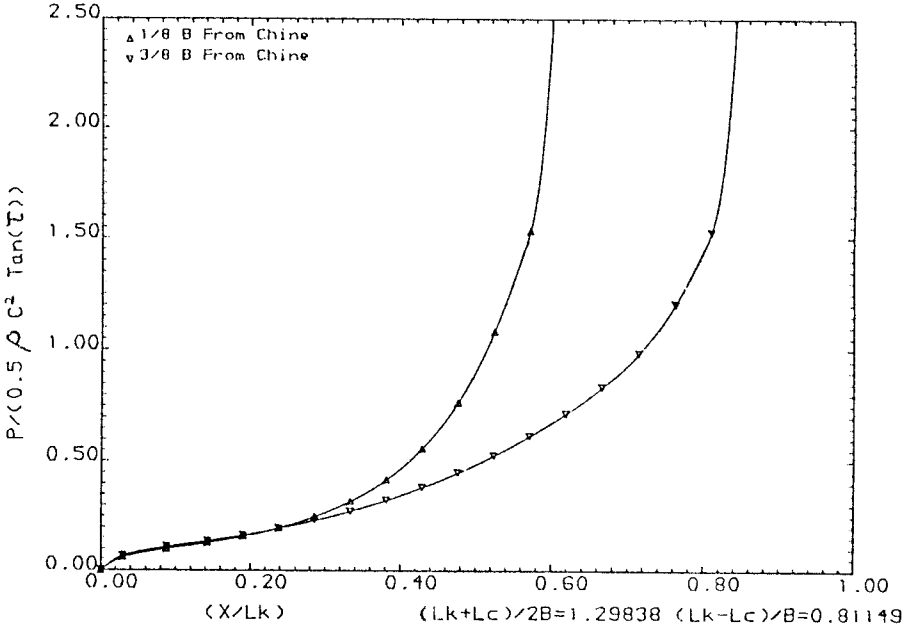

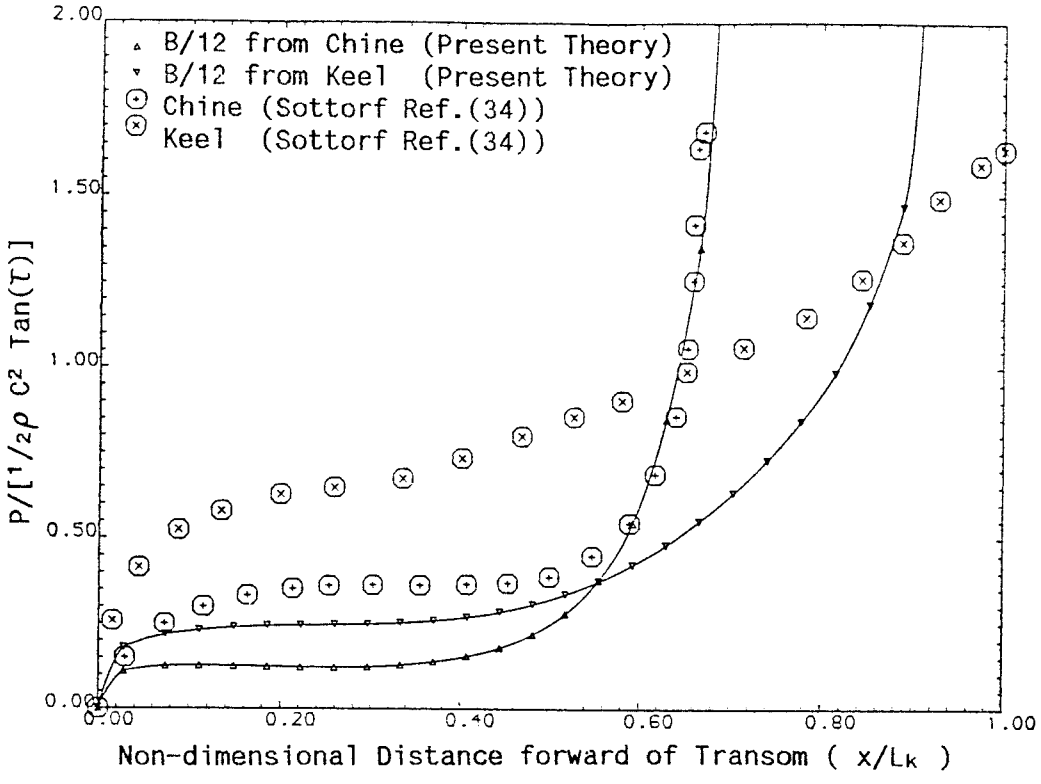

(Cv=3.5 (Lk+Lc)/2B=1.754 (Lk-Lc)/B=0.7017)

Fig.(5.10) Comparison of Pressure Distribution with Experimental Measurements of Sottorf for a 15° Constant Deadrise Surface

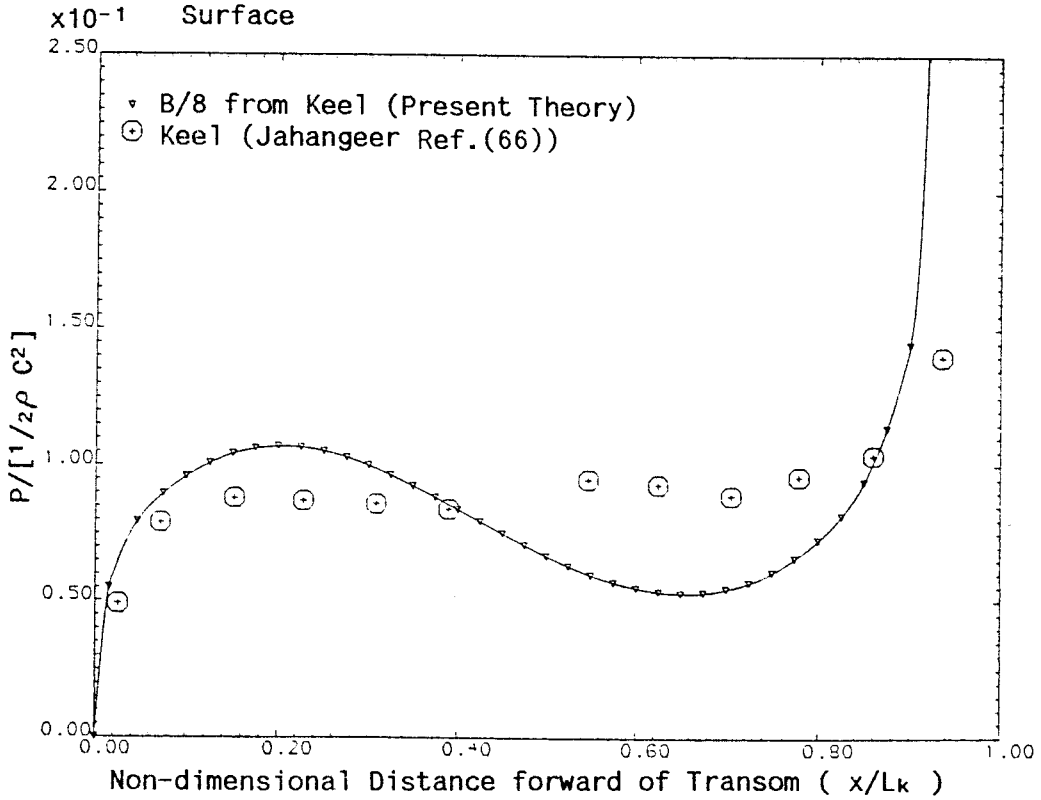

(Cv=2.54 (Lk+Lc)/2B=2.87 (Lk-Lc)/B=0.8115 τ=6°)

Fig.(5.11) Comparison of Keel Pressure Distribution with Experimental Measurements of Jahangeer for a 15° Constant Deadrise Surface

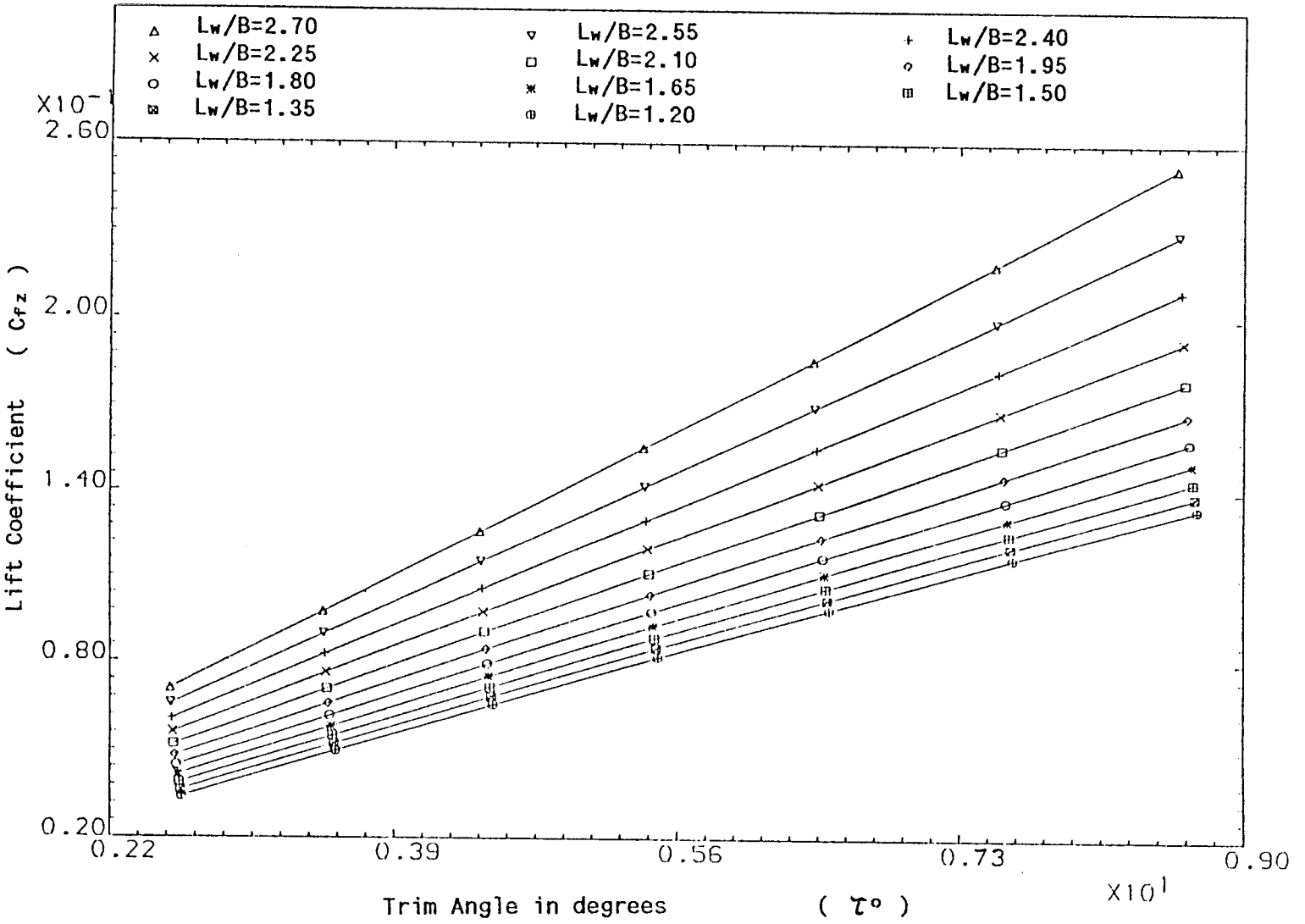

Fig.(5.12a) Computed Lift Coefficient as a function of Trim angle and Mean Lw/B Ratio for 10° Constant Deadrise Surface (Cv=3.0)

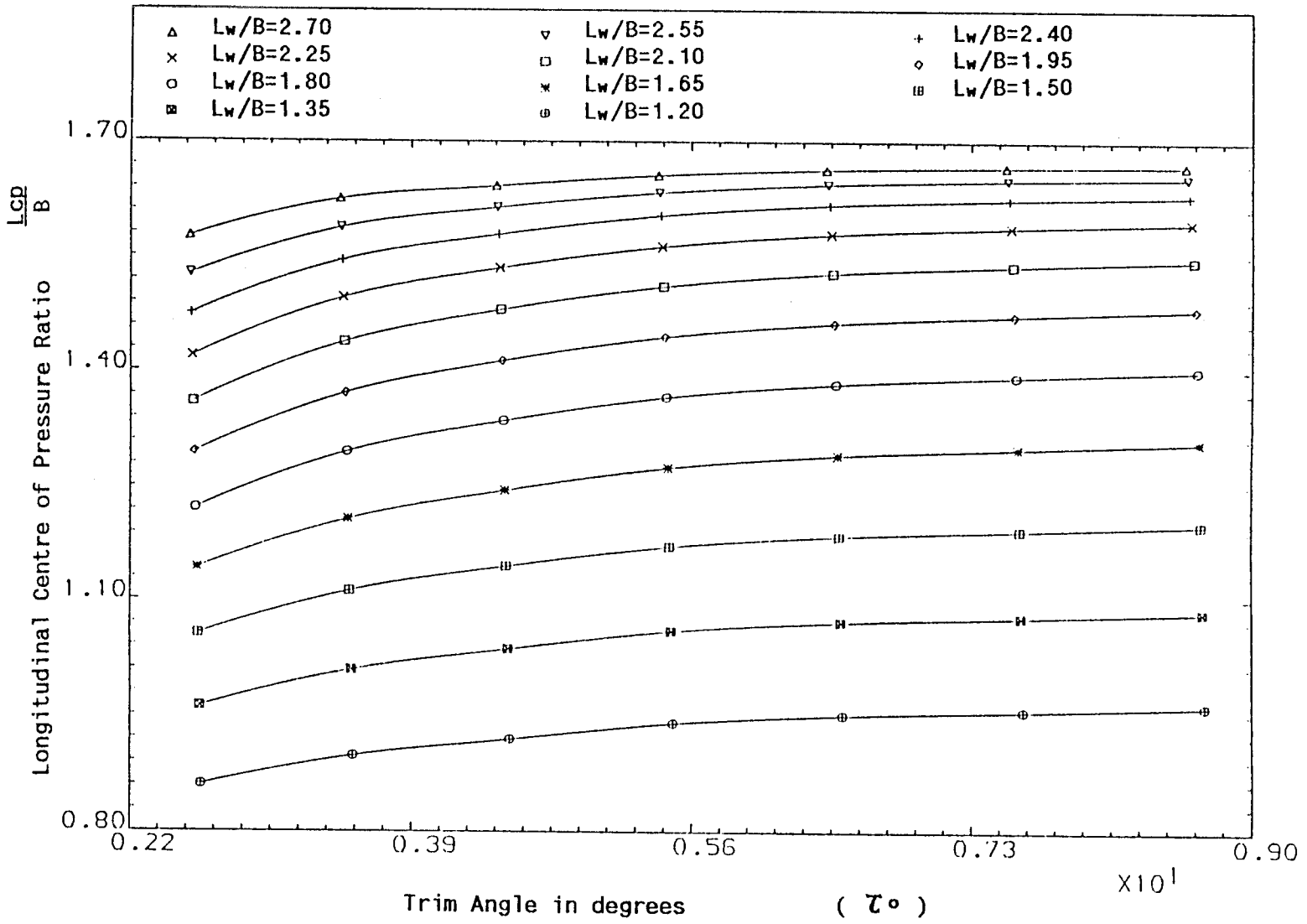

(L_{cp} = Centre of Pressure Location forward of the Transom)

Fig.(5.12b) Computed Centre of Pressure Ratio as a function of Trim Angle and Mean Lw/B Ratio for 10° Constant Deadrise Surface (C_v=3.0)

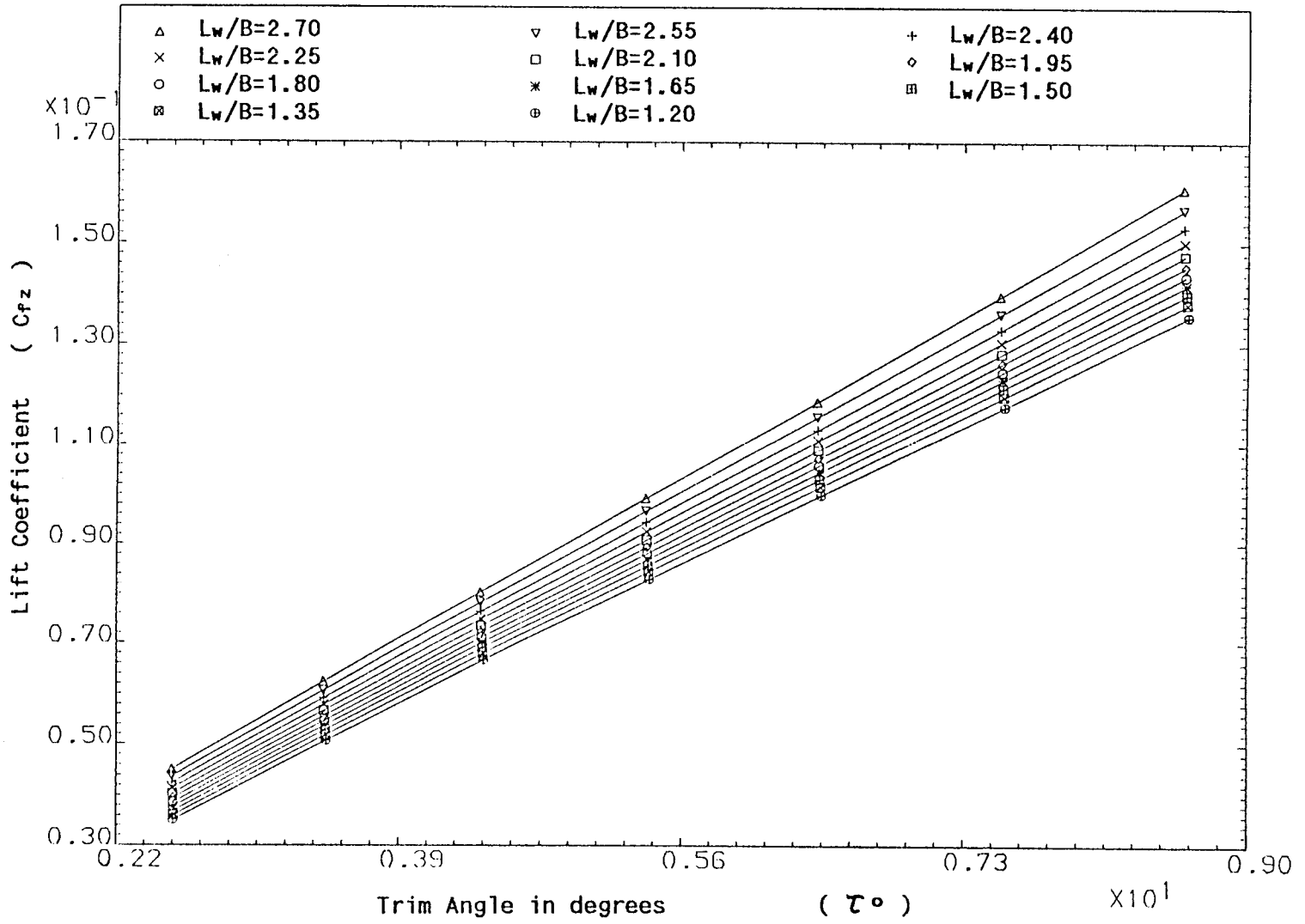

Fig.(5.13a) Computed Lift Coefficient as a function of Trim angle and Mean Lw/B Ratio for 10° Constant Deadrise Surface (C_V=5.0)

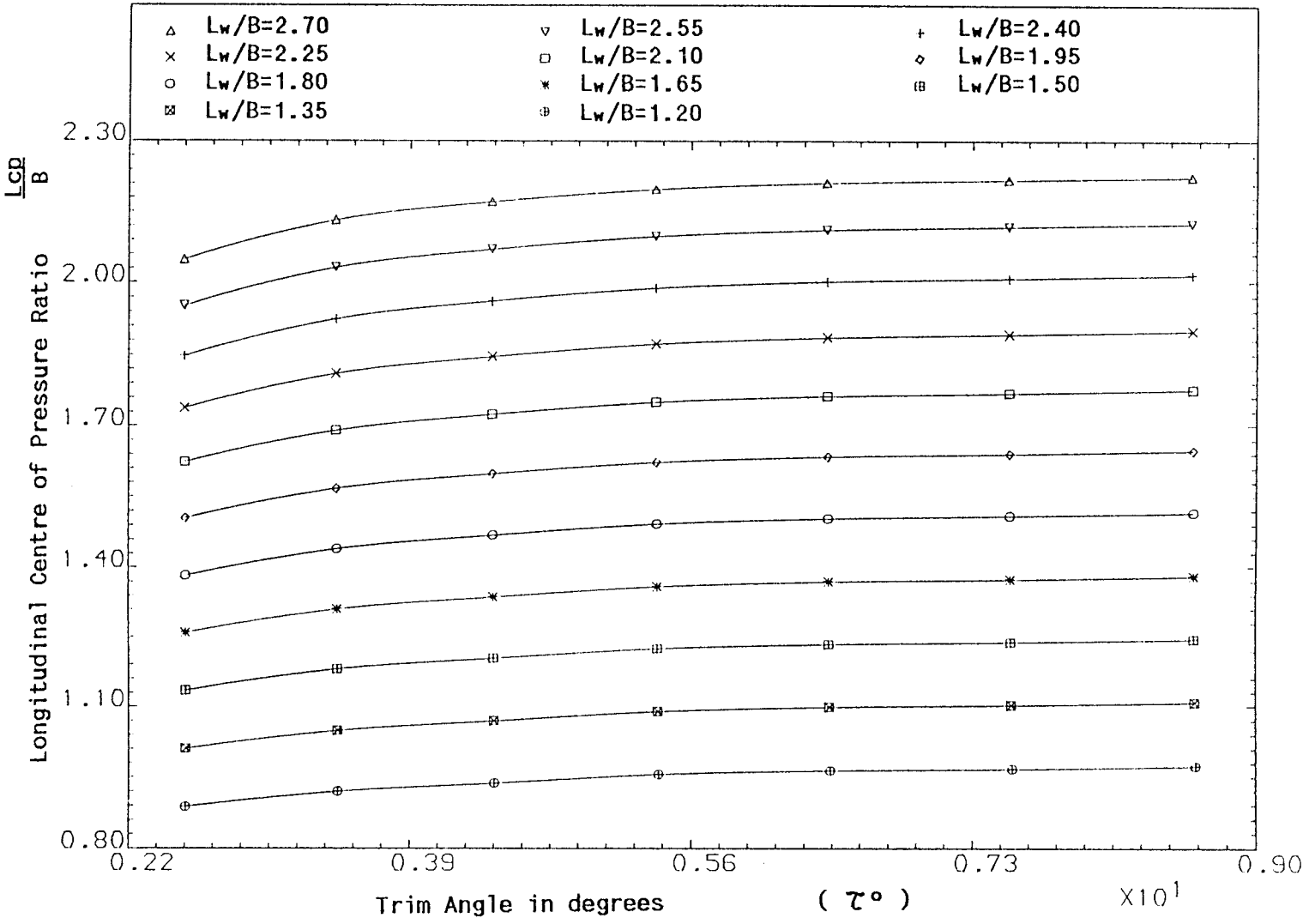

(L_{cp} = Centre of Pressure Location forward of the Transom)

Fig.(5.13b) Computed Centre of Pressure Ratio as a function of Trim Angle and Mean L_w/B Ratio for 10° Constant Deadrise Surface (C_v=5.0)

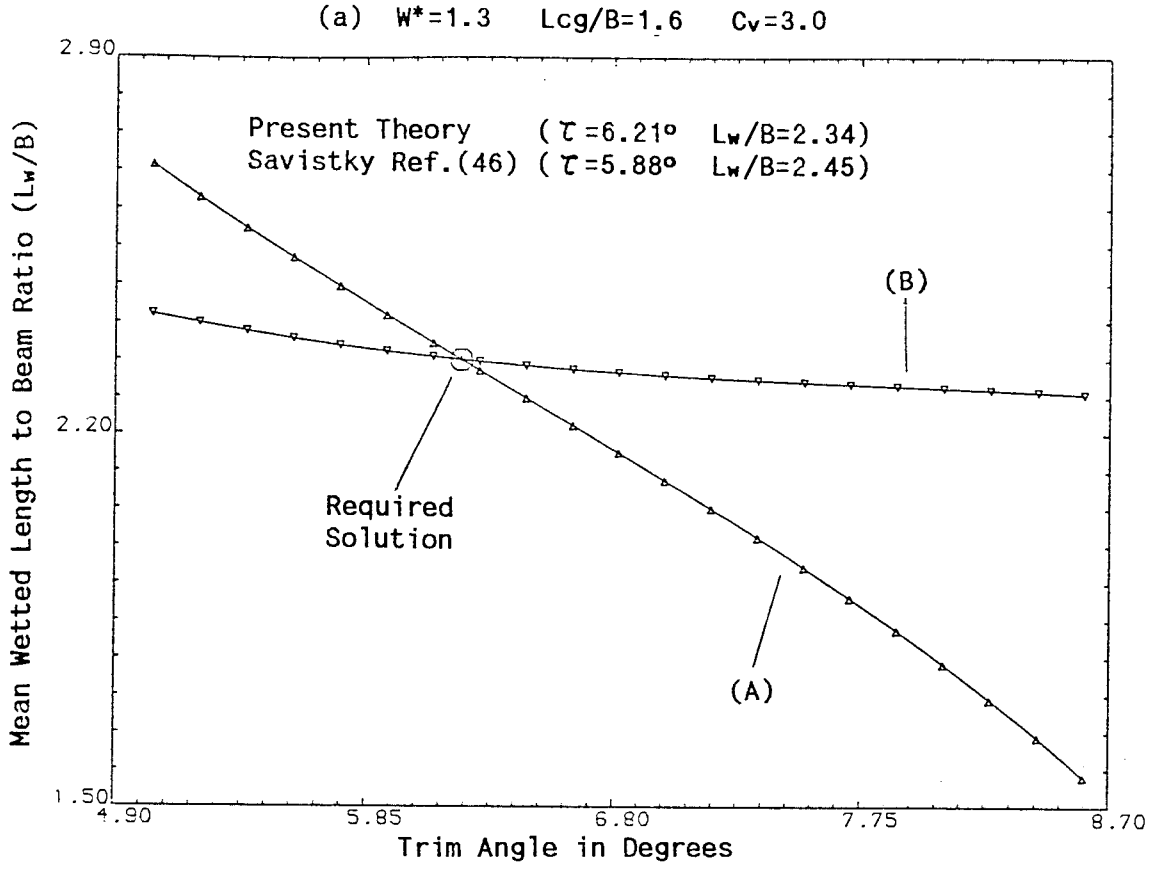

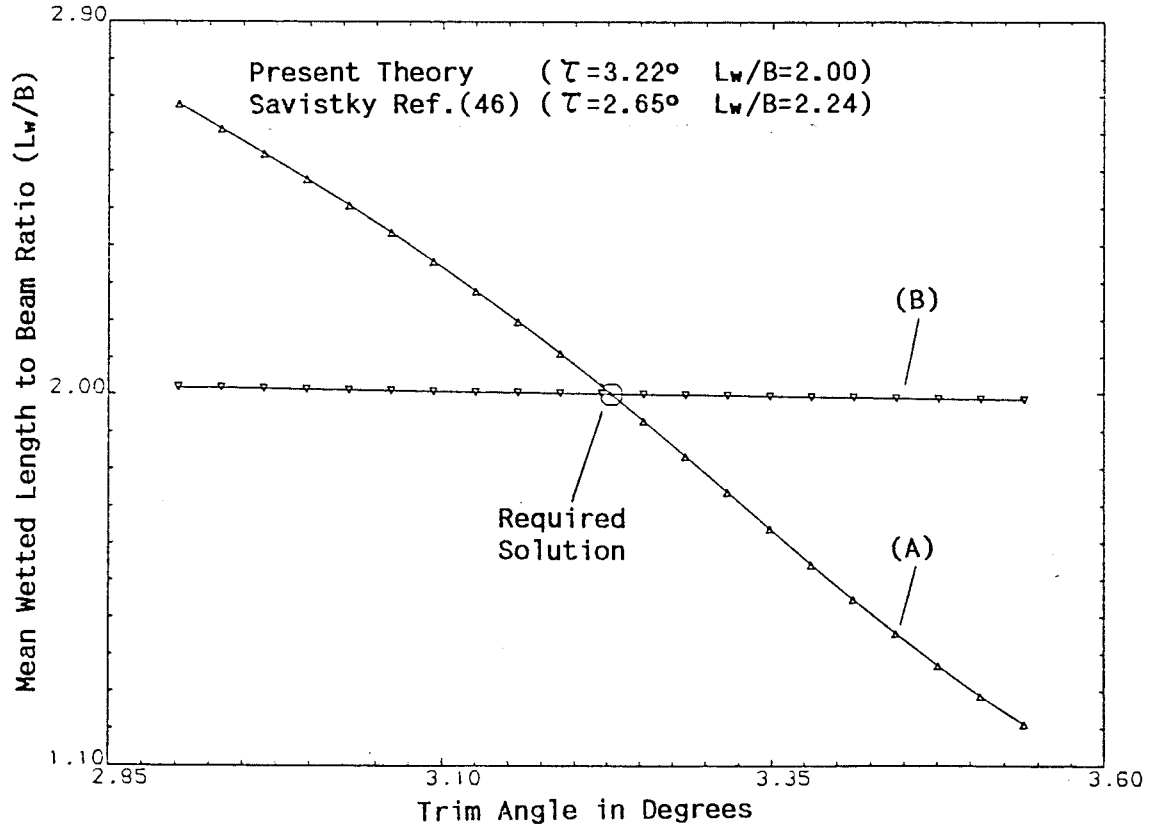

(A) Line of Constant Weight Coefficient (W*)
(B) Line of Constant Lcg/B

Fig.(5.14a,b) Matching Process for determining the Running Trim Angle and Mean Lw/B Ratio for 10° Constant Deadrise Surface

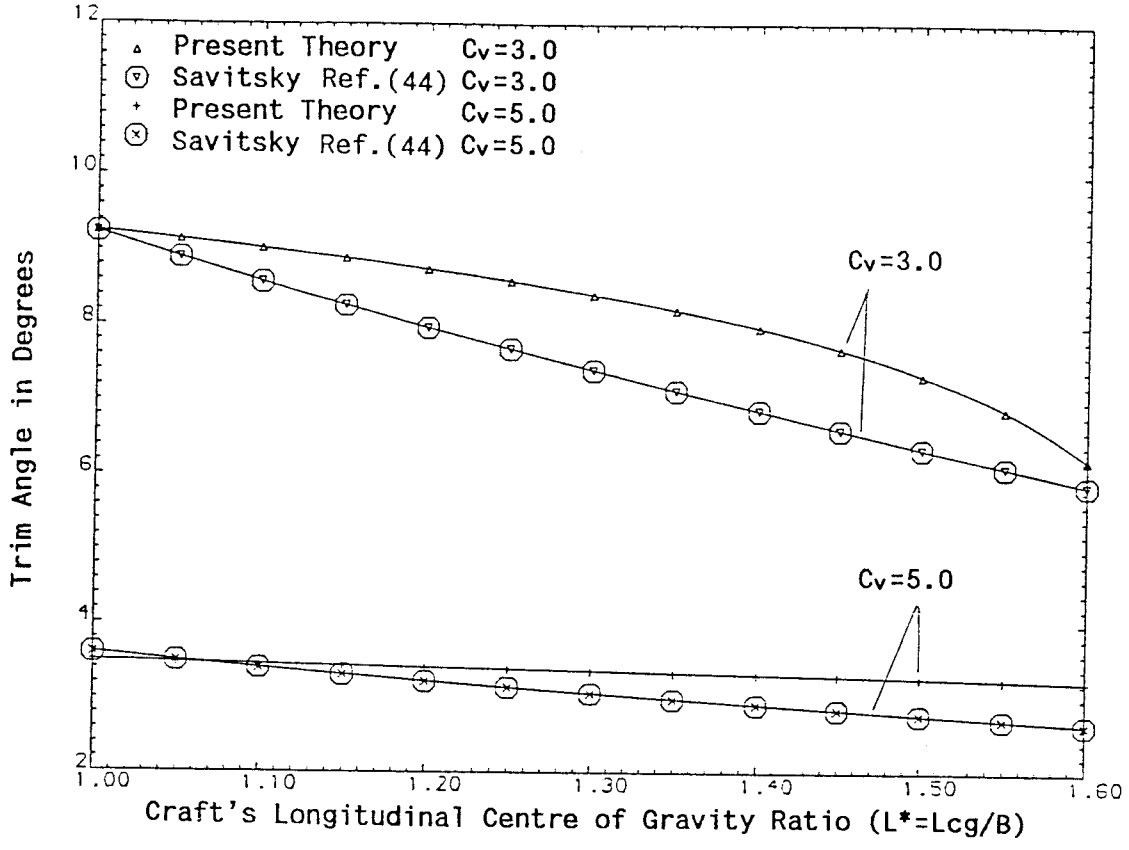

Fig.(5.15a) Variation of Running Trim Angle with Centre of gravity Ratio for 10° Constant Deadrise Surface (W*=1.3)

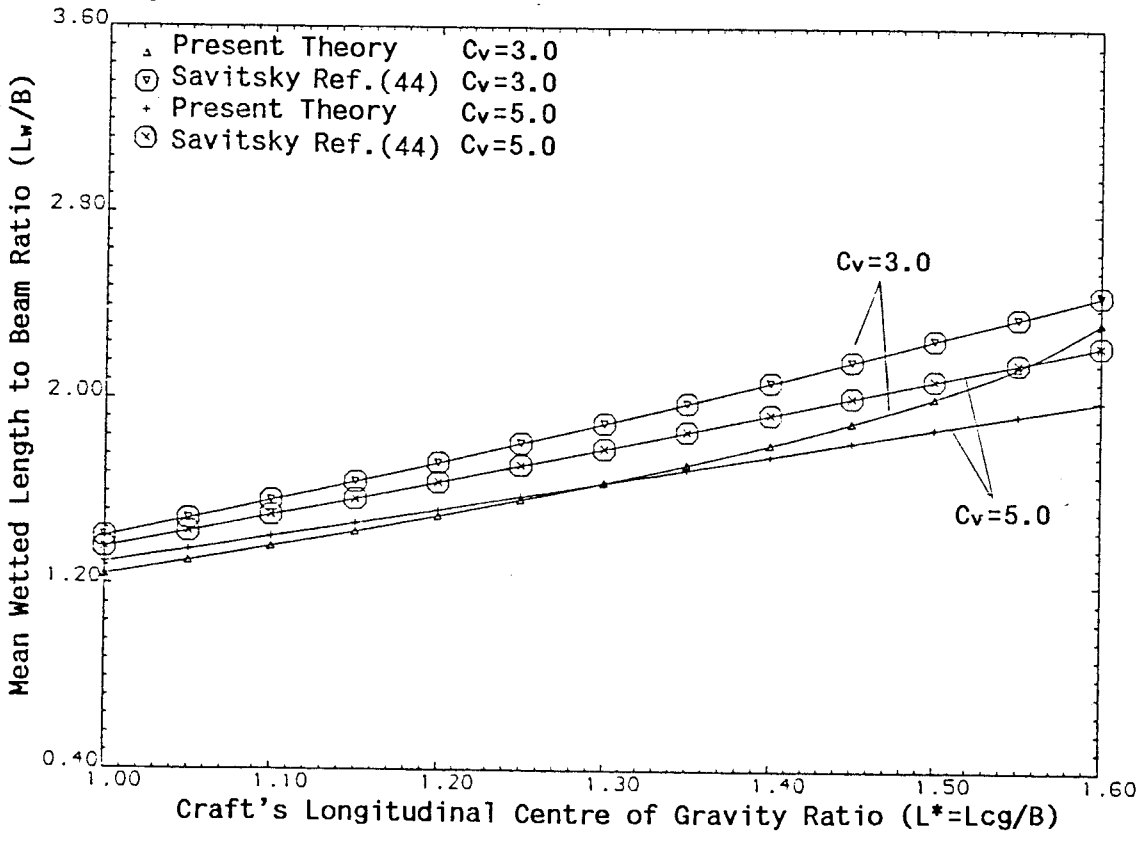

Fig.(5.15b) Variation of Running Mean Wetted Length to Beam Ratio with Centre of Gravity Ratio for 10° Constant Surface (W*=1.3)

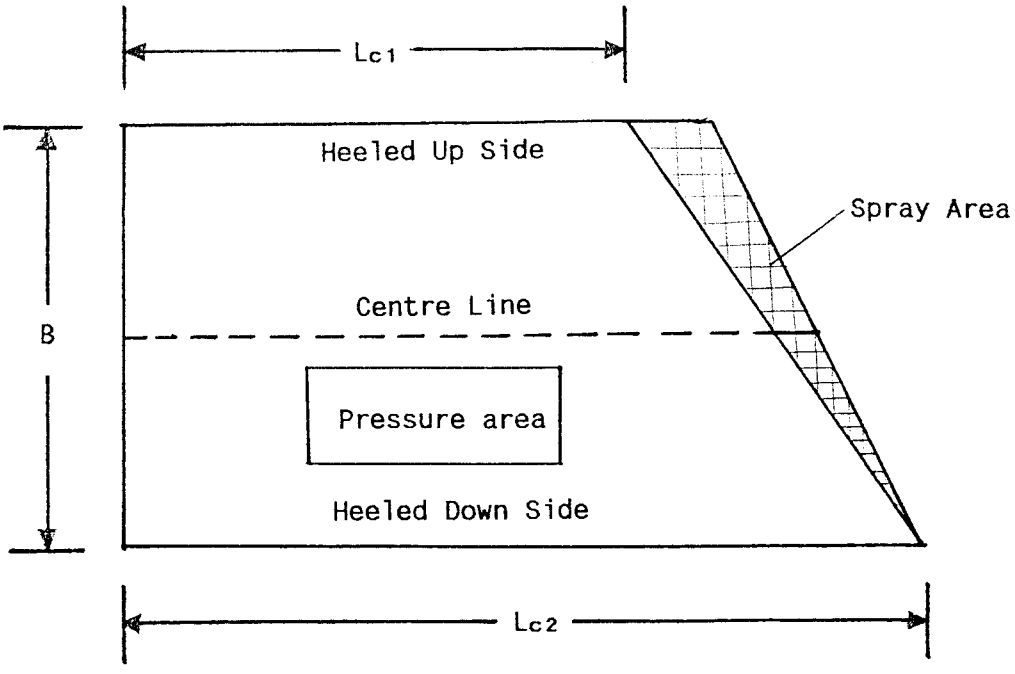

Mean Wetted Length (L_w) = $\frac{(L_{c1} + L_{c2})}{2}$

Fig.(6.1) Projected Wetted Bottom of Planing Flat Plate in Heel Condition

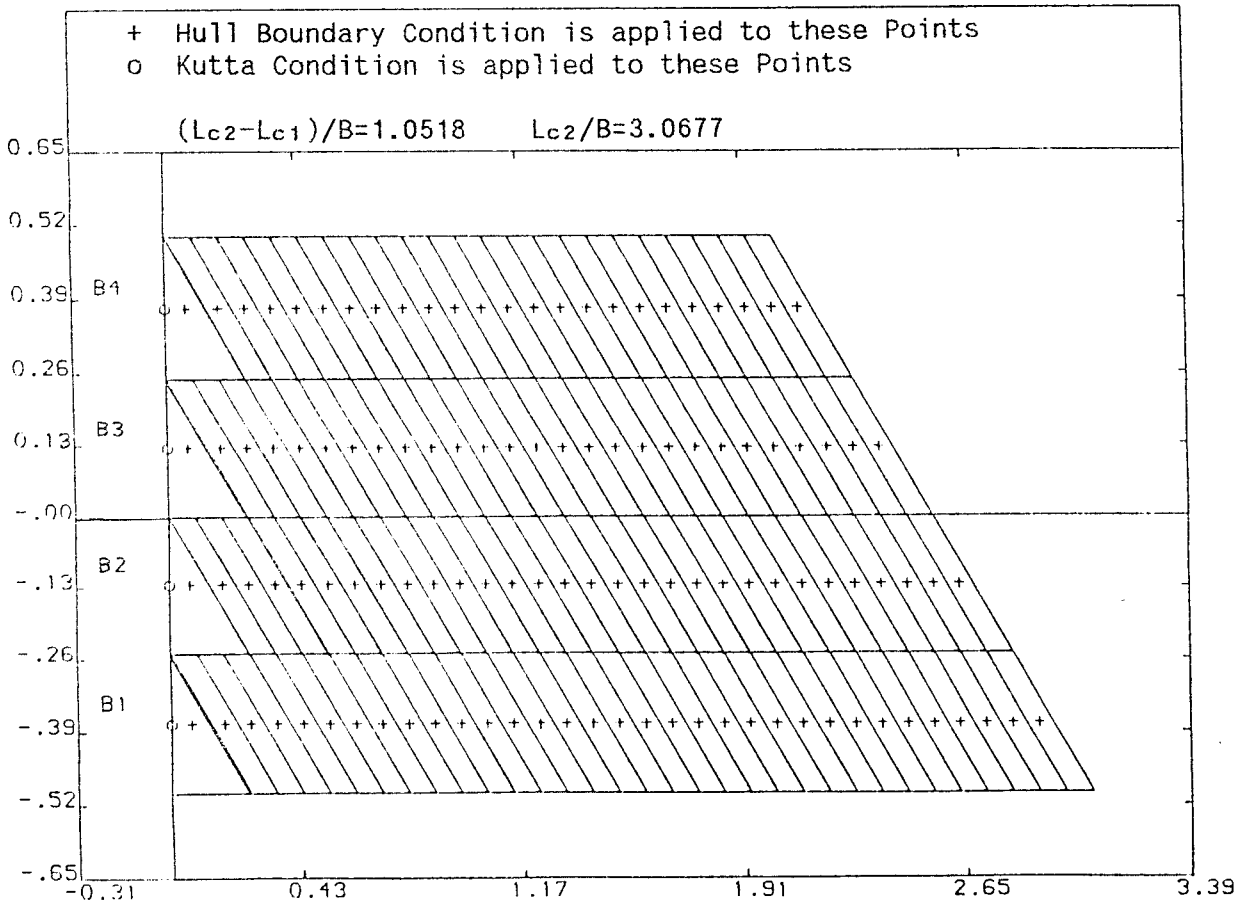

Fig.(6.2) Finite Element Representation of Projected Wetted Bottom

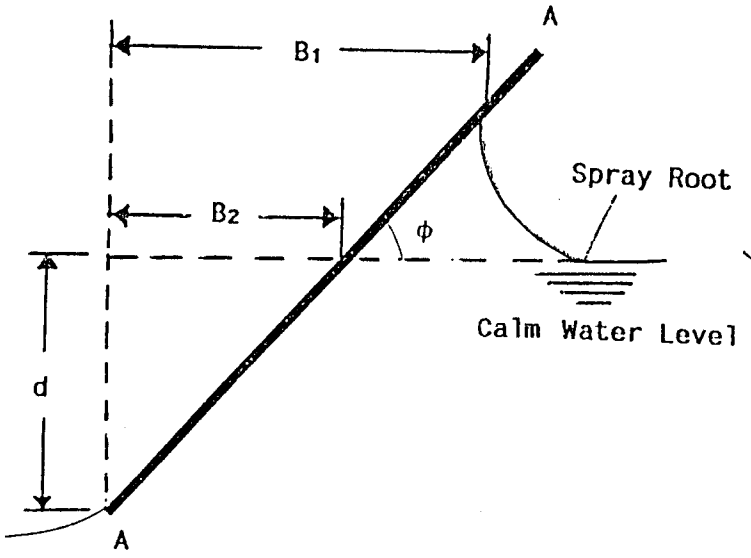

(a) Front View (Section A - A)

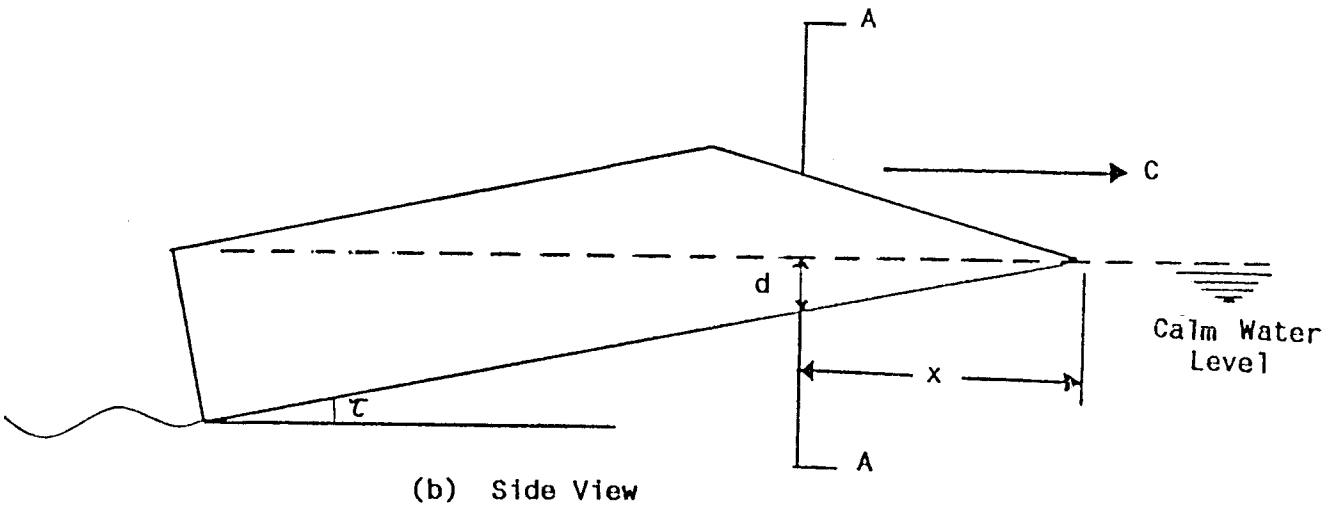

(b) Side View

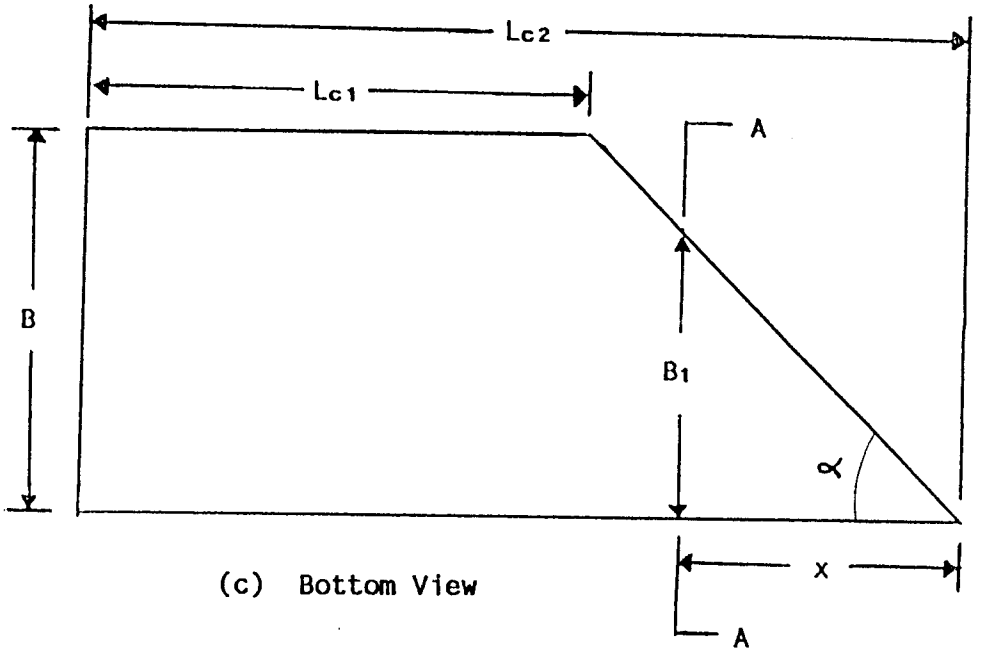

(c) Bottom View

Fig.(6.3a,b,c) Waterline Intersection for Planing Flat Plate in Heel Condition

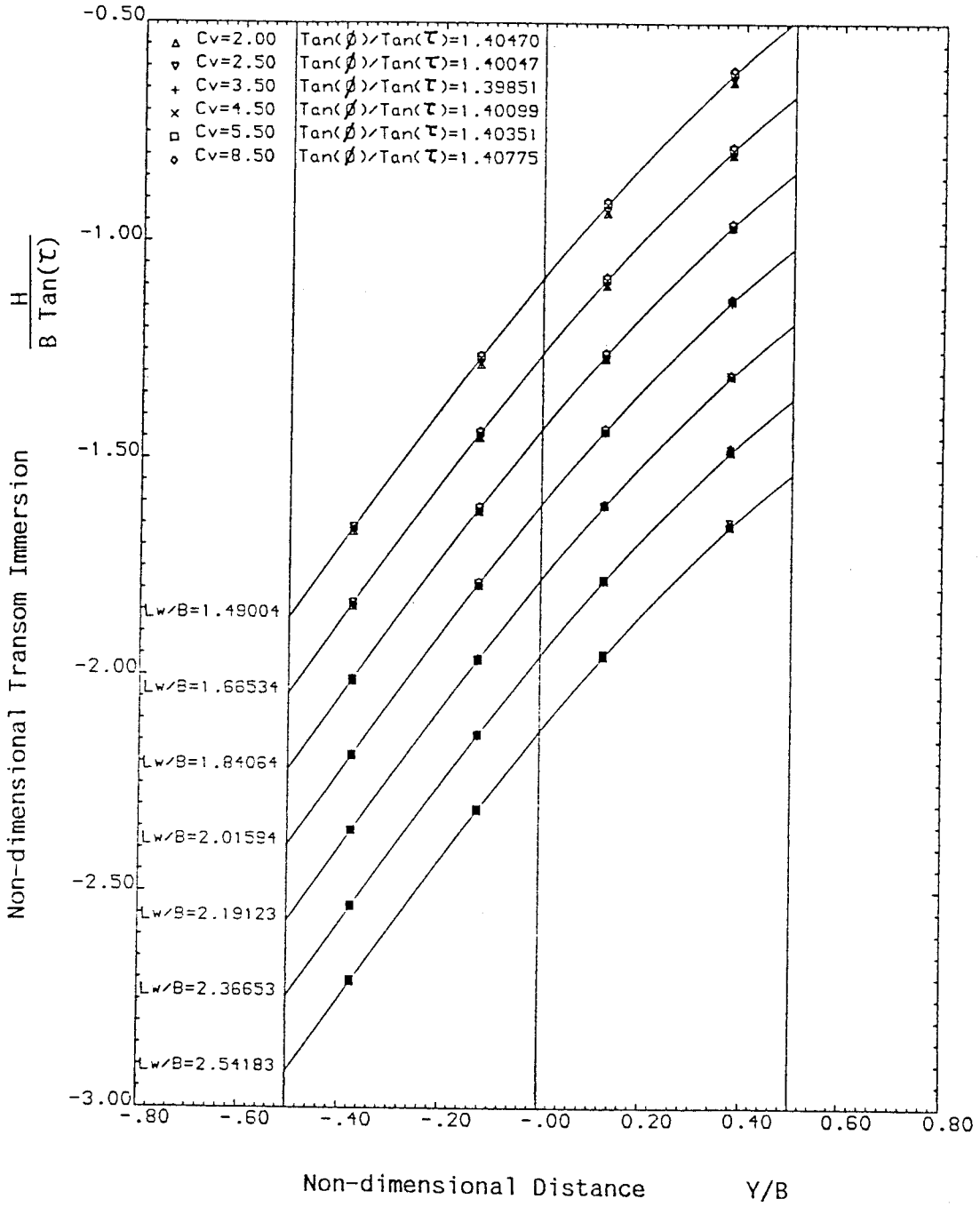

Fig.(6.4) Predicted Transom Shapes and Vertical Locations for Planing Flat Plate in Heel Condition $\frac{(L_{c2}-L_{c1})}{B} = 1.0518$

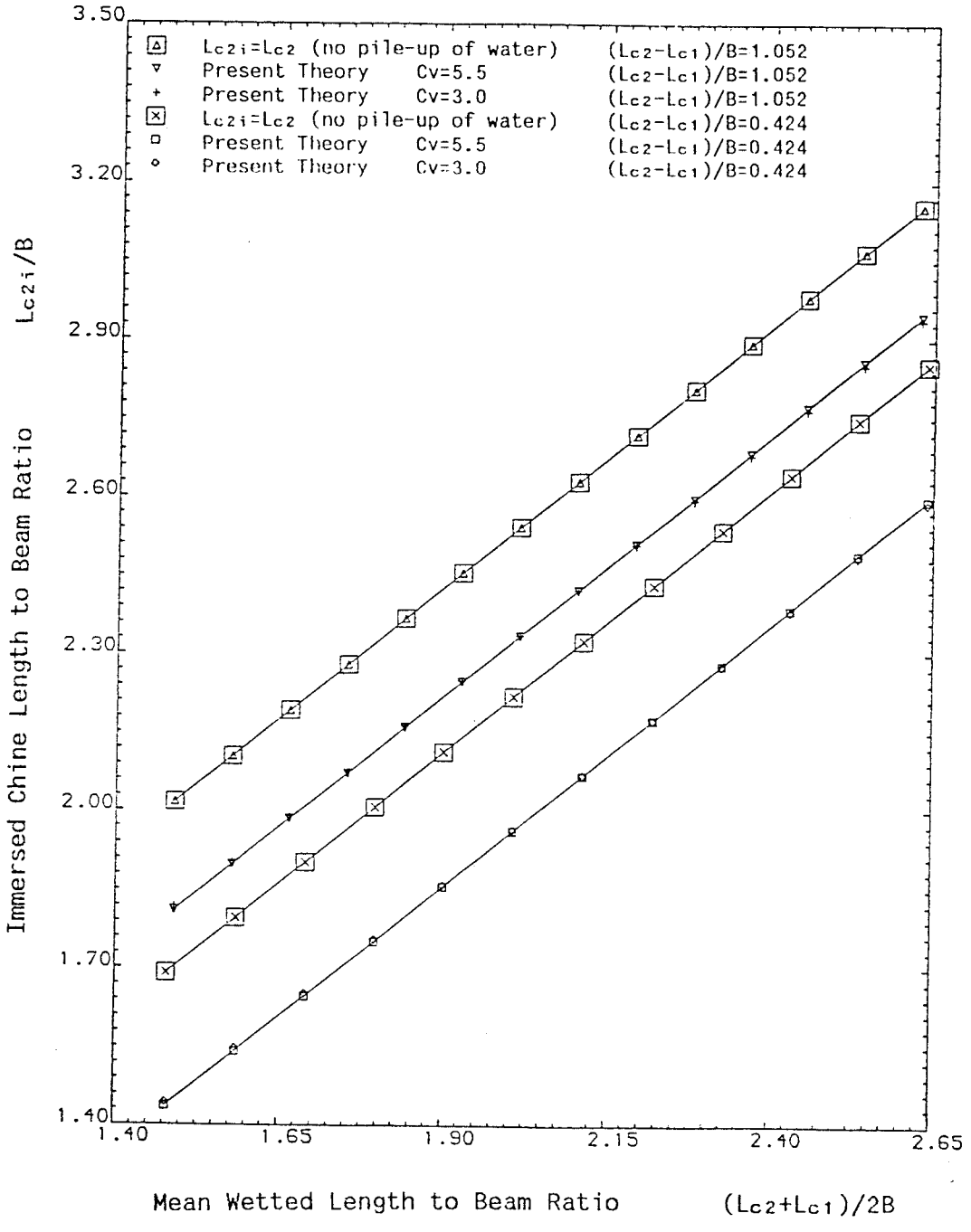

Fig.(6.5) Immersed Chine Length to Beam Ratios (heeled down side) for Heeled Flat Plate

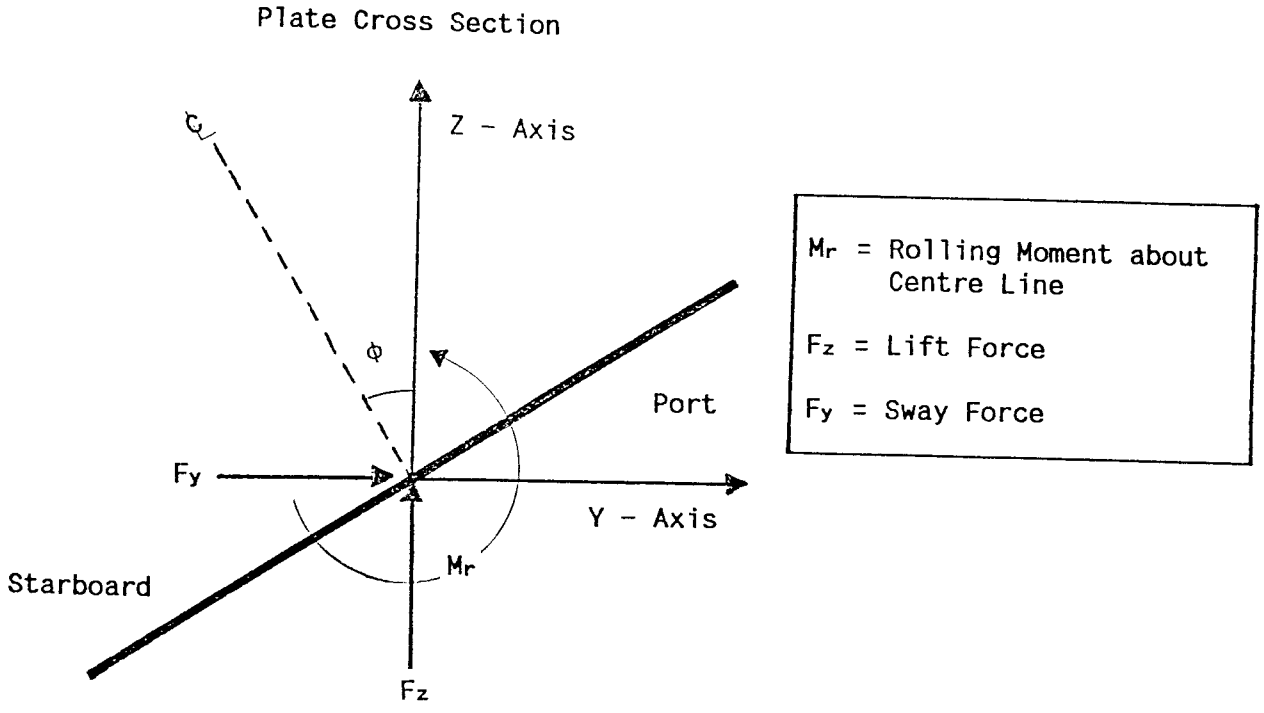

Fig.(6.6a) Sign Conventions for the Forces and Moments acting on a Heeled Planing Flat Plate

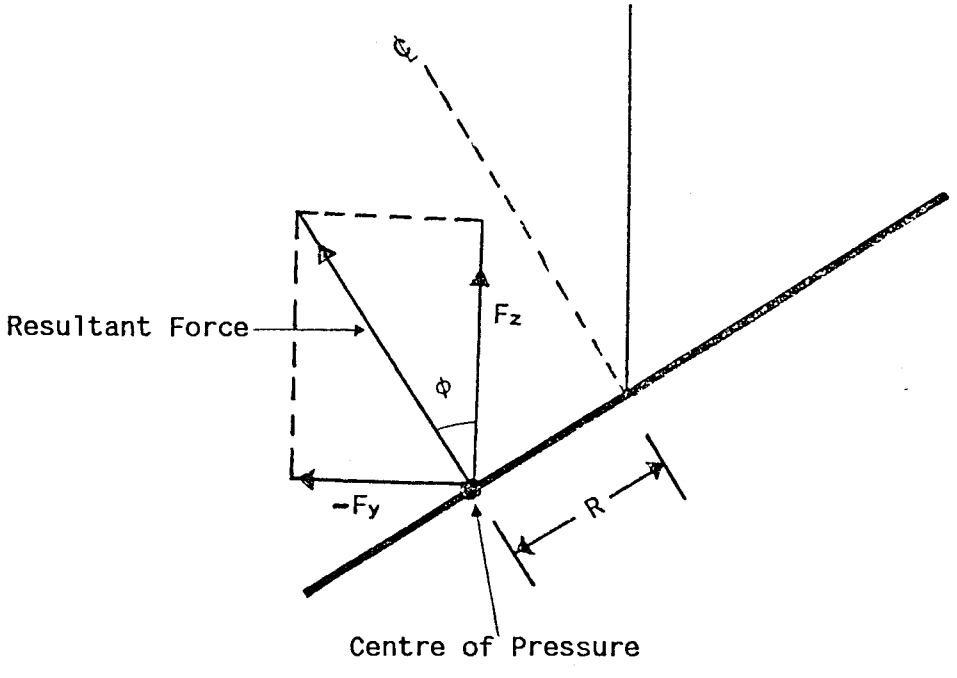

Fig.(6.6b) Hydrodynamic Forces acting on Plate Bottom

Fig.(6.7a) Roll Moment Arm to Beam Ratio for Heeled Flat Plate

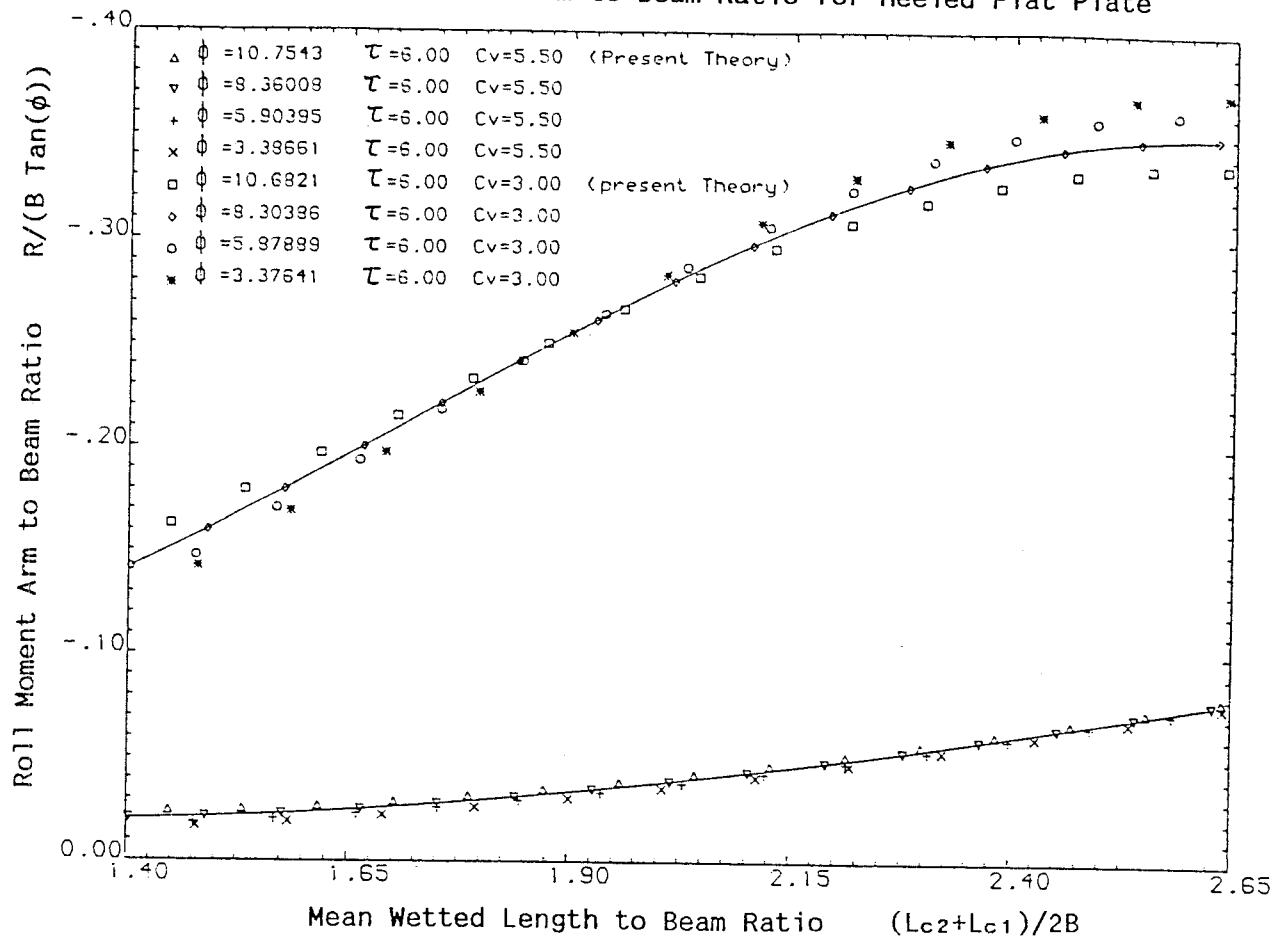

Fig.(6.7b) Roll Moment Coefficient Slopes for Heeled Flat Plate

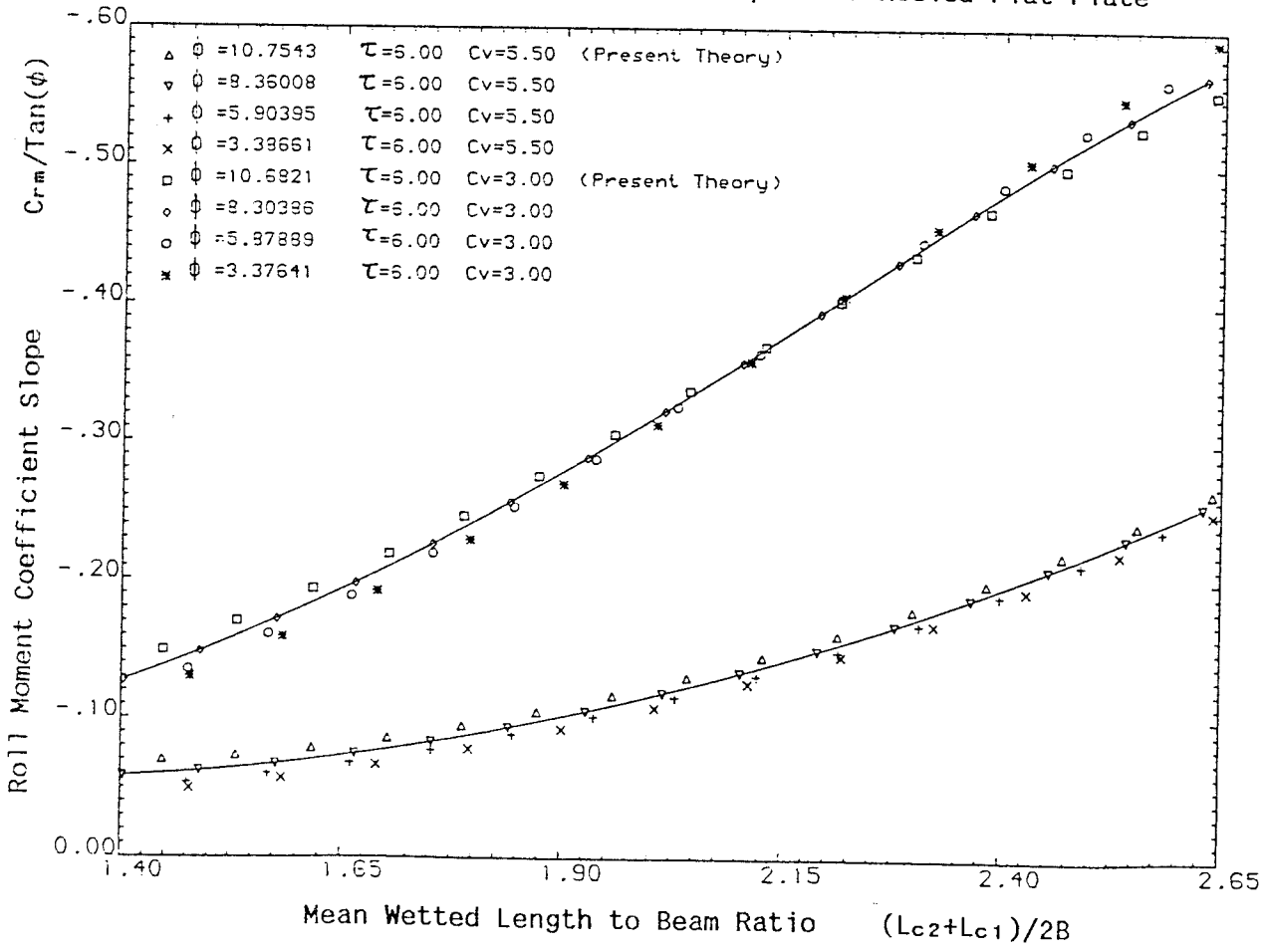

Fig.(6.7c) Lift Coefficient Slopes for Heeled Flat Plate

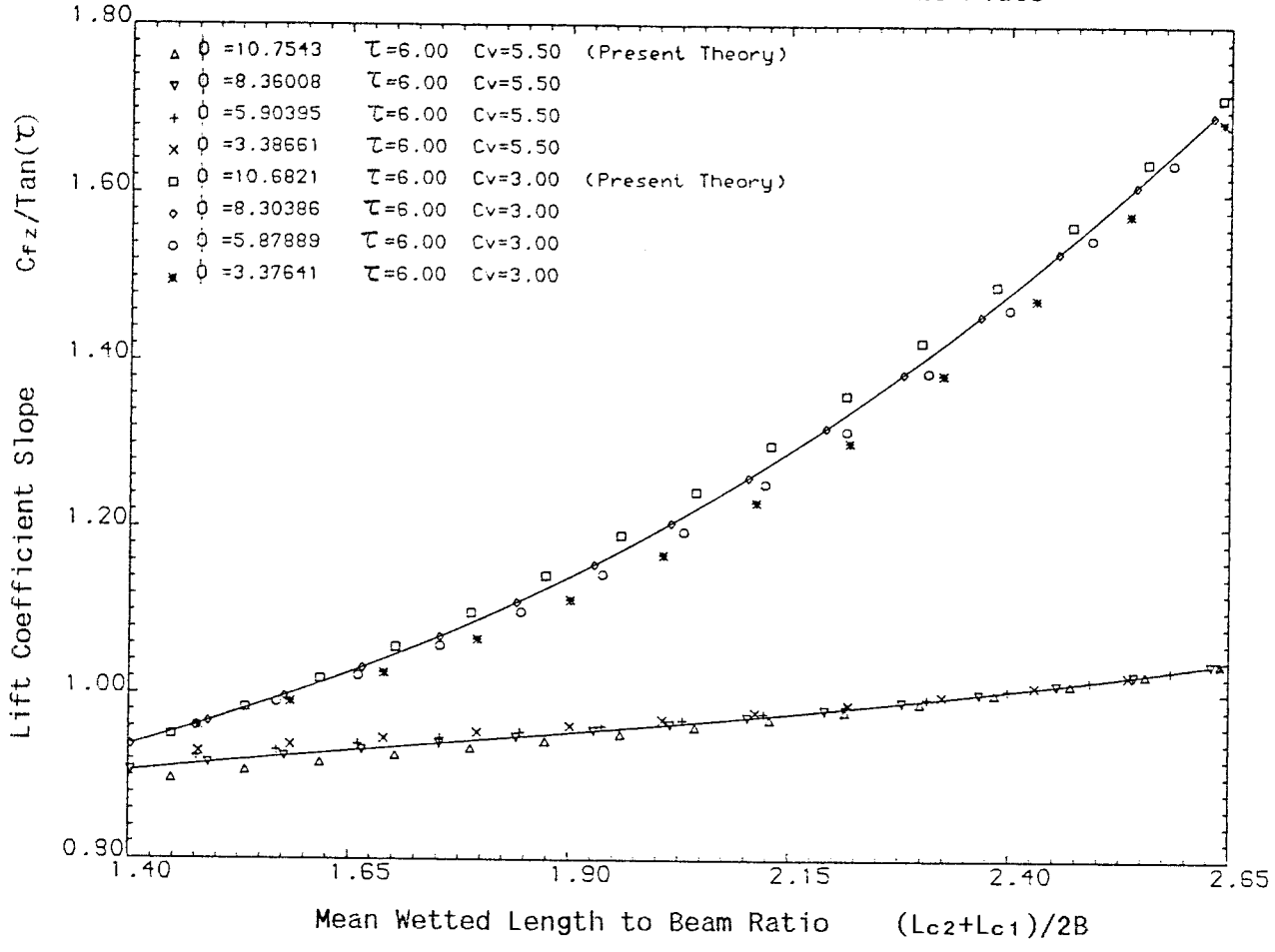

Fig.(6.7d) Centre of Pressure Ratios for Heeled Flat Plate

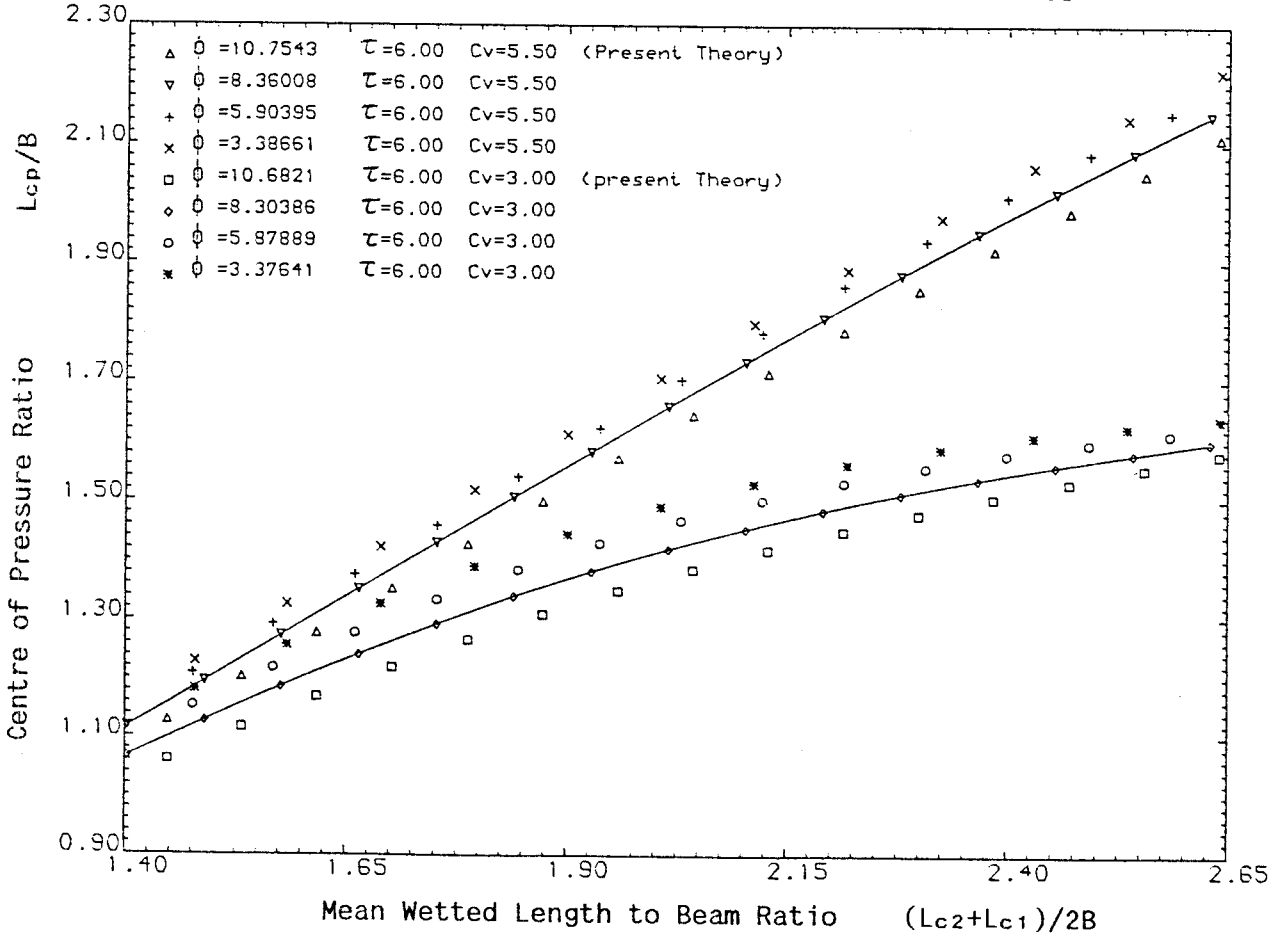

Fig.(6.8a) Comparison of Roll Moment Coefficient slopes with Jahangeer's Results for heeled Flat Plate

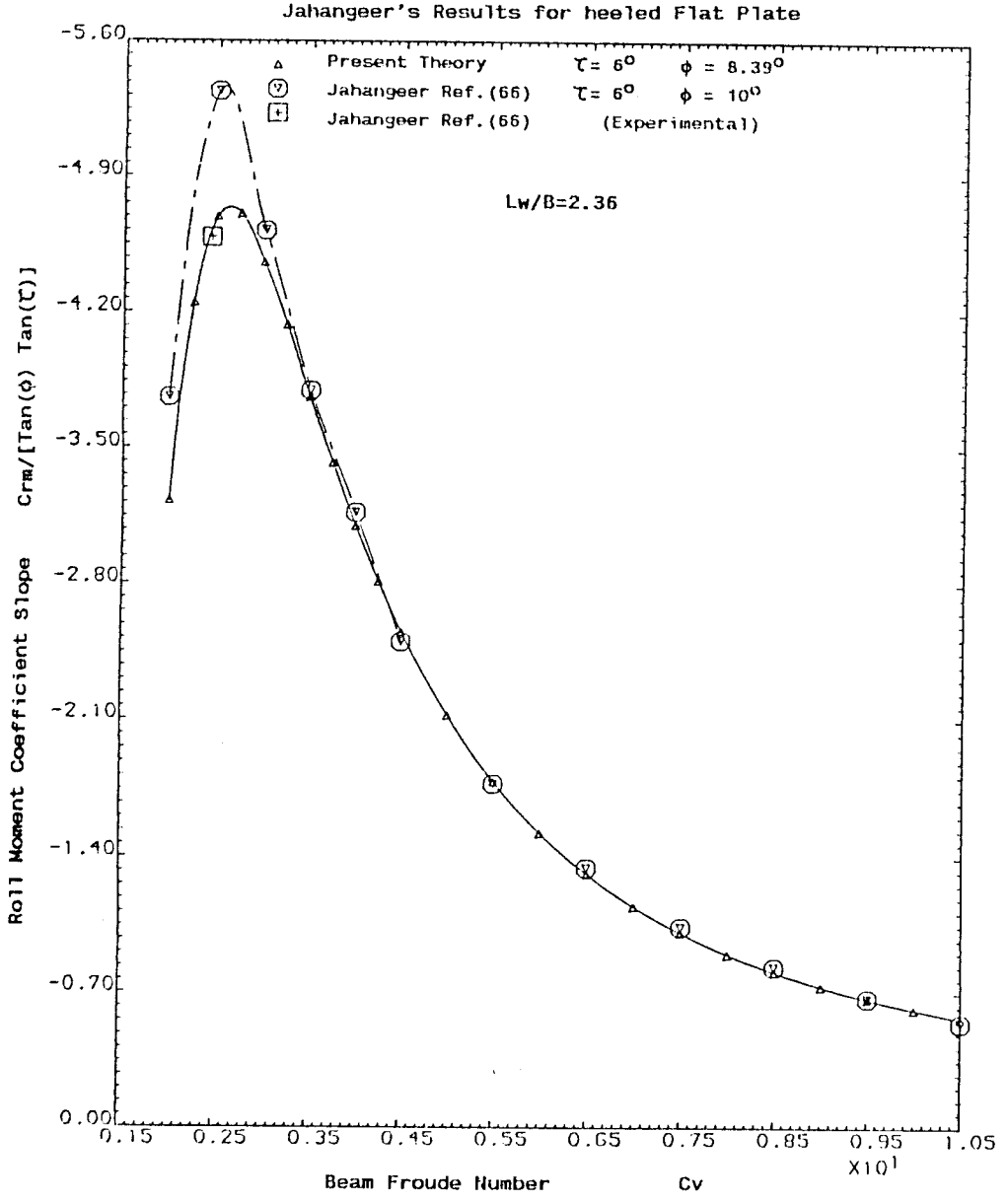

Fig.(6.8b) Comparison of Roll Moment Arm Ratios with Jahangeer's Results for heeled Flat Plate

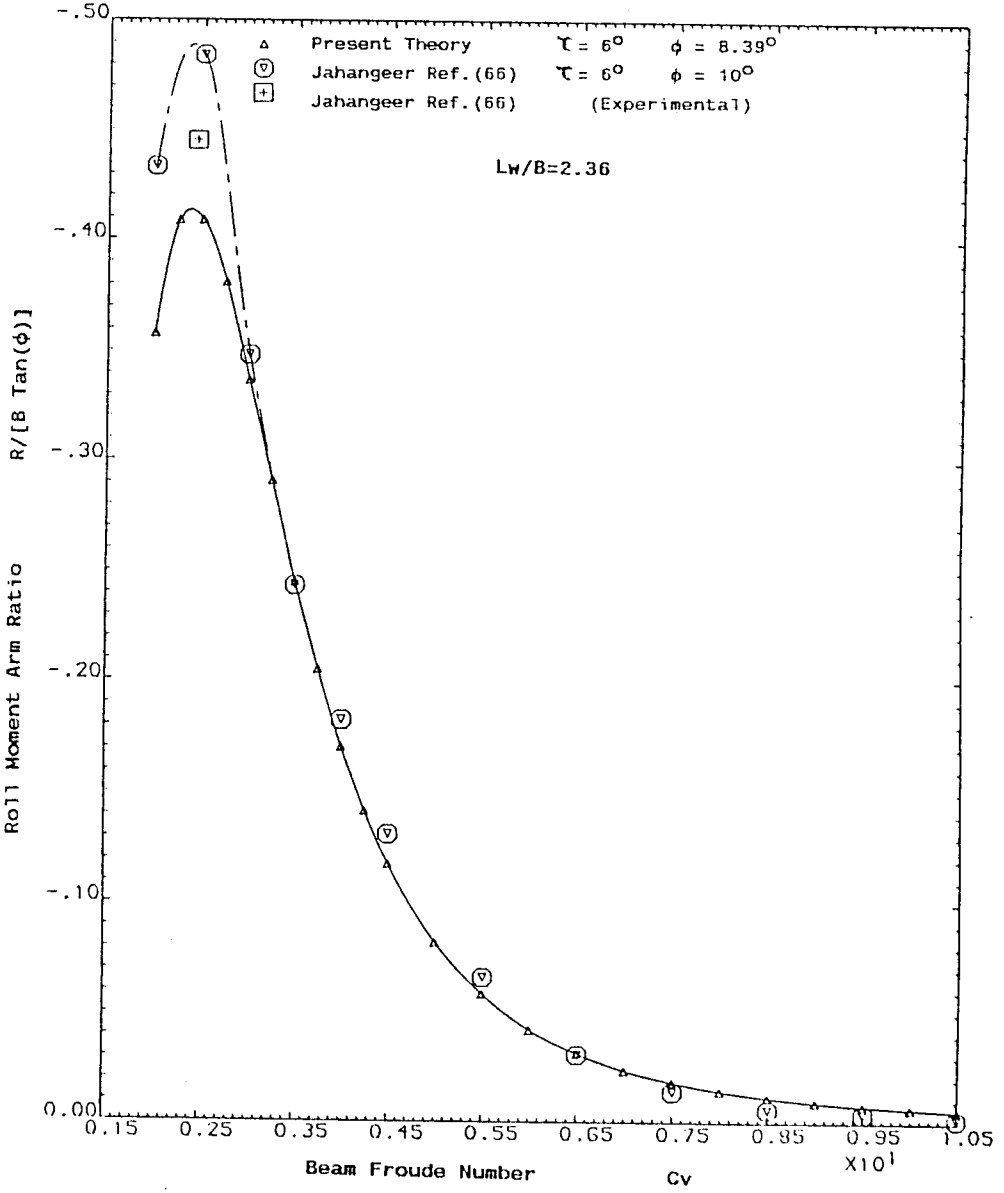

Fig.(6.8c) Comparison of Lift Coefficient Slopes with Jahangeer's Results for heeled Flat Plate

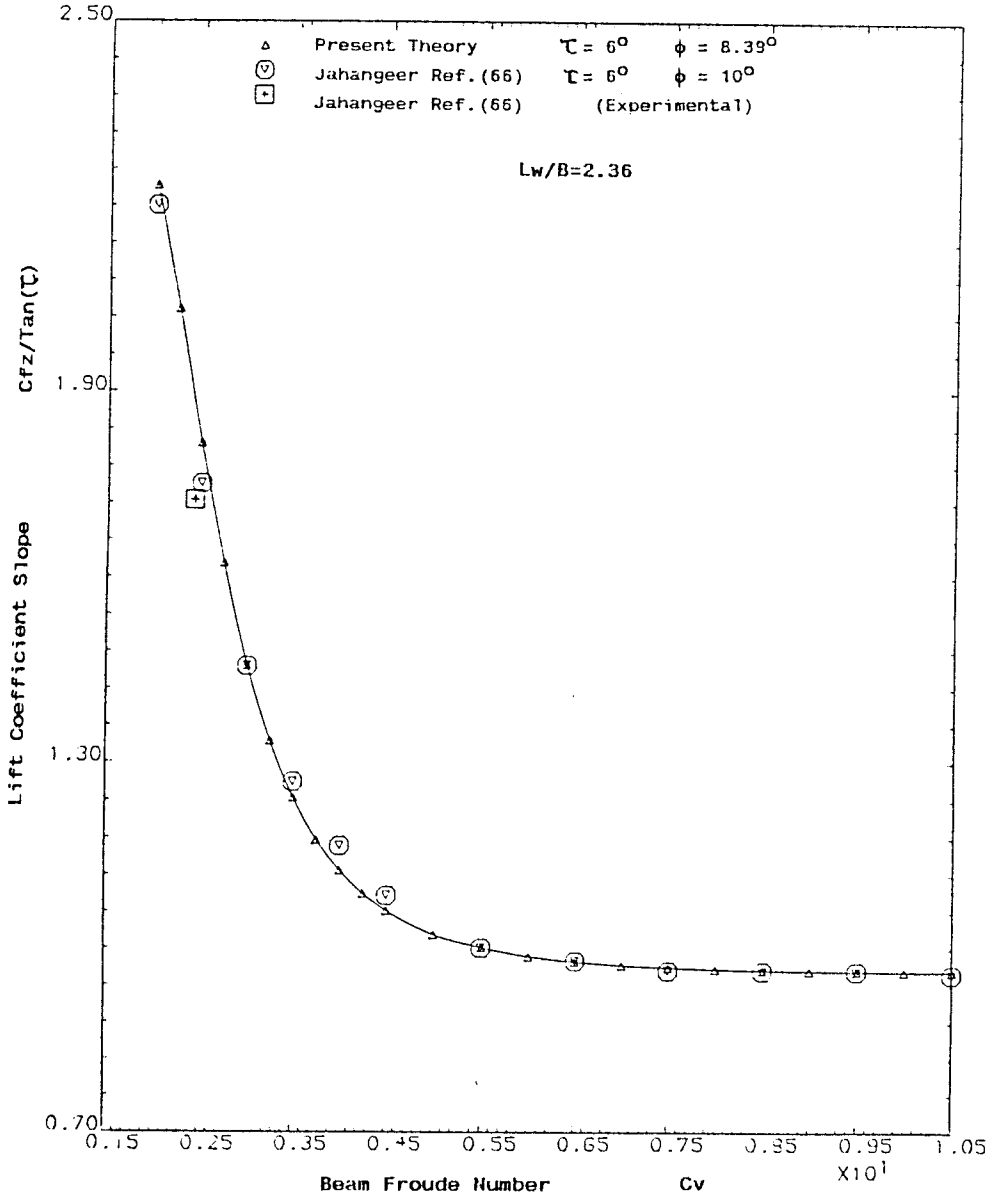

Fig.(6.8d) Comparison of Centre of Pressure Ratios with Jahangeer's Results for heeled Flat Plate

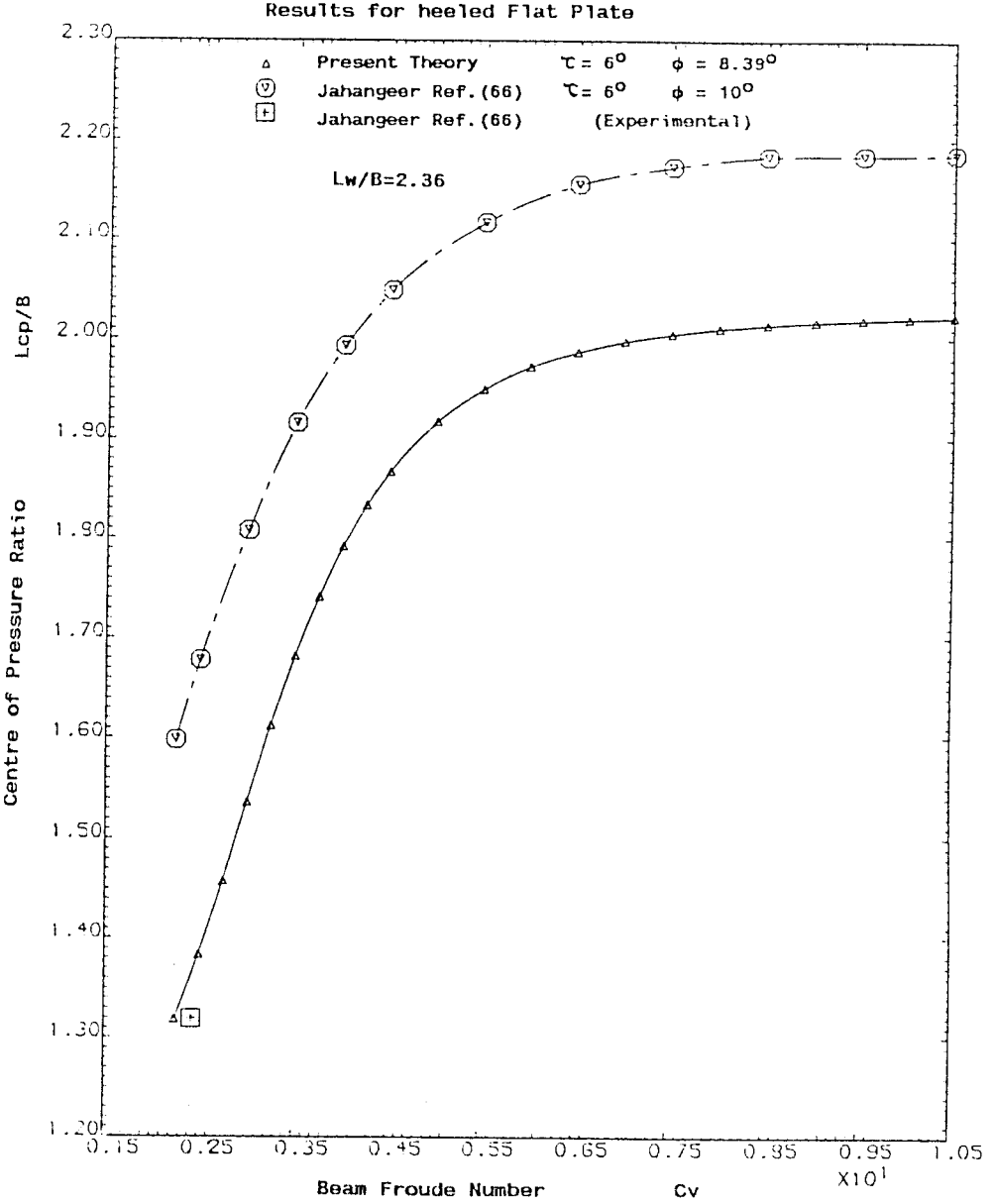

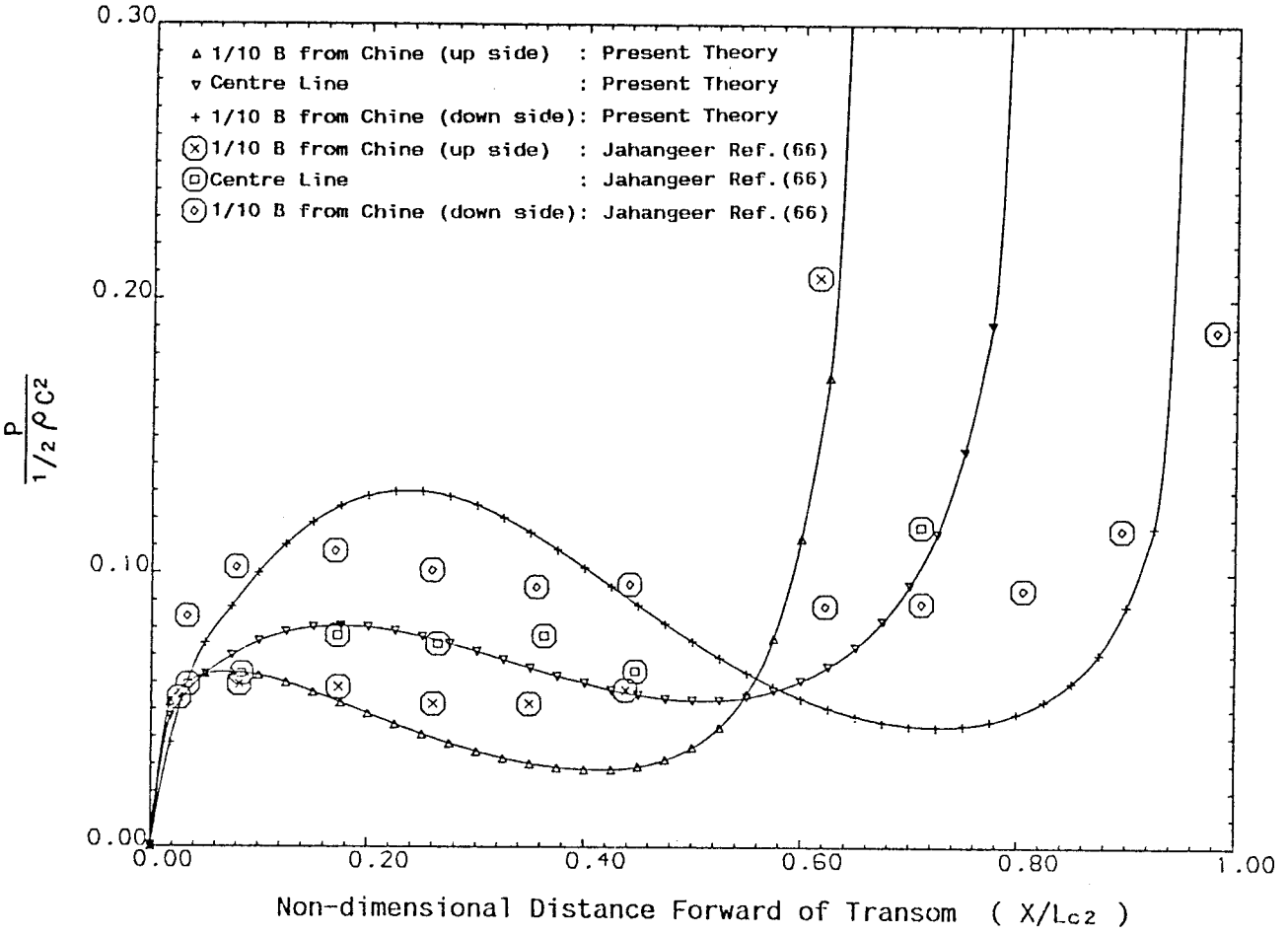

Fig.(6.9) Comparison of Pressure Distribution with Experimental Measurement of Jahangeer for a Heeled Planing Flat Plate

Fig.(6.10a) Computed Lift Coefficient Slopes as a Function of C_v and mean L_w/B for Heeled Planing Flat Plate

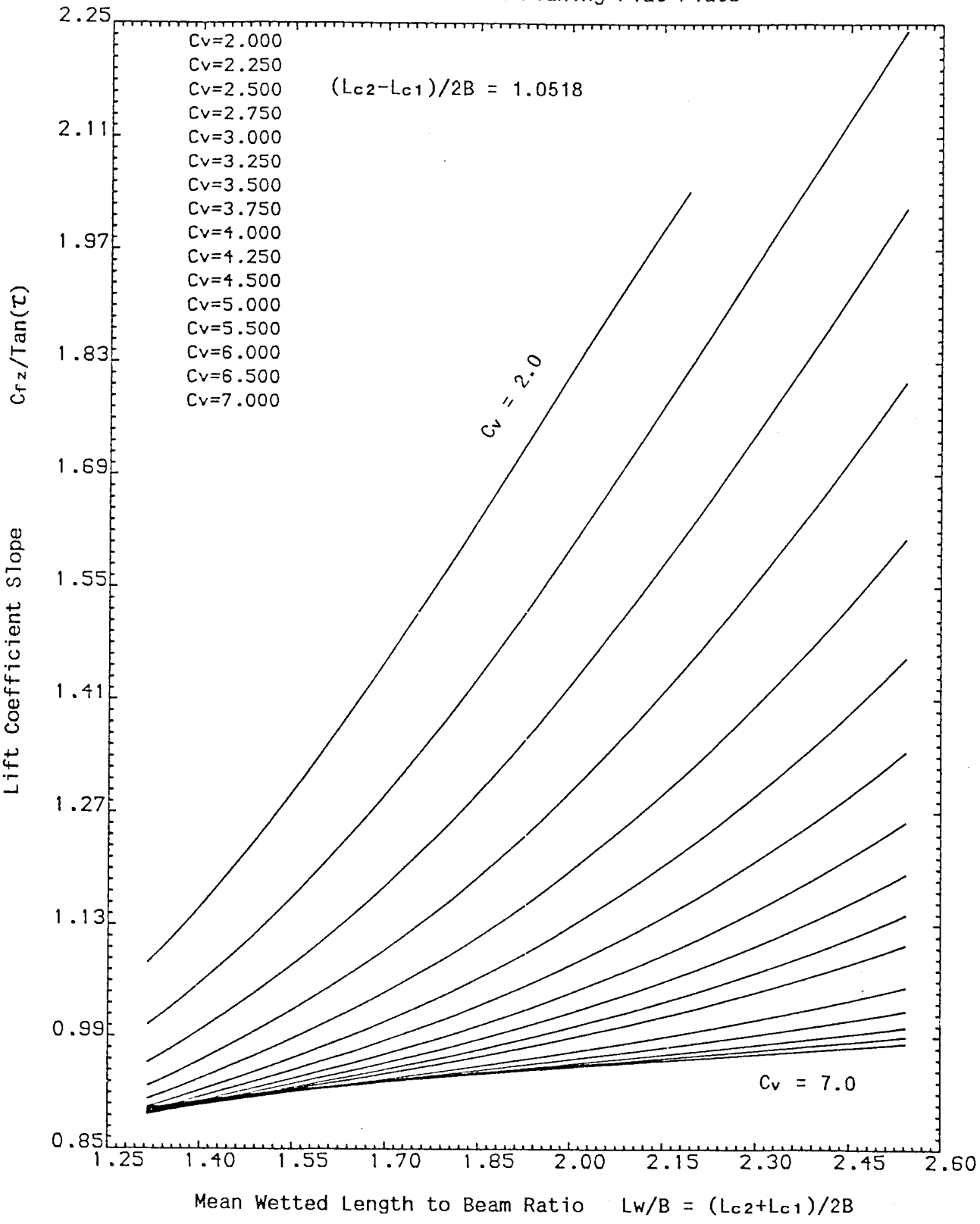

Fig.(6.10b) Computed Centre of Pressure Ratios as a Function of C_v and mean L_w/B for Heeled Planing Flat Plate

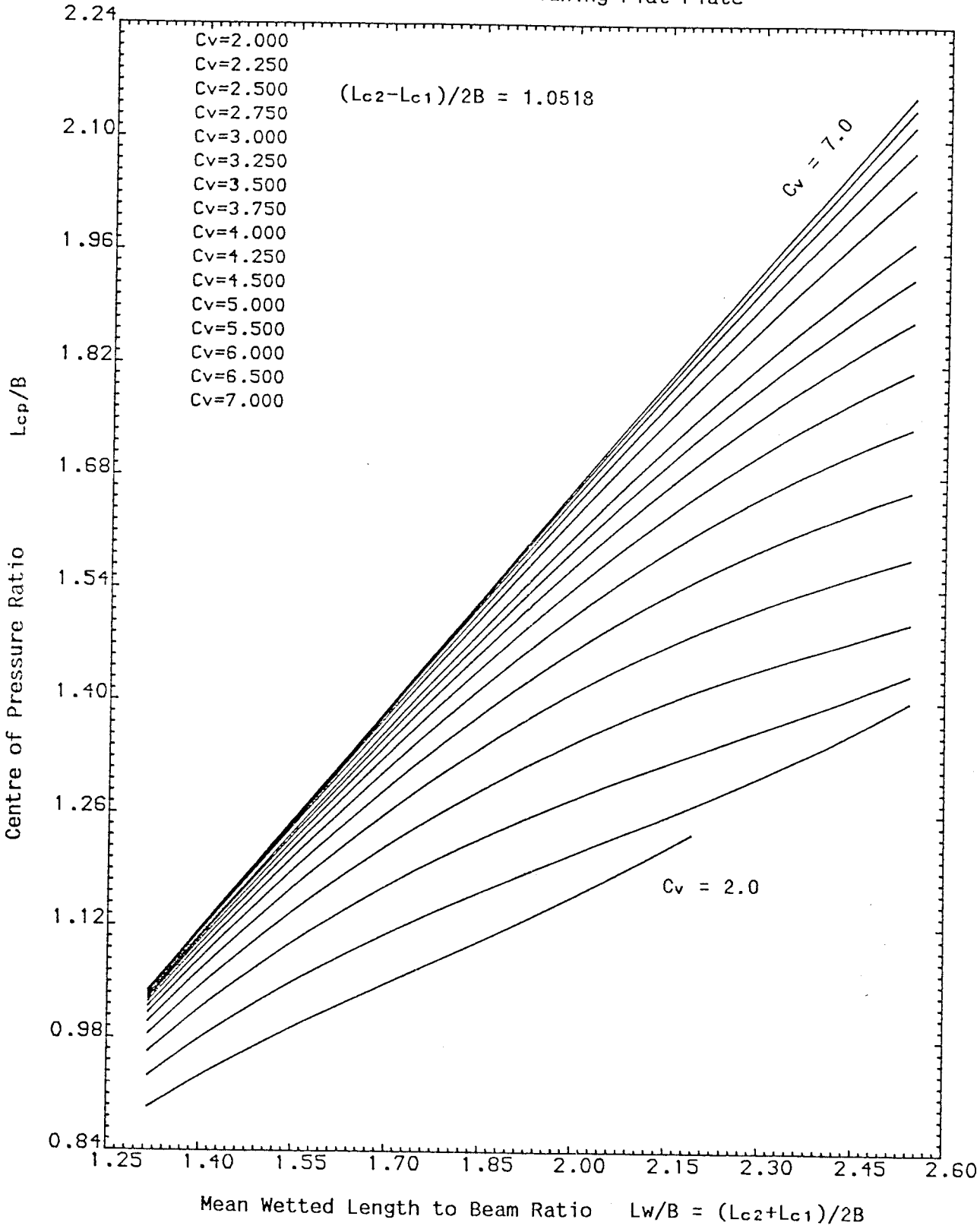

Fig.(6.10c) Computed Roll Moment Coefficient Slope as a Function of Cv and mean Lw/B for Heeled Planing Flat Plate

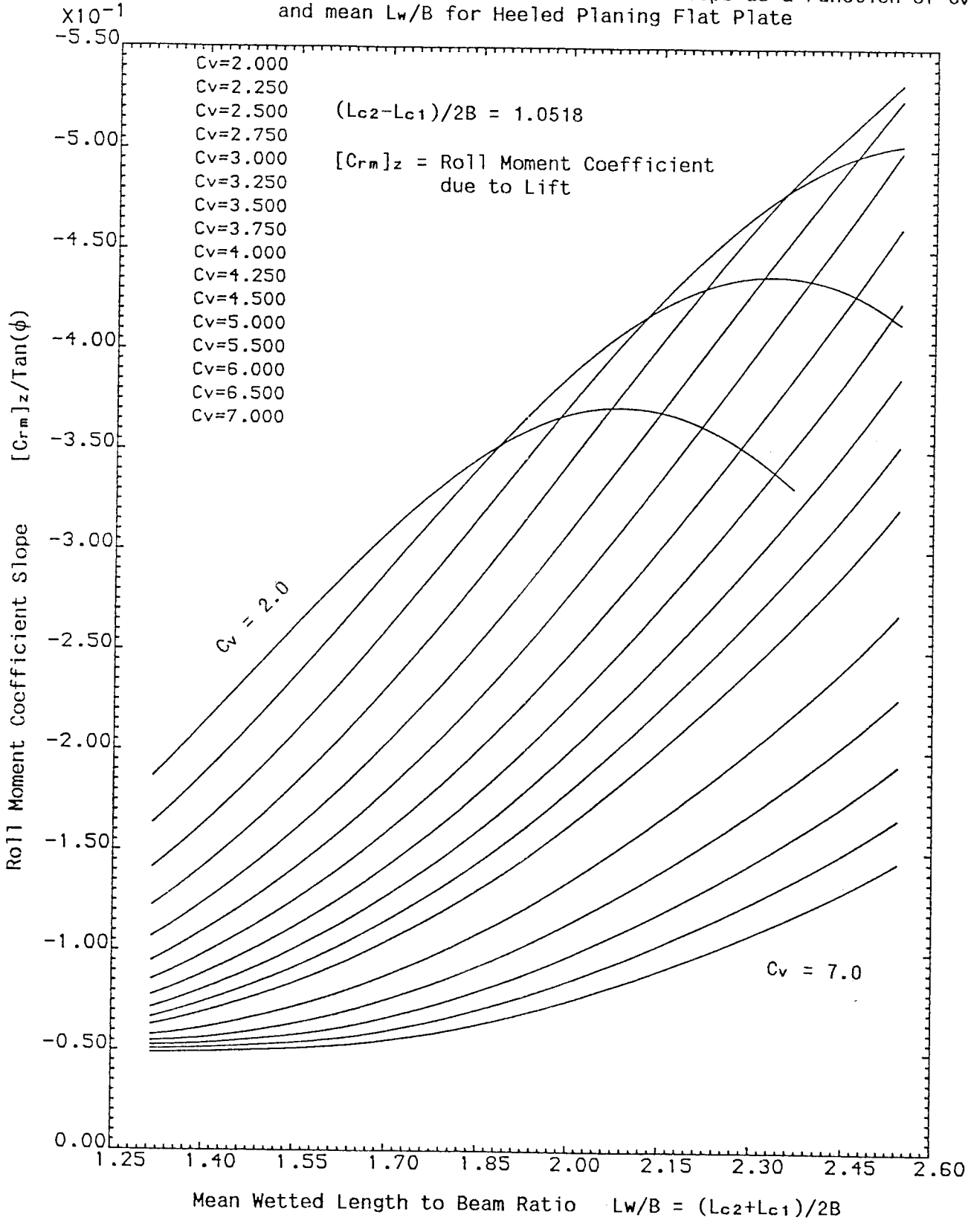

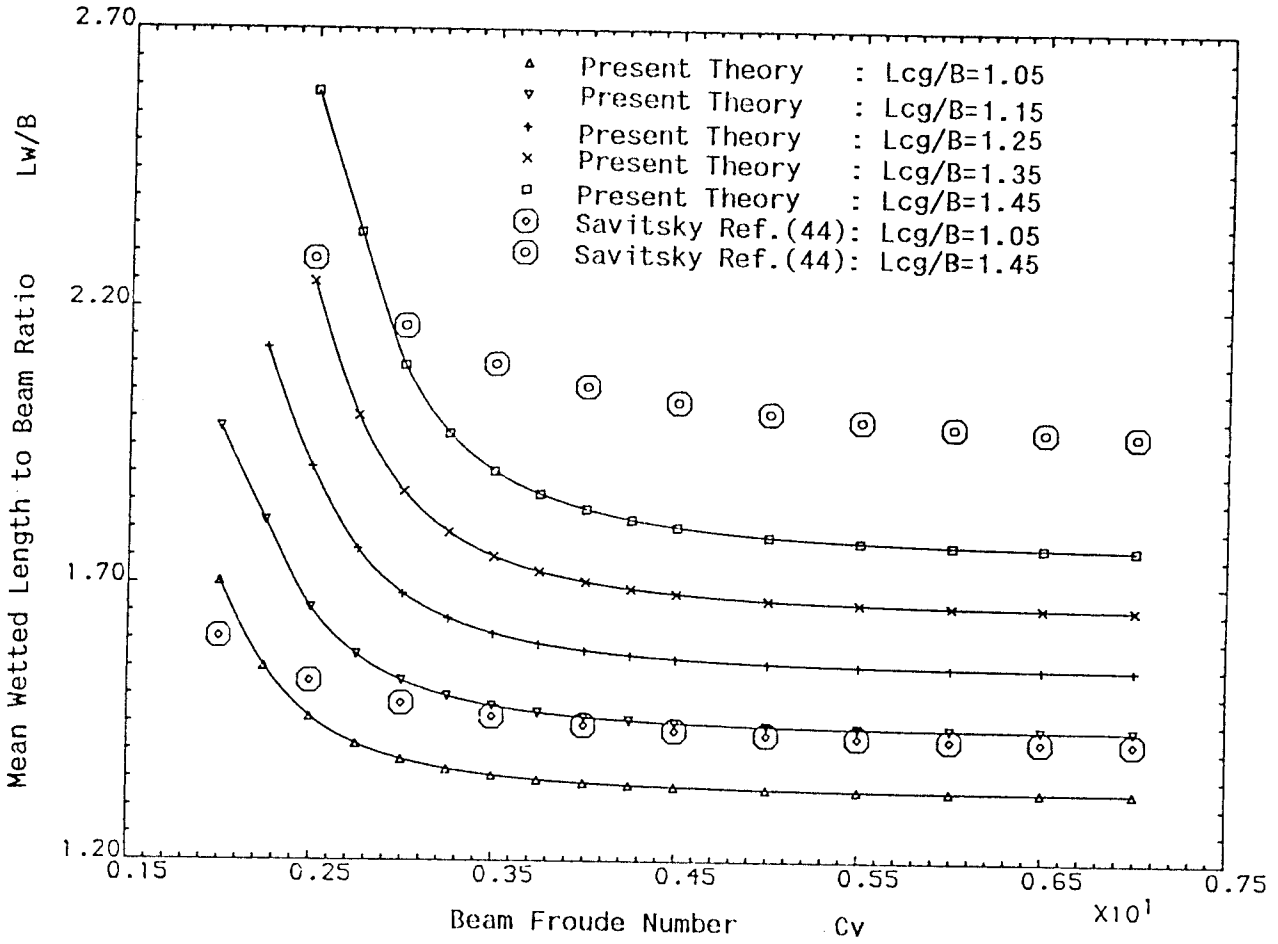

Fig.(6.11a) Variation of Mean Lw/B ratio Against Beam Froude Number for Heeled Planing Flat Plate (Weight Coefficient W* = 1.3)

Fig.(6.11b) Variation of Trim Angle Against Beam Froude Number for Heeled Planing Flat Plate (Weight Coefficient $W^* = 1.3$)

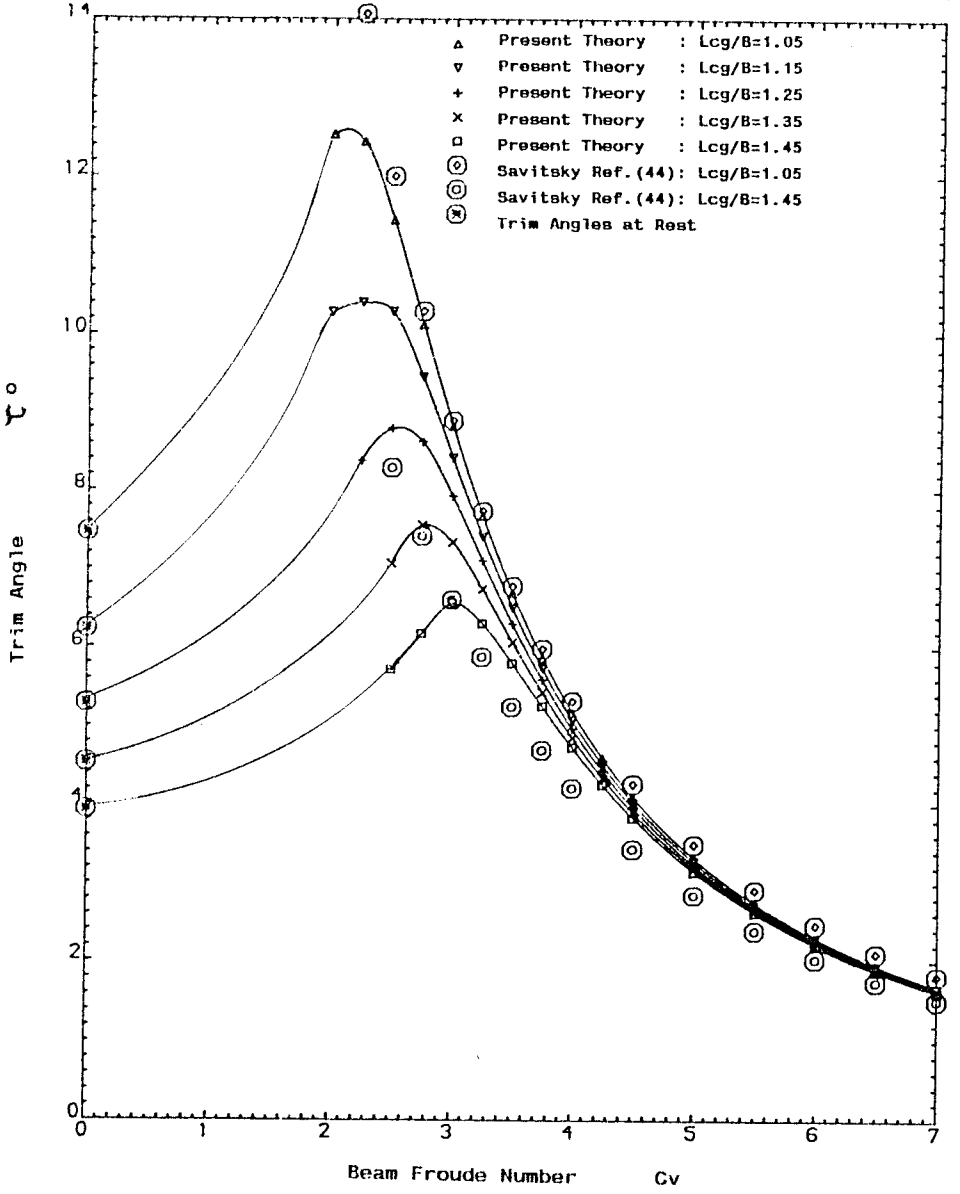

Fig.(6.11c) Variation of Crm/Tan(ϕ) Against Beam Froude Number for Heeled Planing Flat Plate (Weight Coefficient $W^* = 1.3$)

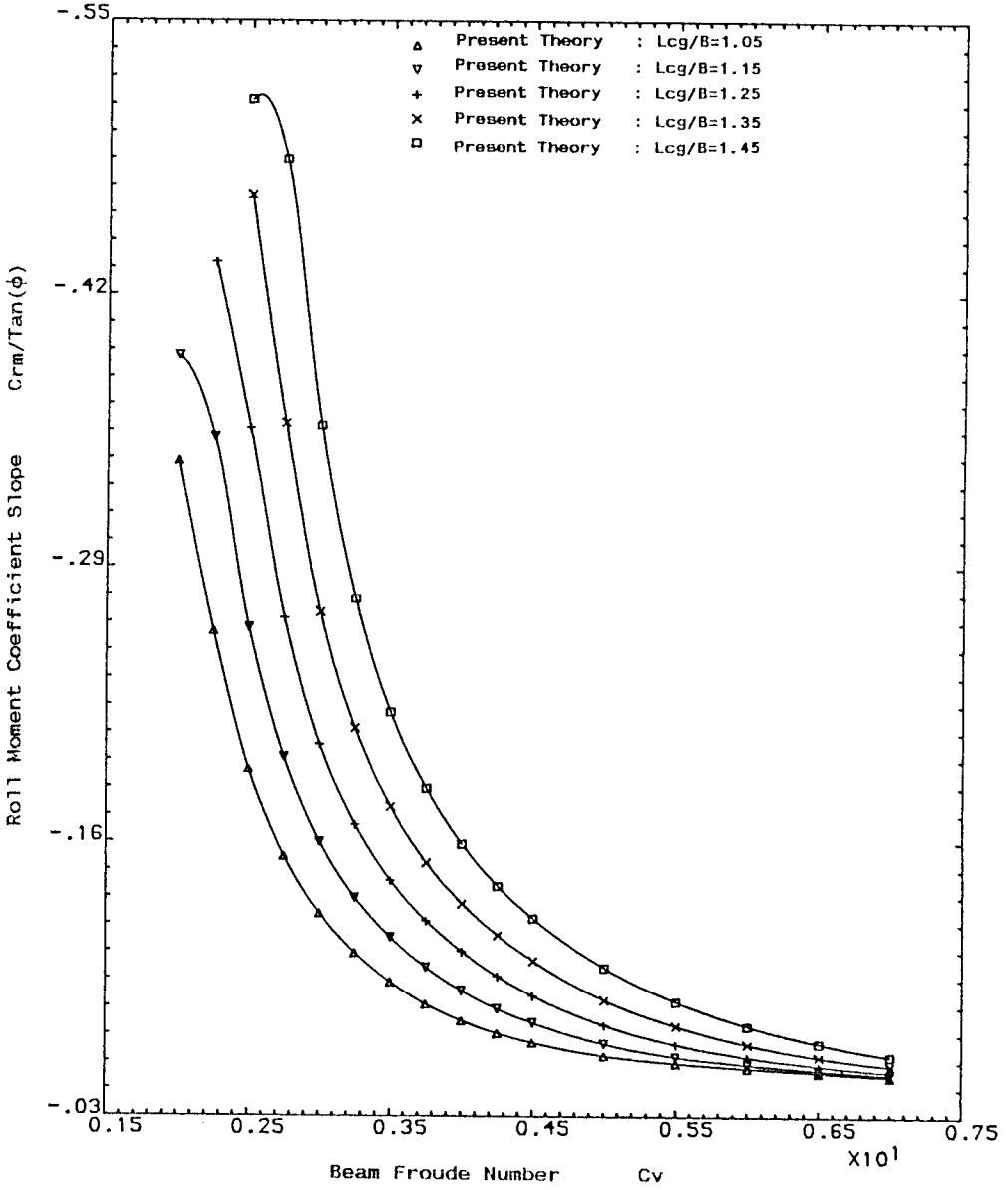

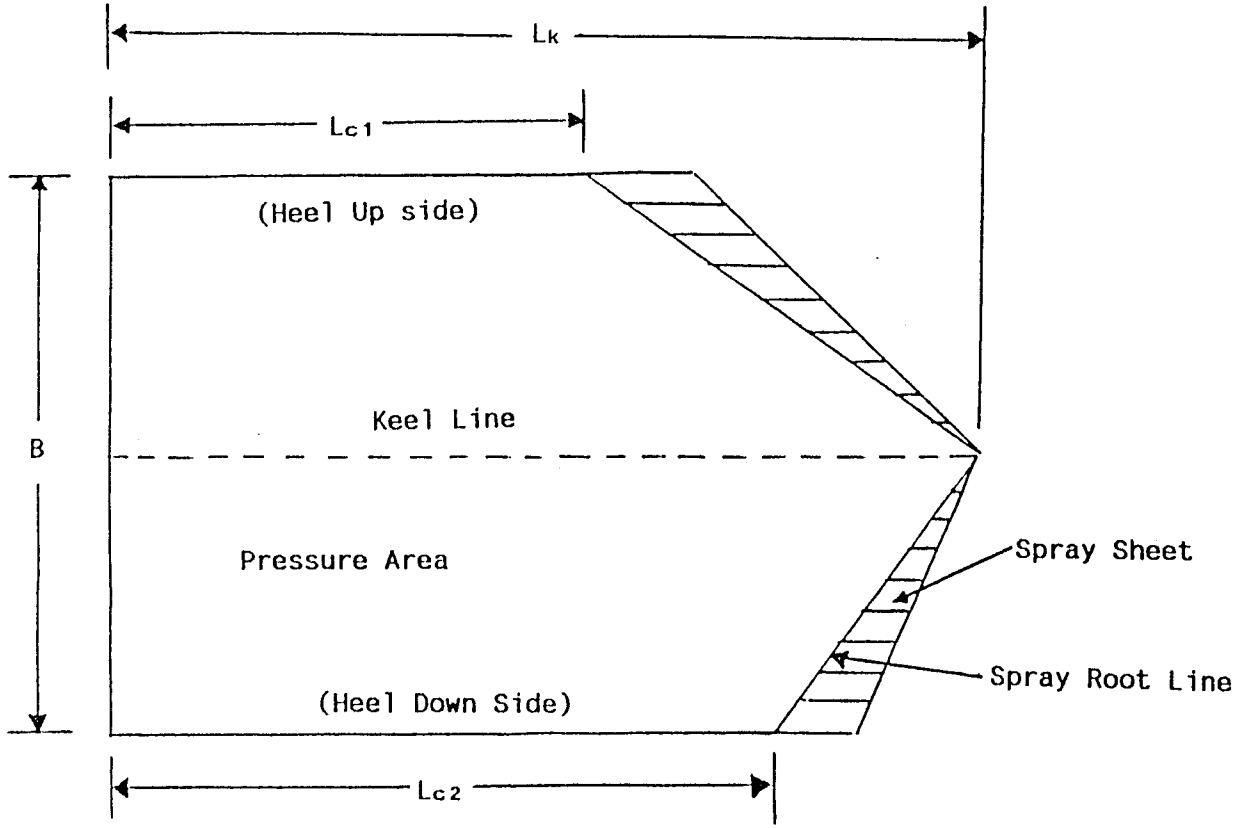

Mean Wetted Length (L_w)

$$= \frac{2L_k + L_{c1} + L_{c2}}{4}$$

Fig.(7.1) A Typical Wetted Bottom of a Planing Constant Deadrise Surface in Heel Condition

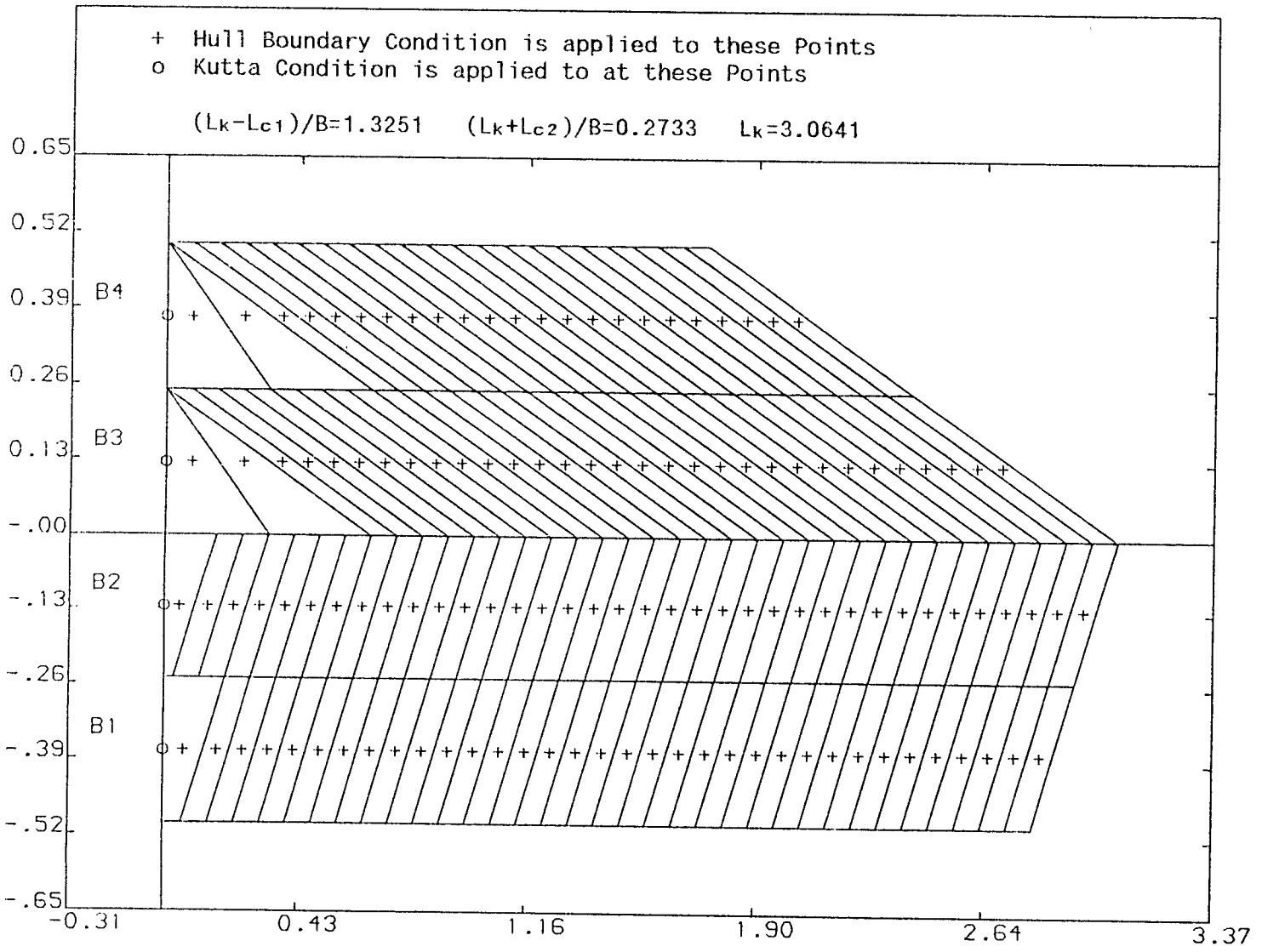

Fig.(7.2) A Typical Finite Element Mesh representing the Projected Wetted Bottom of a Planing Prismatic Surface in Heel Condition

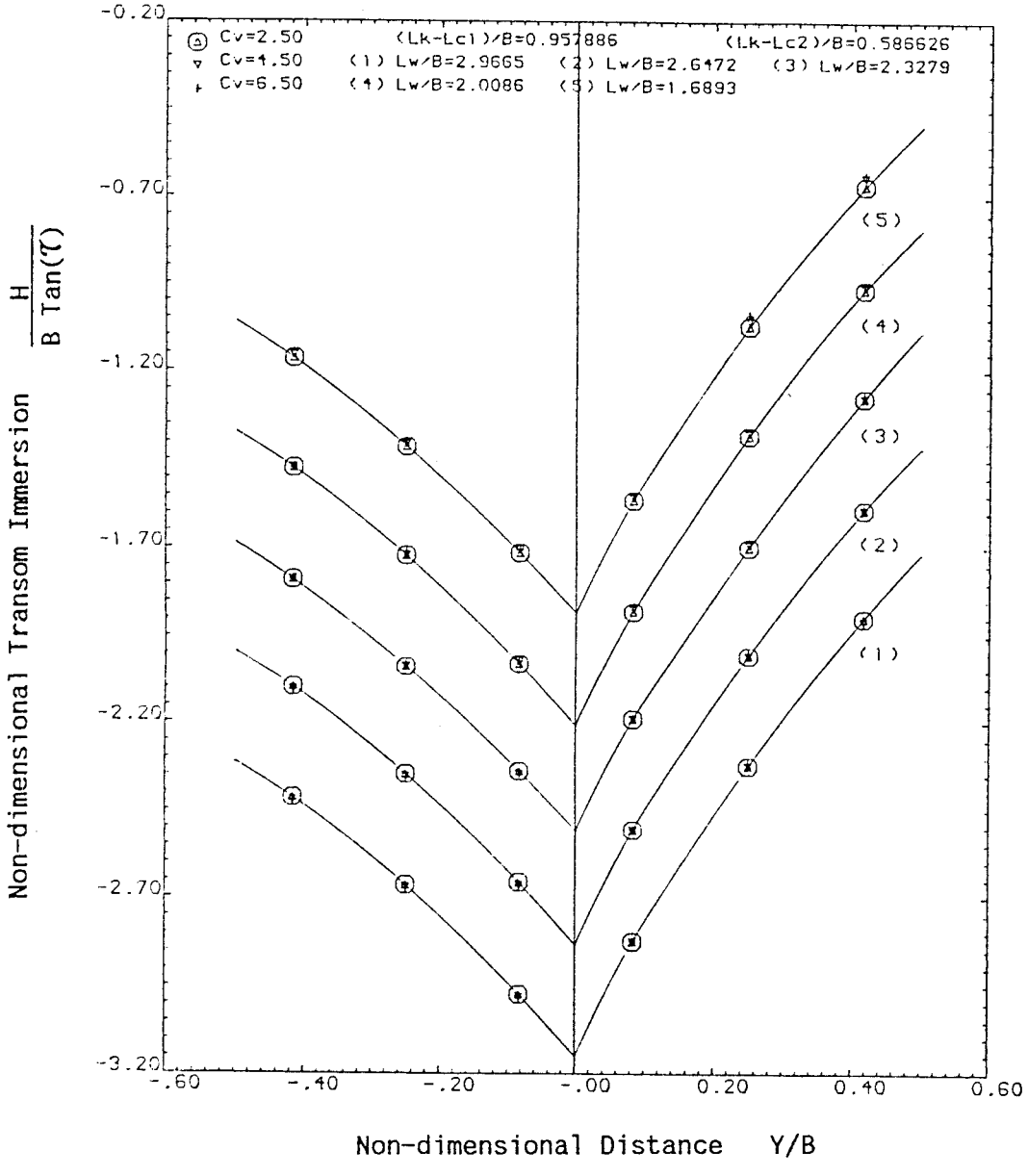

Fig.(7.3) Predicted Transom Shapes for Prismatic Surfaces in Heel

Lw/B=2.850 Deadrise=10.0 (deg.) Cv=2.50

$\frac{(l_k-l_{cf})}{B}$	$\frac{(l_k-l_{cz})}{B}$	Trim Angle in deg. (Theory)	Heel Angle in deg. (Theory)	Trim Angle in deg. (7.2.1a,b)	Heel Angle in deg. (7.2.1a,b)
1.98740	0.93157	2.457256	3.659417	2.19785	3.64937
1.62440	0.76142	3.008811	3.622634	2.68834	3.64937
1.37281	0.64349	3.565894	3.603150	3.18008	3.64937
1.18807	0.55689	4.132985	3.597324	3.67332	3.64937
1.04657	0.49057	4.707944	3.596272	4.16830	3.64937
0.93468	0.43812	5.308470	3.605770	4.66521	3.64937
0.84392	0.39558	5.908997	3.622640	5.16434	3.64937
0.76879	0.36036	6.543208	3.644588	5.66591	3.64937
0.70553	0.33071	7.177579	3.666721	6.17016	3.64937

Lw/B=2.850 Deadrise=10.0 (deg.) Cv=4.00

$\frac{(l_k-l_{cf})}{B}$	$\frac{(l_k-l_{cz})}{B}$	Trim Angle in deg. (Theory)	Heel Angle in deg. (Theory)	Trim Angle in deg. (7.2.1a,b)	Heel Angle in deg. (7.2.1a,b)
1.98740	0.93157	2.470213	3.609942	2.19785	3.64937
1.62440	0.76142	3.016822	3.600651	2.68834	3.64937
1.37281	0.64349	3.572013	3.597329	3.18008	3.64937
1.18807	0.55689	4.140812	3.600211	3.67332	3.64937
1.04657	0.49057	4.719567	3.604848	4.16830	3.64937
0.93468	0.43812	5.326207	3.616546	4.66521	3.64937
0.84392	0.39558	5.932848	3.633467	5.16434	3.64937
0.76879	0.36036	6.575138	3.655072	5.66591	3.64937
0.70553	0.33071	7.217429	3.678372	6.17016	3.64937

Lw/B=2.850 Deadrise=10.0 (deg.) Cv=6.50

$\frac{(l_k-l_{cf})}{B}$	$\frac{(l_k-l_{cz})}{B}$	Trim Angle in deg. (Theory)	Heel Angle in deg. (Theory)	Trim Angle in deg. (7.2.1a,b)	Heel Angle in deg. (7.2.1a,b)
1.98740	0.93157	2.436660	3.639122	2.19785	3.64937
1.62440	0.76142	2.980750	3.632275	2.68834	3.64937
1.37281	0.64349	3.536662	3.627457	3.18008	3.64937
1.18807	0.55689	4.106822	3.626653	3.67332	3.64937
1.04657	0.49057	4.687636	3.628258	4.16830	3.64937
0.93468	0.43812	5.296938	3.635673	4.66521	3.64937
0.84392	0.39558	5.906241	3.652204	5.16434	3.64937

Lw/B=1.800 Deadrise=10.0 (deg.) Cv=2.50

$\frac{(l_k-l_{cf})}{B}$	$\frac{(l_k-l_{cz})}{B}$	Trim Angle in deg. (Theory)	Heel Angle in deg. (Theory)	Trim Angle in deg. (7.2.1a,b)	Heel Angle in deg. (7.2.1a,b)
1.98740	0.93157	2.517780	3.579469	2.19785	3.64937
1.62440	0.76142	3.077517	3.557205	2.68834	3.64937
1.37281	0.64349	3.641351	3.550167	3.18008	3.64937
1.18807	0.55689	4.214999	3.553603	3.67332	3.64937
1.04657	0.49057	4.797727	3.560126	4.16830	3.64937
0.93468	0.43812	5.405682	3.574243	4.66521	3.64937
0.84392	0.39558	6.013637	3.593678	5.16434	3.64937
0.76879	0.36036	6.656134	3.617585	5.66591	3.64937
0.70553	0.33071	7.298632	3.642428	6.17016	3.64937

Lw/B=1.800 Deadrise=10.0 (deg.) Cv=4.00

$\frac{(l_k-l_{cf})}{B}$	$\frac{(l_k-l_{cz})}{B}$	Trim Angle in deg. (Theory)	Heel Angle in deg. (Theory)	Trim Angle in deg. (7.2.1a,b)	Heel Angle in deg. (7.2.1a,b)
1.98740	0.93157	2.487553	3.588668	2.19785	3.64937
1.62440	0.76142	3.041281	3.577631	2.68834	3.64937
1.37281	0.64349	3.597618	3.579081	3.18008	3.64937
1.18807	0.55689	4.166968	3.585934	3.67332	3.64937
1.04657	0.49057	4.746594	3.593316	4.16830	3.64937
0.93468	0.43812	5.354512	3.606972	4.66521	3.64937
0.84392	0.39558	5.962429	3.625170	5.16434	3.64937
0.76879	0.36036	6.606367	3.647689	5.66591	3.64937
0.70553	0.33071	7.250305	3.671753	6.17016	3.64937

Lw/B=1.800 Deadrise=10.0 (deg.) Cv=6.50

$\frac{(l_k-l_{cf})}{B}$	$\frac{(l_k-l_{cz})}{B}$	Trim Angle in deg. (Theory)	Heel Angle in deg. (Theory)	Trim Angle in deg. (7.2.1a,b)	Heel Angle in deg. (7.2.1a,b)
1.98740	0.93157	2.426813	3.663376	2.19785	3.64937
1.62440	0.76142	2.982182	3.633213	2.68834	3.64937
1.37281	0.64349	3.541129	3.624787	3.18008	3.64937
1.18807	0.55689	4.112259	3.623806	3.67332	3.64937
1.04657	0.49057	4.693592	3.625713	4.16830	3.64937
0.93468	0.43812	5.303247	3.633575	4.66521	3.64937
0.84392	0.39558	5.912901	3.650276	5.16434	3.64937

Table (7.1) Comparision of computed Heel and Trim Angles with expressions

(7.2.1a) and (7.2.1b) for a 10° constant deadrise surface

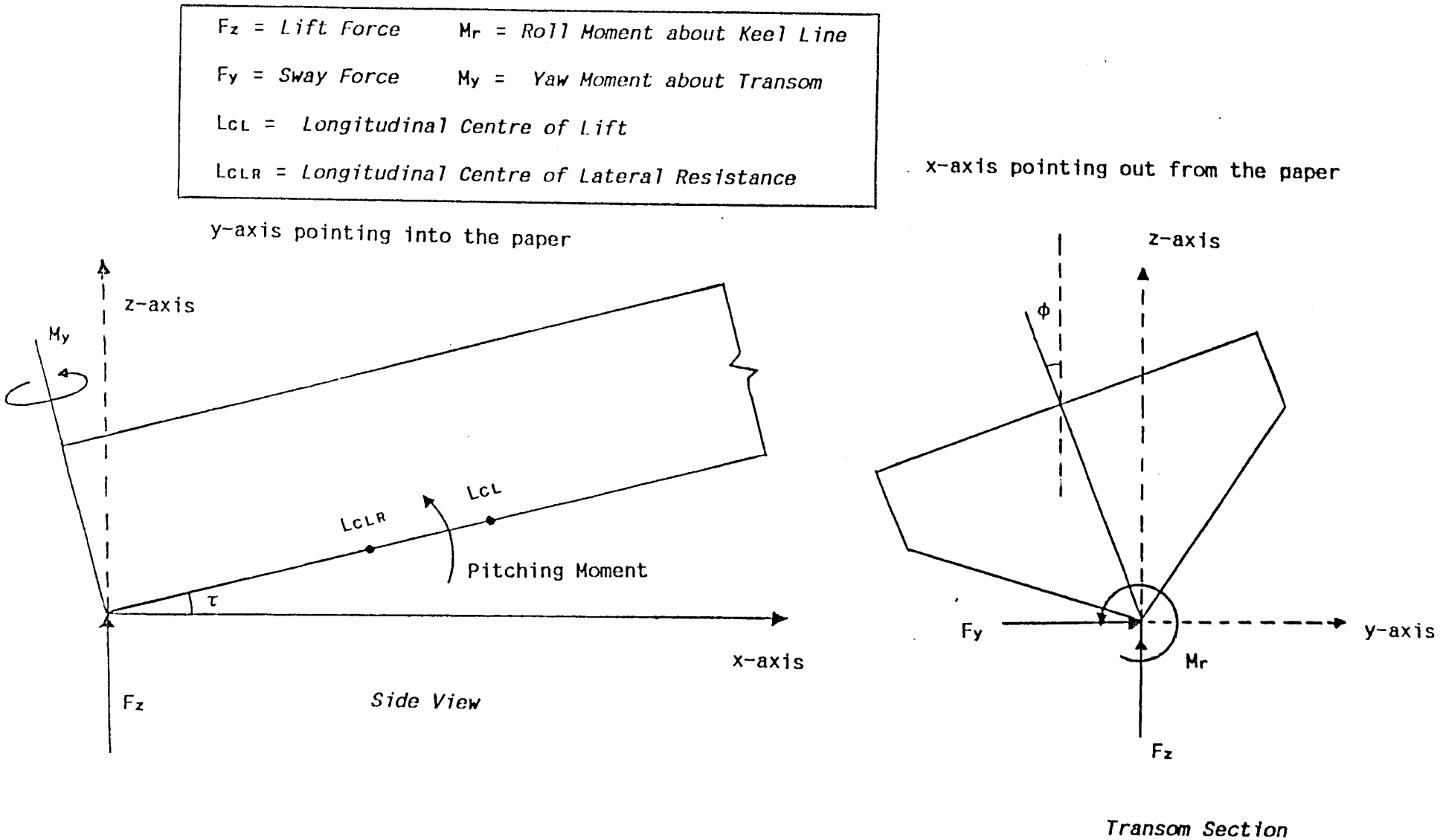

Fig.(7.4) Sign Conventions for the Forces and Moments of a Constant Deadrise Surface in Heel

Fig.(7.5a) Lift Coefficient Slopes for Heeled 15° Constant Deadrise Hull

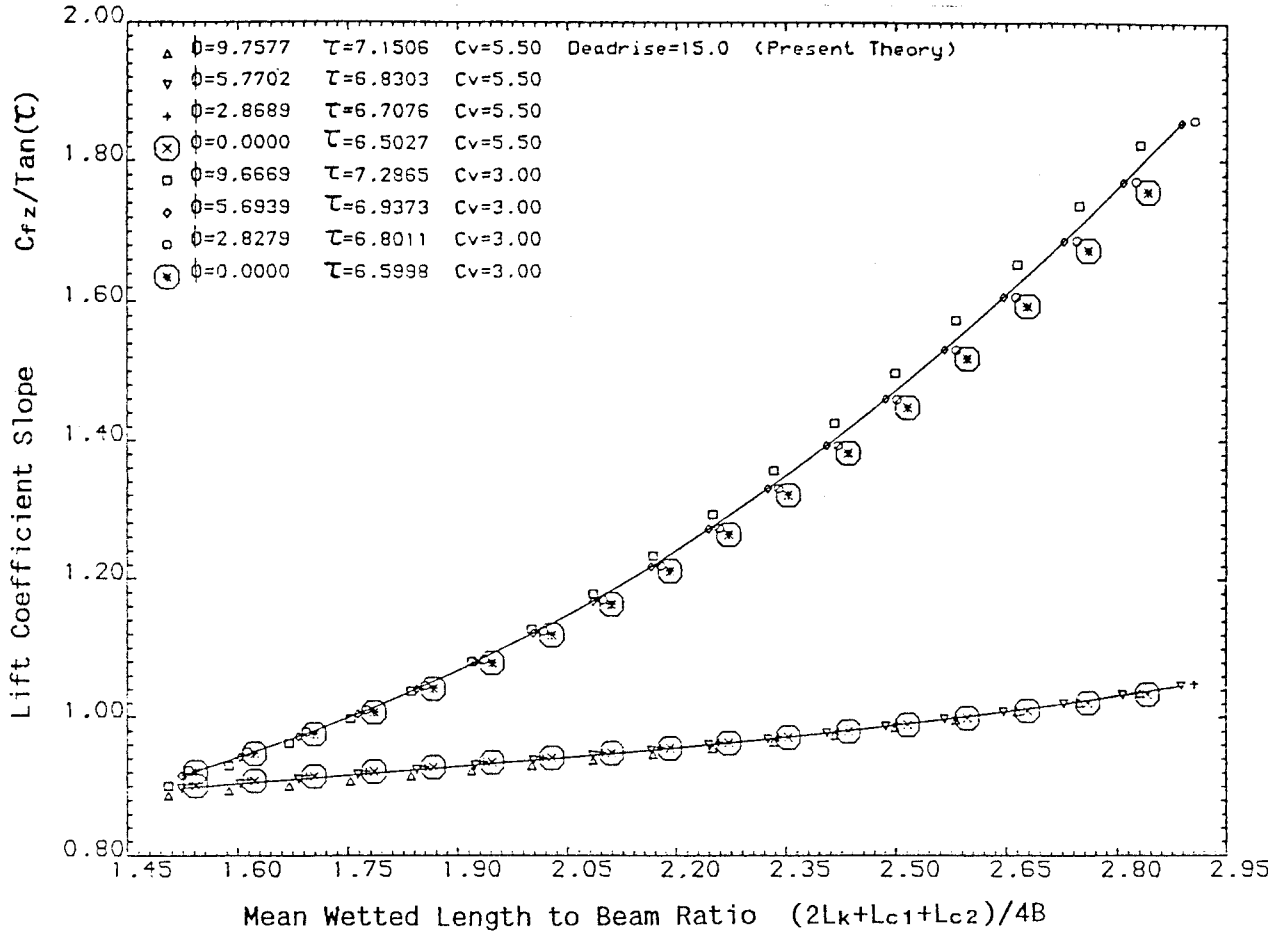

Fig.(7.5b) Centre of Lift Ratios for Heeled 15° Constant Deadrise Hull

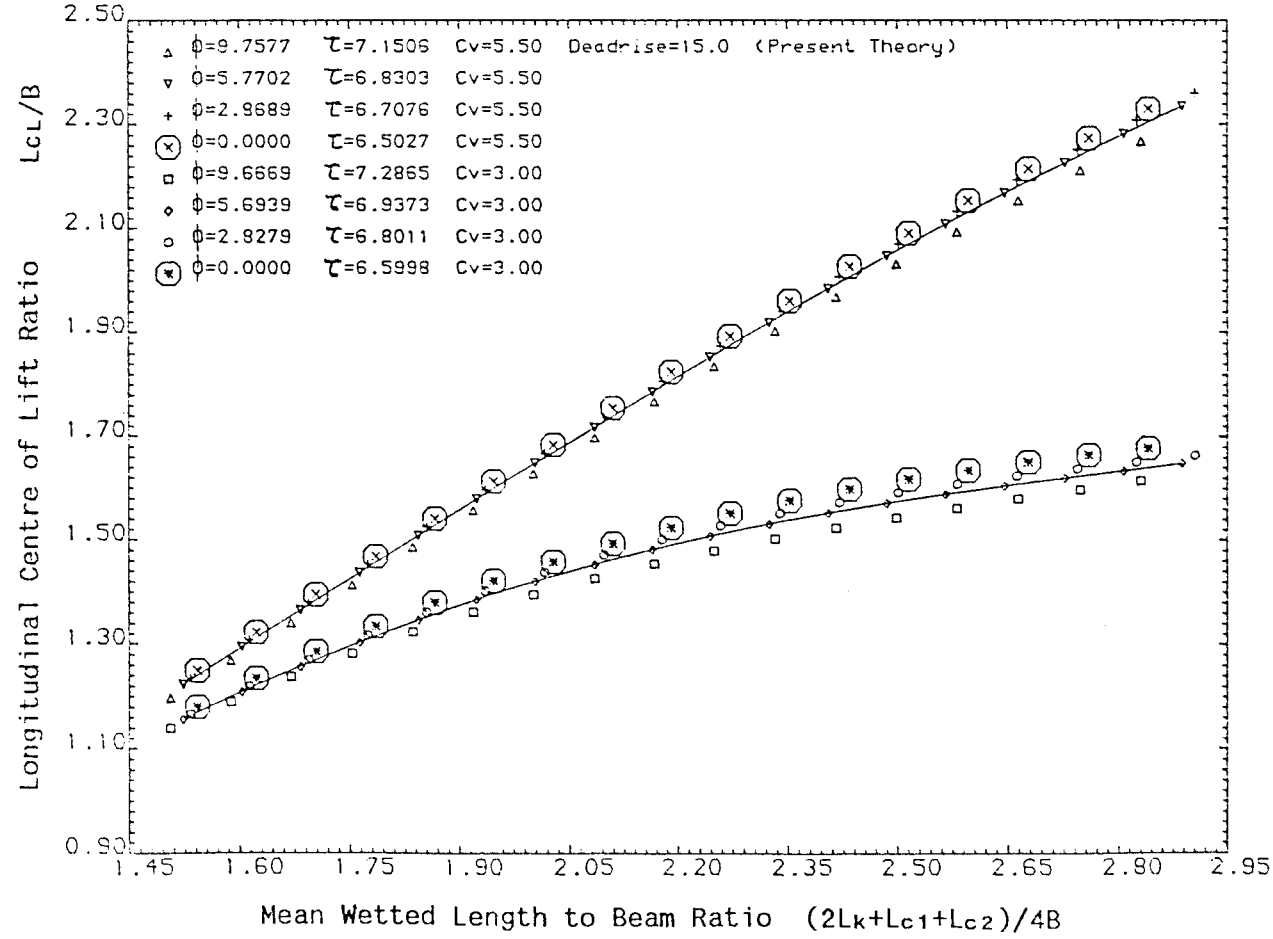

Fig.(7.5c) Roll Moment Coefficient Slopes for Heeled 15° Constant Deadrise Hull

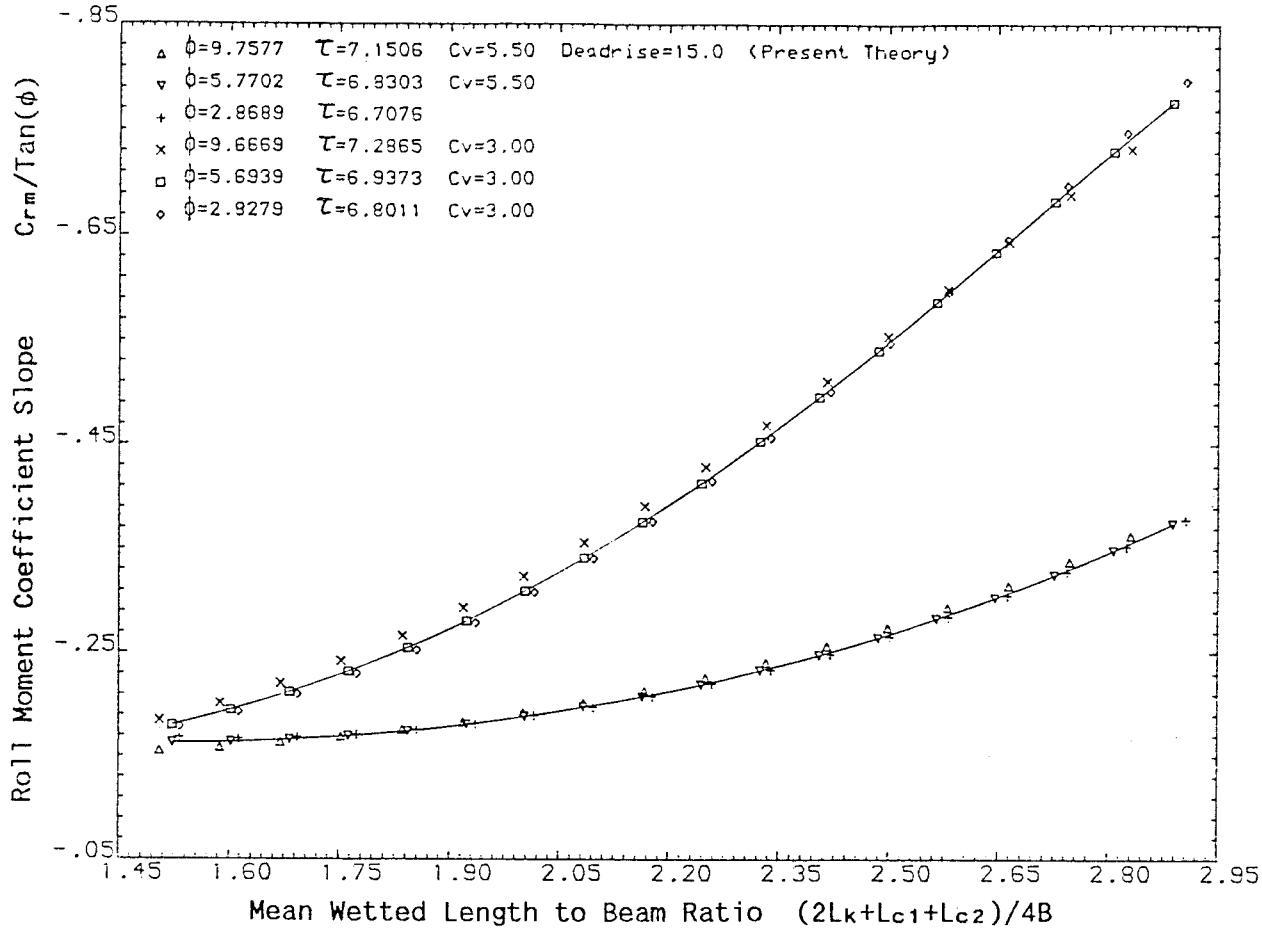

Fig.(7.5d) Righting Moment Arm Ratios for Heeled 15° Constant Deadrise Hull

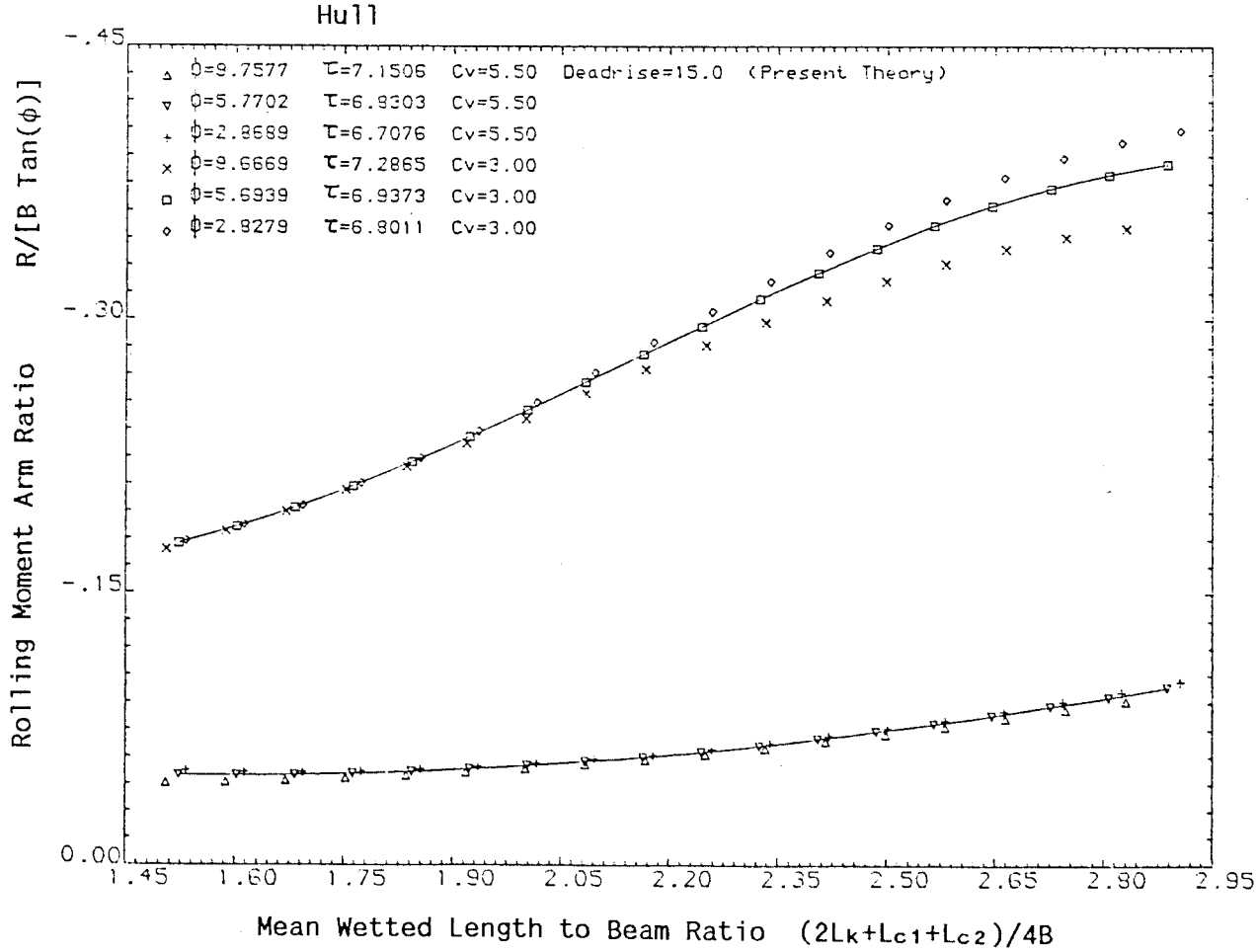

Fig.(7.5e) Sway Force Coefficient Slopes for Heeled 15° Constant Deadrise Hull

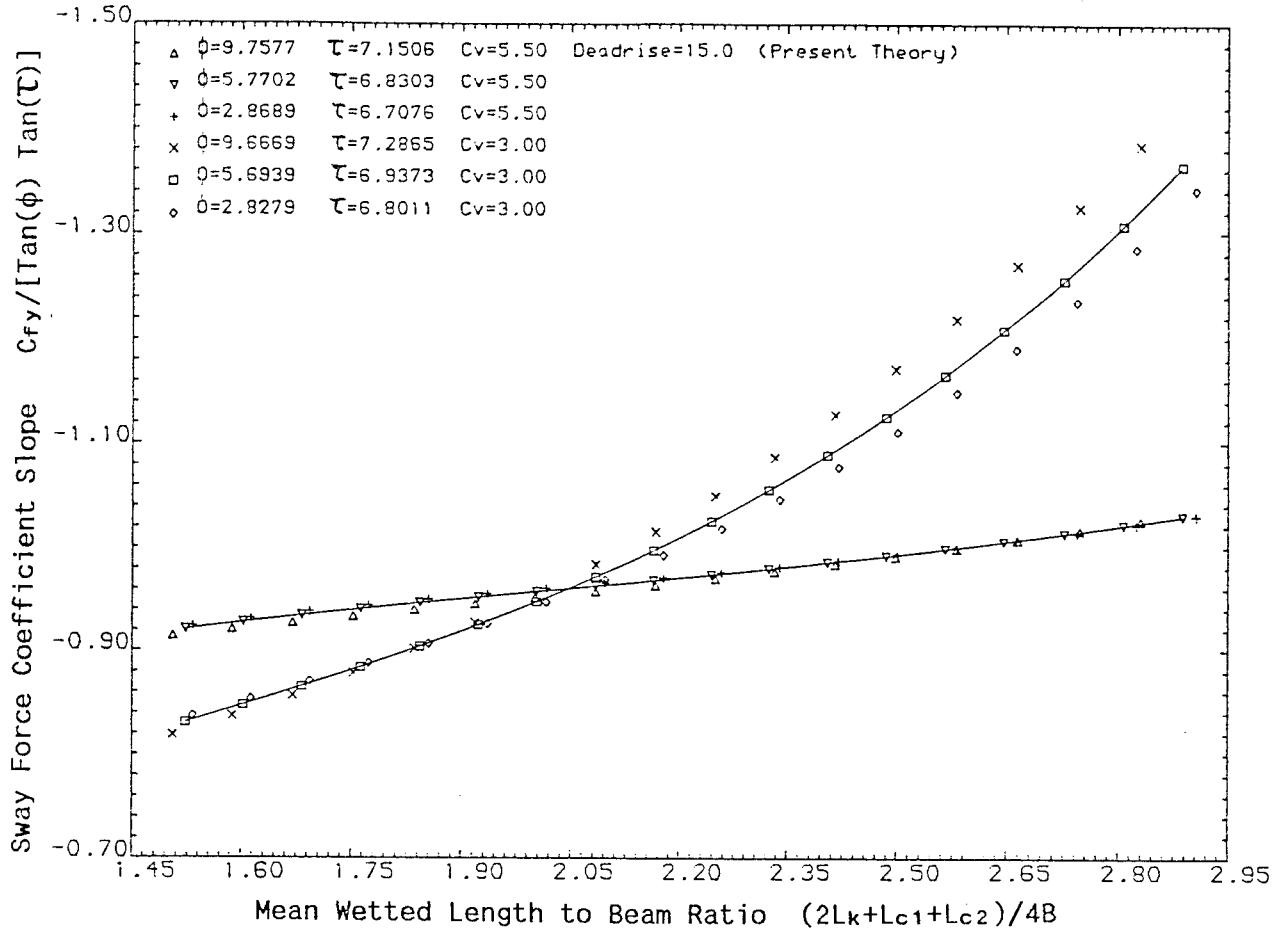

Fig.(7.5f) Yaw Moment Coefficient Slopes for Heeled 15° Constant Deadrise Hull

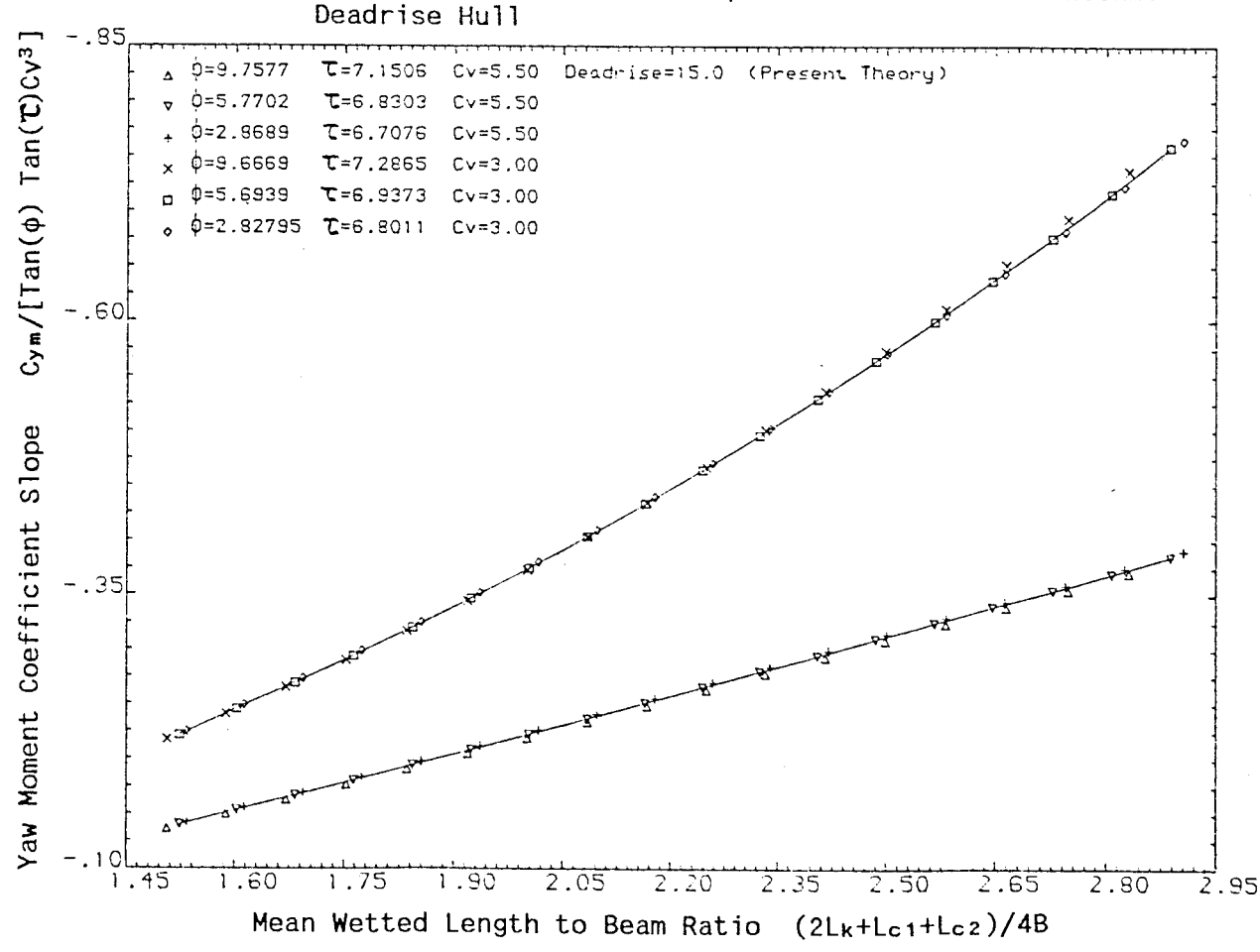

Fig.(7.5g) Centre of Lateral Resistance Ratios for Heeled 15° Constant Deadrise Hull

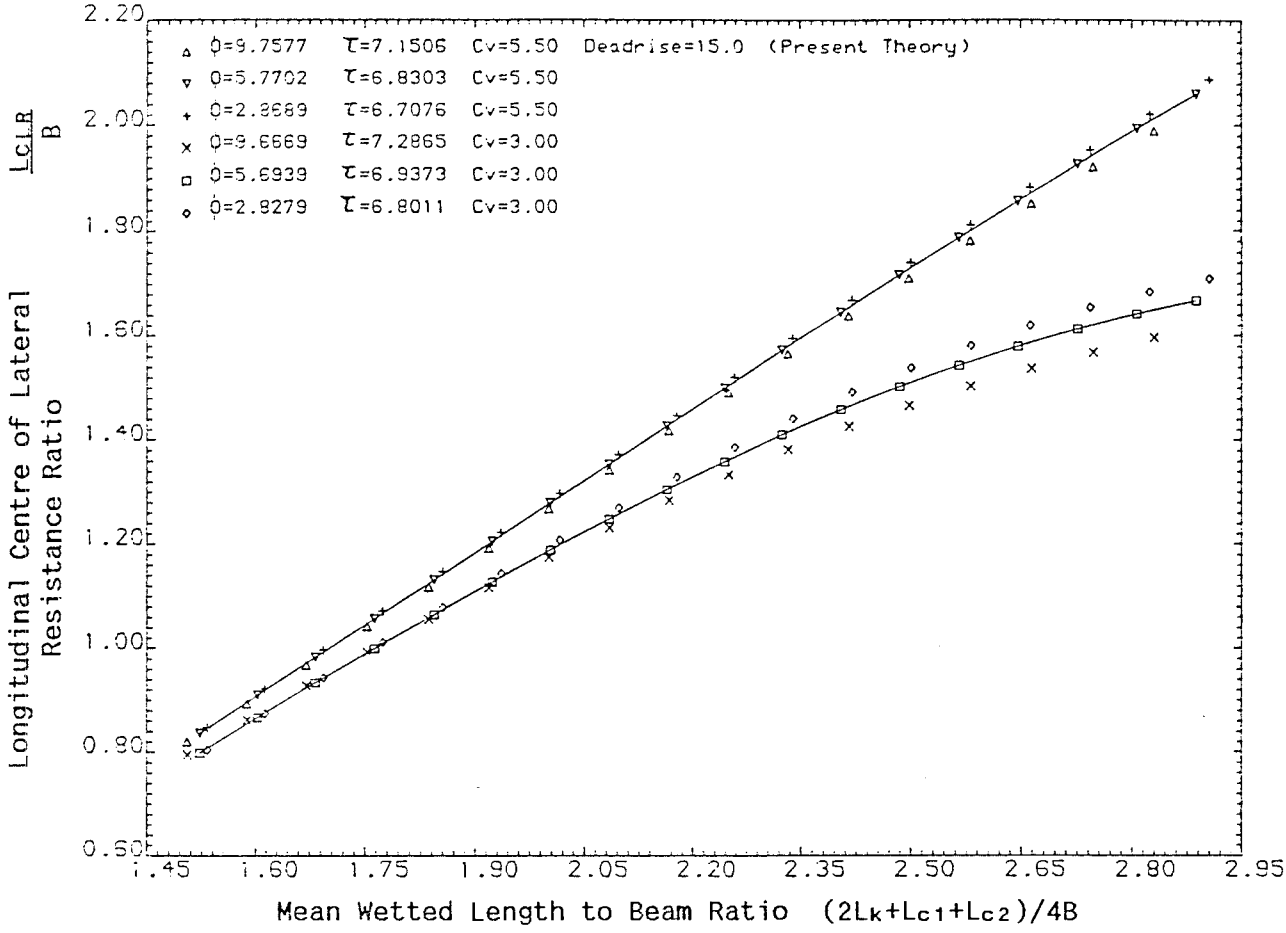

Fig.(7.5h) $(L_{CLR}-L_{CL})/B$ for Heeled 15° Constant Deadrise Hull

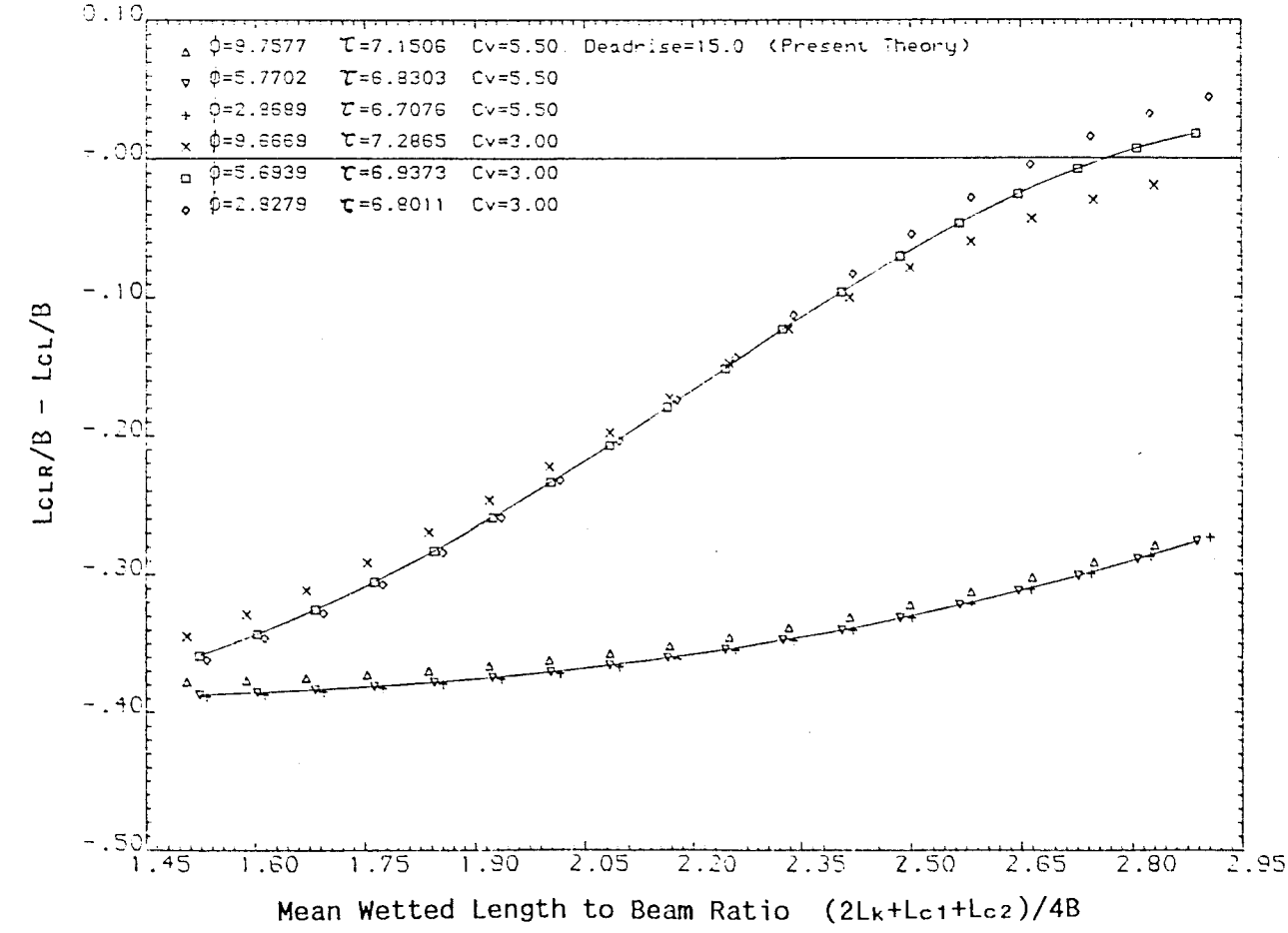

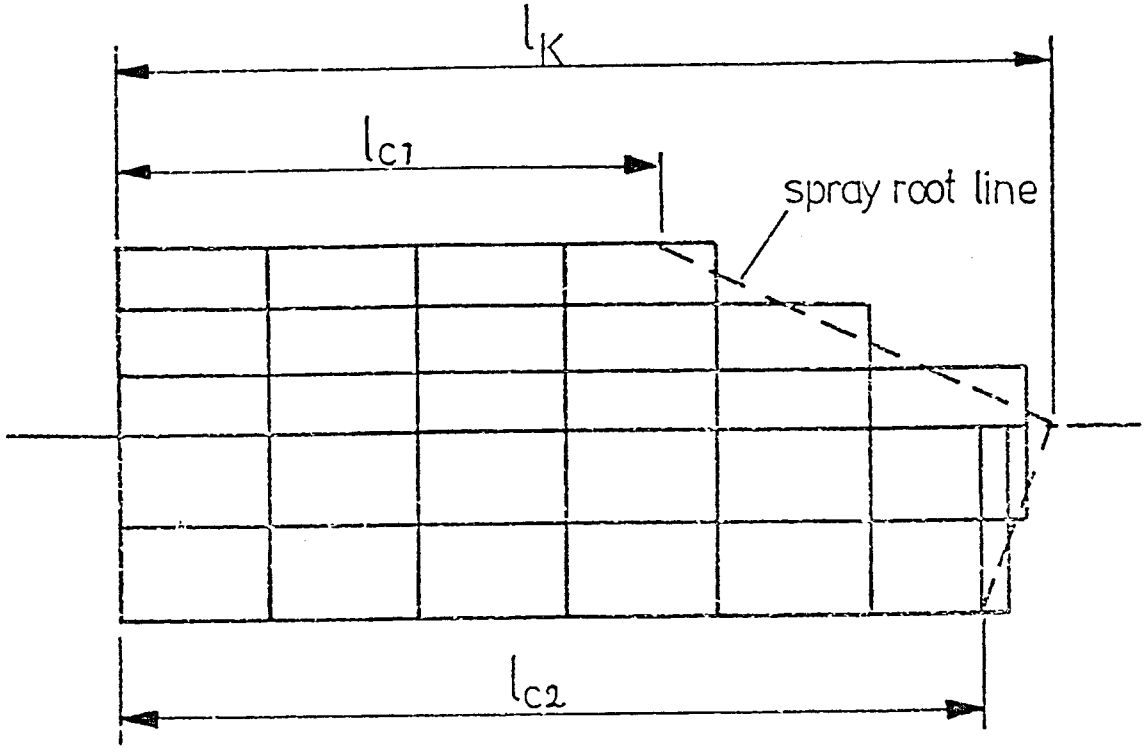

Fig.(7.6) The Wetted Bottom Grid used by Jahangeer (Ref.(66)) with an Asymmetrical Buttocks Layout

Fig.(7.7a) Comparison of Lift Coefficient Slopes with Jahangeer's Results for Heeled 15° Constant Deadrise Hull

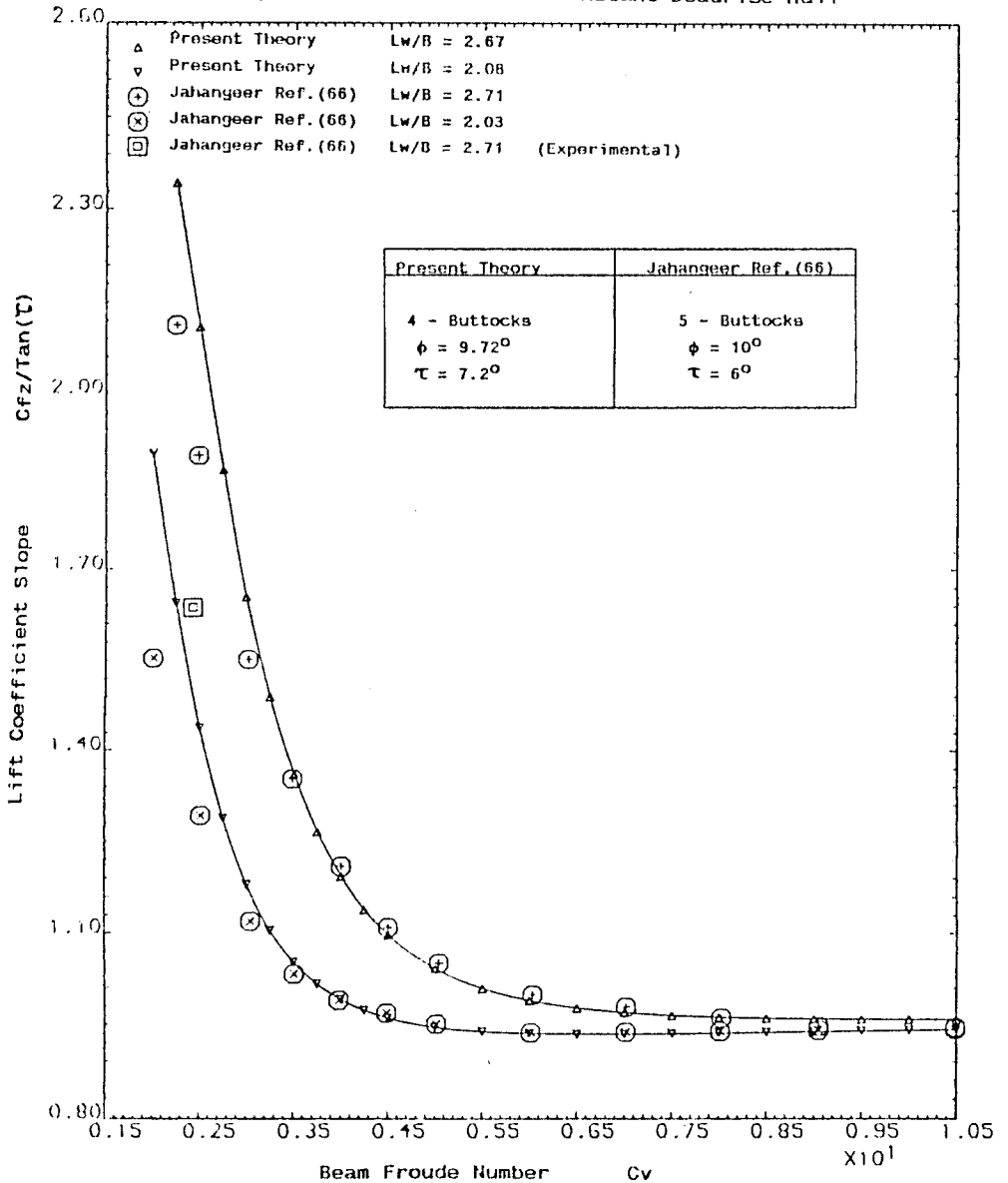

Fig.(7.7b) Comparison of Centre of Lift Ratios with Jahangeer's Results for Heeled 15° Constant Deadrise Hull

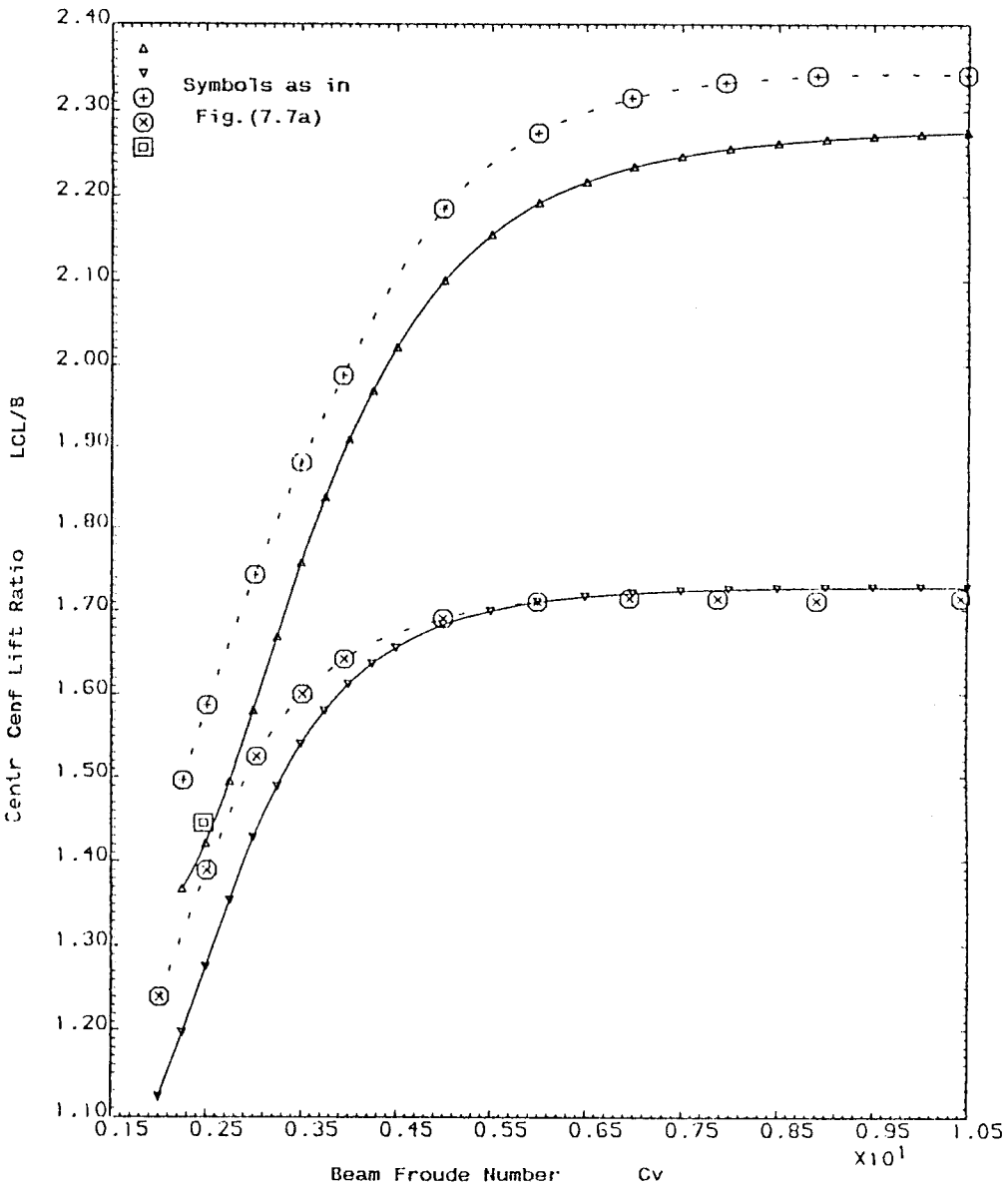

Fig.(7.7c) Comparison of Roll Moment Coefficient Slopes with Jahangeer's Results for Heeled 15° Constant Deadrise Hull

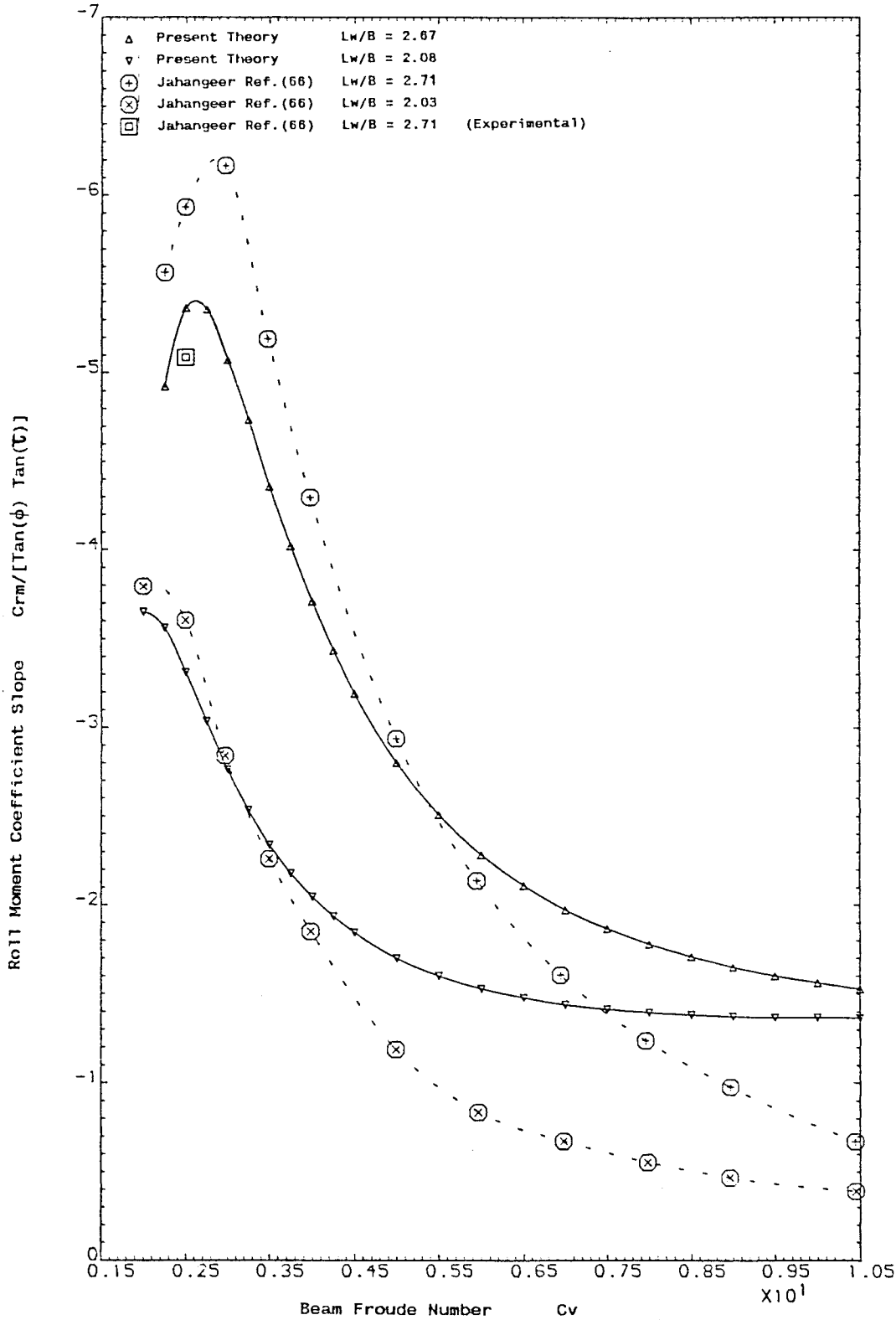

Fig.(7.7d) Comparison of Roll Moment Arm Ratios with Jahangeer's Results for Heeled 15° Constant Deadrise Hull

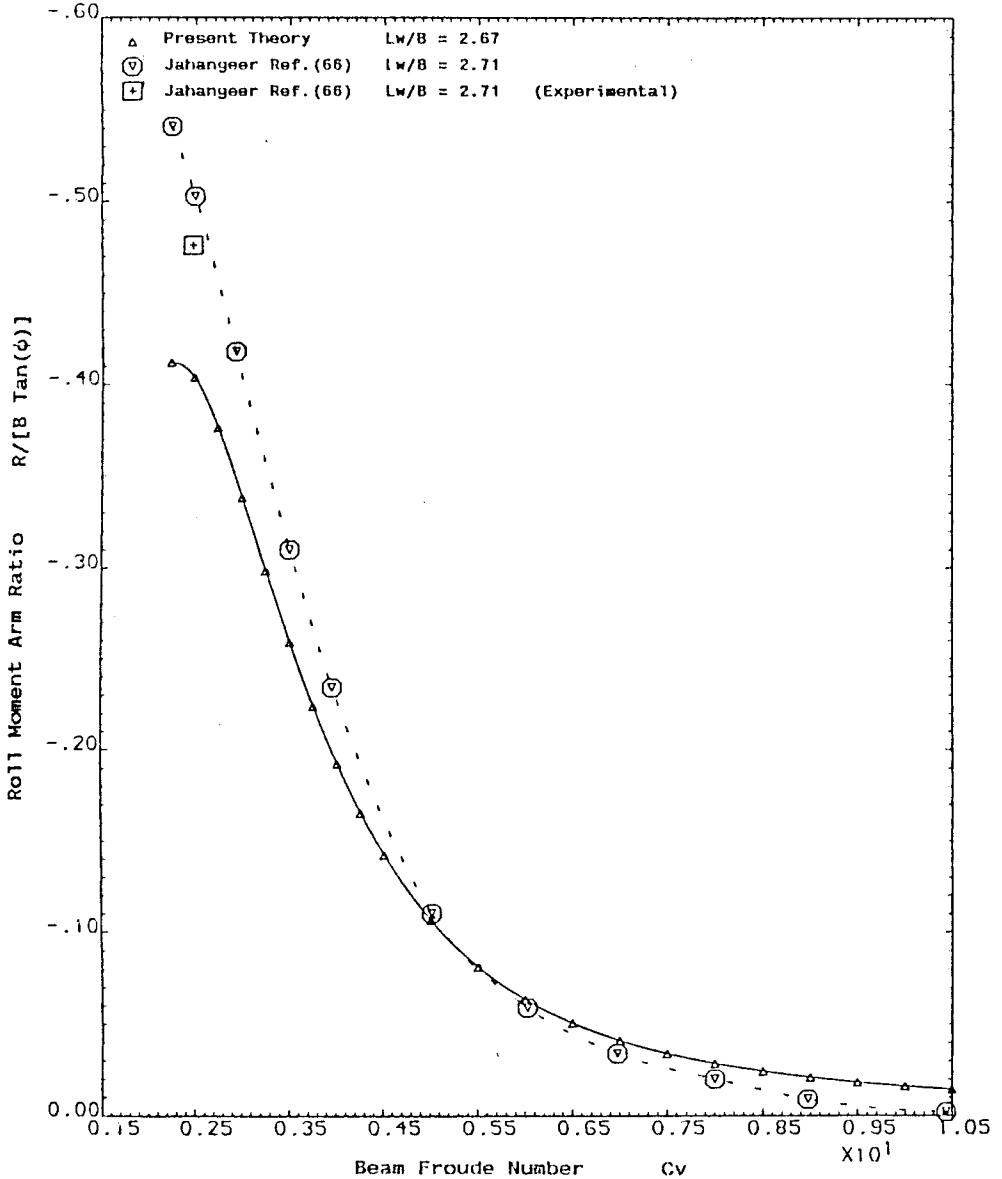

Fig.(7.7d) Comparison of Roll Moment Arm Ratios with Jahangeer's Results for Heeled 15° Constant Deadrise Hull

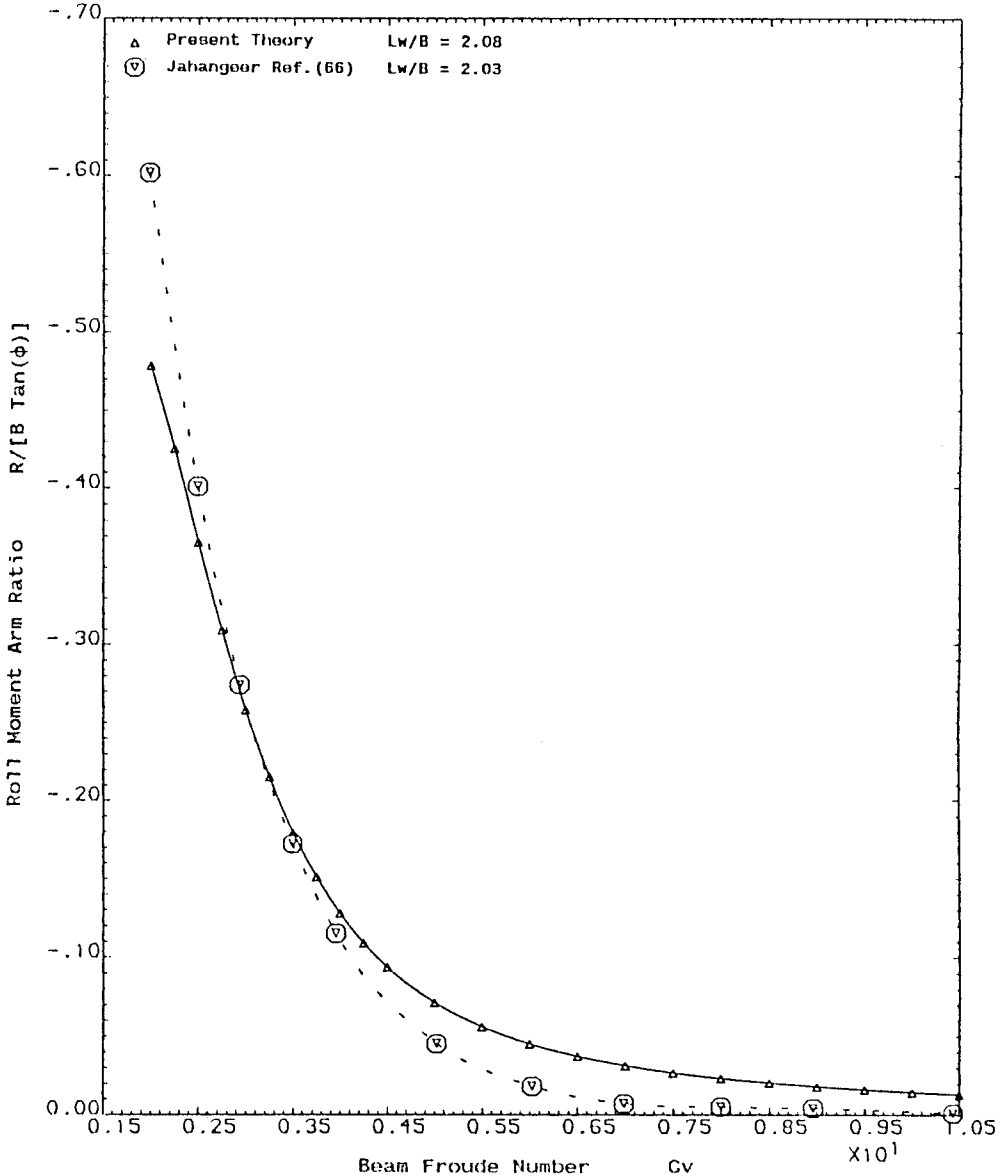

Fig.(7.7e) Variation of Sway Force Coefficient Slope against Beam Froude Number for 15° Constant Deadrise Hull

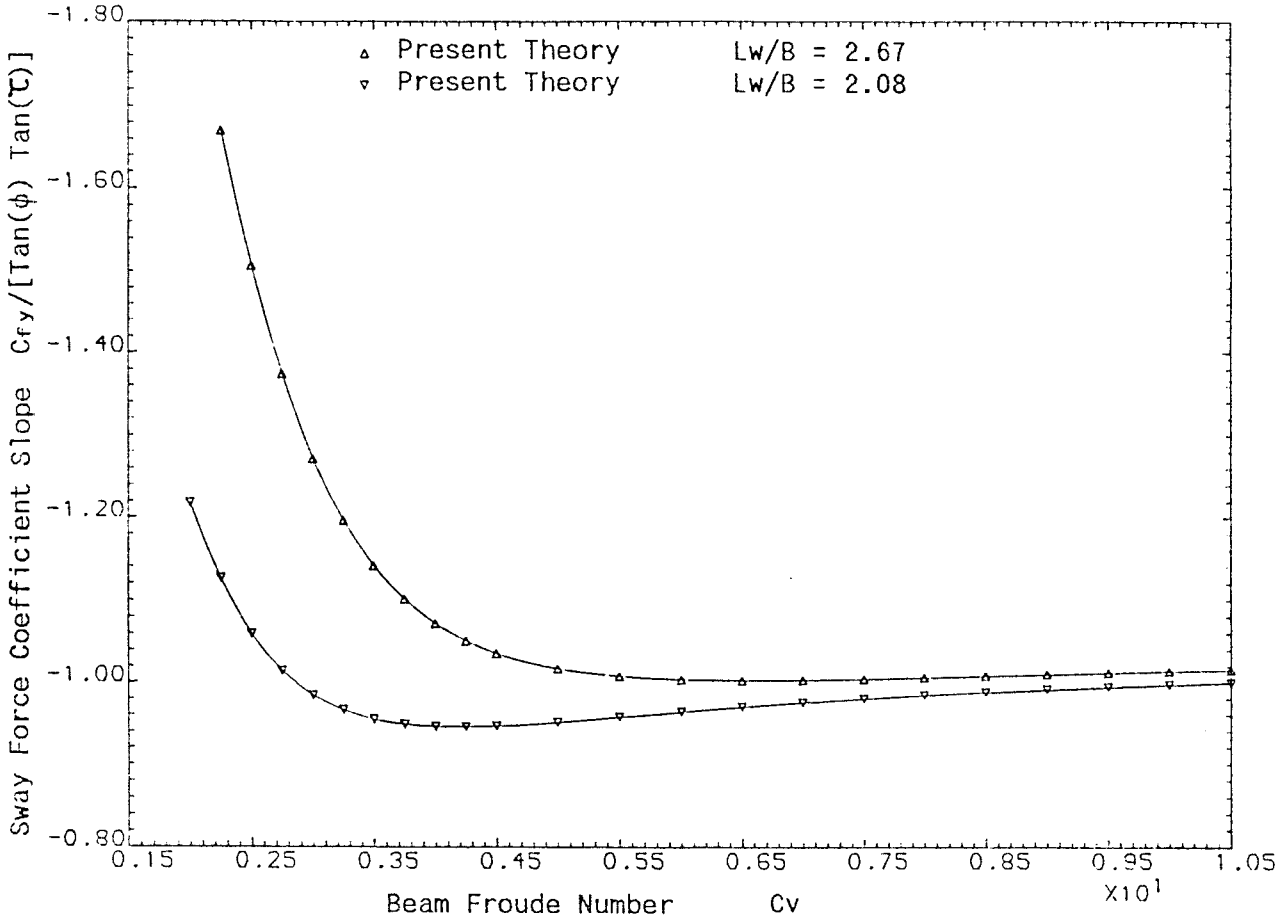

Fig.(7.7f) Variation of Yaw Moment Coefficient Slope (About Transom) against Beam Froude Number for 15° Constant Deadrise Hull

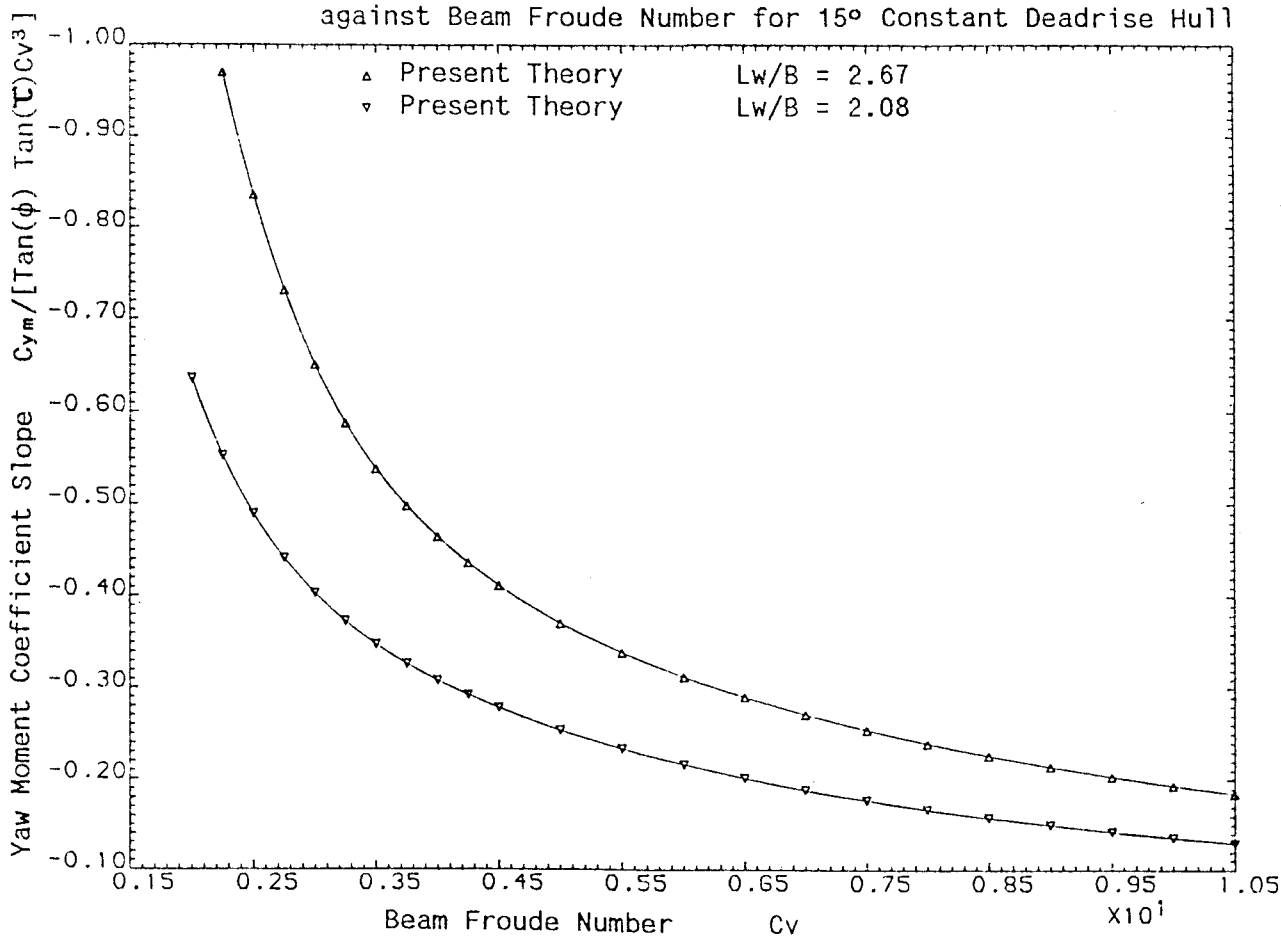

Fig.(7.7g) Variation of Longitudinal Centre of Lateral Resistance Ratio against Beam Froude Number for 15^{O} Constant Deadrise Hull

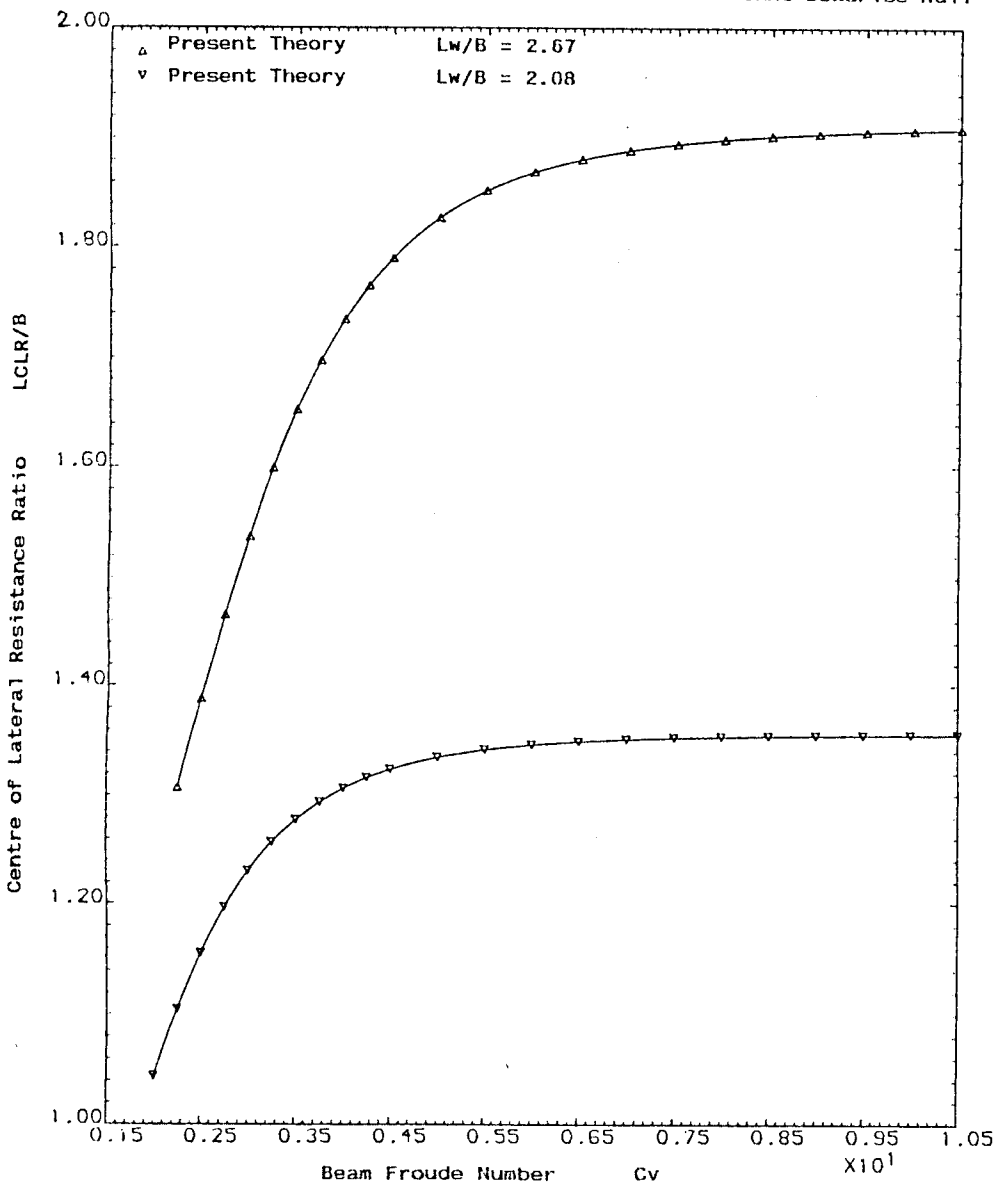

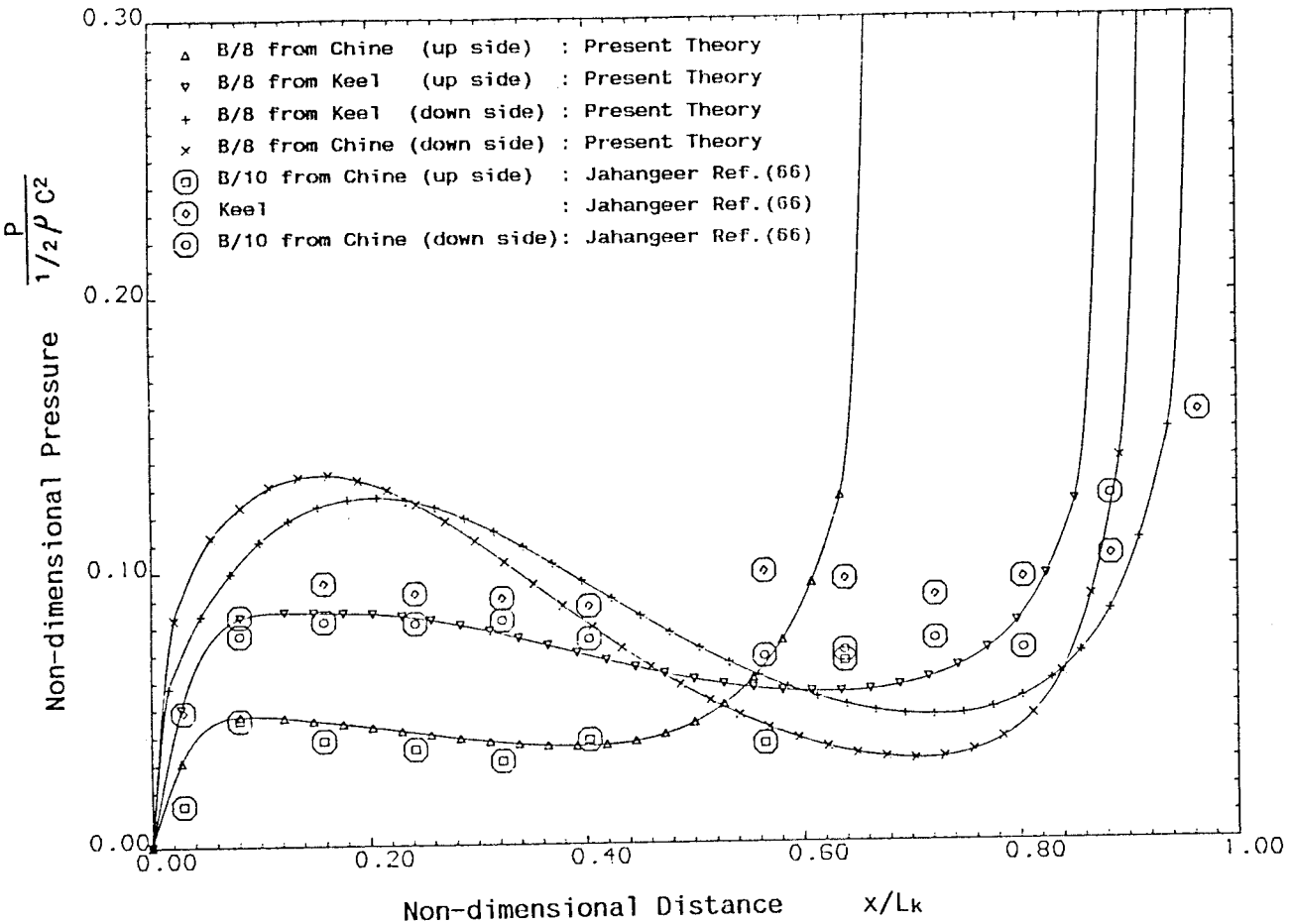

C_V = 2.54 Trim Angle = 6°

Heel Angle = 10° Deadrise Angle = 15°

L_W/B = 2.665

$\frac{L_k - L_{c1}}{B}$ = 1.325 $\frac{L_k - L_{c2}}{B}$ = 0.2733

Fig.(7.8) Comparison of Pressure Distribution with Experimental Measurements of Jahangeer for a 15° Constant Deadrise Hull in Heel Condition

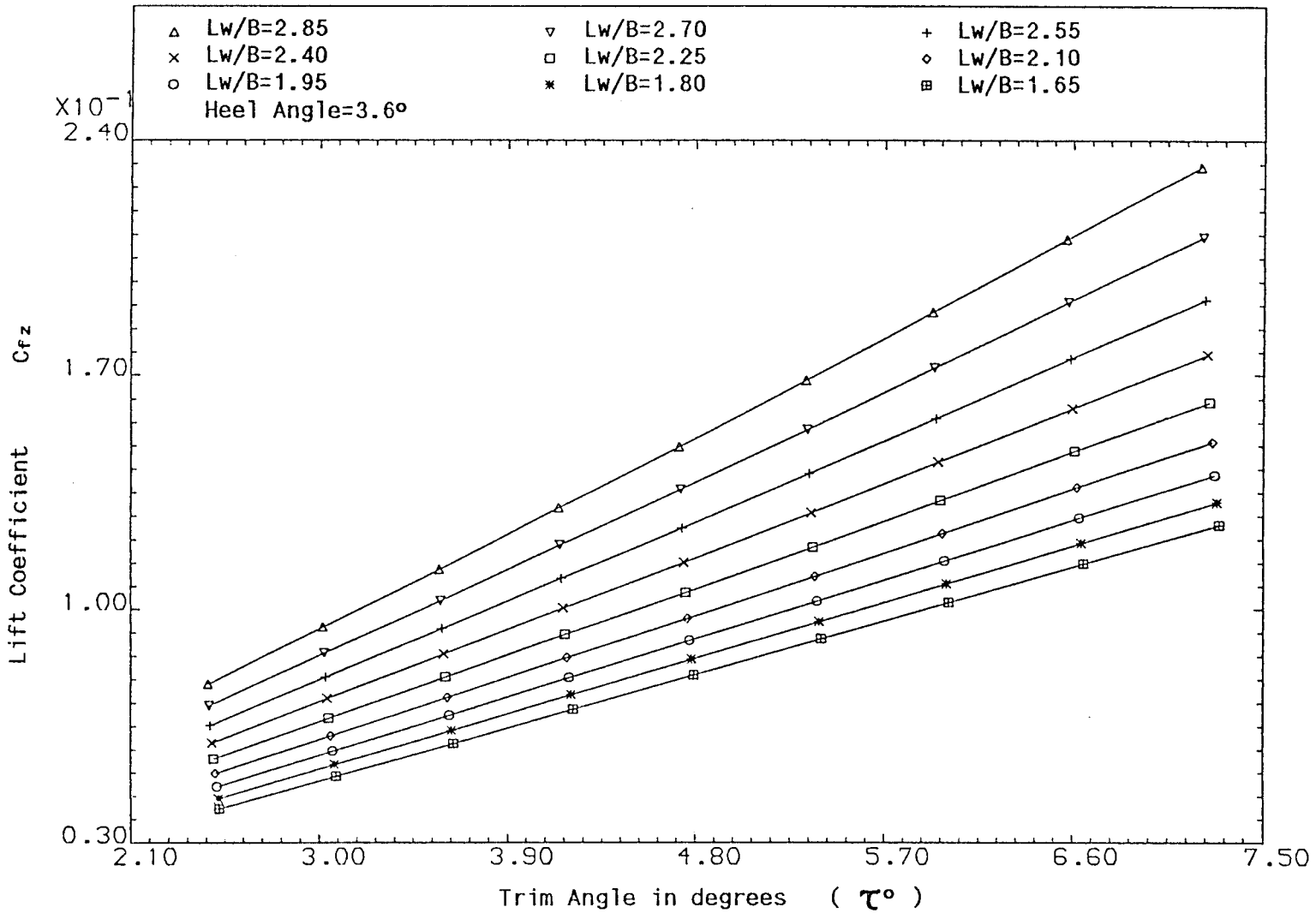

Fig.(7.9.1a) Computed Lift Coefficient as a function of Trim Angle and Mean Lw/B Ratio for 10° Constant Deadrise Hull in Heel Condition (Cv=3.0)

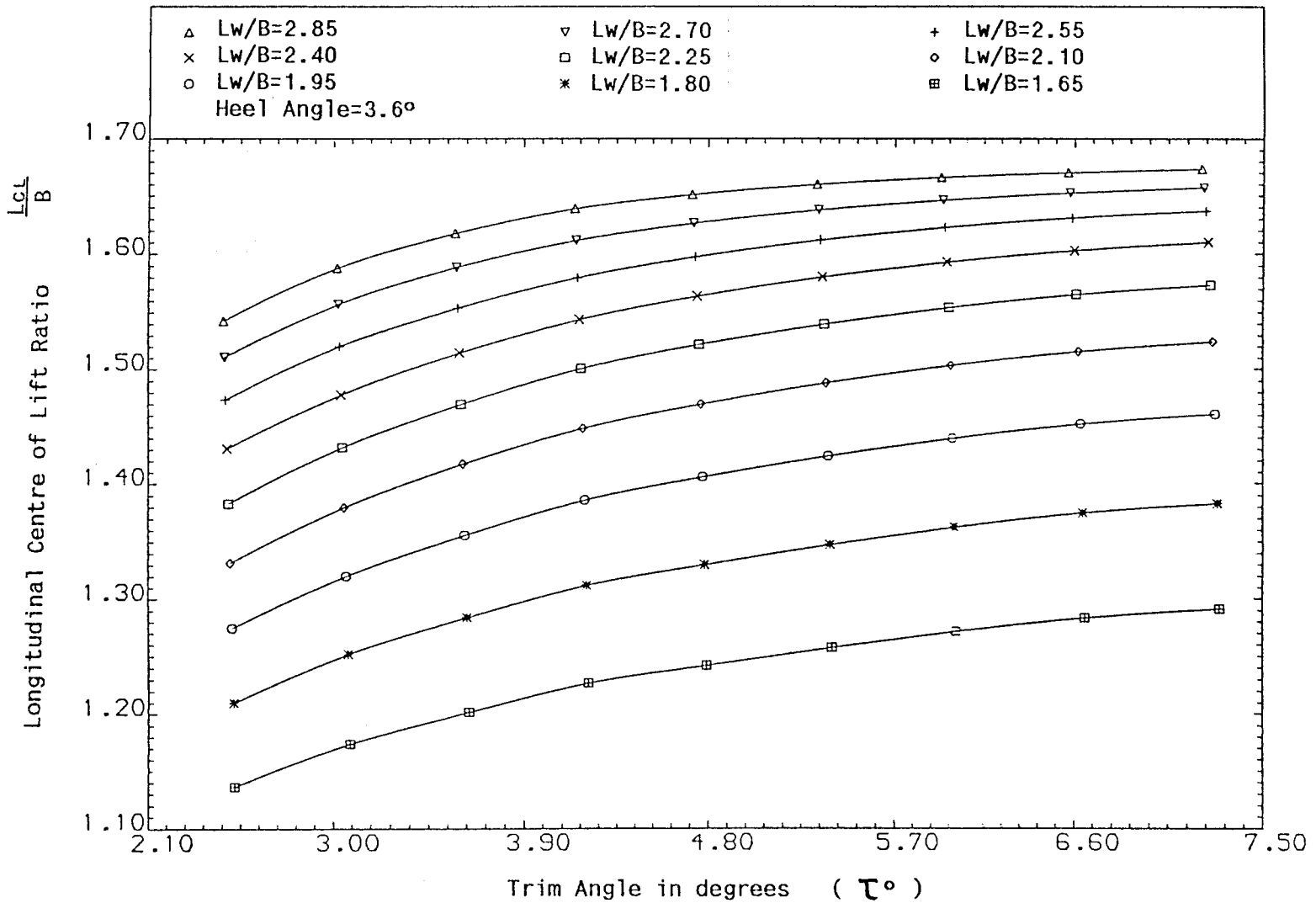

Fig.(7.9.1b) Computed Centre of Lift Ratio as a function of Trim Angle and Mean Lw/B Ratio for 10° Constant Deadrise Hull in Heel Condition (Cv=3.0)

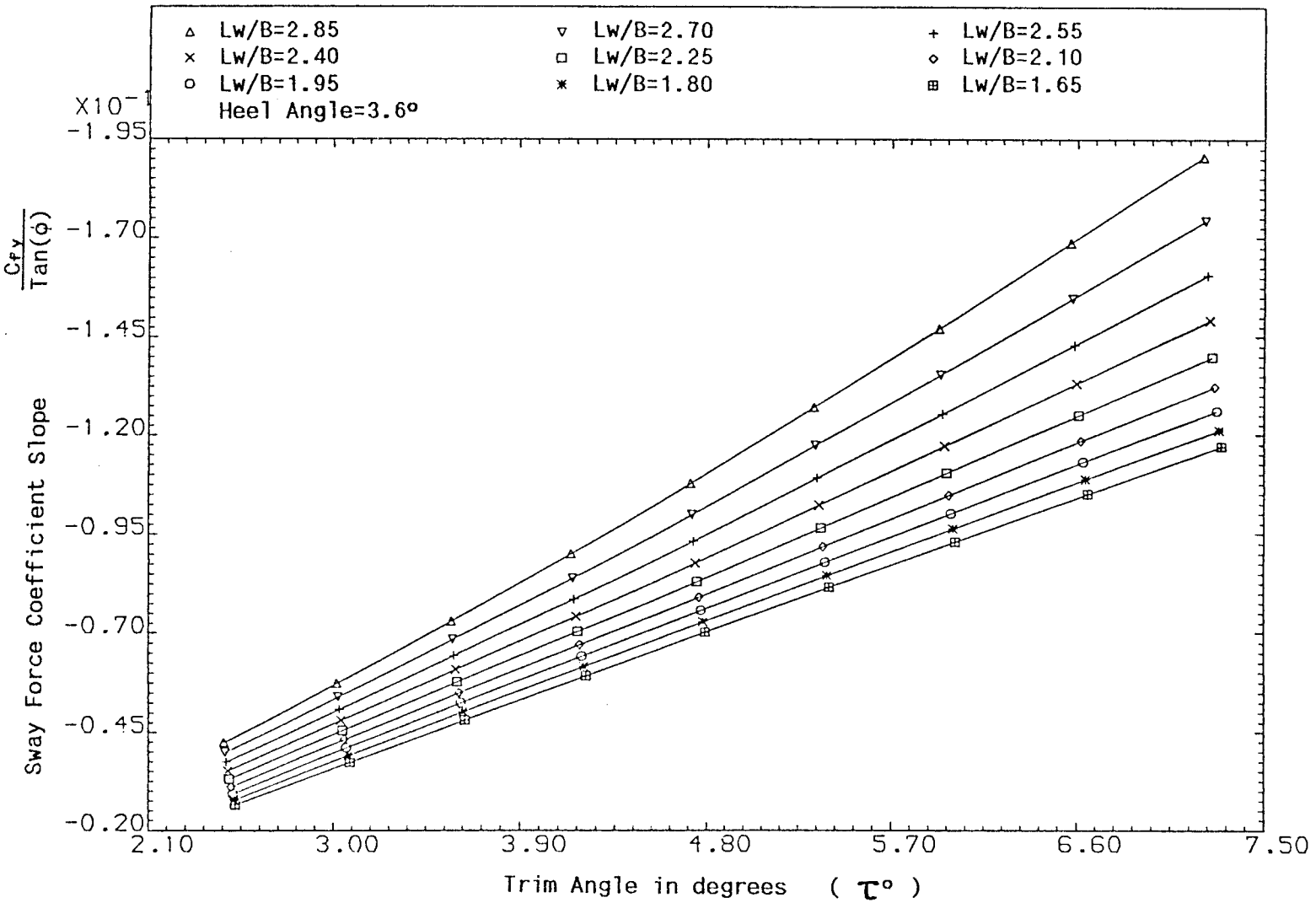

Fig.(7.9.1c) Computed Sway Force Coefficient Slope as a function of Trim Angle and Mean Lw/B Ratio for 10° Constant Deadrise Hull in Heel Condition (Cv=3.0)

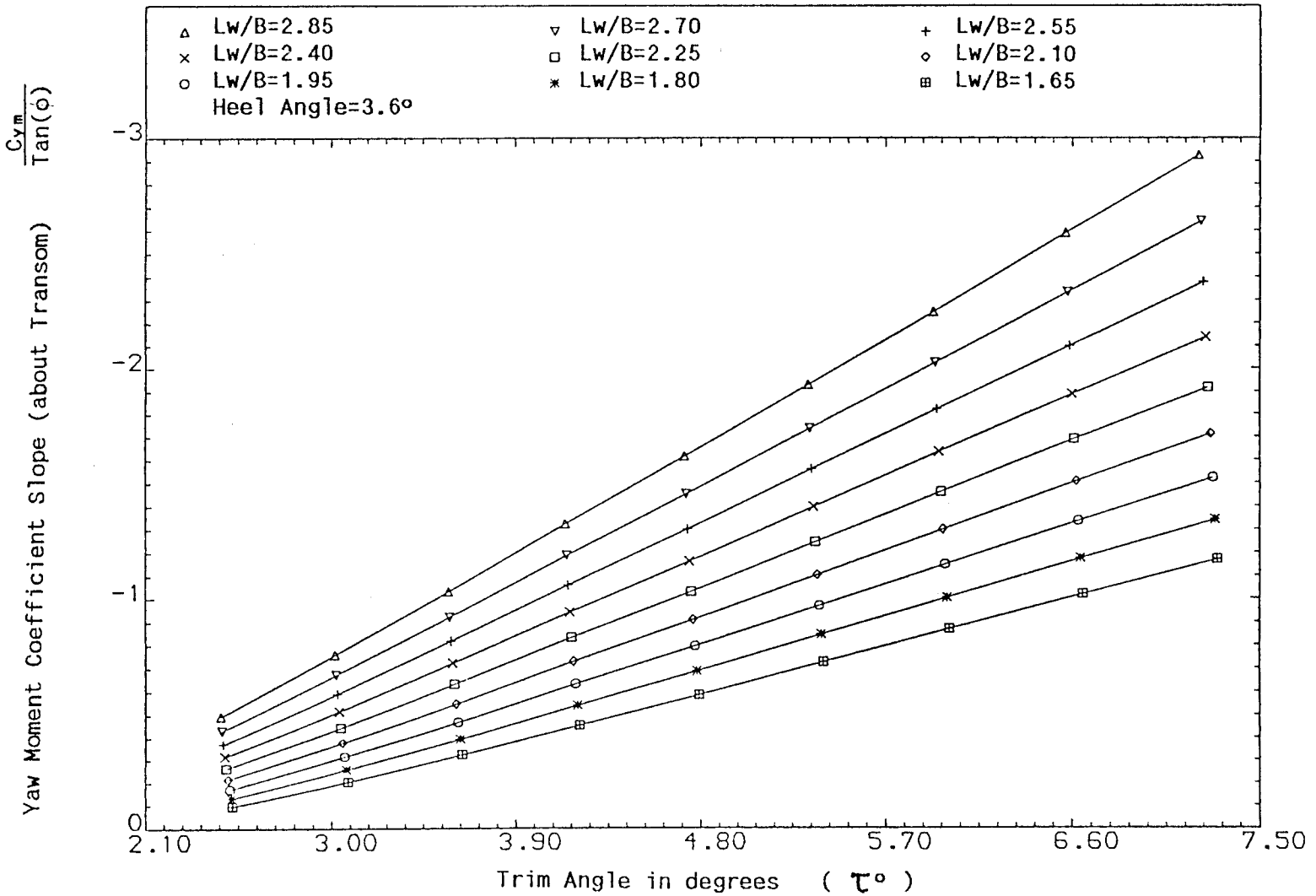

Fig.(7.9.1d) Computed Yaw Moment Coefficient Slope as a function of Trim Angle and Mean Lw/B Ratio for 10° Constant Deadrise Hull in Heel Condition (Cv=3.0)

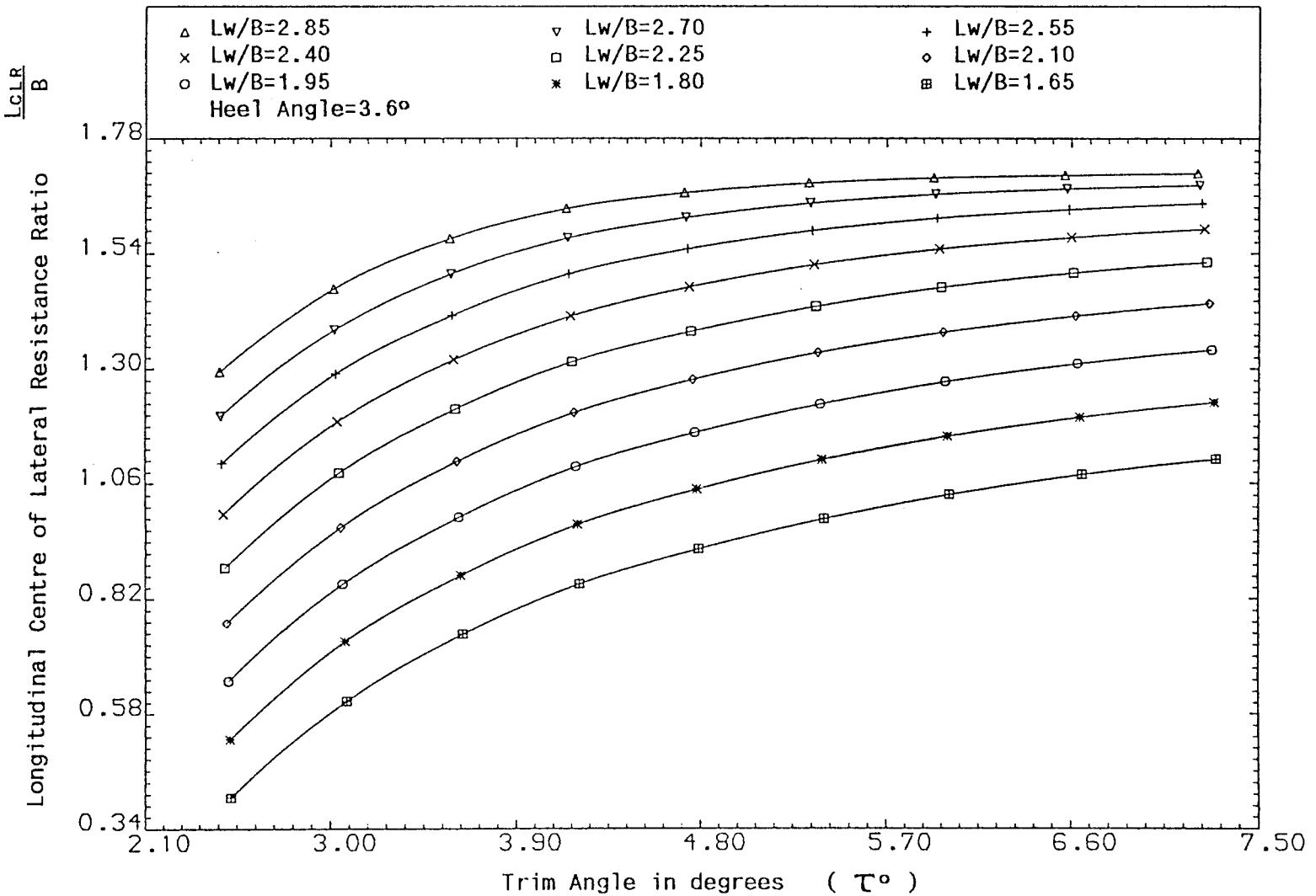

Fig.(7.9.1e) Computed Centre of Lateral Resistance Ratio as a function of Trim Angle and Mean Lw/B Ratio for 10° Constant Deadrise Hull in Heel Condition (Cv=3.0)

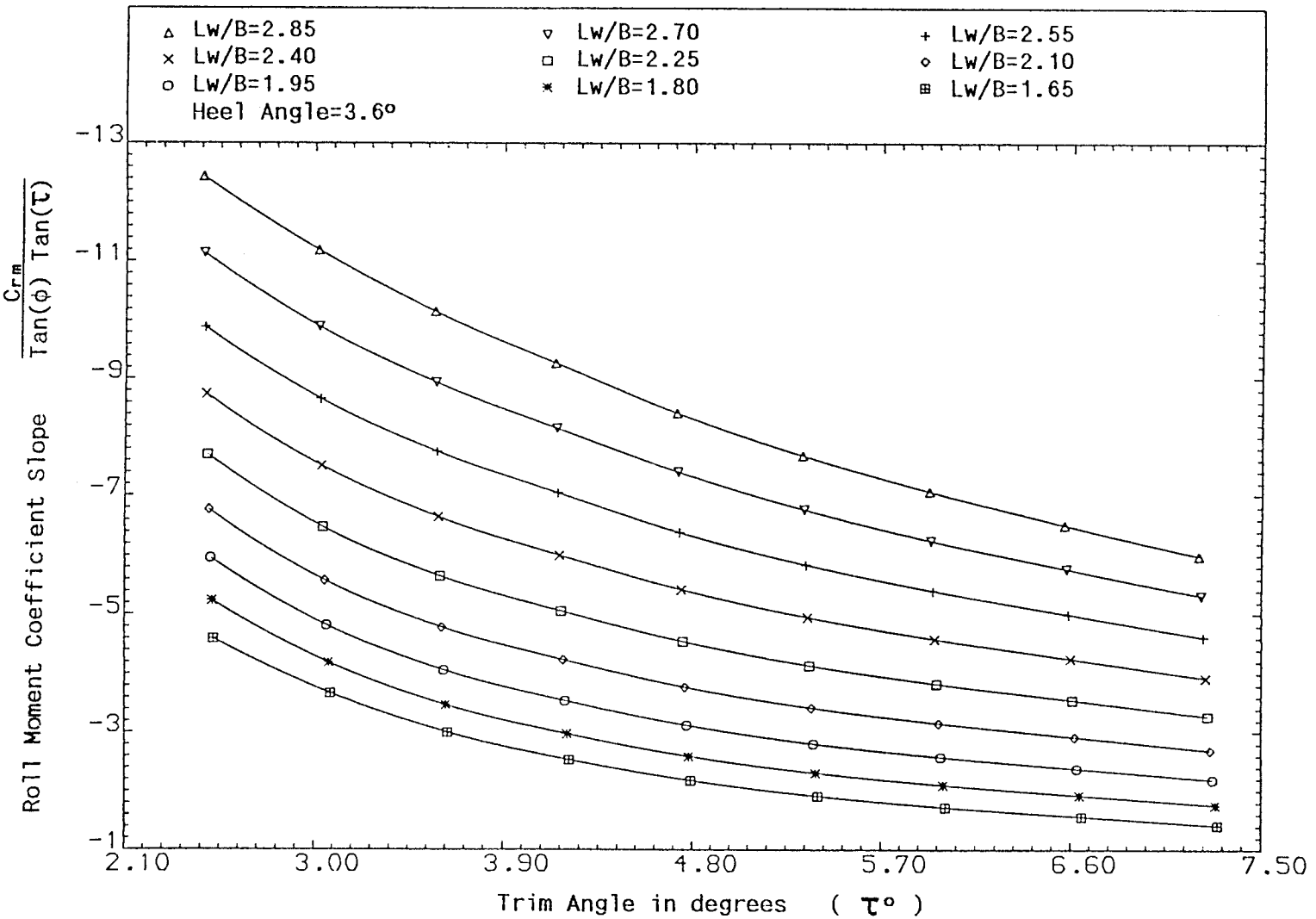

Fig.(7.9.1f) Computed Roll Moment Coefficient Slope as a function of Trim Angle and Mean Lw/B Ratio for 10° Constant Deadrise Hull in Heel Condition (Cv=3.0)

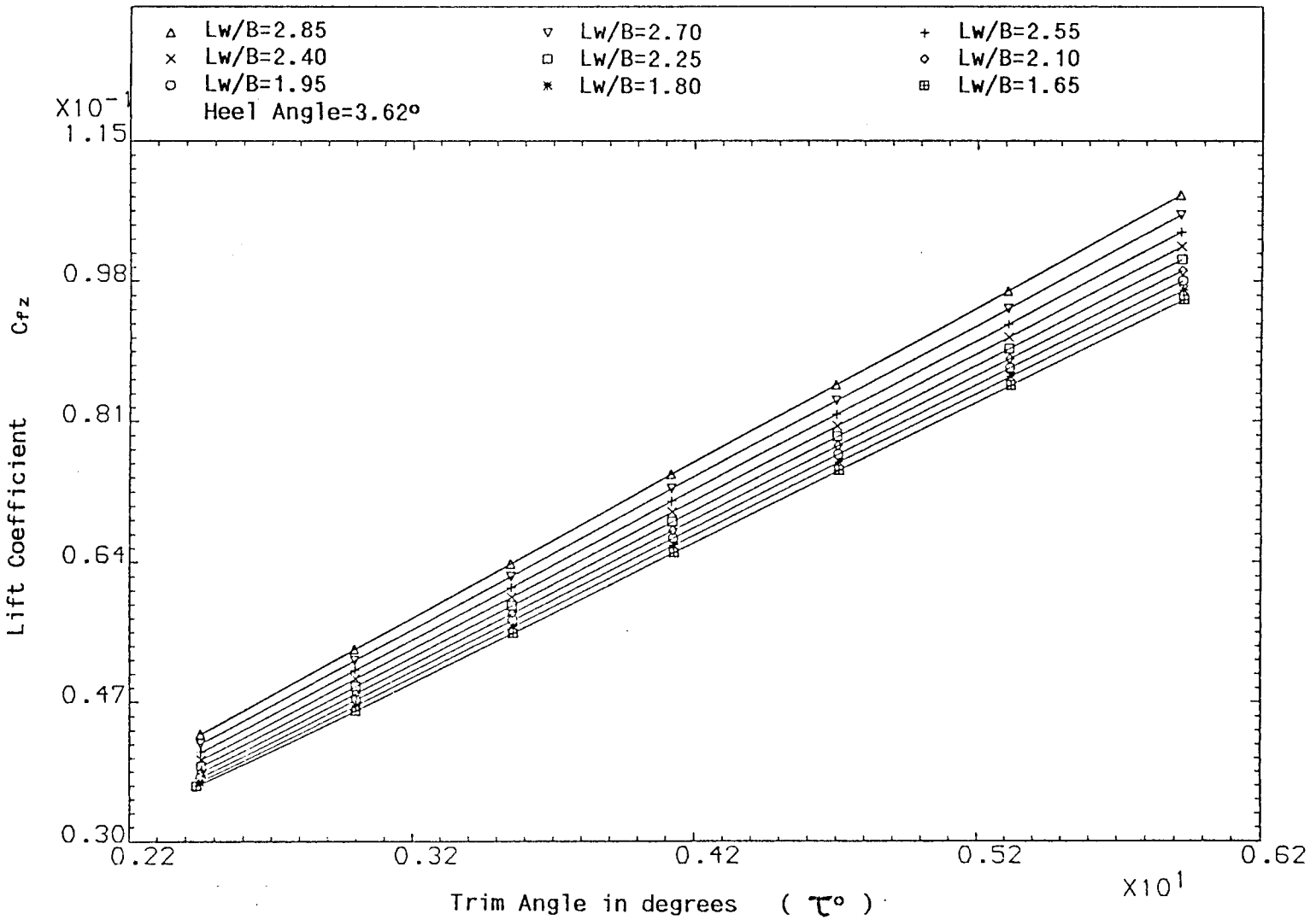

Fig.(7.9.2a) Computed Lift Coefficient as a function of Trim Angle and Mean Lw/B Ratio for 10° Constant Deadrise Hull in Heel Condition (Cv=5.5)

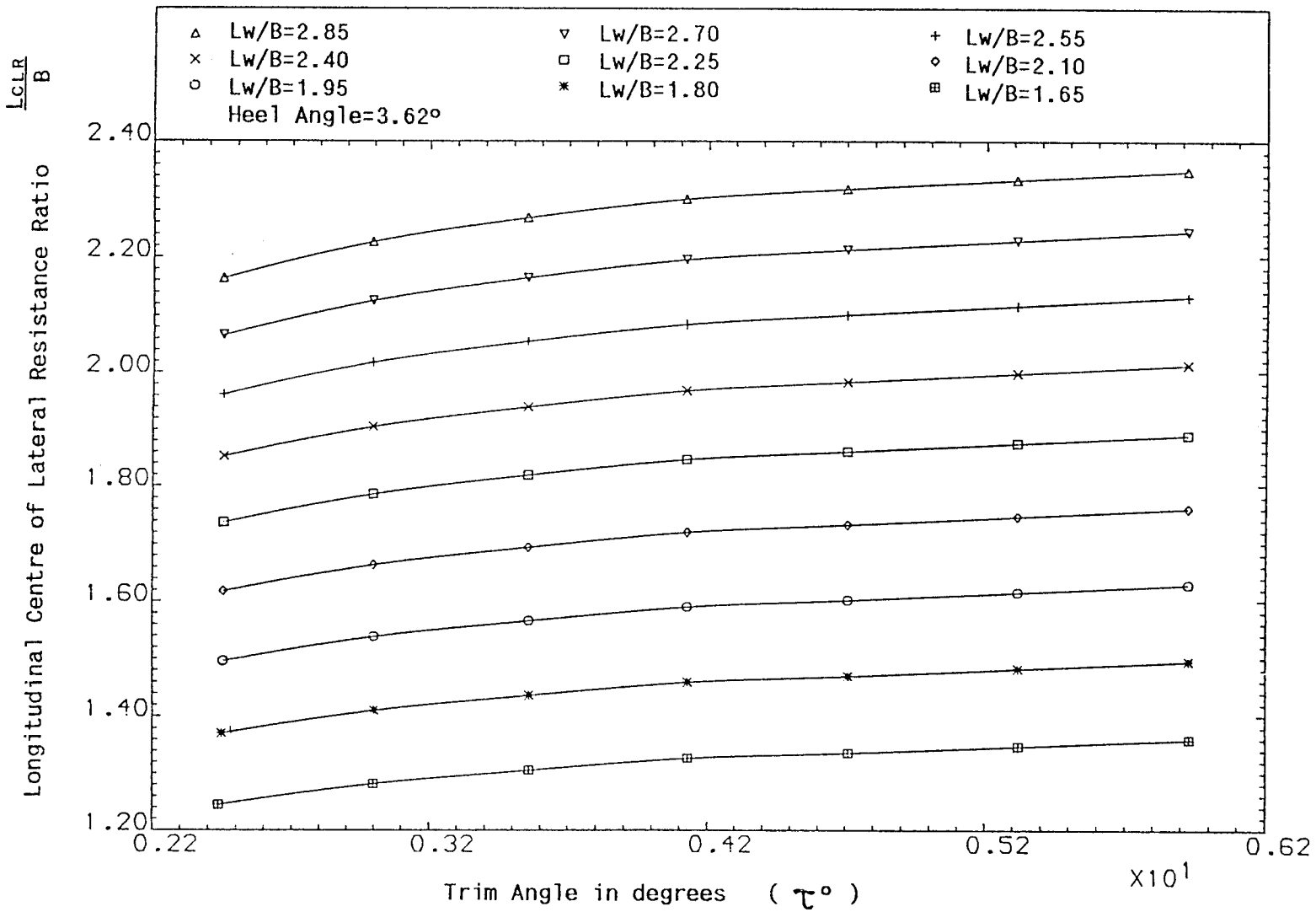

Fig.(7.9.2b) Computed Centre of Lift Ratio as a function of Trim Angle and Mean Lw/B Ratio for 10° Constant Deadrise Hull in Heel Condition (Cv=5.5)

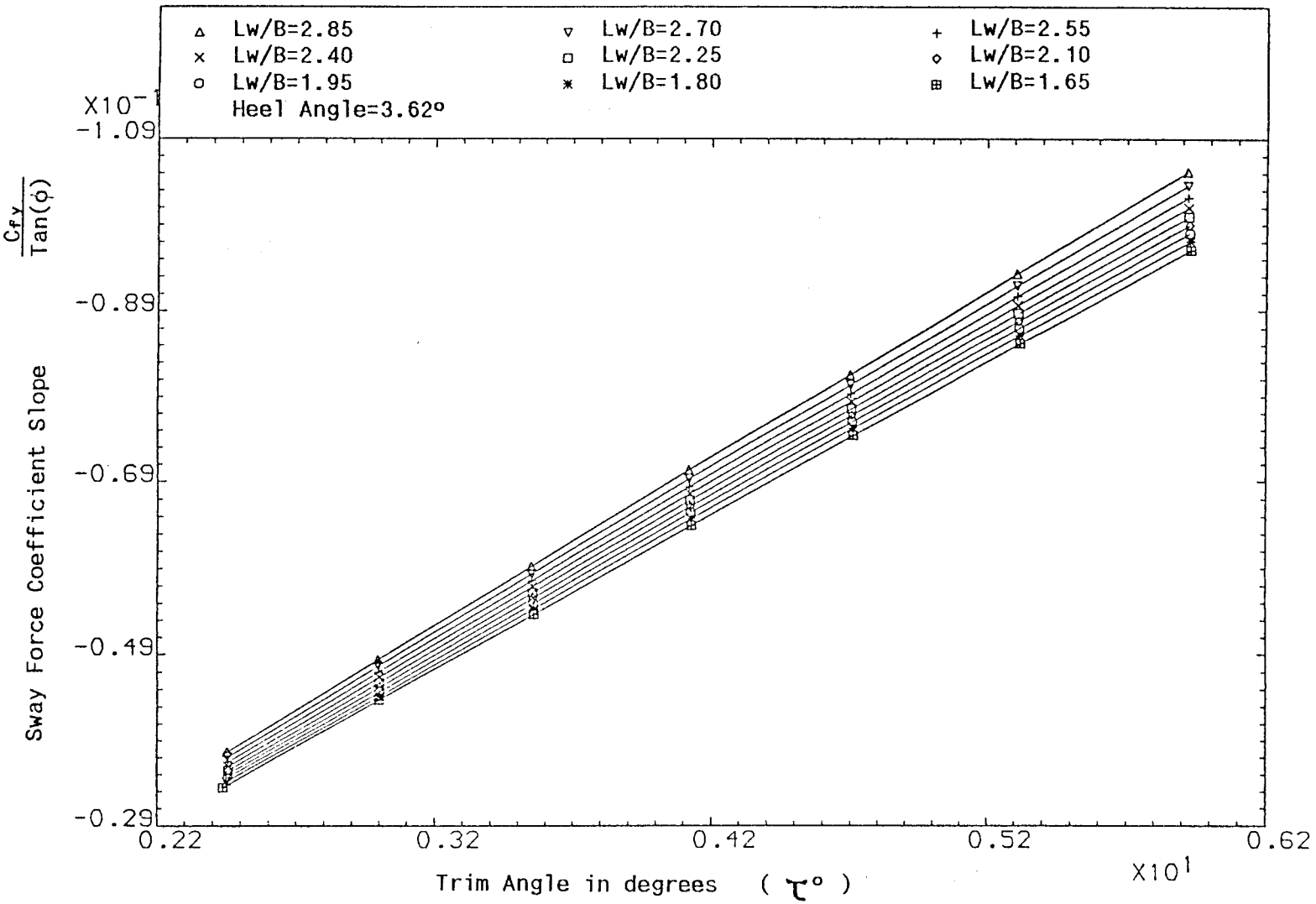

Fig.(7.9.2c) Computed Sway Force Coefficient Slope as a function of Trim Angle and Mean Lw/B Ratio for 10° Constant Deadrise Hull in Heel Condition (Cv=5.5)

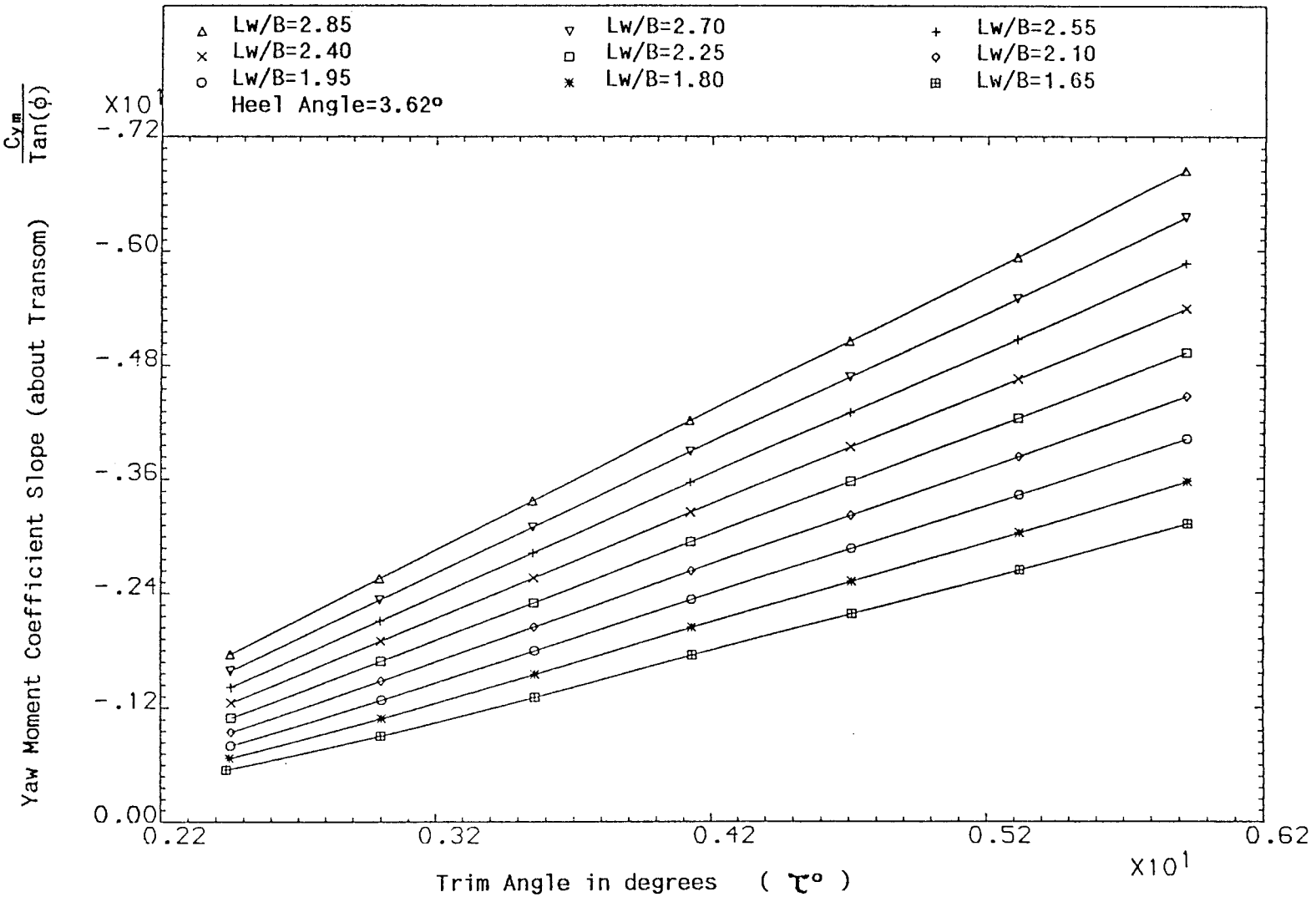

Fig.(7.9.2d) Computed Yaw Moment Coefficient Slope as a function of Trim Angle and Mean Lw/B Ratio for 10° Constant Deadrise Hull in Heel Condition (Cv=5.5)

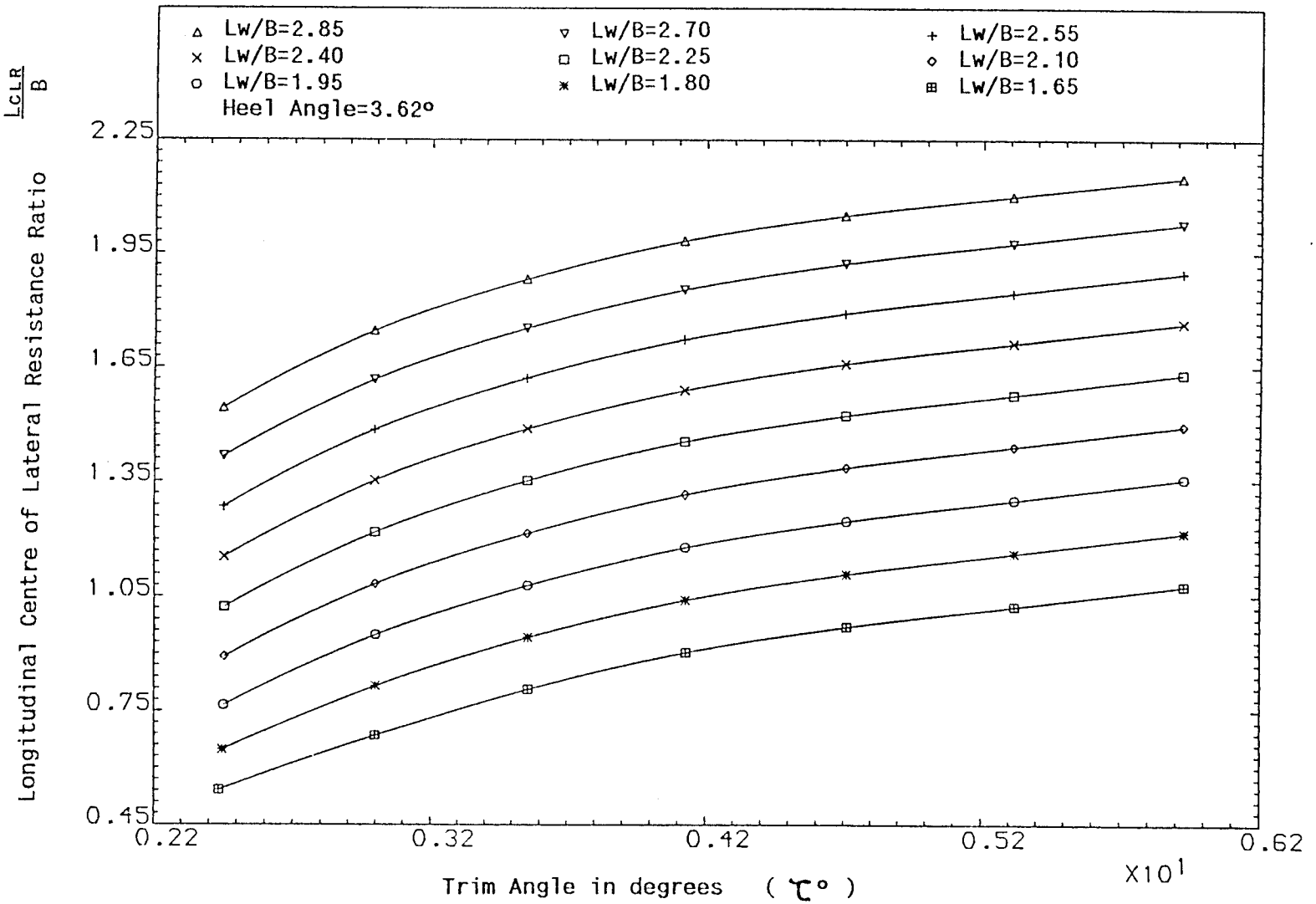

Fig.(7.9.2e) Computed Centre of Lateral Resistance Ratio as a function of Trim Angle and Mean Lw/B Ratio for 10° Constant Deadrise Hull in Heel Condition (Cv=5.5)

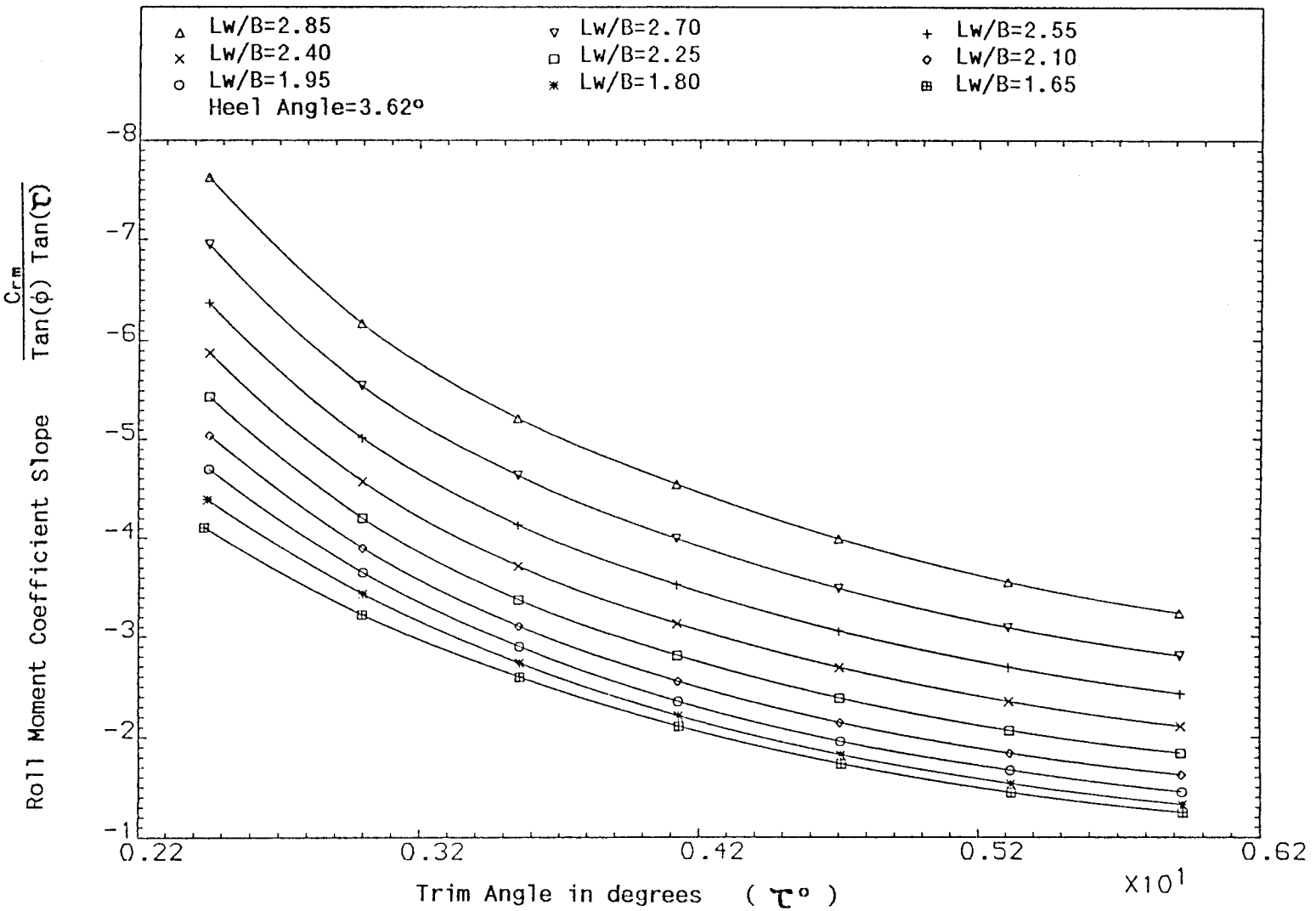

Fig.(7.9.2f) Computed Roll Moment Coefficient Slope as a function of Trim Angle and Mean Lw/B Ratio for 10° Constant Deadrise Hull in Heel Condition (Cv=5.5)

Fig.(7.10a) Variation of Roll Moment Coefficient Slope against Trim Angle for 10° Constant Deadrise Hull in Heel Condition (Cv=3.0)

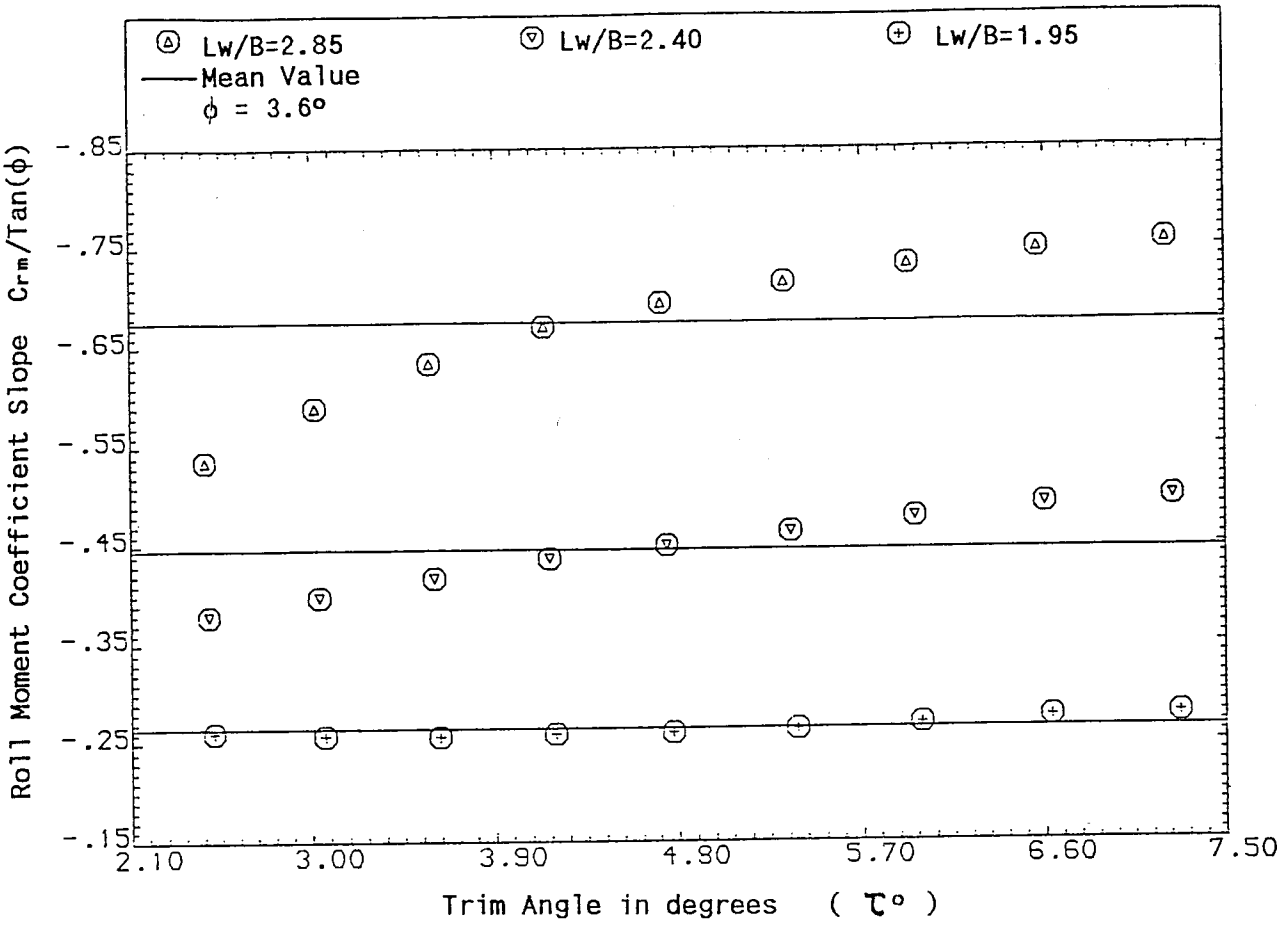

Fig.(7.10b) Variation of Roll Moment Coefficient Slope against Trim Angle for 10° Constant Deadrise Hull in Heel Condition (Cv=5.5)

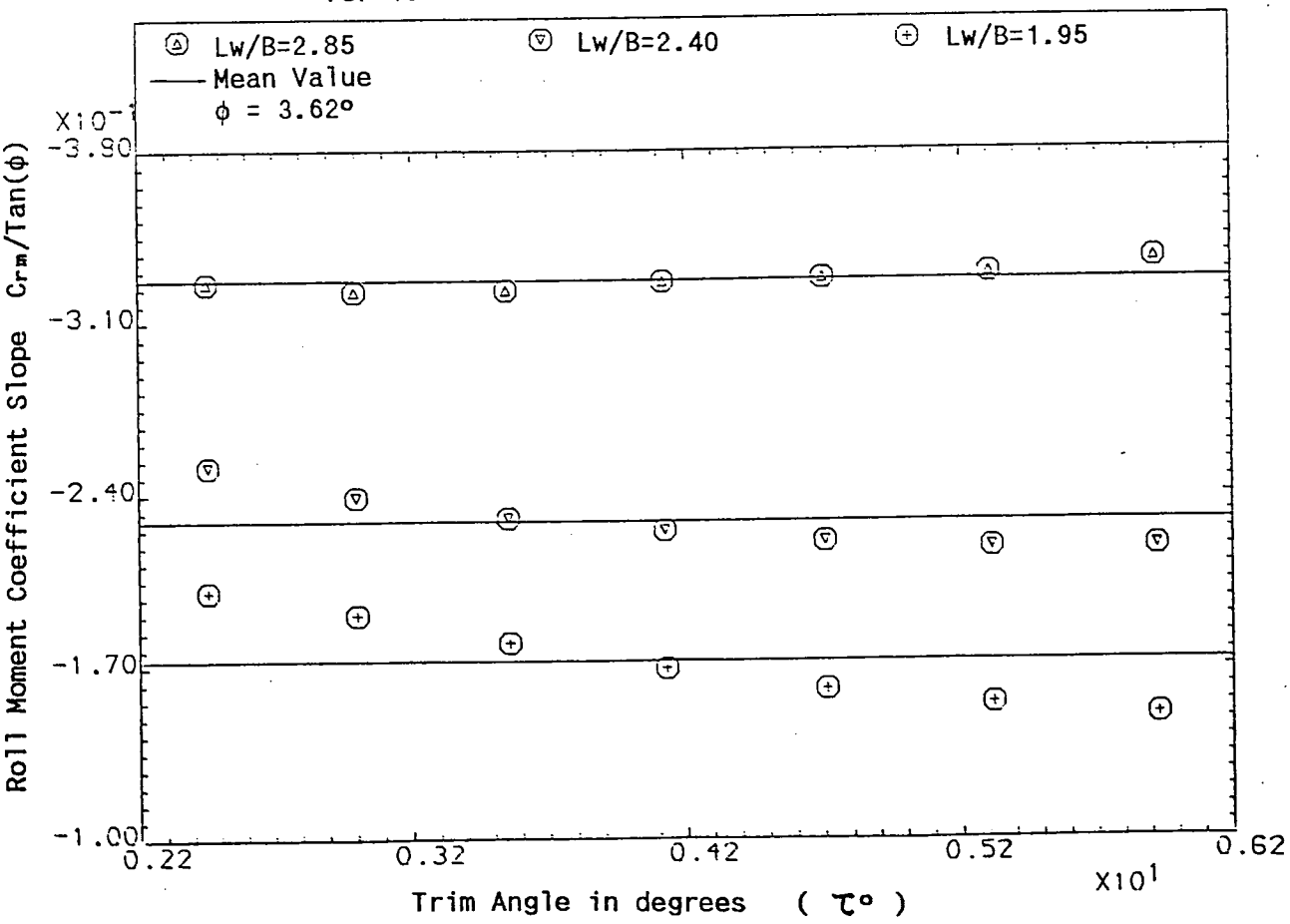

N = Yawing moment F = Sway Force

M = Rolling moment Δ = Lift Force / Weight

Note: Directions of the Sway Force and the Yawing Moment are opposite to those used in the Present Work

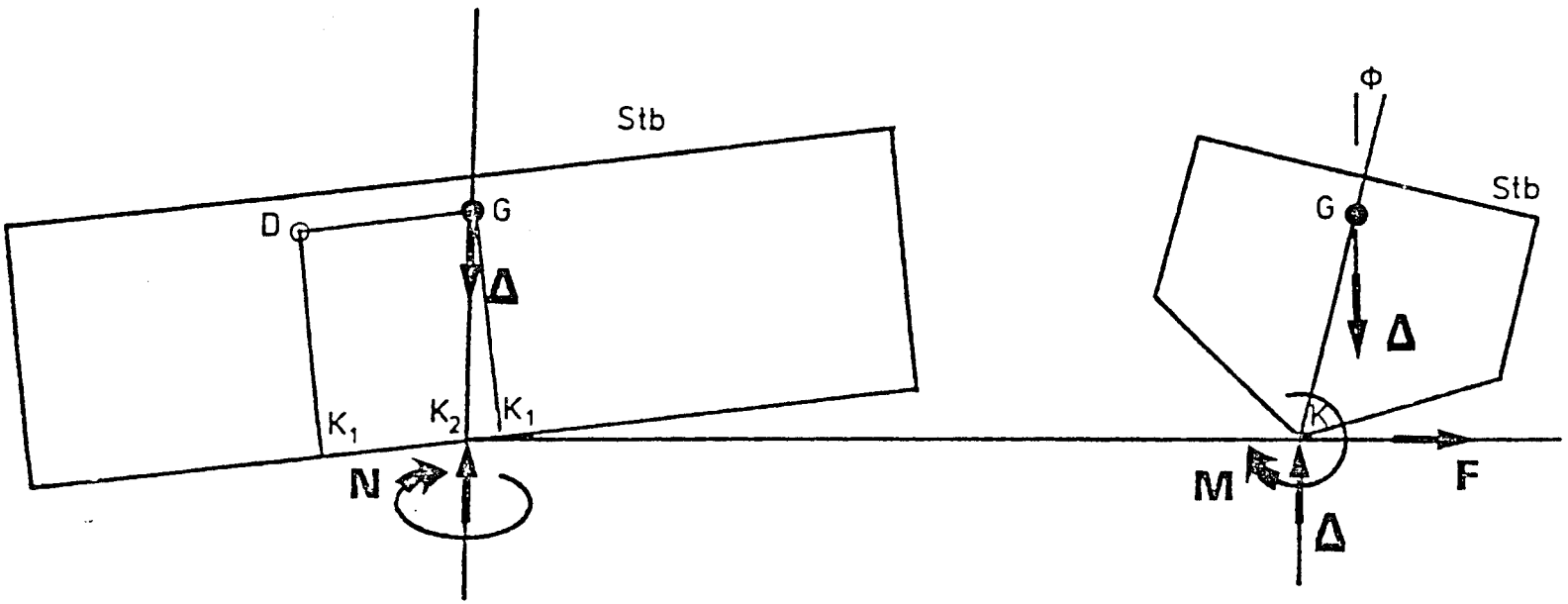

Fig.(7.11) Axes System for Forces and Moments used by Wellicome and Campbell (diagram extracted from Ref.(57))

Fig.(7.12a) F2 for 10^{o} Constant Deadrise Hull
(Cp=7.8, Lk/B=3.0)

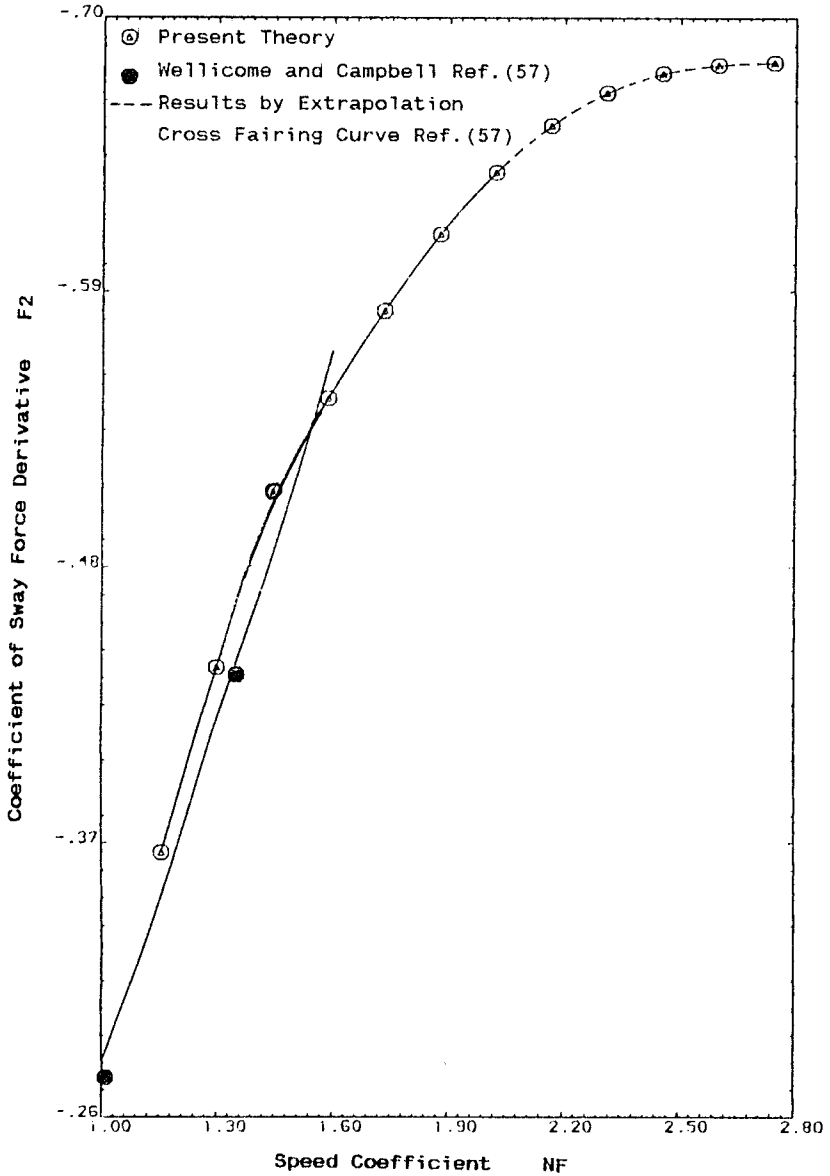

Fig.(7.12b) M2 for 10^{o} Constant Deadrise Hull
(Cp=7.8, Lk/B=3.0)

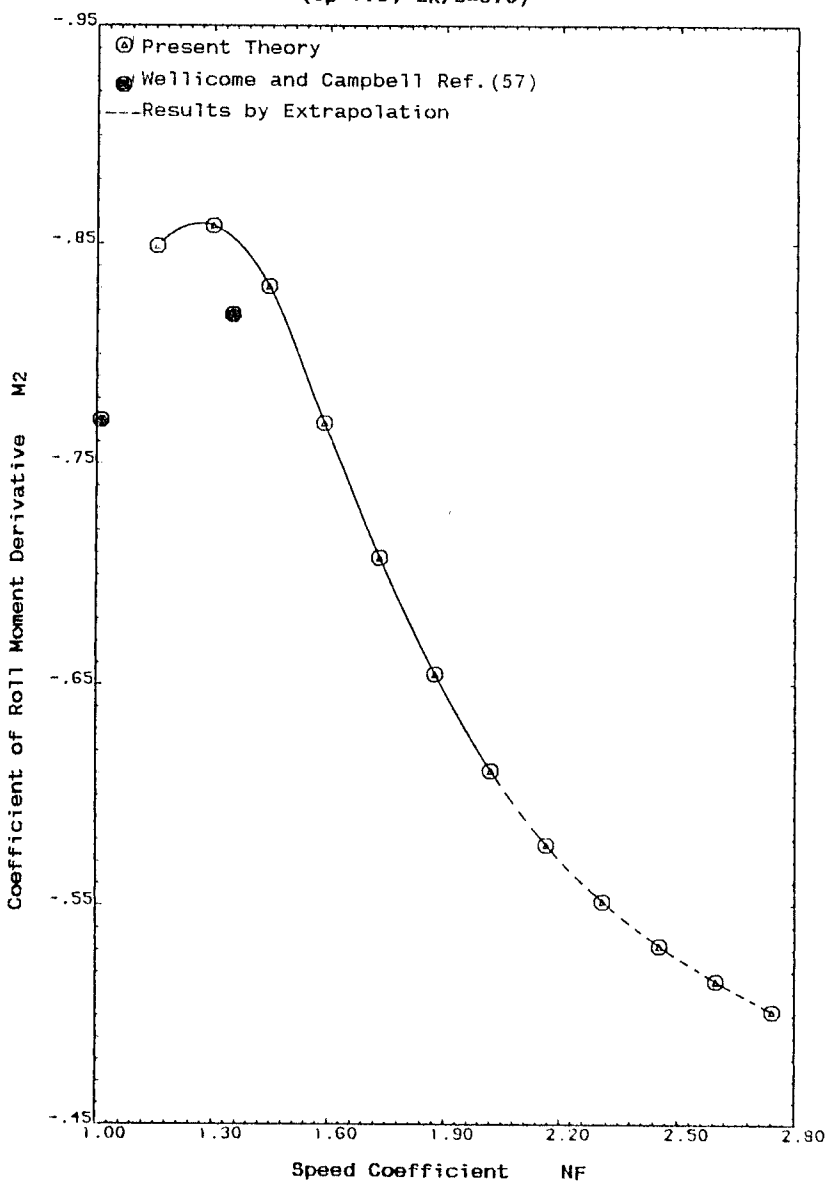

Fig.(7.12c) N2 for 10° Constant Deadrise Hull
(Cp=7.8, Lk/B=3.0)

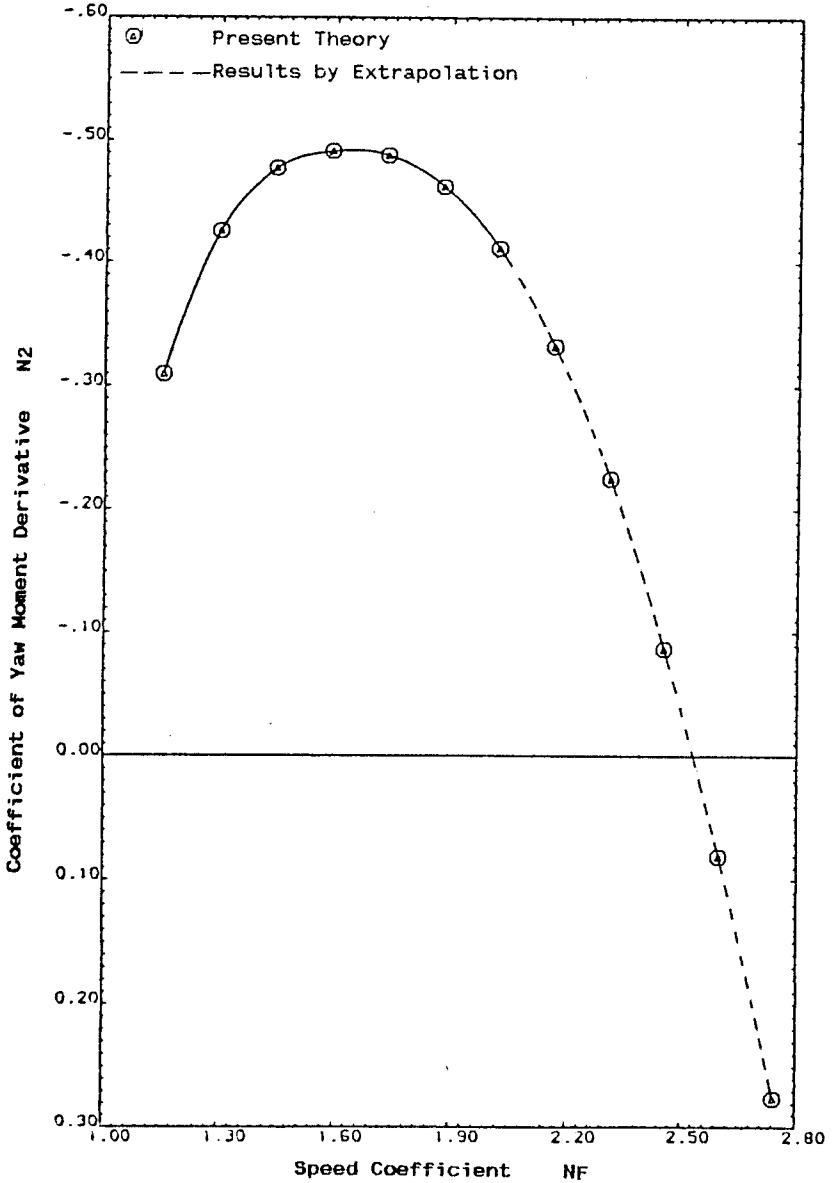

Fig.(7.12d) LCLR/B for 10° Constant Deadrise Hull
(Cp=7.8, Lk/B=3.0)

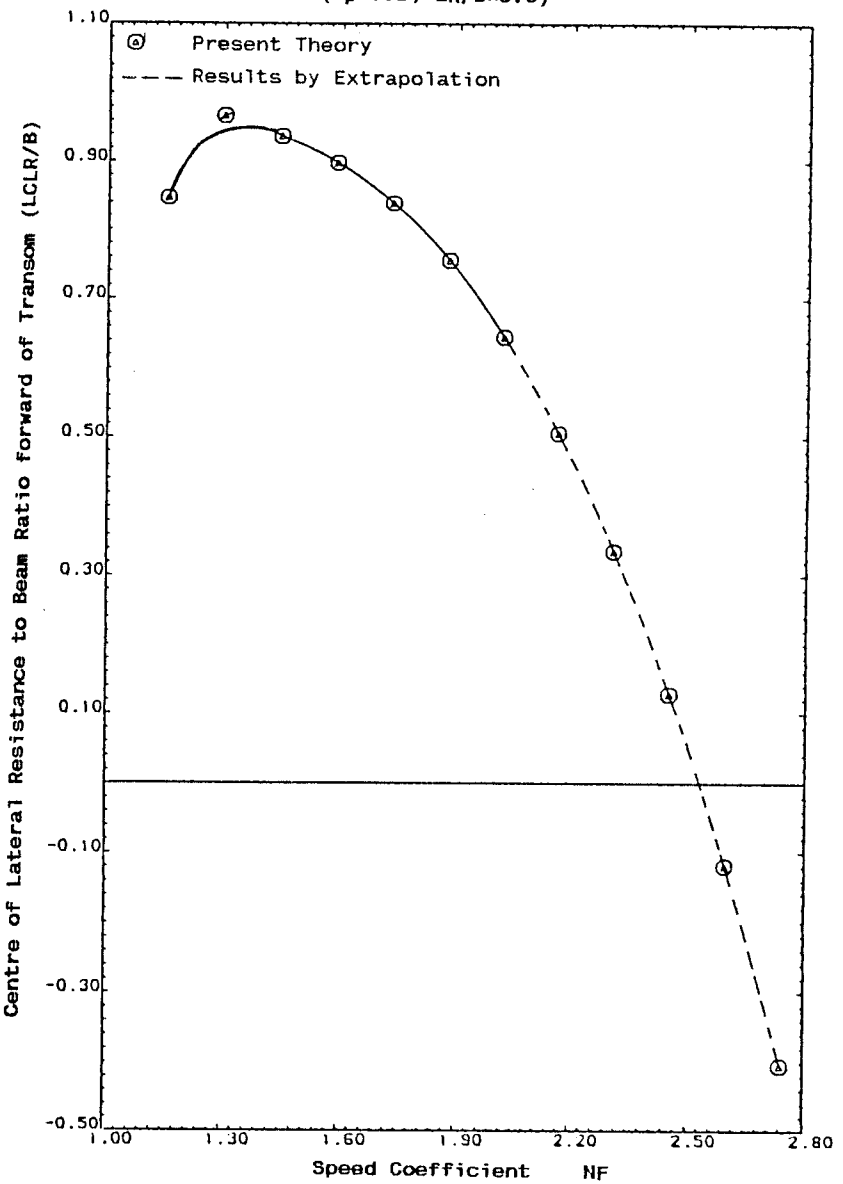

Fig.(7.12e) LCL/B for 10° Constant Deadrise Hull
(Cp=7.8, Lk/B=3.0)

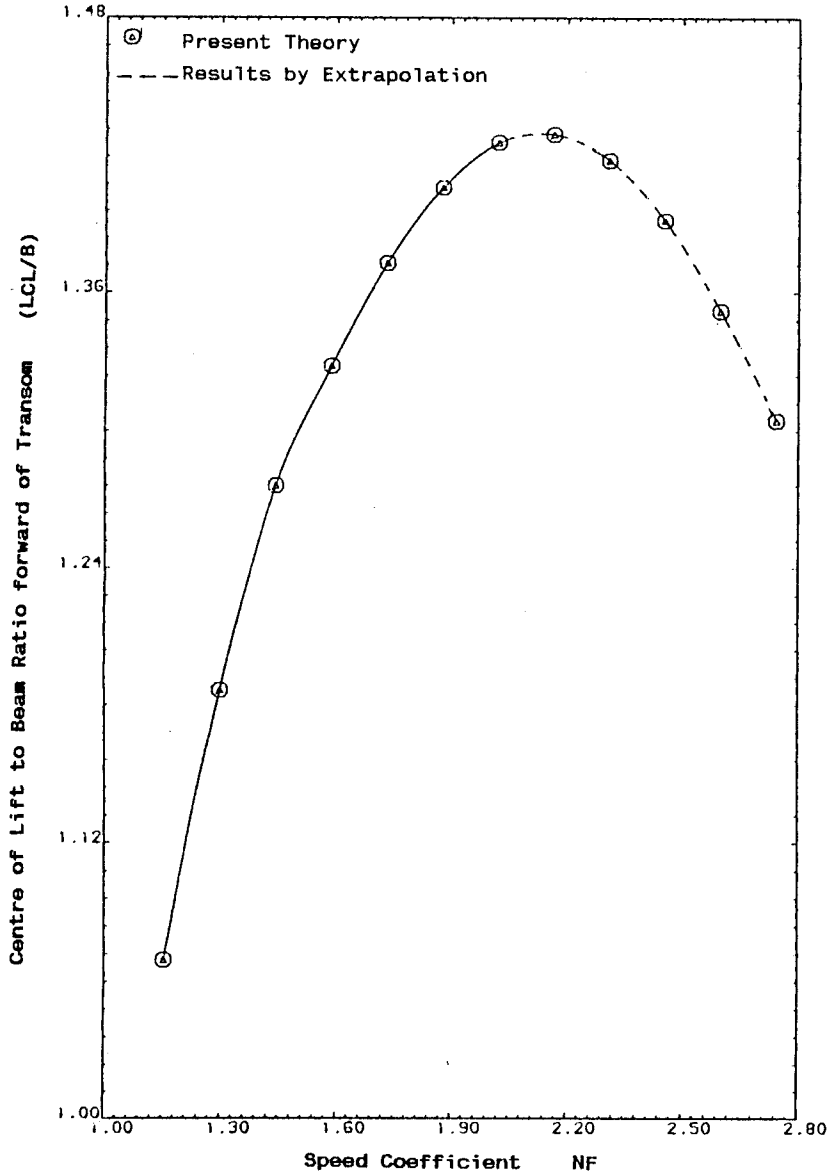

Fig.(7.13a) F2 for 10^{o} Constant Deadrise Hull
(Cp=5.7, Lk/B=3.0)

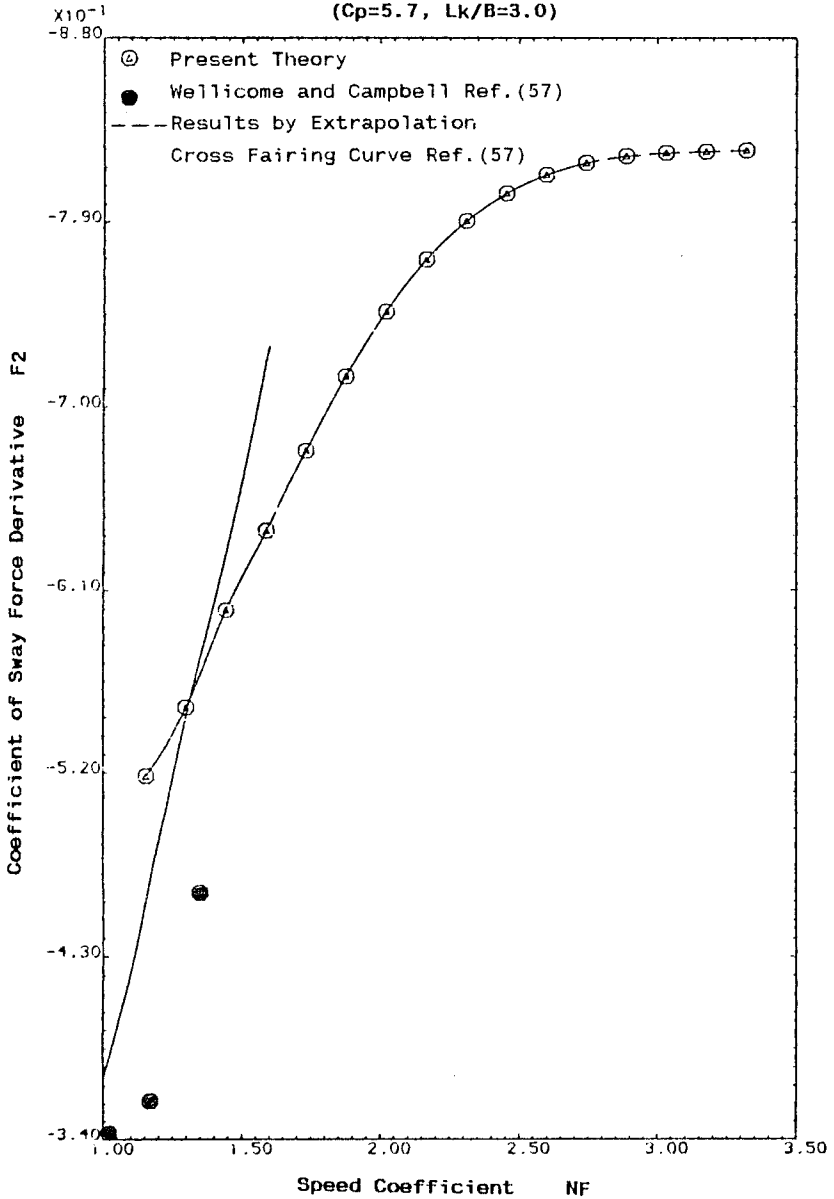

Fig.(7.13b) M2 for 10^{o} Constant Deadrise Hull
(Cp=5.7, Lk/B=3.0)

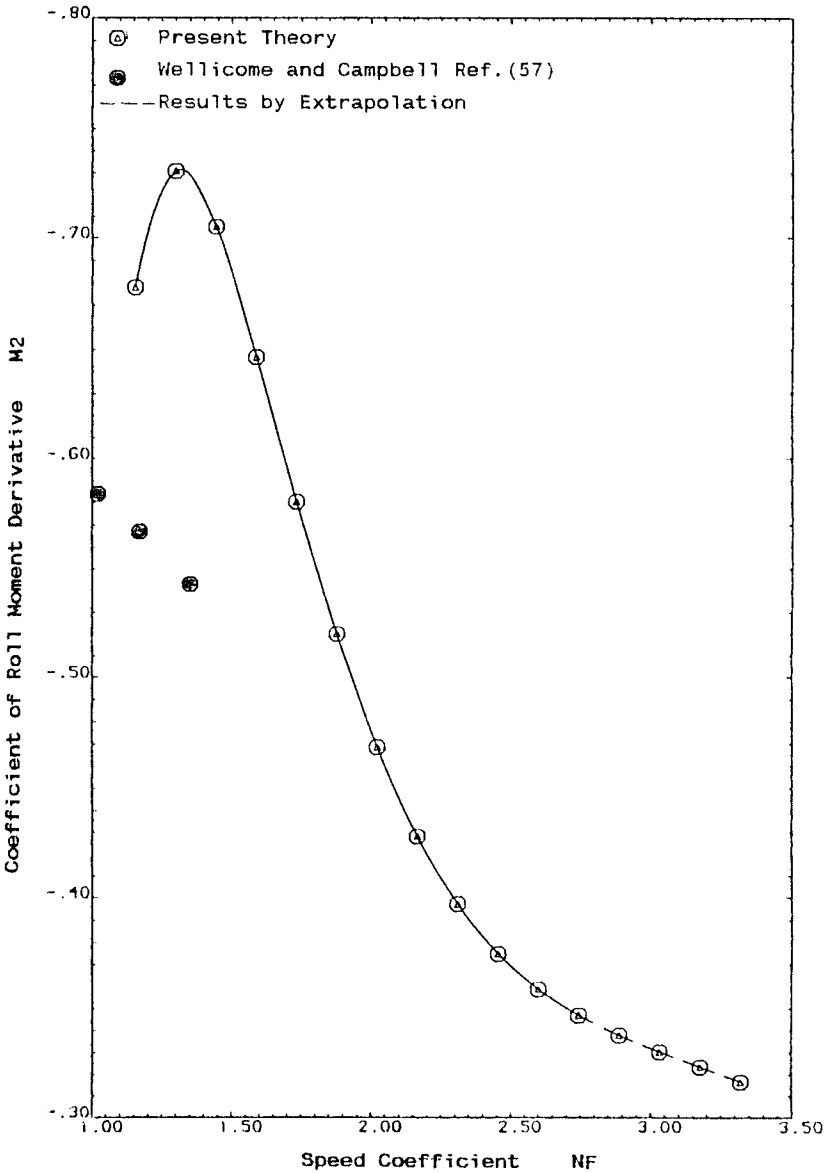

Fig.(7.13c) N2 for 10^{o} Constant Deadrise Hull
(Cp=5.7, Lk/B=3.0)

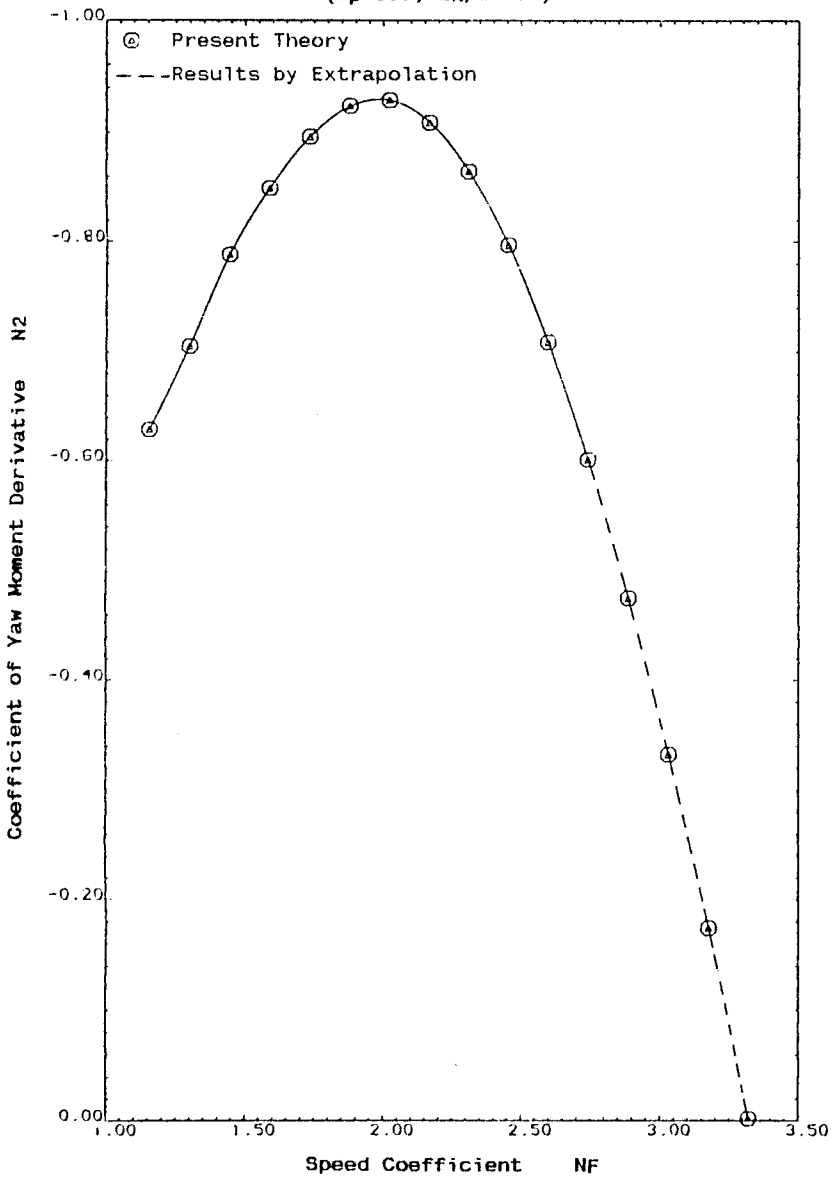

Fig.(7.13d) LCLR/B for 10^{o} Constant Deadrise Hull
(Cp=5.7, Lk/B=3.0)

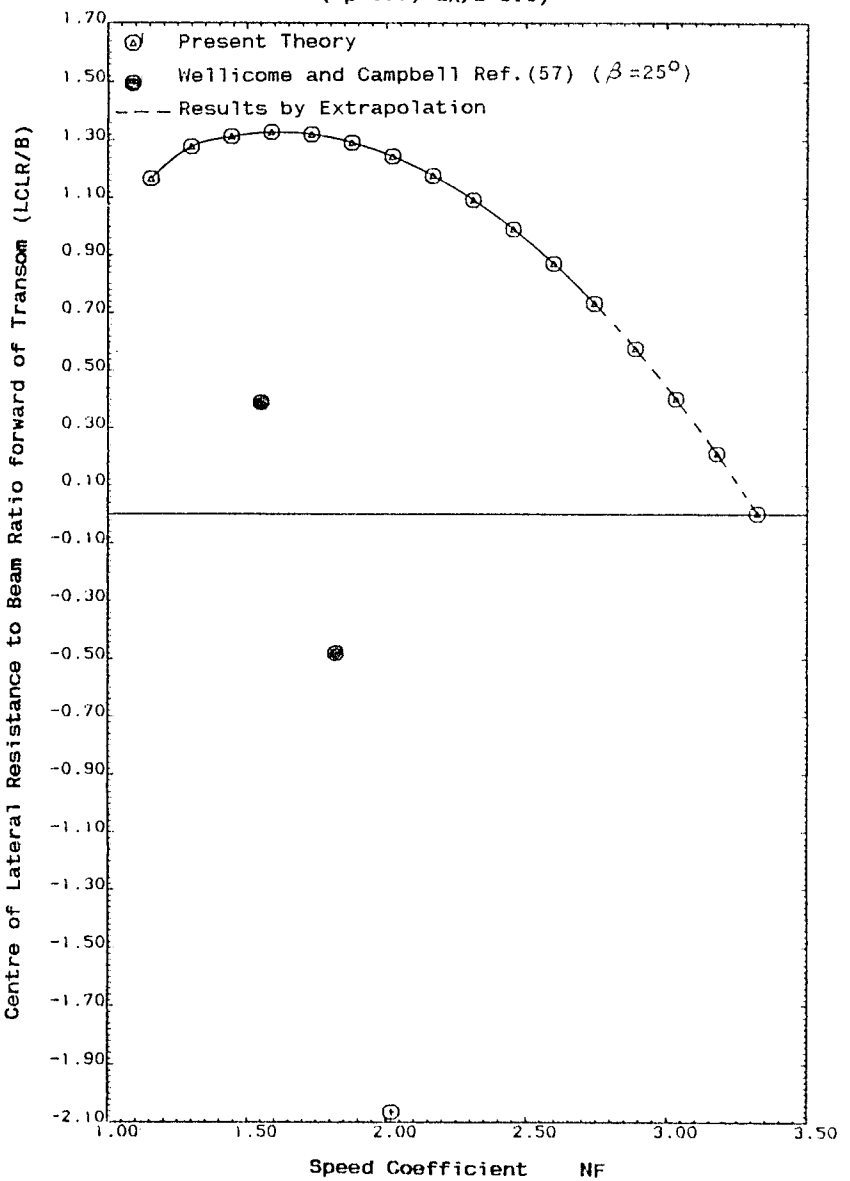

Fig.(7.13e) LCL/B for 10^{0} Constant Deadrise Hull
(Cp=5.7, Lk/B=3.0)

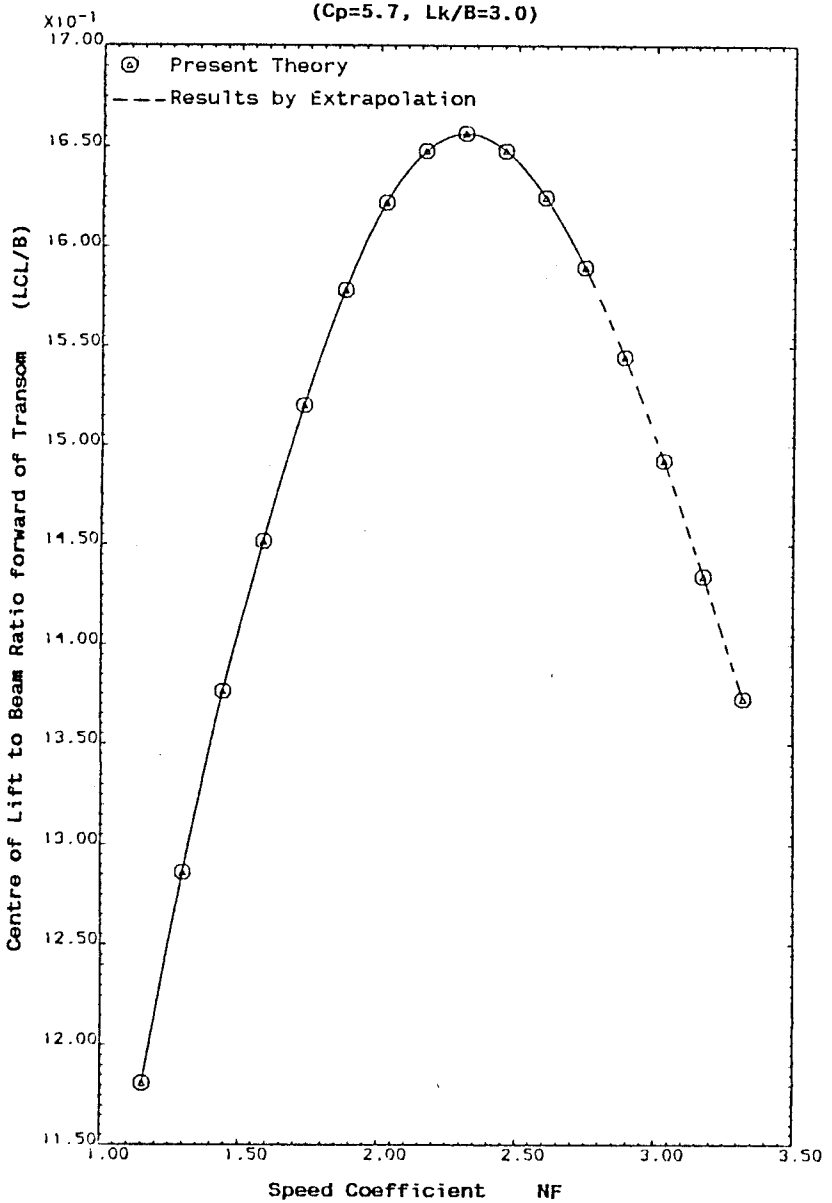

Fig.(7.14a) F2 for 10^{O} Constant Deadrise Hull
(Cp=5.7, Lk/B=2.5)

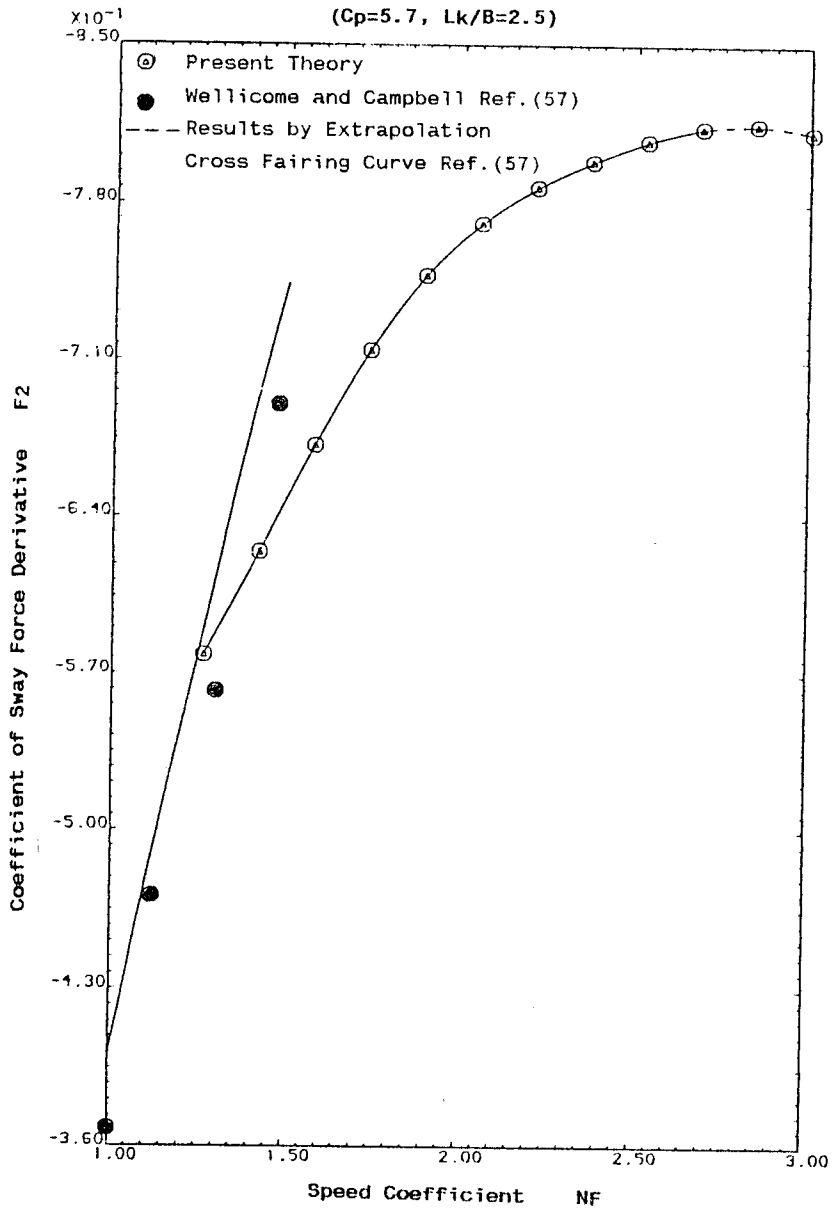

Fig.(7.14b) M2 for 10^{O} Constant Deadrise Hull
(Cp=5.7, Lk/B=2.5)

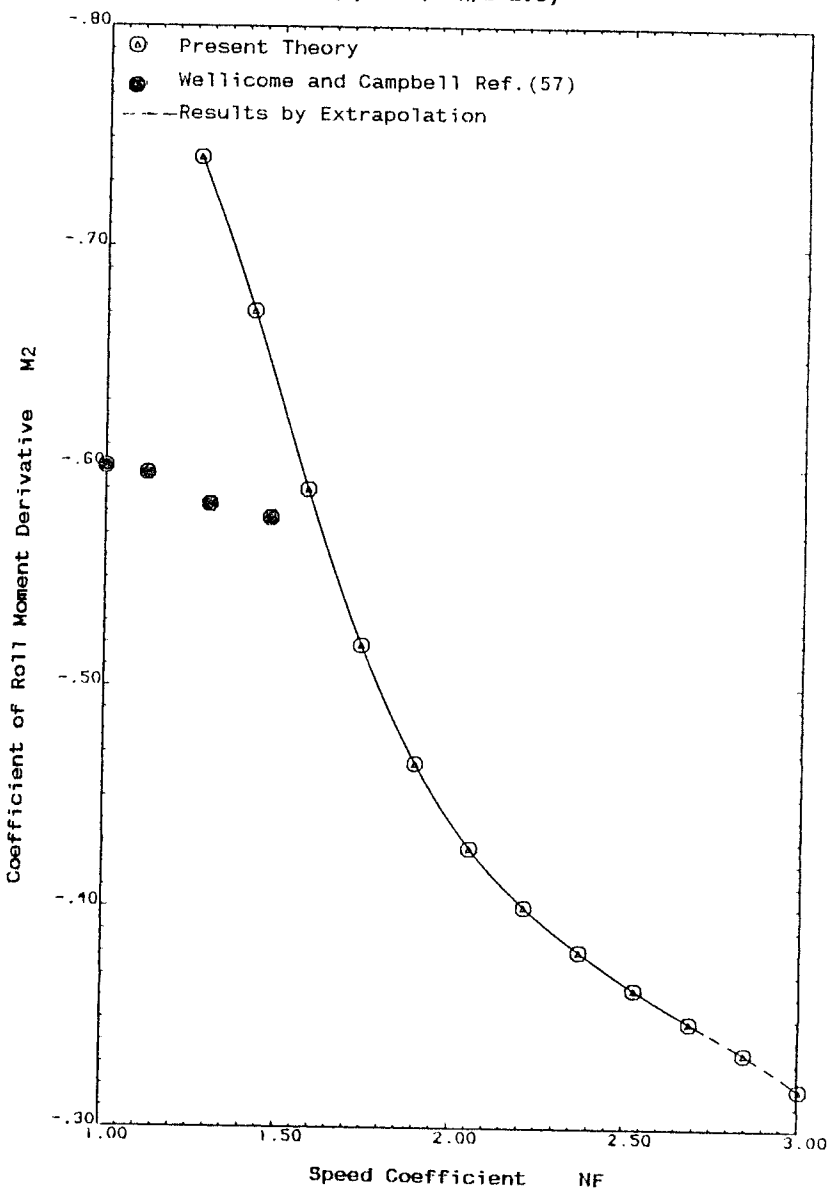

Fig.(7.14c) N2 for 10° Constant Deadrise Hull
(Cp=5.7, Lk/B=2.5)

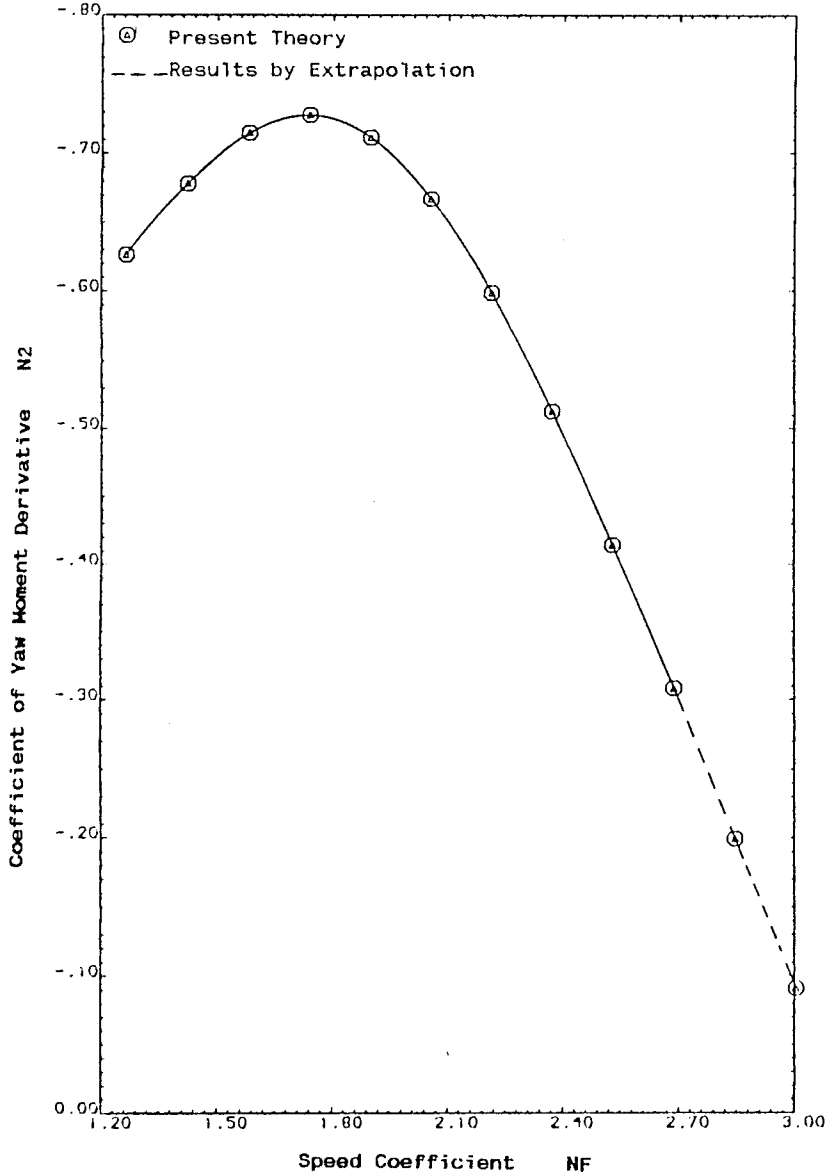

Fig.(7.14d) LCLR/B for 10° Constant Deadrise Hull
(Cp=5.7, Lk/B=2.5)

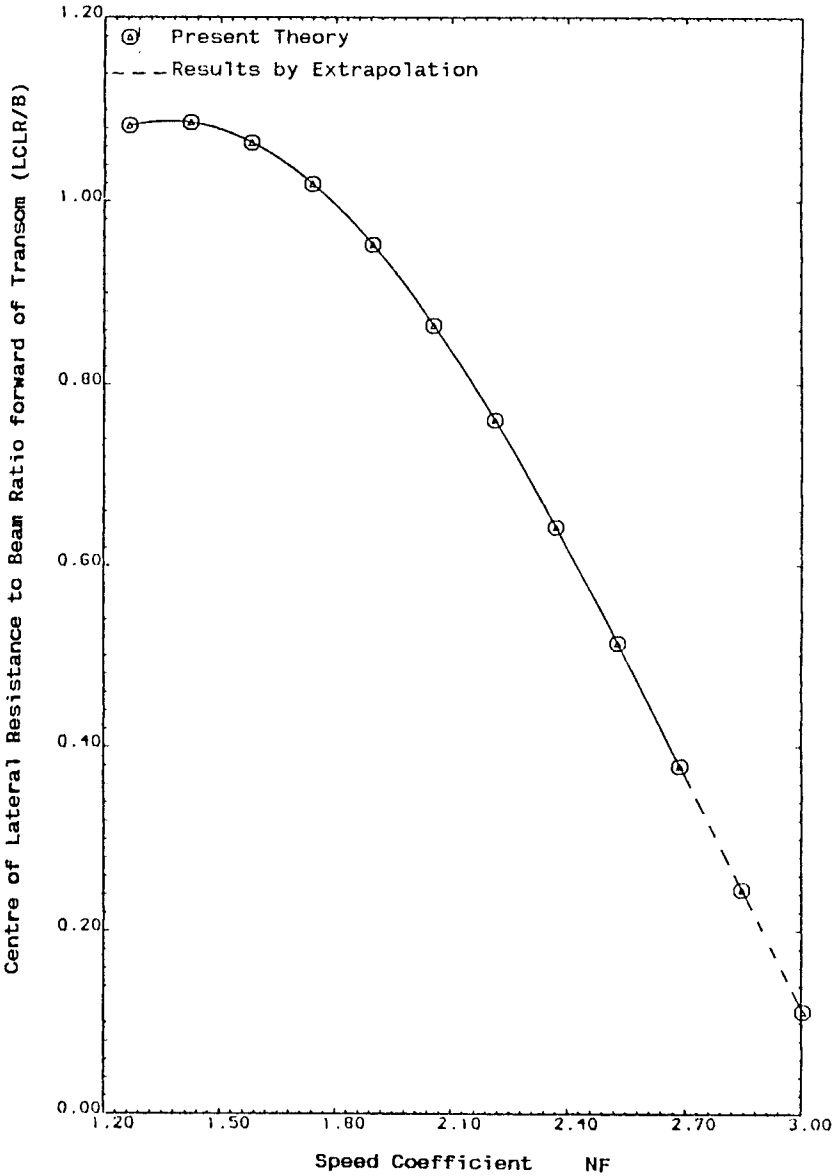

Fig. (7.14e) LCL/B for 10^{O} Constant Deadrise Hull
(Cp=5.7, Lk/B=2.5)

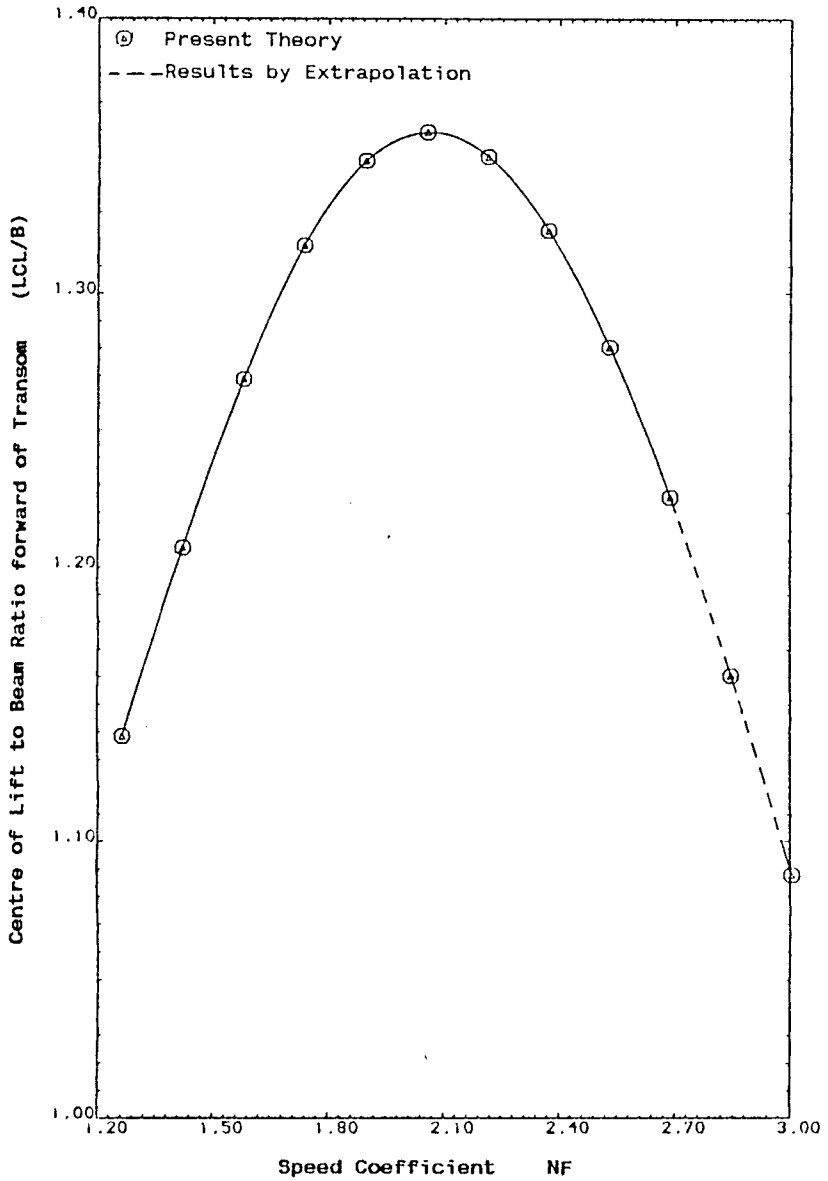

Fig.(7.15a) F2 for 10^{O} Constant Deadrise Hull
(Cp=3.3, Lk/B=3.0)

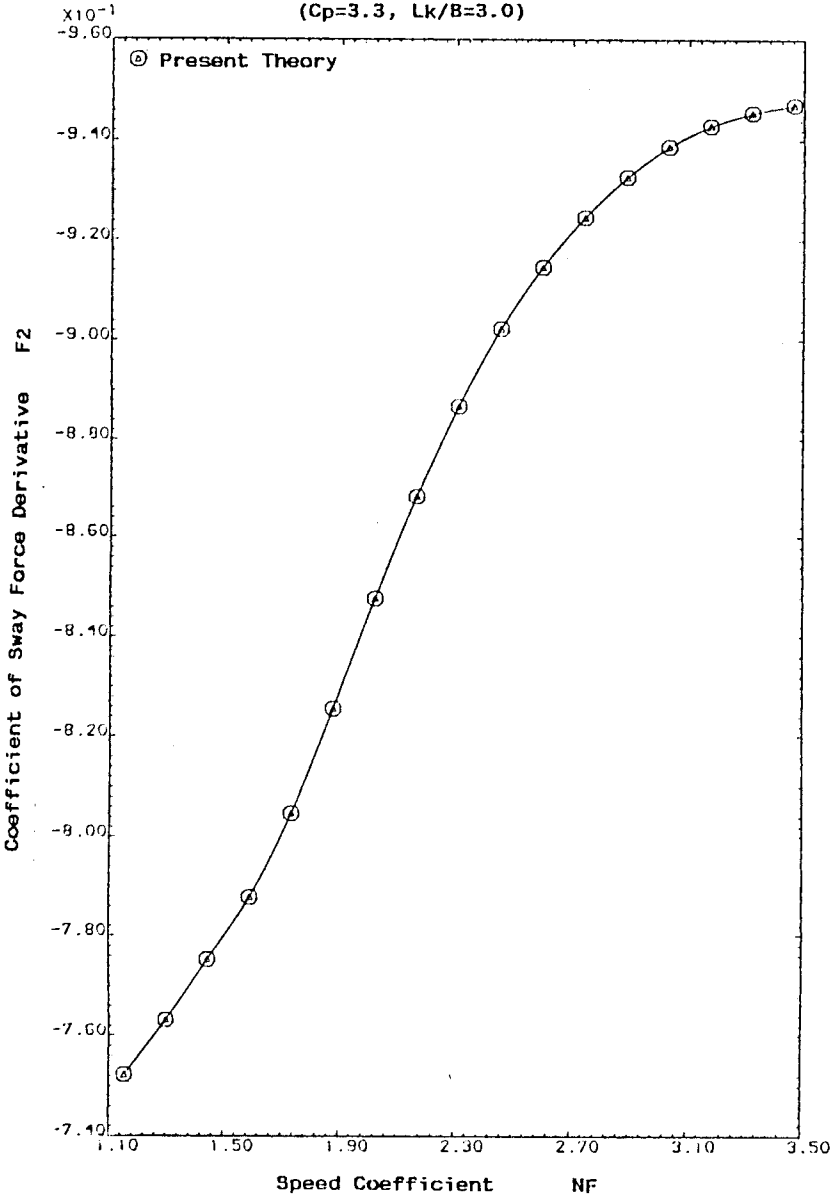

Fig.(7.15b) M2 for 10^{O} Constant Deadrise Hull
(Cp=3.3, Lk/B=3.0)

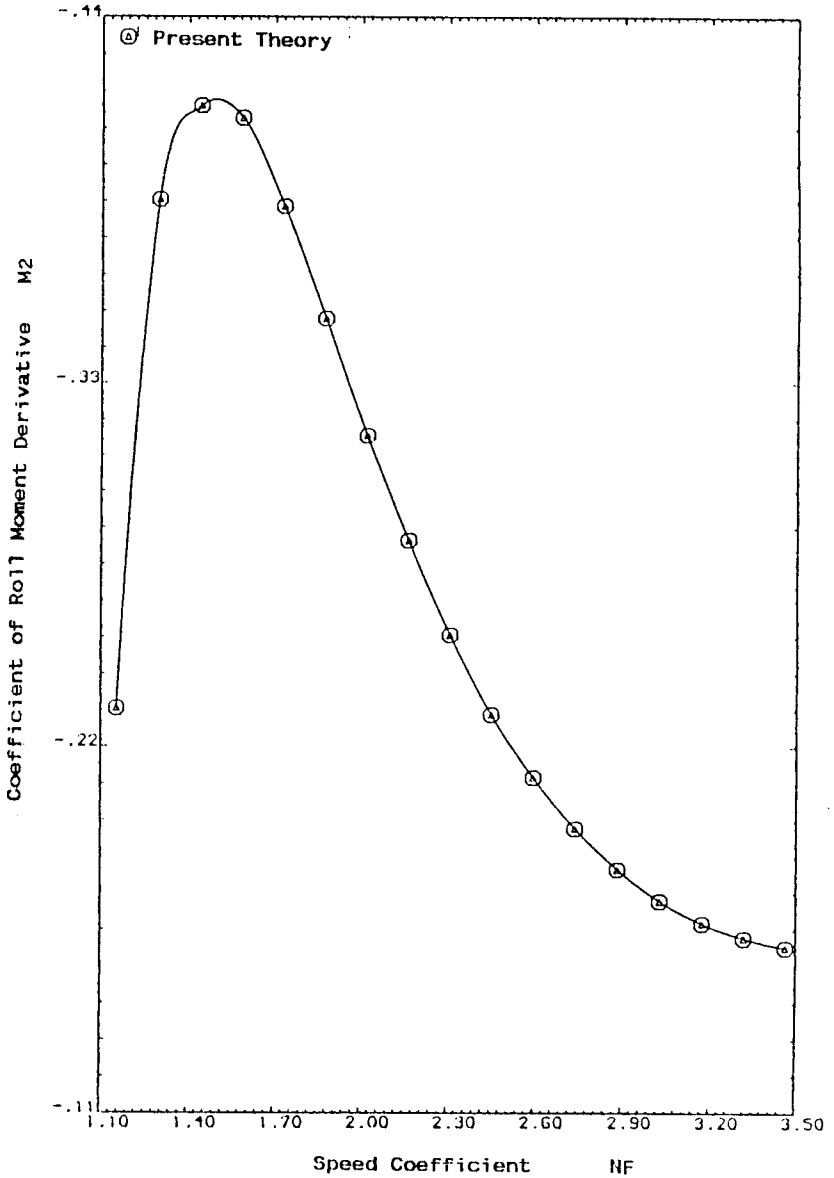

Fig.(7.15c) N2 for 10° Constant Deadrise Hull
(Cp=3.3, Lk/B=3.0)

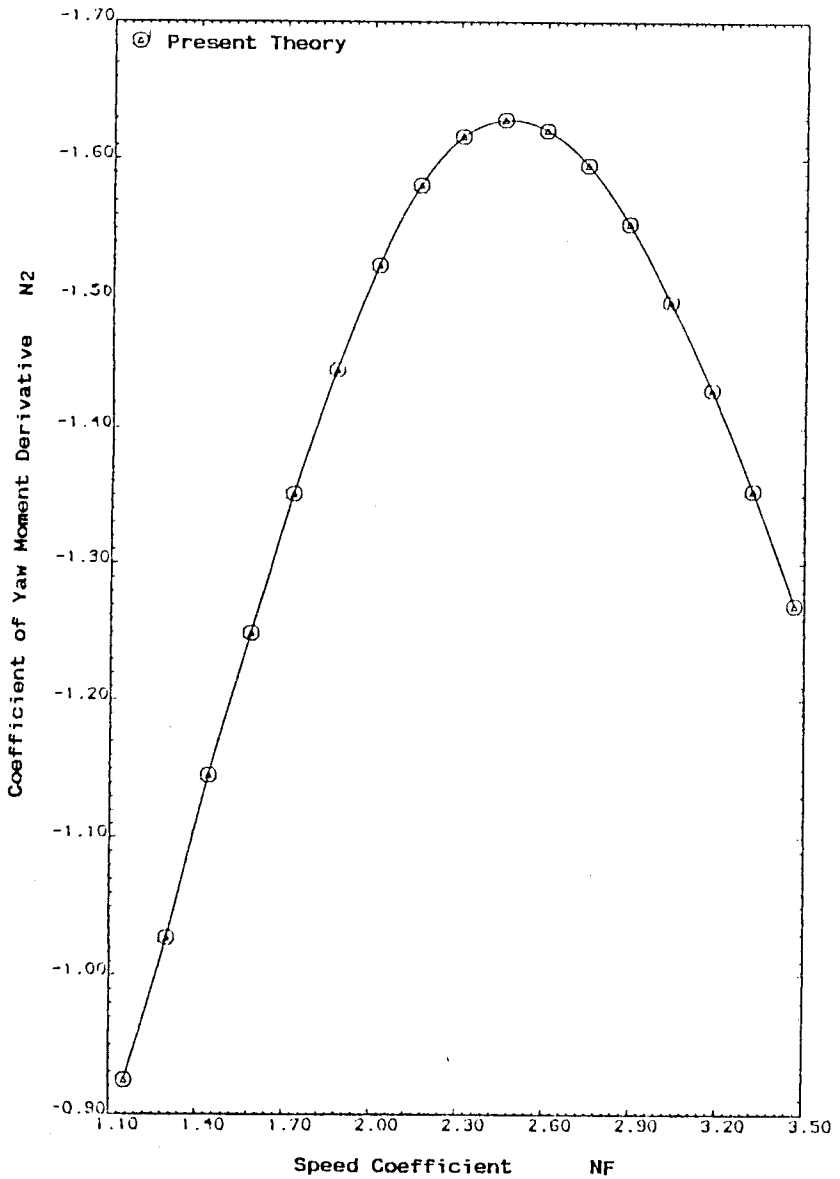

Fig.(7.15d) LCLR/B for 10° Constant Deadrise Hull
(Cp=3.3, Lk/B=3.0)

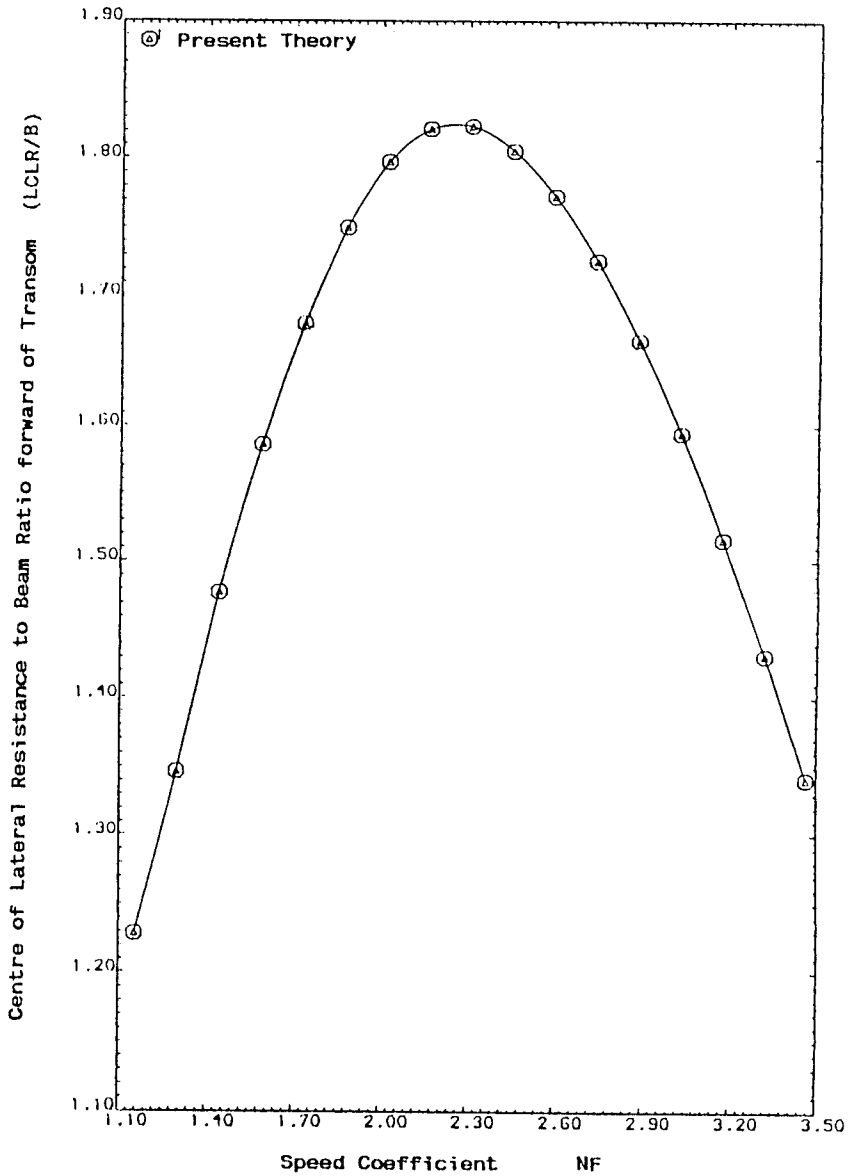

Fig.(7.15e) LCL/B for 10^{O} Constant Deadrise Hull
(Cp=3.3, Lk/B=3.0)

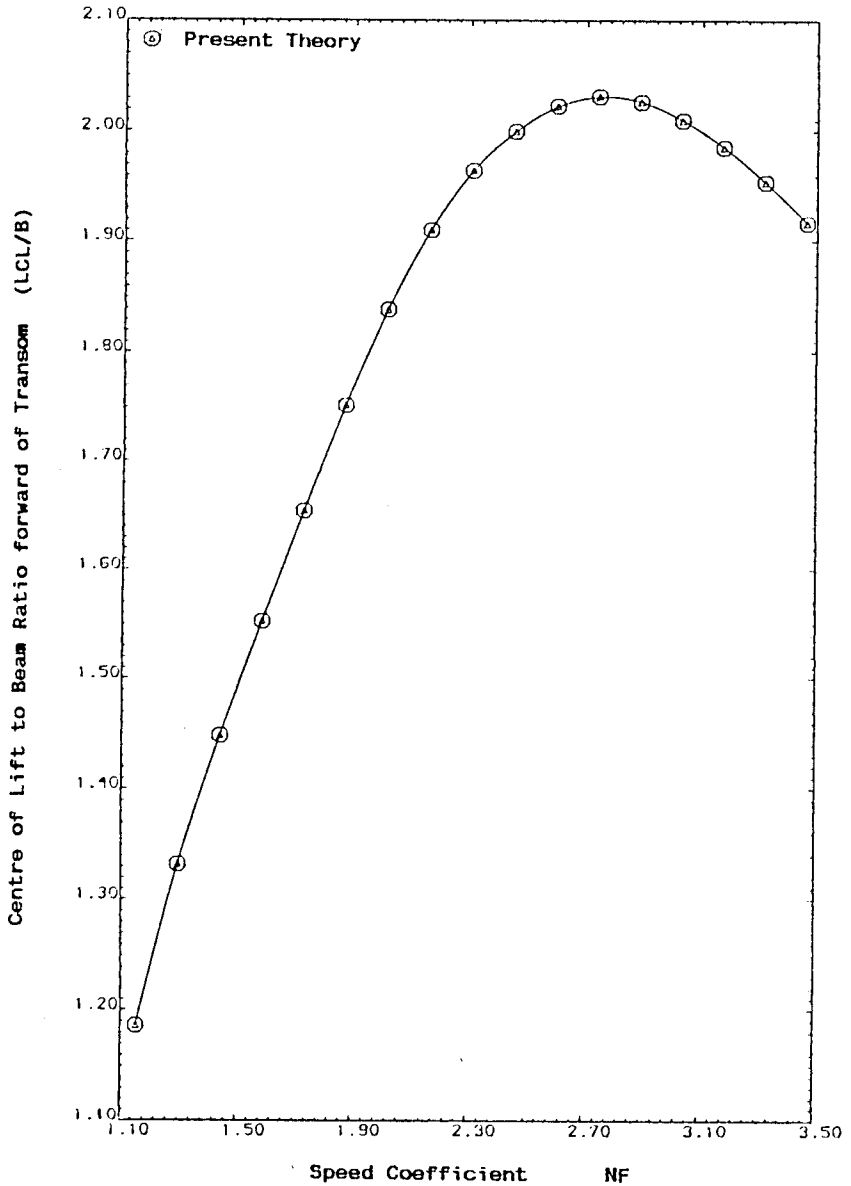

Fig.(7.16a) F2 for 10° Constant Deadrise Hull
(Cp=3.3, Lk/B=2.5)

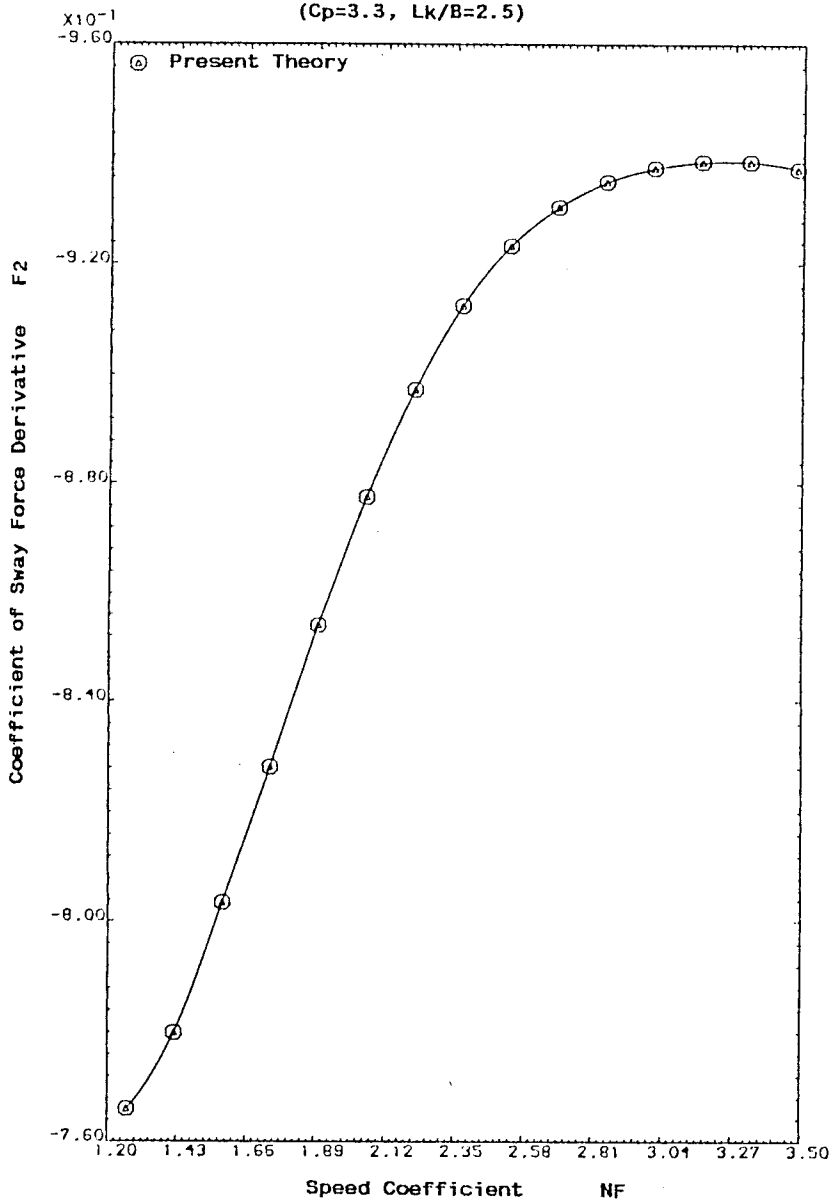

Fig.(7.16b) M2 for 10° Constant Deadrise Hull
(Cp=3.3, Lk/B=2.5)

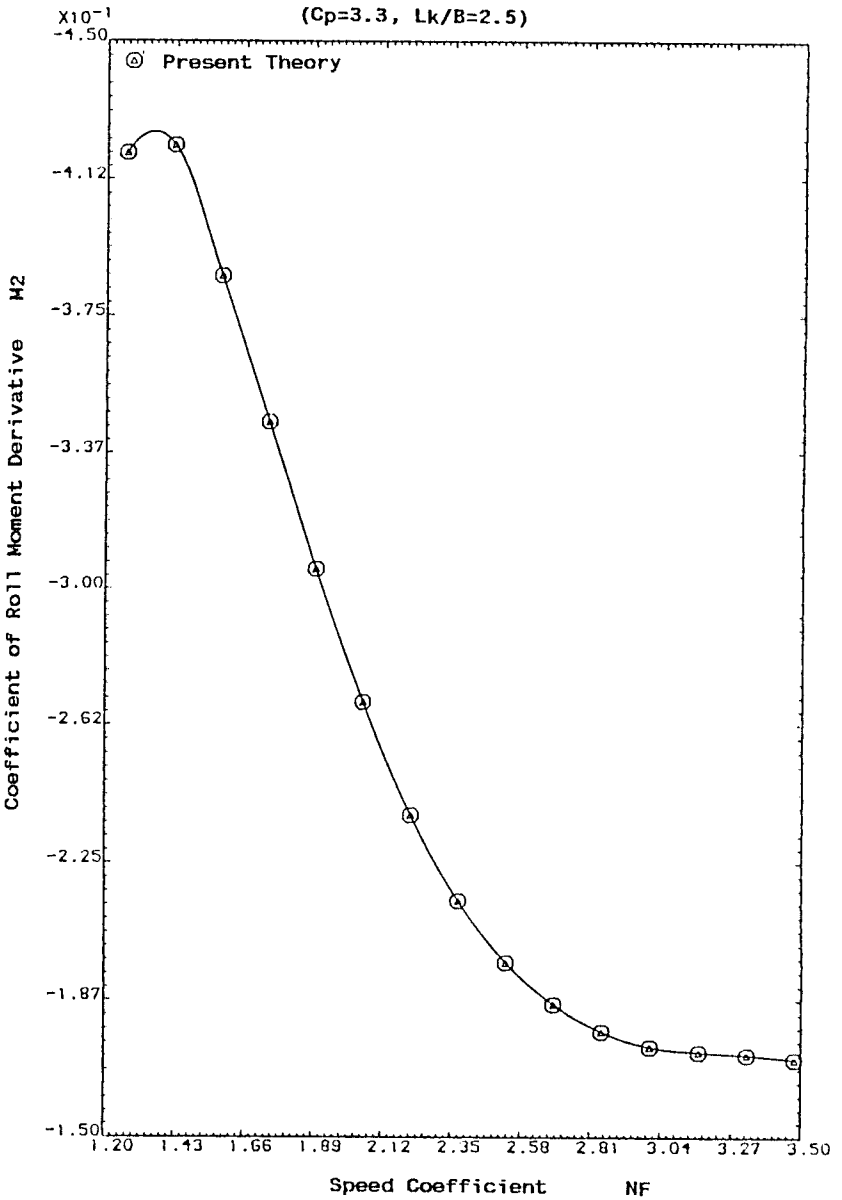

Fig.(7.16c) N2 for 10^{O} Constant Deadrise Hull
(Cp=3.3, Lk/B=2.5)

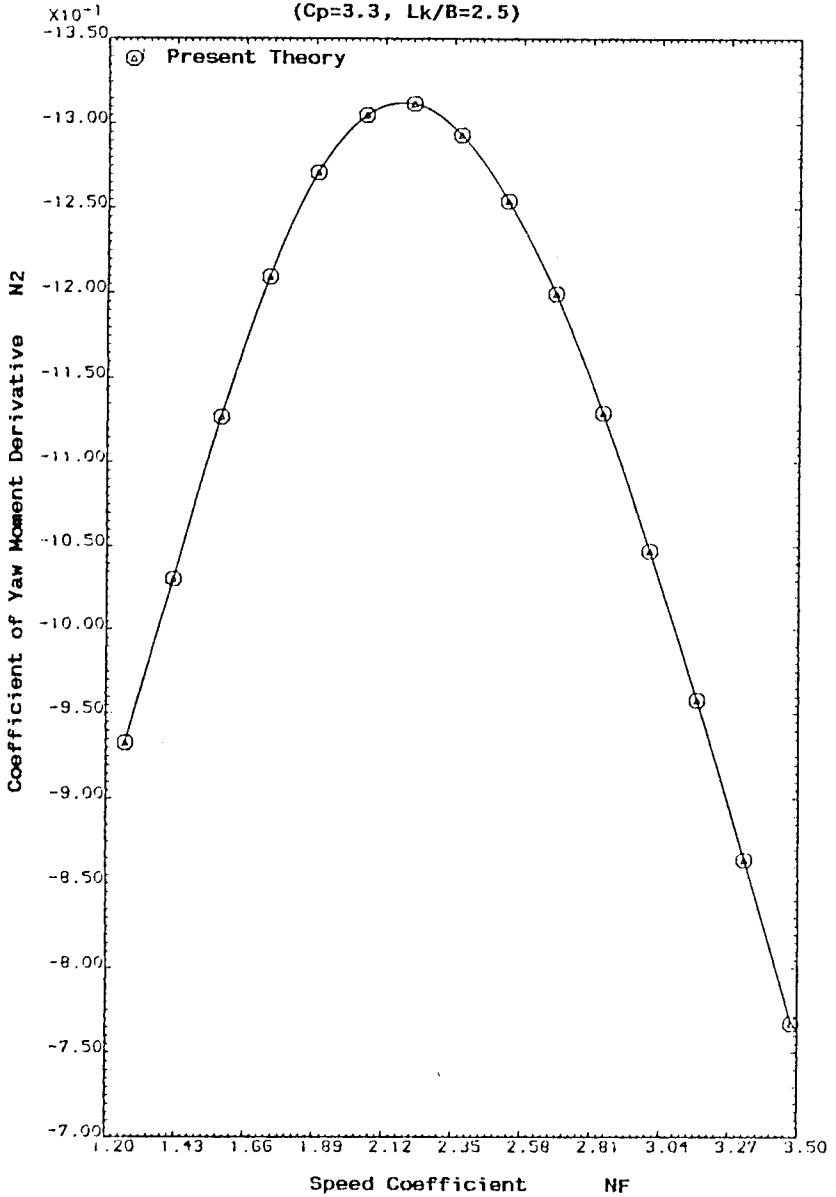

Fig.(7.16d) LCLR/B for 10^{O} Constant Deadrise Hull
(Cp=3.3, Lk/B=2.5)

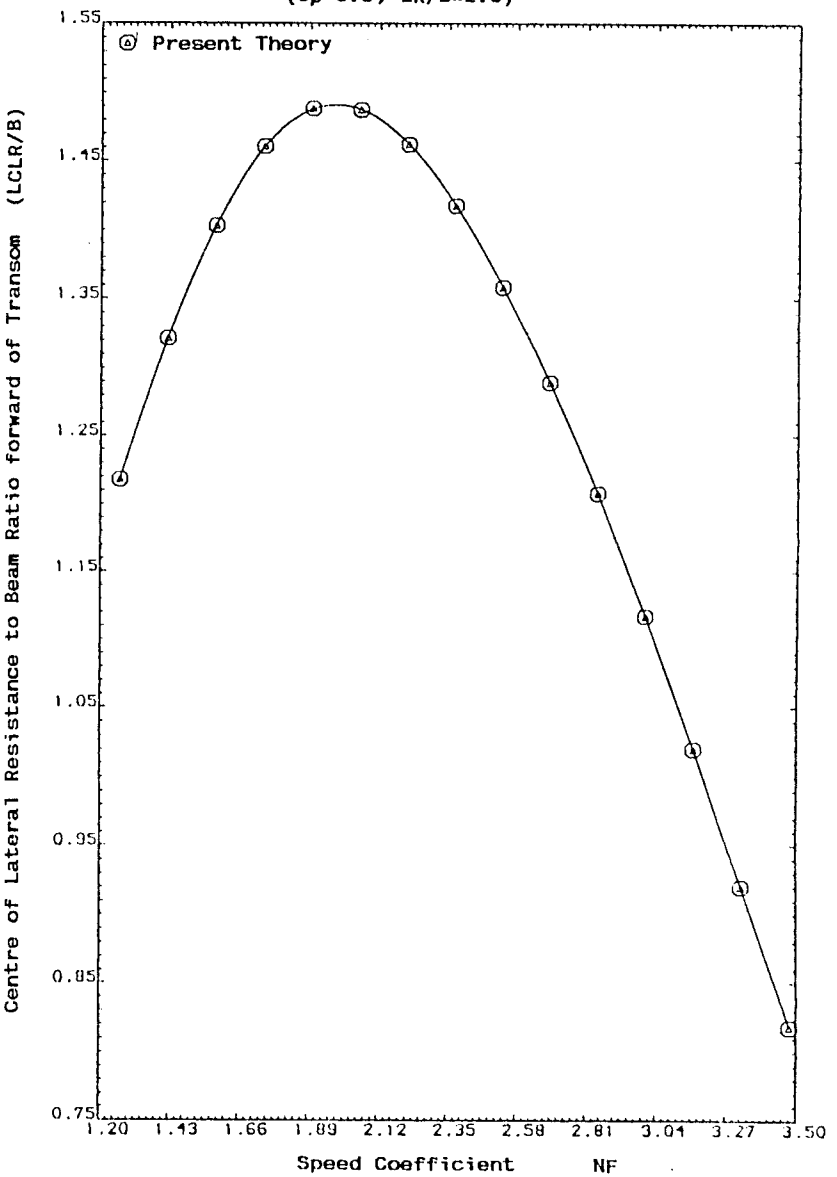

Fig.(7.16e) LCL/B for 10^{O} Constant Deadrise Hull
(Cp=3.3, Lk/B=2.5)

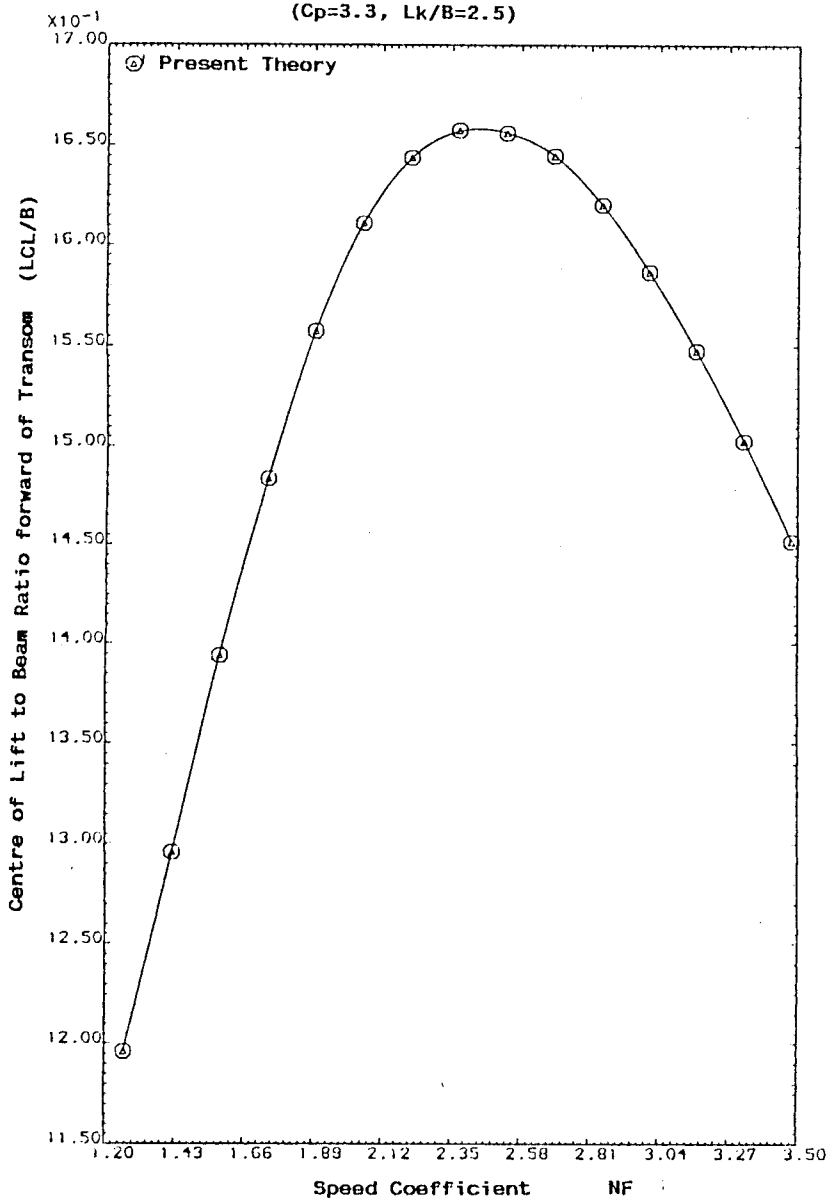

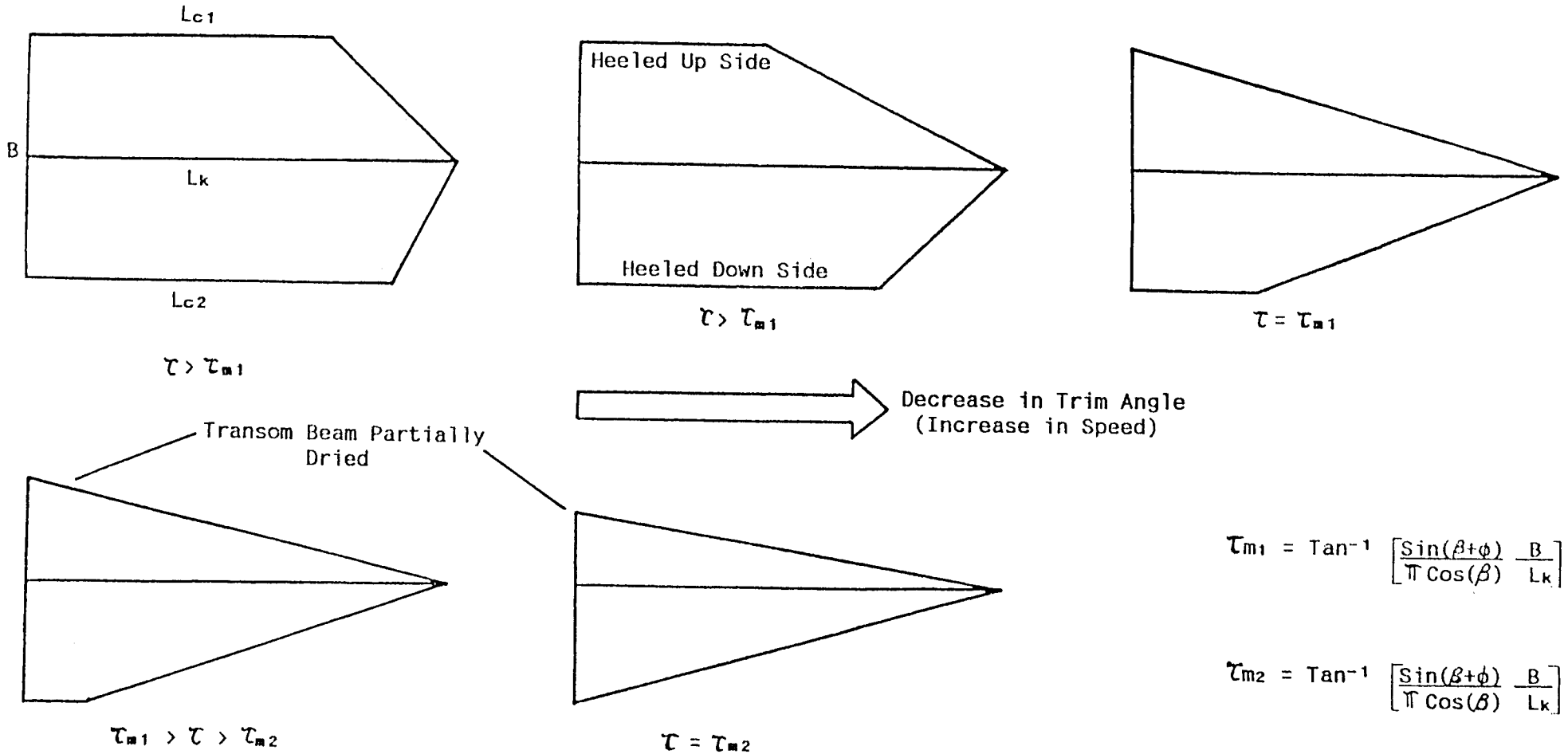

Fig.(7.17) Change in Wetted Bottom Shape against the Decrease in Trim Angle (or Increase in Speed) for a Planing Constant Deadrise Hull in Heel Condition

Table(7.2) F_2, M_2 and L_{CLR}/B calculated from Savitsky's Empirical Equations (5.3.2) and (5.4.1) for High Speed Approximation

Table(7.2a) $L_K/B = 2.5$ $\phi = 3.62°$ $\beta = 10°$

$\tau°$	$\frac{B_U}{B}$	$\frac{B_d}{B}$	$\frac{A_{WU}}{B^2}$	$\frac{A_{Wd}}{B^2}$	$\frac{L_W}{B}$	$\frac{(A_{Wd}-A_{WU})}{B^2}$	F_2	N_2	$\frac{L_{CLR}}{B}$
10.00	0.500	0.500	1.142	1.199	2.341	0.057	-0.997	-1.632	1.636
9.000	0.500	0.500	1.130	1.193	2.323	0.063	-0.993	-1.598	1.609
8.000	0.500	0.500	1.115	1.186	2.301	0.072	-0.988	-1.555	1.574
7.000	0.500	0.500	1.095	1.177	2.272	0.082	-0.981	-1.501	1.530
6.000	0.500	0.500	1.069	1.165	2.234	0.096	-0.971	-1.428	1.470
5.000	0.500	0.500	1.033	1.147	2.180	0.115	-0.957	-1.327	1.386
4.000	0.500	0.500	0.978	1.122	2.099	0.144	-0.935	-1.175	1.256
3.000	0.500	0.500	0.887	1.079	1.966	0.192	-0.894	-0.923	1.032
2.000	0.500	0.500	0.705	0.993	1.698	0.288	-0.792	-0.424	0.535
1.744	0.500	0.500	0.625	0.955	1.580	0.330	-0.736	-0.206	0.280
1.437	0.412	0.500	0.515	0.892	1.407	0.377	-0.388	0.072	-0.186
1.130	0.324	0.500	0.405	0.795	1.200	0.390	-0.003	0.305	-101.6
0.823	0.236	0.500	0.295	0.625	0.920	0.330	0.397	0.372	0.938

Note: $\tau_{m1} = 1.744°$ and $\tau_{m2} = 0.823°$

Table(7.2b) $L_K/B = 2.5$ $\phi = 3.62°$ $\beta = 20°$

$\tau°$	$\frac{B_U}{B}$	$\frac{B_d}{B}$	$\frac{A_{WU}}{B^2}$	$\frac{A_{Wd}}{B^2}$	$\frac{L_W}{B}$	$\frac{(A_{Wd}-A_{WU})}{B^2}$	F_2	N_2	$\frac{L_{CLR}}{B}$
10.00	0.500	0.500	1.058	1.115	2.172	0.057	-1.057	-1.476	1.396
9.000	0.500	0.500	1.036	1.099	2.135	0.063	-1.047	-1.403	1.339
8.000	0.500	0.500	1.009	1.080	2.089	0.072	-1.034	-1.311	1.268
7.000	0.500	0.500	0.974	1.055	2.029	0.082	-1.016	-1.194	1.174
6.000	0.500	0.500	0.927	1.023	1.950	0.096	-0.991	-1.037	1.046
5.000	0.500	0.500	0.862	0.977	1.839	0.115	-0.952	-0.819	0.860
4.000	0.500	0.500	0.765	0.908	1.673	0.144	-0.884	-0.492	0.557
3.107	0.500	0.500	0.625	0.810	1.435	0.185	-0.759	-0.025	0.032
2.801	0.451	0.500	0.563	0.762	1.325	0.199	-0.400	0.162	-0.406
2.495	0.401	0.500	0.502	0.702	1.203	0.200	-0.026	0.295	-11.35
2.188	0.352	0.500	0.440	0.625	1.065	0.185	0.355	0.333	0.938

Note: $\tau_{m1} = 3.107°$ and $\tau_{m2} = 2.188°$

$$F_2 = \frac{\partial F_V}{\partial \phi}\frac{1}{F_Z} \qquad N_2 = \frac{\partial M_Y}{\partial \phi}\frac{1}{B\,F_Z}$$

L_W/B = Total Wetted Area to Beam Square (B^2) Ratio

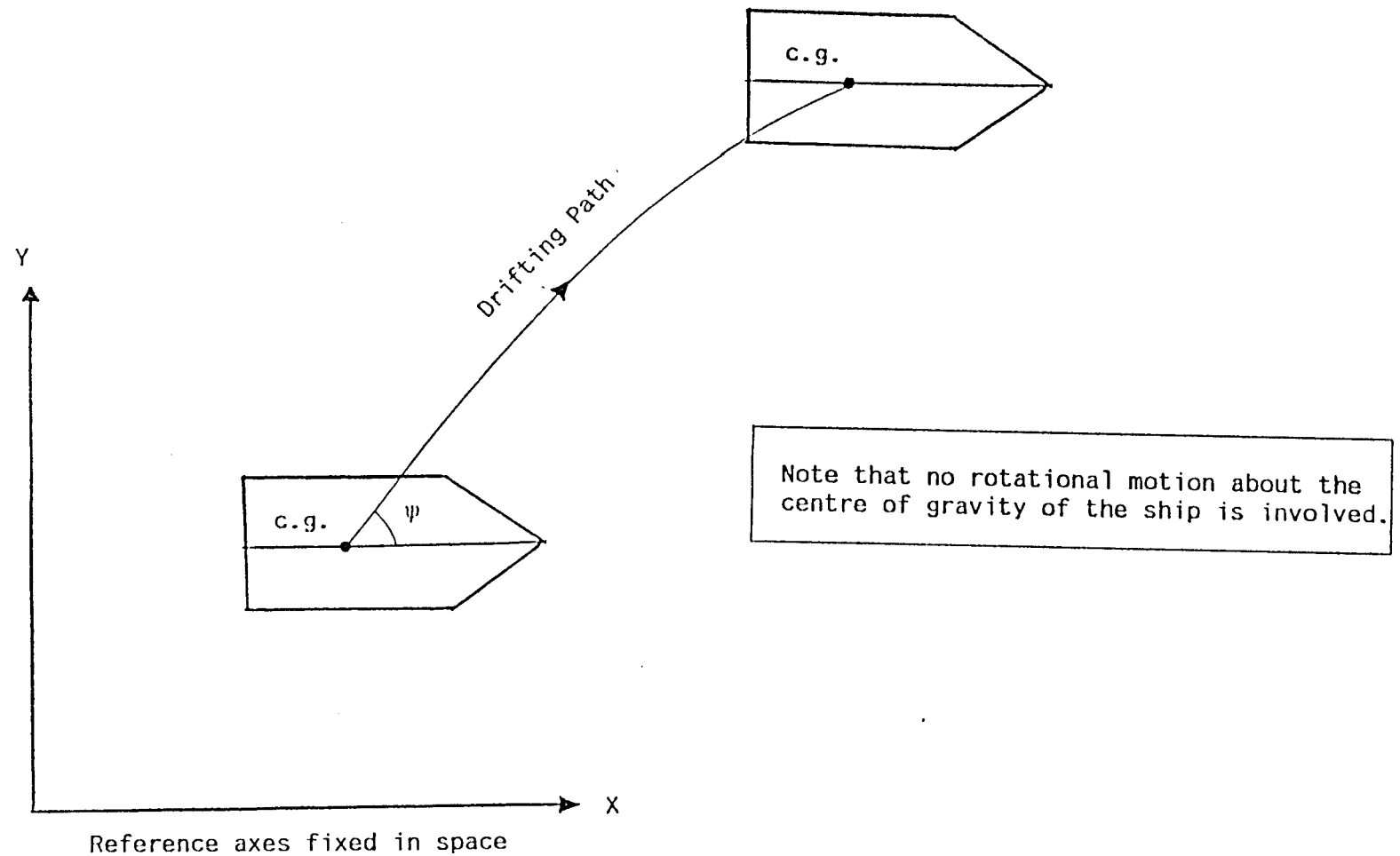

Fig.(8.1) Drifting Motion of a Ship

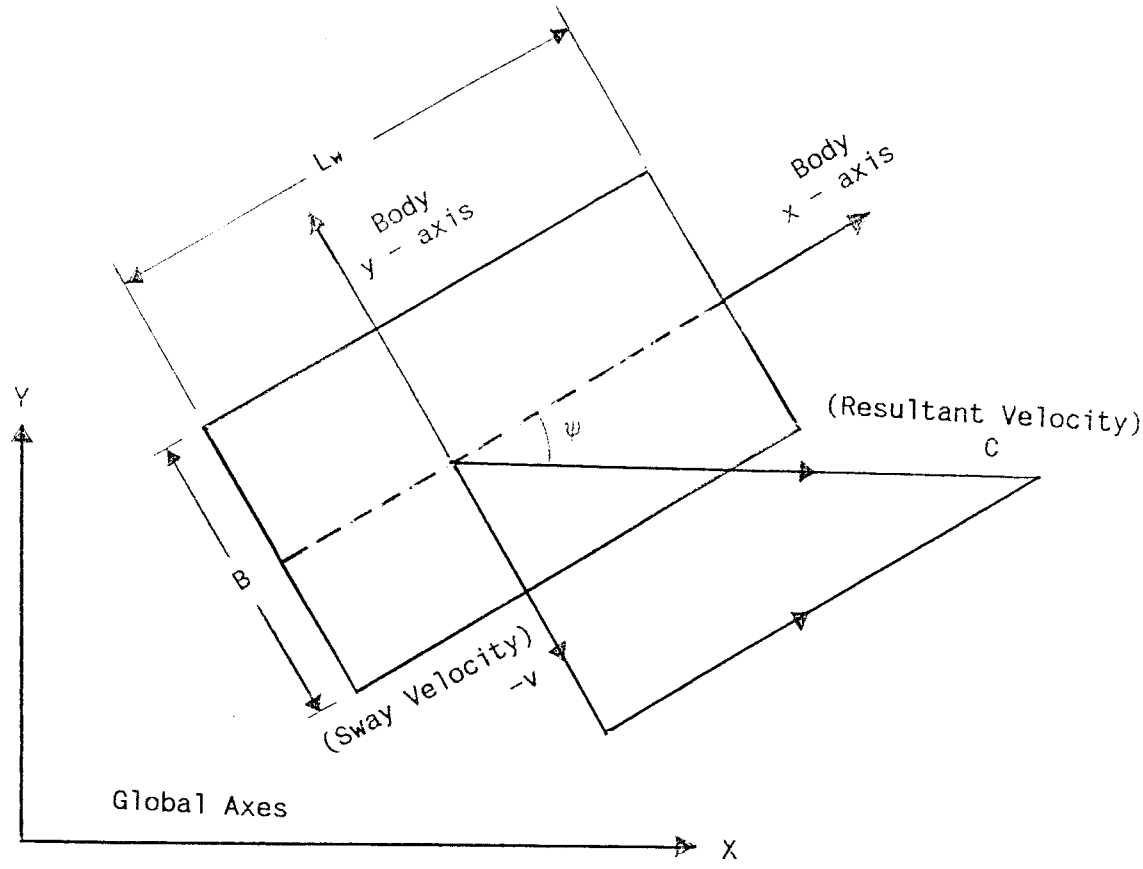

Fig.(8.2) Global Axes and Body Axes of Drifted Planing Flat Plate

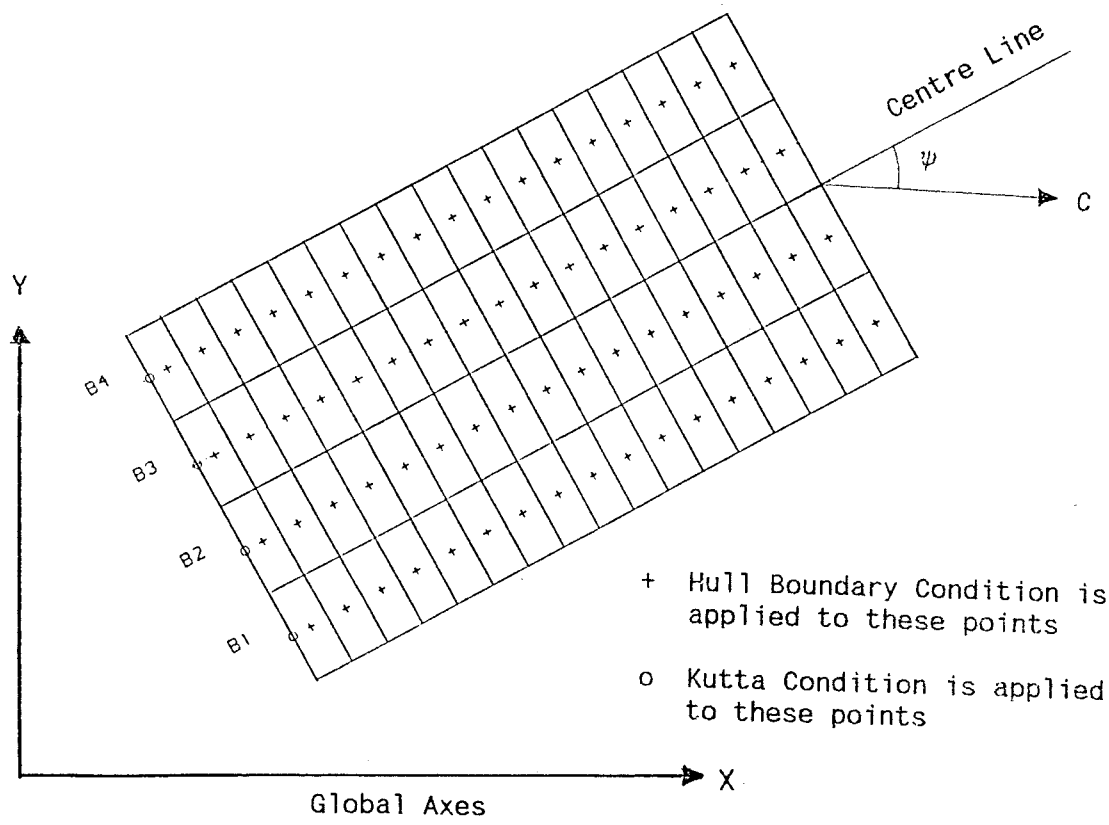

Fig.(8.3) Finite Element Mesh representing the Projected Wetted Bottom of a Drifted Planing Flat Plate

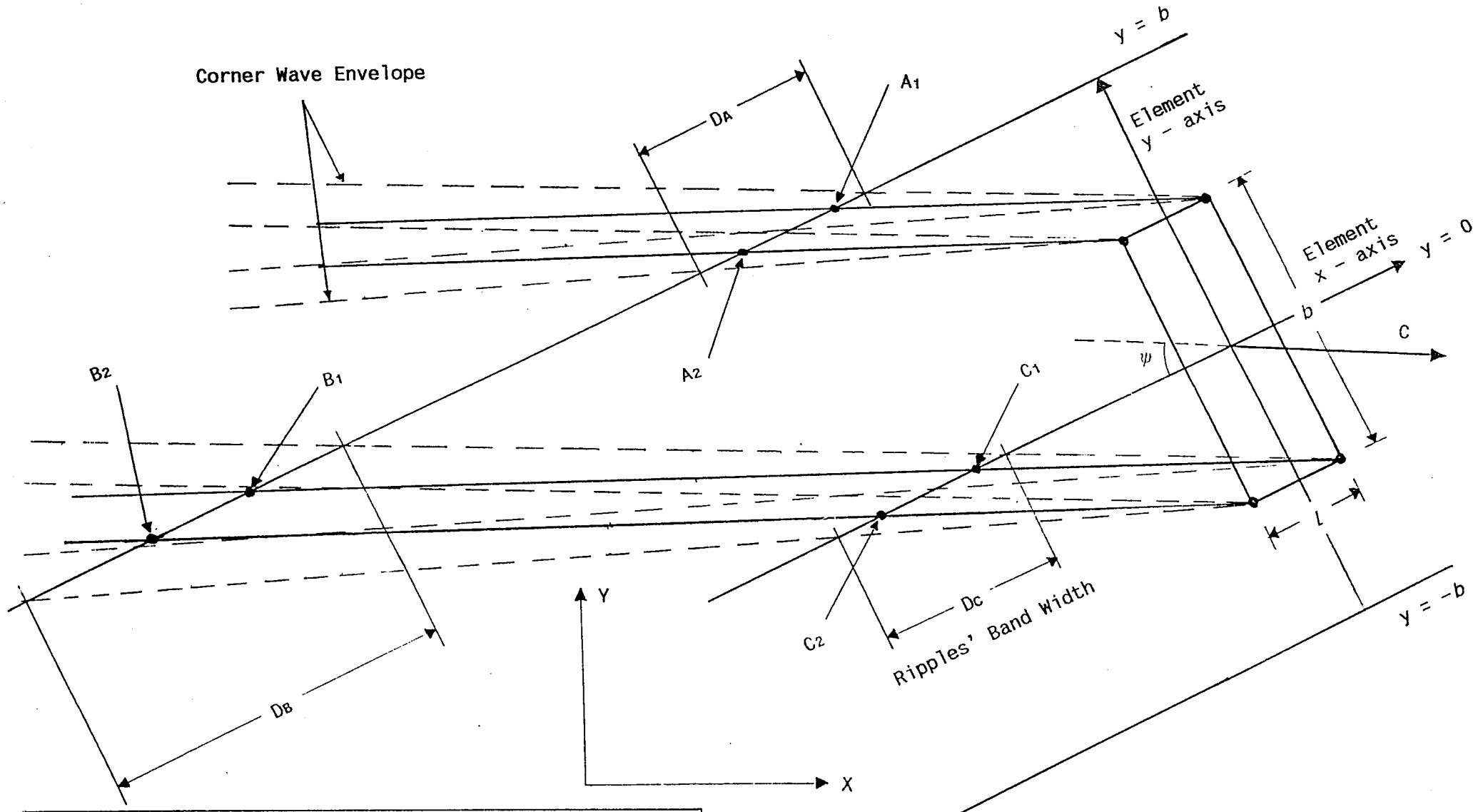

Coordinates with Respect to Element Axes System

A1 $[\{-b/(2\mathrm{Tan}(\psi))+1/2\},b]$	A_2 $[\{-b/2\mathrm{Tan}(\psi)-1/2\},b]$
B_1 $[\{-3b/(2\mathrm{Tan}(\psi))+1/2\},b]$	B_2 $[(\{-3b/(2\mathrm{Tan}(\psi))-1/2\},b]$
C_1 $[\{-b/(2\mathrm{Tan}(\psi))+1/2\},0]$	C_2 $[\{-b/2\mathrm{Tan}(\psi)-1/2\},0]$

Fig.(8.4) Formation of Downstream Wave's Ripples of a Drifted Constant Pressure Rectangular Element

Fig.(8.5a,b,c) Surface Wave Profiles of drifted Rectangular Element

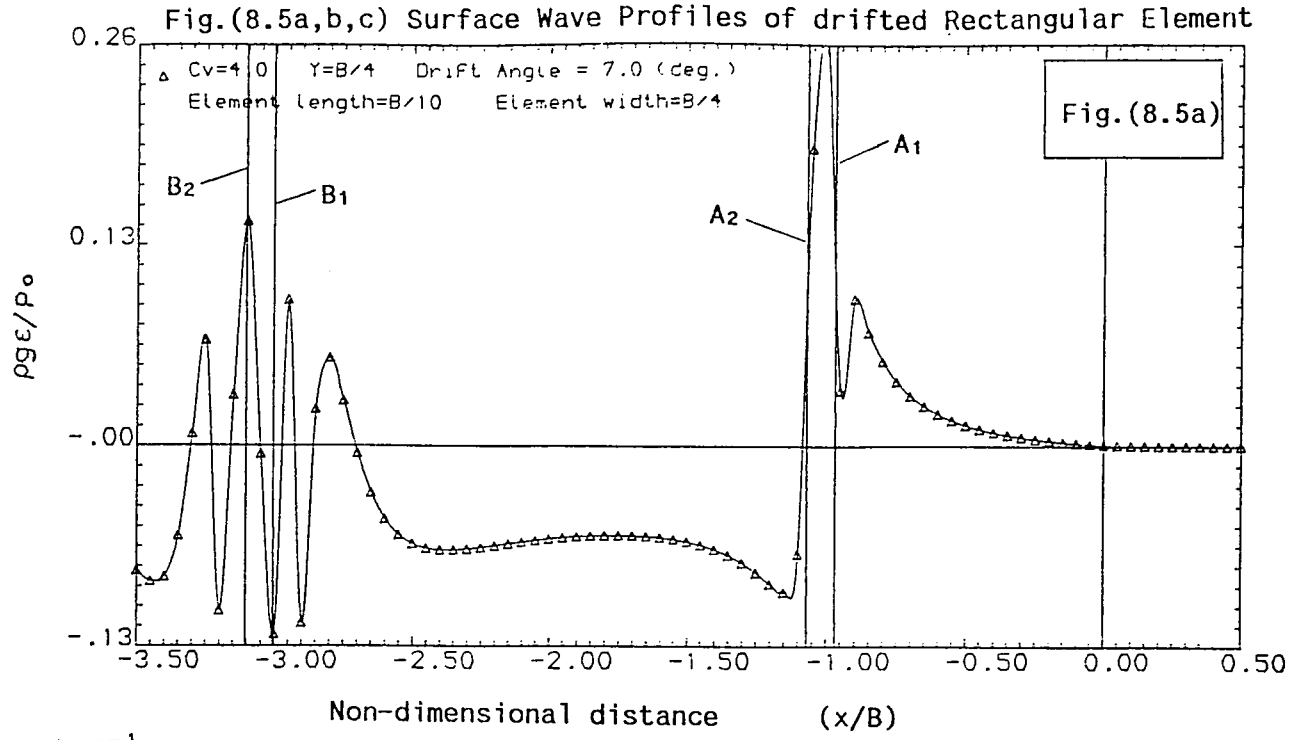

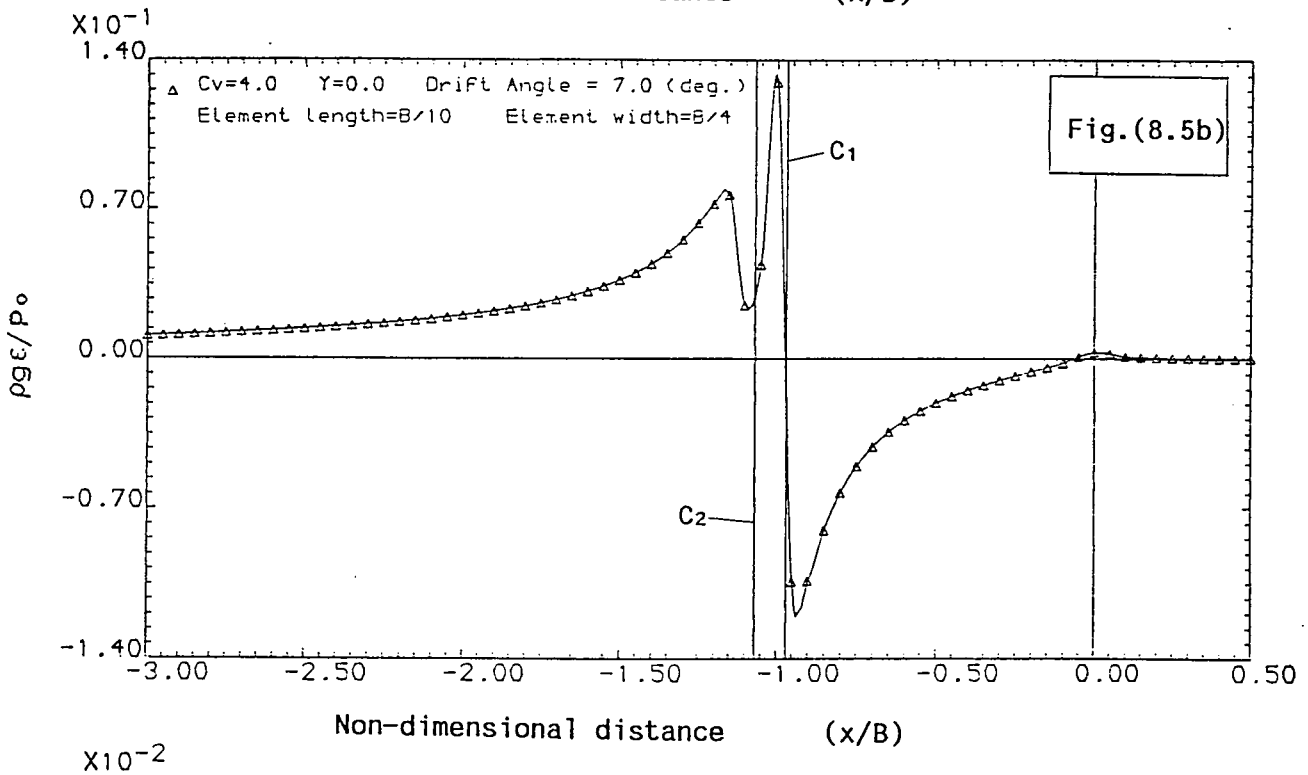

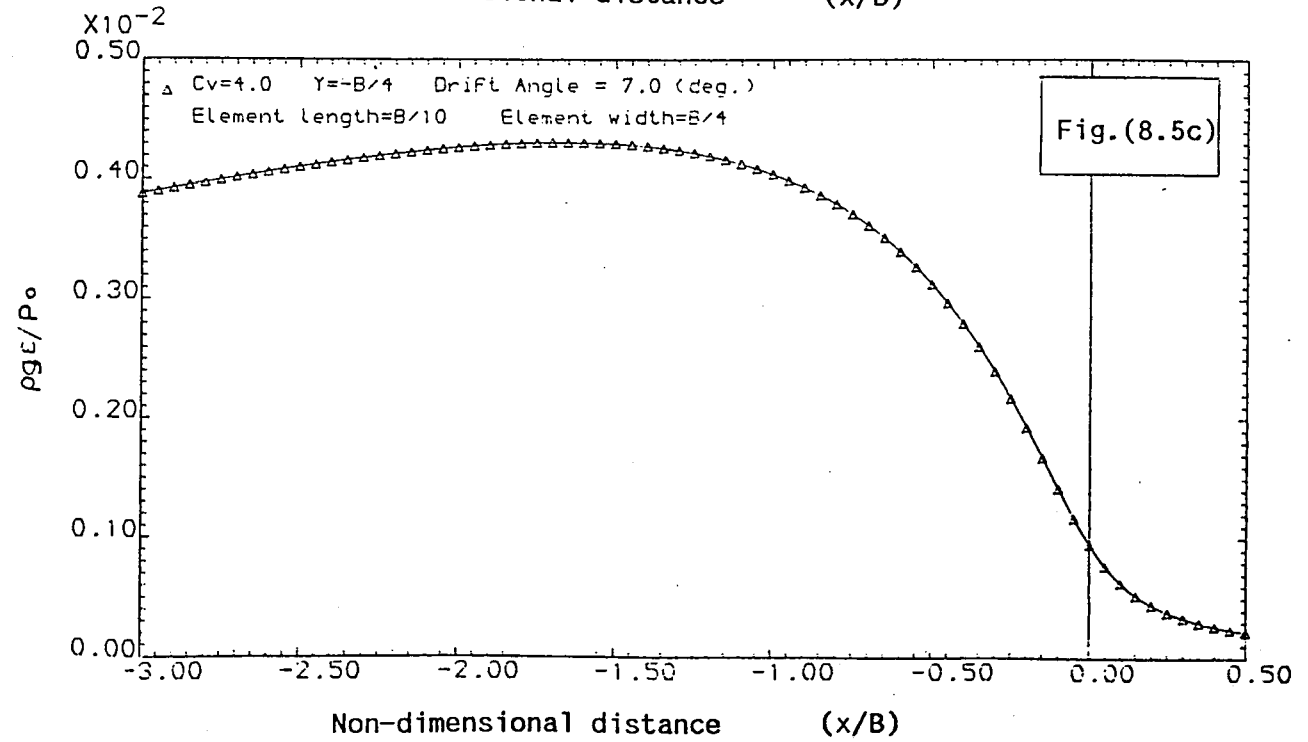

Fig.(8.6a,b,c) Surface Wave Profiles of drifted Rectangular Element

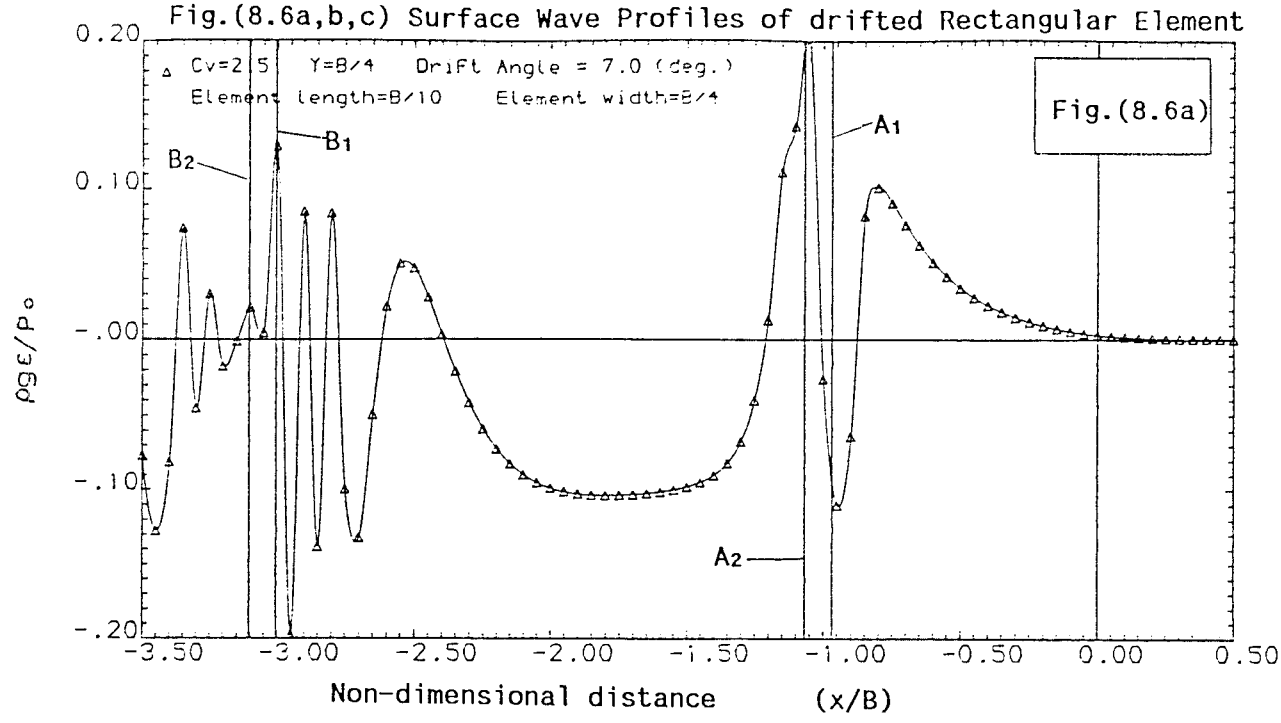

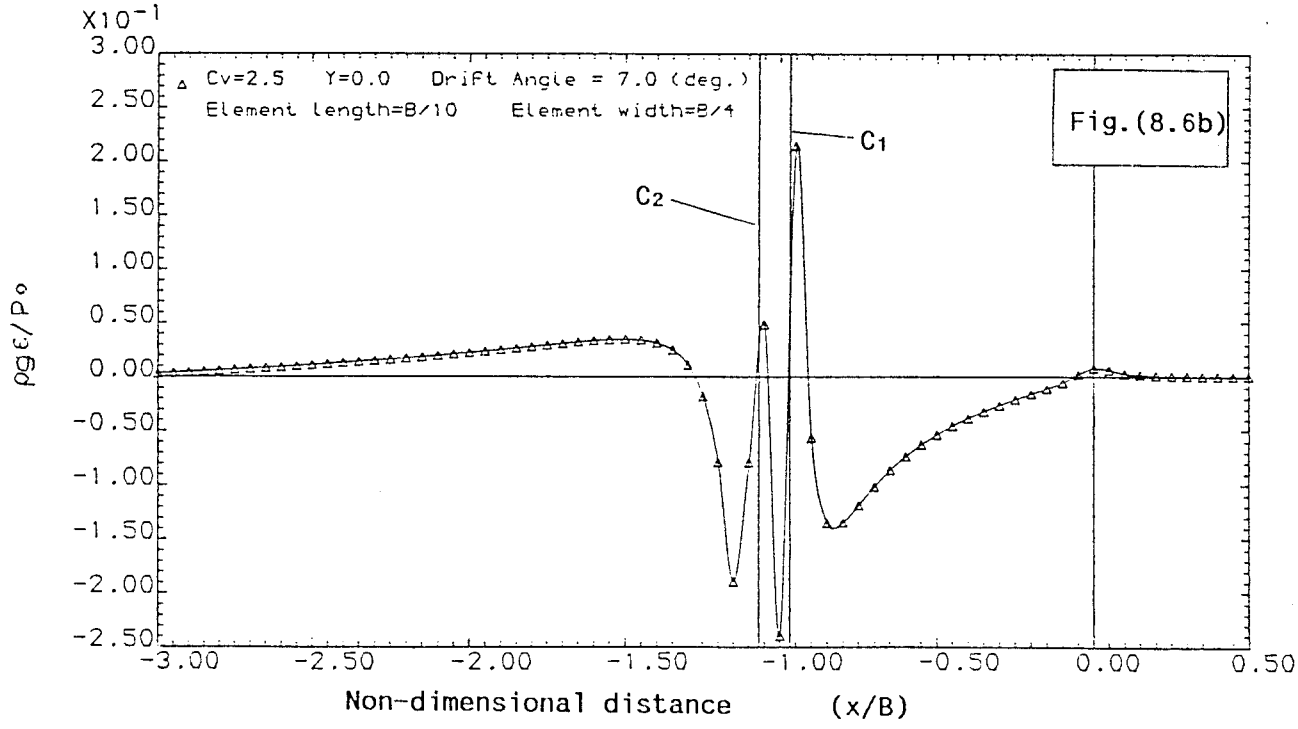

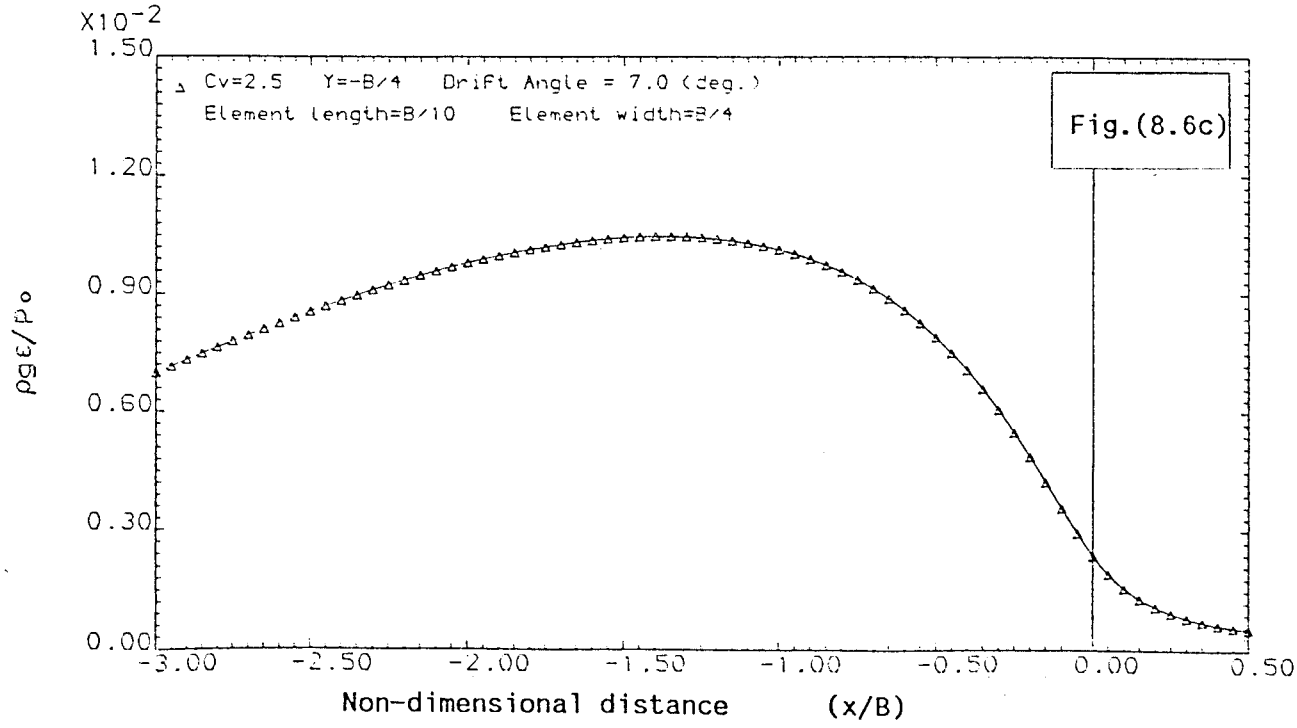

Fig.(8.7a,b,c) Surface Wave Profiles of drifted Rectangular Element

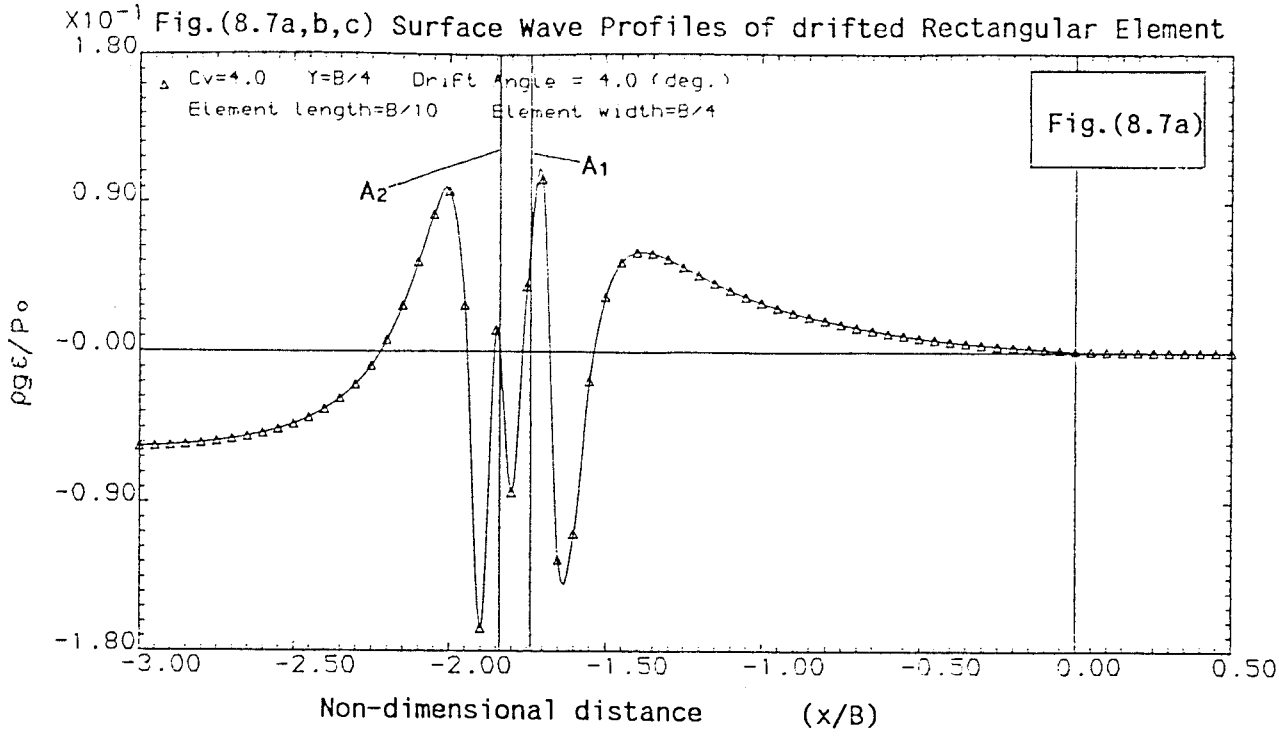

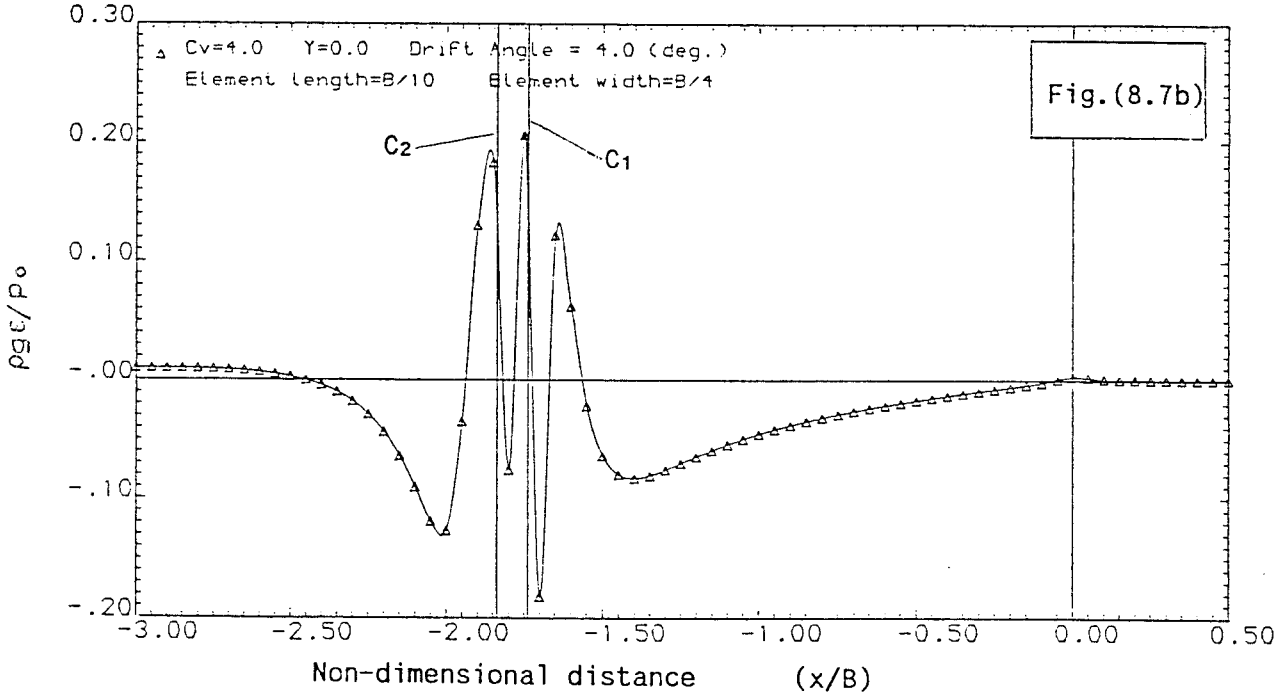

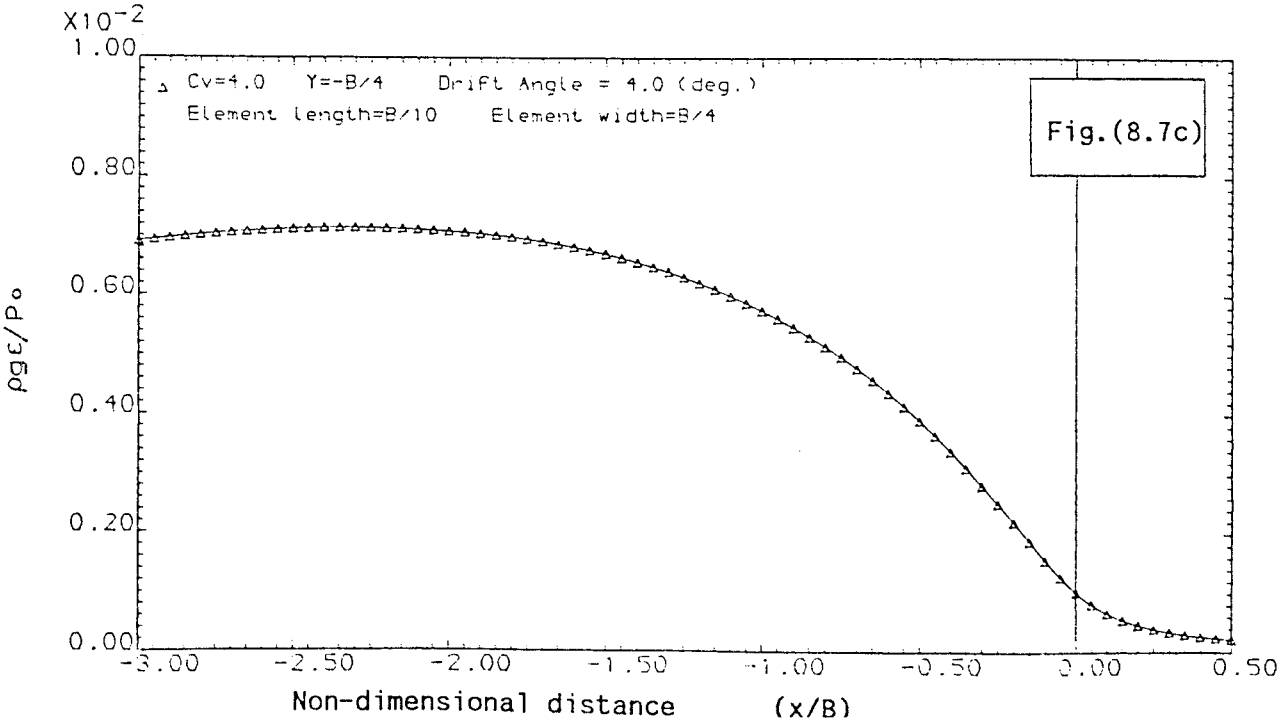

Fig.(8.8a,b,c) Surface Wave Profiles of drifted Rectangular Element

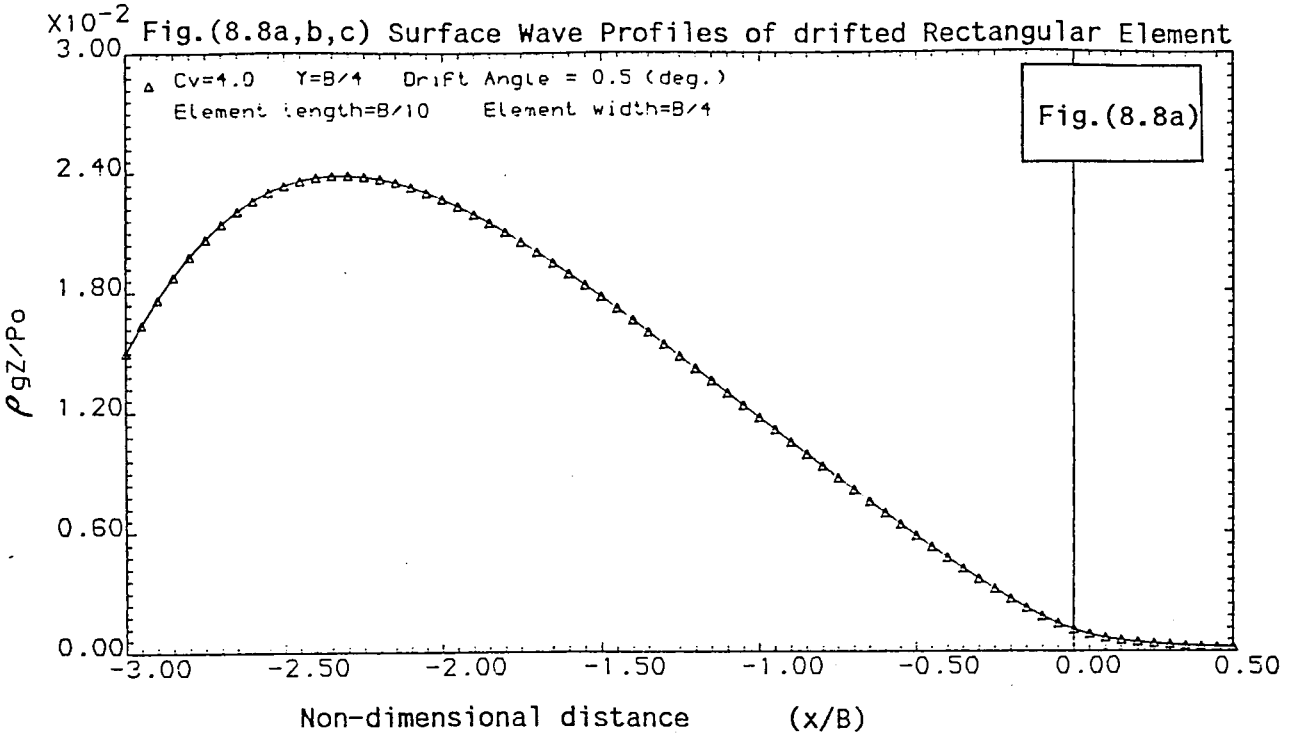

Fig.(8.8a)

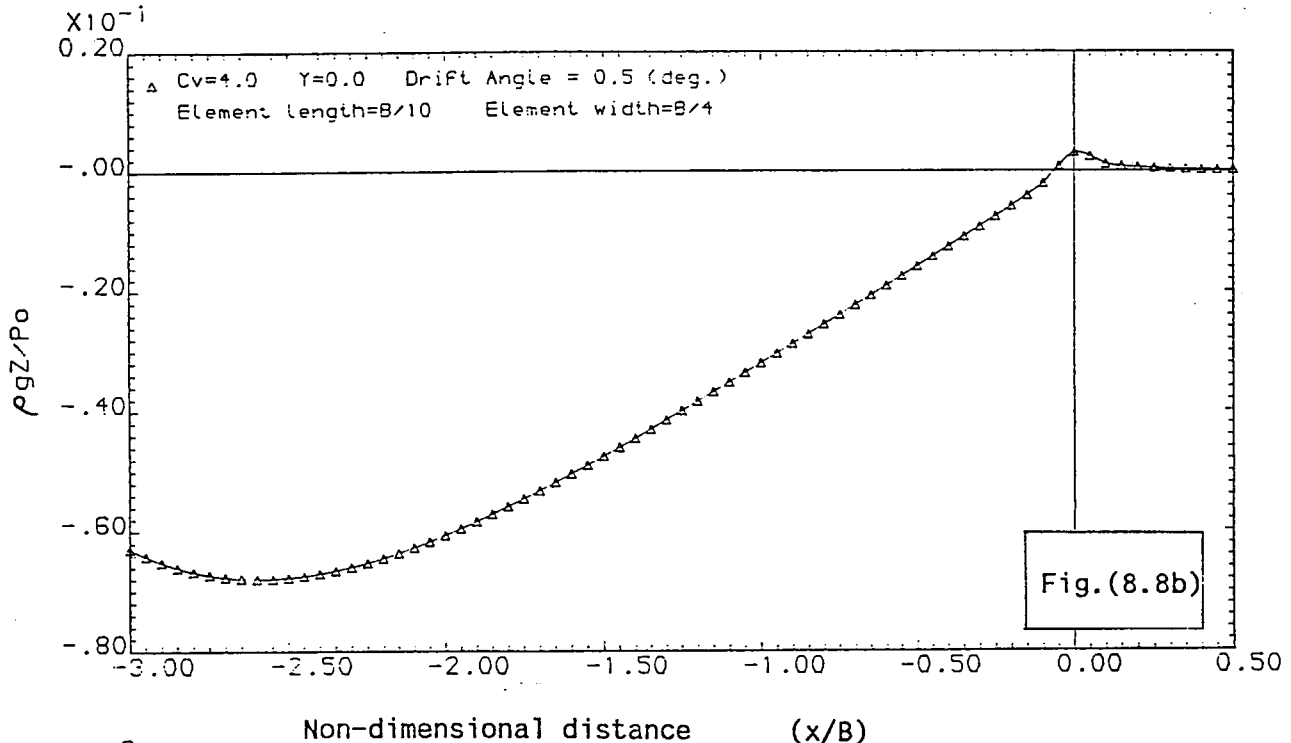

Fig.(8.8b)

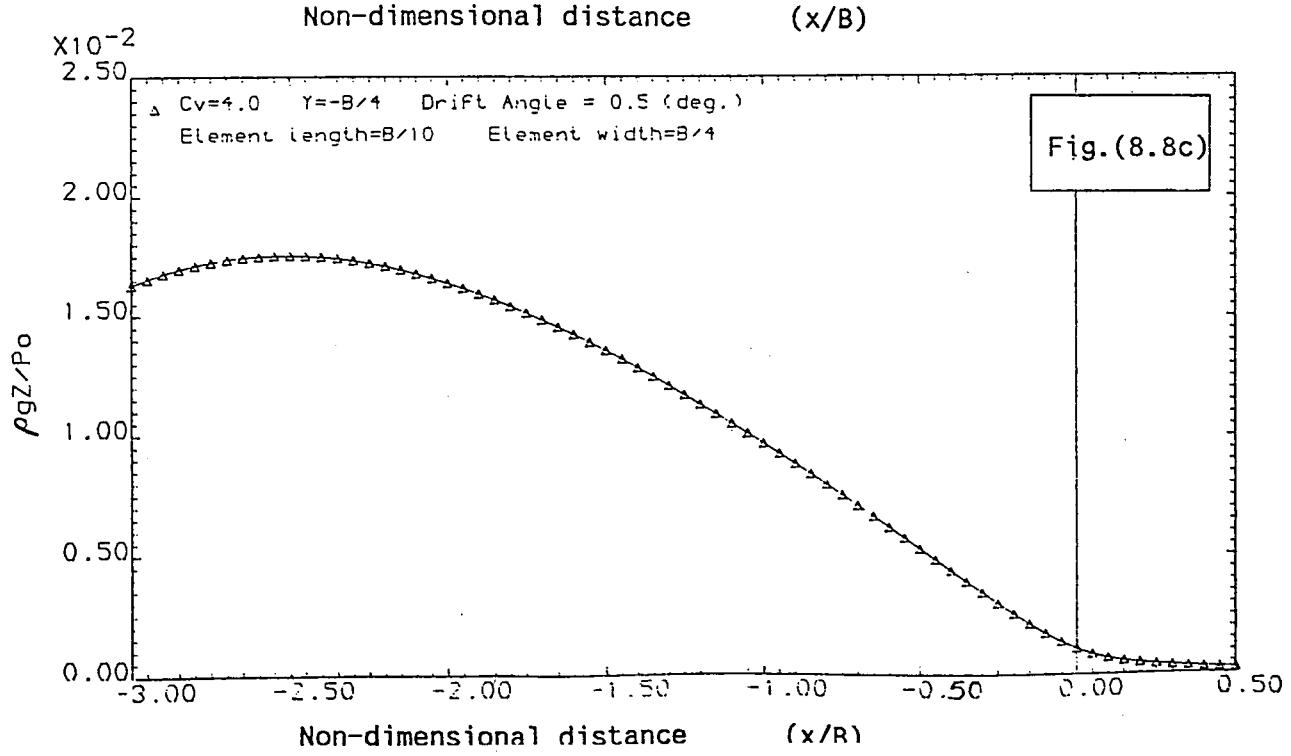

Fig.(8.8c)

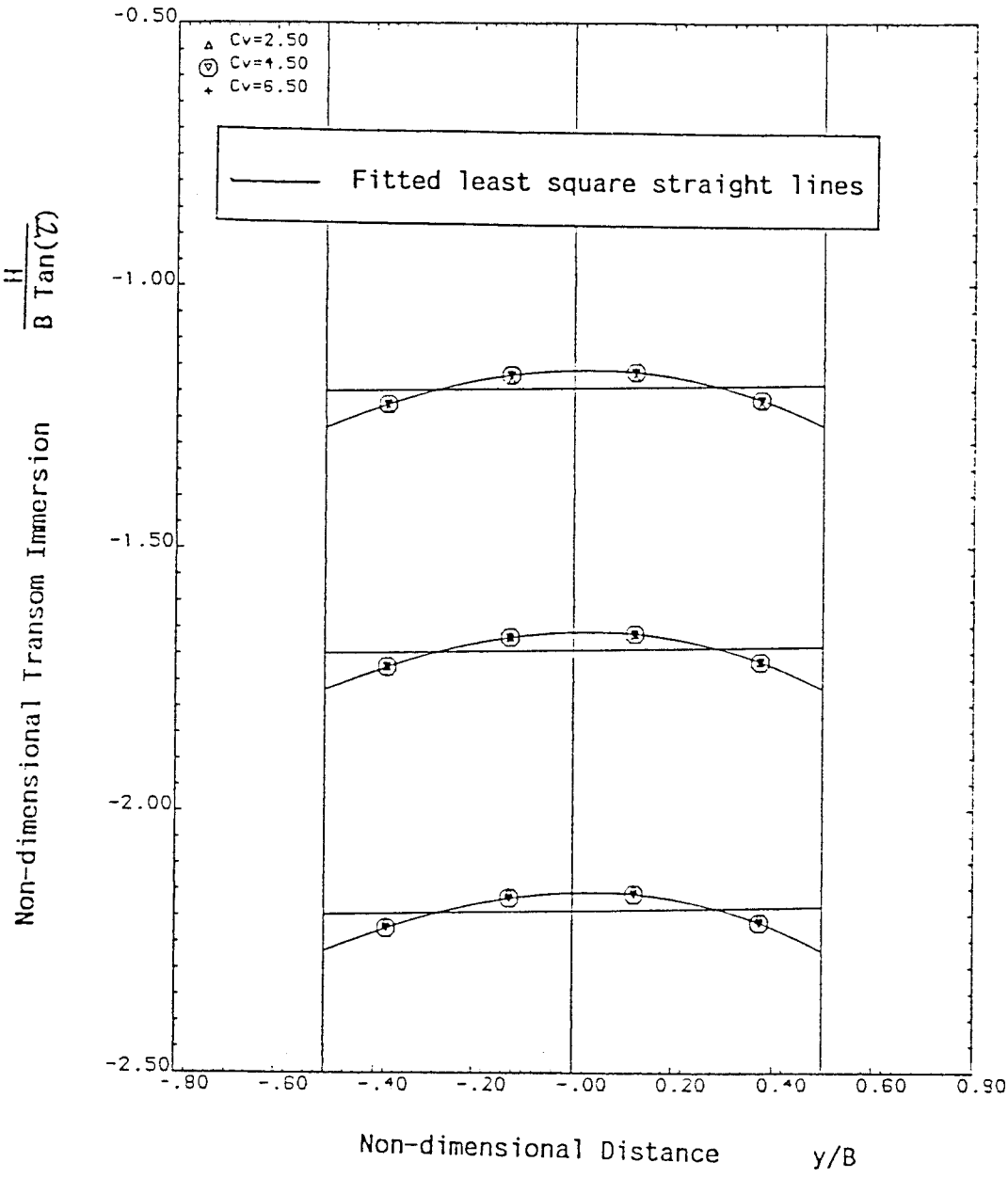

Fig.(8.9) Output Transom Shapes predicted from 0.5°

Drifted Rectangular Wetted Bottom

Fig.(8.10a) Lw/B=2.50

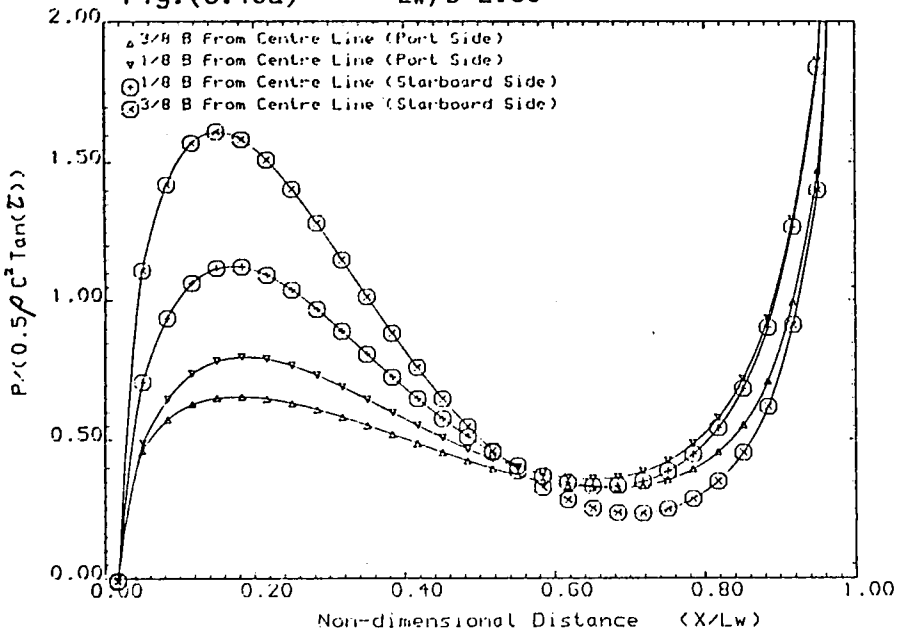

Fig.(8.10b) Lw/B=2.00

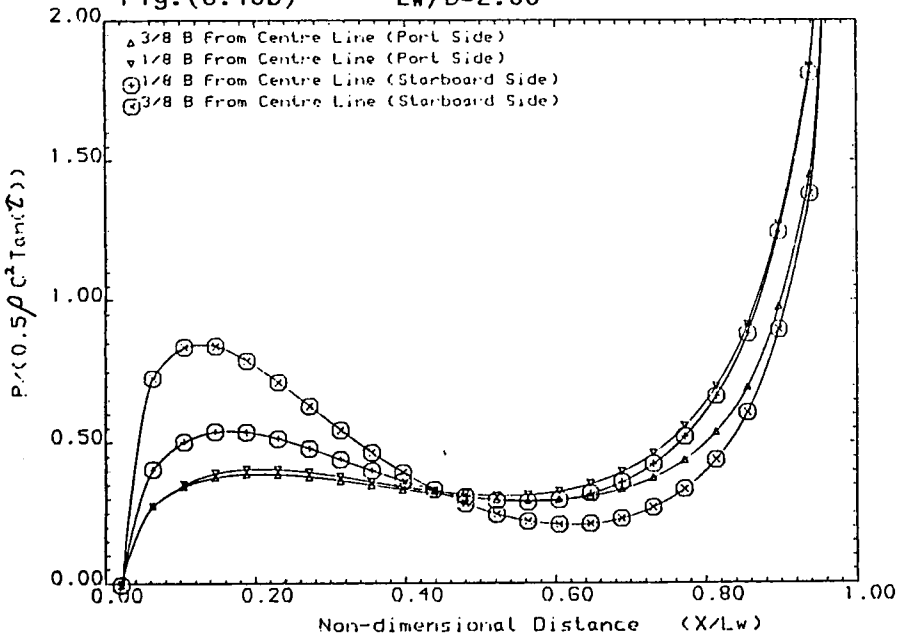

Fig.(8.10c) Lw/B=1.50

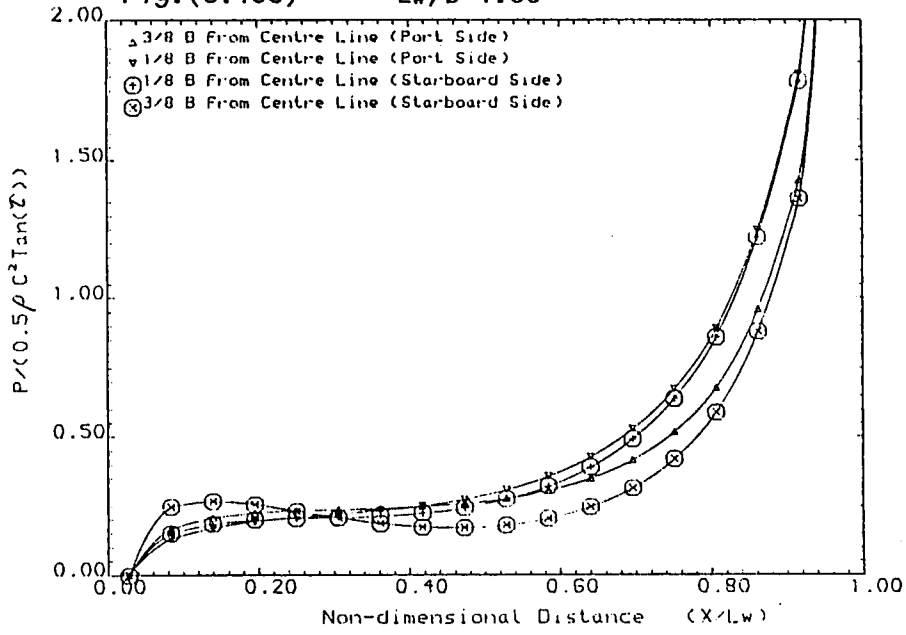

Fig.(8.10a,b,c) Pressure distributions for 0.5° Drifted Planing Flat Plates at Cv=2.50

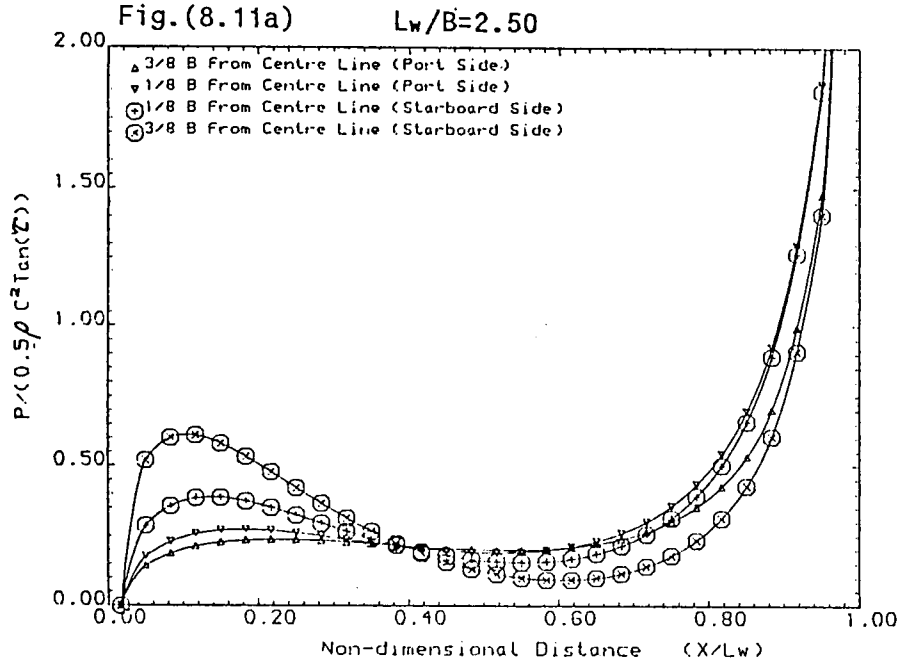

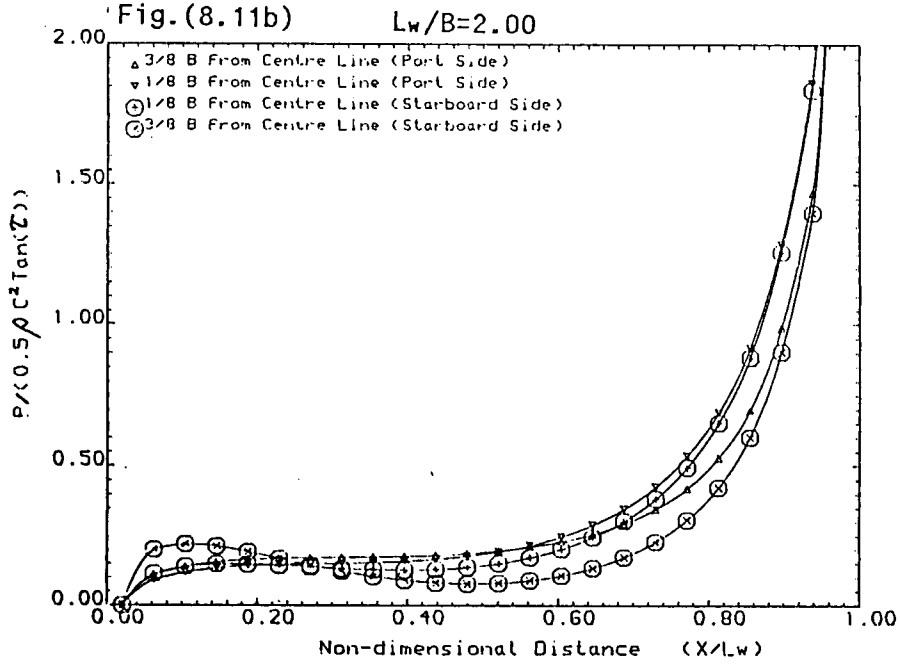

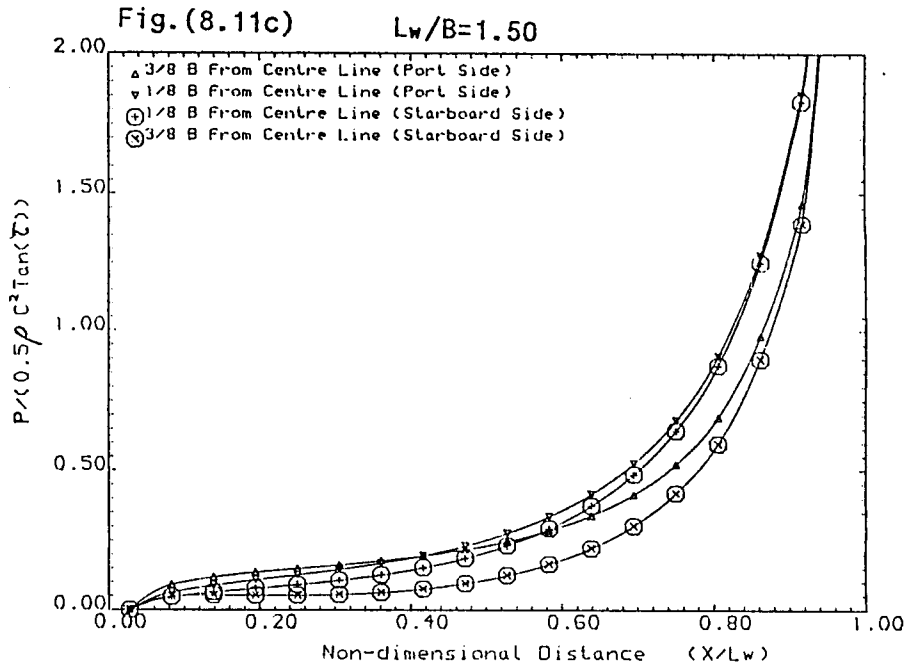

Fig.(8.11a,b,c) Pressure distributions for 0.5° Drifted Planing Flat Plates at Cv=3.50

Fig.(8.12a) Lw/B=2.50

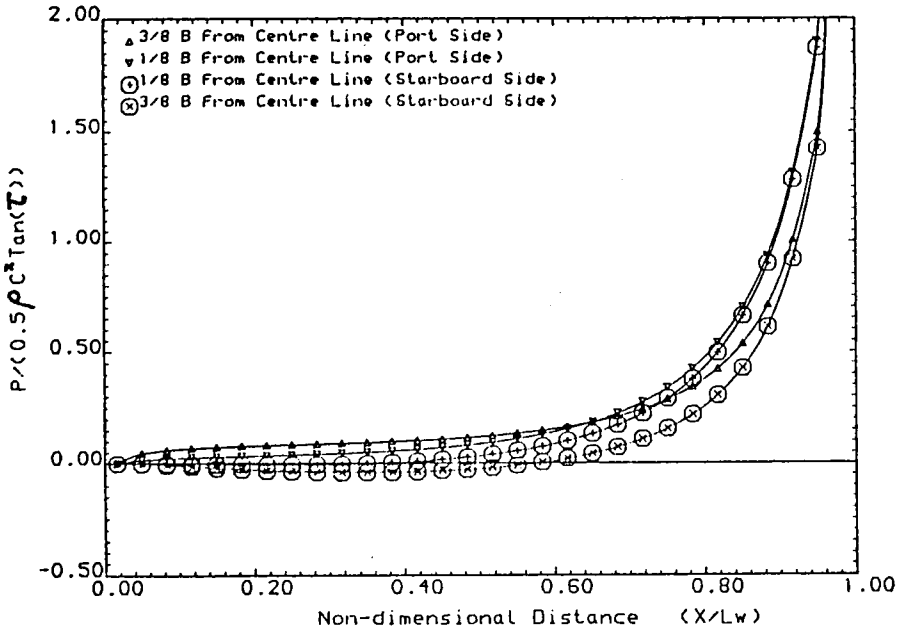

Fig.(8.12b) Lw/B=2.00

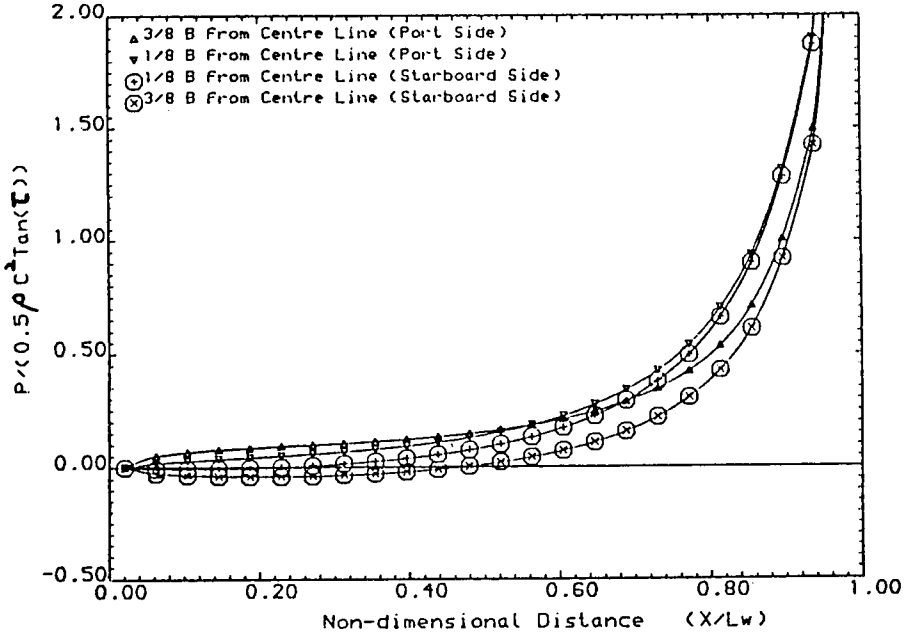

Fig.(8.12c) Lw/B=1.50

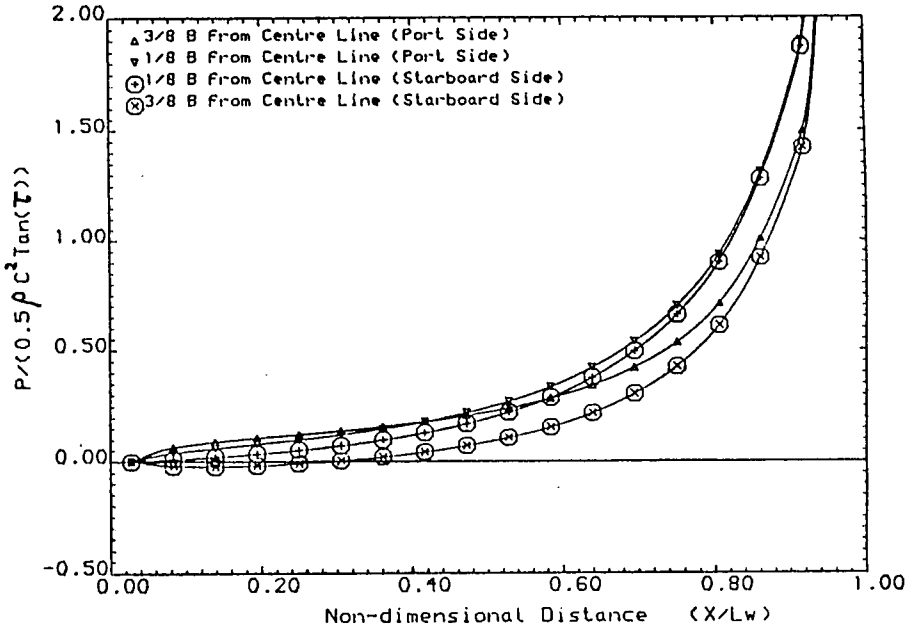

Fig.(8.12a,b,c) Pressure Distributions for 0.5° Drifted Planing Flat Plates at C_v=6.50

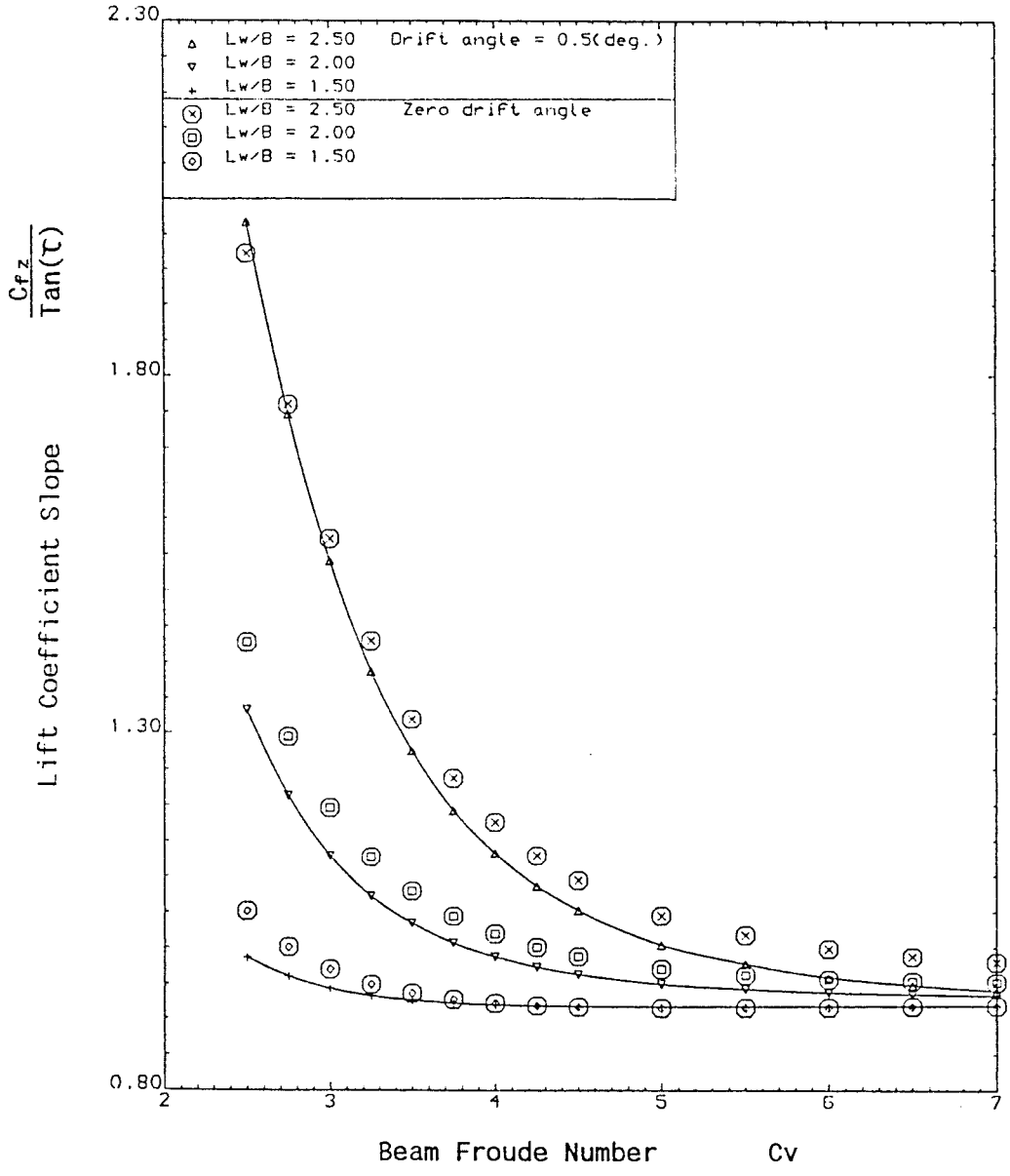

Fig.(8.13a) Computed Lift Coefficient Slopes for Drifted Rectangular Wetted Planforms

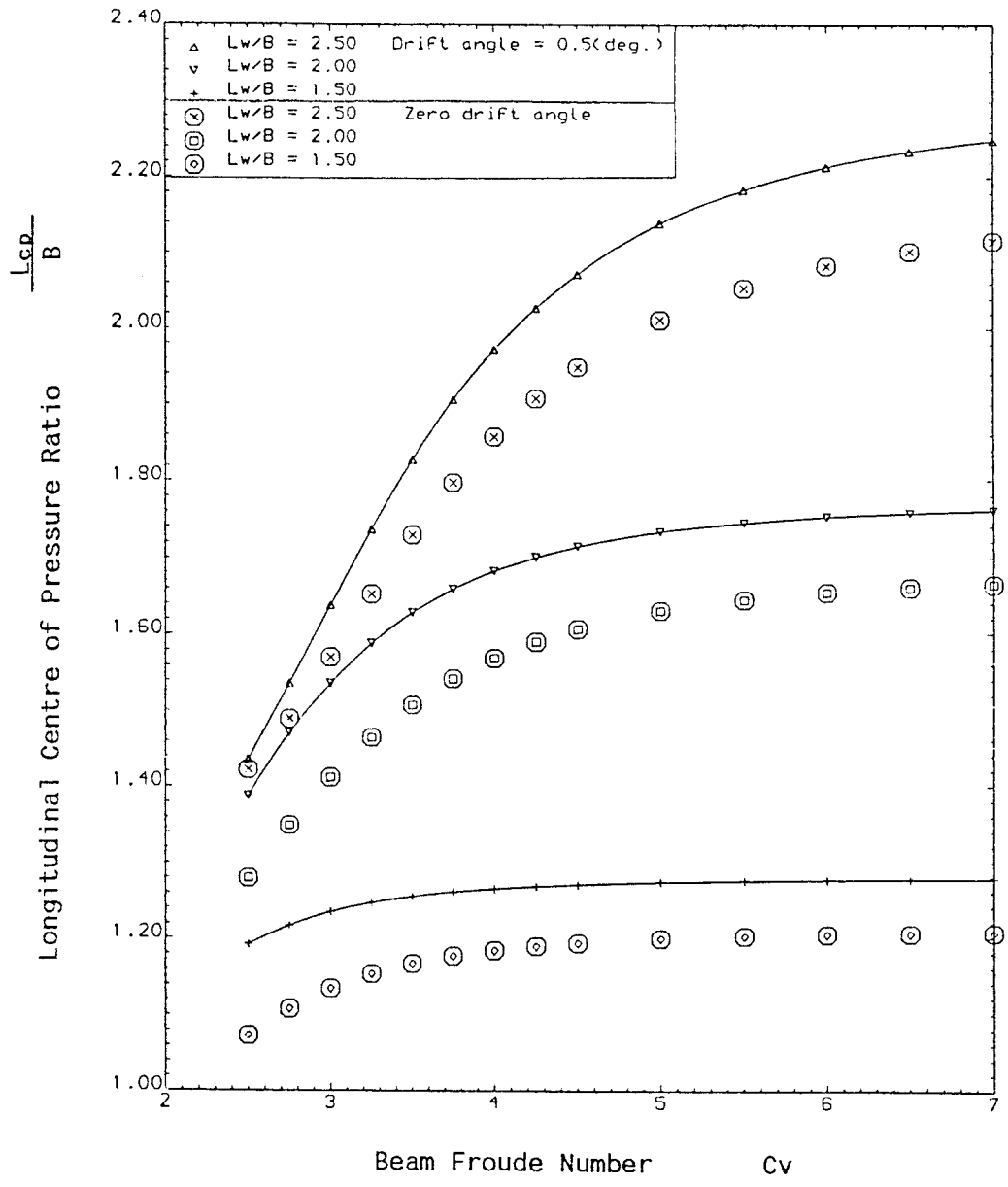

Fig.(8.13b) Computed Longitudinal Centre of Pressure Ratios for Drifted Rectangular Wetted Planforms

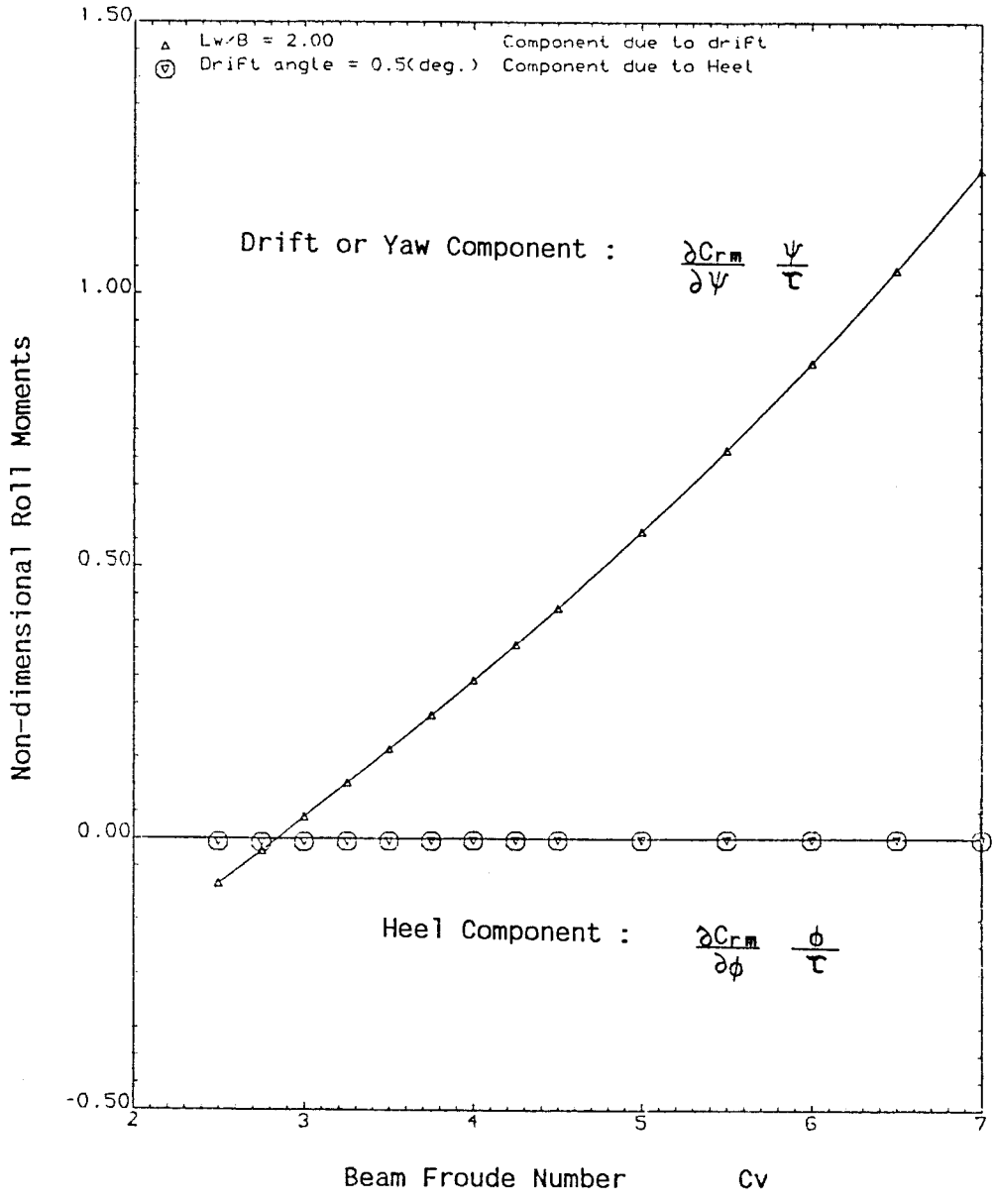

Fig.(8.13c) Computed Roll Moment Components due to Drift and due to Heel for 0.5° Drifted Rectangular Wetted Planform

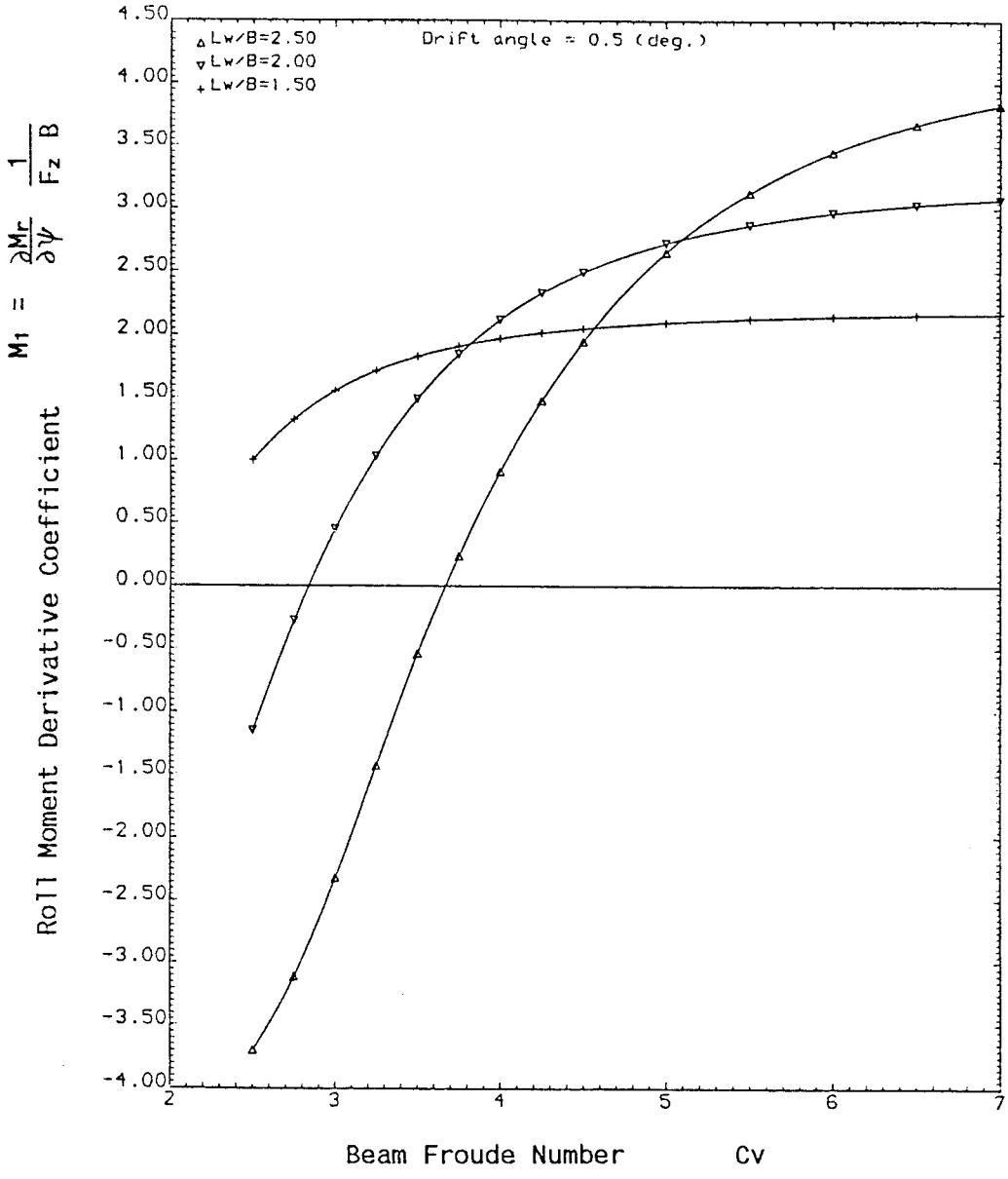

Fig.(8.13d) Computed Roll Moment Derivative Coefficients (M_1)

for Drifted Rectangular Wetted Planforms